Load-bearing capacity of imperfection-sensitive timber members under combined bending and compression

Janusch Töpler

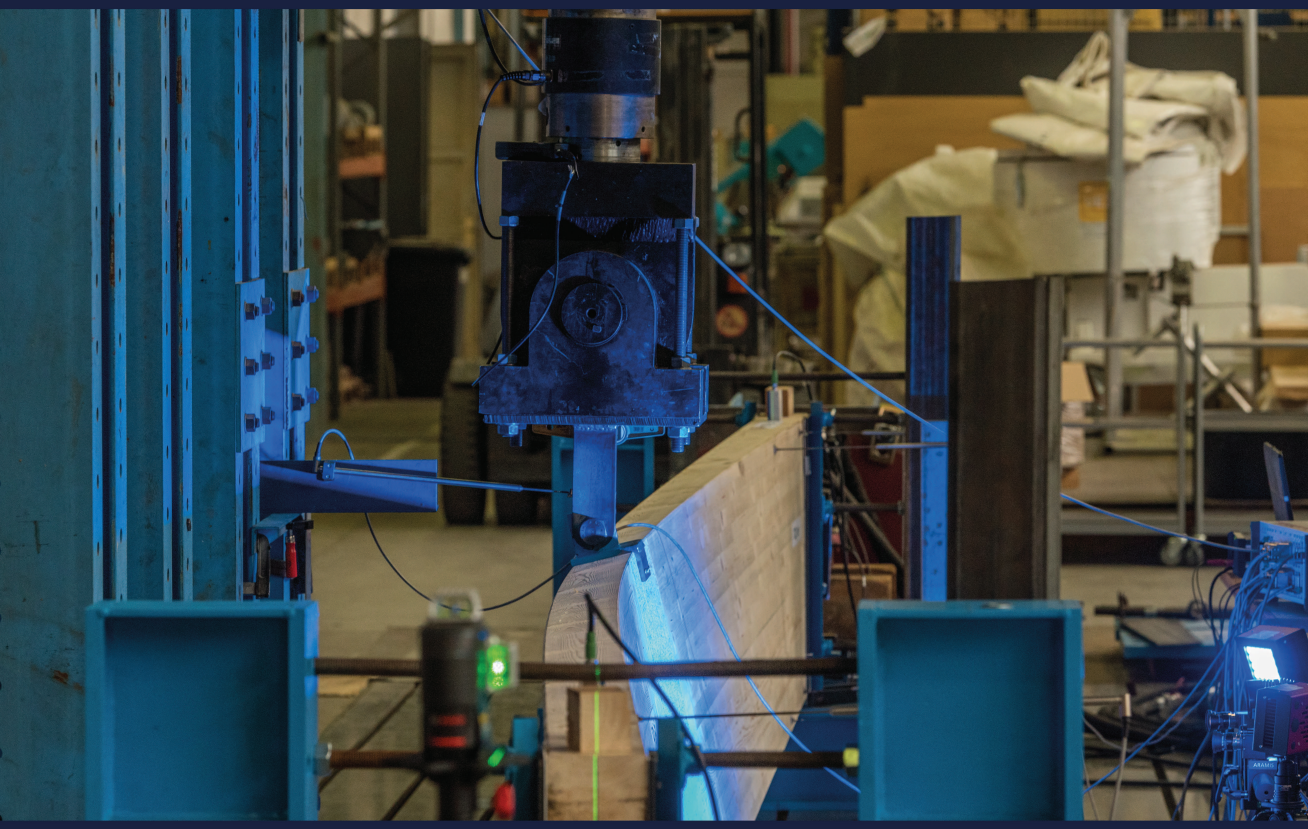

University of Stuttgart
Germany

Cuvillier Verlag Göttingen
Internationaler wissenschaftlicher Fachverlag

Load-bearing capacity of imperfection-sensitive timber members under combined bending and compression

Load-bearing capacity of imperfection-sensitive timber members under combined bending and compression

Von der Fakultät Bau- und Umweltingenieurwissenschaften der Universität Stuttgart
zur Erlangung der Würde eines Doktor-Ingenieurs (Dr.-Ing.) genehmigte Abhandlung

Vorgelegt von
Janusch Töpler
aus Düsseldorf

Hauptberichterin:	Prof. Dr.-Ing. Ulrike Kuhlmann
Mitberichter:	Prof. Dr.-Ing. habil. Jörg Schänzlin
Mitberichter:	Univ.-Prof. Dipl.-Ing. Dr.techn. Gerhard Schickhofer

Tag der mündlichen Prüfung: 11.11.2025

Institut für Konstruktion und Entwurf der Universität Stuttgart

2026

Imprint

Title of the work: Load-bearing capacity of imperfection-sensitive timber members under combined bending and compression
Author: Janusch Töpler
Cuvillier Verlag GmbH
Nonnenstieg 8
37075 Göttingen, Germany
Phone: 0049-551-547240
Website: www.cuvillier.de
E-Mail: info@cuvillier.de

Bibliographic information from the German National Library
The German National Library has listed this book in the Deutsche Nationalbibliografie (German national bibliography); detailed bibliographic information is available online at http://dnb.dnb.de.

1st edition, Göttingen. 2026
authorised dissertation: D 93, Univ. Stuttgart, Diss., 2025

ISBN 978-3-68952-468-5
eISBN 978-3-68952-469-2
ORCID 0000-0002-6015-2220
ISNI 0000000529729687

Zusammenfassung

Diese Arbeit diskutiert das Tragverhalten und die Tragfähigkeit imperfektionsempfindlicher stabförmiger Holzbauteile mit kombinierter Biegung und Druck. Dabei werden die Ergebnisse der drei Forschungsprojekte DIBt - ZP 52-5-13.194, RP 7-1 des Exzellenzclusters IntCDC und IGF No. 21285 N zusammengeführt.

Die wesentlichen Ziele waren, eine Grundlage für ein umfassendes Verständnis des Stabilitätsverhaltens stabförmiger Holzbauteile zu legen und mechanisch sinnvolle, konsistente Nachweisverfahren für das Biegedrillknicken und Biegeknicken stabförmiger Holzbauteile mit kombinierter Biegung und Druck zu formulieren. Der Schwerpunkt lag dabei auf dem Phänomen des Biegedrillknickens. Da die Stabilitätsphänomene des Biegeknickens und des Biegedrillknickens jedoch fließend ineinander übergehen und eine strikte Trennung nicht zwingend mechanisch sinnvoll ist, wurde stets auch das Stabilitätsverhalten ganzheitlich betrachtet.

Für das Verständnis der realen Stabilitätsphänomene und die Generierung von Daten wurden Imperfektionsmessungen an 242 Holzträgern und 57 Holzstützen in 23 Gebäuden, Biegeknickversuche an 27 Buchenfurnierschichtholz GL75 Stützen und Biegedrillknickversuche an 19 Brettschichtholz GL 24h Trägern durchgeführt. Durch analytische Untersuchungen wurde das Wissen um die theoretischen Hintergründe des Stabilitätsverhaltens bei Biegung und Druck erweitert. Für die detaillierte Untersuchung der Einflüsse struktureller und geometrischer Imperfektionen und kombinierter Biegung und Druck wurden numerische Modelle entwickelt. Anhand dieser wurden zudem die experimentellen Ergebnisse durch umfangreiche numerische Parameterstudien und Monte-Carlo-Simulationen erweitert.

Durch das Zusammenführen von experimentellen, analytischen und numerischen Ergebnissen konnte die nichtlineare $N_{x,c}$-$M_{y,1}$-Interaktion der k_c-k_m-Methode validiert werden und konsistente Ersatzimperfektionen für die Bemessung imperfektionsempfindlicher Holzträger und -stützen hergeleitet werden. Dabei zeigte sich, dass das Schub- und Druckplastizieren und die Querschnittsverwölbung infolge Schub einen signifikanten Einfluss auf die Tragfähigkeit (imperfektionsempfindlicher) Holzbauteile haben und in der Bemessung zu berücksichtigen sind.

Darauf aufbauend wurden Vorschläge zur Modifikation und Erweiterung der Nachweise imperfektionsempfindlicher stabförmiger Holzbauteile in FprEN 1995-1-1 [69] entwickelt, die eine zuverlässigere, konsistentere und wirtschaftlichere Bemessung ermöglichen. Teile der Vorschläge, wie die Ersatzimperfektionen und die nichtlineare $N_{x,c}$-$M_{y,1}$-Interaktion des k_c-k_m-Verfahrens, wurden bereits in FprEN 1995-1-1 [69] integriert.

In dieser Arbeit werden erstmalig das Biegeknicken und Biegedrillknicken stabförmiger Holzbauteile auf Basis umfangreicher experimenteller, analytischer und numerischer in konsistenten Berechnungs- und Bemessungsmodellen miteinander verknüpft. Dieses tiefgreifende Verständnis bildet eine fundierte Grundlage, auf der nachfolgende Forschungen, z. B. zu Satteldachträgern und anderen Aspekten, aufbauen und diese erweitern können.

Abstract

This thesis discusses the load-bearing behaviour and capacity of imperfection-sensitive timber members under combined bending and axial compression. It combines the results of three research projects: DIBt - ZP 52-5-13.194, RP 7-1 of the Cluster of Excellence IntCDC, and IGF No. 21285 N.

The main objectives were to establish the basis for a comprehensive understanding of the buckling behaviour of timber members and to formulate mechanically sound, consistent verification methods for the buckling of timber members with combined bending and axial compression. The focus was on the lateral torsional buckling phenomenon. However, as there is a fluent transition between the stability phenomena of flexural buckling and lateral torsional buckling and a separation is not necessarily mechanically reasonable, the stability phenomena were always studied holistically.

For a better understanding of the stability phenomena and generation of a database, imperfection measurements on 242 timber beams and 57 timber columns in 23 buildings, flexural buckling tests on 27 beech LVL GL75 columns, and lateral torsional buckling tests on 19 GL 24h beams were conducted. Through analytical investigations, the knowledge of the theoretical background of the stability behaviour at bending and axial compression was broadened. For the detailed study of the influences of structural and geometrical imperfections and combined bending and axial compression, numerical models were developed. Based on these, the experimental results were extended by extensive numerical parameter studies and Monte Carlo simulations.

By combining experimental, analytical, and numerical results, the nonlinear $N_{x,c}$-$M_{y,1}$-interaction of the k_c-k_m-method was validated, and consistent equivalent imperfections were derived for the design of imperfection-sensitive timber beam-columns. Additionally, the results demonstrated that the shear and compressive plasticising and the cross-sectional warping due to shear have a significant influence on the load-bearing capacity of (imperfection-sensitive) timber members and should be taken into account in the design.

On this basis, proposals were developed for a modification and extension of the verifications of imperfection-sensitive timber members in FprEN 1995-1-1 [69], which allow for a more reliable, consistent, and economical design. Parts of the proposals, such as the equivalent imperfections and the nonlinear $N_{x,c}$-$M_{y,1}$-interaction of the k_c-k_m-method, have already been incorporated into FprEN 1995-1-1 [69].

For the first time, by means of comprehensive experimental, analytical, and numerical investigations, this thesis was able to combine flexural buckling and lateral torsional buckling in consistent analysis and design models. This in-depth understanding provides a sound foundation on which subsequent research, e.g. on double-tapered beams and other aspects, can build and expand.

Acknowledgements

First of all, I would like to express my deepest gratitude to Prof. Dr.-Ing. Ulrike Kuhlmann. Her trust in me, our discussions, her high academic standards, and the many opportunities she has provided me with have been and continue to be of immense value to me, and I am extremely grateful for them.

I would also like to thank Univ.-Prof. Dipl.-Ing. Dr.techn. Gerhard Schickhofer for taking on the role of co-supervisor and the valuable comments.
Likewise, I am very grateful to Prof. Dr.-Ing. habil. Jörg Schänzlin for taking on the co-supervision. I would also like to thank him for his willingness to discuss stability behaviour at length, which occasionally extended the breaks between the timber construction lectures a bit.

The extensive experimental investigations reported in this thesis would not have been possible without the tremendous support of the Department of Building Construction and Component Testing at MPA Stuttgart and the FMPA at BTU Cottbus. Special thanks go to Prof. Dr.-Ing. Mathias Euler and the FMPA team, who hosted me very warmly in Cottbus for a month.
Many thanks also to the Institute of Photogrammetry at the University of Stuttgart and, in particular, to Lena and Edward, who carried out the laser scanning and advised on evaluating the measurements.
The test specimens were generously provided by Pollmeier Massivholz GmbH & Co. KG and Schaffitzel Holzindustrie GmbH + Co. KG. I would like to express my sincere gratitude to the following companies for the uncomplicated provision of timber buildings for the laser scanning: the Architekturbüro Rohloff & Wespel, Blättler Holzbau GmbH, Egger + Ingenieure GmbH, GMS Partner AG, GöSta Hallenbau GmbH, Haas Fertigbau GmbH, Heni Architekten, Implenia Schweiz AG, Pollmeier Massivholz GmbH & Co. KG, Schaffitzel Holzindustrie GmbH & Co. KG, Schnackenberg Holzbau GmbH, and WIEHAG GmbH (in alphabetical order).

The investigations presented in this thesis were in large parts conducted within three research projects. The research project P 52-5- 13.194-2048/19 was supervised by the Deutsches Institut für Bautechnik (DIBt) and carried out with financial support from the Federal States. The research project RP 7-1 of the Cluster of Excellence IntCDC was supported by the Deutsche Forschungsgemeinschaft (DFG, German Research Foundation) under Germany´s Excellence Strategy – EXC 2120/1 – 390831618. The IGF project no. 21285 N was supported by the German Federal Ministry for Economic Affairs and Climate Action on the basis of a decision of the German Bundestag. This support si gratefully acknowledged.

For the many background discussions, practical feedback and research ideas, I would like to thank the members of the 13 AK and, in particular, Prof. Dr.-Ing. Martin H. Kessel and the members of the committees accompanying the research projects.

My sincere thanks also go to Nico, Gabriel, Abdullah, Philip, Julian, Florijan, Keoma, Franz, and Anna (in chronological order), whose bachelor's and master's theses provided

important ideas for this work.

Special thanks also go to my former colleagues at the KE, especially the timber team Julius, Simon, and Lea, as well as Cristóbal and Philippe, with whom there was no shortage of fun in research.

I would also like to express my deepest gratitude to my former colleagues at Breinlinger Ingenieure, Hans-Martin, Thomas, René, and Frank, who taught me structural engineering and encouraged me to return to academia.

Above all, however, I must thank my friends, who always cheered me up and distracted me; my parents and my sister, who taught me the necessary curiosity, enthusiasm for discussion, and perseverance; and my partner, who has always been there for me.

Contents

Conventions and assumptions **XI**

Symbols **XIII**

Abbreviations **XVII**

1 Introduction **1**
1.1 Motivation . . . 1
1.2 Objectives . . . 2
1.3 Scope . . . 2
1.4 Methodology . . . 3
1.5 Outline and Overview . . . 3

2 State of the art **5**
2.1 General . . . 5
2.2 Geometrically nonlinear behaviour . . . 8
2.3 Materially nonlinear behaviour . . . 36
2.4 Failure behaviour and load-bearing resistance . . . 46
2.5 Long-term behaviour . . . 53
2.6 Design verification . . . 58
2.7 Models considering scattering material parameters . . . 75
2.8 Summary and discussion . . . 87

3 Measuring data **89**
3.1 General . . . 89
3.2 Imperfection measurements . . . 90
3.3 Flexural buckling tests on beech LVL columns . . . 113
3.4 Lateral torsional buckling tests on softwood GL beams . . . 125
3.5 Summary . . . 143

4 Analytical derivations and equations **145**
4.1 General . . . 145
4.2 $N_{x,c}$-$M_{y/z,1}$-interaction for flexural buckling . . . 146
4.3 $N_{x,c}$-$M_{y,1}$-interaction for lateral torsional buckling . . . 148
4.4 $N_{x,c}$-$M_{y/z,2}$-interaction . . . 150
4.5 Reduction factor k_m accounting for lateral torsional buckling . . . 153
4.6 Summary . . . 159

5 Numerical modelling and analysis **161**
5.1 General . . . 161
5.2 Finite element based design . . . 162

5.3 Modelling . . . 165
5.4 Verification . . . 180
5.5 Validation . . . 186
5.6 Numerical analysis and parameter studies . . . 194
5.7 Summary . . . 201

6 Results and discussion 203
6.1 General . . . 203
6.2 Basic aspects . . . 204
6.3 Equivalent geometrical imperfections . . . 210
6.4 $N_{x,c}$-$M_{y,1}$-interaction . . . 226
6.5 Summary . . . 244

7 Design proposals 247
7.1 General . . . 247
7.2 Design proposals . . . 248
7.3 Background regarding the design proposals . . . 260
7.4 Discussion . . . 266
7.5 Summary . . . 271

8 Summary and outlook 273
8.1 Summary . . . 273
8.2 Outlook . . . 276

References 277

A Data of flexural buckling tests on beech LVL columns 291
A.1 Flexural buckling tests . . . 291
A.2 Preceding compression tests . . . 300

B Data of lateral torsional buckling tests on glulam beams 303
B.1 Lateral torsional buckling tests . . . 303
B.2 Preceding bending and torsion tests . . . 310
B.3 Preceding compression tests . . . 311

C Reduction factor k_c accounting for flexural buckling 315

D UMAT subroutine for modelling of elastoplastic behaviour of timber 319
D.1 General . . . 319
D.2 Tension in grain direction . . . 319
D.3 Compression in grain direction . . . 319
D.4 Shear . . . 321

E Results of FEA on equivalent geometrical imperfections 323
E.1 Softwood GL beams . . . 323
E.2 Softwood GL columns . . . 329

F Results of FEA on $N_{x,c}$-$M_{y,1}$-interaction **335**
F.1 General 335
F.2 $k_{c/m}$ in dependence of $\lambda_{c/m,rel}$ 335
F.3 $N_{x,c}$-$M_{y,1}$-interaction 343
F.4 Comparison of design proposals with FEA 351

Conventions and assumptions

The coordinate system was chosen with x in the direction of the member length, y in the direction of the member width, and z in the direction of the member height.

Tension is positive and compression negative, unless otherwise specified.

Numbers are usually rounded to the nearest three digits.

The experimental results refer to engineering stresses and the numerical results refer to true stresses. For the discussed phenomena, the differences are negligible.

Symbols

Latin upper-case letters

A	cross-sectional area
A_v	shear area
B	cross-sectional width
E_0	elastic modulus in grain direction
E_{90}	elastic modulus perpendicular to the grain
F	load
F_R	load-bearing capacity
G_0	shear modulus
H	cross-sectional height
H_{pl}	height of plasticised area of the cross-section
I_x	elastic torsional moment of inertia
$I_{y/z}$	elastic moment of inertia about the y or z axis
K_φ	rotational spring stiffness
K_i	factor for determining the KAR value in the *KaReMo*
L	member length
$L_{c,ef}$	effective flexural buckling length
$L_{m,ef}$	effective LTB length
L_s	span of the structural system
$M_{y,cr}$	critical LTB moment
M_x	torsional moment about the x-axis
$M_{y/z}$	bending moment about the y- or z-axis
$M_{y,cr}$	critical bending moment for LTB
N_x	axial force
$N_{y/z,cr}$	critical axial compressive force for flexural buckling about the y- or z-axis
R^2	coefficient of determination
R	resistance
$V_{y/z}$	shear force in y- or z-direction
$W_{y/z}$	section modulus about the y- or z-axis

Latin lower-case letters

e	error term
$e_{y/z}$	bow imperfections in y- or z-direction
e_{ϕ}	sway imperfection
e_{θ}	twist imperfection
f	strength
k_c	relative flexural buckling load-bearing capacity
k_{def}	creep deformation factor
k_m	relative LTB load-bearing capacity
k_{mod}	strength modification factor for the effect of load-duration and moisture content
$k_{pl,c}$	factor for considering the material-specific stiffness reduction due to compressive plasticising
$k_{pl,m}$	factor for considering the material-specific stiffness reduction due to shear plasticising
k_{red}	factor for considering the positive size effect on the bending strength at biaxial bending
k_{shape}	factor for considering the effect of the shape of the cross-section in the shear design verification
$k_{v,xy/xz}$	adjustment factor of the shear strength
q	line load
r	distance to the pith
u, v, w	deformation in x-, y-, z-direction

Greek lower-case letters

α_c	amplification factor of the axial compressive force due to flexural buckling
α_m	amplification factor of the bending moment due to LTB
β_c	fitting factor of the k_c-method
$\beta_{m/\theta}$	fitting factors of the k_m-method
γ	shear strain
γ_{FE}	partial factor for modelling
γ_M	partial factor for material property
$\delta_{y/z}$	Dischinger-coefficient accounting for the distribution of $M_{y/z,1}$

ϵ	strain
θ	rotation or twist about the x-axis
$\lambda_{c,rel}$	relative flexural buckling slenderness ratio
λ_{ef}	slenderness ratio according to DIN EN 1995-1-1/NA [40] NCI to 9.2.5.3
$\lambda_{m,rel}$	relative LTB slenderness ratio
μ	utilisation ratio or standard deviation
$\nu_{LR/LT/RT}$	Poisson's ratios, where the first index defines the direction of the load and the second index the direction of the deformation
ρ	density
ρ_0	dry density
σ	stress or mean value
$\sigma_{m,y,cr}$	critical LTB stress
τ	shear stress
ϕ_c	intermediate parameter for the calculation of k_c
ϕ_m	intermediate parameter for the calculation of k_m

Subscripts

0, 90	in grain direction or perpendicular to the grain
05, 95	5% or 95% quantile value
1, 2	according to 1st- or 2nd-order theory, i.e. geometrically linear or nonlinear calculation
ap	apex
c, t, m, v, tor	compression, tension, bending, shear, or torsion
char, qper	characteristic or quasi-permanent combination of actions according to EN 1990 [55]
cr	critical
d, k	design or characteristic value
dyn, stat	dynamic or static value
edge, flat	edgewise or flatwise bending of lamellas
ef	effective
el, pl	elastic or plastic value
eq	equivalent

est	estimated value
exp, meas	experimentally determined or measured value
g, s, g+s	geometrical, structural, or geometrical and structural imperfections
i, j	increment
j	finger joint
l, r	left or right side of a board
lin	the beginning of the plasticising, i.e. proportionality limit
max, min	maximum or minimum value
mean	mean value
mid	midspan
mod	modified value
P, S	permanent or short term
pith	pith
pro	design proposal
R	resistance
sc	shear centre
T	tangent modulus
t=50a	at a time of 50 years
x, y, z	in case of bending or buckling, about the x-, y-, or z-axis, in other cases, in x-, y-, or z-direction
xy, xz, yz	xy-, xz-, or yz-plane

Abbreviations

COV	coefficient of variation
DOF	degree of freedom
EC5	EN 1995-1-1 [57] or FprEN 1995-1-1 [69]
FE	finite element
FEA	finite element analysis
FEM	finite element method
GL	glued laminated timber
GMNIA	geometrically and materially nonlinear analyses with imperfections
KAR	knot area ratio
KaReMo	Karlsruher Rechenmodell, see, e.g. Blaß et al. [14]
KW	calendar week
L	longitudinal
LBA	linear bifurcation analysis
LN	log-normal distribution
LTB	lateral torsional buckling
LVL	laminated veneer lumber
N	normal distribution
NS	Norway spruce
R	radial
SC	service class
SL	structural lumber
SLS	serviceability limit state
SRQ	system response quantity
T	tangential
T1O	1st-order theory
T2O	2nd-order theory
TS	technical specification
ULS	ultimate limit state

1 Introduction

1.1 Motivation

For the design of bar-shaped timber members, the stability verifications for flexural buckling and lateral torsional buckling are essential. Such members are usually loaded by a combination of axial forces and bending moments. In the design, the longitudinal stresses from axial forces and bending moments, the shear stresses from shear force and torsion, and the deformations are compared with the corresponding resistances.

The equations for stability verification of columns in EN 1995-1-1 [57] and FprEN 1995-1-1 [69] were derived on the basis of extensive experimental, analytical, and numerical investigations on softwood columns and provide reliable and economic results for their design within the safety concept of the Eurocodes. But only a limited number of studies were conducted on columns made of other European wood species or wood products, and no studies were known on the novel material beech laminated veneer lumber GL75.
For lateral torsional buckling, only a few experimental investigations were known, even fewer on full-size softwood glued laminated timber beams, and none on softwood glued laminated timber beam-columns loaded by combined axial compression and bending. The lateral torsional buckling verifications in EN 1995-1-1 [57] and FprEN 1995-1-1 [69] are therefore mainly based on investigations with analytical models, which were not sufficiently validated by full-scale lateral torsional buckling tests yet. Thus, e.g. the background of the nonlinear $N_{x,c}$-$M_{y,1}$-interaction of the k_c-k_m-method was the subject of extensive discussions in the revision of EN 1995-1-1 [57] as there were no experimental results for validation available. Furthermore, the main part of the k_m-method for lateral torsional buckling verification in EN 1995-1-1 [57] is a pure regression model that does not fully consider all relevant parameters. Finally, there were no systematic investigations of geometrical and structural imperfections of timber beams, and the imperfection assumptions of the flexural buckling and lateral torsional buckling verifications in EN 1995-1-1 [57] are inconsistent.

Given these known shortcomings of the lateral-torsional buckling verification method in EN 1995-1-1 [57] and the inconsistencies of the flexural buckling and lateral torsional buckling verification methods, it is likely that the verification methods in EN 1995-1-1 [57] provide partly uneconomical results of varying reliability.

Within three research projects, conducted at the Institute of Structural Design of the University of Stuttgart from 2019 to 2024, systematic measurements of geometrical imperfections of timber beams were carried out in the research project DIBt - ZP 52-5-13.194 [107], flexural buckling tests on beech laminated veneer lumber columns in the research project RP 7-1 of the Cluster of Excellence IntCDC [109], and lateral torsional buckling tests on softwood glued laminated timber beam-columns in the research project IGF No. 21285 N [108]. This thesis combines the results of these three research projects.

1.2 Objectives

The main objective of this thesis was to formulate mechanically sound, consistent verification methods for imperfection-sensitive timber members with combined bending and axial compression, i.e. timber beam-columns. These methods should be capable of considering all relevant effects for both softwood glued laminated timber and novel timber products, including geometrically and materially nonlinear behaviour, geometrical and structural imperfections, size effects, and long-term behaviour.
This resulted in the sub-goals: (i) to experimentally investigate the lateral-torsional buckling behaviour of softwood glued laminated timber beams with combined bending and axial compression; (ii) to experimentally investigate the flexural buckling behaviour of columns made of the novel material beech laminated veneer lumber GL75; (iii) to create a representative database of geometrical imperfections of timber beams; (iv) to develop analytical and numerical models to simulate the buckling behaviour of timber beam-columns and to validate these models with before mentioned experimental results; (v) to develop a model for investigating the scattering structural imperfections of softwood glued laminated timber beams; (vi) to carry out numerical parameter studies on the load-bearing behaviour of imperfection-sensitive timber beam-columns with combined bending and axial compression; and (vii) to evaluate the buckling verifications in FprEN 1995-1-1 [69] and to further develop them for a more reliable, consistent, and economical design of timber beam-columns.
The focus was on lateral torsional buckling. However, as there is a fluent transition between flexural buckling and lateral torsional buckling and a separation is not necessarily mechanically reasonable, the stability phenomena were always studied holistically.
The overarching objective of this thesis was to link the flexural buckling and lateral-torsional buckling of timber members on the basis of extensive experimental, analytical, and numerical calculations and thereby establish the basis for a comprehensive understanding of the buckling phenomena of timber members. To this end, the emphasis was on examining elementary cases, such as single-span beams with a constant rectangular cross-section. This in-depth understanding should provide a sound foundation on which subsequent research can build on and expand.

1.3 Scope

The investigations in this thesis cover: (i) single span bar-shaped members with a constant rectangular cross-section and fork supports; (ii) loading by axial compressive forces and uniaxial bending moments; (iii) softwood glued laminated timber and beech laminated veneer lumber GL75 according to EN 14080 [54] and ETA-14/0354 [63]; (iv) ultimate limit state verifications of stresses in grain direction; and (v) short-term and long-term load-bearing behaviour. The majority of the investigations refer to service class 1, but methods for considering the creep deformation in service classes 2 and 3 are discussed.
Concerning the influence of eigenmodes, eigenvalues, and equivalent member lengths, it is referred to the relevant literature. The verifications in the event of fire or under cyclic loading and the verifications of adjacent members such as fork supports, bracings, and connections are not discussed.

1.4 Methodology

The most important methods utilised in this work were (i) on-site measurements and laboratory experiments, (ii) the finite element method and finite element based design according to FprEN 1993-1-14 [68] and Töpler and Kuhlmann [162], and (iii) the Monte Carlo method.
The on-site measurements were performed to analyse the real geometrical imperfections of timber members in buildings and to create a database for the numerical parameter studies. The laboratory experiments were conducted to investigate which physical phenomena have a relevant influence on the load-bearing capacity of imperfection-sensitive timber beam-columns and to collect data for the validation of the prediction models.
The finite element method was applied to model the lateral torsional buckling and flexural buckling behaviour of timber beam-columns. Finite element based design embraces newly developed methodologies and design concepts that are integrated into the 2nd generation of the Eurocodes, see FprEN 1993-1-14 [68]. These enable the generation of numerical test results by means of a verified and validated finite element model and the application of these results for design.
Furthermore, analytical models can be used to describe stability phenomena, see e.g. Hörsting [90] and Section 4. As significant simplifications have to be made in analytical models, e.g. a constant bilinear plasticising over the member length and beam theory, there are significant differences between these models and the experimentally and numerically observed stability behaviour, e.g. the variable non-linear plasticising over the member length and the cross-sectional warping, see Sections 3.3.3.2, 3.4.3.2, and 6.2.1. While analytical models are useful for building practice, they were not suitable for scientifically investigating the load-bearing behaviour of imperfection-sensitive timber members in this thesis. For this reason, this thesis refrains from discussing the refined analytical model of [90] that was presented in earlier publications, see Köppel et al. [104] and Lukas et al. [120].
The Monte Carlo method was utilised to consider the influence of scattering geometrical imperfections and scattering material parameters on the load-bearing capacity of slender timber beam-columns in finite element analyses.

1.5 Outline and Overview

The structure of this thesis follows the research questions, see Section 1.2, and the methods used, see Section 1.4. The basis of the thesis is the discussion of the state of the art in Section 2, in which the main research questions are developed and the knowledge, data, models, and methods required for this thesis are compiled. The imperfection measurements, the flexural buckling tests on beech laminated veneer lumber columns, and the lateral torsional buckling tests on softwood glued laminated timber beam-columns are described in Section 3. Section 4 discusses analytical investigations on the mechanical background of the stability phenomena. The numerical models, the implementation of material models and scattering geometrical and structural imperfections, the model verification and validation, and the numerical parameter studies are presented in Section 5. An overview of the finite element based design methods in FprEN 1993-1-14 [68] and Töpler and Kuhlmann [162] is

provided in the same section. The results of the numerical parameter studies on equivalent imperfections and the $N_{x,c}$-$M_{y,1}$-interaction are given in Section 6, compared with the experimental and analytical investigations, and discussed in the context of the literature. The design model, which was developed based on these results, is presented in Section 7. The thesis closes with the conclusions and outlook in Section 8. The annexes contain the relevant measurement results and background information on the numerical models.

2 State of the art

2.1 General

Whether stability phenomena can occur for straight members depends on whether the unavoidable imperfections and deformations lead to significant additional internal forces. In the following, therefore, the terms *imperfection-sensitive members* and *non-imperfection-sensitive members* are used if all stability phenomena are addressed. The stability phenomena of bar-shaped members can be verbally subdivided into *flexural buckling*, *torsional buckling*, and *Lateral Torsional Buckling* (LTB). However, in reality, the transitions between these phenomena are fluid, and often a clear distinction is hardly possible. Since torsional buckling is not relevant for the closed cross-sections typical in timber construction, it is not discussed.

The characteristic deformation behaviour of imperfection-sensitive timber members with closed cross-section loaded by (combined) bending and axial compression, also referred to as *imperfection-sensitive timber beam-columns*, is illustrated in Figure 2.1. In addition, the corresponding internal forces $M_{x,2}$, $M_{y,2}$, and $M_{z,2}$ are specified. These internal forces are based on the equations given in Sections 2.2.1 and 2.2.2, with the associated simplifying assumptions. A distinction is made between (i) loading by axial compressive forces $N_{x,c}$, bending moments $M_{y,1}$, or $N_{x,c}$-$M_{y,1}$-interaction; (ii) bow imperfections in y- or z-direction, e_y or e_z, or twist imperfections e_θ; and (iii) cross-sections with $H \approx B$ or $H \gg B$. Cases for which no stability phenomenon occurs are greyed out. The slenderness and the load are each sufficiently high for a stability phenomenon to occur.
A basic distinction can be made between the stability behaviour of (i) members with cross-sections of similar height and width, $H \approx B$, and (ii) members with cross-sections of significantly larger height than width, $H \gg B$.
For slender cross-sections with $H \approx B$, stability behaviour can occur for $N_{x,c}$ combined with bow imperfections $e_{y/z}$ or generally for $N_{x,c}$-$M_{y,1}$-interaction. The particularity of the latter case is that the stability behaviour due to $N_{x,c}$ is caused by the deformations w_1 due to bending $M_{y,1}$, and no imperfections are necessary. Stability behaviour for approximately square cross-sections is therefore always caused by $N_{x,c}$ combined with bow imperfections or deformations. Pure $M_{y,1}$ or twist imperfections e_θ do not cause any stability behaviour.
For slender cross-sections with $H \gg B$, stability behaviour can only occur for $N_{x,c}$ combined with bow imperfections in the y-direction e_y and for $M_{y,1}$ combined with bow imperfections in the y-direction e_y or twist imperfections e_θ. Bow imperfections in the z-direction e_z or $N_{x,c}$ combined with twist imperfections e_θ do not cause any stability behaviour.
For approximately square cross-sections with $H \approx B$, there are no significant additional twists due to stability behaviour. Only additional flexural deformations v_2 and w_2 in the same plane as the imperfections and $M_{y,1}$ are caused. This case is therefore known as *flexural buckling*. For slender cross-sections with $H \gg B$ loaded by $M_{y,1}$ (and $N_{x,c}$) there are no significant deformations in the z-direction, the strong member axis, but only twists and lateral deformations in the y-direction due to stability behaviour. This case is therefore

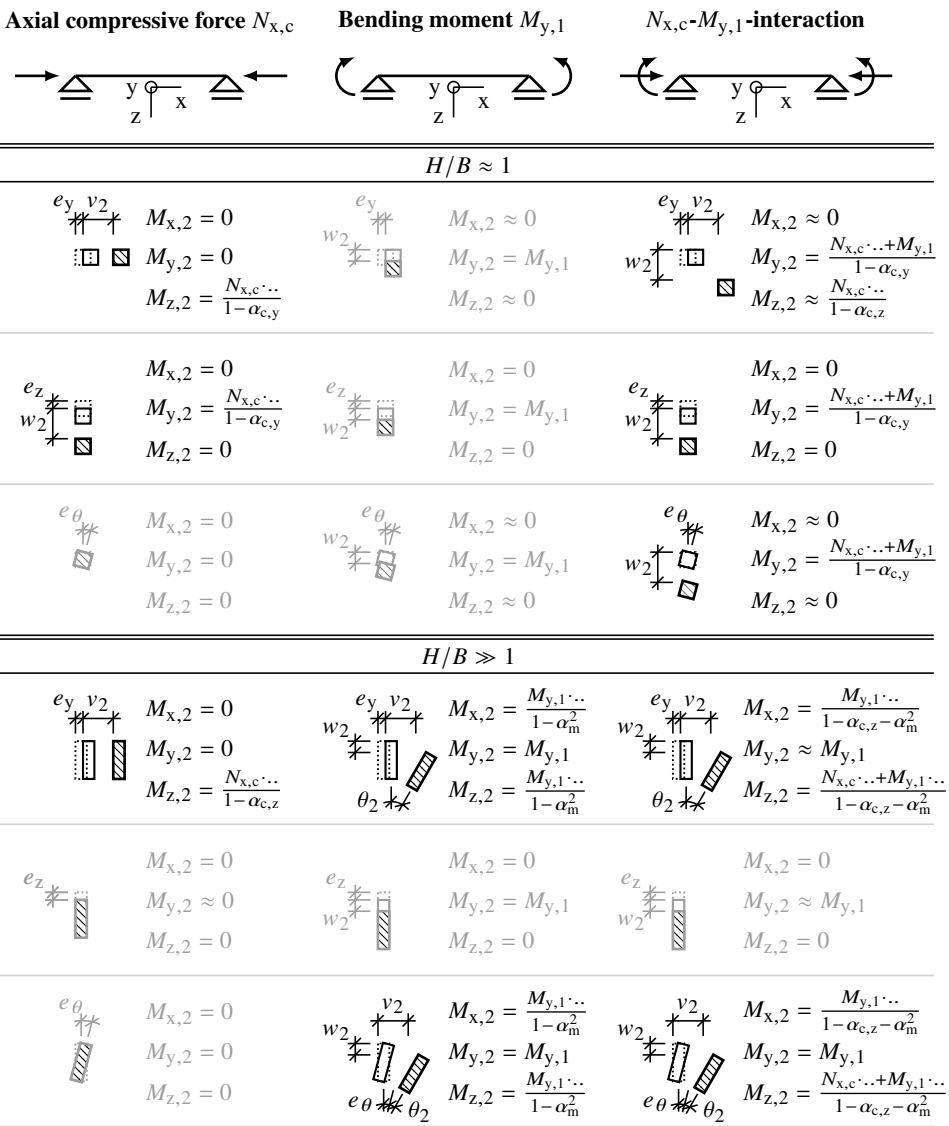

Figure 2.1: Deformation behaviour and corresponding internal forces of imperfection-sensitive timber members with closed cross-section loaded by compression and bending at midspan; top: structural systems; middle: deformation behaviour of cross-sections with $H \approx B$; bottom: deformation behaviour of cross-sections with $H \gg B$; greyed out are cases for which no stability behaviour occurs.

known as *Lateral Torsional Buckling* (LTB). For slender cross-sections with $H \gg B$, loaded only by $N_{x,c}$ and with pure bow imperfections e_y, no twist deformations occur, and the case can be categorised as flexural buckling.
The additional internal forces $M_{x,2}$, $M_{y,2}$, and $M_{z,2}$ due to stability behaviour occur analogously to the additional deformations θ_2, v_2, and w_2.
If the correct stability phenomenon is determined based on the cross-sectional slenderness, loading, and imperfections according to Figure 2.1, this will also reveal which additional deformations and internal forces should be considered in the design.

In building practice, there is practically always a combination of the three basic imperfections e_y, e_z, and e_θ due to growth-related material inhomogeneities as well as production- and assembly-related tolerances. In addition, load-eccentricities that are not planned but which are practically unavoidable, can also lead to significant additional internal forces. Thus, there is practically always a more or less pronounced combination of several of the stability phenomena illustrated in Figure 2.1. For building practice, it is therefore important to define limit criteria for which pure flexural buckling and pure LTB can be assumed and simplified design equations can be applied.

The stability behaviour of imperfection-sensitive timber beam-columns is characterised by a nonlinear increase in deformations and internal forces as the loading increases, see Figure 2.2. The load-bearing capacity of such members is governed either by a member failure due to exceeding the strength (C1), by the maximum of the load-deformation curve (C2), or by a deformation limit criterion (C3). Phenomenologically, this nonlinear stability behaviour can be subdivided into the *geometrically nonlinear load-bearing behaviour* and the *materially nonlinear load-bearing behaviour*.

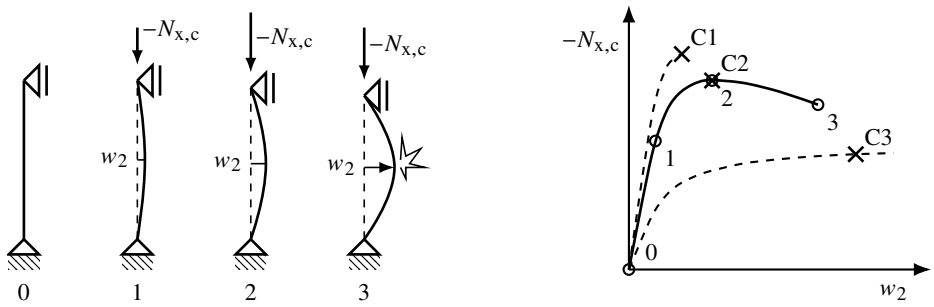

Figure 2.2: Load-deformation behaviour of a timber column with flexural buckling; the flexural buckling behaviour can be caused by geometrical imperfections, load-eccentricities, etc.; left: structural system and three stages of deformations, with 0 being the unloaded column, 1 being the moderately loaded column with a small geometrically nonlinear lateral deformation w_2, 2 being the column at maximum load with a moderate geometrically nonlinear deformation w_2, and 3 being the column at tensile failure due to a significant geometrically nonlinear deformation w_2; right: three possible load-deformation curves with the one of the column on the left as a solid line.

In Sections 2.2 and 2.3, the geometrically nonlinear behaviour and the materially nonlinear behaviour of timber beam-columns are discussed. Within geometrically nonlinear behaviour, flexural buckling and LTB are considered as special cases, and imperfections are discussed as an essential influencing parameter. Concerning the influence of eigenmodes, eigenvalues, and effective lengths, it is referred to the relevant literature. Section 2.3 about materially nonlinear behaviour examines the relevant tensile, compressive, and shear behaviour in grain direction. The failure behaviour of wood in tension, compression, and shear in grain direction is described in Section 2.4. Section 2.5 provides a brief excursus on long-term behaviour. An overview of the stability design methods for timber beam-columns in EN 1995-1-1 [57] and FprEN 1995-1-1 [69] is given in Section 2.6. Section 2.7 discusses methods for simulating scattering material properties of timber. The section closes with the summary and discussions in Section 2.8.
In most cases, the focus is on timber-related aspects, but some topics are also discussed across different materials.

2.2 Geometrically nonlinear behaviour

2.2.1 Flexural buckling

2.2.1.1 General

If the loading of imperfection-sensitive timber (beam-) columns by $N_{x,c}$ (and $M_{y,1}$) leads to significant deformations in the xy- and/or xz-plane and bending moments about the y- and/or z-axis but not twisting or torsional moments, this is referred to as *flexural buckling*, see Figures 2.1 and 2.2. Such members are subsequently referred to as *columns*. Their load-bearing behaviour is characterised by a nonlinear increase in deformations and internal forces, see Figures 2.2 and 2.3.
The experimentally determined load-deformation curve of an eccentrically loaded GL 24h column with dimensions $140 \cdot 160 \cdot 2300$ mm^3 from Frangi and Theiler [71] is presented in Figure 2.3. The x-axis displays the horizontal deformation at midspan w, and the y-axis exhibits the axial compressive force $N_{x,c}$. The behaviour was nonlinear from the beginning. After the load-bearing capacity $N_{x,c,R}$, i.e. the peak, was reached, the horizontal deformations further increased at a moderate load decrease.
The flexural buckling behaviour of timber columns is influenced by the member geometry, the structural system, the actions, the bow imperfections, the sway imperfections, and the material properties, in particular the elastic modulus, the compressive strength, the compressive plasticity, and the tensile strength in grain direction. For timber products with low shear stiffness and strength, e.g. CLT due to its rolling shear behaviour, see Narcy et al. [123], the shear strength and stiffness can influence the flexural buckling behaviour. Rautenstrauch and Becker [133] demonstrated that the influence of the shear stiffness, and therefore presumedly also the influence of the shear strength, is negligible for softwood *Glued Laminated timber* (GL) columns.

Extensive flexural buckling tests on *Structural Lumber* (SL) and GL columns made of softwood were reported in literature, e.g. earlier by Buchanan et al. [25] and Zahn [182], and

later by Frangi and Theiler [71], Lam and Oh [110], Steiger and Fontana [150], and Zahn and Rammer [185]. Ehrhart [49] carried out flexural buckling tests on beech GL columns and demonstrated that these behave similarly to softwood columns but observed higher compressive plasticising in grain direction and therefore reduced load-bearing capacities compared to softwood GL columns. No experiments on beech *Laminated Veneer Lumber* (LVL) GL75 columns were known.

In the following, the physical behaviour of flexural buckling is illustrated, and prediction models for describing the observed load-deformation behaviour are discussed.

2.2.1.2 Slenderness dependent load-bearing and failure behaviour

The experimental studies on flexural buckling by Buchanan et al. [25], Frangi and Theiler [71], Lam and Oh [110], Steiger and Fontana [150], Zahn [182], and Zahn and Rammer [185] demonstrated the decreasing load-bearing capacity of timber columns with axial compression with increasing slenderness due to flexural buckling, see Figure 2.4. This curve of the reduction in load-bearing capacity of columns due to flexural buckling plotted over the slenderness is often referred to as *buckling curve*. The slenderness increases with increasing length and decreasing cross-sectional height or width in the direction of flexural buckling, see Equation (2.11).
With increasing slenderness, the member failure mode changes, as described below according to Buchanan [24] and [71]. While the load-bearing capacity of short, stocky columns depends on the compressive strength in grain direction and compressive failure occurs, see also Section 2.4.3, stability failure occurs for long, slender columns. For the latter, the

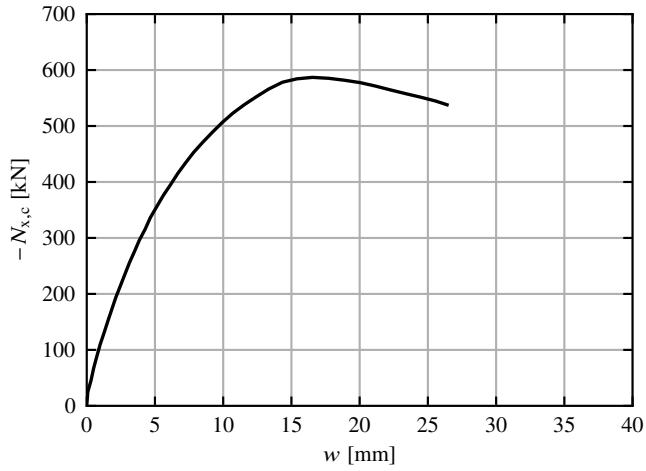

Figure 2.3: Experimentally determined flexural buckling load-deformation curve of an eccentrically loaded GL 24h column with dimensions of $140 \cdot 160 \cdot 2300$ mm^3; axial compressive force $N_{x,c}$ plotted over the horizontal deformation at midspan v; from Frangi and Theiler [71].

load-bearing capacity approaches the critical load and depends on the structural system, the column dimensions, and the elastic modulus in grain direction, or, in summary, the stiffness, see Figure 2.4. With displacement-controlled loading, the load-drop in the load-deformation curve after the peak is exceeded can be mapped, see C2 in Figure 2.2 and Figure 2.3, and columns can be loaded until material failure in tension, which causes member failure. The load drop after the peak is caused by the reduced member stiffness due to compressive plasticising in grain direction. If the load is applied force-controlled, sudden, severe deformations occur when the maximum is reached, which has given the phenomenon the name *stability failure*. This is instantaneously followed by a material failure in tension, causing member failure. For columns with medium slenderness, a transition between compressive failure and stability failure takes place, and the load-bearing capacity is influenced by both compressive strength and stiffness and, additionally, the imperfections, see Figure 2.4. The reduction of the load-bearing capacity compared to the cross-sectional resistance and the critical load, see Figure 2.4, is caused by the geometrically nonlinear behaviour and the materially nonlinear behaviour (compressive plasticising in grain direction) and hence increased internal forces, see Zahn [183] and [185].
As Zahn [183] noted, it is therefore reasonable to utilise a strength criterion for stocky members and a stability criterion for slender members in the design, given the slenderness-dependent failure mode.
In addition to the described member failure behaviour, Ehrhart [49], Frangi and Theiler [71], and Steiger and Fontana [150] reported a local compressive failure in the form of local fibre buckling, which led to a reduction in stiffness and lower load-bearing capacities but not to member failure.
There is no universal definition of where the boundaries between stocky, medium-slender, and slender columns are. In Figure 2.4, a deviation of 10% from the cross-sectional resistance and the critical load was utilised as a criterion, which is reasonable in the

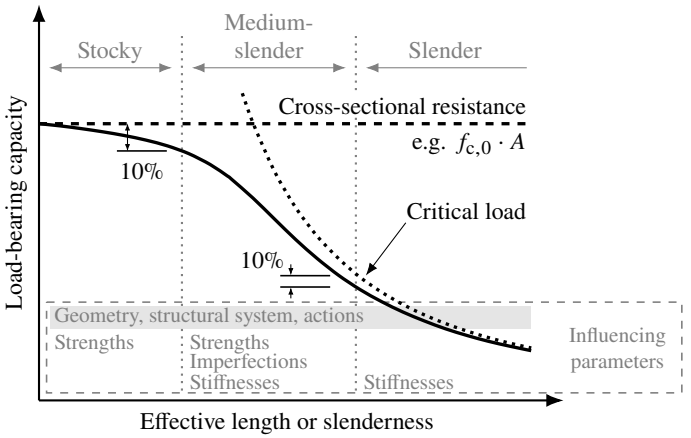

Figure 2.4: Load-bearing capacity of timber beams or columns (solid line) plotted over the effective length or slenderness; with critical load and cross-sectional resistance; illustration of slenderness ranges and associated influencing parameters.

context of structural design and employed in FprEN 1995-1-1 [69] for defining whether geometrically nonlinear behaviour has to be considered or not.

2.2.1.3 Internal forces

Figure 2.5 from Buchanan et al. [25] illustrates the internal forces $N_{x,c}$ and M_y of a column with a defined load-eccentricity or bow imperfection if $N_{x,c}$ is increased from 0 until the load-bearing capacity is reached. The bending moments from geometrically linear analysis $M_{y,1}$ (dot-dashed grey line) and the bending moments from geometrically nonlinear analysis $M_{y,2}$ (dot-dashed black line) are given. The subscript "1" denotes internal forces and deformations according to *1st-order theory* (T1O), i.e. geometrically linear calculations. The subscript "2" denotes internal forces and deformations according to *2nd-order theory* (T2O), i.e. geometrically nonlinear calculations. The increase in bending moment from $M_{y,1}$ to $M_{y,2}$ due to geometrically nonlinear behaviour is obvious. A smaller load-eccentricity or bow imperfection would result in steeper curves of the internal forces $M_{y,1}$ and $M_{y,2}$, and a larger load-eccentricity or bow imperfection would result in flatter curves.
Additionally, the $N_{x,c}$-M_y-interaction curve of the cross-sectional resistance is plotted (solid black line). Finally, the $N_{x,c}$-M_y-interaction curves of the flexural buckling resistance are displayed, which can be determined by varying the load-eccentricity or the bow imperfection (dashed lines). It is differentiated between the flexural buckling resistance if $M_{y,1}$ is evaluated (T1O, grey dashed line) and the flexural buckling resistance if $M_{y,2}$ is evaluated (T2O, black dashed line). Due to the geometrically nonlinear bending moment $M_{y,2}$, the flexural buckling resistance can be significantly smaller than the cross-sectional resistance. A cross-sectional failure would only occur before a stability failure in the case of large eccentricities or bow imperfections.
A larger length or slenderness would increase $M_{y,2}$ and would reduce the flexural buckling resistance. The flexural buckling resistance curves in Figure 2.5 would therefore get pushed down by the maximum critical axial compressive force N_{cr}.

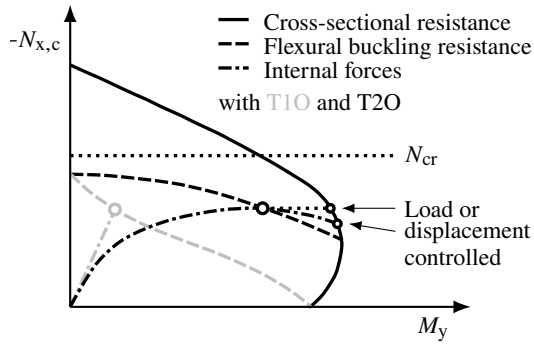

Figure 2.5: Internal forces, cross-sectional resistance, and flexural buckling resistance of a timber column with defined load-eccentricity or bow imperfection; axial compressive load $N_{x,c}$ plotted over bending moment M_y; with critical axial compressive force N_{cr}; adaptation of Buchanan et al. [25].

2.2.1.4 $N_{x,c}$-$M_{y,1}$-interaction

For stocky columns, the $N_{x,c}$-$M_{y,1}$ and the $N_{x,c}$-$M_{y,2}$-interaction curves of the load-bearing capacity are almost identical and resemble the cross-sectional resistance in Figure 2.5. The nonlinearity of the curve is caused by compressive plasticising in grain direction, see discussions in Section 2.3.3 and Blaß [8], [25], Hörsting [90], Steiger and Fontana [150], and Zahn [183]. With increasing slenderness, the plasticising (materially nonlinear behaviour) decreases as the maximum compressive stress in the cross-section decreases due to the smaller critical axial compressive force. At the same time, the geometrically nonlinear behaviour becomes more relevant. Therefore, the difference between $M_{y,1}$ and $M_{y,2}$ increases. For slender columns, the $N_{x,c}$-$M_{y,1}$-interaction curve of the load-bearing capacity is almost linear, as no plasticising occurs before reaching the peak of the load-deformation curve. The $N_{x,c}$-$M_{y,2}$-interaction curve of the load-bearing capacity is still nonlinear due to the geometrically nonlinear behaviour.

2.2.1.5 Miscellaneous

The presentation of test results by Taras [153] is also of interest. By (i) referring load-bearing capacities and slendernesses to *nominal* geometries and material values, he evaluated the safety level of design methods, and by (ii) referring to *actual* (measured or estimated mean) geometries and material values, he evaluated the accuracy of prediction models. This is visualised utilising the experimental results of Frangi and Theiler [71] for GL 24h in Figures 2.6 and 2.7.

In Figure 2.6, the relative load-bearing capacity k_c and relative flexural buckling slenderness ratio $\lambda_{c,rel}$ of the experimental results (Exp) were analysed with nominal geometries and material values according to EN 14080 [54]. The design with calculations using T2O was conducted according to Equations (2.1) to (2.3) and interaction Equation (2.54) from EN 1995-1-1 [57] with the same nominal geometry and material values, just like the critical axial compressive force N_{cr}. Figure 2.6 illustrates that all experimental results were clearly on the safe side compared to the design according to EN 1995-1-1 [57]. This is due to the underestimation of the compressive strength in grain direction $f_{c,0,k}$ of softwood GL in SC 1 in EN 14080 [54], see Schilling et al. [141]. The scattering load-bearing capacities for the individual slendernesses can be used to determine characteristic and design load-bearing capacities and to derive new design recommendations.

In Figure 2.7, the relative load-bearing capacity k_c and relative flexural buckling slenderness ratio $\lambda_{c,rel}$ of the experimental results (Exp) were analysed with measured or estimated mean values of geometry and material parameters according to [71] and Schilling et al. [141]. The design with calculations using T2O was conducted according to Equations (2.1) to (2.3) and interaction Equation (2.54) from EN 1995-1-1 [57] with the same geometry and material values, just like the critical axial compressive force N_{cr}. Figure 2.7 illustrates that T2O provides a reasonable fit to the experimental results with still some optimisation potential of this prediction model and its input values. Such a comparison can be used for validating prediction models, see Sections 5.2 and 5.5.

These two illustrations with nominal and actual values are also used in this thesis.

2.2.1.6 Prediction models

The most common models for predicting the internal forces and deformations of columns are (i) "exact" analytical models, (ii) a combination of regression models and "exact" analytical models, (iii) strain-based models, and (iv) FE models. Energy methods, as presented, e.g. by Chen and Atsuta [28], are not discussed here, as no relevant publications on these for flexural buckling of timber members were known.

2.2.1.7 Prediction models - "exact" analytical model

The basis of the discussed "exact" analytical model is the solution of the differential equations of the flexural buckling phenomenon of a hinged column, Euler buckling case 2, see, e.g. Schänzlin [137]. The quotation marks at "exact" indicate that although this is the exact solution of the system of differential equations, simplifying assumptions were made for its formulation and solution. According to Hörsting [90], these simplifying assumptions are (i) an isotropic, homogeneous, and linearly elastic material; (ii) a rectangular cross-section that is constant over the length; (iii) small deformations ($\sin\phi = \phi$ and $\cos\phi = 1$); (iv) deformations due to shear forces are negligible; (v) sinusoidal half-wave bow imperfections; (vi) actions act in the member axis; (vii) actions $N_{x,c}$ (and $M_{y/z,1}$) cause sinusoidal half-wave deformations, which implies that $M_{y/z,1}$ is a sinusoidal half-wave; (viii) the cross-sectional shape is maintained; (ix) the changes in length due to axial loading

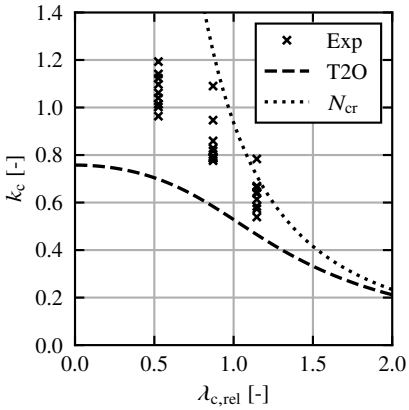

Figure 2.6: Experimentally determined relative flexural buckling load-bearing capacities k_c of GL 24h columns plotted over the relative flexural buckling slenderness ratio $\lambda_{c,rel}$; in comparison with results of T2O calculations with nominal values; k_c and $\lambda_{c,rel}$ calculated with *nominal* geometries and material values; from Frangi and Theiler [71].

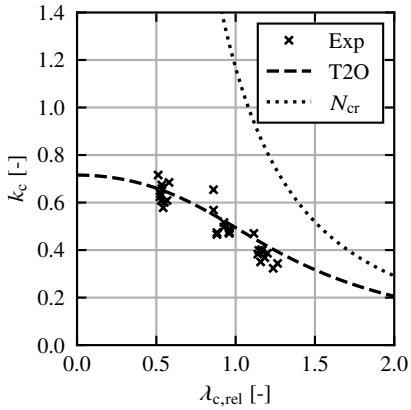

Figure 2.7: Experimentally determined relative flexural buckling load-bearing capacities k_c of GL 24h columns plotted over the relative flexural buckling slenderness ratio $\lambda_{c,rel}$; in comparison with results of T2O calculations with nominal values; k_c and $\lambda_{c,rel}$ calculated with *actual* geometries and material values; from Frangi and Theiler [71].

are negligible; (x) the direction of loads stays the same if deformations occur; and, partly, (xi) flat surfaces remain flat. This "exact" analytical model with small deformations is also known as *T2O*.

The equations given below were taken from recent timber-specific publications Hörsting [90], prEN 1995-1-1 [132], and Schänzlin [137]. The subscript "2" denotes internal forces and deformations according to T2O, geometrically nonlinear calculations. The subscript "1" denotes internal forces and deformations according to T1O, i.e. geometrically linear calculations.
The maximum bending moment about the y- or z-axis at midspan due to geometrically nonlinear behaviour can be calculated as

$$M_{\mathrm{y/z,2}} = \frac{-N_{\mathrm{x,c}} e_{\mathrm{z/y}} + M_{\mathrm{y/z,1}} \cdot (1 + \alpha_{\mathrm{c,y/z}} \delta_{\mathrm{y/z}})}{1 - \alpha_{\mathrm{c,y/z}}} \quad , \tag{2.1}$$

with

$$\alpha_{\mathrm{c,y/z}} = \frac{N_{\mathrm{x,c}}}{N_{\mathrm{y/z,cr}}} \quad , \tag{2.2}$$

$$N_{\mathrm{y/z,cr}} = -\frac{\pi^2 E_{\mathrm{0,el}} I_{\mathrm{y/z}}}{L^2_{\mathrm{c,y/z,ef}}} \quad , \tag{2.3}$$

$$I_{\mathrm{y}} = \frac{BH^3}{12} \quad , \tag{2.4}$$

$$I_{\mathrm{z}} = \frac{B^3 H}{12} \quad , \tag{2.5}$$

where $N_{\mathrm{x,c}}$ is the axial compressive force with a negative sign for compression, $e_{\mathrm{z/y}}$ is the bow imperfection in the z- or y-direction, $M_{\mathrm{y/z,1}}$ is the bending moment about the y- or z-axis according to geometrically linear calculations, $\alpha_{\mathrm{c,y/z}}$ is the amplification factor of the axial compressive force due to flexural buckling about the y- or z-axis, $\delta_{\mathrm{y/z}}$ is the Dischinger-coefficient that accounts for the distribution of $M_{\mathrm{y/z,1}}$ if it deviates from a sinusoidal half-wave, see, e.g. prEN 1995-1-1 [132], $N_{\mathrm{y/z,cr}}$ is the critical axial compressive force for flexural buckling about the y- or z-axis, $E_{\mathrm{0,el}}$ is the elastic modulus in grain direction, $I_{\mathrm{y/z}}$ is the elastic moment of inertia about the y- or z-axis, and $L_{\mathrm{c,y/z,ef}}$ is the effective flexural buckling length about the y- or z-axis according to literature, e.g. DIN EN 1995-1-1/NA [40].
The corresponding maxima of the sinusoidal half-wave deformations at midspan are

$$v_2 = \frac{\alpha_{\mathrm{c,z}} e_{\mathrm{y}} + \frac{M_{\mathrm{y,1}}}{-N_{\mathrm{z,cr}}} \cdot (1 + \alpha_{\mathrm{c,z}} \delta_{\mathrm{z}})}{1 - \alpha_{\mathrm{c,z}}} \quad , \tag{2.6}$$

$$w_2 = \frac{\alpha_{c,y} e_z + \frac{M_{z,1}}{-N_{y,cr}} \cdot (1 + \alpha_{c,y} \delta_y)}{1 - \alpha_{c,y}} \quad . \tag{2.7}$$

If considering shear deformations, the critical axial compressive force for flexural buckling can be calculated according to Engesser [61] as

$$N_{y/z,cr,v} = N_{y/z,cr} \cdot \frac{1}{1 + \frac{N_{y/z,cr}}{G_{0,el} A_s}} \quad , \tag{2.8}$$

where $G_{0,el}$ is the shear modulus in grain direction, A_v is the shear area with $A_s = A/1.2$ for rectangular cross-sections, and $N_{y/z,cr}$ according to Equation (2.3). $N_{y/z,cr,v}$ can be applied instead of $N_{y/z,cr}$ in Equations (2.1) to (2.7).
For determining the load-bearing capacities of columns, the internal forces $N_{x,c}$, $M_{y,2}$, and $M_{z,2}$ can be inserted in respective design interaction equations, e.g. Equations (2.54) and (2.55) from EN 1995-1-1 [57].

If utilising T2O with linear-elastic material behaviour, see Equation (2.1), it is not possible to reproduce the maximum and subsequent load-drop of load-deformation curves of columns observed in experiments, see Figure 2.3, as this would require a stiffness reduction by nonlinear material behaviour. Thus, if applying T2O with Equation (2.1), stability failure cannot occur before the cross-sectional resistance is reached, which does not represent reality accurately.

Advantages of the "exact" analytical model are that (i) the Equations (2.3) to (2.7) provide exact results for geometrically nonlinear internal forces and deformations under the assumptions discussed, (ii) the coupling of geometrically nonlinear behaviour due to bending moments $M_{y,1}$ and axial compressive forces $N_{x,c}$ is directly included in the equations for calculating internal forces, and (iii) the mechanical behaviour is evident from the equations. Disadvantages are that (i) no linear addition (superposition) of internal forces of different load cases is possible; (ii) structural systems deviating from the pinned column with a constant axial compressive force, Euler buckling case 2, have to be considered by modifying the effective flexural buckling length $L_{c,ef}$ and the Dischinger-coefficient $\delta_{y/z}$, which are in some cases unknown; (iii) elastic material behaviour is assumed (plasticising can be considered with the approaches described in Section 2.3.3); and (iv) reasonable equivalent geometrical imperfection assumptions are required to consider the actual geometrical and structural imperfections.

2.2.1.8 Prediction models - combined regression and analytical models

Models that combine "exact" analytical derivations with curve fitting, also referred to as fitted analytical models, are the *Ayrton-Perry approach*, also known as the *Perry–Robertson formula* or *Robertson formula*, and a similar model presented by Ylinen [179], which were discussed by Taras [153], Zahn [183], and Zahn [184]. Similar equations were presented by

Larsen and Theilgaard [113], Leicester [116], and Schänzlin [137].

The *Ayrton-Perry approach* was derived for pure axial compressive forces $N_{x,c}$ (no bending moment $M_{y,1}$), Euler buckling case 2, sinusoidal bow imperfections, $M_{y,2}$ according to T2O from Equation (2.1), and a linear interaction of compressive and bending stresses, i.e. linear elastic material behaviour, see Taras [153]. For an utilisation ratio $\mu = 1.0$ (with Equation (C.2)) the *Ayrton-Perry approach* represents the exact solution of the differential equations, see Schänzlin [137]. For $\mu \leq 1.0$, the *Ayrton-Perry approach* overestimates geometrically nonlinear behaviour and the utilisation ratio, see [137]. The derivation is discussed in Annex C. According to the *Ayrton-Perry approach*, see [137] and [153], the relative flexural buckling load-bearing capacity $k_{c,y/z}$ can be calculated by

$$k_{c,y/z} = \frac{1}{\phi_{c,y/z} + \sqrt{\phi_{c,y/z}^2 - \lambda_{c,y/z,rel}^2}} \quad , \tag{2.9}$$

with

$$\phi_{c,y/z} = 0.5 \cdot \left(1 + \beta_{c,y/z} + \lambda_{c,y/z,rel}^2\right) \quad , \tag{2.10}$$

$$\lambda_{c,y/z,rel} = \sqrt{\frac{N_{x,c,R}}{N_{y/z,cr}}} = \sqrt{\frac{f_{c,0}A}{N_{y/z,cr}}} = \frac{L_{c,y/z,ef}}{\pi \cdot \sqrt{\frac{I_{y/z}}{A}}} \cdot \sqrt{\frac{f_{c,0}}{E_{0,el}}} = \frac{\lambda_{c,y/z}}{\pi} \cdot \sqrt{\frac{f_{c,0}}{E_{0,el}}} \quad , \tag{2.11}$$

where $\phi_{c,y/z}$ is the intermediate parameter for the calculation of $k_{c,y/z}$ about the y- or z-axis, $\lambda_{c,y/z,rel}$ is the relative slenderness ratio for flexural buckling about the y- or z-axis, $\beta_{c,y/z}$ is the fitting factor for flexural buckling about the y- or z-axis, A is the cross-sectional area, $N_{x,c,R}$ is the axial compressive load-bearing capacity of the cross-section, $N_{y/z,cr}$ is the critical axial compressive force for flexural buckling about the y- or z-axis with a positive sign according to Equation (2.3), $f_{c,0}$ is the compressive strength in grain direction with a positive sign, $E_{0,el}$ is the elastic modulus in grain direction, $L_{c,y/z,ef}$ is the effective flexural buckling length about the y- or z-axis according to literature, e.g. DIN EN 1995-1-1/NA [40], $I_{y/z}$ is the elastic moment of inertia about the y- or z-axis, and $\lambda_{c,y/z}$ is the slenderness ratio for flexural buckling about the y- or z-axis.
Bending moments $M_{y,1}$, deviating critical loads and flexural buckling lengths, and sway imperfections (e.g. for cantilever columns) need to be considered additionally for a general application on column design, see [137]. The additional geometrically nonlinear internal forces due to bending moments $M_{y/z,1}$ can be considered according to Kessel et al. [100] and [137].
To include an artificial plateau of $k_{c,y/z}$, Rondal and Maquoi [134] proposed the modification of Equation (2.10) as

$$\phi_{y/z} = 0.5 \cdot (1 + \beta_{c,y/z} \cdot (\lambda_{c,y/z,rel} - \lambda_{c,y/z,rel,0}) + \lambda_{c,y/z,rel}^2) \quad , \tag{2.12}$$

where $\lambda_{c,y/z,rel,0}$ is the limit value of the artificial plateau.

Equations (2.9), (2.11), and (2.12) were included into EN 1993-1-1 [56], EN 1995-1-1 [57], and FprEN 1995-1-1 [69], where they are used for the flexural buckling design, see Sections 2.6.2.1.3 and 2.6.4.1.3.

The ratio of $E_{0,\mathrm{el}}$ to $f_{\mathrm{c},0}$ to f_{m} and the influences of geometrical and structural imperfections, plasticising, and, in steel construction, residual stresses are taken into account by means of a factor, here named $\beta_{\mathrm{c,y/z}}$, see Taras [153] and Zahn and Rammer [185]. This factor, here named $\beta_{\mathrm{c,y/z}}$, is therefore determined by curve fitting to experimental or numerical results, as demonstrated by Blaß [8] and Zahn [184]. However, according to [153], the definition of a fixed factor, here named $\beta_{\mathrm{c,y/z}}$, leads to non-constant reliability over the slenderness, since geometrical and structural imperfections, plasticising, and residual stresses do not depend on the slenderness to the same extent.
For the k_{c}-method in EN 1995-1-1 [57], see Section 2.6.2.1.3, this factor was determined on the basis of the investigations by [8] which are also briefly described in Section 2.2.1.9. In FprEN 1995-1-1 [69] Equation (2.76) for determining $\beta_{\mathrm{c,y/z}}$ is given, which can be derived from the exact solution of design with calculations using T2O by assuming linear-elastic material behaviour as demonstrated by Schänzlin [137], see also Annex C.

Taras [153] demonstrated that the *Ayrton-Perry approach* further developed by Rondal and Maquoi [134], see Equations (2.9) to (2.12), is well suited for modelling the effect of flexural buckling on the load-bearing capacity, see also Figure 2.8.

Figure 2.8 displays the comparison of the relative flexural buckling load-bearing capacities

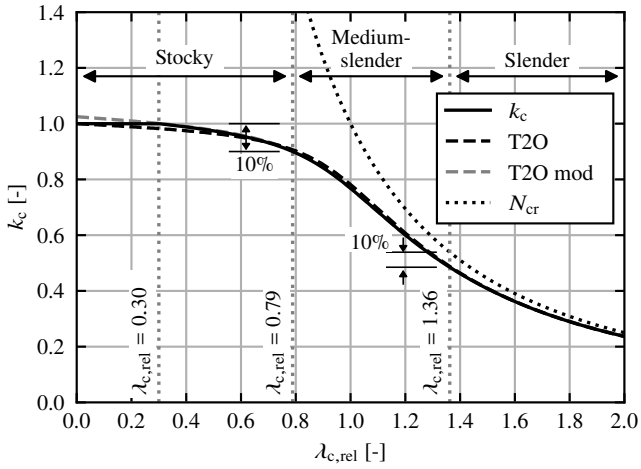

Figure 2.8: Relative flexural buckling load-bearing capacity k_{c} according to the k_{c}-method and calculations using T2O according to EN 1995-1-1 [57] plotted over the relative flexural buckling slenderness ratio $\lambda_{\mathrm{c,rel}}$; with critical axial compressive force N_{cr} according to EN 1995-1-1 [57].

determined with Equations (2.9), (2.11), and (2.12) with $\lambda_{c,y/z,rel,0} = 0.3$ according to EN 1995-1-1 [57] (k_c-method) and calculations using T20, interaction according to Equation (2.54), $M_{y,2}$ according to Equation (2.1), and $e_z = L/1000$ according to FprEN 1995-1-1 [69] for GL 24h according to EN 14080 [54] with column dimensions of $B \cdot H = 120 \cdot 120$ mm^2. In addition, calculations with T2O with $e_z = L/750$ and a modified compressive strength $f_{c,0,k,mod}$, so that $k_c(\lambda_{c,rel} = 0.3) = 1.0$ applies, are presented (T2O mod). The modification of $f_{c,0,k,mod}$ has a similar effect to the term $(\lambda_{c,y/z,rel} - \lambda_{c,y/z,rel,0})$ in Equation (2.12). Figure 2.9 displays a detail of Figure 2.8, which illustrates the influence of the term $(\lambda_{c,y/z,rel} - \lambda_{c,y/z,rel,0})$ and the modification of the compressive strength for $k_c(\lambda_{c,rel} = 0.3) = 1.0$.
Calculations with T2O with $e_z = L/750$ and $f_{c,0,k,mod}$ (T2O mod) mechanically correctly describe the flexural buckling behaviour, which can be depicted in a simplified way by T2O with $e_z = L/1000$ and $f_{c,0,k}$ (T2O) or the k_c-method with $e_z = L/1000$ and $\lambda_{c,y/z,rel,0} = 0.3$ (k_c). The background of $\lambda_{c,y/z,rel,0} = 0.3$ is discussed at Equation (2.59).

Advantages of such fitted analytical models are that (i) a linear interaction (superposition) of internal forces of different load cases is possible; (ii) plasticising can be taken into account by means of a fitting factor, here named $\beta_{c,y/z}$; (iii) the equations are supposedly easier to handle than T2O equations; and (iv) the results of the equations can be tabulated. Disadvantages are that (i) the coupling of geometrically nonlinear behaviour due to bending moments $M_{y/z,1}$ and axial compressive forces $N_{x,c}$ has to be considered in the stress interaction equation for design, which is a problematic mixing of stability and strength criteria; (ii) the geometrically nonlinear part of $M_{y/z,2}$ due to $M_{y/z,1}$, see Equation (2.1),

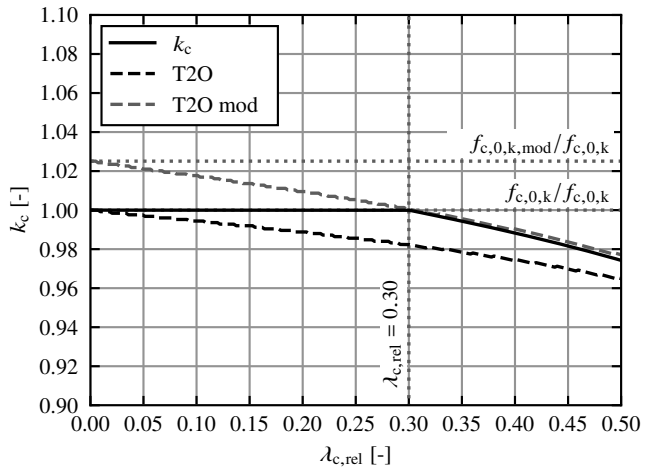

Figure 2.9: Relative flexural buckling load-bearing capacity k_c according to the k_c-method and calculations using T2O according to EN 1995-1-1 [57] plotted over the relative flexural buckling slenderness ratio $\lambda_{c,rel}$; detail of Figure 2.8.

is neglected; (iii) the actual internal forces $M_{y/z,2}$ remain unknown; (iv) the deformations remain unknown; (v) the utilisation is overestimated for utilisation ratios smaller than 1.0; (vi) the mechanical behaviour is not evident from the equations, see Equations (2.9) to (2.11); (vii) structural systems deviating from the pinned column with a constant axial compressive force, Euler buckling case 2, have to be considered by modifying the effective flexural buckling length $L_{c,ef}$ which is unknown in some cases; (viii) for cantilever columns sway imperfections have to be taken into account additionally, e.g. by modifying the effective flexural buckling length $L_{c,ef}$ according to Schänzlin [137]; and (ix) reasonable assumptions for equivalent bow imperfection are required to take account of the actual geometrical and structural bow imperfections.

2.2.1.9 Prediction models - strain-based models

Strain-based models with numerical analyses such as the one applied by Blaß [9], Theiler [154], and Ehrhart [49] are powerful tools for investigating the load-bearing capacity of timber beam-columns.

Blaß [9] utilised such a model for parameter studies on flexural buckling with scattering material parameters over the column length and height and scattering geometrical imperfections. This model contained an early version of the *Karlsruher Rechenmodell*, see Section 2.7, and accounted for a realistic nonlinear stress-strain behaviour in compression according to Glos [77]. It was therefore capable of performing numerical simulations of flexural buckling tests on softwood GL columns, resulting in realistically scattering load-bearing capacities.

Advantages of such strain-based models are that (i) under the assumptions made, they provide exact results for internal forces and deformations; (ii) the coupling of geometrically nonlinear behaviour due to bending moments $M_{y,1}$ and axial compressive forces $N_{x,c}$ is directly considered in the calculation of the internal forces; (iii) realistic materially nonlinear behaviour with a nonlinear stress-strain relationship can be taken into account; (iv) material scattering, respectively, structural imperfections, can be taken into account; (v) any geometrical imperfections can be taken into account; and (vi) any structural systems, boundary conditions, and loads can be realised. Disadvantages are that (i) an application in building practice is only possible, if such a model is already implemented in commercial software; (ii) the quality of the results is highly dependent on correct modelling and input values; and (iii) the mechanical behaviour is not evident from equations.

2.2.1.10 Prediction models - FE models

FE models are one of the most powerful tools for stability analyses and can be regarded as state-of-the-art if conducting computer-based stability analyses. They are utilised in building practice, e.g. RFEM by Dlubal [41], typically with beam and shell elements, and in research, e.g. Abaqus by Dassault Systèmes [1], with beam, shell, and solid elements.

Advantages of FE models are that (i) under the assumptions made, they provide precise results

for internal forces and deformations; (ii) the coupling of geometrically nonlinear behaviour due to bending moments $M_{y,1}$ and axial compressive forces $N_{x,c}$ is directly considered in the calculation of the internal forces; (iii) realistic materially nonlinear behaviour with nonlinear stress-strain relationships can be taken into account; (iv) material scattering, respectively, structural imperfections, can be taken into account; (v) any geometrical imperfections can be taken into account; (vi) any structural systems and loads can be realised; and (vii) they are already implemented in commercial software for the use in building practice. Disadvantages are that (i) the quality of the results is highly dependent on correct modelling and input values, and (ii) the mechanical behaviour is not evident from equations.
Although there are clear advantages if using FE models in flexural buckling investigations in timber construction, they were only rarely employed in this context. Hörsting [90] and Zahn [181] were two exceptions. This may be because the majority of flexural buckling investigations were conducted at a time when the FE method was not yet widely adopted.

2.2.1.11 Summary

It is illustrated that the flexural buckling behaviour of softwood GL columns is sufficiently well investigated and known. However, there were few studies on other European wood species and wood products, such as by Ehrhart et al. [52] on beech GL. In particular, for the novel material beech LVL GL75, see ETA-14/0354 [63], which is of particular interest for highly loaded columns in multi-story buildings, there were no experimental studies to validate and potentially calibrate the discussed prediction models.
Flexural buckling tests on beech LVL GL75 columns were thus required to check the reliability of the prediction models and the design equations in EN 1995-1-1 [57] and FprEN 1995-1-1 [69], see Section 2.6.

2.2.2 Lateral torsional buckling

2.2.2.1 General

If the loading of imperfection-sensitive timber beams (-columns) by $M_{y,1}$ (and $N_{x,c}$) leads to significant deformations in the y-direction, twists about the x-axis, bending moments about the z-axis, and torsional moments, this is referred to as *Lateral Torsional Buckling* (LTB), see Figures 2.1 and 2.10. Such members are subsequently referred to as *beams* for a loading by bending $M_{y,1}$ or *beams-columns* a loading combined by bending and axial compression. Their load-bearing behaviour is characterised by a nonlinear increase in deformations and internal forces, see Figures 2.10 and 2.11.
The experimentally determined load-deformation curve of a GL 30h beam with dimensions $100 \cdot 600 \cdot 6500\,\text{mm}^3$ and 3-point bending from Wilden et al. [176] is presented in Figure 2.11. The x-axis displays the horizontal deformation at midspan v, and the y-axis exhibits the vertical force at midspan F_z. The load-bearing behaviour was nonlinear from the beginning. After about 80% of the load-bearing capacity was reached, large horizontal deformations occurred, leading to a pronounced plateau in the load-deformation curve. Unlike columns, see Figure 2.3, usually a horizontal plateau without a pronounced peak or a significant load-drop was observed by Wilden et al. [174] and [176]. This was probably because the plasticising and, thus, the drop in stiffness are significantly smaller for beams than

for columns. For 2 of the 12 LTB tests, [176] reported an overcritical behaviour due to geometrical bow and twist imperfections opposing each other, see schematic curve with C3 in Figure 2.10. Overcritical behaviour was also reported by Lecomte [114] for LTB of two 3-pin timber arches and by Taras [153] for stocky steel sections.
The load-twist curve presented by [174] was similar to the load-horizontal deformation curve illustrated in Figure 2.11.
The LTB behaviour of timber beams (-columns) is influenced by the member geometry, the structural system, the actions, the bow imperfections, the twist imperfections, and the material properties, in particular the elastic and shear moduli, the compressive strength, the

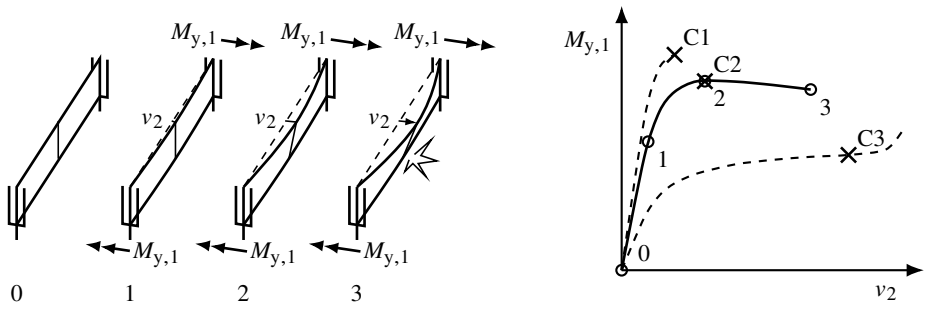

Figure 2.10: Load-deformation behaviour of a timber beam with LTB; the LTB behaviour can be caused by geometrical imperfections, load-eccentricities, etc.; left: structural system and three stages of deformations; right: three possible load-deformation curves with the one of the beam on the left as a solid line.

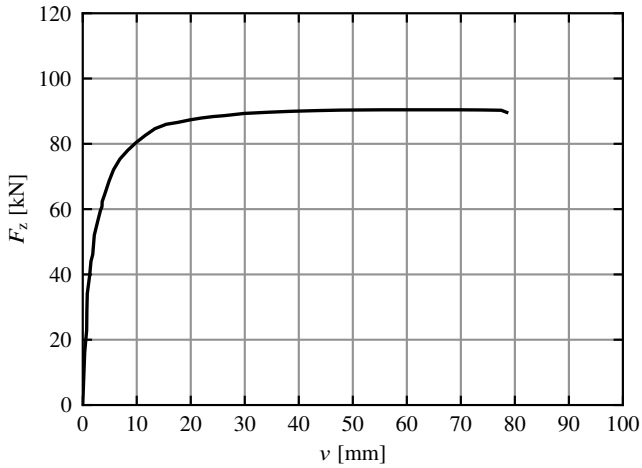

Figure 2.11: Experimentally determined LTB load-deformation curve of a GL 30h beam with dimensions $100 \cdot 600 \cdot 6500$ mm^3 at 3-point bending; vertical force at midspan F_z plotted over the horizontal deformation at midspan v; 1st loading cycle; from Wilden et al. [176].

compressive plasticity, the tensile strength, and the shear strength in grain direction.

There were very few LTB tests on full-size softwood GL beams reported in the literature: several tests on 1 beam by Brüninghoff [20], 18 tests on spruce-pine-fir GL beams by Xiao [178], and, lately, 5 tests on GL 30h and KertoS beams by Wilden et al. [174] and 12 additional tests on GL 30h by Wilden et al. [176]. And some more LTB tests on SL: 33 small-scale tests on clear Douglas Fir beams by Hooley and Madsen [89] and 39 small-scale tests on sawn redwood of structural quality by Larsen [111]. The only known LTB tests with combined bending and axial compression were the small-scale tests by [111].

In the following, the physical behaviour of LTB is illustrated, and prediction models for describing the observed load-deformation behaviour are discussed.

2.2.2.2 Slenderness dependent load-bearing and failure behaviour

The experimental studies on LTB by Brüninghoff [20], Hooley and Madsen [89], Larsen [111], Wilden et al. [174], Wilden et al. [176], and Xiao [178] and the analytical investigations, e.g. by Heimeshoff [86] and [111], demonstrated the decreasing load-bearing capacity of timber beams with uniaxial bending $M_{y,1}$ with increasing slenderness due to LTB, see Figure 2.4. The curve of the reduction in load-bearing capacity of beams due to LTB plotted over the slenderness is often referred to as *lateral torsional buckling curve*. The slenderness increases with increasing length and cross-sectional height and decreasing cross-sectional width, see also Equation (2.23).
As with columns, see Section 2.2.1, the failure mode for beams changes with increasing slenderness. Only [176] and [178] were known to have described the experimentally observed failure behaviour at LTB, so the following explanations are based partly on these sources and partly on analytical considerations. While the load-bearing capacity of short, stocky beams depends on the tensile/bending and shear strength in grain direction, see, e.g. Brandner et al. [18], see C1 in Figure 2.10, see Sections 2.4.2 and 2.4.4, stability failure occurs for long, slender beams, see C2 in Figure 2.10. For the latter, the load-bearing capacity approaches the critical load and depends on the structural system, the beam dimensions, and the elastic and shear moduli in grain direction, or, in summary, the stiffness, see Figure 2.4. With displacement-controlled loading, a possible load-drop in the load-deformation curve after a peak is exceeded can be mapped, see C2 in Figure 2.10, and beams can be loaded until material failure in tension or shear, which causes member failure. If the load is applied force-controlled, as by [178], sudden, severe deformations occur when the maximum is reached, which has given the phenomenon the name *stability failure*. This is instantaneously followed by a material failure in tension or shear, causing member failure. For beams with medium slenderness, a transition between tensile/shear failure and stability failure takes place, and the load-bearing capacity is influenced by both the tensile/shear strengths and the stiffness and, additionally, the imperfections, see Figure 2.4. The reduction of the load-bearing capacity compared to the cross-sectional resistance and the critical load, see Figure 2.4, is caused by geometrically nonlinear behaviour and materially nonlinear behaviour (compressive plasticising) and hence increased internal forces, see Heimeshoff [86].

As Zahn [183] noted, it is therefore reasonable to utilise a strength criterion for stocky members and a stability criterion for slender members in the design, given the slenderness-dependent failure mode.
If tensile failure occurred mainly due to strong axis bending, [178] observed additional compressive failure on the opposite side of the cross-section. He also observed shear failure caused by torsion, which occurred at mid-height of the beams and from midspan to the end. In 1 of the 12 LTB tests, [176] also observed shear failure due to torsion and shear force before bending failure.
There is no clear definition of where the boundaries between stocky, medium-slender, and slender are. In Figure 2.4, a deviation of 10% from the cross-sectional resistance and the critical load was utilised as a criterion, which is reasonable in the context of structural design.

2.2.2.3 Internal forces

Figures 2.12 and 2.13 illustrate the internal forces $M_{y,2}$ and $M_{z,2}$ according to T2O, see Equation (2.15), that result due to LTB if a pure bending moment $M_{y,1}$ is applied to a beam and increased and bow imperfections e_y and lengths L are varied. Additionally, the cross-sectional resistance considering the size effect on the tensile/bending strength for biaxial bending according to Buchanan et al. [25], see Equation (2.32), and the critical bending moment $M_{y,cr}$, see Equation (2.17), are displayed. The calculations were conducted for single-span beams with a concentrated force at the upper edge, mean material properties for GL 24h according to Table 5.1, initial dimensions of $120 \cdot 720 \cdot 8000$ mm^3, and initial

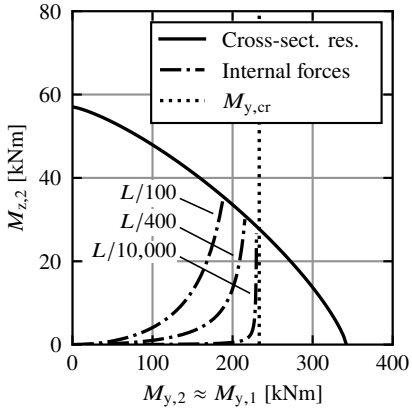

Figure 2.12: Cross-sectional resistance, internal forces according to T2O, and critical bending moments $M_{y,cr}$ of beams with *varying bow imperfections* e_y; bending moment $M_{z,2}$ plotted over the bending moment $M_{y,2}$, with $M_{y,2} \approx M_{y,1}$.

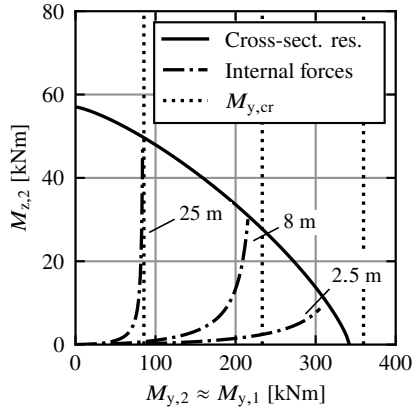

Figure 2.13: Cross-sectional resistance, internal forces according to T2O, and critical bending moments $M_{y,cr}$ of beams with *varying lengths* L; bending moment $M_{z,2}$ plotted over the bending moment $M_{y,2}$, with $M_{y,2} \approx M_{y,1}$.

bow imperfections of $e_y = L/400$ mm. The nonlinearity of the $M_{y,2}$-$M_{z,2}$-interaction curve of the cross-sectional resistance is caused by the size effect, see also Section 2.4.2. There is no notable increase of $M_{y,2}$ due to geometrically nonlinear behaviour and $M_{y,2} \approx M_{y,1}$, which is usually valid for LTB. The nonlinear increase of $M_{z,2}$ due to geometrically nonlinear behaviour is obvious. Smaller bow imperfections result in a smaller $M_{z,2}$, a more pronounced kink in the curve of the internal forces, and the critical load is approached more closely before reaching the tensile strength, see Figure 2.12. The previously described influence of the slenderness on the LTB load-bearing behaviour is illustrated by Figure 2.13. For short beams with 2.5 m, $M_{z,1/2}$ is small, $M_{y,2}$ governs the load-bearing behaviour, and the strength criterion is governing. For slender beams with 25 m, $M_{y,1/2}$ is small, $M_{z,2}$ governs the load-bearing behaviour, and the stability criterion, i.e. the critical bending moment $M_{y,cr}$, is governing.

2.2.2.4 $N_{x,c}$-$M_{y,1}$-interaction

No systematic investigations of the LTB load-bearing behaviour at combined bending and axial compression were known. There were a few experimental investigations by Larsen [111], selective analytical and numerical investigations by Leicester [117], Eggen [43], and Hörsting [90], and proposals for a revision of the design concept in DIN 1052 [38] by Brüninghoff and Klapp [21]. The following fragmented picture emerged from these investigations. For stocky beam-columns, the $N_{x,c}$-$M_{y,1}$- and the $N_{x,c}$-$M_{y,2}$-interaction curves of the load-bearing capacity are almost identical, as $M_{y,2} \approx M_{y,1}$ and $M_{z,2} \approx 0$, see Figure 2.14, and resemble the cross-sectional resistance, see Figure 2.5. Where $N_{x,c}$ is

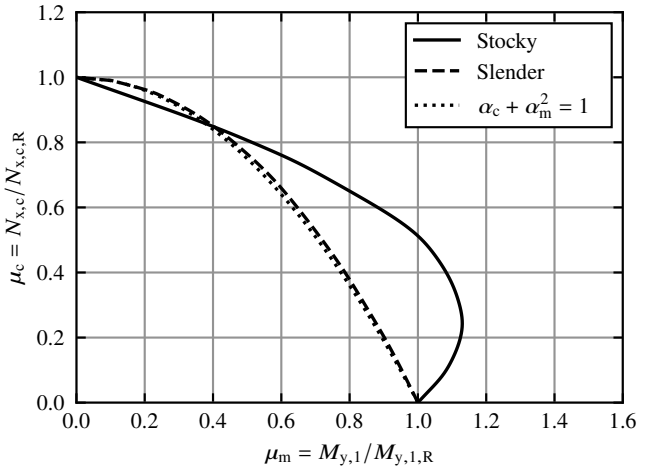

Figure 2.14: Relative compressive load-bearing capacity $\mu_c = N_{c,x}/N_{x,c,R}$ for LTB with combined bending and axial compression plotted over the relative bending load-bearing capacity $\mu_m = M_{y,1}/M_{y,1,R}$; numerical results from Hörsting [90] for stocky beam-columns made of GL 24h; numerical results from Eggen [43] for slender beam-columns made of GL 36c.

the axial compressive force, $N_{x,c,R}$ is the compressive load-bearing capacity with flexural buckling, μ_c is the relative compressive load-bearing capacity, $M_{y,1}$ is the bending moment about the y-axis according to geometrically linear calculations, $M_{y,1,R}$ is the bending load-bearing capacity with lateral torsional buckling, and μ_m is the relative bending load-bearing capacity. The nonlinearity of the curve is caused by compressive plasticising in grain direction, see discussions in Section 2.3.3. With increasing slenderness, the plasticising (materially nonlinear behaviour) decreases as the maximum compressive stress in the cross-section decreases due to the smaller critical axial compressive force. At the same time, the geometrically nonlinear behaviour becomes more relevant. For slender beam-columns, the $N_{x,c}$-$M_{y,1}$-interaction curve of the load-bearing capacity still seems to be nonlinear, but its shape has changed, see Figure 2.14. The shape seems to be similar to the critical LTB load, which is given according to Hörsting [90] by

$$\alpha_{c,z} + \alpha_m^2 = 1 \quad , \tag{2.13}$$

where $\alpha_{c,z}$ is the amplification factor of the axial compressive force due to flexural buckling about the z-axis according to Equation (2.2), and α_m is the amplification factor of the bending moment due to LTB according to Equation (2.16).
The $N_{x,c}$-$M_{y,2}$-interaction curve remains unchanged for all slendernesses and resembles the cross-sectional resistance.
The analytical derivation by Leicester [117] is discussed in more detail in Section 4.3.

2.2.2.5 Miscellaneous

Attention is drawn at this point to the presentation of the test results by Taras [153], which distinguishes between (i) load-bearing capacities and slendernesses referring to *nominal* geometries and material values for evaluating the safety level of design methods and (ii) load-bearing capacities and slendernesses referring to *actual* (measured or estimated mean) geometries and material values for evaluating the accuracy of prediction models, which is discussed in Section 2.2.1 with Figures 2.6 and 2.7.

2.2.2.6 Prediction models

The most common models for predicting the internal forces and deformations of beams are (i) "exact" analytical models, (ii) a combination of regression models and "exact" analytical models, and (iii) FE models. Energy methods, as presented, e.g. by Chen and Atsuta [29], and strain-based models are not discussed here, as no relevant publications on these for LTB of timber members were known.

2.2.2.7 Prediction models - "exact" analytical model

The basis of the "exact" analytical models is the solution of the differential equations of the LTB phenomenon of a single-span beam (-column) with a constant bending moment $M_{y,1}$ (and a constant axial compressive force $N_{x,c}$). The quotation marks at "exact" indicate that although this is the exact solution of the system of differential equations, simplifying assumptions were made for its formulation, see Section 2.2.1. This "exact" analytical model

with small deformations is also known as *T2O*.

The equations given below were taken from recent timber-specific publications: Hörsting [90], prEN 1995-1-1 [132], and Schänzlin [139]. The subscript "2" denotes internal forces and deformations according to T2O, geometrically nonlinear calculations. The subscript "1" denotes internal forces and deformations according to T1O, i.e. geometrically linear calculations.
The maximum bending moment about the y-axis at midspan due to geometrically nonlinear behaviour $M_{y,2}$ can be calculated with Equation (2.1). The maxima of the cosinusoidal half-wave torsional moment at the fork supports $M_{x,2}$ and of the sinusoidal bending moment about the z-axis at midspan due to geometrically nonlinear behaviour $M_{z,2}$ can be calculated as

$$M_{x,2} = \frac{\pi}{L_{m,ef}} \cdot \frac{M_{y,1} e_y + \alpha_m^2 G_{0,el} I_x e_\theta}{1 - \alpha_{c,z} - \alpha_m^2} \quad , \tag{2.14}$$

$$M_{z,2} = \frac{\left(-N_{x,c} + \frac{M_{y,1}^2}{G_{0,el} I_x}\right) \cdot e_y + M_{y,1} e_\theta}{1 - \alpha_{c,z} - \alpha_m^2} \quad , \tag{2.15}$$

with

$$\alpha_m = \frac{M_{y,1}}{M_{y,cr}} \quad , \tag{2.16}$$

$$M_{y,cr} = \frac{\pi}{L_{m,ef}} \cdot \sqrt{E_{0,el} I_z G_{0,el} I_x} \quad , \tag{2.17}$$

$$I_x \approx \frac{B^3 H}{12} \cdot \left(1 - 0.63 \cdot \frac{B}{H} \cdot \left(1 - \frac{B^4}{12H}\right)\right) \quad , \tag{2.18}$$

where $L_{m,ef}$ is the effective LTB length according to literature, e.g. FprEN 1995-1-1 [69], $M_{y,1}$ is the bending moment about the y-axis according to geometrically linear calculations, e_y is the bow imperfection in y-direction, α_m is the amplification factor of the bending moment due to LTB, $G_{0,el}$ is the shear modulus in grain direction, I_x is the elastic torsional moment of inertia according to Equation (2.18), e_θ is the twist imperfection, $\alpha_{c,z}$ is the amplification factor of the axial compressive force due to flexural buckling about the z-axis, $N_{x,c}$ is the axial compressive force with a negative sign for compression, $M_{y,cr}$ is the critical bending moment for LTB, $E_{0,el}$ is the elastic modulus in grain direction, and I_z is the elastic moment of inertia about the z-axis according to Equation (2.5).
The corresponding maxima of the sinusoidal half-wave twists and horizontal deformation at

midspan are

$$\theta_2 = \frac{\frac{M_{y,1}}{G_{0,el} I_x} \cdot e_y + \alpha_m^2 e_\theta}{1 - \alpha_{c,z} - \alpha_m^2} \quad , \tag{2.19}$$

$$v_2 = \frac{(\alpha_{c,z} + \alpha_m^2) \cdot e_y + \alpha_m \cdot \frac{G_{0,el} I_x}{M_{y,cr}} \cdot e_\theta}{1 - \alpha_{c,z} - \alpha_m^2} \quad , \tag{2.20}$$

where $N_{z,cr}$ is the critical axial compressive force for flexural buckling about the z-axis according to Equation (2.3).
For Equations (2.14) to (2.20), $N_{z,cr}$ and $M_{y,cr}$ are the critical loads of the same eigenmode coupled by Equation (2.13) with the same effective length $L_{c,z,ef} = L_{m,ef}$.
For determining the load-bearing capacities of beams, the internal forces $N_{x,c}$, $M_{x,2}$, $M_{y,2}$, $M_{z,2}$ and the shear forces V_y and V_z can be inserted in the respective design equations, e.g. from EN 1995-1-1 [57].

If utilising T2O with linear-elastic material behaviour, see Equations (2.1), (2.14), and (2.15), it is not possible to reproduce the maximum and subsequent load-drop of load-deformation curves of beams sometimes observed in experiments, see Figure 2.10 and Wilden et al. [176], as this would require a stiffness reduction by nonlinear material behaviour. Thus, if applying T2O with Equations (2.1), (2.14), and (2.15), stability failure cannot occur before the cross-sectional resistance is reached, which does not represent reality accurately.

Advantages and disadvantages of the "exact" analytical model are analogous to the discussions in Section 2.2.1.7.

2.2.2.8 Prediction models - combined regression and analytical models

Three models that combine exact analytical derivations with curve fitting, also referred to as fitted analytical models, are discussed in the following.

Leicester [116], Leicester [118], and Taras [153] demonstrated that the cubic form of the LTB resistance equation derived with Equation (2.15), see, e.g. Heimeshoff [86], can be simplified to a quadratic form by assuming imperfections e_y and e_θ affine to the 1st eigenmode. This enables a mechanically sound derivation of the reduction factor k_m accounting for LTB. The same approach was adopted by Wilden et al. [175]. The resulting equations are given below. The derivation is discussed in Section 4.5, as it was extended for this thesis by considering the size effect on the tensile strength due to biaxial bending with k_{red} and formulated with bow imperfections e_y instead of the up to now common formulation with twist imperfections e_θ. According to [116], [118], [153], and [175], the

relative LTB load-bearing capacity k_m can be calculated by

$$k_\mathrm{m} = \frac{1}{\phi_\mathrm{m} + \sqrt{\phi_\mathrm{m}^2 - \lambda_\mathrm{m,rel}^2}} \quad , \tag{2.21}$$

with

$$\phi_\mathrm{m} = 0.5 \cdot \left(1 + \beta_\mathrm{m} + \lambda_\mathrm{m,rel}^2\right) \quad , \tag{2.22}$$

$$\lambda_\mathrm{m,rel} = \sqrt{\frac{f_\mathrm{m} W_\mathrm{y}}{M_\mathrm{y,cr}}} = \sqrt{\frac{M_\mathrm{y,R}}{M_\mathrm{y,cr}}} \quad , \tag{2.23}$$

$$\beta_\mathrm{m} = e_\theta \cdot \frac{H}{B} \quad , \tag{2.24}$$

where ϕ_m is the intermediate parameter for the calculation of k_m, $\lambda_\mathrm{m,rel}$ is the relative slenderness ratio for LTB, β_m is the fitting factor for LTB, f_m is the bending strength, W_y is the section modulus about the y-axis, $M_\mathrm{y,R}$ is the bending load-bearing capacity of the cross-section about the y-axis, and $M_\mathrm{y,cr}$ is the critical bending moment for LTB according to Equation (2.17).
Same as for columns, see Section 2.2.1, the height-to-width ratio and the influence of geometrical and structural imperfections, plasticising, and, in steel construction, residual stresses is taken into account by means of a factor, here β_m, see [153]. Although Equation (2.24) gives a decomposition of β_m, the factor has to be determined by curve fitting with experimental or numerical results to cover all of these effects and not only the imperfections. However, according to [153], the definition of a fixed factor leads to non-constant reliability over the slenderness as geometrical and structural imperfections, plasticising, and residual stresses do not depend on the slenderness to the same extent.
Equations (2.21) to (2.24) are the exact solution of the differential equations for LTB for single-span beams with a constant rectangular cross-section, constant bending moment $M_\mathrm{y,1}$, bow and twist imperfections affine to the 1st eigenmode, and linear elastic material behaviour, see also the derivation in Section 4.5. For considering the relevant effects of cross-sectional dimensions, geometrical and structural imperfections, plasticising, and, in steel construction, residual stresses, a factor, here named β_m, is determined by curve fitting. This model is therefore a combination of regression and analytical models.

The fitted analytical model, which is currently implemented in EN 1995-1-1 [57], i.e. the *k_m-method*, see also Section 2.6.2.1.4, was discussed by Heimeshoff [86]. It was probably derived by curve fitting to the load-bearing capacities determined with calculations using T20 and a linear stress interaction for $M_\mathrm{y,2}$ and $M_\mathrm{z,2}$ according to

$$\frac{M_\mathrm{y,2}}{W_\mathrm{y} f_\mathrm{m}} + \frac{M_\mathrm{z,2}}{W_\mathrm{z} f_\mathrm{m}} = 1 \quad . \tag{2.25}$$

Heimeshoff [86] conducted such investigations with interaction according to Equation (2.25), $M_{y,2} = M_{y,1}$, $M_{z,2}$ according to Equation (2.15), H/B ratios of 4 and 10, $E_{0,el}/G_{0,el} = 22$, and bow imperfections of $e_y = L/288$ and $L/577$.
Figure 2.15 displays the comparison of the relative LTB load-bearing capacities determined with the k_m-method from EN 1995-1-1 [57], see Equations (2.61) to (2.63) and calculations using T20, interaction according to Equation (2.25), $M_{y,2} = M_{y,1}$, $M_{z,2}$ according to Equation (2.15), and $e_y = L/400$ according to EN 1995-1-1 [57]. For GL 24h according to EN 14080 [54] with column dimensions of $B \cdot H = 100 \cdot 1000$ mm^2. The k_m-method splits the LTB curve into three segments, where (i) for $\lambda_{m,rel} \leq 0.75$ the effects of LTB can be neglected, i.e. $k_m = 1.0$; (ii) for $0.75 < \lambda_{m,rel} \leq 1.40$ the effects of LTB are accounted for by a regression line, i.e. $k_m = 1.56 - 0.75\lambda_{m,rel}$; and (iii) for $1.40 < \lambda_{m,rel}$ the LTB load-bearing capacity is equal to the relative critical bending moment, i.e. $k_m = 1/\lambda^2_{m,rel} = M_{y,cr}/W_y f_m$. Schänzlin [139] demonstrated in a parameter study that the deviations between this fitted model of the k_m-method and design with calculations using T2O are small, see also Figure 2.15.

Brüninghoff and Klapp [22] proposed a LTB design with Equations (2.26) to (2.28), which consider the coupling of geometrically nonlinear behaviour due to bending moments $M_{y,1}$ and axial compressive forces $N_{x,c}$ more realistically.

$$\frac{\sigma_{c,0,d}}{f_{c,0,d}} + \frac{\sigma_{m,y,d}}{k_{c,m} f_{m,d}} = 1 \quad , \tag{2.26}$$

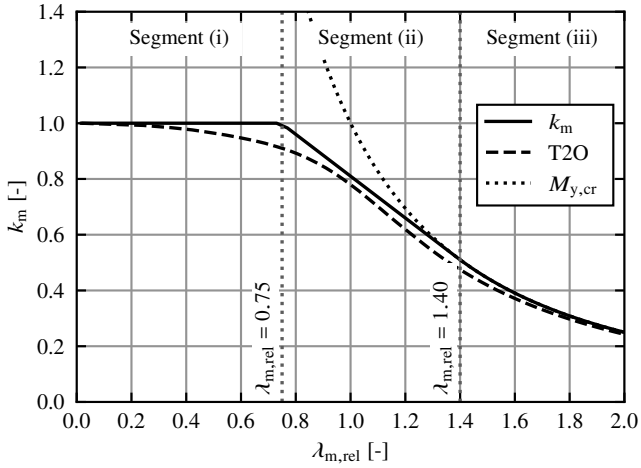

Figure 2.15: Relative LTB load-bearing capacity k_m according to the k_m-method and calculations using T2O according to EN 1995-1-1 [57] plotted over the relative LTB slenderness ratio $\lambda_{m,rel}$; with critical bending moment $M_{y,cr}$ according to EN 1995-1-1 [57].

with

$$k_{c,m} = k_m \cdot \sqrt{1 - \left(\frac{\sigma_{c,0,d}}{k_{c,z} f_{c,0,d}}\right)^n} \quad , \tag{2.27}$$

$$n = \max\begin{cases} 3.25 - 2.5\lambda_{m,rel} \\ 1 \end{cases} \quad . \tag{2.28}$$

where $\sigma_{c,0,d}$ is the design axial compressive stress, $f_{c,0,d}$ is the design compressive strength in grain direction, $\sigma_{m,y,d}$ is the design bending stress about the y-axis, $k_{c,m}$ is the reduction factor accounting for flexural buckling and LTB, $f_{m,d}$ is the design bending strength, k_m is the reduction factor accounting for LTB, $k_{c,z}$ is the reduction factor accounting for flexural buckling, n is a fitting factor, and $\lambda_{m,rel}$ is the relative slenderness ratio for LTB. These equations were derived by curve fitting to the results of calculations using T2O. The underlying nonlinearity of the $N_{x,c}$-$M_{y,1}$-interaction for LTB was supported by the results of numerical analyses by Eggen [43].

If comparing the fitted analytical model by Leicester [116], Leicester [118], and Taras [153], see Equations (2.21) to (2.24), with the k_m-method in EN 1995-1-1 [57], the k_m-method in EN 1995-1-1 [57] represents a further simplification that does not fully account for the actual influence of the H/B ratio, material properties, and imperfections. However, the differences are small in the context of expected design accuracies, see Schänzlin [139].

Advantages and disadvantages of both fitted analytical models are analogous to the discussions in Section 2.2.1.8.

2.2.2.9 Prediction models - FE models

The discussion of FE models in Section 2.2.1.10 also applies to LTB. FEA were applied much more frequently in research for investigating LTB of beams than for flexural buckling of columns, e.g. by Eggen [43], Hörsting [90], Schulte [142], Wilden et al. [174], and Xiao [178].

2.2.2.10 Summary

There were few LTB tests reported on in the literature, e.g. by Hooley and Madsen [89] and Larsen [111]. Even fewer reports on LTB tests on full-size softwood GL beams were known, only one by Brüninghoff [20], 3 by Wilden et al. [174], 12 by Wilden et al. [176], and 18 by Xiao [178]. No LTB tests on softwood GL beam-columns loaded by combined bending and axial compression or on beams made of new materials like beech LVL GL75, see ETA-14/0354 [63], were known at all. In addition, only [176] and [178] briefly discussed experimentally observed failure behaviour. Many parameters that are relevant for the LTB design of softwood GL beams (-columns), such as the influence of slenderness on the load-bearing capacity and the failure behaviour, and the influence of axial compressive loads on the LTB resistance, are assumed purely based on analytical investigations.

Many assumptions for LTB design could therefore not be validated with experimental results of full-size GL beams up to now, which was urgently required to check the reliability of prediction models and the design equations in EN 1995-1-1 [57] and FprEN 1995-1-1 [69], see Section 2.6.

2.2.3 Imperfections

2.2.3.1 General

Imperfections in structural engineering are unplanned deviations of the actual geometry, position, loading, and boundary conditions of a structure from the ideally planned structure, as well as material scatter. These are practically unavoidable and result in additional deformations and internal forces. Unplanned deviations of the actual geometry and position of structures are called *geometrical imperfections*, and the effects of material scattering are called *structural imperfections*. Imperfections that cover the influence of geometrical and/or structural imperfections in the design are called *equivalent geometrical imperfections* covering the effects of geometrical and/or structural imperfections.
In this thesis, only the geometrical and structural imperfections of single members are discussed.

2.2.3.2 Geometrical imperfections

Geometrical imperfections can be deviations of the length, width, and height of a member from the ideally planned geometry, whereby the latter can vary over the member length. In addition, three types of pre-deformations can occur, bow imperfections $e_{y/z}$, twist imperfections e_θ, and sway imperfections e_ϕ, see Figure 2.16. If the actual position of the member axis between two supports deviates from the ideally planned position in the y- or z-direction, this is referred to as *bow imperfection*. Pre-twists of a cross-section about the x-axis over the length are called *twist imperfections*. If a member is subjected to a rigid body rotation, this is referred to as *sway imperfections*.
Geometrical imperfections can change over time due to the viscoplastic behaviour of wood, i.e. creep, shrinkage, and swelling.

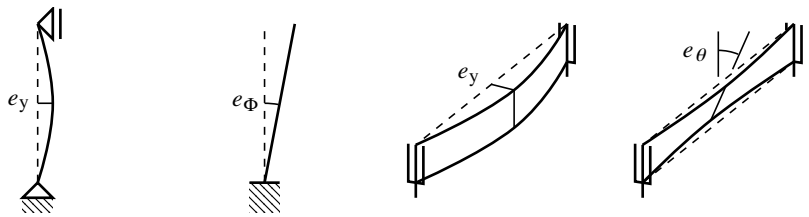

Figure 2.16: Different types of geometrical imperfections of timber beams and columns.

For the deviations of the cross-sectional dimensions of GL columns, Ehlbeck and Blaß [44] determined a mean value, standard deviation, and 5% quantile value of 1.0029, 0.00766, and 0.9894. Schulte [142] found similar values. EN 14080 [54] specifies a permissible deviation of 2 mm in width and max(1%, 4 mm) in height, which corresponds to the 5% quantile value of [44] for a dimension of 200 mm. For this 5% quantile value, the differences between the ideally planned and actual elastic moments of inertia and section modulus are 3.15% and 2.11%, respectively. As beams usually have a significantly larger height, the influence is usually even smaller.
For the member length, the deviations measured by [44] were less than 0.05%. The mean value of the deviation determined by [142] was surprisingly high with 0.1%. EN 14080 [54] specifies a maximum deviation in length of GL members for standard dimensions of min(0.1%, 20 mm). For 0.1%, this results in a deviation of the critical axial compressive force of 0.12% and of the critical bending moment of 0.10%, see Equations (2.3) and (2.17). The influence of the deviation of the member dimensions on the member load-bearing capacity of timber beam-columns can therefore usually be neglected.

Bow imperfections influence the deformations and internal forces of medium-slender timber columns, see Equation (2.1). Bow imperfections and twist imperfections influence the deformations and internal forces of medium-slender timber beams, see Equations (2.14) and (2.15). Sway imperfections influence the load-bearing capacity of clamped columns and of structural systems comprising more than one member.
Measurements of bow, twist, and sway imperfections of timber members were known by Brüninghoff [20], Dietsch and Henke [34], Ehlbeck and Blaß [44], Kessel [96], Kessel et al. [98], Kessel and Mertinaschk [99], Larsen [111], Pawlowski et al. [127], Schulte [142], Wilden et al. [174], and Wilden et al. [176]. Not discussed here are: [96], [98], and [99] as they deal with nail plate trusses; [111] because only small SL specimens were investigated; [127] because it deals with monitoring; and [142] because the measurements on GL beams were conducted directly after production and do not include the governing effects of assembly.
Brüninghoff [20] surveyed 13 softwood GL beams of one roof structure spanning each 21.7 m and coupled to two roof bracings directly after assembly and alignment. The mean, maximum, and minimum values of the horizontal bow imperfections at midspan were $L/780$, $L/660$, and $L/900$. No twist imperfections were observed.
Dietsch and Henke [34] surveyed one softwood GL beam in each of seven buildings that were directly connected to the roof bracing. The measurements were carried out with a laser scanner on existing buildings of more recent construction dates. The mean, maximum, and minimum values of the maximum horizontal bow imperfection of the beam axes were $L/1720$, $L/530$, and $L/5750$. Additionally, they observed the difference of the bow imperfection of the upper to the lower edge of the beams, which yielded the twist imperfections with mean, maximum, and minimum values of 0.0035 rad, 0.0094 rad, and 0.0008 rad.
Ehlbeck and Blaß [44] systematically measured the geometrical imperfections of timber columns in 13 buildings. Both loaded and unloaded timber columns in existing buildings of different construction dates were examined, whereby the influence of loading and long-term behaviour was neglected in the evaluation on the safe side, as it could not be determined.

The sway imperfections, bow imperfections, and wood moisture content of 142 softwood SL and 176 softwood GL columns were documented. The mean and 95% quantile values of the sway imperfections of the softwood GL columns were $1/490$ rad and $1/190$ rad. The bow imperfections were determined as the amplitude of a sinusoidal half-wave using nonlinear regression and the least squares method for fitting to the measured y- and z-coordinates at the quarter points of the columns. The mean and 95% quantile values of the bow imperfections of softwood GL columns were $L/2820$ and $L/1140$. The frequency distributions of the measured imperfections could be fitted well by normal distributions with a mean of 0. The determined distribution functions of the bow imperfections were used as input values for parameter studies with scattering geometrical imperfections and material properties, i.e. structural imperfections, stiffnesses, and strengths. Based on the results, the β_c value of the k_c-method in DIN 1052 [38] and later EN 1995-1-1 [57] was calibrated, see also Sections 2.2.1 and 2.6.2.
Wilden et al. [174] and Wilden et al. [176] measured the bow and twist imperfections of 17 softwood GL test specimens before the LTB tests with a tachymeter. The bow imperfections were bow-shaped and usually smaller $L/1000$, with one beam having $L/850$. The twist imperfections could not be assigned to a specific shape and were smaller than $1^\circ \mathrel{\hat{=}} 0.017$ rad.

Lindner and Giezelt [119] carried out imperfection measurements on 266 steel columns in eight buildings to determine the sway imperfections of columns. Based on the measured values, equivalent geometrical imperfections were determined, taking into account residual stresses and plasticising. The measurements resulted in a 95% quantile value of the geometric sway imperfection of about $1/400$ rad, which can be used for elastic design. By increasing this value to $1/200$ rad, the influence of residual stresses and plasticising can be taken into account. So it was differentiated between values for design with elastic or plastic cross-sectional resistance. These values were adopted in EN 1993-1-1 [56]. The sway imperfections of columns, which are assembly-related, were harmonised for different materials in the Eurocodes, and similar values can be found in EN 1995-1-1 [57] and FprEN 1995-1-1 [69].

Ballio and Mazzolani [6], Ersvik and Alpsten [62], and Schulz [143] demonstrated that the influence of the amplitude of bow imperfections far outweighs the influence of its shape. Furthermore, according to Kessel [97] and [143], an idealised sinusoidal half-wave is sufficient to represent the real, arbitrary shape of a bow imperfection if determining the flexural buckling load-bearing capacity.

Kessel [97] pointed out that if modelling geometrical imperfections, the shape of the applied imperfections does not have to comply with the boundary conditions. e.g. the sway of a cantilever column or the twist at the supports of a beam with fork-bearings actually violate the boundary conditions but have to be considered nonetheless. He further stated that it is only reasonable to relate the imperfections to the effective length L_{ef} if L_{ef} is smaller than the member length L, as in the case of laterally braced beams. Imperfections should therefore refer to $L_{imp} = \min(L, L_{ef})$.

Taras [153] proposed to define the imperfections depending on the slenderness, not the

length, as this is advantageous for the calibration of the fitting factor in design models similar to the *Ayrton-Perry approach*, e.g. the k_c-method in EN 1995-1-1 [57], see Equations (2.10) and (2.22).

2.2.3.3 Structural imperfections

Structural imperfections in the context of this thesis are the scattering of the material properties of timber over the member length, width, and height that lead to a deviation of the actual from the ideal shear centre. Therefore, all material scattering in a member that influences the stiffness and thus the stress-strain relationship in grain direction is of relevance. The LTB behaviour of beams is mainly influenced by the scattering of material properties in the y-direction, and the flexural buckling behaviour of columns is mainly influenced by the scattering of material properties in the z-direction, see Sections 2.2.1 and 2.2.2. A detailed overview of material scattering and how it can be modelled is given in Section 2.7.

The only known measurements of structural imperfections of timber members were carried out by Theiler [154]. He determined the position of the shear centre z_{sc} of columns with four lamellas by measuring the dynamic elastic modulus of the individual lamellas and calculating the resulting eccentricity of the shear centre by

$$z_{sc} = \frac{\sum_{i=1}^{n} E_{0,dyn,i} t_i y_i}{\sum_{i=1}^{n} E_{0,dyn,i} t_i} \quad , \tag{2.29}$$

where $E_{0,dyn,i}$ is the dynamic elastic modulus of the i^{th} lamella in grain direction, t_i is the thickness of the i^{th} lamella, and y_i is the y-coordinate of the centre of the i^{th} lamella. Of 50 columns, the maxima of z_{sc} was 8.3 mm, which was about 5% of the cross-sectional height, see also Figure 2.39.

Taras [153] reported that in steel construction, structural imperfections from residual stresses are independent of the length, in contrast to geometric imperfections.

Blaß [9] developed and applied a model for taking into account the structural imperfections of imperfection-sensitive softwood GL columns. It was a combination of a strain-based model, see Section 2.2.1, and a model for simulating scattering material parameters. The latter was an early version of the *Karlsruher Rechenmodell*, see Section 2.7. Scattering material parameters were simulated over the lamella length, i.e. in the x-direction, and between different lamellas, in the z-direction. The variation of material properties in the z-direction, i.e. between different lamellas, is most relevant for the flexural buckling of columns. The results of Blaß [9] were utilised to calibrate the fitting factor β_c of the k_c-method. An explicit decomposition of the influence of structural imperfections was not carried out. Theiler [154] conducted similar analyses with a similar model.

It is generally assumed that, due to the lamination effect of large GL beams, the influence of geometrical imperfections far outweighs the influence of structural imperfections on the LTB load-bearing capacity. However, no investigations were known to validate this

assumption. In general, no models were known that could be used to take into account structural imperfections across the lamella width, i.e. in y-direction, that are relevant for LTB of beams.

2.2.3.4 Summary

A sufficiently large database of measured geometrical imperfections only existed for softwood columns. These data were included in the derivation of the k_c-method in EN 1995-1-1 [57]. For softwood GL beams and beam-columns made of new materials such as beech LVL GL75, see ETA-14/0354 [63], there were no reliable data on geometrical imperfections. The situation was similar with regard to structural imperfections. While models such as the *Karlsruher Rechenmodell* can be applied to take into account the scattering of material properties within a member in z-direction, which is relevant for flexural buckling, there was no model known that can take into account the scattering across the lamella width, i.e. in y-direction, which is relevant for LTB.
In order to conduct a meaningful investigation of LTB, it was necessary to create a database of geometrical imperfections of softwood GL beams by means of measurements and to develop a model to simulate the scattering material behaviour across the lamella width.

2.3 Materially nonlinear behaviour

2.3.1 General

The material behaviour of wood is distinctly anisotropic in terms of elastic, plastic, and failure behaviour. For mechanical analyses at the member level, a transversely isotropic material behaviour is usually assumed for GL by distinguishing longitudinal and transverse to the grain direction. For LVL, an orthotropic material behaviour is usually assumed by distinguishing longitudinal, radial (flatwise), and tangential (edgewise) directions. Additionally, it needs to be differentiated between the tensile and compressive behaviour in the two or three material directions. Furthermore, the shear behaviour also depends on the loading plane. For softwood GL and beech LVL, the differences between the elastic moduli in tension and compression are negligible according to Glos [78], Niemz and Sonderegger [125], and Töpler and Kuhlmann [161]. However, the plastic and failure behaviour differs significantly for tension and compression.

Typical stress distributions that are relevant for the design of imperfection-sensitive timber members with a rectangular cross-section and combined axial compression and bending are displayed in Figure 2.17. These are (i) longitudinal stresses σ_x from bending $M_{y/z}$ and axial compressive forces $N_{x,c}$ and (ii) longitudinal shear stresses τ from shear forces V_z and torsion M_x. Stresses perpendicular to the grain are not addressed in this thesis. The description of the tensile and compressive behaviour includes the bending behaviour in grain direction, which is not discussed separately.

The following section addresses the influence of nonlinear material behaviour in tension, compression, and shear in grain direction on the load-deformation behaviour of imperfection-sensitive timber members. The associated failure behaviours and strengths are discussed in Section 2.4.

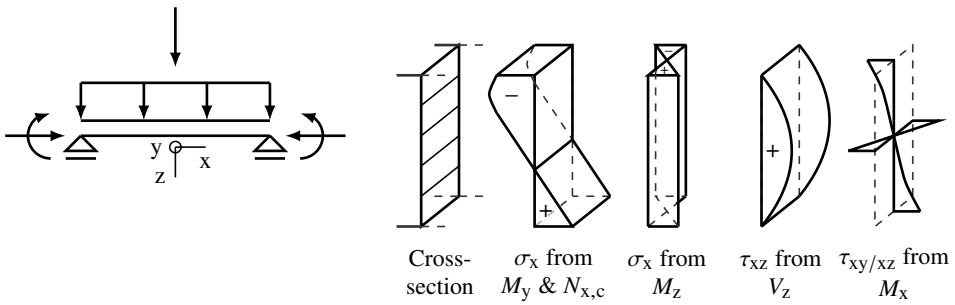

Figure 2.17: Left: structural system discussed in this thesis; right: typical stress distributions relevant for the design of imperfection-sensitive timber members with a rectangular cross-section and combined axial compression and bending.

2.3.2 Tension in grain direction

The typical load-deformation behaviour of timber members with tensile loading in grain direction with cross-sectional dimensions commonly used in timber construction is displayed in Figure 2.18. The load F is plotted over the deformations u. This behaviour is linearly elastic. According to Frese [73], local failure can lead to slightly nonlinear behaviour and, according to Dietsch et al. [33], to a load drop shortly before component failure. Thus, the load-deformation curve can exhibit minor nonlinearities with saw-tooth shape around the maximum load, see Figure 2.18. The failure is a complex interaction of tensile and shear failure at the fibre level and around material defects, e.g. knots, see Bodig and Jayne [16]. If defining stress-strain curves for tension in grain direction for building-practice-orientated investigations, saw-tooth behaviour can be neglected and linear-elastic behaviour can be assumed until failure, see [78].
Thus, there is no influence of a nonlinear tension behaviour in grain direction on the $N_{x,c}$-$M_{z,2}$-interaction relationship of the cross-sectional resistance, which is mostly linear, except for the influence of the size effect, see Section 2.4.2, as demonstrated by Steiger and Fontana [150].

2.3.3 Compression in grain direction

2.3.3.1 General

The typical stress-strain behaviour of timber members with compressive load in grain direction with cross-sectional dimensions commonly used in timber construction is displayed in Figure 2.19. The stresses in grain direction σ_0 are plotted over the strains in grain direction ϵ_0. The following descriptions are based on Bodig and Jayne [16] and Grosse [83]. Up to the linearity limit $f_{c,0,lin}$, also known as the *proportional limit*, the behaviour is linearly elastic. Above the proportionality limit, buckling of cellulose

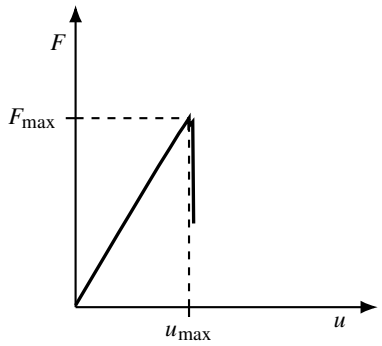

Figure 2.18: Typical load-deformation curve of softwood for tension in grain direction with the load F plotted of the deformation u; data from Dietsch et al. [33].

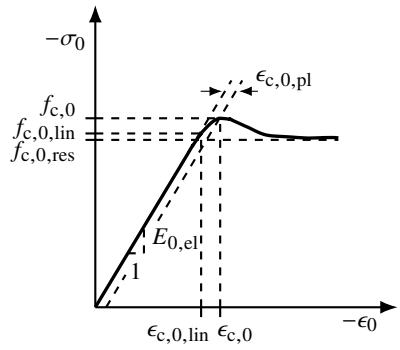

Figure 2.19: Typical stress-strain curve of softwood for compression in grain direction with the stress in grain direction σ_0 plotted over the strain in grain direction ϵ_0; data from Glos [77].

fibrils occurs, and the resulting microscopic kink bands cause plastic deformations, which lead to nonlinear behaviour and flattening of the stress-strain curve. The appearance of kink bands causes the curve to peak and thus defines the compressive strength $f_{c,0}$. This is followed by ductile behaviour with a varying degree of load drop to a residual strength.

Since only the elastic modulus and the compressive strength are usually evaluated in experimental investigations, only very little data on the nonlinear characteristics of the stress-strain relationship are available, despite a large number of publications on compression tests, e.g. by Dill-Langer and Aicher [35], Ehrhart et al. [53], Frese et al. [75], and Glos [78]. Experiments on small, defect-free wood specimens are not discussed here, since defects significantly influence the mechanical behaviour of timber members with compression in grain direction with cross-sectional dimensions commonly used in timber construction.
For the proportionality limit $f_{c,0,lin}$, Grosse [83] reported experimentally determined values of about 70% of the compressive strength of softwood, and Ehrhart [49] reported values of about 85% of the compressive strength for beech GL. In extensive tests on softwood, [78] determined the plastic strain at which the compressive strength is reached $\epsilon_{c,0,pl}$ to be 25% of the elastic strain $\epsilon_{c,0,el} = f_{c,0}/E_0$ and [49] for beech GL at $\epsilon_{c,0,pl} = 0.25$ to $0.45\,\epsilon_{c,0,el}$. For the residual strength, [78] and [83] determined values of about 85% of the compressive strength for softwood. Published values for beech LVL GL75 were not known.

The nonlinear material behaviour with compression in grain direction, also referred to as *compressive plasticising*, leads to a nonlinear stress distribution across the cross-section if the proportionality limit is exceeded, see Figure 2.17. Furthermore, plastic strains occur, which reduce the stiffness in grain direction E_0.
Due to the plastic stress redistribution within the cross-section, the maximum tensile stress in grain direction $\sigma_{t,0}$ relevant for the design can no longer be determined utilising the linear interaction relationship

$$\sigma_{t,0} = \frac{N_{x,c}}{A} + \frac{M_{y,2}}{W_y} + \frac{M_{y,2}}{W_z} \quad , \tag{2.30}$$

where $N_{x,c}$ is the axial compressive force, A is the cross-sectional area, $M_{y/z,2}$ is the bending moment about the y- or z-axis according to geometrically nonlinear calculations, and $W_{y/z}$ is the section modulus about the y- or z-axis.
The modification of the linear interaction in Equation (2.30) to represent the influence of the nonlinear material behaviour in grain direction was the subject of extensive investigations, which are discussed in Sections 2.3.3.2 and 2.3.3.3.
The reduction of the elastic modulus increases $M_{x,2}$, $M_{y,2}$, and $M_{z,2}$, see, e.g. Equations (2.1), (2.14), and (2.15). This is discussed in Section 2.3.3.4.

2.3.3.2 Influence on the load-bearing capacity at $N_{x,c}$-$M_{y/z,2}$-interaction

Blaß [9], Buchanan et al. [25], Hörsting [90], Steiger and Fontana [150], and Zahn [183] demonstrated that the influence of plasticising on the load-bearing capacity depends on the slenderness of the beam-columns, as described below.

Figures 2.20 and 2.21 illustrate the 5% quantile, mean, and 95% quantile values of the load-bearing capacities for flexural buckling of stocky and slender beam-columns with varying eccentricity of the axial compressive force determined experimentally and with the strength model by Buchanan et al. [25]. Each circle represents the result of a large number of experiments.

For stocky beam-columns, plasticising at $N_{x,c}$-$M_{y/z,2}$-interaction leads to a favourable stress distribution with a large compressive stress block, see Figure 2.17, but a reduced internal lever arm. This results in a favourable nonlinear interaction curve of the load-bearing capacity at combined axial compression and bending, see Figure 2.20. The curve of the 5% quantile values of the load-bearing capacity at $N_{x,c}$-$M_{y/z,1/2}$-interaction is more nonlinear than the one of the mean and 95% quantile values, as the ratio of $f_m/f_{c,0}$ is the lowest. This is due to the higher scattering of f_m than $f_{c,0}$. The higher ratio of $f_m/f_{c,0}$ at the level of the 95% quantile values means that already significant plasticising occurs at pure uniaxial bending. Therefore, a smaller beneficial effect due to stress-redistribution can be utilised with increasing compressive force at 95% quantile level than at the 5% quantile level, and the nonlinearity of the curve is less pronounced. There is no need to differentiate between the bending moments according to linear and geometrically nonlinear calculations $M_{y/z,1}$ and $M_{y/z,2}$ in Figure 2.20, as no significant geometrically nonlinear behaviour occurs and the linear and $M_{y/z,1} \approx M_{y/z,2}$.

With increasing slenderness, the stability failure governs, see Figures 2.4 and 2.5, the critical load decreases and the geometrically nonlinear component of $M_{y/z,2}$ increases, see Equations (2.1) and (2.15). The beam-columns can resist lower axial compressive forces,

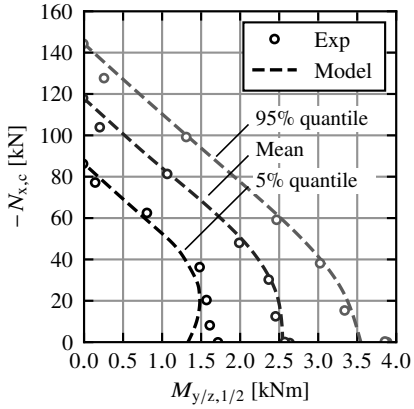

Figure 2.20: Experimentally determined 5% quantile, mean, and 95% quantile values of the $N_{x,c}$-$M_{y/z,1/2}$ load-bearing capacity of eccentrically loaded *stocky* timber columns with flexural buckling; in comparison with results of calculations with a strength model; from Buchanan et al. [25].

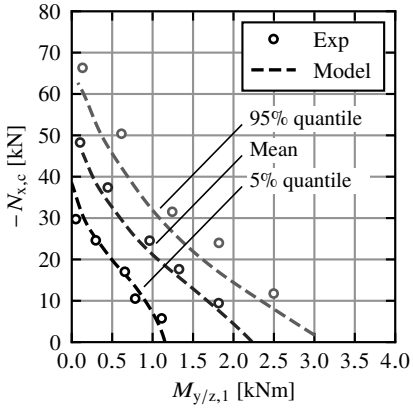

Figure 2.21: Experimentally determined 5% quantile, mean, and 95% quantile values of the $N_{x,c}$-$M_{y/z,1}$ load-bearing capacity of eccentrically loaded *slender* timber columns with flexural buckling; in comparison with results of calculations with a strength model; from Buchanan et al. [25].

and consequently less plasticising occurs.
For very slender beam-columns, plasticising only occurs after the stability failure. There is a significant geometrically nonlinear behaviour and it has to be differentiated between the bending moments according to linear and geometrically nonlinear calculations $M_{y/z,1}$ and $M_{y/z,2}$. While the nonlinear $N_{x,c}$-$M_{y/z,2}$-interaction presented in Figure 2.20 still applies to the load-bearing capacity for geometrically nonlinear internal forces, the $N_{x,c}$-$M_{y/z,1}$-interaction curve of the load-bearing capacity at flexural buckling is approximately linear, see Figure 2.21. The $N_{x,c}$-$M_{y/z,1}$-interaction curve of the load-bearing capacity at LTB is nonlinear, see Figure 2.14.
For flexural buckling, the influence of the slenderness and the difference of the $N_{x,c}$-$M_{y/z}$-interaction between linearly and nonlinearly determined bending moments is illustrated by Figures 2.22 and 2.23. These graphs were derived by [25] with their strength model.

Zahn [183] proposed to consider the positive influence of plasticising on the load-bearing capacity at $N_{x,c}$-$M_{y/z,2}$-interaction by the exponent 2 at the compressive force component in the interaction equation, as this was a good approximation to the experimental results of him and Buchanan et al. [25]. A similar proposal was made by Blaß [8]. This resulted in the following design equation

$$\left(\frac{N_{c,x}}{N_{x,c,R}}\right)^2 + \frac{M_{y,2}}{M_{y,R}} + \frac{M_{z,2}}{M_{z,R}} \leq 1 \quad , \tag{2.31}$$

where $N_{c,x}$ is the axial compressive force, $N_{x,c,R} = A f_{c,0}$ is the axial compressive load-

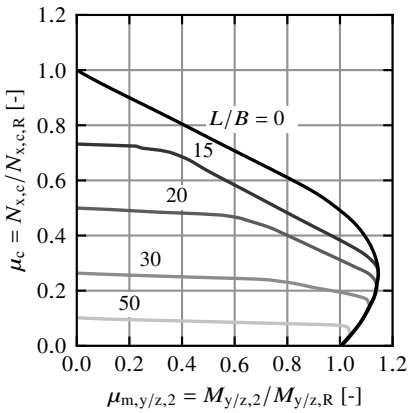

Figure 2.22: Relative load-bearing capacities for $N_{x,c}$-$M_{y/z,2}$-interaction of timber beam-columns with flexural buckling determined with a strength model; with varying slendernesses; from Buchanan et al. [25].

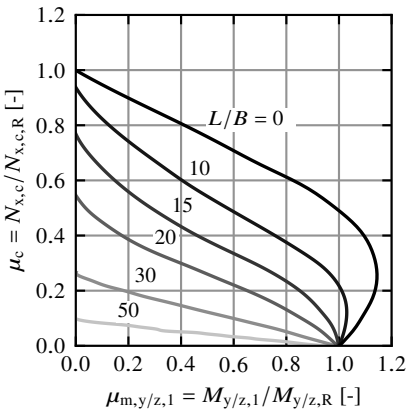

Figure 2.23: Relative load-bearing capacities for $N_{x,c}$-$M_{y/z,1}$-interaction of timber beam-columns with flexural buckling determined with a strength model; with varying slendernesses; from Buchanan et al. [25].

bearing capacity of the cross-section, $M_{y/z,2}$ is the bending moment about the y- or z-axis according to geometrically nonlinear calculations, and $M_{y/z,R} = W_{y/z}f_m$ is the bending load-bearing capacity of the cross-section. This interaction equation was also included in EN 1995-1-1 [57]. The part of the interaction equation for compression and uniaxial bending was validated experimentally by Steiger and Fontana [150] and numerically by Blaß [8].

Different analytical and numerical models for considering the materially nonlinear behaviour in compression in grain direction of timber beam-columns were discussed by, e.g. Blaß [9], Buchanan [24], Hörsting [90], Kersken-Bradley [95], and Theiler [154] and yielded similar results as discussed before.

2.3.3.3 Influence on the load-bearing capacity at $N_{x,c}$-$M_{y,2}$-$M_{z,2}$-interaction

Buchanan et al. [25] and Hörsting [90] also investigated the load-bearing capacity at $N_{x,c}$-$M_{y,2}$-$M_{z,2}$-interaction with their strength models. Results of [25] for a stocky beam-column with square cross-section are presented in Figures 2.24 and 2.25. Plasticising does not only cause a nonlinear curve of the load-bearing capacity at combined axial compression and bending, see Figures 2.20 and 2.22, but also a pronounced nonlinear curve of the load-bearing capacity at combined loading by $M_{y,2}$ and $M_{z,2}$. For combined loading by $M_{y,2}$ and $M_{z,2}$, the nonlinearity increases with increasing compressive force, see Figure 2.24. The magnitude of this nonlinearity depends on the ratio of the bending strength to the

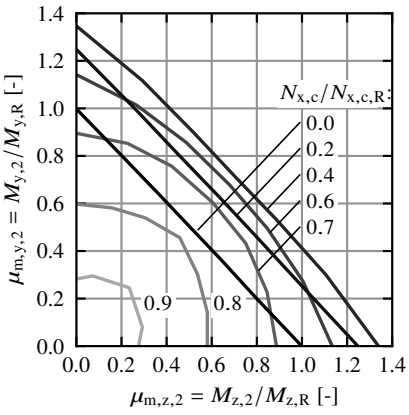

Figure 2.24: Relative load-bearing capacities for $M_{y,2}$-$M_{z,2}$-interaction of square timber cross-sections with different utilisation ratios of the axial compressive force $N_{x,c}/N_{x,c,R}$; pure plasticising without size effect; from Buchanan et al. [25].

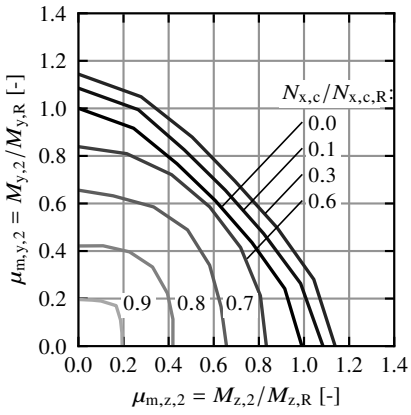

Figure 2.25: Relative load-bearing capacities for $M_{y,2}$-$M_{z,2}$-interaction of square timber cross-sections with different utilisation ratios of the axial compressive force $N_{x,c}/N_{x,c,R}$; with consideration of the size effect on the tensile strength due to biaxial bending; from Buchanan et al. [25].

compressive strength $f_m/f_{c,0}$, the proportionality limit $f_{c,0,lin}$, and the plastic strain at which the compressive strength is reached $\epsilon_{c,0,pl}$. Additionally, [25] included the size effect on the tensile/bending strength according to Weibull theory in their investigations, which resulted in the curves displayed in Figure 2.25. For low axial compressive forces, the size effect further increases the nonlinearity of the curve of the load-bearing capacity. The results were confirmed by [90].
[25] proposed to consider the positive influence of plasticising and size effect on the load-bearing capacity at $N_{x,c}$-$M_{y,2}$-$M_{z,2}$-interaction by the design equation

$$\left(\frac{M_{y,2}}{M_{y,R}}\right)^{\alpha} + \left(\frac{M_{z,2}}{M_{z,R}}\right)^{\alpha} \leq 1 \quad , \tag{2.32}$$

with

$$\alpha = 1.3 - \frac{\frac{N_{x,c}}{N_{x,c,R}}}{2\ln\left(\frac{N_{x,c}}{N_{x,c,R}}\right)} \quad , \tag{2.33}$$

where $M_{y/z,2}$ are the bending moments about the y- and z-axes according to geometrically nonlinear calculations, $M_{y/z,R} = W_{y/z} f_m$ are the bending load-bearing capacities of the cross-section, $N_{x,c}$ is the negative axial compressive force (tensile forces are neglected), and $N_{x,c,R} = A f_{c,0}$ is the axial compressive load-bearing capacity of the cross-section with a negative sign.

2.3.3.4 Influence on the internal forces

The experimental and numerical investigations by Buchanan et al. [25], Hörsting [90], Steiger and Fontana [150], and Zahn [184] on flexural buckling of beam-columns demonstrated that the moment magnification at failure due to compressive plasticising is significantly larger than given by Equation (2.1). This reduces the load-bearing capacity.

For the geometrically nonlinear calculation of internal forces at flexural buckling of softwood beam-columns, see Section 2.2.1, Buchanan et al. [25] therefore proposed an empirically determined modification of the amplification factor of the internal forces from

$$\frac{M_{y/z,2}}{M_{y/z,1}} = \frac{1}{1 - \alpha_{c,y/z}} \quad \text{(old)} \quad , \tag{2.34}$$

to

$$\frac{M_{y/z,2}}{M_{y/z,1}} = \frac{1 + \alpha_{c,y/z}}{1 - \alpha_{c,y/z}} \quad \text{(new)} \quad , \tag{2.35}$$

where $M_{y/z,2}$ is the bending moment about the y- or z-axis according to geometrically nonlinear calculations, $M_{y/z,1}$ is the bending moment about the y- or z-axis according to geometrically linear calculations, and $\alpha_{c,y/z}$ is the amplification factor of the axial compressive force due to flexural buckling about the y- or z-axis according to Equation (2.2).

The author suspects that the Dischinger coefficient in Equation (2.1) was not taken into account by [25] and could have been responsible for some of the deviations that were attributed entirely to compressive plasticising by Steiger and Fontana [150].
Alternatively, Steiger and Fontana [150] suggested considering the stiffness loss at flexural buckling of softwood beam-columns by compressive plasticising by using the tangent modulus $E_{0,T} \approx 0.8E_{0,el}$ for the calculation of the amplification factor $\alpha_{c,y/z}$ in Equation (2.34).
In the k_c-method in EN 1995-1-1 [57], the influence of compressive plasticising on the internal forces is included in β_c that was determined by curve fitting by Blaß [8], see Sections 2.2.1 and 2.6.2.

No investigations on the influence of materially nonlinear behaviour on the internal forces at LTB were known.

2.3.3.5 Summary

There are very little data on the nonlinear characteristics of the stress-strain relationship available, despite a large number of publications. Nonetheless, the positive influence of the compressive plasticising in grain direction on the $N_{x,c}$-$M_{y,2}$-interaction relationship of the cross-sectional resistance is well documented. For flexural buckling of softwood beam-columns, there were also numerous studies on the influence of the compressive plasticising in grain direction on the load-bearing capacity. No such investigations were known for flexural buckling of beech LVL beam-columns and LTB of softwood beam-columns.

2.3.4 Shear in grain direction

Due to the fundamentally different stress distribution in the cross-section, see Figure 2.17, and the correspondingly different possibilities for load redistribution, a distinction has to be made between shear from shear force and shear from torsion.

The typical stress-deformation behaviour of a softwood GL beam for shear in grain direction from shear force is displayed in Figure 2.26. Shear stresses in grain direction τ_{xz} are plotted over the vertical deformations w. The following descriptions are based on Aicher and Ohnesorge [5], Bodig and Jayne [16], Grosse [83]. A premature local shear failure can cause a flattening of the load-deformation curve, see Figure 2.26. The shear failure occurs due to similar failure mechanisms as a transverse tensile failure. At microscopic level, in softwood (typically ring-porous) timber, shear failure may involve (i) fracture of the cell wall parallel to the grain in the weaker early wood and (ii) fracture between adjacent cells in the late wood or compression wood by splitting of the middle lamella (intercell failure) or peeling of the S1 from the S2 layer (interwall failure). At macroscopic level, shear failure in softwood occurs as tangential cracks in the undamaged wood, which, depending on the loading direction and shrinkage cracks, extends in a zigzag pattern radially. The failure behaviour of diffuse-porous wood such as beech differs. In glued timber products such as GL and LVL, interface/bond line failure may also occur. Shear failure in the plane perpendicular to the grain is not possible.

According to Franke et al. [72], the nonlinear behaviour due to premature local failure can usually be neglected in the definition of the stress-strain relationship in building-practice-orientated investigations, and a linear-elastic behaviour up to failure can be assumed.

The typical moment-rotation behaviour of a GL beam for shear in grain direction from torsion is displayed in Figure 2.27. The torsional moments M_x are plotted over the rotations about the x-axis θ. The following descriptions are based on Aicher [3], Gupta and Siller [84], Khokhar et al. [102]. Depending on the wood product, a ductile, gradual failure can occur. Premature local failure, which is sometimes clearly visible and audible, leads to a reduction in stiffness and consequently to nonlinearly increasing deformations and rotations. No experimental data on the nonlinear parameters of the shear stress-strain relationship of full-scale softwood GL or beech LVL members at torsion were available. There was also a lack of published test data from which these parameters could be derived. In the tests by [3], a warping restraint was deliberately applied. Force-controlled tests such as those by Xiao [178] are not suitable for determining the nonlinear parameters of the stress-strain relationship. The duration of the tests in which Möhler and Hemmer [121] determined the moment-rotation behaviour was about 1 s, and the results were therefore not utilised. Therefore, experimental results of small, defect-free softwood samples were utilised in this thesis.As a simplified approach for taking into account the nonlinear behaviour, Dahl and Malo [31] proposed a bilinear shear stress-strain relationship. [31] and Yoshihara and Suzuki [180] experimentally observed values of the proportionality limit $f_{v,lin}$ between 40% and 70% of the shear strength in grain direction and about 55% of the rolling shear strength. The tangent gradient G_T after exceeding the proportionality limits was about 50% to 70% of the elastic shear stiffness in grain direction and about 30% to 40% of the elastic rolling shear stiffness, according to [31].

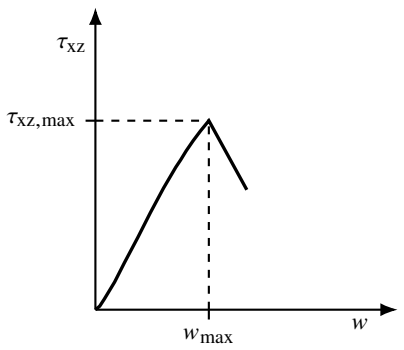

Figure 2.26: Typical stress-deformation curve of a softwood GL beam for shear in grain direction from shear force with the shear stresses τ_{xz} plotted over the vertical deformations w; data from Blaß and Krüger [15].

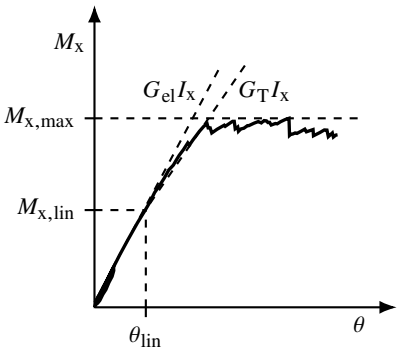

Figure 2.27: Typical torsional moment-rotation curve of a softwood GL beam for torsion with the torsional moment M_x plotted over angle of twist θ; data from Aicher [3].

No investigations on the influence of a nonlinear shear stress-strain relationship on the flexural buckling load-bearing capacity of softwood GL columns were known. As there are only small shear forces in timber columns, the proportionality limit for shear should not be reached, and no influence of shear plasticising should occur. An exception can be timber products with low shear stiffnesses such as CLT, see Narcy et al. [123].
No investigations on the influence of a nonlinear shear stress-strain relationship on the LTB load-bearing capacity of softwood GL beams were known. As significant torsional stresses occur at LTB of slender timber beams due to twisting of the cross-section, see Equation (2.14), an according shear failure behaviour is plausible.

2.3.5 Summary

If wood is subjected to compression in grain direction and shear from torsion, significant nonlinear material behaviour occurs. For other types of stresses and strains in grain direction, linear-elastic material behaviour can be assumed.
Compressive plasticizing increases (i) the cross-sectional load-bearing capacity due to the redistribution of compressive stresses, but also (ii) the internal forces due to the reduction in material stiffness. The extent to which both effects influence the load-bearing capacity of imperfection-sensitive timber members depends on the magnitude of the axial compressive stresses and the slenderness. There were numerous investigations of these effects for flexural buckling of softwood (beam-) columns, but no investigations for flexural buckling of beech LVL (beam-) columns.
No investigations on the influence of a nonlinear shear stress-strain relationship on the LTB behaviour of timber beams (-columns) were known.

2.4 Failure behaviour and load-bearing resistance

2.4.1 General

For imperfection-sensitive timber members loaded by (combined) bending and axial compression, tensile, compressive, and shear failure in grain direction can occur due to the stresses displayed in Figure 2.17.

The load-bearing capacities of timber members in bending, tension, and shear are decisively influenced by local material defects, and a size effect has to be taken into account for the corresponding strengths, see, e.g. Blank et al. [7], Brandner et al. [18], and Frese [74]. With increasing member volume, in which high tensile or shear stresses are present, the probability of material defects within this volume increases. These material defects are decisive for the member failure and the load-bearing capacity. Consequently, the strength decreases with increasing size of the stressed volume, which is known as *size effect*. This behaviour can be considered analytically, e.g. with the weakest link theory described by Weibull [173]. The *Weibull theory*, which assumes brittle material behaviour, was extended by [7] and Tapia and Aicher [152] for the actual *quasi*-brittle material behaviour of wood with tensile and shear stress. According to [152], this extension of the *Weibull theory* enables a more accurate representation of experimental results of the size effect for large volumes.
Due to the ductile behaviour of wood under compression, see Figure 2.19, stress redistribution is possible for such loading. Therefore, according to Buchanan [24] and Schilling et al. [141], the size effect is less pronounced for compressive stresses and can usually be neglected.
For this thesis, only the size effect on the tensile strength due to biaxial bending was considered and is described in more detail below. Other size effects were not explicitly examined and are therefore only briefly mentioned below.

Stress interactions can have a decisive influence on the tensile, compression, and shear strengths of wood, e.g. if shear and transverse tensile stresses interact, see Spengler [148]. In the investigated imperfection-sensitive members, the maximum longitudinal stresses occurred at midspan at the beam edges, and the maximum longitudinal shear stresses from torsion and shear force occurred towards the supports at midheight of the beam sides, see Figure 2.17. Due to the different positions of the maximum longitudinal and shear stresses, the influence of this stress interaction on the strength could be neglected.
Significant transverse stresses occurred in the investigated beams only at the supports and the load introduction. As, with the common supports at the lower edge of a beam and loading at the upper edge of a beam, there was only an interaction of compressive stresses perpendicular to the grain with compressive stresses in grain direction, which (i) was locally very limited, (ii) the material behaviour according to Eberhardsteiner [42] is extremely ductile, and (iii) the LTB tests in Section 3.4 were reinforced with fully threaded screws at the supports and the load introduction, an influence on the load-bearing behaviour was neglected in this thesis.
Furthermore, there was no significant interaction of transversal stresses and shear stresses at any point in the investigated members, which could lead to a reduction in strength.

According to Möhler and Hemmer [122], an interaction of different shear stress components leads to a reduction in strength and has to be taken into account.

The failure behaviour of imperfection-sensitive timber members with tensile, compression, and shear stresses in grain direction is discussed below, and it is outlined how this affects the load-bearing capacity.

2.4.2 Tension and bending in grain direction

In timber construction, the common colloquial term *bending failure* refers to tensile failure due to bending and subsequent failure modes. Therefore, tensile failure due to bending and the associated subsequent failure modes are discussed below.

A typical tensile failure of a GL member subjected to bending according to Fink et al. [65] is displayed in Figure 2.28. After the tensile failure of the outer lamella in the zone of high bending moments, the failure propagates as combined shear and transverse tensile failure, the lamellas fan out, and a significant increase in load is almost impossible, see Frese [74]. The failure criterion for member failure is therefore, according to [74], usually the fracture of the outermost tensile lamella. With regard to the causes of tensile failure of lamellas, Ehlbeck and Colling [46] distinguished between wood failure and finger-joint failure. [65] observed wood failure at knots, knot clusters, and clear wood. Some information on tensile failure of wood at microscopic level is given in Section 2.3.2.
There were no publications known that described the tensile failure behaviour of beech LVL members subjected to bending.

Glos [77] illustrated that the tensile strength of lamellas is decisively influenced by the type of wood, the density (proportion of cell walls), the knottiness, and the wood moisture content. In addition, according to Ehlbeck et al. [48], lamellas with and without finger joints have to be distinguished. [48] provided regression equations for determining the tensile strength of softwood GL lamellas depending on these parameters, see Equations (2.86) to (2.93), which did not lose their validity up to now, see Frese [74]. In addition, the influence of the size effect has to be taken into account, see [48].
The experimentally and numerically determined bending strengths of softwood GL at uniaxial bending were in the range of just under 15 N/mm^2 to over 60 N/mm^2 depending on

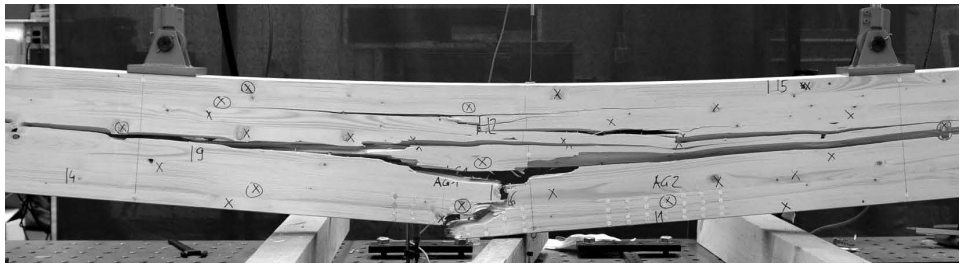

Figure 2.28: Bending failure of a 4-point bending test on a softwood GL beam; from Fink et al. [65].

the density, knottiness, wood moisture content, and finger joints, see Ehlbeck et al. [47], Fink et al. [65], and Frese [74]. The large scattering of the bending strengths highlights its dependence on the grading of the lamellas, see also [74]. But even within a grading or strength class and at a defined wood moisture content, the scattering was considerable, with a COV of about 0.15 according to [74] and Schilling et al. [141].
Experimentally determined bending strengths of beech LVL, ETA-14/0354 [63], at uniaxial bending were in the range of just under 80 N/mm^2 to over 120 N/mm^2 with a COV of less than 0.15, according to Dill-Langer and Aicher [37].
The size effect on the tensile strength of softwood GL with uniaxial bending was discussed, e.g. by [46] and Ehlbeck and Colling [45], and for beech LVL by [37].

Buchanan et al. [25] examined the size effect for biaxial bending utilising the *Weibull theory*, see Weibull [173], assuming that the scattering of tensile strength can be described by a two-parameter Weibull distribution with a shape parameter of $k = 8.0$. The resulting load-bearing capacities were approximated by Equations (2.32) and (2.33) for $M_{y,2}$-$M_{y,2}$-interaction, which also included the positive effect of plasticising.
To further simplify this approach, van der Put [171] suggested to omit the influence of the compressive plasticising and to introducing a k_{red} factor of 0.7 to

$$\frac{M_{y,2}}{M_{y,R}} + 0.7 \cdot \frac{M_{z,2}}{M_{z,R}} \leq 1 \quad , \tag{2.36}$$

$$0.7 \cdot \frac{M_{y,2}}{M_{y,R}} + \frac{M_{z,2}}{M_{z,R}} \leq 1 \quad , \tag{2.37}$$

where $M_{y/z,2}$ is the bending moment about the y- or z-axis according to geometrically nonlinear calculations, and $M_{y/z,R} = W_{y/z} f_m$ is the bending load-bearing capacity of the cross-section. This was also implemented in EN 1995-1-1 [57] and FprEN 1995-1-1 [69], see Equations (2.50), (2.51), (2.54), (2.54), (2.56), and (2.57).

The influence of the tensile strength on the load-bearing capacity of imperfection-sensitive timber members depends on the member slenderness, see Figure 2.4 and the more detailed descriptions in Sections 2.2.1 and 2.2.2. For stocky members, the load-bearing capacity increases proportionally to the tensile strength if neglecting the effects of compressive plasticising and other failure modes. The load-bearing capacity of slender members is not influenced by the tensile strength, only by the stiffness in grain direction. For medium-slender members, there is a transition between the behaviour of stocky and slender members.

In analytical models, a deterministic value of the tensile or bending strength is usually assumed as the limit criterion to take into account tensile failure, see, e.g. Hörsting [90]. In numerical models, alternatively, realistically scattering tensile strengths can be assumed over the member volume, applying approaches such as the *Weibull-Theory* or the *Karlsruher Rechenmodell*, see, e.g. Blaß et al. [14]. In this way, e.g. a large number of numerical test results for 4-point bending tests were generated utilising the *Karlsruher Rechenmodell* and

FEA, the distribution functions of the bending load-bearing capacity were determined, and the bending strength of softwood GL for EN 14080 [54] was determined, see Frese [74]. This approach is described in Section 2.7.
The *Weibull-Theory* was the only known approach for considering the size effect on the tensile strength due to biaxial bending.

2.4.3 Compression in grain direction

Figures 2.29 and 2.30 display a typical compressive failure of spruce GL and beech LVL members with loading in grain direction. Ehrhart et al. [53] and Poulsen [129] observed local compressive wrinkles in softwood GL, which can expand into a kink band across the entire cross-sectional width at further loading. Finally, splitting in grain direction usually occurs due to local transverse tensile failure, e.g. at knots, which leads to a drop in load, see [53], [129]. A similar failure was reported for beech LVL by Dill-Langer and Aicher [35], [53] and Kuck [105].
Some information on compressive failure of wood at microscopic level is given in Section 2.3.3.

Glos [77] illustrated that the compressive strength is decisively influenced by the type of wood, the density (cell wall content), the finger joints, and the wood moisture content. In addition, according to Ehlbeck et al. [48], lamellas with and without finger joints have to be distinguished. [48] provided regression equations for determining the compressive strength of softwood GL lamellas as a function of these parameters, see Equations (2.86) to (2.93), which did not lose their validity up to now, see Frese [74].
Experimentally and numerically determined values of the compressive strength of softwood GL ranged between -21 N/mm^2 and -50 N/mm^2, see Ehrhart et al. [53], Frese et al. [75], and Glos [78]. According to [74] and [75], scatter within a grading or strength class at a defined wood moisture content was low with a COV of less than 0.10.
Experimentally determined compressive strengths of beech LVL from Dill-Langer and Aicher [37] were in the range of -55 N/mm^2 to over -80 N/mm^2 with a COV of less than 0.06.

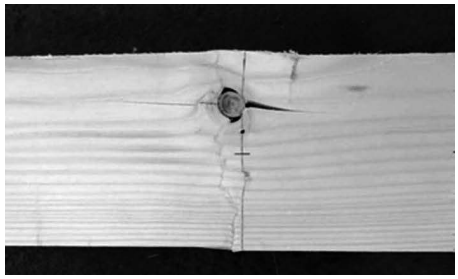

Figure 2.29: Failure of spruce GL at compression in grain direction; from Ehrhart et al. [53]

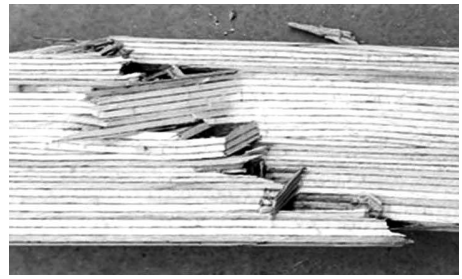

Figure 2.30: Failure of beech LVL at compression in grain direction; from Ehrhart et al. [53]

The influence of the compressive strength on the load-bearing capacity of imperfection-sensitive timber members depends on the member slenderness, see Figure 2.4 and the more detailed descriptions in Sections 2.2.1.2 and 2.2.2.2. Only the load-bearing capacity of stocky columns is directly influenced by the compressive strength. For medium-slender and slender timber members, which are imperfection-sensitive, member failure occurs due to stability, tensile, or shear failure. Nonetheless, for medium-slender members, the compressive strength influences the amount of plasticising and thus the stiffness and load-bearing capacity of the members. This influence is discussed in Section 2.3.3. The load-bearing capacity of slender members is not influenced by the compressive strength, only by the stiffness in grain direction.

A limitation of the compressive stresses in analytical and numerical models is usually not appropriate, due to the extremely ductile compressive behaviour in grain direction. Instead, Blaß [9] limited the mean axial compressive stress in a cross-section to the compressive strength. In addition, he limited the compressive strains $\epsilon_{c,0}$ to a maximum value of 5%. Frese et al. [75] experimentally determined mean strains between 0.25% and 0.55% in compression tests at a measuring length of 320 mm when the compressive strength was reached. Based on further comparative FEA, they recommended a limit strain of 0.5% for determining compressive strengths with FEA and dimensions according to EN 408 [60].

2.4.4 Shear in grain direction

A typical longitudinal shear failure of spruce GL and SL at loading by shear force according to Franke et al. [72] and Gatternig [76] is displayed in Figures 2.31 and 2.32. In ring-porous woods, i.e. softwoods, longitudinal shear failure occurs primarily along annual ring boundaries in the early wood, i.e. tangentially, due to the lower shear strength, see Glos and Denzler [79]. According to [79] and Grosse [83], longitudinal shear stresses radial to the annual rings or shrinkage cracks can cause a zigzag-shaped crack propagation across annual ring boundaries. In the case of softwood GL, side boards with horizontal annual rings are preferably used. Therefore, the shear failure usually follows the grain and annual ring pattern, with occasional jumps across annual ring boundaries, see Figure 2.31, [72],

Figure 2.31: Failure of spruce GL at shear in grain direction; cracks highlighted with a marker; from Franke et al. [72].

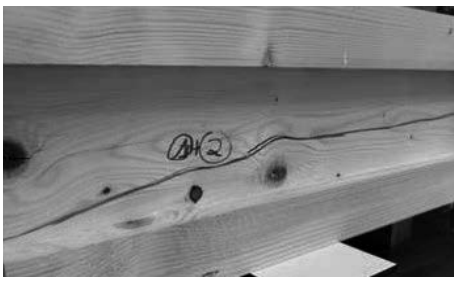

Figure 2.32: Failure of spruce SL at shear in grain direction; cracks highlighted with a marker; from Gatternig [76].

and [79]. In diffuse-porous woods such as beech, longitudinal shear failure does not occur along annual rings, according to Aicher and Ohnesorge [5]. In addition to the wood failure, [5] reported of an interface/bond line failure between two lamellas. Shear cracks can be significantly less obvious than tensile or compressive failure, as illustrated by Blaß and Krüger [15]. In the case of GL beams, according to [15], load increases are generally no longer possible after shear failure occurred. There were no publications known that described the longitudinal shear failure behaviour of beech LVL.
Some information on shear failure of wood at microscopic level is given in Section 2.3.4.

Brandner et al. [18] and Glos and Denzler [79] illustrated that the shear strength is decisively influenced by the type of wood, the density (cell wall content), the annual ring width, the shrinkage cracks, and the wood moisture content. In addition, the influence of the size effect has to be taken into account, see [18]. The influence of the material grade on the shear strength is not significant, according to [18] and [79].
The experimentally determined values of longitudinal shear strength of softwood from [18], [79], Möhler and Hemmer [122], and Spengler [148] were in the range of 3 N/mm^2 to 11 N/mm^2, with a COV between 0.15 and 0.20. Mean values of the longitudinal shear strength at 12% wood moisture content were about 5.3 N/mm^2 in measurements by [79] and [148], and 5% quantile values were between 3.5 N/mm^2 and 4.0 N/mm^2 in measurements by [79] and [122].
Experimentally determined values of the longitudinal shear strength of beech LVL from Dill-Langer and Aicher [36] were in the range of 4 N/mm^2 to 12 N/mm^2, with a COV between 0.15 and 0.20. For 600 mm high beams and service class (SC) 1, they determined mean values of longitudinal shear strength between 6.0 N/mm^2 and 7.5 N/mm^2, and 5% quantile values between 4.0 N/mm^2 and 5.5 N/mm^2.
The size effect on the shear strength of softwood GL was discussed, e.g. by Brandner et al. [18] and for beech LVL by Dill-Langer and Aicher [37].

As there are only small shear forces in timber columns, the shear strength does usually not influence flexural buckling load-bearing capacity. An exception can be timber products with low (rolling) shear strengths, such as CLT, see Narcy et al. [123].
Hörsting [90] investigated the influence of the shear strength on the LTB load-bearing capacity of softwood GL beams. In analytical and numerical calculations, he observed that, due to significant torsional moments, the shear load-bearing capacity became decisive compared to the bending load-bearing capacity for slender beams. However, the determined shear load-bearing capacities were only slightly smaller than the bending load-bearing capacities. For the design of slender members at risk of LTB, he recommended checking both the shear and the tensile load-bearing capacities. Since, according to EN 14080 [54], the bending strength increases with increasing material quality but the shear strength does not, [90] expected that shear failure due to torsion is more relevant for slender beams made of higher-quality materials.
Wilden et al. [176] and Xiao [178] observed shear failure at LTB tests before bending failure.

In analytical models, a deterministic value of the shear strength is usually assumed as the

limit criterion to take into account the shear failure, see, e.g. Hörsting [90]. In numerical models, alternatively, realistically scattering shear strengths can be assumed over the member volume, e.g. according to Brüninghoff and Klapp [21]. This approach is described in Section 2.7.

2.4.5 Summary

For imperfection-sensitive timber members loaded by (combined) bending and axial compression, tensile, compressive, and shear failure in grain direction can occur. The relevant tensile, compression, and shear stresses arise at different locations in the member, and no strength reduction due to stress interaction needs to be taken into account. However, the size effect on the shear and tensile strength due to (quasi-) brittle behaviour has to be considered.
The influence of the tensile, compressive, and shear strengths on the load-bearing capacity of imperfection-sensitive timber members depends on the member slenderness. For stocky members, the load-bearing capacity depends directly on the tensile or compressive strengths. For slender members, the load-bearing capacity depends on the stiffness but may be reduced at LTB due to torsion-induced shear failure. For medium-slender members, there is a transition between the behaviour of stocky and slender members.
There were numerous investigations on the influence of tensile/bending strengths at softwood beam-columns, but only little investigations on the shear strength at LTB and no investigations for beech LVL columns.

2.5 Long-term behaviour

2.5.1 General

In addition to the short-term behaviour described in Sections 2.2 to 2.4, timber members are subject to (i) additional deformations over time, i.e. creep deformations, (ii) decreasing strengths, i.e. duration of load effect, aka creep strength, and (iii) cracks and other material degradation, see Bodig and Jayne [16] and Brandner [17].
In the following, some investigations from literature on creep deformations are briefly described, which are referred to again in the design proposals in Section 7. Creep strength and material degradation are not discussed, as these can be handled independently from the geometrically and materially nonlinear LTB and flexural buckling behaviour.

An exemplary creep behaviour of timber from Kenel and Meierhofer [94] is displayed in Figure 2.33. According to Kenel and Meierhofer [94], creep deformations can be divided into three phases: the primary creep, the secondary creep, and the tertiary creep. The reaching of the tertiary phase depends on the load history. For ensuring the resistance of a structure, tertiary creep, which causes disproportional deformations, should not occur during the lifetime of a building, see [94] and [136].
Blaß [10] and Schulte [142] stated that the creep behaviour is influenced by the material itself, e.g. the dry density, annual ring width, knottiness, fibre deviation, etc., and the type of loading (bending, shear, compression, tension), the direction of loading (longitudinal, radial, tangential), the load history, the wood moisture content and moisture content changes, the temperature, etc. Experimental results of the creep deformation factors, k_{def} in EN 1995-1-1 [57], for different types of loading in grain direction from Gressel [82] are displayed in Figure 2.34. The highest creep deformations occurred for shear and the lowest for tension.

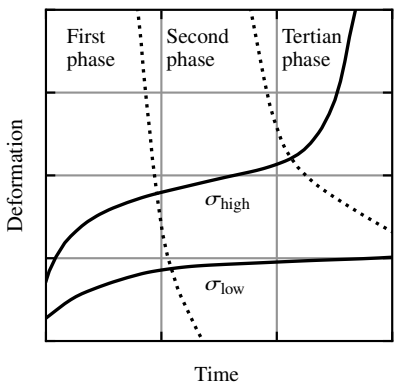

Figure 2.33: Total deformations for low and high stresses σ plotted over the time; with creep phases; from Kenel and Meierhofer [94].

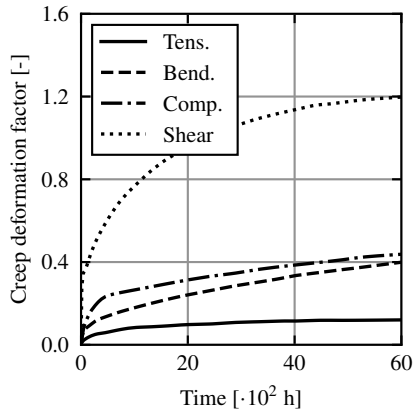

Figure 2.34: Experimentally determined creep deformation factors for spruce plotted over the time for different loadings; from Gressel [82].

2.5.2 Flexural buckling

Blaß [10] and Rautenstrauch and Becker [133] demonstrated that the influence of creep on the flexural buckling load-bearing capacity depends on the column slenderness and stress level. [10] reported no influence for low slendernesses as no significant geometrically and materially nonlinear deformations occur and the load-bearing capacity depends on the compressive strength. For medium slendernesses, he found the highest influence, as the geometrically and materially nonlinear deformations influence the load-bearing capacity and significant stresses are present. For higher slendernesses, as the stresses decrease due to decreasing critical loads N_{cr}, see Equation (2.3), the influence of creep also decreases.

Blaß [10] proposed to consider the influence of creep in the k_c-method for flexural buckling design, see Section 2.6.2, by increasing the fitting factor β_c.

Hartnack and Rautenstrauch [85] recommended to considered creep in flexural buckling design for SC 2 and 3, and if permanent and long-term acting loads exceed 75% and 50% of the design flexural buckling load-bearing capacity. For calculating the long-term load-bearing capacity of columns they recommended several rather complex methods.

Abeysekera et al. [2] recommended to increase the bow imperfections for considering the creep deformations in calculations with T2O to

$$e_{z/y,t=50a} = e_{z/y} \cdot \frac{1-\alpha_{c,y/z}}{1-\alpha_{c,y/z,t=50a}} - \frac{M_{y/z,1}}{N_{x,c}} \cdot \left(\frac{1-\alpha_{c,y/z}}{1-\alpha_{c,y/z,t=50a}} - 1 \right) \quad , \tag{2.38}$$

with

$$\alpha_{c,y/z,t=50a} = \alpha_{c,y/z} \cdot (1 + k_{def}) \quad , \tag{2.39}$$

where $e_{z/y,t=50a}$ is the creep amplified bow imperfection in the z- or y-direction, $e_{z/y}$ is the bow imperfection, $\alpha_{c,y/z}$ is the short-term amplification factor of the axial compressive force due to flexural buckling about the y- or z-axis according to Equation (2.2), $\alpha_{c,y/z,t=50a}$ is the long-term amplification factor, $M_{y/z,1}$ is the bending moment about the y- or z-axis according to geometrically linear calculations with the quasi-permanent combination of loads for SLS, $N_{x,c}$ is the negative axial compressive force with the quasi-permanent combination of loads for SLS.

Schänzlin [137] derived from the differential equations for flexural buckling with pure axial compressive forces (no bending) that creep can be considered by increasing the deformations in Equation (2.6) to

$$v_{2,t=50a} = \frac{\alpha_{c,z} e_y}{1 - \alpha_{c,z} \cdot (1 + k_{def,ef})} \quad , \tag{2.40}$$

with

$$k_{\mathrm{def,ef}} = \frac{N_{\mathrm{x,P,d}}}{N_{\mathrm{x,P,d}} + N_{\mathrm{x,S,d}}} \cdot k_{\mathrm{def}} \quad , \tag{2.41}$$

and therefore the bending moment in Equation (2.1) to

$$M_{\mathrm{y/z,2}} = \frac{-N_{\mathrm{x,c}} e_{\mathrm{z/y}}}{1 - \alpha_{\mathrm{c,y/z}} \cdot (1 + k_{\mathrm{def,ef}})} \quad , \tag{2.42}$$

where $k_{\mathrm{def,ef}}$ is the effective creep deformation coefficient, $N_{\mathrm{x,P,d}}$ and $N_{\mathrm{x,S,d}}$ are the design values of the permanent and the short-term acting axial compressive loads.
They further demonstrated that this can be included in the k_{c}-method from EN 1995-1-1 [57] by modifying the fitting factor $\beta_{\mathrm{c,y/z}}$ in Equation (2.76) to

$$\beta_{\mathrm{c,y/z,t=50a}} = \frac{e_{\mathrm{z/y}}}{L} \cdot \pi \cdot \sqrt{\frac{3E_{\mathrm{0,el}}}{f_{\mathrm{c,0}} \cdot (1 + k_{\mathrm{def,ef}})}} \cdot \frac{f_{\mathrm{c,0}}}{f_{\mathrm{m}}} \quad , \tag{2.43}$$

and the relative slenderness ratio for flexural buckling $\lambda_{\mathrm{c,y/z,rel}}$ in Equation (2.60) to

$$\lambda_{\mathrm{c,y/z,rel,t=50a}} = \sqrt{\frac{f_{\mathrm{c,0}} A \cdot (1 + k_{\mathrm{def,ef}})}{N_{\mathrm{y/z,cr}}}} \quad , \tag{2.44}$$

where L is the member length, $E_{\mathrm{0,el}}$ is the elastic modulus in grain direction, $f_{\mathrm{c,0}}$ and f_{m} are the compressive and bending strengths in grain direction, A is the cross-sectional area, and $N_{\mathrm{y/z,cr}}$ is the critical axial compressive force for flexural buckling about the y- or z-axis with a positive sign according to Equation (2.3). Equation (2.43) does not account for the relevant materially nonlinear behaviour (compressive plasticising in grain direction) of columns, see also Section 2.2.1. Equations (2.43) and (2.44) are the same as k_{c}-method in FprEN 1995-1-1 [69] plus the reduction factor $(1 + k_{\mathrm{def}})$.

Inserting Equation (2.38) in Equation (2.1) for pure axial compressive forces (no bending) results in the same deformation v_2 as Equation (2.40). Both Equations (2.38) and (2.40) are exact solutions of the differential equations for flexural buckling. The proposals of Abeysekera et al. [2] and Schänzlin [137] should therefore yield similar results.

2.5.3 Lateral torsional buckling

Hofmann [87] demonstrated that the influence of creep on the LTB load-bearing capacity depends on the beam slenderness. For low slendernesses, he found no influence as the load-bearing capacity depends on the tensile/bending strength and no significant geometrically or materially nonlinear deformations occur. For medium and high slendernesses and a proportion of the permanent load of 50% and more of the total load, he observed a significant reduction of the LTB load-bearing capacity. He proposed to consider creep in LTB design in SC 1 by a modification of the k_{m}-method from EN 1995-1-1 [57].

Schänzlin [139] derived from the differential equations for LTB with pure bending moment (no axial compressive forces) that creep can be considered by increasing the rotations and deformations in Equations (2.19) and (2.20) to

$$\theta_{2,\mathrm{t=50a}} = \frac{\frac{M_{\mathrm{y},1}}{G_{0,\mathrm{el}} I_{\mathrm{x}}} \cdot e_{\mathrm{y}} + \alpha_{\mathrm{m}}^2 e_{\theta} \cdot (1 + k_{\mathrm{def,v,ef}})}{1 - \alpha_{\mathrm{m}}^2 \cdot (1 + k_{\mathrm{def},\theta,\mathrm{ef}}) \cdot (1 + k_{\mathrm{def,v,ef}})} \quad , \tag{2.45}$$

$$v_{2,\mathrm{t=50a}} = \frac{\alpha_{\mathrm{m}}^2 e_{\mathrm{y}} \cdot (1 + k_{\mathrm{def},\theta,\mathrm{ef}}) + \frac{M_{\mathrm{y},1}}{N_{\mathrm{z,cr}}} \cdot e_{\theta}}{1 - \alpha_{\mathrm{m}}^2 \cdot (1 + k_{\mathrm{def},\theta,\mathrm{ef}}) \cdot (1 + k_{\mathrm{def,v,ef}})} \quad , \tag{2.46}$$

with

$$k_{\mathrm{def},\theta/\mathrm{v,ef}} = \frac{M_{\mathrm{y},1,\mathrm{P,d}}}{M_{\mathrm{y},1,\mathrm{P,d}} + M_{\mathrm{y},1,\mathrm{S,d}}} \cdot k_{\mathrm{def},\theta/\mathrm{v}} \quad , \tag{2.47}$$

and therefore the bending moment in Equation (2.15) to

$$M_{\mathrm{z},2,\mathrm{t=50a}} = \frac{\frac{M_{\mathrm{y},1}^2}{G_{0,\mathrm{el}} I_{\mathrm{x}}} \cdot e_{\mathrm{y}} \cdot (1 + k_{\mathrm{def},\theta,\mathrm{ef}}) + M_{\mathrm{y},1} e_{\theta}}{1 - \alpha_{\mathrm{m}}^2 \cdot (1 + k_{\mathrm{def},\theta,\mathrm{ef}}) \cdot (1 + k_{\mathrm{def,v,ef}})} \quad , \tag{2.48}$$

where $M_{\mathrm{y},1}$ is the bending moment about the y-axis according to geometrically linear calculations, $G_{0,\mathrm{el}}$ is the shear modulus in grain direction, I_{x} is the elastic torsional moment of inertia according to Equation (2.18), e_{y} is the bow imperfection in y-direction, α_{m} is the amplification factor of the bending moment due to LTB according to Equation (2.16), e_{θ} is the twist imperfection, $k_{\mathrm{def},\mathrm{v}/\theta,\mathrm{ef}}$ is the effective creep deformation factor for deformations v or rotations θ, $N_{\mathrm{z,cr}}$ is the critical axial compressive force for flexural buckling about the z-axis according to Equation (2.3), $k_{\mathrm{def},\theta/\mathrm{v}}$ is the creep deformation factor for rotations θ or deformations v, $M_{\mathrm{y},1,\mathrm{P,d}}$ and $M_{\mathrm{y},1,\mathrm{S,d}}$ are the design values of the permanent and the short-term acting bending moments with load-combinations according to EN 1990 [55].
They further demonstrated that this can be included in the k_{m}-method from EN 1995-1-1 [57] by modifying the critical bending moment $M_{\mathrm{y,cr}}$ in Equation (2.17) to

$$M_{\mathrm{y,cr,t=50a}} = \frac{\pi}{L_{\mathrm{m,ef}}} \cdot \sqrt{E_{0,\mathrm{el}} I_{\mathrm{z}} G_{0,\mathrm{el}} I_{\mathrm{x}}} \cdot \frac{1}{\sqrt{(1 + k_{\mathrm{def},\theta,\mathrm{ef}}) \cdot (1 + k_{\mathrm{def,v,ef}})}} \quad . \tag{2.49}$$

2.5.4 Summary

For imperfection-sensitive timber members loaded by (combined) bending and axial compression, creep can significantly increase the deformations and internal forces and therefore decrease the load-bearing capacity.
The influence of creep depends on the member slenderness. Whereas no influence can be found for low slenderness, a high influence can be observed for medium and high

slenderness.
There were numerous experimental, numerical, and analytical investigations on the influence of creep on the flexural buckling load-bearing capacity, and various proposals on the consideration of creep in flexural buckling design exist. For LTB, only a few analytical and numerical investigations and no experimental investigations on creep were known, and design recommendations were scarce in the literature.

2.6 Design verification

2.6.1 General

The design methods for imperfection-sensitive timber members in EN 1995-1-1 [57], DIN EN 1995-1-1/NA [40], and FprEN 1995-1-1 [69] are discussed below. The standards differentiate between (i) ultimate limit state (ULS) design, which deals with the failure of a structure, and (ii) serviceability limit state (SLS) design, which deals with the service-requirements of a structure. The SLS design is only addressed briefly, as it is not the focus of this thesis. Additionally, between (i) design with unmagnified internal forces, i.e. geometrically linear calculations (T1O), and (ii) design with magnified internal forces, i.e. geometrically nonlinear calculations (T2O).
Materially nonlinear calculations are not intended by the standards, see EN 1995-1-1 [57] 2.2.2 (1) and FprEN 1995-1-1 [69] 7.3.3 (1), but some effects of plasticising are considered in the design equations.

The symbols in the design equations from the standards were adapted to correspond to the notation in this thesis. Equations (2.50), (2.51), (2.56), (2.57), (2.61), (2.67), and (2.77) are written in a slightly modified form compared to EN 1995-1-1 [57], DIN EN 1995-1-1/NA [40], and FprEN 1995-1-1 [69], and the internal forces are given instead of the stresses in order to clarify how the stresses shall be determined.

2.6.2 EN 1995-1-1:2004

2.6.2.1 ULS design for bending and compression

2.6.2.1.1 General

For rectangular cross-sections with combined axial compression and bending, the following should be satisfied according to EN 1995-1-1 [57] 6.2.4:

$$\left(\frac{N_{x,c,d}}{A f_{c,0,d}}\right)^2 + \frac{M_{y,1,d}}{W_y f_{m,y,d}} + k_{red} \cdot \frac{M_{z,1,d}}{W_z f_{m,z,d}} \leq 1.0 \quad , \tag{2.50}$$

$$\left(\frac{N_{x,c,d}}{A f_{c,0,d}}\right)^2 + k_{red} \cdot \frac{M_{y,1,d}}{W_y f_{m,y,d}} + \frac{M_{z,1,d}}{W_z f_{m,z,d}} \leq 1.0 \quad , \tag{2.51}$$

where $N_{x,c,d}$ is the design axial compressive force, A is the cross-sectional area, $f_{c,0,d}$ is the design compressive strength, $M_{y/z,1,d}$ is the design bending moment about the y- or z-axis according to geometrically linear calculations, $W_{y/z}$ is the section modulus about the y- or z-axis, $f_{m,y/z,d}$ is the design bending strength about the y- or z-axis, and k_{red} is a factor for considering the positive size effect on the bending strength at biaxial bending. EN 1995-1-1 [57] 6.1.6 (2) recommends $k_{red} = 0.7$ for rectangular cross-sections.
The exponent 2 at the compressive force component takes into account the positive influence of compressive plasticising on the cross-sectional resistance, which was derived by Blaß [8], Buchanan et al. [25], and Zahn [183] for softwood, see also Section 2.3.3. $k_{red} = 0.7$ takes into account the size effect on the bending strength at biaxial bending, which was derived by Buchanan et al. [25] and van der Put [171] for softwood, see also discussions concerning Equations (2.36) and (2.37).

2.6.2.1.2 Imperfection-sensitive members with geometrically nonlinear calculation of internal forces

There is no explicit advice for the bending design of imperfection-sensitive (slender) members with geometrically nonlinear calculation of internal forces in EN 1995-1-1 [57].

Internal forces and deformations can be calculated manually, e.g. with T2O, see Equations (2.1) to (2.7) and (2.14) to (2.20), or suitable software. Design elastic and shear moduli should be used according to EN 1995-1-1 [57] 2.2.2 (1). With regard to equivalent geometrical imperfections for design, EN 1995-1-1 [57] only specifies values for bow imperfections and sway imperfections of columns. Twist imperfections of beams, see Figure 2.16, are not mentioned.

EN 1995-1-1 [57] 5.4.4 (2) gives a minimum equivalent bow imperfection for plane frames and arches of

$$e_y = 0.0025L = \frac{L}{400} \quad , \tag{2.52}$$

where L is the member length. This equivalent bow imperfection is probably also supposed to be applied for geometrically nonlinear calculation of internal forces at flexural buckling and LTB, even if this is not stated in EN 1995-1-1 [57]. It is not differentiated between SL and GL, in contrast to the k_c-method, which includes the material-dependent fitting factor β_c, see Equation (2.59).
The background of the value $L/400$ was unclear to the author. It could be based on engineering judgement supported by imperfection measurements on one building by Brüninghoff [20], see Section 2.2.3. The value is significantly more conservative than the measured bow imperfections of softwood GL columns by Ehlbeck and Blaß [44] with a 95% quantile value of $L/1140$, see Section 2.2.3.
Flexural buckling design of GL columns with calculations using T2O and $e_y = L/400$ results in more conservative load-bearing capacities than the k_c-method, see Figure 2.8. This is not surprising, as the fitting factor β_c of the k_c-method was derived with the above mentioned more favourable bow imperfections of GL columns measured by [44], see Sections 2.6.2.1.3.
LTB design of timber beams with calculations using T2O and $e_y = L/400$ results in similar load-bearing capacities as the k_m-method, see Figure 2.15 and Section 2.6.2.1.4.

EN 1995-1-1 [57] 5.4.4 (2) gives a minimum sway imperfection for plane frames and arches of

$$e_\phi = \begin{cases} \frac{1}{200} & \text{for} \quad h \leq 5 \text{ m} \quad , \\ \frac{1}{200} \cdot \sqrt{\frac{5}{H}} & \text{for} \quad h > 5 \text{ m} \quad , \end{cases} \tag{2.53}$$

where H is the height of the structure or member length in m.
Equation (2.53) is based on the measurements of Lindner and Giezelt [119] on steel structures, see Section 2.2.3. Measurements by Ehlbeck and Blaß [44] on softwood GL columns yielded a 95% quantile value of $e_\phi = 1/187$, which is similar to the design value given in Equation (2.53).

For ultimate limit state (ULS) design of rectangular cross-sections, the following should be satisfied according to EN 1995-1-1 [57] 6.2.4:

$$\left(\frac{N_{x,c,d}}{A f_{c,0,d}}\right)^2 + \frac{M_{y,2,d}}{W_y f_{m,y,d}} + k_{red} \cdot \frac{M_{z,2,d}}{W_z f_{m,z,d}} \leq 1.0 \quad , \tag{2.54}$$

$$\left(\frac{N_{x,c,d}}{A f_{c,0,d}}\right)^2 + k_{red} \cdot \frac{M_{y,2,d}}{W_y f_{m,y,d}} + \frac{M_{z,2,d}}{W_z f_{m,z,d}} \leq 1.0 \quad , \tag{2.55}$$

where $N_{x,c,d}$ is the design axial compressive force, A is the cross-sectional area, $f_{c,0,d}$ is the design compressive strength, $M_{y/z,2,d}$ is the design bending moment about the y- or z-axis according to geometrically nonlinear calculations, $W_{y/z}$ is the section modulus about the y- or z-axis, $f_{m,y/z,d}$ is the design bending strength about the y- or z-axis, and k_{red} is a

factor for considering the positive size effect on the bending strength at biaxial bending. Equations (2.54) and (2.55) are the same as Equations (2.50) and (2.51), and the mechanical background is also identical.

2.6.2.1.3 Imperfection-sensitive columns with geometrically linear calculation of internal forces (k_c-method)

According to EN 1995-1-1 [57] 6.3.2 (2), columns with $\lambda_{c,y/z,rel} > 0.3$ should be treated as imperfection-sensitive and be designed for flexural buckling (additionally to cross-sectional design according to Equations (2.50) and (2.51)).

For flexural buckling of members with combined axial compression and bending, the following should be satisfied according to EN 1995-1-1 [57] 6.3.2:

$$\frac{N_{x,c,d}}{k_{c,y} A f_{c,0,d}} + \frac{M_{y,1,d}}{W_y f_{m,y,d}} + k_{red} \cdot \frac{M_{z,1,d}}{W_z f_{m,z,d}} \leq 1.0 \quad , \tag{2.56}$$

$$\frac{N_{x,c,d}}{k_{c,z} A f_{c,0,d}} + k_{red} \cdot \frac{M_{y,1,d}}{W_y f_{m,y,d}} + \frac{M_{z,1,d}}{W_z f_{m,z,d}} \leq 1.0 \quad , \tag{2.57}$$

with

$$k_{c,y/z} = \frac{1}{\phi_{c,y/z} + \sqrt{\phi^2_{c,y/z} - \lambda^2_{c,y/z,rel}}} \quad , \tag{2.58}$$

$$\phi_{c,y/z} = 0.5 \cdot (1 + \beta_c \cdot (\lambda_{c,y/z,rel} - 0.3) + \lambda^2_{c,y/z,rel}) \quad , \tag{2.59}$$

$$\lambda_{c,y/z,rel} = \frac{\lambda_{y/z}}{\pi} \cdot \sqrt{\frac{f_{c,0,k}}{E_{0,k}}} \quad , \tag{2.60}$$

where $N_{x,c,d}$ is the design axial compressive force, $k_{c,y/z}$ is the relative flexural buckling load-bearing capacity for flexural buckling about the y- or z-axis, A is the cross-sectional area, $f_{c,0,d}$ is the design compressive strength, $M_{y/z,1,d}$ is the design bending moment about the y- or z-axis according to geometrically linear calculations, $W_{y/z}$ is the section modulus about the y- or z-axis, $f_{m,y/z,d}$ is the design bending strength about the y- or z-axis, k_{red} is a factor for considering the positive size effect on the bending strength at biaxial bending, $\phi_{c,y/z}$ is the intermediate parameter for the calculation of $k_{c,y/z}$ about the y- or z-axis, $\lambda_{c,y/z,rel}$ is the relative slenderness ratio for flexural buckling about the y- or z-axis, β_c is a fitting factor (0.1 for GL and LVL and 0.2 for SL), $\lambda_{y/z}$ is the slenderness ratio for flexural buckling about the y- or z-axis including the effective flexural buckling length $L_{c,y/z,ef}$, and $E_{0,k}$ is the characteristic elastic modulus in grain direction. EN 1995-1-1 [57] 6.1.6 (2)

recommends $k_{red} = 0.7$ for rectangular cross-sections.
It was demonstrated by Blaß [8], Buchanan et al. [25], Zahn [183], that for slender timber columns no significant plasticising occurs and therefore the linear $N_{x,c}$-$M_{y,1}$-interaction in Equations (2.56) and (2.57) should be assumed, see also Section 2.3.3. The derivation of Equations (2.58) to (2.60) for calculating the $k_{c,y/z}$ factor, which accounts for the increase of internal forces due to geometrically nonlinear behaviour at flexural buckling with pure axial compressive forces $N_{x,c,d}$, is discussed in Section 2.2.1. Equations (2.56) to (2.60) neglect the geometrically nonlinear behaviour due to bending moments $M_{y,1,d}$ and $M_{z,1,d}$. The fitting factor β_c, which accounts for the ratio of $E_{0,el}$ to $f_{c,0}$ to f_m and the effects of geometrical and structural imperfections, and plasticising, was calibrated by means of curve fitting to the results of numerical calculations with scattering input values and realistic stress-strain behaviour by Blaß [9], see also Section 2.2.1.8. Within the standardisation process, β_c was adjusted from the value 0.13 proposed by Blaß [8] to 0.10 as given in EN 1995-1-1 [57] for GL. The investigations by [8] only covered softwood, but EN 1995-1-1 [57] recommends β_c values independently of the wood species. The transfer to hardwoods is questionable in the light of recent investigations by Ehrhart et al. [52], who found a value of $\beta_c = 0.25$ for beech GL.
According to Brüninghoff and Klapp [22], the compressive strength $f_{c,0,k}$ covers the geometrically and materially nonlinear effects from the experiments with which it was determined, see EN 408 [60]. Assuming Euler buckling case 2, compression test dimensions from EN 408 [60] and typical characteristic material properties of SL and GL according to EN 384 [59] and EN 14080 [54] result in $\lambda_{c,z,rel} \approx 0.3$ as demonstrated by Schänzlin [137]. Therefore, it is not reasonable to include a reduction of load-bearing capacity due to flexural buckling for $\lambda_{c,y/z,rel} \leq 0.3$, as these effects are already covered by the $f_{c,0,k}$, see [22].

Effects of load-eccentricities and sway imperfections are not included in the k_c-method and should be considered additionally, see Schänzlin [137].

2.6.2.1.4 Imperfection-sensitive beam-columns with geometrically linear calculation of internal forces (k_m-method)

According to EN 1995-1-1 [57], beams and beam-columns with $\lambda_{m,rel} > 0.75$ should be treated as imperfection-sensitive and be designed for LTB (additionally to design according to Equations (2.50) and (2.51)).

For LTB of members with combined bending and axial compression, the following should be satisfied according to EN 1995-1-1 [57] 6.3.3:

$$\frac{N_{x,c,d}}{k_{c,z} A f_{c,0,d}} + \left(\frac{M_{y,1,d}}{k_m W_y f_{m,y,d}} \right)^2 \leq 1.0 \quad , \tag{2.61}$$

with

$$k_{\mathrm{m}} = \begin{cases} 1 & \text{for} \quad \lambda_{\mathrm{m,rel}} \leq 0.75 \quad , \\ 1.56 - 0.75\lambda_{\mathrm{m,rel}} & \text{for} \quad 0.75 < \lambda_{\mathrm{m,rel}} \leq 1.40 \quad , \\ \frac{1}{\lambda_{\mathrm{m,rel}}^2} & \text{for} \quad 1.40 < \lambda_{\mathrm{m,rel}} \quad , \end{cases} \tag{2.62}$$

$$\lambda_{\mathrm{m,rel}} = \sqrt{\frac{f_{\mathrm{m,k}}}{\sigma_{\mathrm{m,y,cr}}}} \quad , \tag{2.63}$$

$$\sigma_{\mathrm{m,y,cr}} = \frac{M_{\mathrm{y,cr}}}{W_{\mathrm{y}}} = \frac{\pi \cdot \sqrt{E_{0,\mathrm{k}} I_{\mathrm{y}} G_{0,\mathrm{k}} I_{\mathrm{x}}}}{L_{\mathrm{m,ef}} W_{\mathrm{y}}} \quad , \tag{2.64}$$

where $N_{\mathrm{x,c,d}}$ is the design axial compressive force, $k_{\mathrm{c,z}}$ is the relative flexural buckling load-bearing capacity about the z-axis according to Equation (2.58), A is the cross-sectional area, $f_{\mathrm{c,0,d}}$ is the design compressive strength, $M_{\mathrm{y,1,d}}$ is the design bending moment about the y-axis according to geometrically linear calculations, k_{m} is the relative LTB load-bearing capacity, W_{y} is the section modulus about the y-axis, $f_{\mathrm{m,y,d}}$ is the design bending strength about the y-axis, $\lambda_{\mathrm{m,rel}}$ is the relative slenderness ratio for LTB, $f_{\mathrm{m,k}}$ is the characteristic bending strength, $\sigma_{\mathrm{m,y,cr}}$ is the critical LTB stress, $M_{\mathrm{y,cr}}$ is the critical bending moment for LTB, $E_{0,\mathrm{k}}$ and $G_{0,\mathrm{k}}$ are the characteristic elastic and shear moduli in grain direction, I_{x} and I_{y} are the moments of inertia according to Equations (2.18) and (2.4), and $L_{\mathrm{m,ef}}$ is the effective LTB length. In contrast to the k_{c}-method, it is not differentiated between SL and GL.

Leicester [117] briefly discussed that for slender beams, the nonlinear interaction with exponent 2 at the $M_{\mathrm{y,1}}$ component in Equation (2.61) can be assumed. This corresponds to the $N_{\mathrm{x,c}}$-$M_{\mathrm{y,1}}$-interaction of the critical LTB load in Equation (2.13). The analytical derivation of Equation (2.61) is discussed in more detail in Section 4.3. In few numerical investigations, Eggen [43] confirmed the nonlinearity of the $N_{\mathrm{x,c}}$-$M_{\mathrm{y,1}}$-interaction for LTB, see Section 2.2.2.1 and Figure 2.14.

The origin of Equation (2.62) for calculating the k_{m}-factor was unclear to the author. The first known mentioning was in the Finnish timber code from 1978, see Suomen rakentamismääräyskokoelma B 10 [151]. Heimeshoff [86] demonstrated that for H/B ratios of 4 and 10 and bow imperfections of $e_{\mathrm{y}} = L/288$ and $L/577$, Equation (2.62) is a reasonable approximation of design with calculations using T2O, which was confirmed by Schänzlin [139], see Figure 2.15. Nonetheless, the k_{m}-factor in Equation (2.62) only partially covers the influence of the H/B ratio, material properties, and imperfections, see also Section 2.2.1.8.

Effects of load-eccentricities are not included in the k_{m}-method and should be considered additionally.

2.6.2.2 ULS design for shear

2.6.2.2.1 Imperfection-sensitive members with geometrically nonlinear calculation of internal forces

There is no explicit advice for the shear design of imperfection-sensitive (slender) members with geometrically nonlinear calculation of internal forces in EN 1995-1-1 [57].

Relevant shear stresses can occur due to shear forces and torsional moments. The additional torsional moments due to LTB need to be considered, see, e.g. Equation (2.14).

For rectangular cross-sections, the following should be satisfied for shear stresses from torsion according to EN 1995-1-1 [57] 6.1.8:

$$\tau_{\mathrm{tor,d}} \leq k_{\mathrm{shape}} f_{\mathrm{v,d}} \quad , \tag{2.65}$$

with

$$k_{\mathrm{shape}} = \min \begin{cases} 1 + 0.05 \cdot \frac{H}{B} & , \\ 1.3 & , \end{cases} \tag{2.66}$$

where $\tau_{\mathrm{tor,d}}$ is the design shear stress from torsion, k_{shape} is the factor for considering the effect of the shape of the cross-section, $f_{\mathrm{v,d}}$ is the design shear strength in grain direction, and H and B are the cross-sectional height and width.

Design for shear from shear forces should be carried out according to EN 1995-1-1 [57] 6.1.7. No interaction of shear stresses from torsion and shear forces is considered.

2.6.2.2.2 Imperfection-sensitive members with geometrically linear calculation of internal forces

There is no advice in EN 1995-1-1 [57] on the shear design of members with torsional moments due to geometrically nonlinear behaviour, i.e. LTB.

2.6.2.3 SLS design

A SLS design that considers the geometrically nonlinear deformations is not possible with the k_{c}- and the k_{m}-method as the deformations remain unknown.

With geometrically nonlinear calculations, a SLS design can be conducted by limiting the instantaneous and long-term bending deformations. No equations for determining the geometrically nonlinear deformations are given.

2.6.3 DIN EN 1995-1-1:2013/NA

2.6.3.1 General

DIN EN 1995-1-1/NA [40] NCI NA.5.7 (NA.1) allows to determine internal forces with calculations using T1O if the geometrically nonlinear behaviour would increase the internal forces by less than 10%. In this case, design may be conducted according to Section 2.6.2.1.1, and a reduction in load-bearing capacity due to flexural buckling or LTB may be neglected.

According to DIN EN 1995-1-1/NA [40] NCI NA.5.9 (NA.1), the influence of creep should be considered for compression members in SC 2 and 3 if the design value of the permanent and quasi-permanent action is more than 70% of the total action. In this case, creep may be taken into account by reducing the stiffness by the factor $1/(1 + k_{\mathrm{def}})$.
The background on this limit criterion was discussed by Hartnack and Rautenstrauch [85] who proposed limits of 75% for SC 2 and 50% for SC 3. The discussions between these values and the chosen limit of 70% in DIN EN 1995-1-1/NA [40] were unknown to the author.

2.6.3.2 ULS design for bending

For GL, the product of the elastic modulus and the shear modulus $E_{0,\mathrm{k}}G_{0,\mathrm{k}}$ in Equation (2.64) may be increased by a factor of 1.4 according to DIN EN 1995-1-1/NA [40] NCI Zu 6.3.3 (2).
Blaß [11] conducted investigations on the product E_0G_0 of softwood GL beams with the *Karlsruher Rechenmodell*, see Section 2.7.2. He found 5% quantile values of the product E_0G_0, which were 5% to 10% below the product of the mean values $E_{0,\mathrm{mean}}G_{0,\mathrm{mean}}$. As the positive influences of torsional warping, see, e.g. Hörsting [90], and the increase of bending strength at edgewise bending are neglected in the k_{m}-method, see Section 2.6.2.1.4, he concluded that the product of the mean values $E_{0,\mathrm{mean}}G_{0,\mathrm{mean}}$ can be used in Equation (2.64) for calculating the critical bending moment at LTB in the k_{m}-method. This is similar to increasing $E_{0,\mathrm{k}}G_{0,\mathrm{k}}$ by $1.4 \approx 1.2 \cdot 1.2$, as $E_{0,\mathrm{mean}} \approx 1.2E_{0,\mathrm{k}}$ and $G_{0,\mathrm{mean}} \approx 1.2G_{0,\mathrm{k}}$ according to DIN EN 1995-1-1/NA [40] and EN 14080 [54].
Similar investigations supplemented by experimental results were conducted by Brandner et al. [19] who proposed a factor of $1.3 = 0.9 \cdot 1.2 \cdot 1.2$ for increasing the product $E_{0,\mathrm{k}}G_{0,\mathrm{k}}$.

DIN EN 1995-1-1/NA [40] provides Equations (2.67) and (2.68) for $N_{\mathrm{x,c}}$-$M_{\mathrm{y},1}$-$M_{\mathrm{z},1}$-interaction:

$$\frac{N_{\mathrm{x,c,d}}}{k_{\mathrm{c,y}}Af_{\mathrm{c,0,d}}} + \frac{M_{\mathrm{y},1,\mathrm{d}}}{k_{\mathrm{m}}W_{\mathrm{y}}f_{\mathrm{m,y,d}}} + \left(\frac{M_{\mathrm{z},1,\mathrm{d}}}{W_{\mathrm{z}}f_{\mathrm{m,z,d}}}\right)^2 \leq 1.0 \quad , \tag{2.67}$$

$$\frac{N_{\mathrm{x,c,d}}}{k_{\mathrm{c,z}}Af_{\mathrm{c,0,d}}} + \left(\frac{M_{\mathrm{y},1,\mathrm{d}}}{k_{\mathrm{m}}W_{\mathrm{y}}f_{\mathrm{m,y,d}}}\right)^2 + \frac{M_{\mathrm{z},1,\mathrm{d}}}{W_{\mathrm{z}}f_{\mathrm{m,z,d}}} \leq 1.0 \quad , \tag{2.68}$$

where $N_{\mathrm{x,c,d}}$ is the design axial compressive force, $k_{\mathrm{c,y/z}}$ are the relative flexural buckling

load-bearing capacities about the y- or z-axis according to Equation (2.58), A is the cross-sectional area, $f_{c,0,d}$ is the design compressive strength, $M_{y/z,1,d}$ are the design bending moments about the y- or z-axis according to geometrically linear calculations, k_m is the relative LTB load-bearing capacity, $W_{y/z}$ are the section moduli about the y- or z-axis, and $f_{m,y/z,d}$ are the design bending strengths about the y- or z-axis.
Equation (2.67) is mechanically not reasonable as flexural buckling about the z-axis cannot occur together with LTB, see Figure 2.1. Therefore, it should not be applied for design.

2.6.3.3 ULS design for shear

According to DIN EN 1995-1-1/NA [40] NCI NA.6.1.9 (NA.1), the following should be satisfied for combined shear stresses from torsion and shear forces:

$$\frac{\tau_{tor,d}}{k_{shape} f_{v,d}} + \left(\frac{\tau_{y,d}}{f_{v,d}}\right)^2 + \left(\frac{\tau_{z,d}}{f_{v,d}}\right)^2 \leq 1.0 \quad , \tag{2.69}$$

where $\tau_{tor,d}$ is the design shear stress from torsion, k_{shape} is the factor for considering the effect of the shape of the cross-section according to Equation (2.66), $f_{v,d}$ is the design shear strength in grain direction, and $\tau_{y/z,d}$ are the design shear stresses from shear forces in y- and z-direction.

DIN EN 1995-1-1/NA [40] NCI to 9.2.5.3 (NA.4) allows to neglect shear stresses from torsion if conducing the cross-sectional design of members at the fork supports if the slenderness fulfils following requirement:

$$\lambda_{ef} = \frac{L_{ef} H}{B^2} \leq 225 \quad , \tag{2.70}$$

where L is the effective LTB length, H is the cross-sectional height, and B is the cross-sectional width.
According to R. Hofmann (personal communication, September 25, 2024), this limit criterion was proposed during the discussions of DIN EN 1995-1-1/NA [40]. For common softwood GL grades and H/B ratios larger than 4, the criterion $\lambda_{ef} \leq 225$ is similar to $\lambda_{m,rel} \leq 0.90$, which yields $k_m \geq 0.89$, see Equation (2.62). Therefore, the geometrically nonlinear effects and the additional torsional moments $M_{x,2}$ are small. Since no cases of damage were known, the limit criterion in Equation (2.70) was introduced for facilitating an economic design. No publications on this were known.

2.6.3.4 SLS design

DIN EN 1995-1-1/NA [40] NDP to 7.2 (2) recommends bending deformation limits.

2.6.4 FprEN 1995-1-1:2024

2.6.4.1 ULS design for bending and compression

2.6.4.1.1 General

The design in FprEN 1995-1-1 [69] is identical to EN 1995-1-1 [57], see Section 2.6.2.1.1.

2.6.4.1.2 Imperfection-sensitive members with geometrically nonlinear calculation of internal forces

The design of imperfection-sensitive members with geometrically nonlinear calculation of internal forces in FprEN 1995-1-1 [69] is basically identical to EN 1995-1-1 [57], see Section 2.6.2.1.2. However, FprEN 1995-1-1 [69] also provides explicit rules for such design.

FprEN 1995-1-1 [69] explicitly names geometrical nonlinear calculation of moments with numerical, computational, or analytical methods for stability verification in clause 8.2.1 (2). Equations for analytical calculations using T2O are given in FprEN 1995-1-1 [69] Annex B.4. These represent a more general formulation of Equations (2.1) to (2.5) and Equations (2.14) to (2.18). For analysis on member level without the possibility of load redistribution, lower 5% fractile values of stiffnesses should be assumed according to FprEN 1995-1-1 [69] 7.2.2 (1). Similarly to DIN EN 1995-1-1/NA [40], see Section 2.6.3.1, the geometrically nonlinear behaviour may be neglected if it increases results of calculations using T1O by 10% or less, see FprEN 1995-1-1 [69] 7.3.3 (2).
Likewise DIN EN 1995-1-1/NA [40], see Section 2.6.3.1, the influence of creep should be considered for single columns and beams if the design value of the permanent and quasi-permanent action is more than 70% of the total action by reducing the stiffness by the factor $1/(1 + k_{\mathrm{def}})$. However, this is mistakenly also applied to SC 1, and not only to SC 2 and 3, which will hopefully be corrected in the final version of the standard. As an alternative approach to the reduction of stiffness properties by $(1 + k_{\mathrm{def}})$, creep may be considered by increasing the imperfections according to FprEN 1995-1-1 [69] Annex B.4.6. The latter approach is based on the investigations by Abeysekera et al. [2], see also Section 2.5.2.

FprEN 1995-1-1 [69] 7.4.1 provides with Equations (2.71) to (2.73) values for equivalent bow imperfections $e_{\mathrm{y/z}}$, twist imperfections e_{θ}, and sway imperfections e_{ϕ}, which cover the effects of geometrical and structural imperfections. Effects of (un)planned load-eccentricities are not included in these values according to FprEN 1995-1-1 [69] 7.3.2 (1) Note 2.

$$e_{\mathrm{y/z}} = \begin{cases} \frac{L}{400} & \text{for SL} \quad , \\ \frac{L}{1000} & \text{for GL and LVL} \quad , \end{cases} \tag{2.71}$$

$$e_{\theta,\mathrm{mid}} = \frac{L}{1500 H_{\mathrm{ap}}} \quad , \tag{2.72}$$

$$e_{\theta,\mathrm{supp}} = \begin{cases} \frac{1}{150} & \text{for} \quad \text{fork support with small tolerances} \quad , \\ \frac{1}{100} & \text{for} \quad \text{fork support with large tolerances} \quad , \end{cases} \tag{2.73}$$

where L is the effective length or the real length of a member, whichever is decisive for the design, and H_{ap} is the height of the beam at the apex.
For simplification, instead of assuming twist imperfections both at midspan and at the fork supports, only a twist imperfection at midspan with the following magnitude may be assumed according to FprEN 1995-1-1 [69] 7.4.1 (6):

$$e_{\theta,\mathrm{max}} = 0.5 \cdot (e_{\theta,\mathrm{mid}} + e_{\theta,\mathrm{supp}}) \quad , \tag{2.74}$$

where $e_{\theta,\mathrm{mid}}$ is the twist imperfection at midspan according to Equation (2.72), and $e_{\theta,\mathrm{supp}}$ is the twist imperfection at the fork supports according to Equation (2.73).
For further simplification, for beams with $H < L/15$, the following equivalent bow imperfection of the upper edge may be assumed according to FprEN 1995-1-1 [69] 7.4.1 (8):

$$e_{\mathrm{y,ef}} = \begin{cases} \frac{L}{550} & \text{for} \quad \text{fork support with small tolerances} \quad , \\ \frac{L}{500} & \text{for} \quad \text{fork support with large tolerances} \quad . \end{cases} \tag{2.75}$$

For the sway imperfections, the same values as in EN 1995-1-1 [57] are recommended, see Equation (2.53).
The twist imperfections are based on the investigations presented in this thesis, see Sections 3.2 and 6.3. The bow imperfections are based on the investigations by Blaß [8] on softwood SL and GL columns, on the investigations by Kessel et al. [98] on nail plate trusses, and on the investigations presented in this thesis on GL and LVL beams and columns, see Sections 3.2 and 6.3.

As an alternative to equivalent geometrical imperfections, equivalent actions may be applied according to FprEN 1995-1-1 [69] 7.4.2 (1).

2.6.4.1.3 Imperfection-sensitive columns with geometrically linear calculation of internal forces (k_c-method)

The design of imperfection-sensitive columns with geometrically linear calculation of internal forces in FprEN 1995-1-1 [69] is identical to EN 1995-1-1 [57], see Section 2.6.2.1.3. The only difference is that Equation (2.76) for direct calculation of β_c is given instead of the fixed β_c values defined in EN 1995-1-1 [57].

$$\beta_{\mathrm{c,y/z}} = \frac{e_{\mathrm{z/y}}}{L} \cdot \pi \cdot \sqrt{\frac{3E_{0,\mathrm{k}}}{f_{\mathrm{c,0,k}}}} \cdot \frac{f_{\mathrm{c,0,k}}}{f_{\mathrm{m,y/z,k}}} \quad , \tag{2.76}$$

where $e_{z/y}$ is the equivalent bow imperfection in z- or y-direction according to Equation (2.71), L is the effective length or the real length of a member, whichever is decisive for the design, $E_{0,k}$ is the characteristic elastic modulus in grain direction, $f_{c,0,k}$ is the characteristic compressive strength in grain direction, and $f_{m,y/z,k}$ is the characteristic bending strength about the y- or z-axis.
Equation (2.76) represents the exact solution of design with calculations using T2O and linear elastic material behaviour as demonstrated by Schänzlin [137], see also Section 2.2.1.8 and Annex C. In contrast to the fixed β_c values defined in EN 1995-1-1 [57], see Section 2.6.2.1.3, Equation (2.76) does not account for the effects of plasticising, see discussions in Section 2.2.2.8, Blaß [9], Taras [153], and Zahn and Rammer [185].

2.6.4.1.4 Imperfection-sensitive beam-columns with geometrically linear calculation of internal forces (k_m-method)

In FprEN 1995-1-1 [69], a new set of regression functions is given for the k_m-method. Beams and beam-columns with $\lambda_{m,rel} > 0.55$ should be treated as imperfection-sensitive and be designed for LTB (additionally to design according to Equations (2.50) and (2.51)).

For LTB of members with combined bending and axial compression, the following should be satisfied according to FprEN 1995-1-1 [69] 8.2.2.3:

$$\frac{N_{x,c,d}}{k_{c,z} A f_{c,0,d}} + \left(\frac{M_{y,1,d}}{k_m W_y f_{m,y,d}}\right)^2 + k_{red} \cdot \frac{M_{z,1,d}}{W_z f_{m,z,d}} \leq 1.0 \quad , \tag{2.77}$$

with

$$k_m = \frac{1}{\phi_m + \sqrt{\phi_m^2 - \lambda_{m,rel}^2}} \quad , \tag{2.78}$$

$$\phi_m = 0.5 \cdot (1 + \beta_\theta + \beta_m \cdot (\lambda_{m,rel} - 0.55) + \lambda_{m,rel}^2) \quad , \tag{2.79}$$

$$\lambda_{m,rel} = \sqrt{\frac{f_{m,y,k} W_y}{M_{y,cr}}} \quad , \tag{2.80}$$

$$\beta_\theta = e_{\theta,mid} \cdot \frac{H}{B} \quad , \tag{2.81}$$

$$\beta_m = \frac{e_y}{L} \cdot \frac{H}{B} \cdot \frac{\pi}{2} \cdot \sqrt{\frac{E_{0,k}}{G_{0,k}}} \quad , \tag{2.82}$$

where $N_{x,c,d}$ is the design axial compressive force, $k_{c,z}$ is the relative flexural buckling load-bearing capacity for flexural buckling about the z-axis according to Equation (2.58), A is the cross-sectional area, $f_{c,0,d}$ is the design compressive strength in grain direction, $M_{y/z,1,d}$ is the design bending moment about the y- or z-axis according to geometrically linear calculations, k_m is the relative LTB load-bearing capacity, $W_{y/z}$ is the section modulus about the y- or z-axis, $f_{m,y/z,d}$ is the design bending strength about the y- or z-axis, k_{red} is a factor for considering the positive size effect on the bending strength at biaxial bending, ϕ_m is the intermediate parameter for the calculation of k_m, $\lambda_{m,rel}$ is the relative slenderness ratio for LTB, β_θ and β_m are fitting factors considering the effects of twist and bow imperfections, $M_{y,cr}$ is the critical bending moment for LTB according to Equation (2.64), $e_{\theta,mid}$ is the equivalent twist imperfection according to Equation (2.74), H and B are the cross-sectional height and width, e_y is the equivalent bow imperfection according to Equation (2.71), and $E_{0,k}$ and $G_{0,k}$ are the characteristic elastic and shear moduli in grain direction. FprEN 1995-1-1 [69] 8.1.8.1 (2) recommends $k_{red} = 0.7$ for rectangular cross-sections.
The $N_{x,c}$-$M_{y,1}$-$M_{z,1}$-interaction in Equation (2.78) is the same as in DIN EN 1995-1-1/NA [40], see Equation (2.68), except for the k_{red} factor. k_{red} was introduced for consistency with Equations (2.50), (2.54), and (2.56). There were no investigations known to the author which validated the introduction of k_{red} in Equation (2.77).
The new format of the k_m-method was derived during the drafting process of FprEN 1995-1-1 [69], see prEN 1995-1-1 [131]. Its format was chosen based on the similarity to the k_c-method and the similarity to the solution of the design equations with calculations using T2O, see prEN 1995-1-1 [131]. In contrast to the k_c-method, see Section 2.2.1.8, it is a regression function. The exact solutions discussed in Sections 2.2.2.8 and 4.5 were unknown when drafting FprEN 1995-1-1 [69]. The threshold of 0.55 in Equation (2.79) is supposed to represent the relative slenderness ratio for LTB $\lambda_{m,rel}$ at which the geometrically nonlinear effects increase the effects of actions by 10%. For determining the threshold the following equation, which represents the increase in deformations v, see Equation (2.20), was evaluated:

$$\frac{\alpha_m^2}{1-\alpha_m^2} > 0.1 \quad , \tag{2.83}$$

where α_m is the amplification factor of the bending moment due to LTB according to Equation (2.16). As demonstrated in prEN 1995-1-1 [131], Equation (2.83) can be reformulated to $\lambda_{m,rel}^4 > 0.091$ or $\lambda_{m,rel} > 0.55$.

2.6.4.2 ULS design for shear

2.6.4.2.1 Imperfection-sensitive members with geometrically nonlinear calculation of internal forces

There is no explicit advice for the shear design of imperfection-sensitive (slender) members with geometrically nonlinear calculation of internal forces in FprEN 1995-1-1 [69].

According to FprEN 1995-1-1 [69] 8.1.12 (1), the following should be satisfied for combined

shear stresses from torsion and shear forces:

$$\frac{\tau_{\mathrm{tor,d}}}{k_{\mathrm{shape}} f_{\mathrm{v,d}}} + \left(\frac{\tau_{\mathrm{xy,d}}}{k_{\mathrm{v,xy}} f_{\mathrm{v,xy,d}}}\right)^2 + \left(\frac{\tau_{\mathrm{xz,d}}}{k_{\mathrm{v,xz}} f_{\mathrm{v,xz,d}}}\right)^2 \leq 1.0 \quad , \tag{2.84}$$

where $\tau_{\mathrm{tor,d}}$ is the design shear stress from torsion, k_{shape} is the factor for considering the effect of the shape of the cross-section according to Equation (2.66), $f_{\mathrm{v,(xy/xz,)d}}$ is the respective design shear strength, $\tau_{\mathrm{xy/xz,d}}$ is the design shear stress from shear forces in y- or z-direction, and $k_{\mathrm{v,xy/xz}}$ is an adjustment factor of the shear strength.
Equations for analytical calculations of torsional moments using T2O are given in FprEN 1995-1-1 [69] Annex B.4. These represent a more general formulation of Equations (2.14) to (2.18).

Similarly to DIN EN 1995-1-1/NA [40], the shear stresses from torsion at the fork supports may be disregarded in design if the limit in Equation (2.70) is met.

2.6.4.2.2 Imperfection-sensitive members with geometrically linear calculation of internal forces

There is no advice in FprEN 1995-1-1 [69] on the shear design of members with torsional moments due to geometrically nonlinear behaviour, i.e. LTB.

2.6.4.3 SLS design

SLS design with considering the geometrically nonlinear deformations is not possible with the k_{c}- and the k_{m}-method as the deformations remain unknown.

With geometrically nonlinear calculations, a SLS design can be conducted by limiting the instantaneous and long-term bending deformations. FprEN 1995-1-1 [69] Annex B.4 gives equations for determining the geometrically nonlinear deformations.

2.6.5 Discussion and Summary

The various design methods for compression and bending of imperfection-sensitive timber members in EN 1995-1-1 [57] and DIN EN 1995-1-1/NA [40] are (i) partly inconsistent in their assumptions; (ii) some essential influencing parameters are neglected or not sufficiently taken into account; (iii) they result in load-bearing capacity jumps in the transition area between the different verifications; (iv) and some of them are insufficiently described. These deficits were recognised during the revision of FprEN 1995-1-1 [69] and were at least partially resolved.

EN 1995-1-1 [57] does not provide any information on how to perform a compression and bending design of imperfection-sensitive timber members with geometrically nonlinear internal forces. This deficit is resolved in FprEN 1995-1-1 [69], although the equations given in FprEN 1995-1-1 [69] Annex B.4 for calculating internal forces and deformations at LTB are challenging for building practice.
A major advantage of the flexural buckling and LTB verification with geometrically nonlinear internal forces is that the design method provides continuous results, most of which were validated by comprehensive experimental or numerical investigations, and enable a realistic bending design of timber members. Only by neglecting the geometric nonlinear behaviour if its influence is less than 10‰, a discontinuity is introduced.

The k_c- and k_m-methods provide simplified equations for compression and bending design at flexural buckling and LTB. While the separate k_c- and k_m-methods for pure compression or bending provide good approximations of the actual geometric nonlinear behaviour, see Figures 2.8 and 2.15, the interaction of both methods inevitably results in larger deviations from geometric nonlinear solutions, see Figure 2.35. In addition, the different interaction equations of the k_c-method and the k_m-method, see Equations (2.56), (2.57), and (2.61), lead to discontinuities in the calculated load-bearing capacities between the different design methods, see Figure 2.35.
The k_c-methods in EN 1995-1-1 [57] and FprEN 1995-1-1 [69] are almost identical and supported by extensive investigations by Blaß [9], Buchanan et al. [25], and Zahn [183]. However, the equation given in FprEN 1995-1-1 [69] for calculating β_c omits that β_c in EN 1995-1-1 [57] was calibrated by means of curve fitting to the results of numerical calculations with scattering input values and realistic stress-strain behaviour, see [9]. Thus, β_c in EN 1995-1-1 [57] also includes the effects of compressive plasticising in grain direction, which is not considered in FprEN 1995-1-1 [69]. From the comparison of geometrical imperfections and calculation results of [9] with the k_c-method in EN 1995-1-1 [57], it can be concluded that plasticising apparently has no significant influence on the load-bearing capacity of columns made of common softwoods and that in this case, neglecting plasticising is fine. For other wood products, e.g. beech GL, the more pronounced compressive plasticising can, however, have a significant influence on the load-bearing capacity and must be taken into account if determining β_c, see Ehrhart et al. [52]. Therefore, the general extension of β_c, which was derived by [9] for softwood SL and GL, to other wood products and species appears questionable. The geometrically nonlinear behaviour due to bending moments $M_{y,1,d}$ and $M_{z,1,d}$ is neglected in the k_c-method.

The nonlinear $N_{x,c}$-$M_{y,1}$-interaction in the k_m-method in EN 1995-1-1 [57], see Equation (2.61), was discussed extensively during the revision of FprEN 1995-1-1 [69] in favour of a more conservative linear interaction, see also prEN 1995-1-1 [132]. On the basis of the results of this thesis, the more favourable nonlinear interaction could be kept.
The k_m-method in EN 1995-1-1 [57], Equation (2.62) is a regression model that is not fully considering all relevant parameters. Therefore, it was replaced in FprEN 1995-1-1 [69] by a regression model that better takes into account the relevant parameters. The exact solution discussed in Sections 2.2.2.8 and 4.5 was not known when FprEN 1995-1-1 [69] was drafted. The decrease of the limit value for considering LTB from 0.75 in EN 1995-1-1 [57] to 0.55 in FprEN 1995-1-1 [69] leads in building practice to significantly more cases where the more complex LTB verifications have to be carried out. The limit value of 0.55 was not derived on the basis of the new equivalent geometrical imperfections and T2O equations in FprEN 1995-1-1 [69], but rather on a simplified estimation of the geometrically nonlinear behaviour using Equation (2.83). However, this does not accurately reflect the reduction in load-bearing capacity due to geometrically non-linear behaviour since the influence of imperfections is neglected, see also Equation (2.15). This tightening of the verification by reducing the limit value seems all the more astonishing since no damage cases were known that would justify such a tightening.
The introduction of this k_{red} factor in the k_m-method in FprEN 1995-1-1 [69], see Equation (2.77), is questionable, as no investigations were known that would have supported it.

The equivalent bow imperfection of softwood GL given in EN 1995-1-1 [57] for geometrically

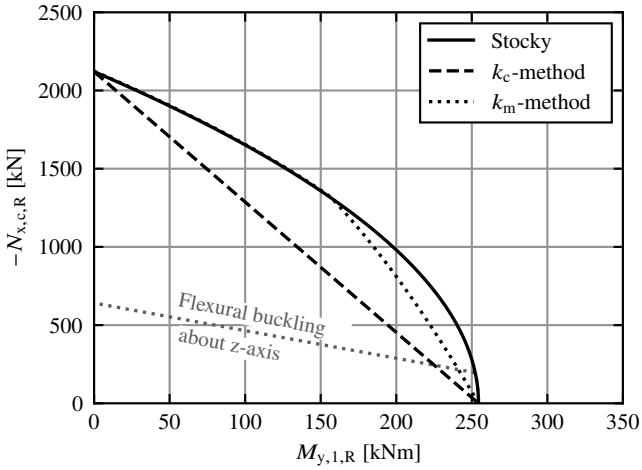

Figure 2.35: Compressive load-bearing capacity $N_{x,c,R}$ with combined axial compression and bending plotted over the bending load-bearing capacity $M_{y,1,R}$; beam-columns made of GL 24h with $\lambda_{c,z,rel} = 0.30$ and $\lambda_{m,rel} = 0.75$; stocky beams without the k_c- or k_m-method, k_c-method for flexural buckling about the y-axis, and k_m-method according to EN 1995-1-1 [57]; k_c-method for flexural buckling about the z-axis separately added.

nonlinear analyses, $L/400$, is inconsistent with the bow imperfections that are included in the flexural buckling design with the k_c-method, $\approx L/1000$ to $\approx L/750$, and LTB design with the k_m-method, $L/288$ to $L/577$. In addition, the k_c-method differentiates between SL and GL, but this differentiation is not available for geometrically non-linear calculations and the k_m-method. Thus, the actually more accurate geometrically nonlinear calculations provide lower load-bearing capacities for GL columns than the simplified k_c-method.
Furthermore, EN 1995-1-1 [57] does not specify any twist imperfections of beams, although these can occur in building practice, see Dietsch and Henke [34].
These deficits were resolved in FprEN 1995-1-1 [69] on the basis of the research presented in this thesis, and (i) separate values for bow and twist imperfections are given, which (ii) are to be applied equally to geometrically nonlinear calculations and the simplified k_c/k_m-methods.

The verification of torsional shear stresses from LTB is not mentioned in EN 1995-1-1 [57]. DIN EN 1995-1-1/NA [40] and FprEN 1995-1-1 [69] specify a limit criterion by which this can be neglected. Deviating from the standards, this limit criterion should not be applied for materials with significantly different ratios of $E_{0,k}$ to $G_{0,k}$ to $f_{m,k}$ than softwood GL, like beech LVL GL75 according to ETA-14/0354 [63]. In FprEN 1995-1-1 [69] Annex B.4, equations for calculating the torsional moment are given, but these are hardly suitable for building practice. Due to insufficient rules in the standards, it can be assumed that the verification of torsional shear stresses from LTB is generally not carried out in practice, even if shear failure can be decisive for LTB; see Wilden et al. [176] and Xiao [178].

The following research questions emerged for imperfection-sensitive timber members from this discussion of the standards: (i) a user-friendly description of the bending design with geometric nonlinear calculations; (ii) a description of the shear design with torsional stresses due to LTB; (iii) the reduction of discontinuities in the load-bearing capacities between the various simplified design methods; (iv) the validation of the nonlinear $N_{x,c}$-$M_{y,1}$-interaction of the k_c-k_m-method; (v) the specification of a complete set of equivalent geometrical imperfections and their consistent implementation in the different design methods; (vi) the provision of mechanically derived equations of the k_m-method; and (vii) the validation of the design methods for wood-based products and materials other than softwood SL and GL.

2.7 Models considering scattering material parameters

2.7.1 General

The mechanical properties of timber and the industrial timber products made from it substantially depend on random and systematic influences, see, e.g. Glos [77]. These influences manifest themselves in the natural growth phase of trees and during industrial processing into finished timber products and lead to scattering of the mechanical properties within and between timber members. Influences arising from the further utilisation of products after manufacturing, e.g. during assembly and service life, are not considered in this section.
According to [77], the growth conditions shape the microscopic and macroscopic structure of a tree. Relevant macroscopic properties for the stiffness and strength of softwoods are:

- the density, which depends, among other things, on
- the annual ring width and
- the proportion of late and early wood.

Altogether, these three parameters describe the cell wall proportion and thus the proportion of load-bearing structure of wood. Although microfibril angle and spiral growth are usually not measured in building practice, they significantly influence the mechanical properties of wood, according to Ormarsson and Cown [126].
According to [77] and Schänzlin [138], growth irregularities that significantly influence the mechanical properties are:

- structural defects such as knots, deviations in fibre angle, compression wood, etc.,
- shape deformations such as severe tapering, crookedness, etc.,
- mechanically caused defects such as cracks from growth, shrinkage, frost, etc.,
- biologically destructive influences such as fungal and insect defects.

[77] described the following additional influences that occur during industrial processing:

- the cross-sectional dimensions of the board, e.g. reduced due to wane,
- the annual ring pattern in the cross-section of the board,
- the angle of the grain to the longitudinal axis of the board and
- the finger joints.

Through grading during industrial processing, shape deformations, cracks, and biologically destructive influences are largely excluded. Hence, the influence of the cell wall proportion (represented by the density, the microfibril angle, and spiral growth), structural defects, and influences from industrial processing need to be discussed subsequently. Scattering of the cross-section dimensions is usually negligibly small, see Blaß [9] and Section 2.2.3.

As an example, according to Glos [77], the scattering of the dry density of softwood GL, see Figure 2.36, leads to significant scatter in the stress-strain relationship for compression in grain direction, see Figure 2.37. The scatter in the stress-strain relationships for compression and tension in grain direction, in turn, causes significant scattering of the bending strength of softwood GL beams, according to Frese [74], see Figure 2.38. In addition, for imperfection-sensitive timber beam-columns, the deviation of the position of the shear centre from the member axis, see Figures 2.39 and 2.40, due to the scattering of the stiffness over the cross-section needs to be considered, see, e.g. Theiler [154].

The mechanical properties of timber, the scattering of which can have a significant influence on the load-bearing capacities of imperfection-sensitive timber members, are indicated by Equations (2.1) to (2.5) and (2.15) to (2.18) and are:

a. stress-strain relationships in tension and compression in grain direction,

b. stress-strain relationships in shear in the LR- and LT-planes,

c. distance of member axis and shear centre in y-direction y_{sc},

d. distance of member axis and shear centre in z-direction z_{sc}, see Figure 2.40.

Whereby the influence of the strengths and stiffnesses from a. and b. on flexural buckling and LTB is obvious, the influence of c. and d. is included in the imperfection assumptions in Equations (2.1), (2.14), and (2.15) and is also known by the term *structural imperfections*, see Section 2.2.3.3.
Comprehensive experimental investigations for describing the scattering of the mechanical properties of softwood as a function of the discussed random and systematic influences

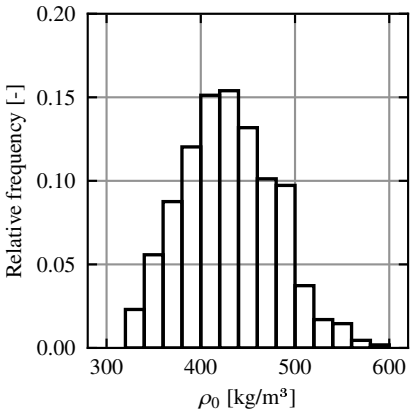

Figure 2.36: Frequency distribution of the dry density ρ_0 of 820 softwood boards; from Glos [77].

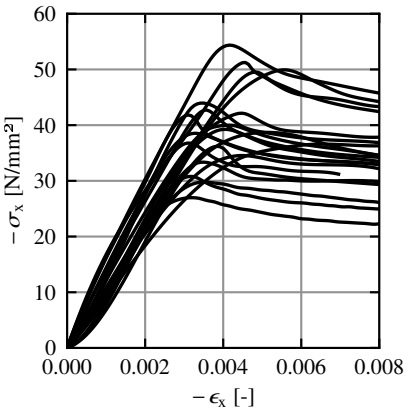

Figure 2.37: Experimentally determined stress-strain curves for compression in grain direction of 20 softwood boards; from Glos [77].

were performed, among others, by Burger [26], Colling [30], Ehlbeck and Blaß [44], Fink [64], Glos [77], Görlacher [80], Görlacher and Kürth [81], Sieder and Brandner [146], and Spengler [148].
Ehlbeck et al. [47], [64], and [146] developed various models for softwood GL that consider the scattering of a. and thus implicitly also of d. on the basis of the decisive random and systematic influences.

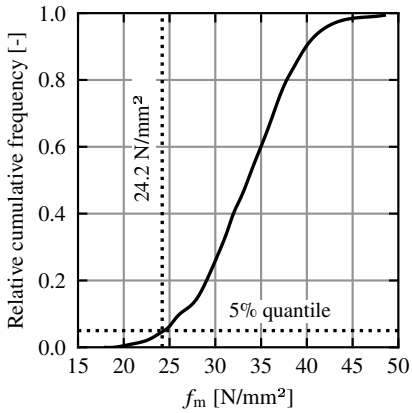

Figure 2.38: Cumulative frequency of the bending strength f_m of softwood GL beams from 1000 computations for visual grading VIS-2; from Frese [74].

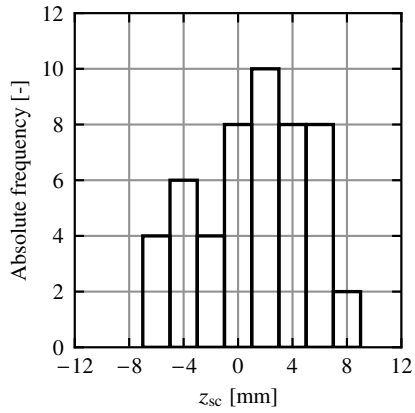

Figure 2.39: Histogram of the position of the shear centre $z_{sc} \triangleq$ structural imperfections of 50 column test specimen made of GL 24h and GL 32h; with L = 1400 mm to 3200 mm and H = 160 mm; from Theiler [154].

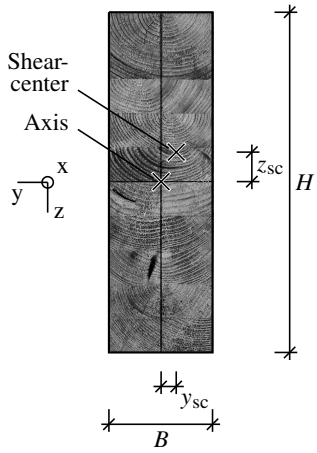

Figure 2.40: Cross-section of a GL beam with imperfect position of the shear centre due to scattering material properties.

Models for taking into account scattering shear strengths and shear moduli of softwood GL, b., were presented by Blaß [11] and Brüninghoff and Klapp [21]. [81] and [148] reported on experimental results of scattering shear stiffnesses.
[146] developed a model for split boards in softwood GL that could possibly be adapted for c.. However, due to the required mesh density and the available computing capacities, it was not suitable for stochastic numerical investigations of imperfection-sensitive timber members. Dahlblom et al. [32], Johansson [93], Kollmann and Côté [103], Ormarsson and Cown [126], and Steffen et al. [149], however, provided experimental results that can be used to derive such a model.

Thus, there was no model known that could take into account the scatter of a., b., c., and d. for softwood GL, which are relevant for the load-bearing capacity of imperfection-sensitive timber members. Since the so-called *Karlsruher Rechenmodell*, which was developed by, among others, Ehlbeck et al. [47], was calibrated for softwood GL, allowed for an easy implementation in the FE model applied in this thesis, was the benchmark for GL strength models, considers a. and d., and could be extended by b. and c., it was chosen as the basis for the numerical modelling of the material scattering in this thesis. The model is described in more detail in Sections 2.7.2 and 5.3.3.

Furthermore, the models for taking into account scattering shear strengths and scattering shear moduli by Blaß [11] and Brüninghoff and Klapp [21] are presented in Section 2.7.3. In addition, the experimental results of Glos and Denzler [79], Görlacher and Kürth [81] and Spengler [148] on scattering shear strengths and stiffnesses are discussed. Based on these, the *Karlsruher Rechenmodell* was extended by b. in this thesis.

Subsequently, the experimental and numerical results obtained by Dahlblom et al. [32], Johansson [93], Ormarsson and Cown [126], and Steffen et al. [149] on scattering stiffnesses over the cross-section are discussed in Section 2.7.4 Based on these, the *Karlsruher Rechenmodell* was extended by c. in this thesis.

2.7.2 Karlsruher Rechenmodell for softwood GL

The *Karlsruher RechenModell* (KaReMo) was developed for conducting numerical experiments to determine the uniaxial bending load-bearing capacity $M_{y,R}$ of GL beams, taking into account the scattering mechanical properties of timber based on the decisive random and systematic influences. The model was first presented by Ehlbeck et al. [47] and was further developed over the last decades, among others, by Ehlbeck and Colling [45], Blaß et al. [14], up to Frese [74]. The investigations by Glos [77], [78] were the starting point. In this section, the parts of the most recent published version of the *KaReMo* that are relevant for this thesis are described on the basis of the literature.

In the model, the GL beams are divided into 30 mm high lamellas, which in turn are divided into 150 mm long cells, see Figure 2.41 and Frese [74]. The lamellas are separated by the finger joints into individual boards.

According to Frese [74], if the decisive random and systematic influences, (i) the dry density ρ_0; (ii) the knot area ratio $tKAR$ of the individual cells; (iii) the wood moisture content u; and (iv) the location of the finger joints are known, each cell can be assigned tensile and compressive strengths and elastic moduli in grain direction by means of regression equations. Influences that cannot be covered by the regression equations can be taken into account by means of residual scatter / residuals / error terms. If this is implemented in a numerical model, experiments can be recalculated with it. [74]
Alternatively, stochastic investigations of the load-bearing behaviour of GL members can be carried out with a numerical model based on [74] by means of scattering random and systematic influences, i.e. numerical Monte Carlo simulations. For these numerical calculations, an endless lamella with scattering random and systematic influences is simulated. First, the position of the finger joints in the endless lamella is randomly determined based on an assumed statistical distribution. Then, each board is randomly assigned a dry density ρ_0, and, in addition, each cell is randomly assigned a knot area ratio KAR based on statistical distributions. Thus, the dry density is assumed to be constant in a board, while the knot area ratio varies from cell to cell. For cells with finger joints, the lower dry density of the two adjacent boards is used, and KAR is set to zero. Due to technical drying, a constant value of the wood moisture content u is assumed over the endless lamella. The endless lamella generated in this way is divided into individual lamellas, which are assembled to form GL beams, see Figure 2.41. According to Blaß [9], several columns are usually cut out of a longer member. The properties of adjacent lamellas of a column are thus statistically independent. For GL beams, this may not apply depending on the production process and the member length.

Larsen [112] found a mean value of the distance between the finger joints or the length of the board to be between 4.50 m and 4.62 m with a standard deviation of 0.67 m to 0.71 m. For the *KaReMo*, Blaß et al. [14] chose a normal distribution with $N(4500, 700^2)$ in mm. Grading has a decisive influence on dry density and knot area ratio. Various visual and

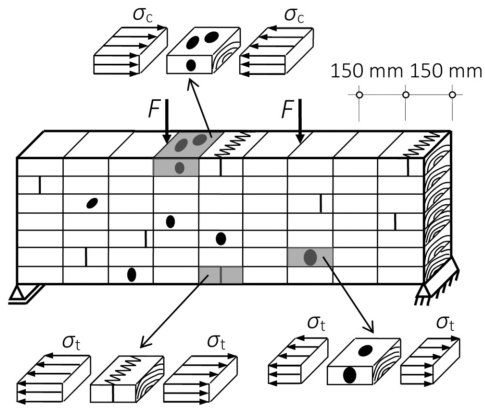

Figure 2.41: GL beam with bending, discretised for the *KaReMo*, and selected idealised stress conditions; from Frese [74].

mechanical grading methods for boards were discussed by [14]. Since lamellas for GL 24h can be graded with the visual grading VIS-2 according to Frese [74], this is applied in the following.
The dry density can be assumed to be constant over the length of a board, according to Ehlbeck et al. [47]. For the dry density, [14] picked a random value for each board from the beta distribution for VIS-2 with $\beta(424, 51.5^2)$ in kg/m^3.
For the knottiness, the definition as knot area ratio KAR and the model of Görlacher [80] are employed. According to [14] and [80], first the largest KAR value per board is determined by drawing a random value from the beta distribution for VIS-2, see [14], with $\beta(0.262, 0.093^2)$. The next smaller KAR value is determined based on the next larger KAR value in the same board, where

$$KAR_{i+1} = K_i \cdot KAR_i \quad , \tag{2.85}$$

where KAR_{i+1} is the next smaller KAR value, K_i is randomly assigned based on a beta distribution with parameters $\alpha = 7.796$, $\beta = 1.14$ according to [14], and KAR_i is the next larger KAR value. The calculation according to Equation (2.85) is repeated as long as $KAR_i \geq 0.05$. Finally, the knot area ratios determined in this way are randomly distributed among the cells of a board. Cells with finger joints are excluded from this, and $KAR = 0$ applies. This model results in 2/3 of the cells of the endless lamella containing no knots and 1/3 of the cells containing knots, i.e. $KAR \geq 0.05$.

According to Frese [74], the regression Equations (2.86) to (2.93) can be used to determine the stiffnesses and strengths for tension and compression in grain direction for each cell for which the wood moisture content, dry density, and knottiness are known. The subscript j indicates the regression equations for cells with finger joints.

$$\begin{aligned} \ln(E_{c,0,el}) = {} & 8.22 + 3.19 \cdot 10^{-3} \cdot \rho_0 - 0.602 \cdot KAR \\ & - 1.36 \cdot 10^{-6} \cdot \rho_0 \cdot u^2 - 1.10 \cdot 10^{-3} \cdot KAR \cdot u^2 + e \end{aligned} \tag{2.86}$$

$$\ln(-f_{c,0}) = 3.23 + 2.80 \cdot 10^{-3} \cdot \rho_0 - 0.825 \cdot KAR - 0.0537 \cdot u + e \tag{2.87}$$

$$\ln(E_{t,0,el}) = 8.20 + 3.13 \cdot 10^{-3} \cdot \rho_0 - 1.17 \cdot KAR + e \tag{2.88}$$

$$\ln(f_{t,0}) = -4.22 + \ln(E_t) \cdot (0.876 - 0.093 \cdot KAR) + e \tag{2.89}$$

$$\ln(E_{c,j,0,el}) = 8.43 + 2.53 \cdot 10^{-3} \cdot \rho_{0,min} - 1.03 \cdot 10^{-3} \cdot u^2 + e \tag{2.90}$$

$$\begin{aligned} \ln(-f_{c,j,0}) = {} & -3.05 + 0.816 \cdot \ln(E_{c,j}) + 6.84 \cdot 10^{-6} \cdot \rho_{0,min} \cdot u^2 \\ & - 0.013 \cdot u \cdot \ln(E_{c,j}) + e \end{aligned} \tag{2.91}$$

$$\ln(E_{t,j,0,el}) = 8.407 + 2.630 \cdot 10^{-3} \cdot \rho_{0,min} + e \tag{2.92}$$

$$\ln(f_{t,j,0}) = 2.72 + 6.14 \cdot 10^{-5} \cdot E_{t,j} + e \tag{2.93}$$

where ρ_0 is the dry density in kg/m^3, KAR is the knot area ratio, u is the wood moisture content in %, and $\rho_{0,min}$ is the minimum dry density of the two adjacent boards in kg/m^3. Results are strengths and stiffnesses in N/mm^2. A scattering error term is added to the expected values of the regression equations to take into account the residual scatter that

Table 2.1: Mean values μ and standard deviations σ of error terms for spruce; from Frese [74].

	$E_{c,0,el}$	$f_{c,0}$	$E_{t,0,el}$	$f_{t,0}$	$E_{c,j,0,el}$	$f_{c,j,0}$	$E_{t,j,0,el}$	$f_{t,j,0}$
μ	0	0	$N(0, 0.160^2)$	$N(0, 0.130^2)$	0	0	0	0
σ	0.142	0.088	$N(0.078, 0.026^2)$	$N(0.1275, 0.0425^2)$	0.231	0.116	0.135	0.195

cannot be explained by the regression equations, see [44]. For the error terms, random values from normal distributions with mean values and standard deviations according to Table 2.1 are drawn for each cell. For the scattering of the error terms of $E_{t,0,el}$ and $f_{t,0}$, specific rules need to be considered according to Frese [74] due to their apparent auto-correlation within a board. In this case, the entire error e is divided into a portion per board and a portion per cell. The mean value μ of the error term per board can be drawn from a normal distribution with parameters according to Table 2.1. The standard deviation σ of the error term per board can be determined in the same way. σ is to be limited to positive values. If μ and σ were determined for a board, the error term per cell of this board can be drawn from the corresponding normal distribution. μ and σ for $E_{t,0,el}$ and $f_{t,0}$ thus vary between boards but are constant within a board.

To exclude unreasonable values for the strengths and stiffnesses of the cells, Blaß [9] limited them to:

$$2000 \leq E_{c,0,el} \leq 24{,}000 \quad \mathrm{N/mm^2} \tag{2.94}$$

$$-15 \leq f_{c,0} \leq -75 \quad \mathrm{N/mm^2} \tag{2.95}$$

$$2000 \leq E_{t,0,el} \leq 24{,}000 \quad \mathrm{N/mm^2} \tag{2.96}$$

$$0 \leq f_{t,0} \leq 100 \quad \mathrm{N/mm^2} \tag{2.97}$$

If values are outside these limits, the corresponding error terms are drawn again.

For the tensile strength of finger joints, as an alternative to Equation (2.92), (i) predefined discrete values were assumed, or (ii) the distribution function of the tensile strength of finger joints was shifted after calculating the endless lamella so that a predefined characteristic value was obtained, see Blaß et al. [14] and Frese [73].

For a simulation of strength grading of the boards that were generated in this way within the endless lamella, it can be checked whether the knot area ratio, the density, and the dynamic or static elastic modulus lie within certain limits. Limit values depending on the grading are given in Blaß et al. [14]. The static and dynamic elastic moduli are given by [14] as

$$E_{0,stat} = \frac{N}{\sum_{i=1}^{N} \frac{1}{E_{0,i}}} \quad , \tag{2.98}$$

$$E_{0,dyn} \approx \frac{E_{0,stat}}{0.95} \quad , \tag{2.99}$$

where $E_{0,\mathrm{stat}}$ is the static elastic modulus in grain direction of a board, N is the number of cells of a board, and $E_{0,\mathrm{i}}$ is the elastic modulus of a cell according to Equations (2.86), (2.88), (2.90), and (2.92), and $E_{0,\mathrm{dyn}}$ is the dynamic elastic modulus of a board.

The *KaReMo* was implemented in a two-dimensional finite element model as outlined by Frese [74]. 4-node shell elements with two degrees of freedom per node were applied. Each cell corresponded to a FE element, see Figure 2.41.
Ehlbeck et al. [47] utilised an orthotropic material model with $G_{0,\mathrm{el}} = 650$ N/mm^2, $E_{90} = 400$ N/mm^2, and Poisson's ratio $\nu_{90,0} = 0.035$ according to Neuhaus [124]. Tension in grain direction was modelled linearly elastic. For compression parallel to the grain, Blaß [9] used the approximation curve developed by Glos [77], which is similar to Figure 2.19. However, since the influence of such a realistic compressive stress-strain relationship is small for bending tests, [74] assumed a linear elastic or a bilinear elastoplastic material behaviour instead. The von Mises yield criterion was used, as the influence of stresses perpendicular to the grain was negligible for the investigated problems.
The compression and tensile elastic moduli of a cell can be determined using the regression Equations (2.86) and (2.88). For $\rho_0 = 430$ kg/m^3 and $u = 12\%$, the tensile elastic modulus is 4% larger than the compressive elastic modulus. However, if modelling wood, no distinction is usually made between the elastic moduli in tension and compression. As [74] explained, the tensile strength is crucial for the bending load-bearing capacity. Since the size of the tensile stress is affected by the tensile elastic modulus, it is of primary importance to model the tensile elastic modulus as realistically as possible. For non-single-span beam systems, [74] therefore generally selected the tensile elastic modulus for all cells. This resulted in a 2% to 3% increased bending elasticity modulus and slightly higher bending strengths.
As explained by Frese [73] and [74], during the development of the model, the tensile failure of the outermost edge lamella has emerged as the decisive criterion for member failure in beams subjected to bending. In the model, it was assumed that exceeding the tensile strength at the integration point of the decisive finite element would immediately lead to member failure. The integration points for the 4-node shell elements used are in the centre of the cell. The evaluation of the tensile stresses was thus carried out at a distance of 15 mm from the lower edge of the beam. Crack formation in internal lamellas before reaching the load-bearing capacity was allowed in the model and modelled by full plasticising of the corresponding cell. For members subjected to axial tension, the failure criterion was extended to both edge lamellas. For the modelling of compression tests, Frese et al. [75] used a limitation of the total strains to 0.5% as the failure criterion.

The model was validated by Ehlbeck et al. [47], Ehlbeck and Colling [45], and Ehlbeck and Colling [46] by means of bending tests. For this purpose, the position of the finger joints, the densities, the elastic moduli, and the knot area ratio of the test specimens were documented and reproduced in the model, see Frese [74]. Experimental and numerical load-bearing capacities determined in this way agreed very well.

Applications of the model for softwood GL for the numerical determination of (i) the bending strength were presented, among others, by Blaß et al. [14], Ehlbeck and Colling [45], and Frese [74], (ii) the flexural buckling load-bearing capacity of columns by Blaß [9],

(iii) the tensile strength by Blaß et al. [12] and Frese [74], (iv) the compressive strength by [74] and Frese et al. [75], and (v) the influence of the structural system by [74].

2.7.3 Scattering shear stiffnesses and strengths in grain direction of softwood GL

Brüninghoff and Klapp [21] presented a model for considering the influence of scattering shear strengths of boards on the shear resistance of softwood GL beams at uniaxial bending. This model is based on the results of 272 shear tests by Glos and Denzler [79] with varying knottiness, dry densities, orientations of annual rings, and occurrence of piths. With the model, the size effect on the shear strength of softwood GL beams was investigated by [21]. [21] modelled the GL lamellas with a height of 35 mm. They assigned a constant shear strength value to each board based on a normal distribution. A normal distribution with mean and characteristic values of 5.3 N/mm^2 and 3.8 N/mm^2 was utilised analogous to the results of Glos and Denzler [79] and Spengler [148]. This corresponds to a standard deviation of 0.17. They assumed that brittle failure at reaching the shear strength directly leads to member failure.
In contrast to the *KaReMo*, scattering mechanical material properties were directly determined, which implicitly cover the effects of the macroscopic structure, growth irregularities, and industrial processing.

According to Glos and Denzler [79] and Spengler [148], the shear strength increases with increasing shear modulus and increasing (dry) density. However, the influence of a shear strength increase between 0 N/mm^2 and 0.5 N/mm^2 per 100 kg/m^3 change in density is less significant in the light of the general scattering of shear strength between 3 N/mm^2 and 9 N/mm^2, see [79]. [79] also found the influence of knottiness and pith to be negligible, and [148] could not observe a correlation between the elastic modulus and shear strength. This is consistent with the observation of [79] that the material grade has no significant influence on shear strength. On the other hand, the shear strength is significantly larger for radial annual rings than for tangential annual rings, see [79] and Section 2.4.4. Due to the composition of GL, a wide variety of annual ring patterns are present within a GL member, which ruled out differentiating according to the annual ring pattern in this thesis.

On the basis of dynamic measurements on 1188 board sections with a length of 150 mm from 48 boards, Görlacher and Kürth [81] found that the ratio of the elastic modulus to the shear modulus can be described by a regression equation as

$$\frac{E_{0,\mathrm{dyn}}}{G_{\mathrm{tor,dyn}}} = 0.00112 \cdot E_{0,\mathrm{dyn}} + 5.43 \quad \text{with} \quad r = 0.66 \quad , \tag{2.100}$$

where $E_{0,\mathrm{dyn}}$ is the dynamic elastic modulus in grain direction in N/mm^2 and $G_{\mathrm{tor,dyn}}$ is the dynamic torsional shear modulus in N/mm^2. The experimental results and the regression equation are displayed in Figure 2.42. The mean value and standard deviation of the shear modulus were 666 N/mm^2 and 91.9 N/mm^2, and of the elastic modulus 13700 N/mm^2 and 2220 N/mm^2. Within boards, the standard deviations of the shear modulus and the

elastic modulus of the board sections, i.e. cells, were lower due to the growth-related autocorrelation. Thus, the standard deviation of the product $E_{0,dyn} \cdot G_{tor,dyn}$ was reduced from $2.15 \cdot 10^6$ N/mm^2 to $1.22 \cdot 10^6$ N/mm^2. Assuming normal distributions for $E_{0,dyn}$ and $G_{tor,dyn}$ with identical coefficients of variation, this results in a reduction factor of the coefficients of variation of $1.22/2.15 = 0.57$ due to the auto-correlation. On the basis of these test results, Blaß [11] derived the increase factor 1.4 of the product $E_{0,el} \cdot G_{0,el}$ for softwood GL if calculating $M_{y,cr}$, see Section 2.6.2.1.4.
The values of the torsional shear modulus were confirmed by dynamic measurements by Blaß [11] on 50 GL beams with dimensions of $600 \cdot 300 \cdot 120$ mm^3 and 1200 to $870 \cdot 456 \cdot 140$ mm^3.

Comprehensive investigations into the influence of the macroscopic structure, growth irregularities, and industrial processing on the shear stiffness of softwood GL were not known.

2.7.4 Scattering stiffnesses over the cross-section of softwood boards

The distance of the shear centre to the member axis in the y-direction y_{cs}, see Figure 2.40, depends on the variation of stiffness in the y-direction, i.e. the scattering of the elastic modulus $E_{0,el}$ and the shear modulus $G_{0,el}$ across the cross-sectional width.

Figures 2.43 and 2.44 display the dynamic elastic moduli of two board sections measured by Steffen et al. [149] with generally increasing values from pith to bark. According to Dahlblom et al. [32] and Ormarsson and Cown [126], the elastic modulus of defect-free

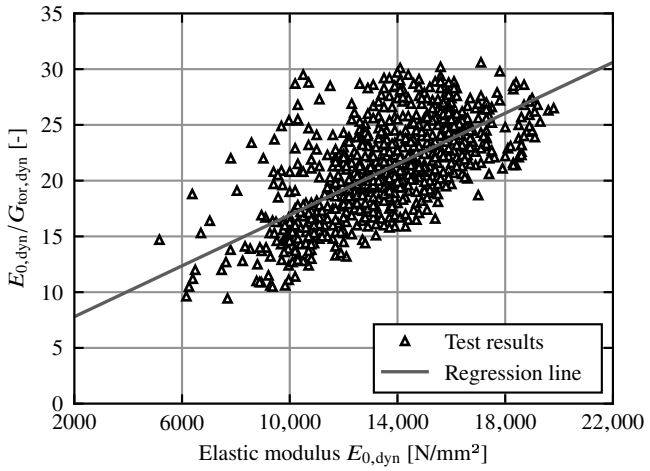

Figure 2.42: Ratio of $E_{0,dyn}/G_{tor,dyn}$ in relation to the dynamic elastic modulus $E_{0,dyn}$; from Görlacher and Kürth [81].

spruce can double from pith to bark from 7500–10,000 N/mm^2 to 15,000 N/mm^2 to 20,000 N/mm^2. Johansson [93] observed that the elastic modulus depends to a large extent on the microfibril angle and the density, and to a lesser extent on the spiral grain. The microfibril angle is halved from pith to bark from just under 30° to below 15°, see [126]. Additionally, the density increases by 0% to 50%, according to Kollmann and Côté [103], [126] and [149]. Maximum values of spiral grain occur close to the pith and rapidly decrease to the bark, see [126]. Local values of the elastic modulus $E_{0,\mathrm{el}}$ can also be significantly influenced by growth irregularities, especially knots, see [149]. [126] determined the dependence of the mean value of the local elastic modulus $E_{0,\mathrm{el,mean}}$ on the distance of the pith r to

$$E_{0,\mathrm{el,mean}} = \begin{cases} 50.58 \cdot r + 7360 & \text{for r} \leq 150 \text{ mm} \\ 15{,}000 & \text{for r} > 150 \text{ mm} \end{cases} , \tag{2.101}$$

where $E_{0,\mathrm{el,mean}}$ is the mean local elastic modulus in grain direction in N/mm^2 and r is the distance to the pith in mm. [126] found lower bounds of the local elastic modulus that were 20% below, and upper bounds that were 20% above, the mean values.

According to Ormarsson and Cown [126], a reduction of the shear modulus only occurs within the first 5 cm of the distance from the pith. From that point to the bark, the values of the shear modulus estimated by [126] using a micro-mechanical simulation model were approximately constant.

2.7.5 Summary

The load-bearing behaviour of timber members is decisively influenced by the scattering of mechanical material properties within and between members due to the natural growth and industrial processing. For imperfection-sensitive timber members, in particular the scattering of (i) the stress-strain relationships in tension, compression, and shear in grain direction over the member volume and (ii) the distance of the member axis and the shear

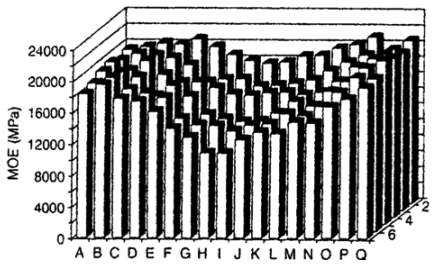

Figure 2.43: Distribution of the dynamic elastic modulus $E_{0,\mathrm{dyn}}$ in a defect-free Norway spruce section with dimensions of $67 \cdot 195$ mm^2 at a wood moisture content of 12%; pith at I-J/6; from Steffen et al. [149].

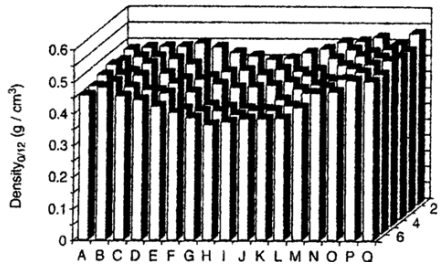

Figure 2.44: Distribution of the density ρ in a defect-free Norway spruce section with dimensions of $67 \cdot 195$ mm^2 at a wood moisture content of 12%; pith at I-J/6; from Steffen et al. [149].

centre in y- and z-directions have a significant influence on the load-bearing capacity. The stress-strain relationships directly influence the stiffness and strength and thus the flexural buckling and LTB load-bearing capacities. The position of the shear centre, on the other hand, represents the contribution of structural imperfections in the imperfection assumptions for geometrically nonlinear calculations, see, e.g. Equations (2.1), (2.14), and (2.15).
Several models were known from the literature that could represent some of these aspects separately, but none that considered the scattering of the mechanical material properties over the width of the lamella, e.g. the position of the shear centre in y-direction. Furthermore, models that simultaneously consider the scattering of the stress-strain relationships in tension and compression in grain direction and the scattering of the stress-strain relationships in shear in grain direction were not known.

2.8 Summary and discussion

The stability phenomena of bar-shaped timber members were the subject of extensive research for over a century and were also incorporated into European standardisation in the 20th century. While some aspects were the subject of in-depth investigation, numerous other aspects were only occasionally or briefly investigated.
There are comprehensive experimental investigations of the flexural buckling behaviour of softwood SL and GL columns, see Section 2.2.2. Nevertheless, only a limited number of studies were conducted on other European wood species or wood products, and no studies were known on the novel material beech LVL GL75. A variety of analytical and numerical models were developed over time, with some allowing for a more precise and others for a more simplified analysis of load-bearing behaviour and load-bearing capacity. The k_c-method recommended in EN 1995-1-1 [57] and FprEN 1995-1-1 [69] was calibrated on the basis of extensive investigations for softwood SL and GL, see Section 2.6. However, it neglects the geometrically nonlinear portion of the applied bending moments $M_{y,1,d}$ and $M_{z,1,d}$, see Section 2.6.2.1.3. Furthermore, the extension of the k_c-method to other European wood species and wood products with more pronounced compressive plasticising in the grain direction appeared to be questionable, given that this can have a significant influence on the load-bearing capacity, see Sections 2.2.1.1 and 2.6.2.1.3.
Only a few experimental investigations of the LTB load-bearing behaviour were known, even fewer on full-size softwood GL beams, and none on softwood GL beam-columns loaded by combined axial compression and bending, see Section 2.2.2. Over time, a number of analytical and numerical models were developed that facilitate a more precise or a more simplified analysis of the load-bearing behaviour and load-bearing capacity. However, some important assumptions underlying these models and their results could not be validated due to the unavailability of measurement data. For example, there were (i) no systematic measurements of the geometrical imperfections of slender timber beams, (ii) no models to estimate the influence of structural imperfections in slender timber beams, and (iii) no investigations of the influence of compressive plasticising in grain direction, see Sections 2.2.2, 2.3, and 2.4. The k_m-methods recommended in EN 1995-1-1 [57] and FprEN 1995-1-1 [69] are regression models that, in general, provide sufficiently accurate results in comparison to geometrically nonlinear calculations, see Section 2.6. During the revision of FprEN 1995-1-1 [69], the nonlinear $N_{x,c}$-$M_{y,1,d}$-interaction in the k_m-method was intensively discussed in favour of a more conservative linear interaction, see Section 2.6.4.1.4. On the basis of the results of this thesis, the more favourable nonlinear interaction could be kept. Furthermore, the unfavourable reduction of the limit value of slenderness, above which a LTB verification has to be carried out, and the favourable introduction of the k_{red} factor in FprEN 1995-1-1 [69] lack sufficient justification.
A further shortcoming of EN 1995-1-1 [57] is the lack of consistency in the imperfection assumptions, which was resolved in FprEN 1995-1-1 [69] on the basis of the investigations presented in this thesis, see Section 2.6.

The principal objectives of this thesis were therefore (i) to derive consistent approaches of imperfections for flexural buckling and LTB design of timber beam-columns and (ii) to derive a mechanically sound, consistent, and experimentally validated design concept for

flexural buckling and LTB of timber beam-columns made of softwood GL and beech LVL. For this purpose it was necessary: (i) to experimentally investigate the flexural buckling load-bearing behaviour of beech LVL columns, see Section 3.3; (ii) to experimentally investigate the LTB load-bearing behaviour of softwood GL beams, see Section 3.4; (iii) to systematically measure the geometrical imperfections of slender timber beams, see Section 3.2; (iv) to develop a model for estimating the influence of structural imperfections in slender timber beams, see Section 5.3.3; (v) to develop a parameterised numerical model, verify and validate it with experimental results, see Section 5; and (vi) to conduct parameter studies on the load-bearing behaviour of imperfection-sensitive timber beam-columns, see Section 5.6.

3 Measuring data

3.1 General

The following experimental investigations and measurements were designed to create the database for answering the research questions raised in the preceding section on the load-bearing capacities of imperfection-sensitive timber members under combined axial compression and bending. For this purpose, a comprehensive database of geometrical imperfections of softwood GL beams was created and merged with measurement data of timber beams and columns from the literature, see Section 3.2. Furthermore, the load-bearing behaviour of full-sized columns made of the innovative material beech LVL GL75 was investigated experimentally, see Section 3.3. Finally, the load-bearing behaviour of full-sized softwood GL beams under combined bending and axial compression was investigated experimentally for the first time, see Section 3.4. Based on the results of these measurements, the FE model described in Section 5 was validated, the design methods in EN 1995-1-1 [57] and FprEN 1995-1-1 [69] were evaluated, see Section 6, and proposals for a modification of the design methods were developed, see Section 7.

3.2 Imperfection measurements

3.2.1 General

Within the research project DIBt - ZP 52-5-13.194 [107], geometrical imperfections of timber members in 23 buildings were determined shortly after assembly with a laser scanner from 2020 to 2022, see Figures 3.1 and 3.2 and Section 3.2.2. Buildings with GL beams made of softwood and beam-columns made of beech LVL were surveyed. The measurements were carried out in cooperation with the Institute for Photogrammetry at the University of Stuttgart. Based on the results, see Section 3.2.3, equivalent geometrical imperfections covering the effects of geometrical imperfections were determined numerically, see Section 3.2.4. These were utilised as input parameters for the numerical analyses and parameter studies in Sections 5.6.2 and 6.3 for determining equivalent geometrical imperfections for flexural buckling and LTB design according to EN 1995-1-1 [57] and FprEN 1995-1-1 [69] covering the effects of geometrical and structural imperfections. A more detailed description is given by Töpler and Kuhlmann [163]. The complete measurement data are available at Töpler and Kuhlmann [165].

3.2.2 Measurement programme, setup and execution

3.2.2.1 Measurement programme

23 buildings were surveyed, and from these 202 softwood GL beams, 38 beech LVL beams, and 57 beech LVL columns were analysed. Many of the measured secondary members, such as purlins or also softwood GL and concrete columns, were not analysed, as this was not the research question of the investigations. The following discussions refer only to the analysed members. The data of the analysed members are given by Töpler and Kuhlmann [163]. The complete measurement data, including not analysed members, are available at Töpler and Kuhlmann [165]. The data sets of the buildings are labelled according to the year, the calendar week (abbreviated KW in German), and, if necessary, a consecutive number. With the exception of three multi-story buildings (2021-KW12, 2021-KW22, and

Figure 3.1: Survey of building 2020-KW34 with a laser scanner Leica ScanStation P20.

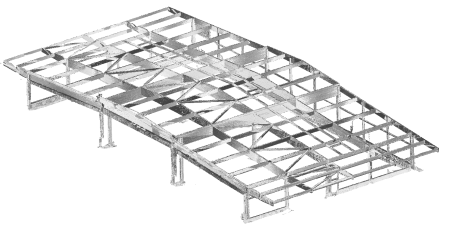

Figure 3.2: Point cloud from laser scan measurements of building 2020-KW34.

2021-KW25), all investigated buildings were single-story halls.
To ensure the representativeness of the sample of timber buildings, typical beam geometries (span, cross-sectional dimensions, and beam shape) and material grades commonly applied in building practice in Austria, Germany, and Switzerland were covered, see Table 3.1. The span of the evaluated beams ranged between 6.9 m and 42.4 m, the height between 0.60 m and 2.7 m, the width between 0.14 m and 0.32 m, and the ratio of the cross-sectional height to width between 2 and 12.6. Beams with constant, double tapered, pitched cambered, and fish-bellied beams with rectangular cross-section were measured. The length of the evaluated columns ranged between 2.8 m and 3.8 m, the height between 0.24 m and 0.48 m, the width between 0.16 m and 0.32 m, and the ratio of cross-sectional height to width between 1.0 and 1.5. All columns had a constant rectangular cross-section. The material grades of the analysed beams were GL 24h, GL 28c, GL 30c, and GL75, and of the analysed columns GL75 according to EN 14080 [54] and ETA-14/0354 [63]. As SL is rarely used as a material for imperfection-sensitive beams due to its small cross-sectional dimensions, it was neglected in the investigations. Beams were measured that were aligned during assembly by means of a roof bracing system, as well as beams without such a roof bracing system for alignment. The timber members were fabricated and the timber buildings erected by different manufacturers and assembly companies.

3.2.2.2 Setup and execution

The measurements were taken directly after the assembly and alignment of the timber structures. In some cases, the structures were loaded by roofing and wall cladding in addition to their self-weight. This was documented along with the magnitude of the estimated permanent actions. The influence of wind actions during the measurements could be neglected, as the 10 min average wind speed at nearby weather stations was always below 6.5 m/s^2 and usually below 5 m/s^2. The measured geometry of the timber members thus particularly includes influences from assembly, transport, and production. Influences from the loading, long-term behaviour, and slip within the connections, which can occur at the first significant loading of the roof structures, are not included in the measurement results or are included only to a negligible extent.

The surveys were carried out with a Leica ScanStation P20 laser scanner, see Figure 3.1, which records measurement points in a grid of $3.1 \cdot 3.1$ mm^2 at a distance of 10 m, see Leica Geosystems AG [115]. Several measurements were carried out for each building, with a distance between the measurement locations of approximately 20 m. The separate point clouds were merged into one three-dimensional point cloud of the entire structure of a building in post-processing, see Figure 3.2. The total measurement time per measurement location was 15 min to 30 min and per building 1 h to 5 h. The measurement method proved to be very reliable and robust over the course of the measurements. Difficulties only arose during the measurement of one building due to a safety net underneath the roof structure with a mesh size of approximately 10 cm, which caused scattering of the laser. These scattering points were filtered out in the post-processing. From this point on, however, only buildings without a safety net were measured. Precipitation was avoided as it can also lead to scattering of the laser.

Table 3.1: Buildings surveyed and members analysed.

Building	Member type	Member shape	Span L [m]	Ratio H / B	Material	Bracing system
2020-KW23	Beams		14.5	5.1	GL 28c	Steel diagonals
2020-KW27	Beams		29.6	12.2	GL 24h	Timber diagonals
2020-KW32	Beams		23.3	9.0	GL 28c	Timber diagonals
2020-KW33	Beams		17.6	8.7	GL 28c	Steel diagonals
2020-KW34	Beams		13.1–17.5	7.2–12.6	GL 24h	Timber diagonals, fixed columns
2020-KW38_1.1	Beams		17.4	5.0	GL 28c	GL roof panel
2020-KW38_1.2	Beams		9.9	3.6	GL 24h	GL roof panel
2020-KW38_1.3	Beams		10.0, 10.1	3.8	GL 24h	GL roof panel
2020-KW38_1.4	Beams		6.9	2.9, 4.8	GL 24h	GL roof panel
2020-KW38_2	Beams		42.4	10.6	GL 28c	Timber diagonals
2020-KW45_1.1	Beams		23.5	9.2	GL 28c	Steel diagonals
2020-KW45_1.2	Beams		26.5	9.3	GL 28c	Steel diagonals
2020-KW49	Beams		20.8	6.8	GL 24h	Timber diagonals
2021-KW12	Beams		15.5	4.0	GL75	GL roof panel
2021-KW16	Beams		20.7	11.1	GL 28c	Steel diagonals
2021-KW22	Beams		16.3	8.0	GL75	GL roof panel
2021-KW24	Beams		42.4	9.4, 10.2	GL 28c, GL 30c	Timber diagonals
2021-KW25	Beams Columns		11.5 3.1–3.8	2.0 1.0, 1.5	GL75	GL roof panel
2021-KW30_1	Beams		24.8	5.7, 6.7	GL 30c	Timber diagonals
2021-KW30_2	Beams		24.7	8.7	GL 30c	Trapezoidal roofing
2021-KW30_3	Beams		24.8	6.7, 7.4	GL 30c	Timber diagonals
2021-KW33_1.1	Beams		24.8, 25.4	7.6	GL 28c	Steel diagonals
2021-KW33_1.2	Beams		28.1, 28.4	7.8	GL 28c	Steel diagonals
2022-KW15	Beams Columns		16.7 2.8	5.5 1.4, 1.5	GL75	GL roof panel

In addition, the air temperature, humidity, and, if possible, the wood moisture content at a depth of approximately 2.5 cm of at least three structural elements per building were determined with a Trotec T2000 multifunction measuring device, see TROTEC GmbH & Co. KG [170]. Furthermore, information was collected concerning the building structure, material, manufacture, transport, assembly process, weathering, surface quality, and any damage to the timber members.

3.2.3 Evaluation and measurement results

3.2.3.1 Evaluation of beams

The point clouds, see Figure 3.2, were automatically evaluated using a developed Matlab script. The Matlab script was published by Töpler and Kuhlmann [165] together with the measuring data. With the Matlab script, (i) the beams were aligned along the x-axis; (ii) the points of the columns and adjacent members were eliminated; (iii) the points of the lower edge and the two side faces of the beams were separated; (iv) these points were further divided into 101 equal segments along the beam length; (v) the points of each segment of the side faces were further divided into 10 equal height segments; (vi) the mean z-coordinates of the lower edge, the beam axis, and the upper edge of each segment were computed; (vii) the mean y-coordinate of the points of each height segment was computed for both sides of the beams; (viii) the mean value of the two mean y-coordinates of both side faces of the beams was computed for each height segment; (ix) the regression lines of the y- and z-coordinates of each segment for both side faces and the middle of the beams were computed; (x) the y-coordinates of the beam axis in each segment were computed by evaluating the respective regression line at mid-beam height; (xi) the twist of the cross-section about the x-axis was derived as the slope of the respective regression line.

The results of the evaluation were the y- and z-coordinates of the beam axis and the twist of the cross-section about the x-axis over the beam length. The y-coordinate of the beam axis represents the bow imperfection, and the twist of the cross-section about the x-axis represents the twist imperfection. As the direction of the y-axis was randomly defined for each building, the absolute values of the geometrical imperfections were generally taken into account in the evaluation. Only if comparing geometrical imperfections on the same beam or between adjacent beams, the signs need to be taken into account.
Figure 3.3 displays typical examples of measured horizontal bow imperfections, and Figure 3.4 displays typical examples of the twist imperfections, both over the beam length. The ideal beam axis and supports are illustrated by the dashed line and circles, respectively.

In the further evaluation, the twist imperfections were split into three parts: the twist imperfections at both supports $e_{\theta,\mathrm{supp},0/\mathrm{L}}$ and the additional twist imperfection at midspan $e_{\theta,\mathrm{mid}}$, see Figure 3.5. The twist imperfections at the supports were obtained directly from the measurements, and the twist imperfections at midspan were determined using the approximation method described in Section 3.2.4.

3.2.3.2 Evaluation of columns

The point clouds of the beech LVL columns were analysed analogously to the beams with the deviations described below. The sway imperfections $e_{\phi,\mathrm{y}}$ and $e_{\phi,\mathrm{z}}$ were determined utilising the mean values of the y- and z-coordinates of the uppermost and lowermost column segments.

To determine the bow imperfections, the sway imperfections $e_{\phi,\mathrm{y}}$ and $e_{\phi,\mathrm{z}}$ were first subtracted from the mean values of the y- and z-coordinates of the column segments. The

least squares method was then applied to determine the regression parabola of the mean values of the y- and z-coordinates of all column segments with zero points at the column head and base. The bow imperfections e_y and e_z were taken as the amplitudes of the regression parabola.
For simplification, the equivalent bow imperfection e_y, which includes the effects of both bow imperfections $e_{y,meas}$ and $e_{z,meas}$, was determined. Therefore, internal forces were calculated using T2O, see Equation (2.1). It was specified that the maximum bending stress from both e_y and e_z should correspond to the maximum bending stress from e_y and

$$\frac{N_{x,c}e_y}{(1-\alpha_{c,y})\cdot W_y} = \frac{N_{x,c}e_{y,meas}}{(1-\alpha_{c,y})\cdot W_y} + \frac{N_{x,c}e_{z,meas}}{(1-\alpha_{c,z})\cdot W_z} \quad , \tag{3.1}$$

which yields

$$e_y = e_{y,meas} + e_{z,meas}\cdot\frac{(1-\alpha_{c,y})\cdot W_y}{(1-\alpha_{c,z})\cdot W_z} \quad , \tag{3.2}$$

where $N_{x,c}$ is the axial compressive force, $\alpha_{c,y/z}$ is the amplification factor of the axial compressive force due to geometrically nonlinear behaviour according to Equation (2.2), and $W_{y/z}$ are the section modulus about the y- or z-axis. Buckling about the z-axis, being the week axis, was assumed.

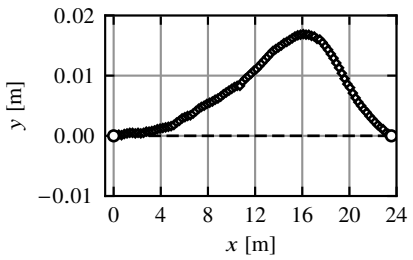

(a) Building 2020-KW32; beam axis 7.

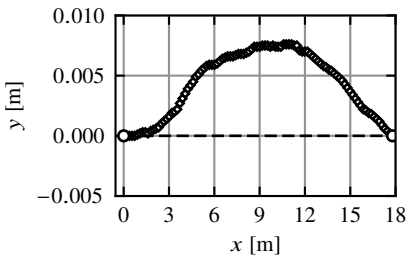

(b) Building 2020-KW33; beam axis 4.

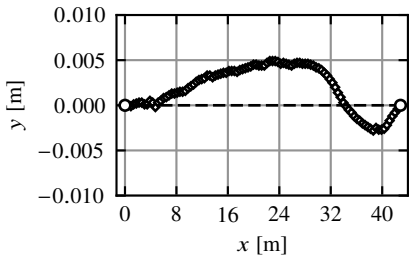

(c) Building 2020-KW38_2; beam axis 25.

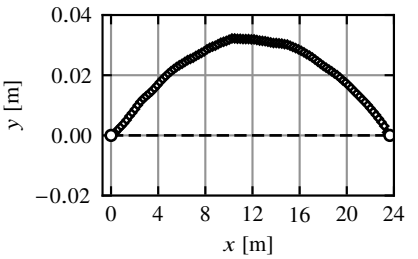

(d) Building 2020-KW45_1.1; beam axis 8.2.

Figure 3.3: Typical curves of the measured horizontal bow imperfections of the beam axis; representing the top view of the beams; with x-axis as longitudinal beam axis.

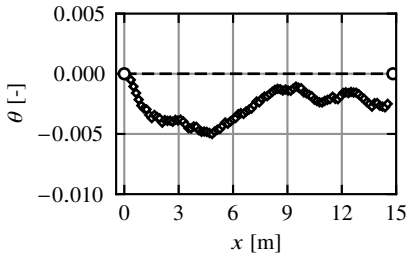

(a) Building 2020-KW23; beam axis 2.

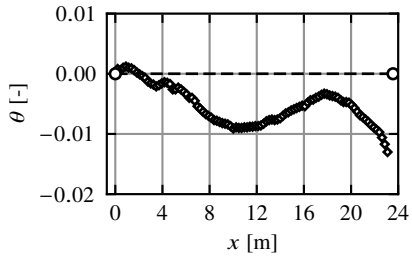

(b) Building 2020-KW32; beam axis 5.

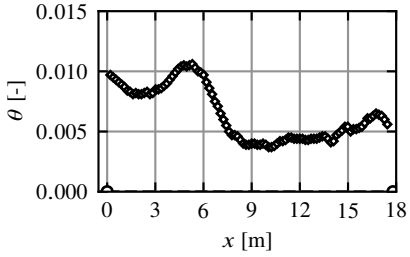

(c) Building 2020-KW33; beam axis 3.

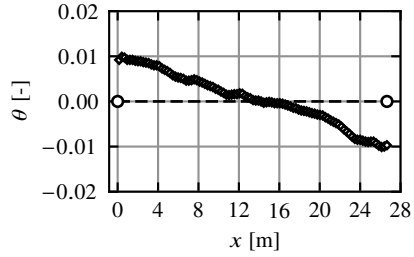

(d) Building 2020-KW45_1.2; beam axis 5.3.

Figure 3.4: Typical curves of the measured twist imperfections about the beam axis; with x-axis as longitudinal beam axis.

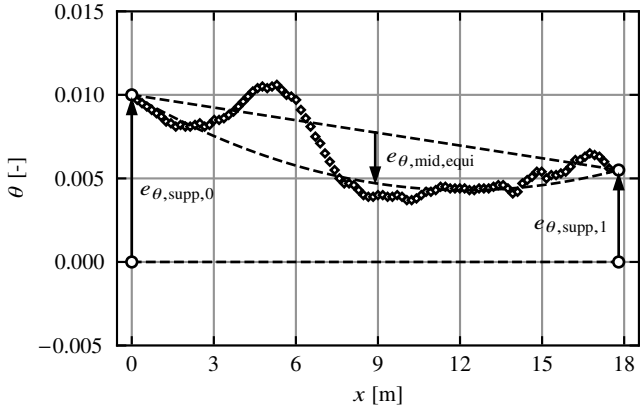

Figure 3.5: Subdivision of the twist imperfections into twist imperfections at the supports $e_{\theta,\mathrm{supp,0/L}}$ and equivalent twist imperfections at midspan $e_{\theta,\mathrm{mid}}$; building 2020-KW33; beam axis 3; with x-axis as longitudinal beam axis.

3.2.3.3 Measuring accuracy

The measurement error of a measurement point at a distance of the laser scanner to the object of 15 m is specified in Leica Geosystems AG [115] as approximately 1 mm in the x-, y-, and z-directions (position accuracy and range noise). This coincides with the observed deviations if evaluating the measurement results of the individual point coordinates. Therefore, in the evaluation, average values of the point coordinates of 200 to 1000 measuring points were calculated, whereby the accuracy of the averaged point coordinates was increased to less than 0.1 mm in the x-, y-, and z-directions at a confidence level of 90% according to Fischer [66]. Since this is a random error, with expected horizontal bow imperfections e_y of the members of approximately $L_{min}/1000 = 6.9$ mm ($L_{min} = 6.9$ m from Table 3.1), the measuring accuracy of the laser scanner was sufficient for the investigations.

3.2.3.4 Results of beams

It was observed that the geometrical imperfections of beams can be split into three parts: the bow imperfections, the twist imperfections at midspan, and the twist imperfections at the fork supports, see Figure 3.6. The total geometrical imperfection of a beam was a superposition of these three parts.
Figure 3.3 displays typical curves of measured horizontal bow imperfections over the beam length (x direction). The ideal beam axis and supports are illustrated by the dashed line and circles, respectively.
The shape of the bow imperfection usually corresponded approximately to a sinusoidal or parabolic curve, see Figures 3.3b and 3.3d. In some cases, a bump shape occurred, see Figure 3.3a. In a few cases, a change in the sign of the bow imperfections was observed at the point of application of a compression purlin, see Figure 3.3c. In general, the bow imperfection curves could be represented by a sinusoidal half-wave.
A continuous change of the beam width over the beam length was observed for some members, see Töpler and Kuhlmann [163].
Figure 3.7 presents the maximum values of the measured horizontal bow imperfections e_y of all evaluated beams, 202 made of softwood GL and 38 made of beech LVL. The x-axis displays the beam span L, and the y-axis exhibits the bow imperfection e_y. Each data point represents the maximum measured horizontal bow imperfection of one beam, which is

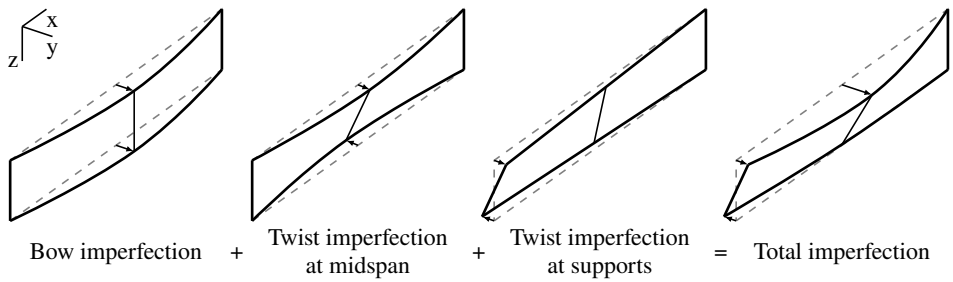

Figure 3.6: Composition of the total geometrical imperfection of timber beam-columns.

not necessarily at midspan, see Figure 3.3. In addition, the equivalent bow imperfection of $L/400$ for design according to EN 1995-1-1 [57] and the value $L/1000$ are displayed. The relationship between bow imperfections e_y and spans L was approximately linear. All measured bow imperfections e_y were below $L/400$. A maximum bow imperfection e_y of $L/1000$ was exceeded by 18 of the 240 evaluated beams. For buildings with beams with $e_y > L/1000$: (i) assembly difficulties were reported due to small tolerances of connectors (2020-KW27), see [3] in Figure 3.7; (ii) the beams were braced by GL roof panels and therefore could not be aligned horizontally during assembly (2020-KW38_1.1), see [1] in Figure 3.7; or (iii) one of two diagonal roof bracings was not aligned properly (2020-KW45_1.1), see [2] in Figure 3.7. The beams of buildings 2020-KW27 and 2020-KW45_1.1 are subsequently referred to as outliers, as the large bow imperfections could have been prevented by an appropriate alignment. The bow imperfections of the beech LVL beams were slightly lower than the ones of the softwood GL beams.
Bow imperfections of adjacent beams coupled by purlins and connected to the same diagonal roof bracing were similar, see Töpler and Kuhlmann [163].

Figure 3.4 displays typical curves of measured twist imperfections over the beam length (x direction). As a result of the sign definition, a positive twist imperfection means a larger positive pre-deformation of the upper edge of the beam in the y-direction in relation to the lower edge of the beam. The ideal beam axis and supports are illustrated by the dashed line and circles, respectively.
Unlike the bow imperfection curves, the shapes of the twist imperfections over the beam length could not be assigned a generally valid curve shape. The maximum twist imperfection

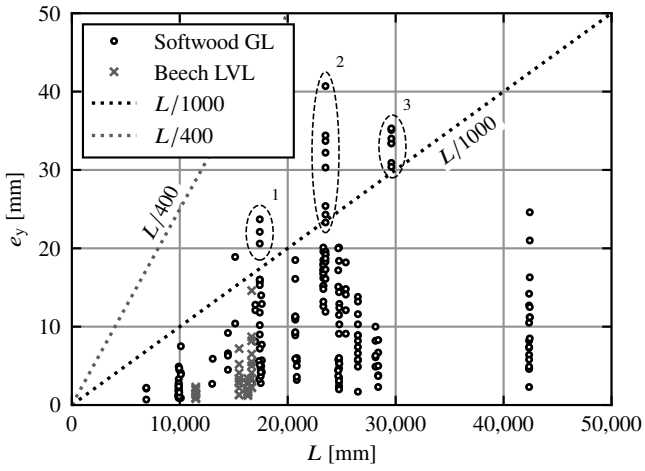

Figure 3.7: Maximum measured horizontal bow imperfections e_y of 202 softwood GL beams and 38 beech LVL beams plotted over the spans L; each data point represents one beam; [1] outliers of 2020-KW38_1.1; [2] outliers of 2020-KW45_1.1; [3] outliers of 2020-KW27.

often occurred at the supports, especially if the fork supports were designed as reinforced concrete pockets. The shape of the twist imperfections along the beam length was, in some cases, approximately sinusoidal or parabolic, see Figure 3.4a. But in general, significant twist imperfections occurred either at one support, see Figure 3.4b, at both supports with the same sign, see Figure 3.4c, or at both supports with opposite signs, see Figure 3.4d.

Absolute values of the twist imperfections at midspan $e_{\theta,\mathrm{mid}}$ are discussed in Section 3.2.4. The imperfections exhibited by the adjacent beams (coupled by purlins and connected to the same diagonal roof bracing) had only minor similarities, see Töpler and Kuhlmann [163].

Figures 3.8 and 3.9 present the frequency distributions of the measured twist imperfections at the supports $e_{\theta,\mathrm{supp}}$. In addition, fitted folded normal distributions are plotted, which represents a good fit to the samples. A distinction was made between supports with large tolerances, such as fork supports by means of reinforced concrete pockets or similar, and supports with small tolerances, such as fork supports by means of lateral timber members or similar, as these significantly influenced the results. There was no significant influence of the span. The mean value, standard deviation, and 95% quantile value of the measured twist imperfections, which resulted from the sample of softwood GL and beech LVL beams with fork supports with large tolerances, were

$$\mu(e_{\theta,\mathrm{supp}}) = 0.0037\ , \quad \sigma(e_{\theta,\mathrm{supp}}) = 0.0033\ , \quad e_{\theta,\mathrm{supp},95} = 0.0102\ .$$

The mean value, standard deviation, and 95% quantile value of the measured twist

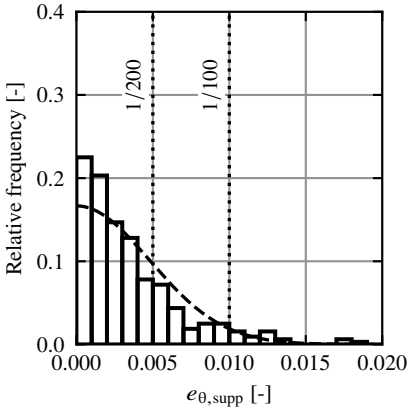

Figure 3.8: Relative frequency distribution of the measured twist imperfections $e_{\theta,\mathrm{supp}}$ at 353 supports of softwood GL and beech LVL beams; with fitted folded normal distribution; fork supports with *large* tolerances.

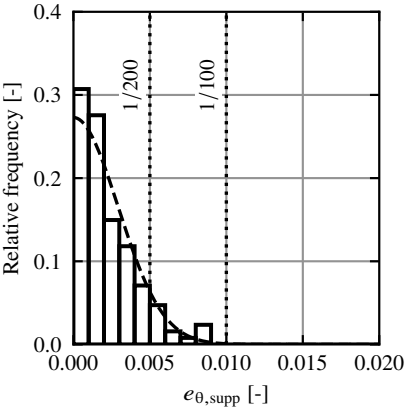

Figure 3.9: Relative frequency distribution of the measured twist imperfections $e_{\theta,\mathrm{supp}}$ at 127 supports of softwood GL and beech LVL beams; with fitted folded normal distribution; fork supports with *small* tolerances.

imperfections, which resulted from the sample of softwood GL and beech LVL beams with fork supports with small tolerances, were

$$\mu(e_{\theta,\mathrm{supp}}) = 0.0022\ , \quad \sigma(e_{\theta,\mathrm{supp}}) = 0.0019\ , \quad e_{\theta,\mathrm{supp},95} = 0.0058\ .$$

3.2.3.5 Results of columns

Figure 3.10 presents the determined equivalent bow imperfections e_y of 57 beech LVL columns. The x-axis displays the column length L, and the y-axis exhibits the determined equivalent bow imperfection e_y. Each data point represents the maximum determined equivalent bow imperfection of one column. In addition, the values $L/1000$ and $L/1500$ are displayed. Due to the small variation in length, no conclusion could be drawn regarding a possible relationship between column lengths and equivalent bow imperfections. A maximum bow imperfection of $L/1000$ and $L/1500$ was exceeded by one and three columns, respectively.

Figure 3.11 displays the relative frequency distribution of the determined equivalent bow imperfections e_y/L. In addition, a fitted folded normal distribution is plotted. None of the distribution functions analysed represented a good approximation of the sample, which might be due to its small size. The mean value, standard deviation, and 95% quantile value of the equivalent bow imperfections, which resulted from the sample of beech LVL columns, were

$$\mu\left(\frac{e_\mathrm{y}}{L}\right) = 0.329\ \frac{\mathrm{mm}}{\mathrm{m}}\ , \quad \sigma\left(\frac{e_\mathrm{y}}{L}\right) = 0.194\ \frac{\mathrm{mm}}{\mathrm{m}}\ , \quad \frac{e_{\mathrm{y},95}}{L} = 0.604\ \frac{\mathrm{mm}}{\mathrm{m}}\ .$$

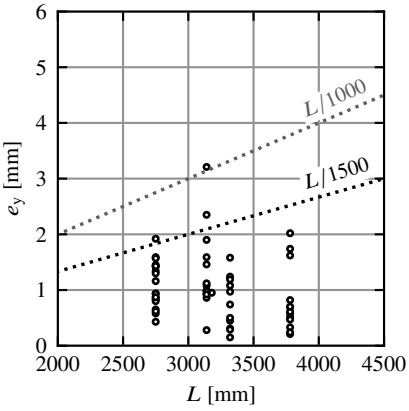

Figure 3.10: Determined equivalent bow imperfections e_y of 57 beech LVL columns plotted over the length L; each data point represents one column.

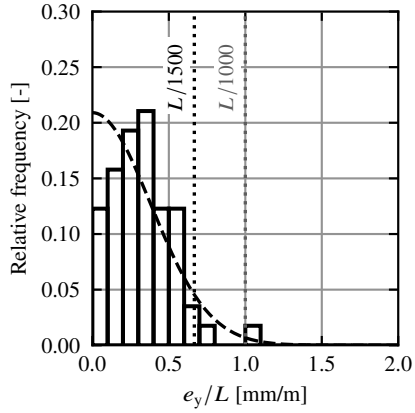

Figure 3.11: Relative frequency distribution of the determined equivalent bow imperfections e_y in relation to the beam spans L of 57 beech LVL columns; with fitted folded normal distribution.

Figure 3.12 presents the sway imperfections e_ϕ of 57 beech LVL columns. For 57 columns and y- and z-directions, this yields 114 values. The x-axis displays the column length L, and the y-axis exhibits the sway imperfection e_ϕ. In addition, the sway imperfection of $1/200$ for design according to EN 1995-1-1 [57], see Equation (2.53), is plotted. A decrease in sway imperfections was observed with increasing column length. This is in line with Equation (2.53) from EN 1995-1-1 [57] for columns longer than 5 m. A maximum sway imperfection of $1/200$ was exceeded by one column.
Figure 3.13 displays the relative frequency distribution of the measured sway imperfections e_ϕ. In addition, a fitted folded normal distribution is plotted, which represents a good fit to the sample. The mean value, standard deviation, and 95% quantile value of the measured sway imperfections, which resulted from the sample of beech LVL columns, were

$$\mu(e_\phi) = 0.00100\,, \quad \sigma(e_\phi) = 0.00088\,, \quad e_{\phi,95} = 0.00244\,.$$

3.2.4 Numerical analysis of equivalent geometrical imperfections of beams

3.2.4.1 General

For design according to EN 1995-1-1 [57], the measured irregular geometrical bow and twist imperfections of the beams, see Figures 3.3 and 3.4, had to be converted into sinusoidal or parabolic equivalent geometrical imperfections. The additional effect of structural imperfections is discussed in Sections 5.6.2 and 6.3.

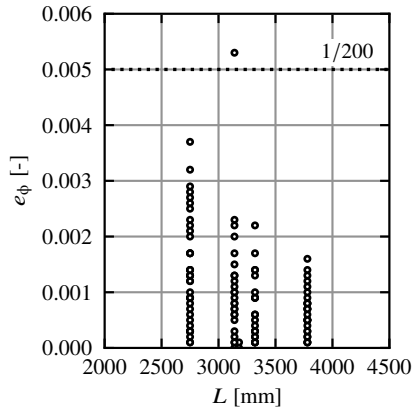

Figure 3.12: Measured sway imperfections e_ϕ of 57 beech LVL columns plotted over the length L; each data point represents the sway of one column in one direction.

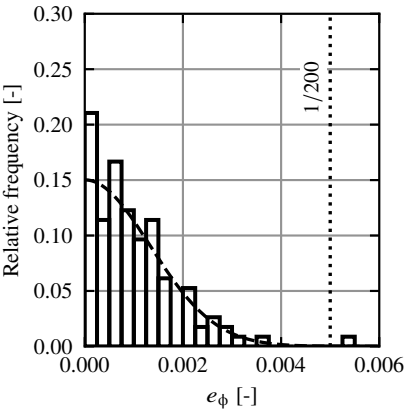

Figure 3.13: Relative frequency distribution of the measured sway imperfections e_y of 57 beech LVL columns; with fitted folded normal distribution.

Equivalent geometrical imperfections in the shape of a sinusoidal half-wave were determined for each of the 240 measured softwood GL and beech LVL beams with an approximation method. The numerical analyses demonstrated that computations with measured and equivalent geometrical imperfections resulted in similar maximum bending stresses and utilisation ratios. For each beam, (i) numerical eigenvalue analyses (model 1); (ii) numerical analyses with measured imperfections (model 2); and (iii) numerical analyses with equivalent geometrical imperfections (model 3) were performed.

3.2.4.2 Modelling and analysis

Abaqus/CAE 2020 was used for the FEA. The beams were modelled individually and with their nominal geometry and material properties. This corresponds with the design method *numerical design calculations with direct resistance check* in the *Guidelines for Finite Element Based Design of Timber Structures* by Töpler and Kuhlmann [162], see Section 5.2. If present, the roof bracing was modelled with an equivalent beam with stiffness determined according to Kessel et al. [101]. If the modelled beam was not a direct part of the roof bracing, the purlins connecting the roof bracing to the beam were modelled by equivalent springs acting only in the y-direction. Joint stiffnesses were taken into account based on the execution drawings. Ideal fork supports were modelled in the beam axis. An orthotropic material model with mean stiffnesses and characteristic strengths according to EN 14080 [54] and ETA-14/0354 [63], Poisson's ratios according to Neuhaus [124] and Töpler and Kuhlmann [161], bilinear elastoplastic material behaviour for compression in grain direction, and linear elastic material behaviour for tension in grain direction was utilised. The grain direction was chosen to be parallel to the bottom edge of the beams. A uniform line load q was applied at the upper edge of the beams. The effects of self-weight were negligible. 20-node quadratic solid elements C3D20R were chosen for meshing. 100 elements were modelled in the beam length, 10 in the height, and 8 in the width. The model was verified and validated according to the *FE guidelines* [162], see Sections 5.4 and 5.5.

In model 1, no imperfections and purely elastic material behaviour were considered. The eigenvalues and eigenmodes of the beams were determined, and the relative LTB slenderness ratios $\lambda_{m,rel}$ and resulting effective lengths $L_{m,ef}$ were computed.
In model 2, the measured irregular imperfections, see Figures 3.3 and 3.4, were considered. The load-bearing capacities and the corresponding uniform line loads q_{max}, at which the characteristic bending strength $f_{m,k}$ was reached, were computed.
In model 3, predetermined equivalent geometrical imperfections were considered, and q_{max} from model 2 was applied. The resulting tensile stresses in grain direction and utilisation ratios $\mu = \sigma_{t,0}/f_{m,k}$ were evaluated.
Iterative approaches for determining the equivalent geometrical imperfections proved infeasible in preliminary investigations, see Töpler and Kuhlmann [163]. Therefore, the amplitudes of the equivalent geometrical imperfections for model 3 were determined analytically using an approximation method. In this approximation method, the measured y-coordinates of the 101 segments of each beam were interpreted as 101 individual horizontal forces with the corresponding magnitude. The resulting horizontal deformation v_j of the j^{th}

segment of a beam was calculated as

$$v_j = \sum_{i=1}^{101} y_i \cdot \frac{1}{6E_{0,el}I_z} \cdot \begin{cases} a_i^2 b_i \cdot \left(1 + \frac{L}{a_i}\right) \cdot \frac{(L-x_j)}{L} - \frac{(L-x_j)^3}{a_i b_i L} & \text{for} \quad i \le j \quad , \\ a_i b_i^2 \cdot \left(1 + \frac{L}{b_i}\right) \cdot \frac{x_j}{L} - \frac{x_j^3}{a_i b_i L} & \text{for} \quad i > j \quad , \end{cases} \tag{3.3}$$

where y_i is the applied horizontal force corresponding to the imperfection of the i^{th} segment, see, e.g. Figure 3.3, a_i is the distance of the i^{th} segment to the support at $x = 0$, b_i is the distance of the i^{th} segment to the support at $x = L$, x_j is the distance of the j^{th} segment to the support at $x = 0$, L is the span, $E_{0,el}$ is the elastic modulus in grain direction, and I_z is the moment of inertia about the z-axis. The amplitude of the equivalent bow imperfections in the shape of a sinusoidal half-wave was selected in such a way that the same maximum horizontal deformation of a beam according to Equation (3.3) was obtained as for the measured bow imperfections. The same procedure was adopted to determine the equivalent twist imperfections, whereby the product of the twist imperfection and the beam height of the i^{th} segment was assumed as individual horizontal loads y_i.

The ratio of the resulting equivalent bow imperfections to measured bow imperfections is displayed in Figure 3.14. The regression line has a slope of 0.98 and a coefficient of determination of $R^2 = 0.98$ as well. Especially for larger values of imperfections, there is a good fit.

The subsequent comparison of the utilisations ratios μ_m of the maximum tensile stresses in grain direction $\sigma_{t,0}$ of models 2 and 3 served as a validation of the approximation method. Other approximation methods were discussed by Töpler and Kuhlmann [163].

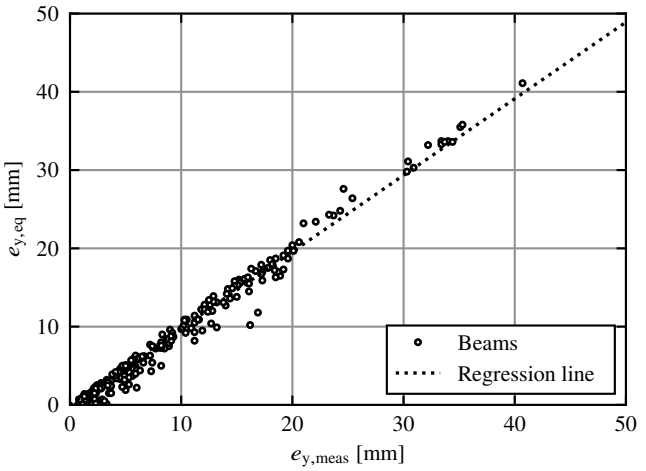

Figure 3.14: Equivalent horizontal bow imperfections $e_{y,eq}$ in comparison with the maximum measured horizontal bow imperfections $e_{y,meas}$ of 202 softwood GL beams and 38 beech LVL beams; each data point represents one beam.

Table 3.2: Numerically determined mean values, minima, maxima, and coefficients of variation (COV) of the relative LTB slenderness ratio $\lambda_{m,rel}$ and the utilisation ratios due to bending $\mu = \sigma_{t,0}/f_{m,k}$, $\mu_{m,y} = M_y/W_y f_{m,k}$, and $\mu_{m,z} = M_z/W_z f_{m,k}$; results of all braced beams.

		Model 2 (measured imp.)			Model 3 (equivalent imp.)		
	$\lambda_{m,rel}$	μ_m	$\mu_{m,y}$	$\mu_{m,z}$	μ_m	$\mu_{m,y}$	$\mu_{m,z}$
Mean	0.77	1.00	0.94	0.06	1.00	0.94	0.06
Minimum	0.52	1.00	0.72	0.00	0.97	0.72	0.00
Maximum	0.96	1.00	1.00	0.28	1.02	1.00	0.30
COV	0.16	0.00	0.07	1.05	0.01	0.07	1.03

The mean, minimum, and maximum utilisation ratios of the maximum tensile stresses $\mu_m = \sigma_{t,0}/f_{m,k}$ and the maximum bending moments about the y and z axis $\mu_{m,y/z} = M_{y/z}/W_{y/z} f_{m,k}$ of all braced beams from analyses with models 2 and 3 are displayed in Table 3.2. Where $\sigma_{t,0}$ is the maximum tensile stress in grain direction from FEA and $M_{y/z}$ is the maximum bending moment about the y or z axis calculated with the nodal stresses in grain direction from FEA.
The mean utilisation ratio μ_m for model 3 was 1.0, and the minima and maxima were 0.97 and 1.02, respectively. The utilisation ratios due to bending about the strong axis $\mu_{m,y}$ were identical in both models, as the same loads q_{max} were applied. The utilisation ratios due to bending about the weak axis $\mu_{m,z}$ in model 3 were also almost identical to those in model 2. It was thus demonstrated that FEAs with equivalent geometrical imperfections, calculated according to the presented approximation method in Equation (3.3), result in almost identical utilisation ratios for bending compared to FEAs with measured geometrical imperfections. The low relative LTB slenderness ratios $\lambda_{m,rel}$ of the braced beams illustrated the high effectiveness of the bracings for the horizontal stabilisation of the surveyed beams. The approximation method was therefore validated and is very well suited for determining the equivalent bow and twist imperfections of timber beams. Using the approximation method, representative equivalent geometrical imperfections can thus be determined based on mechanical principles.

3.2.4.3 Results

Figures 3.15 and 3.16 display the frequency distributions of the determined equivalent bow imperfections e_y/L of 179 softwood GL beams and 95 beech LVL beams and columns, respectively. For softwood GL beams, the results of buildings 2020-KW27 and 2020-KW45_1.1 are not included due to the reported assembly inaccuracies, which could have been avoided by proper alignment and checking. For beech LVL, equivalent geometrical imperfections of 57 columns determined with calculations using T2O and 38 beams determined with the discussed approximation method are combined in Figure 3.16. In addition, fitted folded normal distributions are plotted, which represents a good fit to the samples. The mean value, standard deviation, and 95% quantile value of the equivalent bow imperfections, which resulted from the sample of softwood GL beams neglecting results of buildings 2020-KW27 and 2020-KW45_1.1, were

$$\mu\left(\frac{e_y}{L}\right) = 0.359\ \frac{\text{mm}}{\text{m}}\,,\quad \sigma\left(\frac{e_y}{L}\right) = 0.282\ \frac{\text{mm}}{\text{m}}\,,\quad \frac{e_{y,95}}{L} = 0.847\ \frac{\text{mm}}{\text{m}}\,.$$

The mean value, standard deviation, and 95% quantile value of the equivalent bow imperfections, which resulted from the sample of beech LVL beams and columns, were

$$\mu\left(\frac{e_y}{L}\right) = 0.282\ \frac{\text{mm}}{\text{m}}\,,\quad \sigma\left(\frac{e_y}{L}\right) = 0.190\ \frac{\text{mm}}{\text{m}}\,,\quad \frac{e_{y,95}}{L} = 0.578\ \frac{\text{mm}}{\text{m}}\,.$$

Figure 3.17 presents the determined equivalent twist imperfections at midspan multiplied by the maximum beam height $e_{\theta,\text{mid}}H_{\text{ap}}$ of 202 softwood GL and 38 beech LVL beams. The x-axis displays the beam span L, and the y-axis exhibits the determined equivalent twist imperfections at midspan $e_{\theta,\text{mid}}H_{\text{ap}}$. The product of $e_{\theta,\text{mid}}H_{\text{ap}}$ represents the difference between the bow imperfection of the upper edge and the lower edge of a beam and was chosen because the correlation with the span was higher than for $e_{\theta,\text{mid}}$ alone. Additionally, it allows an illustrative comparison with bow imperfections. Each data point represents the maximum determined equivalent twist imperfection at midspan of one beam. In addition, the value $L/1500$ is plotted. As with the bow imperfections e_y, the relationship between $e_{\theta,\text{mid}}H_{\text{ap}}$ and spans L was approximately linear, see Töpler and Kuhlmann [163].
Figure 3.18 displays the relative frequency distribution of the determined equivalent twist imperfections at midspan $e_{\theta,\text{mid}}H/L$. In addition, a fitted folded normal distribution is plotted, which represents a good fit to the sample. The mean value, standard deviation, and 95% quantile value of the equivalent twist imperfections at midspan, which resulted from the sample of softwood GL and beech LVL beams, were

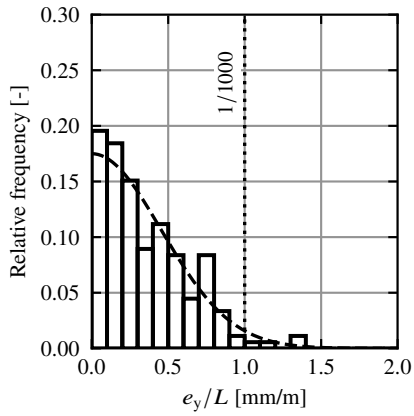

Figure 3.15: Relative frequency distribution of the determined equivalent bow imperfections e_y in relation to the beam spans L of 179 softwood GL beams; with fitted folded normal distribution; neglecting outliers.

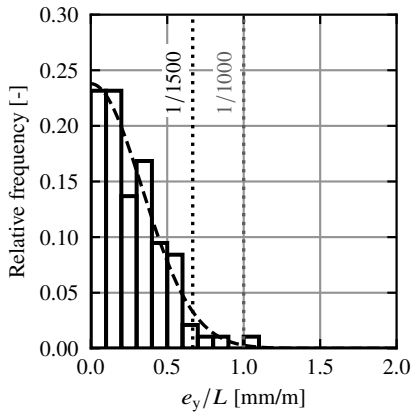

Figure 3.16: Relative frequency distribution of the determined equivalent bow imperfections e_y in relation to the column lengths or beam spans L of 57 beech LVL columns and 38 beech LVL beams; with fitted folded normal distribution.

$$\mu\left(\frac{e_{\theta,\mathrm{mid}}H}{L}\right) = 0.184\ \frac{\mathrm{mm}}{\mathrm{m}}\ ,\quad \sigma\left(\frac{e_{\theta,\mathrm{mid}}H}{L}\right) = 0.193\ \frac{\mathrm{mm}}{\mathrm{m}}\ ,\quad \frac{e_{\theta,\mathrm{mid},95}H}{L} = 0.628\ \frac{\mathrm{mm}}{\mathrm{m}}\ .$$

No significant correlations supported by causality were found between the geometrical bow and twist imperfections of the beams, except for the twist imperfections at both supports. Figure 3.19 presents the measured twist imperfections at both supports $e_{\theta,\mathrm{supp},0}$ and $e_{\theta,\mathrm{supp},1}$ of 202 softwood GL and 38 beech LVL beams. Each data point represents one beam. Neglecting outliers, the regression line through the origin was determined and plotted in the diagram. Its coefficient of determination was rather low, with $R^2 = 0.27$. $e_{\theta,\mathrm{supp},1}$ could be described in dependence on $e_{\theta,\mathrm{supp},0}$ by

$$e_{\theta,\mathrm{supp},1} = 0.5 e_{\theta,\mathrm{supp},0} + e \qquad \text{with } e\text{:} \quad N(0, 0.0042, -) \tag{3.4}$$

where e is a scattering error term and $N(\mu, \sigma, \mathrm{limit})$ are the parameters of its underlying normal distribution. σ was calculated according to Ehlbeck and Colling [46].

3.2.5 Discussion

The comparison of equivalent bow imperfections and measured bow imperfections, see Figure 3.14, emphasised the observation of Ballio and Mazzolani [6], Ersvik and Alpsten [62], and Schulz [143] that the amplitude of the bow imperfection far outweighs the influence of the shape the bow imperfection, see also Section 2.2.3.2. Especially for large imperfection values, equivalent and measured imperfections were almost equal.

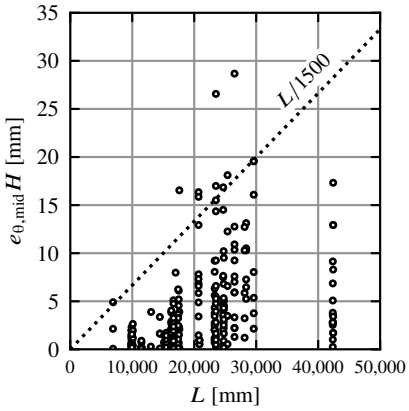

Figure 3.17: Determined equivalent twist imperfections at midspan $e_{\theta,\mathrm{mid}}H_{\mathrm{ap}}$ of 202 softwood GL and 38 beech LVL beams plotted over the spans L; each data point represents one beam.

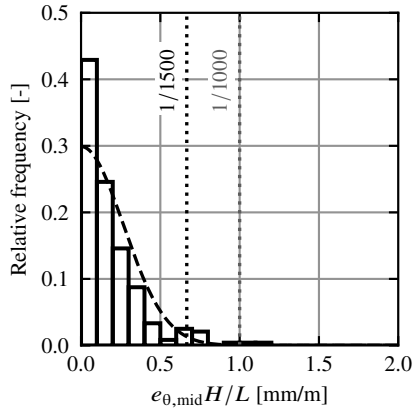

Figure 3.18: Relative frequency distribution of the determined equivalent twist imperfections at midspan $e_{\theta,\mathrm{mid}}H_{\mathrm{ap}}$ in relation to the beam spans L of 202 softwood GL and 38 beech LVL beams; with fitted folded normal distribution.

Tables 3.3, 3.4, 3.5, and 3.6 present the determined (equivalent) geometrical imperfections as well as relevant data from the literature for comparison. The number of measured values n, the mean values of the absolute values of the imperfections $\mu(|e_y|)$, the standard deviations of the absolute values of the imperfections $\sigma(|e_y|)$, the mean values of the imperfections $\mu(e_y)$ that naturally scatter around zero, the standard deviations of the imperfections $\sigma(e_y)$, and the 95% quantile values of the imperfections $e_{y,95}$ are displayed. Depending on the source, these are measured geometrical imperfections or determined equivalent geometrical imperfections covering the effects of geometrical and/or structural imperfections.

The own determined equivalent bow imperfections of softwood GL and beech LVL beams were of similar magnitude, see Table 3.3 and Figure 3.7. However, for beech LVL members, these values were slightly more favourable. On the one hand, this difference could have been positively influenced in favour of the beech LVL beams by (i) their low H/B ratio, see Table 3.1; (ii) the different behaviour of softwood GL and beech LVL during the trimming due to the different densities; and (iii) the protection of beech LVL members from moisture during transport, storage, and assembly. On the other hand, most softwood GL were aligned during assembly with a lateral bracing system, which was not possible for any of the beech LVL members. This and the generally large scatter of the values might explain the observed differences in the bow imperfections of softwood GL beams and beech LVL members. Therefore, the author was hesitant to conclude from these data that the bow imperfections for GL75 beam-columns are generally smaller than for softwood GL beam-columns.
The bow imperfections of softwood GL columns measured by Ehlbeck and Blaß [44] were of the same magnitude as the own results of softwood GL beams, although the former were mostly caused by manufacturing, long-term behaviour, and loading, and the latter

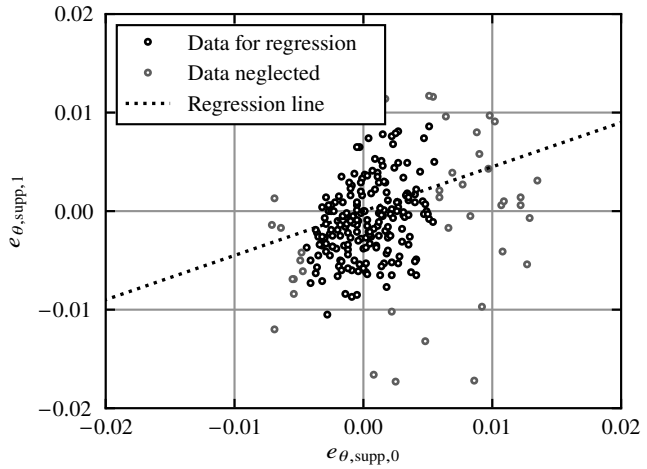

Figure 3.19: Measured twist imperfections at the supports $e_{\theta,\mathrm{supp},0}$ and $e_{\theta,\mathrm{supp},1}$ of 202 softwood GL and 38 beech LVL beams; each data point represents one beam.

by assembly and alignment. The values of the beech LVL columns were again slightly more favourable. Consequently, no significant improvement in production-related bow imperfections appears to have taken place over the past 40 years.
In 1973, Brüninghoff [20] measured the bow imperfections of 13 softwood GL beams that were significantly less favourable than own results. This might be due to improved assembly accuracy and alignment in the past 50 years.
The curves of the measured horizontal bow imperfections of beams in Figure 3.3 were similar to the measurement results of Dietsch and Henke [34]. They measured the bow imperfections of seven softwood GL beams, which were somewhat less favourable than own measurement results. This might be due to the fact that they measured beams that were not only loaded by their self-weight but were also partly subjected to long-term influences.
The assumption of $\beta_c = 0.1$ in the k_c-method in EN 1995-1-1 [57] and FprEN 1995-1-1 [69]

Table 3.3: Comparison of determined bow imperfections e_y of softwood GL and beech LVL beam-columns (upper part of table) with values from literature (lower part of table).

	n	$\mu(\lvert e_y \rvert)$ [mm]	$\sigma(\lvert e_y \rvert)$ [mm]	$\mu(e_y)$ [mm]	$\sigma(e_y)$ [mm]	$e_{y,95}$ [mm]
Softwood GL beams [1]	202	$L/2290$	$L/2800$	0.0	$L/1780$	$L/880$
Softwood GL beams without outliers [1,2]	179	$L/2790$	$L/3550$	0.0	$L/2190$	$L/1180$
Softwood GL and beech LVL beams without outliers [1,2]	217	$L/3040$	$L/3670$	0.0	$L/2340$	$L/1200$
Beech LVL beams and columns [1]	95	$L/3660$	$L/5130$	0.0	$L/2980$	$L/1710$
Softwood GL columns by Ehlbeck and Blaß [44] [3]	176	$L/2820$	$L/3550$	0.0	$L/2230$	$L/1140$
Softwood GL beams by Brüninghoff [20] [3]	13	$L/780$	$L/7000$	-	-	-
Softwood GL beams by Dietsch and Henke [34] [3]	7	$L/1720$	$L/1830$	-	-	-
Softwood GL beams with T2O according to EN 1995-1-1 [57] [4]	-	-	-	-	-	$L/400$
Softwood GL columns with the k_c-method in EN 1995-1-1 [57] [4,5]	-	-	-	-	-	$\approx L/1000$ $\approx L/750$

[1] Equivalent geometrical imperfections covering the effects of geometrical imperfections.
[2] The values of buildings 2020-KW27 and 2020-KW45_1.1 were neglected.
[3] Measured geometrical imperfections.
[4] Equivalent geometrical imperfections covering the effects of geometrical and structural imperfections.
[5] Approximate values recalculated using T2O, $f_{c,0,k}$ or $f_{c,0,k,mod}$, and $\beta_c = 0.1$ from EN 1995-1-1 [57]. $f_{c,0,k}$ results in $\approx L/1000$ and $f_{c,0,k,mod}$ results in $\approx L/750$, see Figures 2.8 and 2.9.

Table 3.4: Comparison of determined equivalent twist imperfections $e_{\theta,\mathrm{mid}}H_{\mathrm{ap}}$ of softwood GL and beech LVL beams at midspan with values from literature.

	n	$\mu(\lvert e_{\theta,\mathrm{mid}}H\rvert)$ [mm]	$\sigma(\lvert e_{\theta,\mathrm{mid}}H\rvert)$ [mm]	$\mu(e_{\theta,\mathrm{mid}}H)$ [mm]	$\sigma(e_{\theta,\mathrm{mid}}H)$ [mm]	$e_{\theta,\mathrm{mid},95}H$ [mm]
Softwood GL and beech LVL beams [1]	240	$L/5430$	$L/5180$	0.0	$L/3750$	$L/1600$
Softwood GL beams by Dietsch and Henke [34] [2]	6	$L/6500$	$L/4490$	-	-	-
EN 1995-1-1 [57]	-	-	-	-	-	-

[1] Equivalent geometrical imperfections.
[2] Measured geometrical imperfections; deviating evaluation, as values are the difference between the maximum horizontal deformation of the upper edge and the lower edge of a beam; twist at the supports was not considered.

Table 3.5: Results of measured twist imperfections $e_{\theta,\mathrm{supp}}$ of softwood GL and beech LVL beams at the supports.

	n	$\mu(\lvert e_{\theta,\mathrm{supp}}\rvert)$ [-]	$\sigma(\lvert e_{\theta,\mathrm{supp}}\rvert)$ [-]	$\mu(e_{\theta,\mathrm{supp}})$ [-]	$\sigma(e_{\theta,\mathrm{supp}})$ [-]	$e_{\theta,\mathrm{supp},95}$ [-]
All beams	480	1/310	1/330	0.0	1/220	1/100
Fork supports with large tolerances	353	1/270	1/310	0.0	1/200	1/100
Fork supports with small tolerances	127	1/450	1/530	0.0	1/340	1/180
EN 1995-1-1 [57]	-	-	-	-	-	-

Table 3.6: Results of measured sway imperfections e_{ϕ} of beech LVL columns.

	n	$\mu(\lvert e_{\phi}\rvert)$ [-]	$\sigma(\lvert e_{\phi}\rvert)$ [-]	$\mu(e_{\phi})$ [-]	$\sigma(e_{\phi})$ [-]	$e_{\phi,95}$ [-]
All beech LVL columns	114	1/1000	1/1140	0.0	1/750	1/380
Softwood GL columns by Ehlbeck and Blaß [44]	176	1/490	1/560	0.0	1/370	1/190
EN 1995-1-1 [57]	-	-	-	-	-	1/200 [1]

[1] For $L > 5$ m a reduction factor depending on L may be applied according to EN 1995-1-1 [57].

can be interpreted as an equivalent bow imperfection of $\approx L/1000$ if $f_{c,0,k}$ is assumed, see Figures 2.8 and 2.9. But, if considering the increase in the compressive strength assumed by the k_c-method due to $k_c(\lambda_{c,rel} = 0.3) = 1.0$, i.e. $f_{c,0,k,mod}$, $\beta_c = 0.1$ results in an equivalent bow imperfection of $\approx L/750$, see Figures 2.8 and 2.9. On the one hand, $\approx L/1000$ is in line with literature and own measurement results of geometrical imperfections. On the other hand, structural imperfections should have a significant influence on the flexural buckling load-bearing capacity, see Figure 2.40. If considering structural imperfections, the larger difference between the measured bow imperfections, $L/1140$, of Ehlbeck and Blaß [44] and equivalent bow imperfections of $\approx L/750$ appears more realistic than just an insignificant difference to equivalent bow imperfections of $L/1140$ to $\approx L/1000$. This is further discussed in Section 6.3.
At first glance, the value of the equivalent bow imperfection of timber members, $L/400$, given in EN 1995-1-1 [57] for T2O seems to be far on the safe side. However, EN 1995-1-1 [57] does not explicitly account for twist imperfections of beams, which might be covered by the difference between $L/400$ and $\approx L/1000$ (or $\approx L/750$). This is further discussed in Section 6.3.

Dietsch and Henke [34] measured similar twist imperfections of beams as own measurement results, see Table 3.4. However, they did not differentiate between twist imperfections at midspan and twist imperfections at the supports. [20] did not determine any twist imperfections. The correlation $e_{\theta,mid} = 0.05B/H$ found by Larsen [111] on solid wood test specimens was not confirmed by own measurement results.
Twist imperfections at supports with large tolerances were approximately two times the size of twist imperfections at supports with small tolerances, see Table 3.5. This significant difference is plausible, as the additional gap in, e.g. reinforced concrete pockets enables significantly larger twist imperfections.
Twist imperfections are not discussed in EN 1995-1-1 [57].

Ehlbeck and Blaß [44] measured sway imperfections of softwood GL columns with approximately twice the size of own measurement results, see Table 3.6. This difference should not be overrated, as own measurements only included two buildings. Values in EN 1995-1-1 [57] are larger than own measurement results but in line with measurement results for softwood GL columns of Ehlbeck and Blaß [44]. At this point, attention should be drawn to the cross-material coordination of sway imperfections in the current Eurocodes, which is discussed in Section 2.2.3. The decrease in sway imperfections at lengths larger than 5 m recommended in EN 1995-1-1 [57] and FprEN 1995-1-1 [69] was observed even for shorter lengths in own measurements, see Figure 3.12.

If comparing different parts of the geometrical imperfections, the determined equivalent twist imperfections at midspan were between 50% and 75% of the equivalent bow imperfections. The 95% quantile values relevant for the design were $L/1600$ and $L/1180$, respectively. The equivalent twist imperfections at midspan were approximately 70% of the measured twist imperfections at the supports if comparing pure rotations.
Worth mentioning are the similarities between the sway imperfections according to Ehlbeck and Blaß [44] and the own measured twist imperfections at the supports with small tolerances.

In the only building in which both imperfections were evaluated, 2022-KW15, a positive correlation between them was found. As beams with fork supports with small tolerances are aligned directly to the columns, e.g. by using lateral timber members, a positive correlation between both is also reasonable.
As previously discussed in Section 3.2.4.3, no significant correlations supported by causality were found between the different parts of the geometrical imperfections of the beams, except for the twist imperfections at both supports. This is reasonable, as twist imperfections at the supports are mainly influenced by the placement of a beam in the fork supports (rigid body rotation of the entire beam), the twisting of the beam along its length due to manufacturing, transport, etc., and the alignment of the beam at the supports (twist of the cross-section at both supports against each other).

Due to the large scattering of the measurement results and despite the large sample size, it was only possible to determine parameters that had a pronounced influence. The linear relationship between bow imperfections and the span of the timber members assumed in EN 1995-1-1 [57] and found by Ehlbeck and Blaß [44] and Larsen [111] was a plausible approximation of the measurement results in Figure 3.7. Surprisingly, no significant differences were found between geometrical imperfections of members with and without roof bracing utilised for alignment. A significant influence of the horizontal beam stiffness on the geometrical imperfections was not found.

The geometrical bow and twist imperfections are affected by manufacturing, transport, storage, assembly, slip in the connections, and long-term behaviour. Sway imperfections of columns are mainly caused by assembly, slip in the connections, and long-term behaviour. The slip in the connections and long-term behaviour are not discussed here, as time $t = 0$ was examined. For members with:

a. relatively small lateral stiffness and lateral supports, geometrical bow and twist imperfections are mainly caused by assembly and can be reduced during alignment;

b. relatively small lateral stiffness but without lateral supports, geometrical bow and twist imperfections are caused by manufacturing, transport, storage, and assembly;

c. relatively high lateral stiffness, geometrical bow and twist imperfections are mainly caused by manufacturing, transport, and storage.

Beams prone to LTB usually belong to categories a. or b.. Columns prone to flexural buckling usually belong to categories b. or c..
This illustrates a major difference between beams and columns. The beams of timber halls often have such low lateral stiffness that they are dependent on lateral supports from roof bracing. Due to the low lateral stiffness of the beams, the geometrical bow and twist imperfections at midspan are significantly influenced by the coupling to a roof bracing and the alignment of this bracing. Conversely, this makes the correct alignment of the roof bracing necessary. Columns, on the other hand, often have relatively high lateral stiffness and no lateral supports. Manufacturing, transport, and storage are therefore decisive for their bow imperfections.

Another major difference between beams and columns are the different internal forces due to different loading. While twist imperfections cause additional internal forces in members subjected to bending (beams), sway imperfections cause additional internal forces in structural systems subjected to axial compressive forces, e.g. columns, see Equations (2.1), (2.14), and (2.15). Therefore, in addition to the horizontal alignment at midspan, the vertical alignment at the fork supports is relevant for beams. For columns, on the other hand, verticality must be ensured.

Following this reasoning, the expectations were confirmed by the relatively large bow imperfections of building 2020-KW38_1.1, which did not have a roof bracing that could be used for alignment. However, the measured values of other beams in roof structures without roof bracing for alignment did not confirm this assumption. For 2021-KW30_2 in particular, the bow imperfections were significantly smaller than the limit value of $L/1000$, with $e_y = L/1200$ to $L/11{,}000$, see Töpler and Kuhlmann [163]. Although no significant influence of the possibility of lateral alignment of the beams during assembly was observed in the measurement results, insufficient alignment during assembly had a significant influence, see 2020-KW27 and 2020-KW45_1.1 in [163]. Such outliers can be prevented by appropriate checks during assembly.

The similarity of the bow imperfections of adjacent beams connected to the same roof bracing, see Töpler and Kuhlmann [163], reinforced the argument that the bow imperfections of slender beams are decisively influenced by the alignment of the roof bracing during assembly.
The measurements of Brüninghoff [20] confirmed the similarity of the bow imperfections of adjacent beams. In a roof structure with 13 beams and two roof bracings, he found differences in the bow imperfections of adjacent beams between 1 mm and 6 mm, with all beams being pre-deformed in the same direction. Absolute values were between 24 mm and 33 mm.
FprEN 1995-3 [70] specifies a maximum permitted deviation of the length of timber beam-columns, e.g. purlins, of 5 mm. This value approximately corresponds to the deviation of the bow imperfections of adjacent beams in the measurements of [20] and [163]. Compared to the maxima of the measured bow imperfections, the 5 mm were rather low, see Figure 3.7. In addition, the length tolerance represents a random error, making it unlikely that the length deviations of several purlins connected in a row add up. Thus, the influence of the deviation of the length of purlins and compression struts on the bow imperfections was small compared to the influence of the alignment of the roof bracing.
Systematic deviations in the beam width are conceivable. Due to their small size, ≤ 2 mm, see BS-Holz-Merkblatt [23], these are, however, of minor importance.

As twist imperfections of adjacent beams coupled by purlins and compression struts showed only minor similarities, see Töpler and Kuhlmann [163], it was concluded that twist imperfections are decisively influenced by the alignment of the individual beams at the fork supports.

3.2.6 Summary

Within the research project DIBt - ZP 52-5-13.194 [107], 23 buildings were surveyed with a laser scanner directly after assembly, and the geometrical imperfections of 202 softwood GL beams, 38 beech LVL beams, and 57 beech LVL columns were analysed, see Section 3.2.2. The obtained point clouds were automatically evaluated with a developed Matlab script, see Section 3.2.3. An approximation method for a simplified calculation of equivalent bow and twist imperfections was developed and validated, see Section 3.2.4.2 and Equation (3.3).
It was observed that the geometrical imperfections of beams can be split into three parts: the bow imperfections e_y, the twist imperfections at midspan $e_{\theta,mid}H_{ap}$, and the twist imperfections at the fork supports $e_{\theta,supp}$, see also Figure 3.6. For the softwood GL beams, the 95% quantile values of the equivalent bow imperfections, the equivalent twist imperfections at midspan, and the twist imperfections at the supports of $L/1180$, $L/1600$, and $1/100$, respectively, were determined, see Section 3.2.5 and Tables 3.3, 3.4, and 3.5. Additionally, the bow and sway imperfections of the beech LVL columns were determined, see Tables 3.3 and 3.6. The determined bow imperfections agreed well with measured values of Ehlbeck and Blaß [44] and Dietsch and Henke [34] and the equivalent bow imperfection underlying the k_c-method in EN 1995-1-1 [57]. The equivalent bow imperfection of timber members given in EN 1995-1-1 [57] for calculations using T2O, $L/400$, seemed to be on the safe side and is further discussed in Section 6.3. Twist imperfections had hardly been reported in the literature and seemed to be not considered in the design of timber beams according to EN 1995-1-1 [57]. However, as the measured twist imperfections were about 70% of the size of the bow imperfections they can have a significant impact on the LTB load-bearing capacity.
The necessary combination of geometrical and structural imperfections into equivalent geometrical imperfections is discussed in Sections 5.6.2 and 6.3. The findings are summarised in the design proposals for standardisation in Section 7, which were already incorporated in FprEN 1995-1-1 [69].

3.3 Flexural buckling tests on beech LVL columns

3.3.1 General

Within the research project RP 7-1 of the Cluster of Excellence *Integrative Computational Design in Architecture and Construction* (IntCDC) [109], 27 flexural buckling tests on full-scale beech LVL columns were conducted at the test facilities of the MPA Stuttgart, see Figures 3.20 and 3.21. The objectives were to investigate the load-bearing behaviour and buckling curves of beech LVL columns, to validate a numerical model with the experimental results, see Section 5.5.2, and to evaluate the design methods in EN 1995-1-1 [57] and FprEN 1995-1-1 [69] for flexural buckling of beech LVL columns, see Section 6.4. In preceding tests, the elastic modulus $E_{0,el}$ of each test specimen and the stress-strain curve of beech LVL for compression in grain direction were determined, as these are relevant input parameters for comparative analyses. A more detailed description is given by Töpler [155]. The complete experimental data are available at Töpler and Kuhlmann [167]. An excerpt of the experimental data is also given in Annex A.

3.3.2 Test programme, setup and execution

3.3.2.1 Test programme

Flexural buckling tests on 27 beech LVL columns made of GL75 according to ETA-14/0354 [63] were conducted. Three parameters were varied: the slenderness by means of the length and cross-sectional dimensions, the eccentricity of the applied axial compressive force, and

Figure 3.20: Flexural buckling test S13; beech LVL column with dimensions of $200 \cdot 200 \cdot 2500$ mm^3.

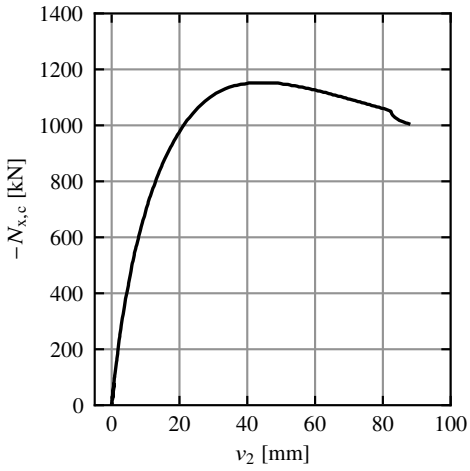

Figure 3.21: Flexural buckling test S08; vertical compressive force $N_{x,c}$ plotted over the horizontal deformation at midspan v_2; experimental results.

Table 3.7: Test programme for flexural buckling of beech LVL GL75 columns.

Specimen number	Number of specimens	L [mm]	H [mm]	B [mm]	$\lambda_{c,rel}$ [1]	Orientation of lamellas	Load-eccentricity
S01–S03	3	3000	120	120	1.89	Flatwise	$B/10$
S04–S06	3	3000	160	160	1.45	Flatwise	$B/10$
S07–S09	3	3000	200	200	1.18	Flatwise	$B/10$
S10–S12	3	2500	200	200	1.00	Flatwise	$B/6.7$
S13–S15	3	2500	200	200	1.00	Edgewise	$B/10$
S16–S18	3	2500	200	200	1.00	Flatwise	$B/10$
S19–S21	3	2500	200	200	1.00	Flatwise	$B/20$
S22–S24	3	2000	200	200	0.821	Flatwise	$B/10$
S25–S27	3	2000	200	200	0.821	Edgewise	$B/10$

[1] Calculated with Equation (2.60), with characteristic material values according to ETA-14/0354 [63], with the size effect on the compressive strength for $H = 160$ mm and 200 mm according to ETA-14/0354 [63], and with $L_{c,ef}$ considering the test setup.

the orientation of the lamellas, see Table 3.7.
The dimensions were chosen to represent typical values of medium-slender columns in building practice. This slenderness range is most interesting if investigating the reduction in load-bearing capacity due to flexural buckling, as strength, stiffness, and imperfections have a relevant influence, see Figure 2.4. In contrast, the load-bearing capacity of stocky columns is governed by the compressive strength $f_{c,0}$ and the load-bearing capacity of slender columns by the elastic modulus $E_{0,el}$, both of which are sufficiently well known, see Section 2 and ETA-14/0354 [63]. As the flatwise bending strength was expected to be lower, this orientation was chosen as the default. To force a flexural buckling in a defined direction and to minimise the influence of the unplanned geometrical and the hardly measurable structural imperfections, the axial load was applied eccentrically similar to the experiments of, e.g. Buchanan et al. [25] and Theiler [154].

For each column test specimen, one elastic bending test was conducted before the destructive flexural buckling tests to determine the bending elastic modulus $E_{0,el}$, see Figure 3.22. The orientation of the lamellas was chosen along the column tests, see Table 3.7.

Five compression tests in grain direction were conducted to determine the compressive strength $f_{c,0}$ and the stress-strain curve of beech LVL GL75 in grain direction, see Figure 3.23. Dimensions of $120 \cdot 50 \cdot 300$ mm^3 were chosen to correspond with EN 408 [60] and compression tests for the determination of the characteristic compressive strength $f_{c,0,k}$ of GL75 carried out by Dill-Langer and Aicher [36]. The test specimens were all milled from the same residual piece of one column. The ratio $H/B = 6$ also defines $\lambda_{c,y/z,rel,0}$ in the k_c-method, see Section 2.2.1.8 and Equation (2.12). The orientation of the lamellas was parallel to the short side, the width.

3.3.2.2 Setup and execution

The preceding elastic 4-point bending tests were conducted according to EN 408 [60] to determine the global bending modulus of elasticity $E_{0,el}$, see Figure 3.22. In the 1st load cycle, a displacement-controlled loading up to 40% of the estimated load-bearing capacity $F_{R,est}$ was applied in approximately 120 s, held for 30 s, unloaded at the same speed to 10% of $F_{R,est}$, held for 30 s, reloaded in the 2nd load cycle at the same speed up to 40% of $F_{R,est}$, held for 30 s, and fully unloaded. The reloading was carried out in accordance with EN 26891 [58] in order to minimise slip in the test setup.

The preceding compression tests in grain direction were conducted according to EN 408 [60] and Dill-Langer and Aicher [36] to determine the compressive strength $f_{c,0}$ and the stress-strain curve of beech LVL GL75 in grain direction, see Figure 3.23. In the 1st load cycle, a displacement-controlled loading up to 40% of the estimated load-bearing capacity $F_{R,est}$ was applied with 0.008 mm/s, held for 30 s, unloaded at the same speed to 10% of $F_{R,est}$, held for 30 s, loaded in the 2nd load cycle at the same speed until exceeding the load-bearing capacity, and a load drop to 300 kN. The vertical deformations were measured with two displacement transducers on both wide sides of the test specimens over a length of 230 mm.

The flexural buckling tests on the beech LVL columns were conducted as compression tests with a defined load-eccentricity, see Figure 3.20. Tilting bearings were arranged on the column top and base to allow a rotation around the z-axis with as little restriction as possible. The structural system thus corresponded to Euler buckling mode 2 with minimal rotational springs at the supports. The rotation points of the tilting bearings had a distance of 153 mm and 154 mm to the column surface at the top and bottom, respectively. The load was applied displacement-controlled from the bottom at a speed of 2 mm/min. The 1st

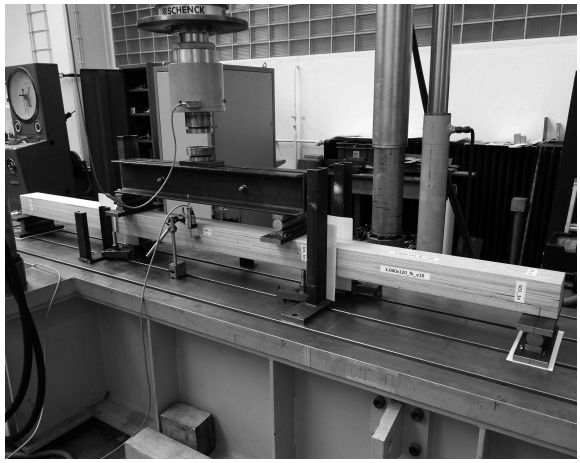

Figure 3.22: Elastic 4-point bending test; S01 with dimensions of $120 \cdot 120 \cdot 3000$ mm^3.

Figure 3.23: Compression test in grain direction.

load cycle was conducted up to 80 kN, and the 2nd load cycle until the columns failed. In tests S09 to S27, in the 2nd load cycle, the machine displacement was held constant every 2 mm for 30 s to 180 s until there was no significant load drop anymore, see Figures in Annex A.1. This allowed for relaxation and creep of the material. However, as the stiffness and load-bearing capacity of wood are dependent on the loading rate, any deviation from the loading procedures for determining the material strengths described in EN 408 [60] can cause systematic deviations in the observed stiffnesses and strengths. In hindsight, it is therefore not advisable to employ the procedure of holding the deformations constant in certain intervals for comparable experiments. The load-eccentricity was realised by the same offset of the columns at both tilting bearings at the top and base. As protection if the columns failed, horizontal timber beams were arranged to prevent the test specimen from falling out of the test facility. The measurement of the complex deformation behaviour at midspan was conducted with the optical measuring system ARAMIS Adjustable 12M. For this purpose, a stochastic pattern was applied to two adjacent sides of the test specimens at midspan. This was supplemented by measurement points at the supports. The measuring system was set up at a 45° angle to the sides of the columns in order to measure both sides with the stochastic pattern in parallel, analogous to the perspective in Figure 3.20.

Exact cross-sectional dimensions and weight were documented directly before each test series. Before and after the testing, the test specimens were wrapped in vapour-proof foil to prevent changes in the wood moisture content. The wood moisture content was not examined because the measurements for the elastic modulus and compressive strength already accounted for its influence, making its precise value irrelevant to the evaluation of the results.

3.3.3 Measurement results

3.3.3.1 Evaluation

The preceding elastic bending tests and the compression tests were evaluated according to EN 408 [60]. In the evaluation of the compression tests, the beginning of the plasticising, i.e. the proportionality limit $f_{c,0,lin}$, was determined, see Figure 2.19. It was defined as the point at which the total strains ϵ_0 exceeded the linear elastic strains $\epsilon_{0,el} = \sigma_0 / E_{0,el}$ by 5%.

For the flexural buckling tests of the beech LVL columns, the horizontal and vertical deformations at midspan and at the supports and the rotations at the supports were analysed. The horizontal deformation at midspan, which is discussed below, is the difference between the horizontal deformation at midspan and the horizontal deformations at the column head and base, see Töpler [155]. The results of column S01 were not included in the evaluation because the calotte of the testing machine was utilised instead of a tilting bearing at the bottom support, which acted rather as a restraint due to high friction. In tests S09 to S27, there was no significant effect of relaxation on the load-bearing capacities, and the results were assessed without consideration of the relaxation.

Table 3.8: Results of the preceding elastic bending tests on the beech LVL GL75 columns.

	$E_{0,el}$ [N/mm^2]	$E_{0,el,flat}$ [N/mm^2]	$E_{0,el,edge}$ [N/mm^2]	ρ [kg/m^3]
Mean	16,400	16,600	15,700	801
Minimum	14,700	15,500	14,700	788
Maximum	18,000	18,000	16,500	820
COV	0.0463	0.0402	0.0377	0.0113

3.3.3.2 Results

The summarised results of the preceding elastic bending tests are given in Table 3.8. The mean value of the elastic bending modulus in grain direction $E_{0,el}$ was 16,400 N/mm^2. The mean elastic modulus for flatwise bending $E_{0,el,flat}$ of 21 test specimens was approximately 6% higher than the one for edgewise bending $E_{0,el,edge}$ of the other 6 test specimens. All results are given in Annex A.1.

The stress-strain curve of the preceding compression test 2.1 is presented as exemplary for all tests in Figure 3.24. The x-axis displays the strain ϵ_0, and the y-axis exhibits the stress σ_0. In addition, the important parameters derived from the stress-strain curves and the curve of an idealised ellipsoid plasticising (Ellipse) are illustrated, see also Figure 5.5. The curve was linear elastic up to approximately 65% of the load-bearing capacity. Subsequently, considerable plasticising occurred until the compressive strength $f_{c,0}$ was reached. A

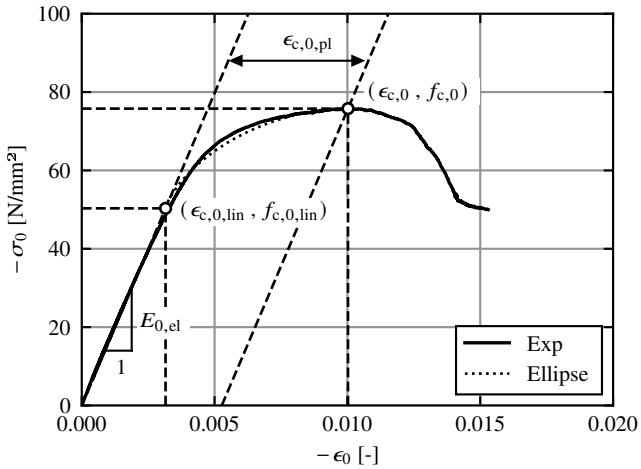

Figure 3.24: Stress-strain curve of test specimen 2.1; compression in grain direction of beech LVL; stresses σ_0 plotted over strains ϵ_0; relevant parameters are highlighted.

Table 3.9: Results of five compression tests in grain direction on beech LVL GL75.

	$E_{0,el}$ [N/mm^2]	$f_{c,0,lin}$ [$\cdot f_{c,0}$]	$f_{c,0}$ [N/mm^2]	$\epsilon_{c,0,pl}$ [$\cdot \epsilon_{c,0,el}$]	ρ [kg/m^3]
Mean	16,200	0.662	−76.9	1.26	798
Minimum	15,600	0.642	−74.3	1.08	794
Maximum	16,900	0.689	−80.4	1.65	802
COV	0.0302	0.0301	0.0384	0.188	0.00411

significant load drop followed. During plasticising, a visible buckling of the fibres occurred at the corners of the test specimen, and, after reaching the compressive strength, the fibre buckling spread over the entire cross-section. The latter manifested itself partly in the form of a kink band with an inclination of approximately 45°. The main results of the tests are summarised in Table 3.9. All results are given in Annex A.2.

The load-deformation curve of the flexural buckling test of column S08 is presented as exemplary for all tests in Figure 3.21. The x-axis displays the horizontal deformation at midspan v, and the y-axis exhibits the compressive force $N_{x,c}$. The curve was nonlinear from the beginning. After the load-bearing capacity $N_{x,c,R}$ was reached, the horizontal deformations increased significantly with a moderate load decrease until the brittle failure of the test specimen occurred. Therefore, the load-bearing capacity was always defined by the peak of the load-deformation curve and not the brittle member failure in tension.

The experimentally determined relative flexural buckling load-bearing capacities k_c of columns S02 to S27 are plotted in Figure 3.25 over the relative flexural buckling slenderness ratio $\lambda_{c,rel}$ and given in Table 3.10.
In this case,

$$k_c = \frac{N_{x,c,R}}{HBf_{c,0}} \quad , \tag{3.5}$$

where $N_{x,c,R}$ is the load-bearing capacity, H and B are the measured cross-sectional dimensions, see Table A.1, and $f_{c,0}$ is the mean compressive strength −76.9 N/mm^2 from the compression tests, see Table 3.9. $\lambda_{c,rel}$ was calculated with Equation (2.11), measured elastic moduli and geometries of each test specimen according to Table A.1, and above mentioned $f_{c,0}$, see also discussion of Figure 2.7. N_{cr} was calculated with Equation (2.3) and the mean elastic modulus $E_{0,el}$ = 16,400 N/mm^2 from the preceding elastic bending tests, see Table 3.8.
The load-bearing capacities followed the expected shape of a buckling curve, and their scatter was low. The load-eccentricity had the expected large influence on the load-bearing capacity. As the load-eccentricity caused a planned bending moment $M_{y,1}$, k_c was always smaller than one. The comparison with results of the k_c-method from EN 1995-1-1 [57] is discussed in Section 3.3.4.

The failure of the columns was announced in 21 cases by an audible cracking. Before member failure, a visible locale tensile failure or compressive failure occurred in two cases each, see Table 3.10. The member failure took place suddenly and with a loud bang. It consisted of a tensile failure at the tension side of the column at midspan and an adjacent combined transverse tensile and shear failure, which expanded to different extents towards the supports, see Figure 3.27. When failing, the column sometimes "jumped" out of the supports due to the released energy, see Figure 3.26. In 16 cases, the tensile failure was highly defibrated, see Figure 3.27. In 8 cases, the tensile failure was moderately defibrated. In 2 cases, the tensile failure was not defibrated and the columns failed along lamella joints. Heavily defibrated means that the length of the defibrated area on the bending side was larger than 15% of the column length. The maximum was 37%. Moderately defibrated means that the length of the defibrated area was less than 15%, but there was no punctual failure. The combined transverse tensile and shear failure occurred in several planes, see Figure 3.27, and, in the case of stocky columns with $B = 200$ mm subjected to flatwise bending, sometimes led to a splitting of the cross-section over the entire width and length. For columns subjected to edgewise bending, the transverse tensile and shear failure was significantly less pronounced, i.e. over 35% to 45% of the column length, i.e. than for columns subjected to flatwise bending, over 27% to 100% of the column length. For stockier columns with $B = 200$ mm and $L \leq 2500$ mm, minor fibre buckling occurred at the cross-sectional corners in the compression zone, between 0.25 and 0.75 of the column length. In 11 out of 18 cases, a kink band formed in the compression zone, see Figure 3.28.

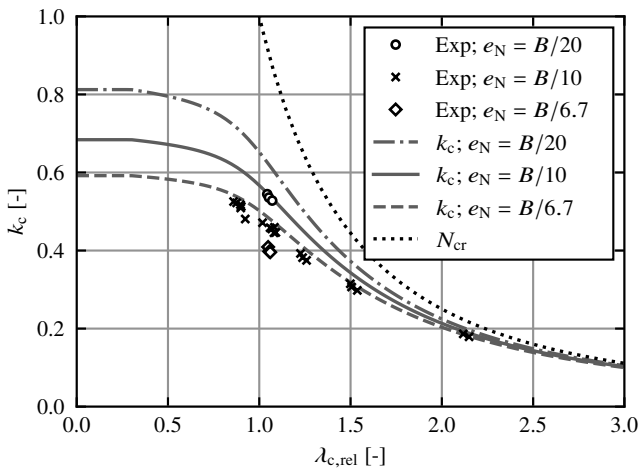

Figure 3.25: Experimentally determined relative flexural buckling load-bearing capacities k_c of columns S02 to S27 plotted over the relative flexural buckling slenderness ratio $\lambda_{c,rel}$; comparison with the relative critical axial compressive forces N_{cr} and results of the k_c-method according to EN 1995-1-1 [57]; k_c and $\lambda_{c,rel}$ calculated with *measured* geometries and material values.

Table 3.10: Results of the flexural buckling tests on beech LVL GL75 columns.

Series number	$\lambda_{c,rel}$ [1]	$N_{x,c,R}$ [kN]	k_c	Failure at the end			Failure before end
				Defibration	Comp. [2]	Kink band	
S02	2.117	−200	0.186	Moderate	-	-	-
S03	2.149	−193	0.179	High	-	-	-
S04	1.537	−569	0.298	High	-	-	-
S05	1.505	−585	0.307	Not	-	-	-
S06	1.499	−601	0.315	Moderate	-	-	-
S07	1.259	−1130	0.375	High	-	-	-
S08	1.237	−1152	0.382	High	-	-	Tensile
S09	1.226	−1183	0.392	Moderate	-	-	-
S10	1.048	−1226	0.409	High	x	x	-
S11	1.055	−1191	0.398	Not	x	x	Compressive
S12	1.060	−1185	0.396	High	x	-	-
S13	1.083	−1359	0.460	High	x	-	-
S14	1.091	−1321	0.446	High	x	-	-
S15	1.069	−1348	0.455	High	x	-	-
S16	1.018	−1418	0.471	High	-	-	-
S17	1.059	−1378	0.458	High	-	-	-
S18	1.081	−1342	0.446	High	-	-	-
S19	1.044	−1634	0.545	Moderate	x	x	-
S20	1.053	−1609	0.536	High	x	x	-
S21	1.071	−1590	0.528	High	x	x	-
S22	0.859	−1576	0.526	Moderate	x	x	-
S23	0.876	−1569	0.522	Moderate	x	x	-
S24	0.898	−1528	0.509	High	x	x	-
S25	0.923	−1439	0.481	Moderate	x	x	-
S26	0.901	−1535	0.513	Moderate	x	x	Compressive
S27	0.897	−1548	0.518	High	x	x	Tensile

[1] Calculated with Equation (2.60), measured elastic moduli and geometries of each test specimen according to Table A.1 and $f_{c,0} = -76.9$ N/mm^2 from the compression tests, see Table 3.9.

[2] Comp. = Compression.

3.3.4 Discussion

$E_{0,el,mean}$ = 16,500 N/mm^2 and 16,200 N/mm^2, which were determined in the preceding elastic bending and axial compression tests, see Tables 3.8 and 3.9, were in good agreement with results from previous tests and literature, see Töpler and Kuhlmann [161] with $E_{0,el,mean}$ = 17,600 N/mm^2, Ehrhart et al. [51] with $E_{0,el,mean}$ = 16,200 N/mm^2 for u = 6.1%, and ETA-14/0354 [63] with $E_{0,el,mean}$ = 16,800 N/mm^2. This also indicated a low wood moisture content of the test specimens of 6% to 7%.

$f_{c,0,mean} = -76.9$ N/mm^2, which was determined in the preceding compression tests, see Table 3.9, was in good agreement with literature values, see Dill-Langer and Aicher [37]

with $f_{c,0} = -60$ N/mm^2 to -80 N/mm^2. The scatter of $f_{c,0}$ was very low because all test specimens were fabricated from the same residual piece of one column test specimen and because beech LVL is a very homogeneous material.
The large plastic strains of beech LVL on reaching compressive strength with a mean of $\epsilon_{c,0,pl} = 1.26\epsilon_{c,0,el}$, see Table 3.9, were remarkable. For softwood, Glos [77] determined a mean value of $\epsilon_{c,0,pl} = 0.25\epsilon_{c,0,el}$, see Section 2.3.3.1. Thus, for beech LVL, the experimentally determined plastic strains were 4 to 6.5 times higher than for European softwood. Fortunately, the experimental data of Ehrhart et al. [53] could be re-evaluated to validate the own results, see Töpler and Kuhlmann [164]. For machine forces larger than 50% of the estimated maximum force, [53] only recorded the cylinder displacements. Therefore, the strains were evaluated based on a corrected value of the cylinder displacements, which is subject to some uncertainty. From the data of [53], plastic strain of $\epsilon_{c,0,pl} \approx 1.5\epsilon_{c,0,el}$ and a proportionality limit of $f_{c,0,lin} \approx 0.75 f_{c,0}$ were determined for wood moisture contents between 6% and 9%. For a wood moisture content of 17%, representing SC 2, smaller plastic strains of $\epsilon_{c,0,pl} \approx 1.15\epsilon_{c,0,el}$ were assessed. These values were in good agreement with own test results.
The plastic strains could be mapped well by means of an ellipse, see Figure 3.24, as proposed by Grosse [83], where $(f_{c,0} - f_{c,0,lin})$ and $\epsilon_{c,0,pl}$ were the ellipse radii. For more details see also Figures 5.5 and 5.4. The analytical equation of the stress-strain relationship of spruce by Glos [77] was not a satisfactory approximation for beech LVL, as the $\epsilon_{c,0,pl}$ value led to a proportionality limit of $f_{c,0,lin} \approx 0.1 f_{c,0}$ in this equation, which was far too small. Based on the results in Table 3.9, $\epsilon_{c,0,pl} = 1.25\epsilon_{c,0,el}$, $f_{c,0,lin} = 0.65 f_{c,0}$, and $f_{c,0} = 40.0$ N/mm^2 were chosen for the FE model described in Section 5.

Figure 3.26: Column S22 after failure; test specimen "jumped" out of the tilting bearings at failure.

Figure 3.27: Combined tensile, transverse tensile, and shear failure at midspan of column S20.

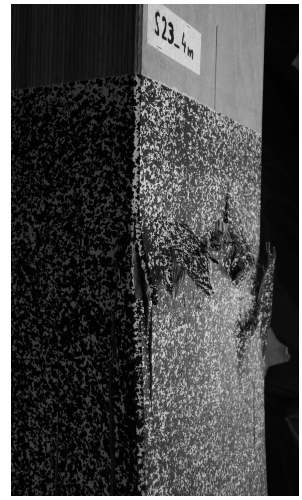

Figure 3.28: Fibre buckling over the entire width of the compression zone, i.e. a kink band, of column S23.

The flexural buckling tests demonstrated that the described test setup is well suited for the experimental investigation of flexural buckling. A planned eccentricity of the axial compressive force is generally advisable, as this enforces a flexural buckling in a defined direction and minimises the influence of unplanned geometrical and hardly measurable structural imperfections. The load-eccentricity can easily be taken into account in FEA. In contrast, this is difficult for structural imperfections, as these can hardly be measured and therefore cannot be considered in models. This is a good example of how the influence of unknown or not-measurable basic variables can be reduced by introducing an additional but known basic variable that exceeds this influence and thereby increases the accuracy of the prediction models.

Figure 3.29 and Table 3.11 present the experimentally determined relative flexural buckling load-bearing capacities k_c and the results of the k_c-method from EN 1995-1-1 [57]. k_c was calculated with Equation (3.5) and characteristic material values according to ETA-14/0354 [63] of $f_{c,0,k} = k_{c,0} \cdot 59.4$ N/mm^2, $f_{m,k} = k_{h,m} \cdot 75$ N/mm^2, and $E_{0,05} = 15{,}300$ N/mm^2, where $k_{c,0}$ and $k_{h,m}$ consider the size effect. For k_c in Figure 3.29, a cross-section with $200 \cdot 200$ mm^2 was assumed. $\lambda_{c,rel}$ and N_{cr} were calculated with Equations (2.64) and (2.3) and the same material values. The characteristic load-bearing capacities according to the k_c-method from EN 1995-1-1 [57] were up to 10% higher than the experimentally determined load-bearing capacities, see Table 3.11. Actually, the characteristic values according to EN 1995-1-1 [57] should be on the safe side to be in line with the semi-probabilistic safety

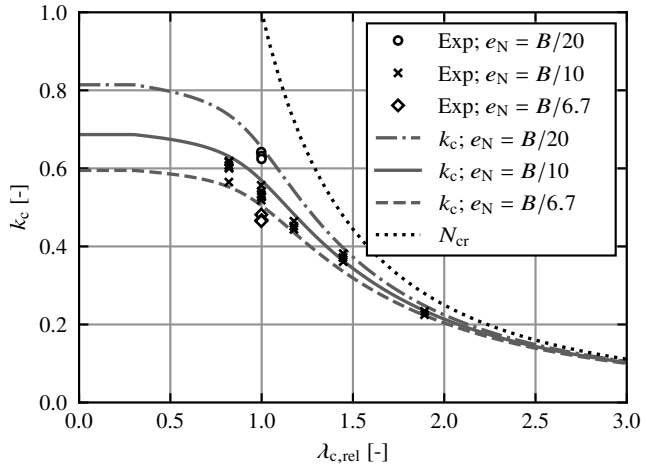

Figure 3.29: Experimentally determined relative flexural buckling load-bearing capacities k_c of columns S02 to S27 plotted over the relative flexural buckling slenderness ratio $\lambda_{c,rel}$; comparison with the relative critical axial compressive forces N_{cr} and results of the k_c-method according to EN 1995-1-1 [57]; k_c and $\lambda_{c,rel}$ calculated with *nominal* geometries and material values.

Table 3.11: Comparison of the experimentally determined flexural buckling load-bearing capacities and the results of the k_c-method from EN 1995-1-1 [57].

Series number	$\lambda_{c,rel}$ [1]	$N_{x,c,R,exp}$ [kN]	$k_{c,exp}$	$k_{c,EC5}$	$\frac{k_{c,exp}}{k_{c,EC5}}$
S02	1.89	−200	0.233	0.238	0.979
S03	1.89	−193	0.225	0.238	0.945
S04	1.45	−569	0.361	0.367	0.984
S05	1.45	−585	0.371	0.367	1.011
S06	1.45	−601	0.382	0.367	1.041
S07	1.18	−1130	0.444	0.483	0.919
S08	1.18	−1152	0.452	0.483	0.936
S09	1.18	−1183	0.464	0.483	0.961
S10	1.00	−1226	0.481	0.505	0.952
S11	1.00	−1191	0.468	0.504	0.929
S12	1.00	−1185	0.465	0.505	0.921
S13	1.00	−1359	0.534	0.570	0.937
S14	1.00	−1321	0.519	0.570	0.911
S15	1.00	−1348	0.529	0.569	0.930
S16	1.00	−1418	0.557	0.570	0.977
S17	1.00	−1378	0.541	0.569	0.951
S18	1.00	−1342	0.527	0.569	0.926
S19	1.00	−1634	0.642	0.655	0.980
S20	1.00	−1609	0.632	0.654	0.966
S21	0.82	−1590	0.624	0.654	0.954
S22	0.82	−1576	0.619	0.631	0.981
S23	0.82	−1569	0.616	0.631	0.976
S24	0.82	−1528	0.600	0.631	0.951
S25	0.82	−1439	0.565	0.631	0.895
S26	0.82	−1535	0.603	0.631	0.956
S27	0.82	−1548	0.608	0.631	0.964

[1] Calculated with Equation (2.60), with characteristic material values according to ETA-14/0354 [63], with the size effect on the compressive strength for H = 160 mm and 200 mm according to ETA-14/0354 [63].

concept of the Eurocodes. The reason for these unexpected differences were the high plastic strains of beech LVL compared to softwood GL. This caused a reduction in the bending stiffness, which led to larger horizontal deformations and thus lower load-bearing capacities. Therefore, the k_c-method in EN 1995-1-1 [57] and FprEN 1995-1-1 [69] should not be applied for the design of beech LVL columns without a modification taking into account the material-specific pronounced compressive plasticising in grain direction of beech LVL.

As a final point, the different reference values in Figures 3.25 and 3.29, which the attentive reader may have noticed, need to be discussed. In Figure 3.25, k_c and $\lambda_{c,rel}$ were determined with *measured* or realistically assumed material and geometry parameters.

This representation is suitable for validating prediction models, e.g. the k_c-method in EN 1995-1-1 [57], as it visualises how well a model represents reality. In contrast, the representation in Figure 3.29, in which k_c and $\lambda_{c,rel}$ were determined with *nominal* material properties in accordance with EN 1995-1-1 [57], is suitable for checking the safety level of design equations. It can be employed to determine characteristic load-bearing capacities based on scattering experimental or numerical results, as it clearly illustrates the scattering of the load-bearing capacities of the planned members. This is also discussed in Figures 2.6 and 2.7.

3.3.5 Summary

Within the research project RP 7-1 of the *Cluster of Excellence Integrative Computational Design in Architecture and Construction* (IntCDC), 27 flexural buckling tests on full-scale beech LVL GL75 columns according to ETA-14/0354 [63] were conducted, and their load-bearing behaviour was investigated.

In preceding tests, the elastic modulus $E_{0,el}$ of each test specimen and the stress-strain curves for compression in grain direction were determined. With a proportionality limit of $f_{c,0,lin} \approx 0.65 f_{c,0}$ and plastic strains of $\epsilon_{c,0,pl} \approx 1.25 \epsilon_{c,0,el}$, beech LVL exhibited three to five times higher plasticising than reported by Glos [77] and from own tests in Section 3.4.3.2 for softwood GL. This should be taken into account in ULS design if internal forces are influenced by a loss of stiffness due to plasticising.

The flexural buckling tests demonstrated that the described test setup is well suited for the experimental investigation of flexural buckling. It is generally advisable to apply the axial compressive force eccentrically, as the eccentricity minimises the influence of unplanned geometrical and hardly measurable structural imperfections.
The load-horizontal displacement behaviour of the columns was pronouncedly nonlinear. The load-bearing capacity was always defined by the peak of the load-deformation curve and not a brittle member failure in tension. The member failure was usually announced by a cracking sound, occurred suddenly with a loud bang, and consisted of a tensile failure at midspan and an adjacent combined transverse tensile and shear failure. The load-bearing capacities for different slendernesses followed the expected shape of a buckling curve, and their scatter was low, see Figure 3.25. The characteristic load-bearing capacities according to EN 1995-1-1 [57] were up to 10% higher than the experimentally determined load-bearing capacities, see Figure 3.29. This was due to bespoken high plastic strains $\epsilon_{c,0,pl}$ on reaching the compressive strength and the resulting decrease of the bending stiffness. Therefore, the design methods in EN 1995-1-1 [57] should be modified before applying them to beech LVL columns.
The influence of plasticising on the load-bearing capacity of beech LVL columns is further discussed in Section 6.4. The findings are summarised in the design proposals for standardisation in Section 7.

3.4 Lateral torsional buckling tests on softwood GL beams

3.4.1 General

Within the research project IGF No. 21285 N [108], 19 LTB tests on full-scale softwood GL beams with combined bending and axial compression were conducted at the test facilities of the FMPA Cottbus, see Figure 3.30. The objectives were to investigate the load-bearing behaviour and buckling curves of softwood GL beams subjected to combined bending and axial compression, to validate a numerical model with the experimental results, see Section 5.5.3, and to evaluate current design formulas in EN 1995-1-1 [57] for LTB of timber beams, see Section 6.4. In preceding tests, elastic bending and torsional stiffnesses of each test specimen and the stress-strain curve of the softwood GL for compression in grain direction were determined, as these are relevant input parameters for comparative analyses. A more detailed description is given by Töpler and Kuhlmann [166]. The complete experimental data are available at Töpler and Kuhlmann [168]. An excerpt of the experimental data is also given in Annex B.

3.4.2 Test programme, setup and execution

3.4.2.1 Test programme

LTB tests on 19 softwood GL beams made of GL 24h according to EN 14080 [54] were conducted. Two parameters were varied: the slenderness ratio $\lambda_{m,rel}$ by means of the beam length and height, and the utilisation ratio μ_c of the axial compressive force $N_{x,c}$ according to the k_c-method in EN 1995-1-1 [57], see Table 3.12. Beams of medium slenderness were

Figure 3.30: LTB test T02; GL beam with dimensions of $720 \cdot 120 \cdot 8000$ mm^3 shortly before failure.

Table 3.12: Test programme for LTB of GL 24h beams.

Specimen number	Number of specimens	L [mm]	H [mm]	B [mm]	$\lambda_{m,rel}$ [1]	Axial compressive force [kN]	μ_c [2]
T01–T03	3	8000	720	120	1.041	0	0.00
T04–T05	2	8000	600	120	0.940	0	0.00
T06–T07	2	8000	600	120	0.940	−25	0.20
T08–T09	2	8000	600	120	0.940	−50	0.40
T10–T11	2	8000	600	120	0.940	−75	0.60
T12–T13	2	6000	480	120	0.747	0	0.00
T14–T15	2	6000	480	120	0.747	−35	0.20
T16–T17	2	6000	480	120	0.747	−70	0.40
T18–T19	2	6000	480	120	0.747	−105	0.60

[1] Calculated with Equation (2.63), with characteristic material values according to EN 14080 [54], with the size effect on the bending strength for $H = 480$ mm according to EN 1995-1-1 [57], with an increase of $E_{0,05}G_{0,05}$ by a factor of 1.4 according to DIN EN 1995-1-1/NA [40], and with $L_{m,ef}$ considering the test setup.

[2] $\mu_c = N_{x,c}/N_{x,c,R,k}$, with $N_{x,c,R,k}$ calculated with the k_c-method according to EN 1995-1-1 [57], see Equations (2.56) to (2.60), with characteristic material values according to EN 14080 [54], and with $L_{c,ef} = L$.

chosen because this slenderness range is most interesting if investigating the reduction in load-bearing capacity due to LTB, as strength, stiffness, and imperfections have a relevant influence, see Figure 2.4. In contrast, the load-bearing capacity of stocky beams is governed by the bending strength f_m, and the load-bearing capacity of slender beams by the elastic and shear moduli $E_{0,el}$ and $G_{0,el}$, which are sufficiently well known, see Section 2 and EN 14080 [54]. The axial compressive force was selected to be approximately 0%, 20%, 40%, and 60% of the characteristic flexural buckling load-bearing capacity according to the k_c-method from EN 1995-1-1 [57], i.e. of utilisation ratio $\mu_c = N_{x,c}/N_{x,c,R,k}$. All beams were of a constant rectangular cross-section. The load introduction and support areas were reinforced with pre-drilled, fully threaded screws. Test specimen T01 was used as a trial to examine the test setup, test execution, and measurement devices.

For each LTB test specimen, elastic bending tests about the strong and weak axes and torsion tests were conducted before the destructive LTB tests to determine the bending elastic modulus $E_{0,el}$ and the shear modulus $G_{0,el}$.

8 compression tests in grain direction were conducted to determine the compressive strength $f_{c,0}$ and the stress-strain curve of GL 24h. Dimensions of $120 \cdot 40 \cdot 300$ mm^3 were chosen. The test specimens were milled from residual pieces of four single GL lamellas, which were stored together with the LTB test specimen.

3.4.2.2 Setup and execution

The preceding elastic bending and torsion tests were conducted as 3-point bending and, respectively, torsion tests, with test setups, speeds, and directions of loading identical to the following LTB tests. For the elastic bending tests about the strong axis and the torsion tests, in contrast to the LTB tests, the load was applied with a load frame and two vertical cylinders at midspan, see Figure 3.31. The two vertical cylinders allowed applying a bending load by inducing the same displacement and a torsional load by inducing the opposite displacement. The deformations and rotations were measured with two vertical and four horizontal displacement transducers at midspan, similar to EN 408 [60]. To reduce the slip, a displacement-controlled load was applied in two load cycles with unloading and reloading between a maximum of 10% and 40% of the estimated load-bearing capacity in accordance with EN 26891 [58].

The preceding compression tests in grain direction were conducted according to EN 408 [60] to determine the compressive strength $f_{c,0}$ and the stress-strain curve of softwood GL GL 24h. A displacement-controlled loading was applied. The load-bearing capacity F_R was reached after approximately 300 s, and tests were stopped at a load drop to 80% of F_R. The vertical deformations were measured with two displacement transducers on both wide sides of the test specimens over a length of 180 mm. Exact cross-sectional dimensions and weight were documented directly before the tests.

The LTB experiments were conducted as 3-point bending tests, see Figure 3.32. The supports were constructed as ideal fork supports with rotation points at a horizontal distance of 60 mm from the beam faces. The resulting span of the structural system was $L_s = L - 2 \cdot 60$ mm. On one end of the beams, a horizontal support was formed by an abutment and a centrally

Figure 3.31: Test setup of preceding elastic bending tests about the strong axis and torsion tests.

arranged calotte. On the other end of the beam, the horizontal load was applied centrally using a cylinder with a yoke joint. The axial compressive force generated friction in the horizontal support and the yoke joint, so these acted as rotational springs about the z-axis. Vertical loading was applied at the upper edge in midspan with a horizontal eccentricity perpendicular to the beam axis of 8 mm for a planned LTB in a defined direction. The distance between the upper edge of the beam and the axis of rotation of the load, the screw axis, resulted in an additional vertical eccentricity of 53 mm, see Figure 3.33. To ensure vertical loading if the beams deformed horizontally, the upper bearing of the vertical cylinder was automatically moved horizontally by up to 220 mm. In the trial T01, the vertical cylinder was first installed without inclination, which led during vertical loading to sudden lateral deflections of the test specimen by 5 cm, followed by a dynamic behaviour of the test set-up. Subsequently, for all tests, the vertical cylinder was inclined by 10 mm to 20 mm over its 2210 mm length for limiting the dynamic behaviour of the test setup. The resulting horizontal force acted in the same direction as the horizontal eccentricity of the vertical load. In addition, the speed of the horizontal displacement of the upper bearing of the vertical cylinder was reduced to a minimum. For the 6 m long test specimens, the horizontal eccentricity and the inclination of the vertical cylinder were partly insufficient to generate a LTB of the beams in the desired direction, see T15 in Figure 3.35. The influence of geometrical and structural imperfections and friction in the supports and load application predominated. For this reason, beams T15 to T19 were aligned horizontally at midspan using a jack.

Beams with and without axial compressive force were tested, see Table 3.12. In order to determine the equivalent bow imperfection of each beam, the tests without a planned axial compressive force were also loaded in advance by a small centric axial compressive force of -20 kN, and the horizontal deformations at midspan were measured. In the case of a planned axial compressive force, this was first applied and force-controlled in 120 s up to

Figure 3.32: LTB test setup.

Figure 3.33: Vertical load introduction for LTB tests.

the levels given in Table 3.12. Vertical forces were applied displacement-controlled at a rate of 4 mm/min to 5 mm/min, which resulted in a member failure in about 10 min to 20 min. The tests were stopped at the event of member failure or a load drop to 80% of the load-bearing capacity. A load cycle to minimise slip was rejected due to an observed unfavourable deformation behaviour under repeated loading.
The measurement of the complex deformation behaviour at midspan was conducted with the optical measuring system ARAMIS Adjustable 12M. For this purpose, a stochastic pattern was applied to one side of the test specimens at midspan. Displacement transducers and tilt sensors measured the rotations about the x-, y-, and z-axes at the supports.

Exact cross-sectional dimensions, weight, and wood moisture content of the beams were documented directly before the elastic bending and torsion tests. The wood moisture content was measured with a Trotec T2000 multifunction measuring device [170] at a depth of approximately 2.5 cm at three points per beam. Before and after the testing, the test specimens were wrapped in vapour-proof foil to prevent changes in the wood moisture content.

3.4.3 Measurement results

3.4.3.1 Evaluation

The preceding elastic bending and torsion tests were evaluated according to EN 408 [60]. The shear modulus was calculated from the results of the torsion test by

$$G_{0,\mathrm{el}} = \frac{M_\mathrm{x} L}{4\theta I_\mathrm{x}} \quad , \tag{3.6}$$

where M_x is the applied torsional moment, L is the span, θ is the measured rotation at midspan, and I_x is the torsional moment of inertia according to Equation (2.18). FEA with solid elements generally lead to a slightly deviating relationship between rotations θ and elastic and shear moduli than Equation (2.18), the values of the elastic and shear moduli for FEA were determined iteratively in FEA, results see Annex B.2. For bending about the weak axis, the analytically and numerically determined elastic moduli were almost identical, see Table B.2. For bending about the strong axis, numerically determined elastic moduli were 2% to 6% larger than analytically determined values. For torsion, numerically determined shear moduli were 5% to 10% smaller than analytically determined values.

The preceding compression tests were evaluated according to EN 408 [60]. Additionally, the beginning of plasticising, i.e. the proportionality limit $f_{\mathrm{c},0,\mathrm{lin}}$, was evaluated, see Figure 2.19. The proportionality limit was defined as the point at which the total strains ϵ_0 exceeded the linear elastic strains $\epsilon_{0,\mathrm{el}} = \sigma_0 / E_{0,\mathrm{el}}$ by 5%. The total strains ϵ_0 were calculated with results of the two displacement transducers.

For the LTB tests, the horizontal and vertical deformations at midspan and the rotations at the supports were evaluated. The equivalent bow imperfections $e_{\mathrm{y,eq}}$ were determined with

Table 3.13: Results of the preceding elastic bending and torsion tests on the GL 24 beams for FEA.

	$E_{0,el,y}$ [N/mm^2]	$E_{0,el,z}$ [N/mm^2]	$E_{0,el,y}/E_{0,el,z}$ [-]	$E_{0,el}$ [N/mm^2]	$G_{0,el}$ [N/mm^2]
Mean	12,100	12,100	1.006	12,100	747
Minimum	10,900	11,200	0.940	11,100	625
Maximum	14,700	13,200	1.120	13,900	812
COV	0.0830	0.0503	0.0463	0.0644	0.0616

the horizontal deformations v_2 at applied axial compressive force $N_{x,c}$ by

$$e_{y,eq} = \frac{v_2 \cdot (1 - \alpha_{c,y})}{\alpha_{c,y}} \quad , \tag{3.7}$$

where $\alpha_{c,y}$ is the amplification factor for critical axial compressive forces according to Equation (2.2). Equation (3.7) is a simplification of Equation (2.6).

3.4.3.2 Results

The results of the preceding elastic bending and torsion tests for FEA are given in Table 3.13. The mean values of the elastic and shear moduli were 12,100 N/mm^2 and 747 N/mm^2, respectively. On average, the elastic moduli for bending about the strong and weak axes were almost identical. Thus, it was assumed that the mean value of $E_{0,el,y}$ and $E_{0,el,z}$ represented a good approximation for the FEAs in the validation, see Section 5.5.3. All results are given in Annex B.2.
The stress-strain curve of the preceding compression test 1.2 is presented as exemplary for all compression tests in Figure 3.34. The x-axis displays the strain ϵ_0, and the y-axis exhibits the stress σ_0. In addition, the important parameters derived from the stress-strain curves and the curve of an idealised ellipsoid plasticising are illustrated, see also Figure 5.5. The curve was linear elastic up to approximately 80% of the load-bearing capacity. Subsequently, plasticising occurred until the compressive strength $f_{c,0}$ was reached. A load drop followed. During the tests, crackling was heard once the proportionality limit was reached. The failure occurred (i) as buckling of the fibres, which ultimately manifested itself in the form of kink bands and led to ductile behaviour after the maximum load was reached; and (ii) as tensile failure perpendicular to the grain in the form of splitting of the test specimens in the grain direction, starting from knots. The main results of the tests are summarised in Table 3.14. All results are given in Annex B.3.

Typical load-deformation curves of the LTB tests are presented in Figure 3.35 for beams T05, T06, and T15. The x-axis displays the horizontal deformation of the beam axis at midspan v, and the y-axis exhibits the vertical cylinder force F_z. The curves of 16 out of 19 tests were pronouncedly nonlinear, see T05 and T06. After about 80% of the load-bearing capacity was reached, large horizontal deformations occurred, see Figure 3.30, leading to a plateau in the load-deformation curves. In some cases, local failure caused sudden

Table 3.14: Results of eight compression tests in grain direction on GL 24h.

	$E_{0,el}$ [N/mm^2]	$f_{c,0,lin}$ [$\cdot f_{c,0}$]	$f_{c,0}$ [N/mm^2]	$\epsilon_{c,0,pl}$ [$\cdot \epsilon_{c,0,el}$]	ρ [kg/m^3]
Mean	12,100	0.706	−43.2	0.452	480
Minimum	8970	0.469	−35.1	0.257	407
Maximum	15,000	0.853	−50.2	0.823	530
COV	0.164	0.168	0.107	0.415	0.0935

load drops, followed by partial load and deformation recovery, see T06. The tests were stopped if either a brittle member failure occurred or the load dropped below 80% of the load-bearing capacity. In three cases, the beams failed in uniaxial bending without showing LTB behaviour, see T15 in Figure 3.35. In these cases, the applied horizontal eccentricity of 8 mm and the inclination of the vertical cylinder were not sufficient to overcome the effects of geometrical and structural imperfections and friction at the supports and load application. The determined equivalent bow imperfections ranged from 1.4 mm to 6.7 mm in the opposite direction to the load-eccentricity, see Table B.1, and therefore only partially explained this behaviour. This could indicate that there were significant structural imperfections. For enforcing LTB behaviour, beams T15 to T19 were aligned horizontally at midspan using a jack.

As the axial compressive force increased, (i) the peak of the load-deformation curve shifted to the left; (ii) the maximum deformations v increased; and (iii) the maximum vertical force F_z decreased, see Figure 3.36.

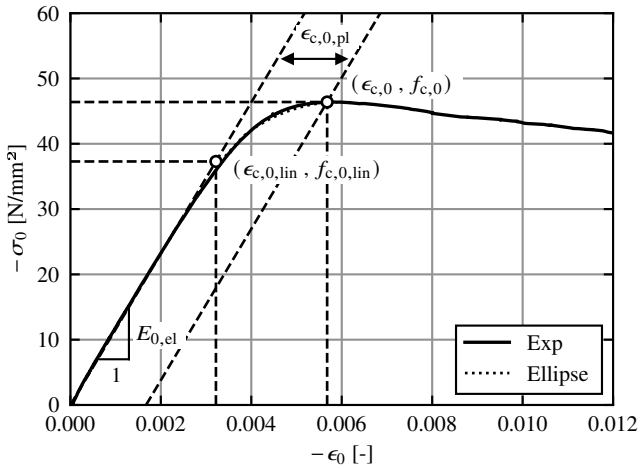

Figure 3.34: Stress-strain curve of test specimen 1.2; compression in grain direction of GL 24h; stresses σ_0 plotted over strains ϵ_0; relevant parameters are highlighted.

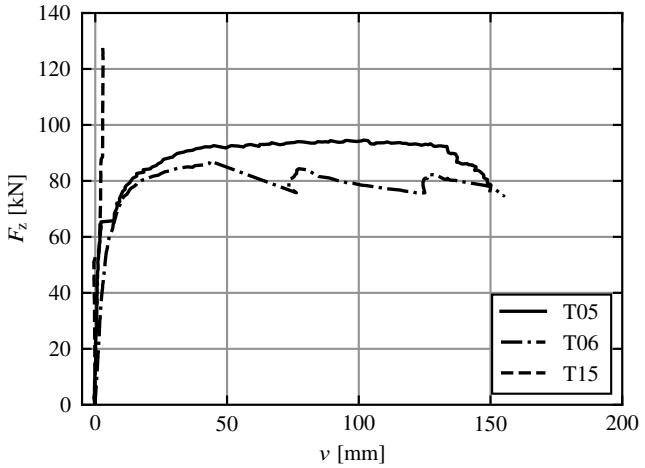

Figure 3.35: LTB tests T05, T06, and T15; vertical force F_z plotted over the horizontal deformation of the beam axis at midspan v; experimental results.

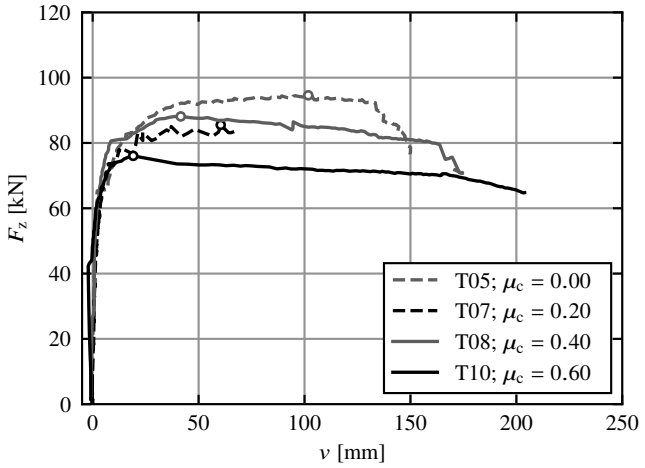

Figure 3.36: LTB tests T05, T07, T08, T10 with $\lambda_{m,rel} = 0.94$; vertical force F_z plotted over the horizontal deformation of the beam axis at midspan v; experimental results; influence of the axial compressive force $N_{x,c}$; circles mark maximum vertical loads (peaks).

The experimentally determined relative load-bearing capacities k_{m} of all beams are plotted over the relative LTB slenderness ratio $\lambda_{\mathrm{m,rel}}$ in Figure 3.37 and are given in Table 3.15. In this case,

$$k_{\mathrm{m}} = \frac{F_{\mathrm{z,R}} \cdot \frac{L_{\mathrm{s}}}{4}}{W_{\mathrm{y}} f_{\mathrm{m,mean}}} \quad , \tag{3.8}$$

where $F_{\mathrm{z,R}}$ is the load-bearing capacity, L_{s} is the span of the structural system, W_{y} is the section modulus about the y-axis, and the mean bending strength $f_{\mathrm{m,mean}}$ = 33.0 N/mm^2 according to Schilling et al. [141]. The experimentally determined load-bearing capacities in Table B.1 and the measured cross-sectional dimensions from Table B.1 were utilised. For design with calculations using T2O, Equation (2.15) for determining $M_{\mathrm{z,2}}$, Equations (2.54) and (2.55) for the bending design verification, and Equation (2.69) for the shear design verification with nominal cross-sectional dimensions from Table 3.12, the experimentally determined mean stiffnesses $E_{0,\mathrm{el}}$ = 12,100 N/mm^2 and $G_{0,\mathrm{el}}$ = 801 N/mm^2, see Table B.2, $f_{\mathrm{m,mean}}$ = 33.0 N/mm^2, and a bow imperfection of 8 mm representing the horizontal load-eccentricity were applied. $M_{\mathrm{y,cr}}$ was calculated with Equation (2.17) and the same cross-sectional dimensions and stiffnesses. $\lambda_{\mathrm{m,rel}}$ was calculated with Equation (2.23), with measured elastic moduli and geometries of each test specimen according to Table B.2, and $f_{\mathrm{m,mean}}$ = 33.0 N/mm^2.
The relative load-bearing capacities decreased with increasing slenderness ratio and followed the expected shape of a buckling curve. For the same dimensions and compressive load,

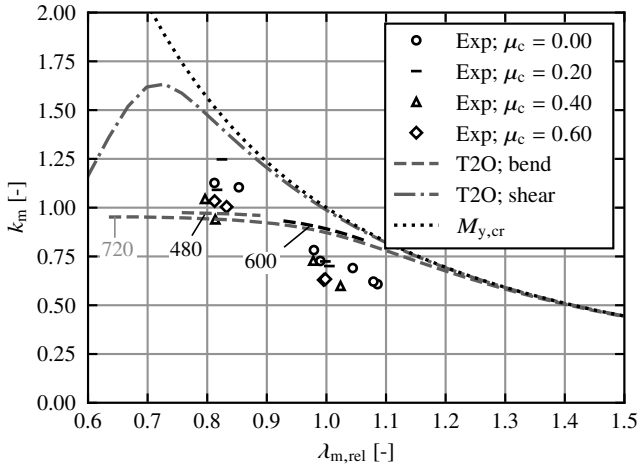

Figure 3.37: Experimentally (Exp) determined relative LTB load-bearing capacities k_{m} plotted over the relative LTB slenderness ratio $\lambda_{\mathrm{m,rel}}$; comparison with the relative critical bending moments $M_{\mathrm{y,cr}}$ and results of bending (bend) and shear design with calculations using T2O according to EN 1995-1-1 [57] with cross-sectional heights 480 mm, 600 mm, and 720 mm; k_{m} and $\lambda_{\mathrm{m,rel}}$ calculated with *measured* or mean geometries and material values.

Table 3.15: Results of the LTB tests on softwood GL 24h beams.

Specimen number	$\lambda_{m,rel}$ [1]	μ_c [2]	$F_{z,R}$ [kN]	k_m
T01	1.086	0.00	106.0	0.608
T02	1.044	0.00	120.5	0.691
T03	1.079	0.00	108.3	0.621
T04	0.990	0.00	88.0	0.727
T05	0.979	0.00	95.1	0.783
T06	0.998	0.20	87.8	0.725
T07	1.005	0.20	85.0	0.701
T08	0.978	0.40	88.3	0.728
T09	1.024	0.40	72.7	0.599
T10	0.995	0.60	76.3	0.630
T11	0.998	0.60	76.9	0.634
T12	0.853	0.00	115.2	1.104
T13	0.812	0.00	117.3	1.127
T14	0.816	0.20	113.9	1.091
T15	0.825	0.20	129.8	1.247
T16	0.814	0.40	97.9	0.940
T17	0.796	0.40	108.9	1.044
T18	0.833	0.60	104.6	1.004
T19	0.812	0.60	107.5	1.034

[1] Calculated with Equation (2.23), with measured elastic moduli and geometries of each test specimen according to Table B.2, and $f_{m,mean} = 33.0$ N/mm^2.

[2] Utilisation ratio of the axial compressive force μ_c, see Table 3.12.

the measured load-bearing capacities scattered by up to 20%. For stocky beams, the 20% scattering was in the same range as the scattering of the bending strength f_m reported by [141] and therefore reasonable, see T12 to T19 in Table 3.15. For the more slender beams, the 20% scattering was surprisingly high, as the scattering of the stiffness reported by [141] is three times smaller than the scattering of the strength, see T01 to T11 in Table 3.15. The comparisons with results of calculations using T2O and the critical bending moment are discussed in Section 3.4.4.

The experimentally determined load-bearing capacities of beams T04 to T19 with combined bending and axial compressive forces are plotted in Figure 3.38. The design with calculations using T2O was carried out analogous to the calculations described in the previous paragraph. The results illustrate the influence of the axial compressive force on the bending and the shear load-bearing capacity. An increase of the axial compressive force from 0% to 60% of the characteristic flexural buckling load-bearing capacity led to a reduction in the bending load-bearing capacity of about 20%. In Section 3.4.4, the experimental results are compared with results of the design methods from EN 1995-1-1 [57].

Three failure modes were observed: tensile failure due to bending, shear failure, and

compression failure, see Figures 3.39 and 3.40. The failure behaviour is documented in Table 3.16. At vertical loadings higher than 20% to 40% of the load-bearing capacity, cracking was audible and indicated minor local failure, being neither visible nor having any significant influence on the load-deformation curves. In 14 out of 18 tests (not documented for T01), loud cracking was audible at vertical loading above 70% of the load-bearing capacity, indicating a significant local failure and leading to a flattening of the load-deformation curves, see Figure 3.35. Only in 4 cases this was visible in the form of local shear or tensile cracks, see Table 3.16. In 12 tests, an abrupt brittle member failure occurred. The remaining 7 tests were aborted if the load dropped below 80% of the load-bearing

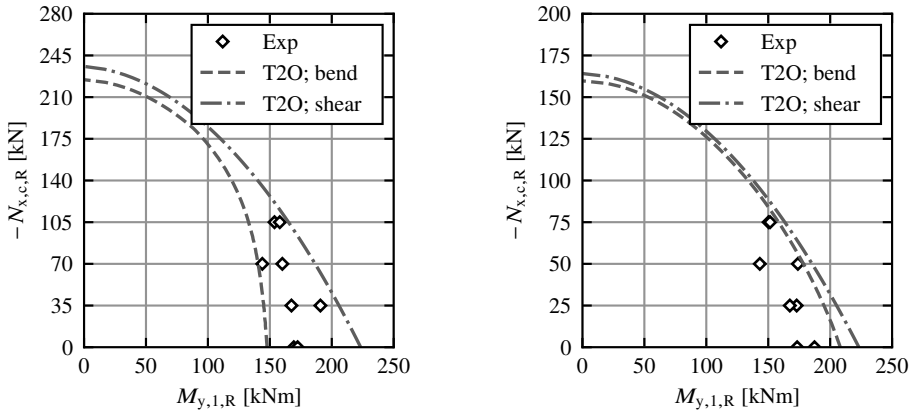

(a) $480 \cdot 120 \cdot 6000$ mm^3. **(b)** $600 \cdot 120 \cdot 8000$ mm^3.

Figure 3.38: Experimentally (Exp) determined absolute LTB load-bearing capacities of beams T04 to T19; comparison with results of bending and shear design with calculations using T2O according to EN 1995-1-1 [57], all with *measured* or mean geometries and material values.

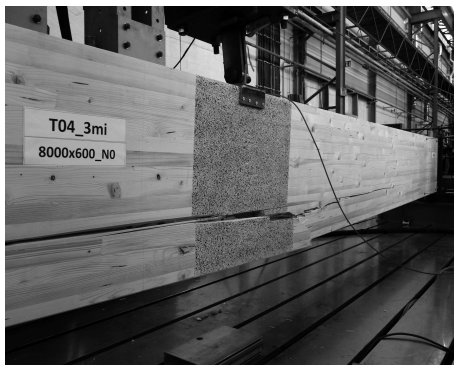

Figure 3.39: Tensile failure of beam T04.

Figure 3.40: Diagonal shear failure of beam T09.

Table 3.16: Visible failure behaviour before and at the end of the LTB tests.

Series number	Member failure	Localised failure at the end			Localised failure before the end	Estimated $f_{v,0,lin}$ [N/mm^2]
		Tensile	Shear	Compression		
T01	-	-	x	[1]	-	[1]
T02	-	-	x	x	-	2.70
T03	Shear	-	x	x	-	1.70
T04	Tensile	x	x	x	-	1.59
T05	-	x	x	x	-	2.00
T06	-	x	x	x	Tensile & shear	1.13
T07	Tensile	x	x	-	-	-
T08	Tensile	x	x	x	Tensile	-
T09	Shear	-	x	x	Shear	1.40
T10	-	-	x	x	-	1.35
T11	-	-	x	x	-	1.35
T12	Tensile	x	-	-	-	1.88
T13	Tensile	x	-	x	-	2.18
T14	Tensile	x	-	x	-	2.01
T15	Tensile	x	-	-	-	2.45
T16	Tensile	x	-	-	-	-
T17	Tensile	x	-	x	-	1.76
T18	Tensile	x	-	x	-	-
T19	-	x	x	x	Tensile & shear	1.83

[1] Not documented.

capacity. In 10 cases, member failure occurred in tension and in 2 cases in shear, expressed as a diagonal crack that partially cut through the cross-section completely from the area where the vertical load was applied to one support, see Figures 3.39 and 3.40. The tensile failure was sometimes rather punctual and sometimes strongly defibrated over a beam length of up to 1.80 m. It affected the lowest one to six lamellas. The tensile failure originated from knots (11 cases) and/or from finger-joints (6 cases). Member failure in tension was always accompanied by tensile failure perpendicular to the grain, see Figure 3.39. Usually, the shear failure was localised and difficult to detect. It occurred along the grain (11 cases), at knots (11 cases), along glue lines (7 cases), and in compression wood (2 cases). Minor local buckling of the wood fibres under compression in grain direction was observed in 14 cases around the area where the vertical load was applied.

Table 3.16 illustrates that the slender beams T01 to T03 failed exclusively in shear, while the stocky beams T12 to T19 usually failed in tension. For T04 to T11, both failure mechanisms were present. As torsional moments increase with increasing slenderness, it was concluded that the shear failure was mainly caused by torsion. The loud cracking above 70% of the load-bearing capacity, which was followed by a flattening of the load-deformation curve, indicated that this local shear failure occurred early and significantly influenced the load-bearing capacity. As the comparative numerical analyses confirmed that a reduction in shear stiffness can cause such an effect, see Section 5.5.3, an attempt was made to determine the point of time of the significant local shear failure. It was assumed that this was the

point of loud, audible cracking. Based on the documented times of the loud cracking, the corresponding vertical loads F_z were determined for each test in which this cracking occurred. The corresponding shear stresses in grain direction for each test were determined in comparative numerical analyses with the FE model described in Section 5. Finally, it was assumed that this stress was equal to the proportionality limit $f_{v,0,lin}$, see Figure 5.3. This resulted in numerically estimated $f_{v,0,lin}$ of 1.13 N/mm^2 to 2.70 N/mm^2. The mean value was 1.81 N/mm^2.
No influence of the axial compressive force on the failure mechanisms was detected.

3.4.4 Discussion

The elastic modulus $E_{0,el}$ = 12,100 N/mm^2, which was determined in the preceding elastic bending tests, see Table 3.13, was in good agreement with literature values, see, e.g. EN 14080 [54] with $E_{0,el,mean}$ = 11,500 N/mm^2, and Schilling et al. [141] with $E_{0,el}$ = 12,800 N/mm^2. $G_{0,el}$ = 747 N/mm^2 from elastic torsion tests, see Table 3.13, was about 15% higher than usually reported in the literature, see EN 14080 [54] and Brandner et al. [19] with $G_{0,mean}$ = 650 N/mm^2. The reasons could be the different structural systems and different stress distributions, but the differences were also within the range of possible material scatter.

The compressive strength in grain direction $f_{c,0}$ = −43.2 N/mm^2, which was determined in the preceding compression tests, see Table 3.14, was in good agreement with literature values, see Glos [77] with $f_{c,0}$ = −39.8 N/mm^2 and Schilling et al. [141] with $f_{c,0}$ = −40.4 N/mm^2. [77] measured plastic strains of $\epsilon_{c,0,pl} = 0.15$ to $0.40\,\epsilon_{c,0,el}$, which were about half the size of own results of $\epsilon_{c,0,pl} = 0.26$ to $0.82\,\epsilon_{c,0,el}$. However, too few values from the literature were available for a conclusive evaluation.
Grosse [83] determined a proportionality limit of $f_{c,0,lin} \approx 0.70\,f_{c,0}$. This was in good agreement with most of the own results, which ranged from $f_{c,0,lin} = 0.64$ to $0.80\,f_{c,0}$. Only for one test a rather low value of $f_{c,0,lin} = 0.47\,f_{c,0}$ was found. The plastic strains could be mapped well by means of an ellipse, see Figure 3.24, as proposed by [83], where $(f_{c,0} - f_{c,0,lin})$ and $\epsilon_{c,0,pl}$ represent the ellipse radii.
Based on the results in Table 3.14, $\epsilon_{c,0,pl} = 0.40\,\epsilon_{c,0,el}$, $f_{c,0,lin} = 0.75\,f_{c,0}$, and $f_{c,0}$ = 40.0 N/mm^2 were chosen for the FEAs in Section 5.

The LTB tests demonstrated that the described test setup is well suited for the experimental investigation of LTB. A planned eccentricity of the vertical force is generally advisable, as this forces a LTB in a defined direction and minimises the influence of unplanned geometrical and hardly measurable structural imperfections. The load-eccentricity can be easily taken into account in the FEA. In contrast, this is difficult for structural imperfections, as these can hardly be measured and therefore cannot be considered in models. This is a good example of how the influence of unknown or not-measurable basic variables can be reduced in experiments by introducing an additional but known basic variable, thereby increasing the accuracy of the prediction models.

Figure 3.41 presents the experimentally determined absolute load-bearing capacities of the beams with $N_{x,c}$-$M_{y,1}$-interaction, the results of FEA with the model described in

Section 5.5.3, and the results of the k_c-k_m-method and calculations using T2O according to EN 1995-1-1 [57]. For the k_c-k_m-method, it is differentiated between the flexural buckling interaction (k_c) from Equations (2.56) and (2.57) and the LTB interaction (k_c-k_m) from Equation (2.61). For the design with calculations using T2O, Equation (2.15) for determining $M_{z,2}$, Equations (2.54) and (2.55) for the bending design verification, and Equation (2.69) for the shear design verification were applied. The design verifications were conducted with characteristic material values according to EN 14080 [54] of $f_{c,0,k}$ = 24.0 N/mm^2, $f_{m,k}$ = 24.0 N/mm^2, $f_{v,0,k}$ = 3.5 N/mm^2, $E_{0,05}$ = 9600 N/mm^2, and $G_{0,05}$ = 540 N/mm^2, where the product $E_{0,05}G_{0,05}$ was increased by a factor of 1.4 according to DIN EN 1995-1-1/NA [40]. For calculations using T2O, a bow imperfection of 8 mm was assumed according to the test setup.
The nonlinear $N_{x,c}$-$M_{y,1}$-interaction in the k_m-method in EN 1995-1-1 [57], see Equation (2.61), was discussed extensively during the revision of FprEN 1995-1-1 [69] in favour of a more conservative linear interaction, see prEN 1995-1-1 [132] and Section 2.6.5. The nonlinear curve of the $N_{x,c}$-$M_{y,1}$-interaction was confirmed by the test results. On the basis of the results of this thesis, the more favourable nonlinear interaction could be kept in FprEN 1995-1-1 [69]. The experimentally determined large load-bearing capacities of the 6 m long beams indicated that the actual bending strength was higher than the assumed mean value in calculations using T2O of 33 N/mm^2.

Figure 3.42 and Table 3.17 present the experimentally determined relative load-bearing capacities k_m and the results of the k_m-method and calculations using T2O according to EN 1995-1-1 [57]. In addition, the limit λ_{ef} = 225 according to DIN EN 1995-1-1/NA

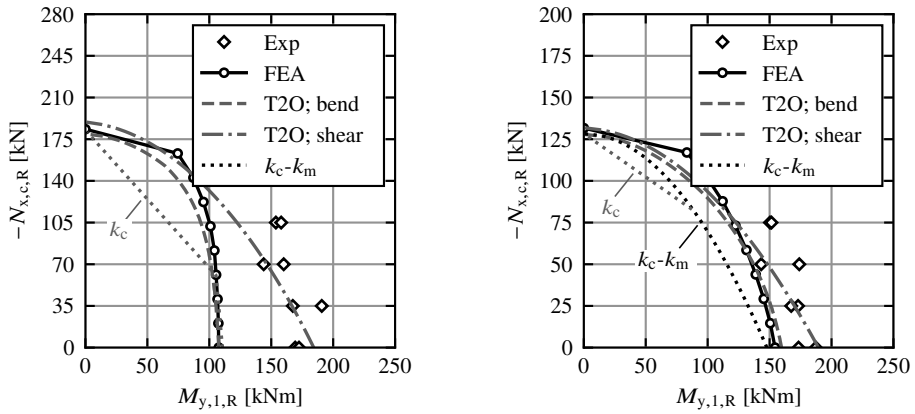

(a) 480 · 120 · 6000 mm^3. **(b)** 600 · 120 · 8000 mm^3.

Figure 3.41: Experimentally (Exp) determined absolute LTB load-bearing capacities of beams T04 to T19; in comparison with results of the k_c-k_m-method and bending (bend) and shear design with calculations using T2O according to EN 1995-1-1 [57] and with results of FE analyses (FEA), all with *nominal* geometries and material values.

[40] is displayed in Figure 3.42, below which the torsional stresses may be neglected if verifying the cross-section at the supports, see also Section 2.6.3.1. k_m was calculated with Equation (3.8), $\lambda_{m,rel}$ with Equation (2.63), and $M_{y,cr}$ with Equation (2.64) and the same material values as discussed in the previous paragraph. For the design with calculations using T2O, Equation (2.15) for determining $M_{z,2}$, Equations (2.54) and (2.55) for the bending design verification with a cross-section of $720 \cdot 120$ mm^2, and Equation (2.69) for the shear design verification with a cross-section of $480 \cdot 120$ mm^2 were utilised. The characteristic material values discussed in the previous paragraph, and, alternatively, the mean material values of $f_{c,0,mean} = 40.0$ N/mm^2 and $f_{m,mean} = 33.0$ N/mm^2 from Schilling et al. [141], $f_{v,0,mean} = 5.3$ N/mm^2 from Glos [78] and Spengler [148], and $E_{0,el,mean} = 11{,}500$ N/mm^2 and $G_{0,mean} = 650$ N/mm^2 from EN 14080 [54], were applied. A bow imperfection of 8 mm was assumed according to the test setup. No axial compressive forces were considered in the calculation of the k_m-method and T2O results displayed in Figure 3.42.
The k_m-method from EN 1995-1-1 [57] was on the safe side compared to the experimental results. The same was valid for the characteristic load-bearing capacities from calculations using T2O. For slendernesses $\lambda_{m,rel} \geq 1.2$, the characteristic and mean load-bearing capacities according to T2O were almost identical because the stiffnesses in characteristic calculations are raised to mean values by the factor 1.4 in the product of $E_{0,05}G_{0,05}$, see Blaß [11].
The experimentally determined load-bearing capacities with $\mu_c = 0.00$ and the small slenderness of $\lambda_{m,rel} = 0.747$ were about 15% higher, and for the larger slendernesses

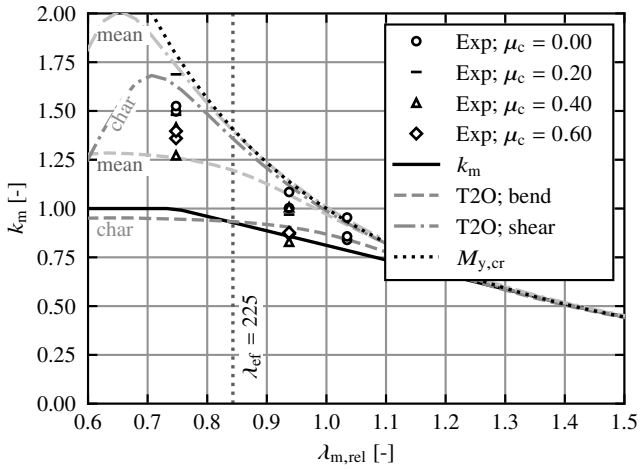

Figure 3.42: Experimentally (Exp) determined relative LTB load-bearing capacities k_m of all beams plotted over the relative LTB slenderness ratio $\lambda_{m,rel}$; in comparison with results of the k_m-method and bending (bend) and shear design with calculations using T2O according to EN 1995-1-1 [57], design with k_m-method with *characteristic* and design with T2O with *characteristic* and *mean* material values; with the relative critical bending moment $M_{y,cr}$; with the limit $\lambda_{ef} = 225$ according to DIN EN 1995-1-1/NA [40]; k_m and $\lambda_{m,rel}$ calculated with *nominal* geometries and material values.

Table 3.17: Comparison of the experimentally determined relative LTB load-bearing capacities and the results of the k_m-method and calculations using T2O according to EN 1995-1-1 [57].

Series number	$\lambda_{m,rel}$ [1]	μ_c [2]	$k_{m,exp}$	k_m according to EN 1995-1-1 [57] and T2O			
				k_c-k_m	T2O bend		T2O shear	
					Char	Mean	Char	Mean
T01	1.041	0.00	0.839	0.779	0.837	0.908	0.896	0.920
T02	1.041	0.00	0.954	0.779	0.837	0.908	0.896	0.920
T03	1.041	0.00	0.857	0.779	0.837	0.908	0.896	0.920
T04	0.940	0.00	1.003	0.855	0.924	1.090	1.096	1.127
T05	0.940	0.00	1.085	0.855	0.924	1.090	1.096	1.127
T06	0.940	0.20	1.001	0.767	0.878	1.010	0.991	1.038
T07	0.940	0.20	0.969	0.767	0.878	1.010	0.991	1.038
T08	0.940	0.40	1.006	0.668	0.800	0.916	0.869	0.938
T09	0.940	0.40	0.829	0.668	0.800	0.916	0.869	0.938
T10	0.940	0.60	0.870	0.551	0.683	0.806	0.724	0.824
T11	0.940	0.60	0.877	0.551	0.683	0.806	0.724	0.824
T12	0.747	0.00	1.497	1.000	0.972	1.313	1.630	1.732
T13	0.747	0.00	1.525	1.000	0.972	1.313	1.630	1.732
T14	0.747	0.20	1.480	0.973	0.952	1.277	1.489	1.603
T15	0.747	0.20	1.688	0.973	0.952	1.277	1.489	1.603
T16	0.747	0.40	1.272	0.881	0.915	1.220	1.320	1.457
T17	0.747	0.40	1.416	0.881	0.915	1.220	1.320	1.457
T18	0.747	0.60	1.360	0.607	0.844	1.124	1.112	1.288
T19	0.747	0.60	1.397	0.607	0.844	1.124	1.112	1.288

Bend = bending design verification, shear = shear design verification, char = characteristic material values, mean = mean material values.

[1] Calculated with Equation (2.23), with measured elastic moduli and geometries of each test specimen according to Table B.2, and $f_{m,mean} = 33.0$ N/mm^2.

[2] Utilisation ratio of the axial compressive force μ_c, see Table 3.12.

$\lambda_{m,rel} = 0.940$ and 1.041 were up to 10% lower than mean values from calculations using T2O, see Table 3.17. This discrepancy was caused by the different failure behaviour of the 6 m and 8 m long beams, see Table 3.16. While the 6 m long beams (with experimentally higher load-bearing capacities than results of calculations using T2O) failed in bending, and their bending strength was obviously higher than the assumed mean value of 33 N/mm^2, early local shear failure occurred in the 8 m long beams (with experimentally lower load-bearing capacities than results of calculations using T2O). For the latter, the high twist of the cross-sections led to high shear stresses, which caused early local shear failures, which led to a reduction of stiffnesses, which resulted in higher deformations, and finally a 10% to 20% reduction in load-bearing capacity. The limit value of $\lambda_{ef} = 225$ according to DIN EN 1995-1-1/NA [40] was, possibly by chance, at the transition point at which only bending failure and no more shear failure occurred in the tests. The experimental results more closely followed the characteristic or mean shear load-bearing capacities than the bending load-bearing capacities. The shear failure was not expected to this extent, as shear

load-bearing capacities according to EN 1995-1-1 [57] with internal forces according to T2O are always higher than bending load-bearing capacities, see Figure 3.42 and Table 3.16. There seemed to be a fundamental shortcoming in the known design formulas for LTB of slender beams, e.g. in EN 1995-1-1 [57] and FprEN 1995-1-1 [69], as these were not able to predict the experimentally observed shear failure mode due to torsion.
This modelling deficit is also highlighted by Figure 3.37, which illustrates the modelling deviations of calculations using T2O from experimental results. If neglecting the early local shear failure, the stiffness of slender beams seems to be significantly overestimated by the design models. The design models in EN 1995-1-1 [57] predict load-bearing capacities which are only slightly smaller than the critical bending moment $M_{y,cr}$, see Figure 3.37.

No test results from the literature were known with which the low proportional limit $f_{v,0,lin} = 1.81$ N/mm^2 could be compared. With a mean value of the shear strength $f_{v,0} = 5.3$ N/mm^2, according to Glos and Denzler [79] and Spengler [148], the results of the LTB tests yielded $f_{v,0,lin} = 0.34 f_{v,0}$. For defect-free test small specimens, values of $f_{v,0,lin} = 0.4$ to $0.7 f_{v,0}$ were measured by Dahl and Malo [31] and Yoshihara and Suzuki [180], see Section 2.3.4. The reason that the value from own tests was lower could have been because large GL beams were tested, which resulted in a high scatter of the shear strength, making local failure more likely to occur early.

As a final point, the different reference values in Figures 3.37 and 3.42 need to be discussed. In Figure 3.37, k_m and $\lambda_{m,rel}$ were determined with *measured* or realistically assumed material and geometry parameters. This representation is suitable for validating prediction models, as it visualises how well a model represents reality. In contrast, the representation in Figure 3.42, in which k_m and $\lambda_{m,rel}$ were determined with *nominal* material properties in accordance with EN 1995-1-1 [57], is suitable for checking the safety level of design equations. It can be employed to determine characteristic load-bearing capacities based on scattering experimental or numerical results, as it clearly illustrates the scattering of the load-bearing capacity of the planned members. This is also discussed in Figures 2.6 and 2.7.

3.4.5 Summary

Within the research project IGF No. 21285 N [108], 19 LTB tests on full-scale softwood GL beams with combined bending and axial compression were conducted, and their load-bearing behaviour was investigated.

In preceding tests, the elastic and shear moduli $E_{0,el}$ and $G_{0,el}$ of each test specimen and the stress-strain curves for compression in grain direction were determined. With a proportionality limit of $f_{c,0,lin} \approx 0.71 f_{c,0}$ and plastic strains of $\epsilon_{c,0,pl} \approx 0.45 \epsilon_{c,0,el}$, the results were in a similar range as reported in literature.
The LTB tests demonstrated that the described test setup is well suited for the experimental investigation of LTB. It is generally advisable to apply the vertical force eccentrically, as the eccentricity minimises the influence of unplanned geometrical and hardly measurable structural imperfections.

However, the chosen horizontal eccentricity of the vertical load of 8 mm = $L/750$ was too low for the least slender test specimens. The author recommends a value of about $L/400$. In contrast to tests in steel construction, see, e.g. Kuhlmann and Jörg [106], due to the sometimes sudden lateral deflection of timber beams in LTB tests, it is recommended not to apply the vertical load ideally vertical but to incline the loading cylinder slightly. This has a stabilising effect during the execution of a test. In principle, it is not essential to keep the loading cylinder vertical over the entire duration of a test, provided that a changing inclination of the cylinder is measured. This can be taken into account in FEA.
The load-deformation behaviour in horizontal direction of 16 out of 19 beams was nonlinear with a pronounced plateau, see Figure 3.35. However, in three tests, a bending failure occurred without prior lateral deflection of the beams. It is therefore possible that, despite their imperfection sensitivity, beams do not exhibit a typical stability failure but a pure bending failure.
Shear failure occurred in the slender test specimens and bending failure in the stockier ones, see Table 3.16 and Figures 3.39 and 3.40. The shear failure was not expected based on a preceding design verification according to EN 1995-1-1 [57]. For the slender test specimens, the high twist of the cross-sections led to high torsional shear stresses, resulting presumably in early local shear failures. These shear failures led to a reduction of stiffnesses, leading to higher deformations and finally reducing the load-bearing capacities. The determined proportionality limit of the shear stress-strain curve $f_{v,0,lin}$ = 1.81 N/mm^2 was surprisingly low. No values of torsion tests from the literature were known for comparison.

The nonlinear curve of the $N_{x,c}$-$M_{y,1}$-interaction, which is assumed in the k_c-k_m-method in EN 1995-1-1 [57] and FprEN 1995-1-1 [69], see Sections 2.6.2.1.4 and 2.6.4.1.4, was confirmed by the test results, see Figure 3.41. The k_c-k_m-method in EN 1995-1-1 [57] was on the safe side compared to experimental results, see Figure 3.42. For calculations using T2O, this was only the case for $\lambda_{m,rel}$ = 0.74 and 0.94, not for $\lambda_{m,rel}$ = 1.04, as the reduction of stiffness due to early local shear failure is not accounted for in EN 1995-1-1 [57] or FprEN 1995-1-1 [69]. Therefore, LTB design methods need to be modified to account for such a shear failure of slender beams due to torsion.

The influence of the shear failure on the load-bearing capacity of softwood GL beams is further discussed in Section 6.4. The findings are summarised in the design proposals for standardisation in Section 7.

3.5 Summary

The measurements and experiments described in Section 3 address the following key research questions and aims of this thesis, which were developed in Section 2: (i) the investigation of the influence of the wood species and the wood product and the correspondingly different compressive plasticising on the flexural buckling load-bearing capacity by experimental investigations on beech LVL GL75 columns; (ii) the investigation of the LTB load-bearing capacity with combined axial compression and bending by experimental investigations on softwood GL beam-columns; and (iii) the creation of a database of geometrical imperfections by the systematic surveying of timber buildings. The results were utilised to validate the numerical models in Section 5.5, to evaluate the design models from EN 1995-1-1 [57] and FprEN 1995-1-1 [69], and to derive the design proposals in Section 7.

23 buildings were surveyed, and the geometrical imperfections of 202 softwood GL beams, 38 beech LVL beams, and 57 beech LVL columns were analysed, see Table 3.1. An approximation method for a simplified calculation of equivalent bow and twist imperfections was developed and validated, see Section 3.2.4.2 and Equation (3.3). It was observed that the geometrical imperfections of beams can be split into three parts: the bow imperfections e_{y}, the twist imperfections at midspan $e_{\theta,\mathrm{mid}}$, and the twist imperfections at the fork supports $e_{\theta,\mathrm{supp}}$, see also Figure 2.16. For softwood GL beams, the 95% quantile values of the equivalent bow imperfections, the equivalent twist imperfections at midspan, and the twist imperfections at the supports were $L/1180$, $L/1600$, and $1/100$, respectively, see Tables 3.3, 3.4, and 3.5. Additionally, bow and sway imperfections of beech LVL columns were determined, see Tables 3.3 and 3.6. The results of bow imperfections agreed well with values from literature and the k_{c}-method in EN 1995-1-1 [57]. Twist imperfections had hardly been reported in the literature and did not seem to be considered in the design of timber beams according to EN 1995-1-1 [57]. However, as the measured twist imperfections were about 70% of the size of the bow imperfections, they can have a significant impact on the LTB load-bearing capacity.
The necessary combination of geometrical and structural imperfections into equivalent geometrical imperfections is discussed in Sections 5.6.2 and 6.3. The findings are summarised in the design proposals for standardisation in Section 7, which were already included in FprEN 1995-1-1 [69].

27 tests on full-scale beech LVL GL75 columns were conducted that illustrated the pronouncedly nonlinear behaviour of flexural buckling, see Figure 3.21. The peak of the load-deformation curve always defined the load-bearing capacity and not a brittle member failure in tension. The load-bearing capacities for different slendernesses followed the expected shape of a buckling curve, and their scatter was low, see Figure 3.29. The characteristic load-bearing capacities according to EN 1995-1-1 [57] were up to 10% higher than the experimentally determined load-bearing capacities, see Figure 3.29. This was due to high plastic strains $\epsilon_{\mathrm{c},0,\mathrm{pl}}$ on reaching the compressive strength and the resulting decrease in bending stiffness, see Figure 3.24. It was observed that beech LVL exhibited three to five times higher plastic strains than softwood GL with $\epsilon_{\mathrm{c},0,\mathrm{pl}} = 1.25\,\epsilon_{\mathrm{c},0}$, see Figure 3.24. Therefore, the design methods in EN 1995-1-1 [57] should be modified before applying

them to beech LVL columns. The influence of plasticising on the load-bearing capacity of beech LVL columns is further discussed in Section 6.4.

19 tests on full-scale softwood GL beams were conducted that illustrated the usually pronouncedly nonlinear behaviour of LTB, see Figure 3.35. However, in three tests, a bending failure occurred without prior lateral deflection of the beams. It is therefore possible that, despite their imperfection sensitivity, beams do not exhibit a typical stability failure before uniaxial bending failure. The load-bearing capacities followed the expected shape of a LTB curve, see Figure 3.37. The nonlinear curve of the $N_{x,c}$-$M_{y,1}$-interaction, which is assumed in EN 1995-1-1 [57] and FprEN 1995-1-1 [69], was confirmed by the test results, see Figure 3.41. The k_c-k_m-method and calculations using T2O according to EN 1995-1-1 [57] were on the safe side compared to experimental results, see Figure 3.42. For the slender test specimens with $\lambda_{m,rel} = 1.04$, the high twist of the cross-sections led to high shear stresses, which presumably caused early local shear failures, which led to a reduction of stiffness, resulting in higher deformations, and finally reducing the load-bearing capacities. The determined proportionality limit $f_{v,0,lin} = 1.81$ N/mm^2 was surprisingly low, see Table 3.16. Even a member shear failure due to torsion occurred in two tests, see Table 3.16. Therefore, LTB design methods need to be modified to account for such a shear failure of slender beams due to torsion. The influence of the shear failure on the load-bearing capacity of softwood GL beams is further discussed in Section 6.4.

The findings of the described measurements and experiments were applied as input values for the FEA in Sections 5 and 6 and combined with the FE results and analytical derivations in Section 4 to develop the design proposals for standardisation in Section 7.

4 Analytical derivations and equations

4.1 General

Analytical models allow for enhancing the understanding of physical phenomena, studying such phenomena in more detail (limitations of experimental measurement techniques) and extending the results of experimental investigations (limitations in number, geometry, boundary conditions, etc. of tests). For the mechanical understanding of structural problems and the development of mechanically meaningful design concepts, the derivation of analytical models is of great advantage. However, setting up and solving such analytical equations can be quite challenging to the point of being practically impossible. Until the rise of FEA, see Section 5, analytical models were the standard methods for investigating stability problems in civil engineering, see, e.g. Larsen [111] and Section 2.

The objective of the presentation of the analytical equations and models in this section is to improve the understanding of the mechanical background of the stability phenomena in timber construction. The

- $N_{x,c}$-$M_{y/z,1}$-interaction for flexural buckling, see Section 4.2,
- $N_{x,c}$-$M_{y,1}$-interaction for LTB, see Section 4.3,
- $N_{x,c}$-$M_{y,2}$-interaction, see Section 4.4, and
- k_m-method for LTB, see Section 4.5,

are discussed. These have to some extent already been discussed by other authors but were sometimes only partially documented, or in a different or more complex shape, and some so far back in time that they might not be remembered anymore.
The derivation of the k_c-method for flexural buckling, see also Sections 2.2.1.8 and 2.6.2.1.3, is provided for information in Annex C, as this thesis does not provide any new contribution to this. The derivation of the T2O equations is discussed in detail by, e.g. Hörsting [90].

The analytical equations derived in the section were incorporated into the evaluation and discussion of the numerical and experimental results in Section 6 and the formulation of the design concept in Section 7.

4.2 $N_{x,c}$-$M_{y/z,1}$-interaction for flexural buckling

For the flexural buckling design with combined axial compression and bending and geometrically linear calculation of internal forces (T1O), e.g. with the k_c-method in EN 1995-1-1 [57] and FprEN 1995-1-1 [69], a mechanically sound $N_{x,c}$-$M_{y/z,1}$-interaction relationship has to be chosen.
Leicester [117] demonstrated that for very slender columns and linear elastic material behaviour, a linear $N_{x,c}$-$M_{y/z,1}$-interaction can be assumed. Since he only partially documented the derivation, the non-affine bending moments and deformations were neglected, and this was so far back in time that it might not be remembered anymore, the complete derivation based on [117] is given here.

For very slender columns, the bending stresses due to flexural buckling govern the design, and

$$\frac{N_{x,c}}{N_{x,c,R}} \to 0 \quad , \tag{4.1}$$

where $N_{x,c}$ is the negative axial compressive force, and $N_{x,c,R} = A f_{c,0}$ is the axial compressive load-bearing capacity of the cross-section with a negative sign.
Therefore, only uniaxial bending stresses need to be considered in the design, which, no matter what the stress interaction equation looks like, yields the limit criterion

$$\frac{M_{y/z,2}}{M_{y/z,R}} \leq 1 \quad , \tag{4.2}$$

where $M_{y/z,2}$ is the bending moment about the y- or z-axis according to geometrically nonlinear calculations with Equation (2.1), and $M_{y/z,R} = W_{y/z} f_m$ is the bending load-bearing capacity of the cross-section.
Inserting Equation (2.1) in Equation (4.2) results in

$$\frac{-N_{x,c} e_{z/y} + M_{y/z,1} \cdot (1 + \alpha_{c,y/z} \delta_{y/z})}{M_{y/z,R} \cdot (1 - \alpha_{c,y/z})} \leq 1 \quad . \tag{4.3}$$

where $e_{z/y}$ is the bow imperfection in the z- or y-direction, $M_{y/z,1}$ is the bending moment about the y- or z-axis according to geometrically linear calculations (T1O), $\alpha_{c,y/z}$ is the amplification factor of the axial compressive force due to flexural buckling about the y- or z-axis according to Equation (2.2), and $\delta_{y/z}$ is the Dischinger-coefficient that accounts for the distribution of $M_{y/z,1}$, see, e.g. prEN 1995-1-1 [132].
Furthermore, for very slender columns

$$k_{c,y/z} N_{x,c,R} \to N_{y/z,cr} \quad , \tag{4.4}$$

where $N_{y/z,cr}$ is the critical axial compressive force for buckling about the y- or z-axis according to Equation (2.3), and $k_{c,y/z}$ is the reduction factor accounting for flexural buckling, e.g. according to Equation (2.58).

For $\alpha_{c,y/z}$ according to Equation (2.2) this yields

$$\frac{N_{x,c}}{k_{c,y/z}N_{x,c,R}} \rightarrow \alpha_{c,y/z} \quad . \tag{4.5}$$

Inserting Equation (4.5) in Equation (4.3) results, after some transformations, in

$$\frac{N_{x,c}}{k_{c,y/z}N_{x,c,R}} + \frac{-N_{x,c}e_{z/y}}{M_{y/z,R}} + \frac{M_{y/z,1}}{M_{y/z,R}} \cdot \left(1 + \frac{N_{x,c}}{k_{c,y/z}N_{x,c,R}} \cdot \delta_{y/z}\right) \leq 1 \quad . \tag{4.6}$$

It can be demonstrated that

$$\frac{-N_{x,c}e_{z/y}}{M_{y/z,R}} \ll \frac{N_{x,c}}{k_{c,y/z}N_{x,c,R}} \quad . \tag{4.7}$$

Therefore, the term $N_{x,c}e_{z/y}/M_{y/z,R}$ in Equation (4.6) can be neglected, which yields

$$\frac{N_{x,c}}{k_{c,y/z}N_{x,c,R}} + \frac{M_{y/z,1}}{M_{y/z,R}} \cdot \left(1 + \frac{N_{x,c}}{k_{c,y/z}N_{x,c,R}} \cdot \delta_{y/z}\right) \leq 1 \quad . \tag{4.8}$$

For very slender columns with $\delta_{y/z} = 0$, i.e. the shape of the bending moment $M_{y/z,1}$ is affine to the deformation v or w, the $N_{x,c}$-$M_{y,1}$-interaction of flexural buckling bearing capacity is thereby linear. For other distributions of the bending moment $M_{y/z,1}$, a non-linearity of the interaction is caused by $\delta_{y/z} \neq 0$.

Equation (4.8) describes the $N_{x,c}$-$M_{y,1}$-interaction for flexural buckling design of very slender columns with geometrically linear internal forces (T1O), e.g. the k_c-method in EN 1995-1-1 [57] and FprEN 1995-1-1 [69], see Sections 2.6.2.1.3 and 2.6.4.1.3. The geometrically nonlinear effects should be considered with $k_{c,y/z}$. Equation (4.8) with $\delta_{y/z} = 0$ is identical to the $N_{x,c}$-$M_{y,1}$-interaction equation for flexural buckling in EN 1995-1-1 [57] and FprEN 1995-1-1 [69], see Equations (2.56).

Figures 4.1 and 4.2 illustrate the relative load-bearing capacities for $N_{x,c}$-$M_{y,1}$-interaction with a constant bending moment, i.e. $\delta_y = 0.273$, and a bending moment due to a concentrated force at midspan, i.e. $\delta_y = -0.189$, for different reduction factors k_c. The constant bending moment has a slightly negative influence on the $N_{x,c}$-$M_{y,1}$-interaction, the triangular bending moment has a slightly positive influence on the $N_{x,c}$-$M_{y,1}$-interaction.

The experimental investigations of Buchanan et al. [25] confirmed the linear $N_{x,c}$-$M_{y/z,1}$-interaction for slender columns and the slightly negative effect of a constant bending moment, see Figure 2.21.

It has to be emphasised that the term $(1+...\delta_{y/z})$ in Equation (4.8) describes the geometrically nonlinear component of the internal forces due to the bending moment $M_{y/z,1}$, which is neglected in the k_c-method, see Section 2.6.2.1.3.

4.3 $N_{x,c}$-$M_{y,1}$-interaction for lateral torsional buckling

For the LTB design with combined axial compression and bending and geometrically linear calculation of internal forces (T1O), e.g. with the k_m-methods in EN 1995-1-1 [57] and FprEN 1995-1-1 [69], a mechanically sound $N_{x,c}$-$M_{y,1}$-interaction relationship has to be chosen.
Leicester [117] demonstrated that for very slender beams and linear elastic material behaviour, a $N_{x,c}$-$M_{y,1}$-interaction with squaring of the bending moment component can be assumed. Since he only partially documented the derivation, and this was so far back in time that it might not be remembered anymore, the complete derivation based on [117] is given here.

For very slender beam-columns, the LTB load-bearing capacity approaches the critical load that is given by the denominator of Equation (2.15):

$$1 - \alpha_{c,z} - \alpha_m^2 = 0 \quad . \tag{4.9}$$

where $\alpha_{c,z}$ is the amplification factor of the axial compressive force due to flexural buckling about the z-axis according to Equation (2.2), and α_m is the amplification factor of the bending moment due to LTB according to Equation (2.16).
Inserting Equations (2.2) and (2.16) in Equation (4.9) yields

$$1 - \frac{N_{x,c}}{N_{z,cr}} - \left(\frac{M_{y,1}}{M_{y,cr}}\right)^2 = 0 \quad , \tag{4.10}$$

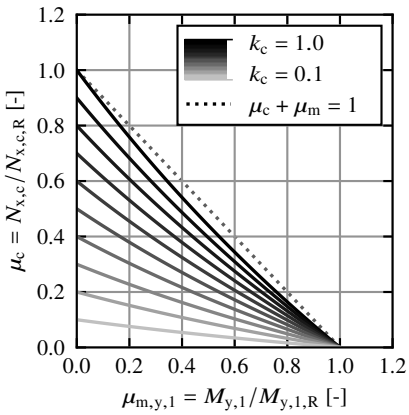

Figure 4.1: Relative load-bearing capacities for $N_{x,c}$-$M_{y,1}$-interaction and different reduction factors k_c according to Equation (4.8); *constant bending moment* $M_{y,1}$.

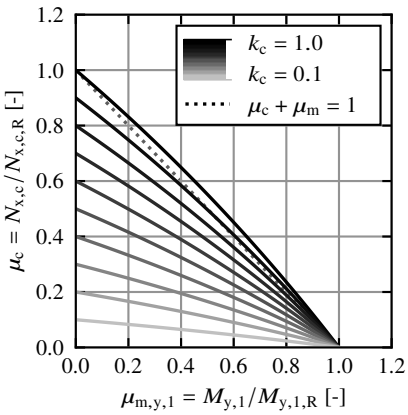

Figure 4.2: Relative load-bearing capacities for $N_{x,c}$-$M_{y,1}$-interaction and different reduction factors k_c according to Equation (4.8); $M_{y,1}$ applied by a *concentrated force at midspan*.

where $N_{x,c}$ is the axial compressive force, $N_{z,cr}$ is the critical axial compressive force for flexural buckling about the z-axis according to Equation (2.3), $M_{y,1}$ is the bending moment about the y-axis according to geometrically linear calculations (T1O), and $M_{y,cr}$ is the critical bending moment according to Equation (2.17).
Furthermore, for very slender beam-columns

$$k_{c,z} N_{x,c,R} \rightarrow N_{z,cr} \quad , \tag{4.11}$$

$$k_m M_{y,R} \rightarrow M_{y,cr} \quad , \tag{4.12}$$

where $k_{c,z}$ is the reduction factor accounting for flexural buckling, e.g. according to Equation (2.58), $N_{x,c,R} = A f_{c,0}$ is the axial compressive load-bearing capacity of the cross-section, k_m is the reduction factor accounting for LTB, e.g. according to Equation (2.62), and $M_{y,R}$ is the bending load-bearing capacity of the cross-section about the y-axis.
With Equations (4.11) and (4.12), Equation (4.10) can be rearranged to

$$\frac{N_{x,c}}{k_{c,z} N_{x,c,R}} + \left(\frac{M_{y,1}}{k_m M_{y,R}} \right)^2 = 1 \quad . \tag{4.13}$$

For very slender beam-columns, the $N_{x,c}$-$M_{y,1}$-interaction of LTB load-bearing capacity is thereby nonlinear.
Equation (4.13) describes the $N_{x,c}$-$M_{y,1}$-interaction for LTB design of very slender beam-columns with geometrically linear internal forces (T1O), e.g. the k_m-methods in EN 1995-1-1 [57] and FprEN 1995-1-1 [69], see Sections 2.6.2.1.4 and 2.6.4.1.4. The geometrically nonlinear effects should be considered with $k_{c,z}$ and k_m. Equation (4.13) is identical to the $N_{x,c}$-$M_{y,1}$-interaction equation for LTB in EN 1995-1-1 [57] and FprEN 1995-1-1 [69], see Equations (2.61) and (2.77).
No size effect may be applied to strengths in this interaction, as it describes the stability failure of very slender beam-columns, which is purely stiffness-dependent.

The nonlinear $N_{x,c}$-$M_{y,1}$-interaction in the k_m-method in EN 1995-1-1 [57], see Equation (2.61), was discussed extensively during the revision of FprEN 1995-1-1 [69] in favour of a more conservative linear interaction, see prEN 1995-1-1 [132] and Section 2.6.5. The described analytical derivation by Leicester [117] provides the mechanical background of the nonlinear $N_{x,c}$-$M_{y,1}$-interaction. On the basis of the results of this thesis, the more favourable nonlinear interaction could be kept in FprEN 1995-1-1 [69].

4.4 $N_{x,c}$-$M_{y/z,2}$-interaction

For a flexural buckling and LTB design of timber beam-columns with combined axial compression and bending and geometrically nonlinear calculation of internal forces (T2O), a mechanically sound $N_{x,c}$-$M_{y/z,2}$-interaction relationship has to be chosen.
For this thesis, the $N_{x,c}$-$M_{y/z,2}$-interaction relationship of the cross-sectional load-bearing capacity was derived analytically, taking into account a bilinear elastoplastic compression behaviour of wood in grain direction. The basis was the analytical model presented by van der Put [171]. The common sign convention of negative compression and positive tension was applied, resulting in slight differences to the equations presented by van der Put [172] and van der Put [171].

Tensile failure was assumed as the failure criterion. The stress distribution over the cross-section in Figure 4.3 results from a combined axial compression and bending loading and a bilinear stress-strain relationship for compression in grain direction for the limit state if the strength f_m, i.e. the cross-sectional load-bearing capacity, is reached. Based on this stress distribution, the relationship between internal forces and strengths can be described by

$$N_{x,c} = f_{c,0} H B + \frac{f_m - f_{c,0}}{2} \cdot (H - H_{pl}) \cdot B \quad , \tag{4.14}$$

$$M_{y/z,2} = \frac{f_m - f_{c,0}}{2} \cdot (H - H_{pl}) \cdot \left(\frac{H}{2} - \frac{H - H_{pl}}{3} \right) \cdot B \quad , \tag{4.15}$$

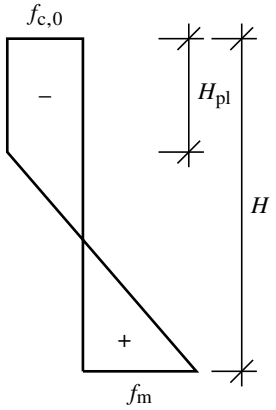

Figure 4.3: Stress distribution in grain direction for combined loading by an axial compressive force $N_{x,c}$ and a bending moment $M_{y,2}$ and bilinear elastoplastic material behaviour.

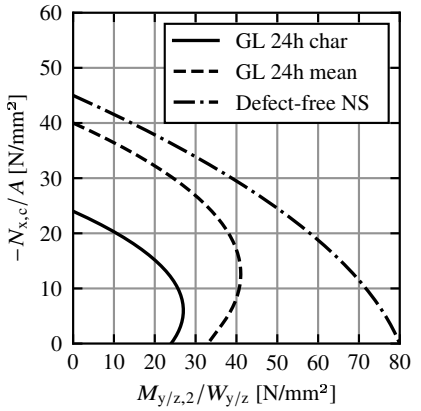

Figure 4.4: Cross-sectional resistances for combined bending and axial compression and bilinear elastoplastic material behaviour with Equation (4.16); with varying $f_{c,0}$ and f_m.

Table 4.1: Values of a and b and interaction equations for different timber materials with the compressive utilisation ratio $\mu_c = N_{x,c}/Af_{c,0}$ and the bending utilisation ratio $\mu_m = M_{y/z,2}/W_{y/z}f_m$.

	$f_{c,0}/f_m$ [1] [N/mm^2]	a $\mu_c = (0, 0.5, 1)$	b	Interaction equation
GL 24c char [2]	-21.0 / 24.0	(0.62, 0.31, 0.01)	0.99	$\mu_c^2 - \mu_c(0.62 - 0.61\mu_c) + \mu_m = 0.99$
GL 24h char [2]	-24.0 / 24.0	(1.00, 0.50, 0.00)	1.00	$\mu_c^2 - \mu_c(1.00 - 1.00\mu_c) + \mu_m = 1.00$
GL 30c char [2]	-24.5 / 30.0	(0.44, 0.23, 0.02)	0.98	$\mu_c^2 - \mu_c(0.44 - 0.42\mu_c) + \mu_m = 0.98$
GL75 char [3]	-59.4 / 75.0	(0.36, 0.20, 0.03)	0.97	$\mu_c^2 - \mu_c(0.36 - 0.33\mu_c) + \mu_m = 0.97$
GL 24h mean [4]	-40.0 / 33.0	(1.68, 0.85, 0.02)	0.98	$\mu_c^2 - \mu_c(1.68 - 1.66\mu_c) + \mu_m = 0.98$
Defect-free NS [5]	-45.0 / 80.0	(-0.24, -0.01, 0.22)	0.78	$\mu_c^2 + \mu_c(0.24 - 0.46\mu_c) + \mu_m = 0.78$

[1] If $-f_{c,0} < f_m$, the input bending strength for Equations (4.16) to (4.18) needs to be chosen higher than f_m for actually reaching the bending resistance $f_m W_y$ due to the plasticizing.

[2] EN 14080 [54]; [3] ETA-14/0354 [63]; [4] Schilling et al. [141]; [5] Norway Spruce (NS) DIN 68364 [39].

where $N_{x,c}$ is the axial compressive force, $f_{c,0}$ and f_m are the compressive and bending strengths in grain direction, H and B are the cross-sectional height and width, H_{pl} is the height of plasticised area of the cross-section, and $M_{y/z,2}$ is the bending moment about the y- or z-axis according to geometrically nonlinear calculations (T2O). Equations (4.14) and (4.15) only apply if compressive plasticising occurs, i.e. $H_{pl} \geq 0$.
Solving Equation (4.14) for H_{pl} and inserting the result in Equation (4.15) yields, after some transformations,

$$\left(\frac{N_{x,c}}{Af_{c,0}}\right)^2 - a \cdot \frac{N_{x,c}}{Af_{c,0}} + \frac{M_{y/z,2}}{W_{y/z}f_m} = b \quad , \tag{4.16}$$

with

$$a = \left(\frac{5f_{c,0}^2 + 3f_{c,0}f_m}{f_m^2 - f_{c,0}f_m} - \frac{4f_{c,0}^2 - f_m^2 + f_{c,0}f_m}{f_m^2 - f_{c,0}f_m} \cdot \frac{N_{x,c}}{Af_{c,0}}\right) \quad , \tag{4.17}$$

$$b = \frac{-3f_{c,0}f_m - f_{c,0}^2}{f_m^2 - f_{c,0}f_m} \quad , \tag{4.18}$$

where A is the cross-sectional area, and $W_{y/z}$ is the section modulus about the y- or z-axis. Hence, the interaction relationship depends on the ratio of $f_{c,0}$ to f_m.
Figure 4.4 illustrates the load-bearing capacities for $N_{x,c}$-$M_{y/z,2}$-interaction and different materials, i.e. different ratios of $f_{c,0}$ to f_m according to Table 4.1. The interaction relationship is clearly nonlinear, with the degree of nonlinearity depending on the ratio of $f_{c,0}$ to f_m. This is consistent with the experimental results of Buchanan [24], see Figure 2.20.
Table 4.1 provides values of a and b and the resulting interaction equations for common timber materials and common ratios of $f_{c,0}$ to f_m. For common values of $f_{c,0,k}$ and $f_{m,k}$, the parameters a and b become $a > 0$ and $b \approx 1$. Therefore, a can be neglected on the safe

side (greyed out in Table 4.1).
On the safe side, Equation (4.16) can thus be simplified to

$$\left(\frac{N_{x,c}}{A f_{c,0}}\right)^2 + \frac{M_{y/z,2}}{W_{y/z} f_m} = 1 \quad . \tag{4.19}$$

This interaction relationship for considering plasticising in Equation (4.19) no longer has an intuitive form if the section modulus $W_{y/z}$ is used. But, as demonstrated, Equation (4.19) is a mechanically reasonable solution of the interaction relationship.
Hence, the empirical $N_{x,c}$-$M_{y/z,2}$-interaction equation in EN 1995-1-1 [57] and FprEN 1995-1-1 [69], see Equation (2.54), which was derived based on the experimental and numerical results of Blaß [9], Buchanan et al. [25], and Zahn [183], can also be derived analytically.

4.5 Reduction factor k_{m} accounting for lateral torsional buckling

In practice, simplified design models are often adopted for LTB design, which assume geometrically linear internal forces (T1O) and a reduction factor k_{m} to account for the LTB. Several design models for calculating k_{m} with regression equations partly based on analytical models are discussed in Sections 2.2.2.8, 2.6.2.1.4, and 2.6.4.1.4.
Leicester [118], Taras [153], and Wilden et al. [175] discussed a mechanically sound analytical derivation of the reduction factor for considering LTB k_{m}. As this analytical derivation of k_{m} was not widely used or known in timber construction when this thesis was prepared, the complete derivation based on [118], [153], and [175] is given here and expanded to enhance its ease of use. Novel elements are the consideration of the size effect due to biaxial bending with k_{red}, the consideration of the creep deformations with $k_{\mathrm{def,ef}}$, and, at least in timber construction, the formulation with bow imperfections e_{y} instead of twist imperfections e_{θ}, which allows consistent imperfection assumptions in the standardisation.

In the first part of the derivation, $M_{\mathrm{z},2}$, according to Equation (2.15), is simplified by reducing the exponent of α_{m} in the denominator from 2 to 1.
The basis for this is the differential equations for LTB with a constant bending moment $M_{\mathrm{y},1}$, see, e.g. Hörsting [90]:

$$G_{0,\mathrm{el}} I_{\mathrm{x}} \cdot \frac{\mathrm{d}^2\theta}{\mathrm{d}x^2} - M_{\mathrm{y},1} \cdot \frac{\mathrm{d}^2(v + e_{\mathrm{y}})}{\mathrm{d}x^2} = 0 \quad , \tag{4.20}$$

$$E_{0,\mathrm{el}} I_{\mathrm{z}} \cdot \frac{\mathrm{d}^4 v}{\mathrm{d}x^4} + M_{\mathrm{y},1} \cdot \frac{\mathrm{d}^2(\theta + e_{\theta})}{\mathrm{d}x^2} = 0 \quad , \tag{4.21}$$

where $G_{0,\mathrm{el}}$ is the shear modulus in grain direction, I_{x} is the elastic torsional moment of inertia according to Equation (2.18), θ is the twist about the x-axis over the member length, $M_{\mathrm{y},1}$ is the applied constant bending moment about the y-axis according to geometrically linear calculations, v is the deformation in y-direction over the member length, e_{y} is the bow imperfection in y-direction over the member length, $E_{0,\mathrm{el}}$ is the elastic modulus in grain direction, I_{z} is the elastic moment of inertia about the z-axis according to Equation (2.5), and e_{θ} is the twist imperfection about the x-axis over the member length.
By means of the initial functions

$$\theta(x) = \theta_2 \sin\left(\pi \cdot \frac{x}{L}\right) \quad , \tag{4.22}$$

$$v(x) = v_2 \sin\left(\pi \cdot \frac{x}{L}\right) \quad , \tag{4.23}$$

$$e_\theta(x) = e_\theta \sin\left(\pi \cdot \frac{x}{L}\right) \quad , \tag{4.24}$$

$$e_y(x) = e_y \sin\left(\pi \cdot \frac{x}{L}\right) \quad , \tag{4.25}$$

where θ_2 is the rotation of the cross-section about the axis at midspan according to geometrically nonlinear calculations, L is the span, v_2 is the deformation of the beam axis at midspan in y-direction according to geometrically nonlinear calculations, e_θ is the twist imperfection about the x-axis at midspan, and e_y is the bow imperfection in y-direction at midspan, the differential equations can be transformed to

$$G_{0,el} I_x \, \theta_2 - M_{y,1} \cdot (v_2 + e_y) = 0 \quad , \tag{4.26}$$

$$\frac{\pi^2}{L^2} \cdot E_{0,el} I_z \, v_2 - M_{y,1} \cdot (\theta_2 + e_\theta) = 0 \quad , \tag{4.27}$$

which are valid at midspan.
The key in the derivation is the assumption that the shape and amplitude of the bow and twist imperfections are affine to the 1st eigenmode. Therefore, according to Sedlacek et al. [145],

$$e_y = k \, v_2 \quad , \tag{4.28}$$

$$e_\theta = k \, \theta_2 \quad , \tag{4.29}$$

where k is a scaling factor.
Inserting Equations (4.28) and (4.29) in Equations (4.26) and (4.27) yields

$$G_{0,el} I_x \, \theta_2 - M_{y,1} \cdot (v_2 + k v_2) = 0 \quad , \tag{4.30}$$

$$\frac{\pi^2}{L^2} \cdot E_{0,el} I_z \, v_2 - M_{y,1} \cdot (\theta_2 + k\theta_2) = 0 \quad . \tag{4.31}$$

Solving Equation (4.30) for k and inserting the result in Equation (4.31) results after several transformations in

$$\frac{v_2}{\theta_2} = \frac{M_{y,cr}}{N_{z,cr}} \quad , \tag{4.32}$$

and with Equations (4.28) and (4.29) in

$$\frac{e_y}{e_\theta} = \frac{M_{y,cr}}{N_{z,cr}} \quad , \tag{4.33}$$

where $M_{y,cr}$ is the critical bending moment for LTB according to Equation (2.17), and $N_{z,cr}$ is the critical axial compressive force for flexural buckling about the z-axis according to Equation (2.3). The 1st eigenmode of a single-span beam with a constant rectangular cross-section and a constant bending moment $M_{y,1}$ is thus given by Equation (4.33).
This coupling of the imperfections by applying them in the shape of the 1st eigenmode is a key in the mechanically sound analytical derivation of the reduction factor k_m, because it allows to reduce the exponent of α_m in the denominator of Equation (2.15) from 2 to 1. The consideration of creep deformations by replacing v and θ in Equations (4.20) and (4.21) with $v \cdot (1 + k_{def,ef})$ and $\theta \cdot (1 + k_{def,ef})$ has no influence on Equation (4.33).
If assuming pure uniaxial bending (no axial compressive forces) and applying Equation (4.33), the bending moment $M_{z,2}$ from Equation (2.48) can be rewritten as

$$M_{z,2} = \frac{-N_{z,cr}\alpha_m e_y}{1 - \alpha_m \cdot (1 + k_{def,ef})} \quad , \tag{4.34}$$

where $k_{def,ef}$ is the effective creep deformation coefficient according to Equation (2.47) with $k_{def,ef} = k_{def,\theta,ef} = k_{def,v,ef}$. From Equation (2.15) to Equation (4.34), the exponent of α_m in the denominator is reduced from 2 to 1.

In the second part of the derivations, a mechanically sound formulation of the reduction factor k_m is presented.
The basis is the linear $M_{y,2}$-$M_{z,2}$-interaction with size effect for biaxial bending according to EN 1995-1-1 [57], see Equation (2.54) and (2.55), where

$$\frac{M_{y,2}}{W_y f_{m,y}} + k_{red} \cdot \frac{M_{z,2}}{W_z f_{m,z}} \leq 1.0 \quad , \tag{4.35}$$

$$k_{red} \cdot \frac{M_{y,2}}{W_y f_{m,y}} + \frac{M_{z,2}}{W_z f_{m,z}} \leq 1.0 \quad , \tag{4.36}$$

where $M_{y/z,2}$ is the bending moment about the y- or z-axis according to geometrically nonlinear calculations, $W_{y/z}$ is the section modulus about the y- or z-axis, $f_{m,y/z}$ is the bending strength about the y- or z-axis, and k_{red} is a factor for considering the positive size effect on the bending strength at biaxial bending according to EN 1995-1-1 [57].
The common assumption is made that the geometrically nonlinear LTB behaviour does not significantly influence the bending moment about the strong axis, and $M_{y,2} = M_{y,1}$ applies.

If inserting this and Equation (4.34) into Equations (4.35) and (4.36), this yields

$$\begin{aligned}&\frac{\sigma_{\mathrm{m,y,1}}^2}{f_{\mathrm{m,y}}^2}\cdot(1+k_{\mathrm{def,ef}})\cdot k_{\mathrm{red,1}}\\&-\frac{\sigma_{\mathrm{m,y,1}}}{f_{\mathrm{m,y}}}\cdot\left(k_{\mathrm{red,1}}\cdot\frac{\sigma_{\mathrm{m,y,cr}}}{f_{\mathrm{m,y}}}+k_{\mathrm{red,2}}\cdot\frac{\pi^2E_{0,\mathrm{el}}I_{\mathrm{z}}}{L^2W_{\mathrm{z}}f_{\mathrm{m,z}}}\cdot e_{\mathrm{y}}+(1+k_{\mathrm{def,ef}})\right)\\&+\frac{\sigma_{\mathrm{m,y,cr}}}{f_{\mathrm{m,y}}}=0\quad,\end{aligned}\tag{4.37}$$

where $\sigma_{\mathrm{m,y,1}}=M_{\mathrm{y,1}}/W_{\mathrm{y}}$ is the bending stresses about the y-axis, $k_{\mathrm{red,1/2}}=k_{\mathrm{red}}$ is a factor for considering the positive size effect on the bending strength at biaxial bending (either $k_{\mathrm{red,1}}$ or $k_{\mathrm{red,2}}$ may be applied), and $\sigma_{\mathrm{m,y,cr}}=M_{\mathrm{y,cr}}/W_{\mathrm{y}}$ is the critical bending stress. $k_{\mathrm{red,1}}$ and $k_{\mathrm{red,2}}$ were introduced to allow for the formulation of Equation (4.37) in one equation instead of two. This equation is the simplified quadratic form of the LTB load-bearing capacity and is similar to the *Ayrton-Perry approach* for flexural buckling discussed in Section 2.2.1.8.
With the definition of the reduction factor for LTB

$$k_{\mathrm{m}}=\frac{\sigma_{\mathrm{m,y,1}}}{f_{\mathrm{m,y}}}\quad,\tag{4.38}$$

the definition of the relative slenderness ratio for LTB

$$\lambda_{\mathrm{m,rel}}^2=\frac{f_{\mathrm{m,y}}\cdot(1+k_{\mathrm{def,ef}})}{\sigma_{\mathrm{m,y,cr}}}\quad,\tag{4.39}$$

and the definition of the fitting factor

$$\beta_{\mathrm{m}}=\frac{\pi^2E_{0,\mathrm{el}}I_{\mathrm{z}}f_{\mathrm{m,y}}}{L^2W_{\mathrm{z}}\sigma_{\mathrm{m,y,cr}}f_{\mathrm{m,z}}}\cdot e_{\mathrm{y}}\quad,\tag{4.40}$$

Equation (4.37) can be simplified to

$$k_{\mathrm{m}}^2\,k_{\mathrm{red,1}}\,\lambda_{\mathrm{m,rel}}^2-k_{\mathrm{m}}\cdot\left(k_{\mathrm{red,1}}+k_{\mathrm{red,2}}\,\beta_{\mathrm{m}}+\lambda_{\mathrm{m,rel}}^2\right)+1=0\quad.\tag{4.41}$$

This quadratic equation can be solved for k_{m}, where the smaller of the two results is

$$\begin{aligned}k_{\mathrm{m}}=&\frac{1}{k_{\mathrm{red,1}}\lambda_{\mathrm{m,rel}}^2}\cdot0.5\cdot\left(k_{\mathrm{red,1}}+k_{\mathrm{red,2}}\,\beta_{\mathrm{m}}+\lambda_{\mathrm{m,rel}}^2\right)\\&-\sqrt{\left(\frac{1}{k_{\mathrm{red,1}}\lambda_{\mathrm{m,rel}}^2}\cdot0.5\cdot\left(k_{\mathrm{red,1}}+k_{\mathrm{red,2}}\,\beta_{\mathrm{m}}+\lambda_{\mathrm{m,rel}}^2\right)\right)^2-\frac{1}{k_{\mathrm{red,1}}\lambda_{\mathrm{m,rel}}^2}}\quad.\end{aligned}\tag{4.42}$$

By the introduction of

$$\phi_m = 0.5 \cdot \left(k_{red,1} + k_{red,2}\, \beta_m + \lambda_{m,rel}^2 \right) \quad , \tag{4.43}$$

Equation (4.42) can be simplified to

$$k_m = \frac{\phi_m - \sqrt{\phi_m^2 - k_{red,1} \lambda_{m,rel}^2}}{k_{red,1} \lambda_{m,rel}^2} \quad . \tag{4.44}$$

Expanding the numerator and denominator by $\phi_m + \sqrt{\phi_m^2 - k_{red,1} \lambda_{m,rel}^2}$ yields

$$k_m = \frac{1}{\phi_m + \sqrt{\phi_m^2 - k_{red,1} \lambda_{m,rel}^2}} \quad . \tag{4.45}$$

The reduction factor for LTB in bending design with geometrically linear calculations k_m can thus be calculated by means of Equations (4.45) and (4.43).

If formulated in accordance with EN 1995-1-1 [57] and FprEN 1995-1-1 [69], the following should be satisfied for LTB of beams with uniaxial bending:

$$\frac{M_{y,1,d}}{k_m W_y f_{m,y,d}} \leq 1.0 \quad , \tag{4.46}$$

with

$$k_m = \min \left\{ \frac{1}{\phi_{m,1} + \sqrt{\phi_{m,1}^2 - k_{red} \lambda_{m,rel}^2}} \, , \, \frac{1}{\phi_{m,2} + \sqrt{\phi_{m,2}^2 - \lambda_{m,rel}^2}} \right\} \quad , \tag{4.47}$$

$$\phi_{m,1} = 0.5 \cdot \left(k_{red} + \beta_m + \lambda_{m,rel}^2 \right) \quad , \tag{4.48}$$

$$\phi_{m,2} = 0.5 \cdot \left(1 + k_{red}\, \beta_m + \lambda_{m,rel}^2 \right) \quad , \tag{4.49}$$

$$\lambda_{m,rel} = \sqrt{\frac{f_{m,y,k} W_y \cdot (1 + k_{def,ef})}{M_{y,cr}}} \quad , \tag{4.50}$$

$$\beta_m = \frac{\pi^2 E_{0,el} I_z f_{m,y,k}}{L^2 W_z \sigma_{m,y,cr} f_{m,z,k}} \cdot e_y \quad , \tag{4.51}$$

where $M_{y,1}$ is the design bending moment about the y-axis according to geometrically linear calculations, k_m is the reduction factor accounting for LTB, $W_{y/z}$ is the section modulus about the y- or z-axis, $f_{m,y/z,d}$ is the bending strength about the y- or z-axis, $\phi_{m,1/2}$ are the intermediate parameters for the calculation of k_m, k_{red} is a factor for considering the positive size effect on the bending strength at biaxial bending according to EN 1995-1-1 [57], $\lambda_{m,rel}$ is the relative slenderness ratio for LTB, β_m is a fitting factor considering the effects of the ratio of, e.g. $E_{0,el}$ to $G_{0,el}$, the influences of geometrical and structural imperfections, and plasticising, $k_{def,ef}$ is the effective creep deformation coefficient according to Equation (2.41), and $M_{y,cr}$ is the critical bending moment according to Equation (2.17). β_m can also be reformulated as

$$\begin{aligned}\beta_m &= \frac{A}{W_z}\cdot\frac{\sigma_{c,y,cr}}{\sigma_{m,y,cr}}\cdot\frac{f_{m,y,k}}{f_{m,z,k}}\cdot e_y = \frac{e_y}{L}\cdot\frac{H}{B\cdot\sqrt{1-0.63\cdot\frac{B}{H}}}\cdot\frac{\pi}{2}\cdot\sqrt{\frac{E_{0,k}}{G_{0,k}}}\cdot\frac{f_{m,y,k}}{f_{m,z,k}}\\ &\approx \frac{e_y}{L}\cdot\frac{H}{B}\cdot\frac{\pi}{2}\cdot\sqrt{\frac{E_{0,k}}{G_{0,k}}}\quad .\end{aligned} \tag{4.52}$$

The equations of the k_m-method in FprEN 1995-1-1 [69], see Section 2.6.4.1.4, are surprisingly similar to Equations (4.47), (4.48), and (4.52) if assuming $f_{m,y} = f_{m,z}$ and $k_{red} = 1$. Only the terms β_θ and $(\lambda_{m,rel} - 0.55)$ are not present in the previously analytically derived equations. However, the introduction of a limit criterion from which LTB is to be considered, as it is a reasonable simplification for building practice, see also Sections 2.6 and 7.2.2.4 (4). Even if the value 0.55 itself is questionable, see Section 2.6.5.

4.6 Summary

Analytical equations and models were presented that improve the understanding of the mechanical background of the stability phenomena in timber construction.

In Section 4.2, it is demonstrated that the $N_{x,c}$-$M_{y/z,1}$-interaction for flexural buckling of very slender columns is predominantly linear. This confirms the linear $N_{x,c}$-$M_{y/z,1}$-interaction of the k_c-method in EN 1995-1-1 [57] and FprEN 1995-1-1 [69]. Furthermore, the geometrically nonlinear component of the internal forces resulting from the bending moment $M_{y/z,1}$, which is disregarded in the k_c-method in EN 1995-1-1 [57] and FprEN 1995-1-1 [69], is derived in Equation (4.8).
In Section 4.3, it is shown that the $N_{x,c}$-$M_{y,1}$-interaction for LTB of very slender beam-columns is nonlinear and represents the limit criterion of the critical load in Equation (4.33). This confirms the nonlinear $N_{x,c}$-$M_{y/z,1}$-interaction of the k_m-method in EN 1995-1-1 [57] and FprEN 1995-1-1 [69].
The $N_{x,c}$-$M_{y,2}$-interaction of the cross-sectional load-bearing capacity with bilinear elasto-plastic compression behaviour in grain direction was analysed in Section 4.4, and it was demonstrated that the nonlinear $N_{x,c}$-$M_{y,2}$-interaction in EN 1995-1-1 [57] and FprEN 1995-1-1 [69] represents a mechanically sound limit criterion.
Finally, an analytical derivation of the k_m-method for LTB is presented, see Section 4.5. New features are the consideration of the size effect due to biaxial bending with k_{red}, the consideration of the creep deformations with $k_{def,ef}$, and, at least in timber construction, the formulation with bow imperfections e_y, which allows consistent imperfection assumptions in the standardisation. The regression equations of the k_m-method in FprEN 1995-1-1 [69] are similar to the analytically derived equations but can still be simplified by omitting the mechanically superfluous term β_θ.
The analytical derivation of the k_c-method for flexural buckling is discussed in Annex C.

The findings were integrated into the evaluation and discussion of the numerical and experimental results presented in Section 6, as well as the formulation of the design concept presented in Section 7

5 Numerical modelling and analysis

5.1 General

Numerical models, like analytical ones, allow for enhancing the understanding of physical phenomena, studying such phenomena in more detail (limitations of experimental measurement techniques), and extending the results of experimental investigations. Moreover, to overcome limitations in number, geometry, boundary conditions, etc. of tests. The flexibility of the *Finite Element Method* (FEM) allows for investigating effects that cannot be represented analytically, such as material scattering over the member volume. As a result, *Finite Element Analysis* (FEA) has become the predominant method for investigating stability problems in civil engineering, see, e.g. Pourostad [130] and Taras [153] and Section 2.

The aim of the application of FEA in this thesis was to examine the load-bearing behaviour of imperfection-sensitive timber members under combined axial compression and bending in more detail and to conduct extensive parameter studies. In particular

- the equivalent geometrical imperfection assumptions for design, see Section 5.6.2, and
- the $N_{x,c}$-$M_{y,1}$-interaction for flexural buckling and LTB, see Section 5.6.3,

are discussed. The relevant physical phenomena established in Sections 2 and 3 had to be considered, which are (i) the geometrically nonlinear behaviour with scattering geometrical and structural imperfections, (ii) the materially nonlinear behaviour for compression in grain direction and shear, and (iii) the failure behaviour with scattering tensile and shear strengths.

For the development, verification, and validation of the FE model and the evaluation of the FE results, the methodology from the *FE guidelines* according to Töpler and Kuhlmann [162] was applied, which is discussed in Section 5.2. The FE model and especially the modelling of the material, structural imperfections, and geometrical imperfections are discussed in Section 5.3. An extensive verification and validation of the FE model was conducted in line with the *FE guidelines*, with the results of flexural buckling and LTB tests described in Sections 3.3 and 3.4, see Sections 5.4 and 5.5. Finally, the analysis and parameter studies on equivalent geometrical imperfections and $N_{x,c}$-$M_{y,1}$-interaction are described in Section 5.6. The results are discussed in Section 6 together with the experimental results from Section 3 and the analytical derivations from Section 4. This culminated in the formulation of the design concept in Section 7.

5.2 Finite element based design

In order to promote the standardisation of FE based design in timber construction, and based on similar developments in steel construction with FprEN 1993-1-14 [68], *Guidelines for Finite Element Based Design of Timber Structures* (*FE guidelines*) were developed by Töpler and Kuhlmann [162] within the Cluster of Excellence *Integrative Computational Design in Architecture and Construction* (IntCDC) at the University of Stuttgart from 2019 to 2022 [109]. These *FE guidelines* were also discussed in Töpler et al. [169] and Töpler et al. [160]. The initiative was adopted in standardisation, and the working group CEN/TC 250/SC 5/WG 11 was established to develop a *Technical Specification* (TS) for *Design assisted by numerical methods* of timber structures. Excerpts relevant to this thesis are presented in this section.

The *FE guidelines* and the TS aim at providing guidance on the use of numerical methods in daily engineering practice and in expert engineering applications. They provide (i) guidance on the use of numerical methods for design and timber-specific modelling issues; (ii) minimum requirements on model and software capabilities for specific applications; (iii) boundaries for the safe and correct application of numerical methods; (iv) methods for verification and validation of models, analyses, and results; (v) benchmarks for model verification and validation; (vi) possibilities for an expert application of numerical analyses within the safety concept of the Eurocodes. Major benefits of the implementation of such rules are the reduction of modelling errors, an increase in the quality of numerical analyses, and, therefore, improved trustworthiness and acceptance of numerical models for design. Furthermore, the possibilities of applying numerical analyses for timber design are extended for complex problems where other methods yield conservative results or are not available.

Within the *FE guidelines* [162], a procedure for FE based design of timber structures is proposed, see Figure 5.1 and also Töpler et al. [169].
In step (1), the problem to be investigated is defined. In step (2), the appropriate design method is chosen. Three design methods are described in Section 4 of the *FE guidelines*, depending on the purpose and the complexity level of the numerical calculations.
In daily engineering practice, FEA are usually utilised to calculate internal forces, deformations, and eigenvalues and to evaluate the load-bearing behaviour of complex three-dimensional structures. The design checks are conducted with the design equations of the Eurocodes. In this case, the design method *numerical design requiring a subsequent design check* can be applied, where the *FE guidelines* provide (i) information on modelling, e.g. creep, stiffness of joints and connections; (ii) minimum requirements and boundaries on model and software if modelling certain problems; (iii) methods for evaluation of the quality of FE results, e.g. mesh density, singularities; (iv) benchmarks for comparison of calculation results.
The possibility of an expert engineering application of FEA beyond the standard cases defined in the Eurocodes is enabled with the design method *numerical design with direct resistance check*. This method introduces the possibility of a complete numerical design within the semi-probabilistic safety concept of the Eurocodes by computing not only the effects of actions but also the resistances numerically. Taking into account the model uncertainties, the load-bearing capacity can thus be directly verified without relying on the

design equations of the Eurocodes. Input values for FEA are nominal values according to EN 1995 (all parts), relevant product standards, or technical approvals. Characteristic resistances R_k can be determined by dividing numerically determined resistances by the partial factor for modelling γ_{FE}. The partial factor for modelling γ_{FE} covers the uncertainties of the numerical model and the type of analysis considering the differences between the numerical model and physical reality. If a normal distribution is assumed for the ratio of the measured (or known) to the computed results, γ_{FE} can be computed as

$$\gamma_{FE} = \frac{1}{m_0 \cdot (1 - k_n \cdot V_0)} \geq 1.0 \quad , \tag{5.1}$$

where m_0 is the mean value of the ratio of the measured (or known) to the computed results for n samples, k_n is the characteristic fractile factor according to EN 1990 [55], Annex D, and V_0 is the coefficient of variation of the ratio of the measured (or known) and the computed results for n samples. Design resistances, R_d, can be obtained by applying the standard partial factors according to EN 1990 and EN 1995 (all parts).
Numerical simulations can be applied in product development and certification and in research for complementing and extending physical experiments. On the highest level, stochastic input values for geometrical and material properties may be used, and a statistical evaluation according to EN 1990 [55] may be performed for determining the test-based resistance (including the actual partial factor).

It is essential to ensure sufficient accuracy of the FEA, hence step (4) in Figure 5.1. For this reason, the terms *verification* and *validation* are defined in FprEN 1993-1-14 [68].

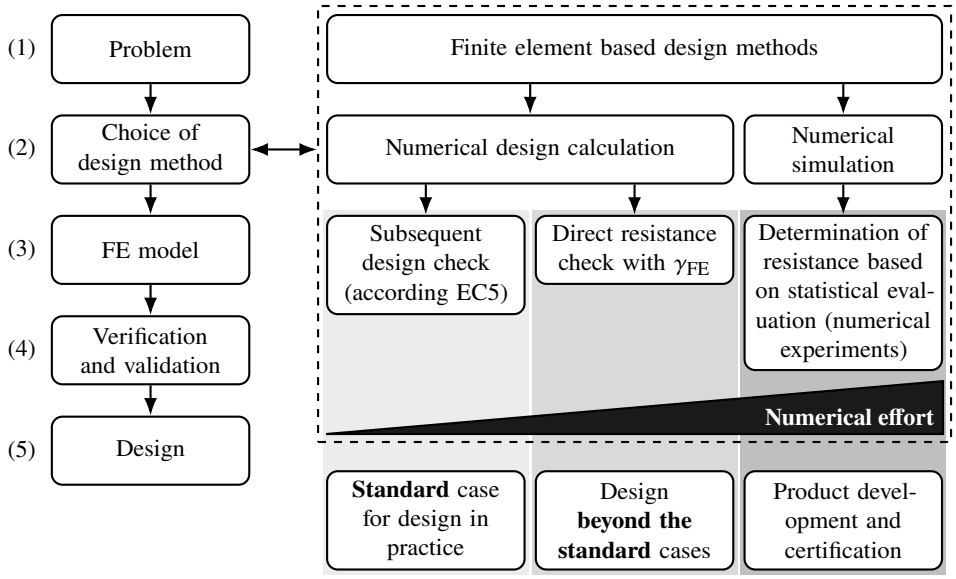

Figure 5.1: Proposed procedure for the FE based design; from Töpler and Kuhlmann [162].

The *verification* ensures, according to the *FE guidelines* [162], that the numerical model and analysis are properly implemented, understood, and applied. Additionally, the verification should confirm that the used numerical solution is a good approximation of exact mathematical solutions, mechanical models, or benchmarks. The verification described in Töpler and Kuhlmann [162] includes the following steps, which are applied in Section 5.4.

1. In the *engineering judgement*, the main calculation results of the FEA (system response quantities (SRQs), which are, e.g. internal forces, deformations, and load-deformation behaviour) are checked using simple mechanical models, benchmarks, or experience.
2. Within the *discretisation check*, it is demonstrated that the chosen element type and size are accurate for the analysed problem. A mesh convergence study is executed to check if the relevant SRQs converge as the mesh is refined. The chosen mesh size should satisfy the 5% test. If computation times are low, a 1% test may be applied.
3. The *solver convergence check* ensures that the SRQs have converged if the computation of a load, displacement, or time step is finished.
4. The *sensitivity check* is a variation of the input parameters determining which parameters are crucial to the relevant SRQs and whether these parameters should be defined with higher precision or not.
5. The *imperfection sensitivity check* examines whether and which imperfections affect the SRQs.

Depending on the chosen design method, see Figure 5.1, steps 2. to 5. may be omitted.
The *validation* ensures, according to the *FE guidelines* [162], that the model correctly or conservatively captures the physical phenomena to be modelled by comparing numerical results with known accurate solutions (benchmarks). Within the validation, the uncertainty of the model can be quantified by evaluation of the differences between numerical results and benchmarks, e.g. by calculation of γ_{FE} with Equation (5.1). The methods are applied in Section 5.5.

For ULS design in step (5) of Figure 5.1 with *numerical design calculations with direct resistance check* and *numerical simulations*, the structural resistance is determined according to the *FE guidelines* [162] by taking the lowest resistance from the following three criteria:

- the ultimate stress;
- the maximum load level of the computed load-deformation path; and
- the largest tolerable deformation (or strain).

The characteristic resistance R_{k} may be determined by dividing the numerical resistance R_{FE} by the partial factor for modelling γ_{FE}. In even more advanced investigations, an actual partial factor may be derived based on statistical evaluation according to EN 1990 [55].

The methods of the *FE guidelines* [162] were applied for this thesis, and their results are discussed, see Sections 5.3 to 6.

5.3 Modelling

5.3.1 General

Abaqus/CAE 2023 [1] was used for the FEA. Modelled member geometries are given in Sections 5.4, 5.5, and 5.6. Geometrical bow and twist imperfections were considered according to Section 5.3.4. Material modelling is discussed in Sections 5.3.2 and 5.3.3, the latter also covering structural imperfections.
20-node quadratic solid elements C3D20R were chosen for meshing. 6 elements were generally used in the width of a member, see Abaqus [1]. The mesh size in member length and height was chosen depending on the application of the *KaReMo*, see Section 5.3.3. If using the *KaReMo*, the element length was set to a divider of 150 mm, and the element height was set to 40 mm according to the selected lamella height. As few elements as possible, but at least 20, were used in the member length. Where *KaReMo* was not used, exactly 20 elements were chosen in the member length and 6 in the height. The verification of the mesh size is described in Section 5.4. For the verification and the validation in Sections 5.4 and 5.5, different mesh sizes were chosen.
The modelled boundary conditions and actions are described in Sections 5.4, 5.5, and 5.6. *Geometrically and materially nonlinear analyses with imperfections* (GMNIA) with the quasi-Newton solution technique of Abaqus [1] were conducted.

5.3.2 Material model

5.3.2.1 General

Softwood GL 24h and GL 30c according to EN 14080 [54] and beech LVL GL75 according to ETA-14/0354 [63] were modelled. Service class 1 at normal temperature without long-term effects was generally assumed. Transversely isotropic material behaviour was chosen for softwood GL and orthotropic material behaviour for beech LVL, see Section 2.3.1. According to the relevant stresses, see Figure 2.17, and in line with Section 2, plasticity and/or failure were only considered for compression and tension in grain direction and for shear.
The influence of a stress interaction on plasticising and failure was only considered for the shear stresses in the three planes LR, LT, and RT, see Annex D.
As there was no material model available in *Abaqus CAE/2023* to model the behaviour described below, a corresponding user-defined material model was developed in the *UMAT* subroutine of Abaqus, see Töpler [159]. A detailed explanation of this material model and the underlying equations is given in Annex D.

5.3.2.2 Tension in grain direction

For tension in grain direction, based on the discussions in Section 2.3.2, a linear-elastic material behaviour up to failure was modelled with the stress-strain relationship in Figure 5.2. Two methods were implemented to consider tensile failure, depending on the application of the model: (i) for the *KaReMo* according to Section 5.3.3, element deletion if the tensile strength $f_{t,0}$ is exceeded at one integration point; (ii) in all other cases, no failure criterion

in the material model, but a check in post-processing whether the tensile strength $f_{t,0}$ is exceeded at an element node. Following Frese [74], for the *KaReMo*, a member failure was assumed if the tensile strength of the outermost lamella was exceeded, see also Section 2.4.2.

5.3.2.3 Compression in grain direction

For compression in grain direction, based on the discussions in Sections 2.3.3, 3.3.3, and 3.4.3, the stress-strain relationship was defined in three parts, see Figure 5.4. In part 1, a linear elastic material behaviour was assumed up to the proportionality limit $f_{c,0,lin}$. In part 2, nonlinearly increasing plastic strains were modelled after exceeding the proportionality limit $f_{c,0,lin}$ and until the compressive strength $f_{c,0}$. The plastic strains were calculated utilising an ellipse with radii $(f_{c,0} - f_{c,0,lin})$ and $\epsilon_{c,0,pl}$, see Figure 5.5. The elliptical shape was chosen because it is simple to implement and provides a good approximation to experimentally determined stress-strain curves, see Section 2.3.3 and Figures 3.24 and 3.34. Experimentally determined stress-strain curves often show a drop in stress after the compressive strength is reached. This was neglected to improve the convergence of the FEA. A linear plasticising with a stiffness $E_{c,0,pl}$ was assumed in part 3, resulting in a minimum overall stiffness of $E_{c,0,T}$. For a continuous stress-strain relationship, the tangent intersection of $E_{c,0,pl}$ with the ellipse was chosen as the transition point from parts 2 to 3. No failure criterion for compression in grain direction was considered in the material model. In post-processing, based on Blaß [9] and Frese et al. [75], a compressive failure was assumed if the total strain $\epsilon_{c,0}$ was exceeded at all element nodes in a section or if the mean compressive stress in the section exceeded the compressive strength, see also Section 2.4.3. It should be noted that these two failure criteria were generally not relevant for the numerically determined load-bearing capacities of imperfection-sensitive timber members.

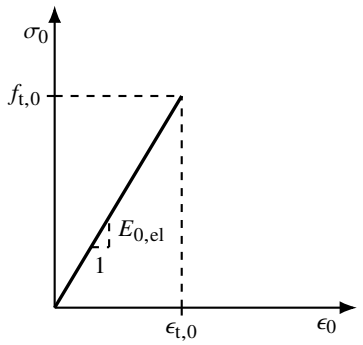

Figure 5.2: Modelled stress-strain relationship for tension in grain direction; stresses σ_0 plotted over strains ϵ_0.

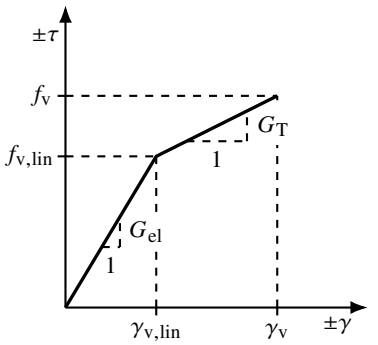

Figure 5.3: Modelled stress-strain relationship for shear; shear stresses τ plotted over shear strains γ.

5.3.2.4 Shear in grain direction

For simplification, and as only a few experimental results are known, see Section 2.3.4, a bilinear stress-strain relationship was modelled for shear, see Figure 5.3. Linear elastic material behaviour was assumed until the proportionality limit $f_{v,lin}$ was reached. This was followed by linear plasticity with stiffness G_{pl}, resulting in an overall stiffness of G_T. No failure criterion was implemented in the material model. Instead, two failure criteria were implemented in the post-processing, depending on the application of the model: (i) for the *KaReMo*^{v} according to Section 5.3.3, a check whether the shear strength f_v is exceeded at the integration points; (ii) in all other cases, a check whether the shear strength f_v is exceeded at the element nodes.
This distinction was made because the tensile failure criterion in the *KaReMo* is also checked at the integration points according to Frese [74]. Stress checks based on EN 1995-1-1 [57], on the other hand, are carried out with edge stresses, i.e. values at the element nodes. In the tests of Blaß and Krüger [15], it was not possible to increase the load after a shear failure due to shear force occurred, see also Section 2.4.4. Therefore, a member failure in shear was assumed as soon as the shear strength was exceeded at any point in a member. Due to the fundamentally different distribution of torsional shear stresses, see Figure 2.17, it is imaginable that in this case a stress redistribution is possible if the shear strength is reached and that the load can further be increased. However, as no experimental results were known, this was not considered.

5.3.2.5 Size effect

The size effects on the tensile and shear strengths in member length and height were implicitly considered in case the *KaReMo*$^{++}$ was utilised, see Section 5.3.3.

Alternatively, the size effect on the tensile strength due to biaxial bending was optionally taken into account in post-processing. The modified tensile strength $f_{t,0,mod}$ was calculated

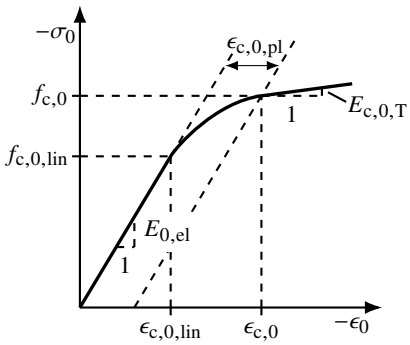

Figure 5.4: Modelled stress-strain relationship for compression in grain direction; stresses σ_0 plotted over strains ϵ_0.

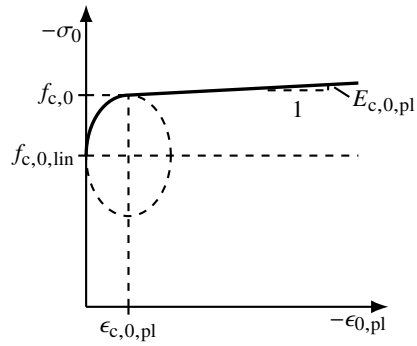

Figure 5.5: Modelled stress-plastic strain relationship for compression in grain direction; stresses σ_0 plotted over plastic strains $\epsilon_{0,pl}$.

with

$$f_{t,0,mod} = f_{t,0} \cdot \min \left\{ \frac{M_{y,2}W_z + M_{z,2}W_y}{k_{red}M_{y,2}W_z + M_{z,2}W_y}; \frac{M_{y,2}W_z + M_{z,2}W_y}{M_{y,2}W_z + k_{red}M_{z,2}W_y} \right\} \quad , \tag{5.2}$$

where $f_{t,0}$ is the tensile strength equivalent to the bending strength f_m given in EN 1995-1-1 [57], $M_{y/z,2}$ is the bending moment about the y- or z-axis according to geometrically nonlinear analyses, $W_{y/z}$ is the section modulus about the y- or z-axis, and $k_{red} = 0.7$ is the reduction factor according to EN 1995-1-1 [57]. Equation (5.2) can be derived directly from Equations (2.54) and (2.55) from EN 1995-1-1 [57] and is a pragmatic estimate of the size effect due to biaxial bending, which considers the proportion of $\sigma_{m,y,2} = M_{y,2}/W_y$ to $\sigma_{m,z,2} = M_{z,2}/W_z$. For uniaxial bending this equation yields $f_{t,0,mod} = f_{t,0}$. The maximum modified tensile strength according to this equation occurs for $\sigma_{m,y,2} = \sigma_{m,z,2}$ and is $f_{t,0,mod} = 1.18 \cdot f_{t,0}$.

5.3.2.6 Material values for GL 24h

The initial values for material modelling of GL 24h are given in Table 5.1 and are reasonable mean values at 12% moisture content. Optionally, some of these values were replaced by scattering material properties according to Section 5.3.3.

Table 5.1: Initial values for material modelling of GL 24h.

	Elastic modulus [N/mm^2]	Proportionality limit [Ratio f_{lin}/f]	Strength [N/mm^2]	Plastic strain at strength [Ratio $\epsilon_{pl}/\epsilon_{el}$]	Plastic modulus [N/mm^2]
Tension in L	11,500	-	33.0 [1,2]	-	-
Compression in L	11,500	0.75	−40.0	0.40	50
Tens. & comp. in R & T	300	-	-	-	-
Shear in LR & LT	650	0.30	5.3 [2]	-	975
Shear in RT	100	0.55	1.6	-	50

[1] The size effect due to biaxial bending may be considered additionally according to Equation (5.2).
[2] The size effect in member length and height may be considered additionally according to *KaReMo*, see Section 5.3.3.

The plastic moduli $E_{c,0,pl}$ and G_{pl} were used for the calculation of plastic strains $\epsilon_{0,pl}$ and γ_{pl}, see Figures 5.3, 5.4, and 5.5. Based on the experimental results of Neuhaus [124] and in line with a transverse isotropic material behaviour, the Poisson's ratios were set to $\nu_{LR} = \nu_{LT} = \nu_{RT} = 0.5$. Moduli of elasticity and shear in the LR- and LT-planes were picked according to EN 14080 [54]. Corresponding values of the LTB specimen, see Table 3.13, were slightly higher, similar to values of Schilling et al. [141] for the elastic moduli. Based on Aicher and Dill-Langer [4], Ehrhart and Brandner [50], and Flaig [67], the rolling shear modulus was assumed to be higher than given in EN 14080 [54]. The tensile strength in grain direction representing the bending strength of beams at a reference beam height of $H = 600$ mm was chosen according to [141]. The parameters for the elastoplastic behaviour at compression in grain direction were derived from own compression tests, see Section 3.4,

and slightly adjusted based on Glos [77] and [141]. For the plastic modulus at compression in grain direction, a reasonable value resulting in a minimum slope of the stress-strain curve was chosen. Shear strengths in the LR- and LT-planes were taken from Glos and Denzler [79] and Spengler [148], and in the RT-plane from Dahl and Malo [31], [50] and [67]. The proportionality limit for shear in grain direction $f_{v,0,lin}$ was chosen according to the results of the LTB tests, see Table 3.16. The other parameters for the elastoplastic shear behaviour were picked according to [31].
The low proportionality limit for shear in the LR- and LT-planes needs to be highlighted. It has a significant influence on the load-deformation behaviour of LTB, see Section 5.4.5, and it was assumed that it represented the point of the first occurrence of a significant local shear failure in the LTB tests, leading to a flattening of the load-deformation curves, see Section 3.4. The low value of $f_{v,0,lin} = 0.3 \cdot 5.3 = 1.6$ N/mm^2, see also Table 3.16, could be due to the fact that large GL beams were tested, which resulted in a high scatter of the shear strength, making it very likely that local failure occurred early. However, as the shear stress distribution due to torsion is well suited for load redistribution, a member shear failure occurred at comparatively high stresses. The value of 0.3 is suitable for modelling shear behaviour with torsion as the decisive action and should not be transferred to shear behaviour with shear force as the decisive action, see also Section 2.3.4.

5.3.2.7 Material values for GL 30c

The initial values for material modelling of GL 30c are given in Table 5.2 and are reasonable mean values at 12% moisture content. No scattering material parameters were taken into account for GL 30c.

Table 5.2: Initial values for material modelling of GL 30c.

	Elastic modulus [N/mm^2]	Proportionality limit [Ratio f_{lin}/f]	Strength [N/mm^2]	Plastic strain at strength [Ratio $\epsilon_{pl}/\epsilon_{el}$]	Plastic modulus [N/mm^2]
Tension in L	13,000	-	41.0 [1,2]	-	-
Compression in L	13,000	0.75	−45.0	0.40	50
Tens. & comp. in R & T	300	-	-	-	-
Shear in LR & LT	650	0.30	5.3 [2]	-	975
Shear in RT	100	0.55	1.6	-	50

[1] The size effect due to biaxial bending may be considered additionally according to Equation (5.2).
[2] The size effect in member length and height may be considered additionally according to *KaReMo*, see Section 5.3.3.

Poisson's ratios were chosen similar to GL 24h. The elastic modulus in grain direction was picked according to EN 14080 [54], the tensile strength in grain direction representing the bending strength of beams at a reference beam height of $H = 600$ mm according to Schilling et al. [141], and the compressive strength according to Ehrhart et al. [51] and Schilling et al. [141]. It should be noted that the elastic moduli in EN 14080 [54] are lower than the values reported by [141]. Other material values were chosen in line with GL 24h,

as no significant effect of the material grade on the shear strength was found by Glos and Denzler [79], and corresponding research on the elastoplastic behaviour was not known.

5.3.2.8 Material values for GL75

The initial values for material modelling of GL made of beech LVL, GL75, are given in Table 5.3 and are reasonable mean values at 5 to 6% moisture content. No scattering material parameters were taken into account for GL75.

Table 5.3: Initial values for material modelling of GL75.

	Elastic modulus [N/mm^2]	Proportionality limit [Ratio f_{lin}/f]	Strength [N/mm^2]	Plastic strain at strength [Ratio $\epsilon_{\text{pl}}/\epsilon_{\text{el}}$]	Plastic modulus [N/mm^2]
Tension in L	16,800	-	90.0 [1]	-	-
Compression in L	16,800	0.65	−77.0	1.25	50
Tens. & comp. in R & T	900	-	-	-	-
Shear in LR	900	-	-	-	-
Shear in LT	1000	-	-	-	-
Shear in RT	150	-	-	-	-

[1] The size effect due to biaxial bending may be considered additionally according to Equation (5.2).

Based on the experimental results of Töpler and Kuhlmann [161], the Poisson's ratios were set to $\nu_{\text{LR}} = 0.3$, $\nu_{\text{LT}} = 0.5$ and, $\nu_{\text{RT}} = 0.2$. The elastic modulus in grain direction was picked according to ETA-14/0354 [63] and is in line with values from own experimental results, see Section 3.3 and Töpler and Kuhlmann [161], and values reported by Ehrhart et al. [51] and Kuck [105]. The elastic moduli in radial and tangential directions were chosen based on own experiments [161] and Windeck and Blaß [177], as values given in ETA-14/0354 [63] are very conservative. Shear moduli in the LR- and LT-planes were assumed based on own experiments [161], and the shear modulus in the RT-plane based on Hütter [91]. The tensile strength in grain direction representing the bending strength of beams at a reference beam height of $H = 600$ mm was chosen according to Dill-Langer and Aicher [37]. The parameters for the elastoplastic behaviour at compression in grain direction were derived from own compression tests, see Section 3.3, and verified based on Dill-Langer and Aicher [37] and a re-evaluation of experimental data of Ehrhart et al. [53], which were generously provided. For the plastic modulus at compression in grain direction, a reasonable value resulting in a minimum slope of the stress-strain curve was chosen. Linear elastic behaviour without failure was assumed in radial and tangential directions as well as in shear, as literature on post-elastic behaviour was scarce.

5.3.3 Scattering material properties and structural imperfections

5.3.3.1 General

As discussed in Section 2.7, scattering material properties influence the load-bearing capacity of imperfection-sensitive timber members by means of the

a. stress-strain relationship in tension and compression in grain direction (considered by the *KaReMo*),

b. stress-strain relationship for shear in the LR- and LT-planes (considered by the *KaReMo*$^{+\nu}$),

c. distance of the member axis and shear centre in y-direction (considered by the *KaReMo*$^{+y}$),

d. distance of the member axis and shear centre in z-direction (considered by the *KaReMo*).

Models that allow for accounting for these influences in FEA are presented below. The modelling approaches are extensions of the *Karlsruher Rechenmodell* (*KaReMo*).
By these models, the material model described in Section 5.3.2 is modified and extended. Depending on the application, the models were used to replace some of the material parameters listed in Tables 5.1 to 5.3. Service class 1 at normal temperature without long-term effects was generally assumed.
The *KaReMo* covers the effects of a. and d. and is described in Section 2.7. The main assumptions and input parameters for this thesis are presented below. The *KaReMo*$^{+\nu}$ covers the effects of b. and is an extension of the *KaReMo* to include scattering shear stiffnesses and strengths in the x- and z-directions, i.e. along a board and between individual boards. The *KaReMo*$^{+y}$ covers the effects of d. and is an extension of the *KaReMo* to include scattering stiffnesses in the y-direction, i.e. along the board width. These three different models can be combined as required. The *KaReMo*$^{++}$ is the combination of the three models mentioned above, which takes into account scattering material stiffnesses along the length, height, and width of the members and scattering material strengths along the length and height of the members. A scattering of the strengths over the width of the member is not considered.
Thus, in FEA with *KaReMo*$^{++}$, the size effect on the tensile and shear strength in the member length and height is implicitly considered. A size effect in the member width cannot be considered by *KaReMo*$^{++}$. The *KaReMo*$^{++}$ was implemented for softwood GL.

In the computation routine for FEA, the generation of the scattering material properties of the *KaReMo*$^{(++)}$ was conducted beforehand with a separate *Python* script, see Figure 5.14. The *Python* script of the *KaReMo*$^{++}$ is published at Töpler [158].

5.3.3.2 *KaReMo*

The *KaReMo* was implemented according to Section 2.7.2 for modelling softwood GL. Scattering material parameters for visual grading VIS-2 according to Blaß et al. [14] were assumed, as lamellas graded in VIS-2 can be used for GL 24h according to Frese [74].

This was also the material grade of the LTB test specimens, see Section 3.4. Less material scatter can be expected with increasing material quality or grade as stated by [14]. GL 24h is currently the lowest material grade used on a large commercial scale for softwood GL in Germany. Therefore, it was expected that the results of the analyses with VIS-2 are on the safe side and can be transferred to the common softwood GL grades available. A wood moisture content of 12% was chosen.
For imperfection-sensitive timber members, stresses in grain direction at the integration points of the FE elements can switch between tension and compression during stepwise loading. Since the tensile strength is decisive for the bending load-bearing capacity and the magnitude of the tensile stress is dependent on the tensile elastic modulus, modelling the tensile elastic modulus as realistic as possible is of paramount importance, see Frese [74] and Section 2.7. Based on [74], the tensile elastic modulus $E_{t,0,el}$ according to Equation (2.88) was therefore generally utilised for all cells of the *KaReMo*. This leads to slightly higher bending load-bearing capacities according to [74].
To avoid unreasonable values of stiffnesses and strengths of individual cells, the limit values of Blaß [9] according to Equations (2.94) bis (2.97) were applied.
Scattering values of the tensile strength of finger-joint according to Equation (2.93) were assumed without modifying the characteristic value.

In contrast to current publications on the *KaReMo*, e.g. Blaß et al. [14] and Frese [74], a nonlinear elastoplastic material behaviour under compression in grain direction according to Section 5.3.2 was considered. The integration points of the 20-node solid elements applied in this work are closer to the element edges than the integration points of the 4-node shell elements that [74] utilised for the implementation. As a result, the ultimate tensile strengths were reached earlier in this thesis, and the bending load-bearing capacities decreased slightly. This counteracted the positive influence of the tensile elastic modulus. A lamella height of 40 mm was utilised instead of the 30 mm in [14].

Due to the complexity of the model and the different model variants, which were not fully documented in the literature, slight deviations of the results of the implementation of the model described in this thesis from results from the literature were expected.

The *KaReMo* can be utilised to determine the elastic modulus $E_{0,el}$, the tensile strength $f_{t,0}$, and the compressive strength $f_{c,0}$ and replace the corresponding values in Tables 5.1 to 5.3. The model can be applied to numerically determine the bending, tensile, and compressive strengths of softwood GL members under flatwise bending and axial forces. Realistic structural imperfections in the x- and z-directions are implicitly taken into account. If performing numerical Monte Carlo simulations with scattering mechanical material properties with this model, these "numerical experiments" can be utilised to determine characteristic and design bending, tensile, and compressive strengths, as well as flexural buckling load-bearing capacities of columns. For FEA of columns, geometrical imperfections should be taken into account.
As the influence of the essential macroscopic properties (dry density), growth irregularities (knots), and industrial processing (finger-jointing) of softwood GL is explicitly taken into account with the generally valid regression models in Equations (2.94) to (2.97), the

KaReMo can map the influence of changes in macroscopic properties, growth irregularities, and industrial processing, e.g. due to changes in the grading process of boards.

5.3.3.3 *KaReMo*$^{+v}$

Scattering shear strengths $f_{v,0}$ of softwood GL were implemented utilising the model of Brüninghoff and Klapp [21], see Section 2.7.3. Each board was assigned a constant value of the shear strength $f_{v,0}$ from a log-normal distribution with $LN(1.65, 0.180^2)$. In contrast to [21], a log-normal distribution was chosen, as this allows a better fitting to the test results of Glos and Denzler [79] and, according to JCSS [92], should be preferred if modelling strengths. In addition, a lamella height of 40 mm was used instead of the 35 mm of [21]. The position of the individual boards was given by the position of the finger joints from the *KaReMo*. For cells of the *KaReMo*$^{+v}$ with finger joints, the lower shear strength of the two adjacent boards was assumed.
Based on the results of the dynamic measurements by Görlacher and Kürth [81], see Section 2.7.3, the shear modulus of a cell was determined as a function of the elastic modulus of the same cell by means of a linear regression as

$$G_{0,el} = 0.015 \cdot E_{0,el} + 450 + e \quad , \tag{5.3}$$

where $G_{0,el}$ is the shear modulus in grain direction in N/mm^2, $E_{0,el}$ is the elastic modulus in grain direction in N/mm^2, and e is the scattering error term in N/mm^2. For the error term, a random value from a normal distribution with $N(0, 110^2)$ in N/mm^2 with lower and upper limits of -250 N/mm^2 and 300 N/mm^2 was selected for each cell. Equation (5.3) was derived based on the data published by [81], see Figure 2.42, assuming that the ratios of $G_{tor,dyn}$ to $E_{0,dyn}$ and $G_{0,el}$ to $E_{0,el}$ are similar. For visual grading VIS-2, the results of $E_{t,0,el}$ and $G_{0,el}$ of 1000 generated cells according to Equation (5.3) are illustrated in Figure 5.6. The mean value and the standard deviation of $E_{t,0,el}$ were 13,100 N/mm^2 and 3170 N/mm^2, and of $G_{0,el}$ 649 N/mm^2 and 114 N/mm^2. Compared to Blaß [11] and [81], there was a larger scatter of $G_{0,el}$ and the product $E_{t,0} \cdot G_{0,el}$, due to the larger standard deviation of $E_{t,0,el}$ of individual cells in VIS-2. The mean values were similar. The autocorrelation of the product $E_{t,0} \cdot G_{0,el}$ within a board considered in [11] was taken into account by the autocorrelation of $E_{t,0,el}$ in a board, see Section 2.7.2, and thus also of $G_{0,el}$ according to Equation (5.3).
A correlation between shear modulus and shear strength, as discussed by Spengler [148], was not taken into account. As stiffnesses attract stresses, this assumption is on the safe side for the 5% quantile value of the shear load-bearing capacity, i.e. it reduces the 5% quantile value of the load-bearing capacity.

The *KaReMo*$^{+v}$ can be utilised to determine the shear modulus $G_{0,el}$ and the shear strength $f_{v,0}$ and replace the corresponding values in Tables 5.1 to 5.3.
The model can be applied to numerically determine the shear strengths of softwood GL members under flatwise bending. Realistic structural imperfections in the x- and z-directions are implicitly taken into account. If performing numerical Monte Carlo simulations with scattering mechanical material properties with this model, the results of these "numerical

experiments" can be utilised to determine characteristic and design shear strengths. An extensive validation of the model based on test results is still pending.
As the influence of the essential macroscopic properties and growth irregularities is not explicitly taken into account, the *KaReMo*$^{+v}$ cannot map the influence of changes in the essential macroscopic properties and growth irregularities. The model is therefore only applicable for softwood GL, where the macroscopic properties and the growth irregularities of the boards are comparable to the experimental investigations of Glos and Denzler [79] and Görlacher and Kürth [81].

5.3.3.4 *KaReMo*$^{+y}$

For the scattering of the material stiffness across the board width, the influences of density, microfibril angle, spiral growth, structural defects, and the effects of industrial processing on elastic modulus and shear modulus discussed in Section 2.7.1 are relevant.
While the influence of the variation of the density over board length and cross-sectional height on the elastic modulus $E_{0,el}$ is taken into account in the *KaReMo*, its variation over the board width is neglected in the *KaReMo*. The microfibril angle and spiral growth are not taken into account in the *KaReMo*, as these are not recorded in building practice. According to Ormarsson and Cown [126], the density increases from pith to bark, while the microfibril angle and spiral growth decrease, see Section 2.7.4. Most of the changes occur within the first 150 mm from the pith, see [126]. Each of the three factors causes an increase in the elastic modulus from pith to bark, see [126]. Thus, the position of the pith has a relevant influence on the variation of the elastic modulus across the board cross-section. There was no significant influence of the distance to the pith on the shear modulus found by [126].

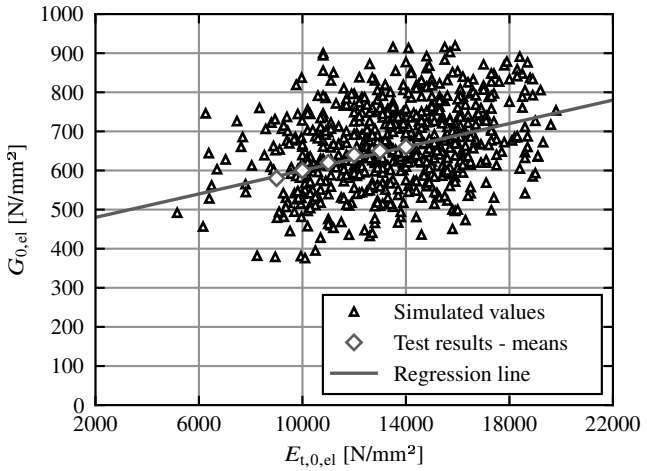

Figure 5.6: With VIS-2 and Equation (5.3) simulated values (n = 1000) of $E_{t,0,el}$ and $G_{0,el}$; Equation (5.3) with e = 0 as regression line; comparison with mean values for different material grades from Görlacher and Kürth [81].

According to Steffen et al. [149], local values of material stiffness can also be significantly influenced by structural defects such as knots or compression wood. Since knots are very limited in size, occur frequently, and are distributed across the board width, their influence on the stiffness is smeared over the cell and board length. Compression wood could not be detected during visual grading by Blaß and Frese [13] and only occurred in two of the machine graded boards of the LTB tests, see Section 3.4.3.2. It was therefore assumed that the influence of structural defects on the scattering of material stiffnesses across the board width can be neglected on the cell and board level.
No publications were known on the variation of finger joint properties across the board width.

The scattering of the elastic modulus $E_{0,\mathrm{el}}$ across the board width was implemented in the *KaReMo*$^{+y}$ on the basis of the previous discussion utilising the regression relationship given by Ormarsson and Cown [126], Equation (2.101), which describes $E_{0,\mathrm{el,mean}}$ as a function of the distance to the pith r. Influences of structural defects, industrial processing, and others not mentioned were taken into account by assumptions on the safe side, i.e. by increasing the assumed scatter. A scattering of the shear modulus $G_{0,\mathrm{el}}$ over the board width was not taken into account.
To determine the typical scattering of the location of the pith in boards of softwood GL members, the photos of the faces of the LTB test specimens, see Section 3.4, were analysed. A typical photo of a face is displayed in Figure 5.7. For determining the location of the pith, a circle was fitted into one representative annual ring of each board cross-section. The distances of the pith to the board centres in y- and z-directions of the 528 visible board cross-section of the LTB test specimens are plotted in Figure 5.7. Each data point represents a pair of values of one board. The values were determined with an accuracy of 1 mm. Mean values of y_{pith} and z_{pith} were 10.7 mm and 46.4 mm at a board height of 40 mm and board width of 120 mm.
In the next step, the cross-section of each board was divided into $10 \cdot 10$ mm^2 segments. For all segments of the 528 board cross-sections, the elastic moduli were determined with Equation (2.101) and the coordinates of the piths in Figure 3.4. The elastic moduli of the left and right halves of each board and of the entire board were determined on the basis of the elastic moduli of the $10 \cdot 10$ mm^2 segments. Finally, the ratio

$$\Delta E_{0,\mathrm{el}} = \frac{E_{0,\mathrm{el,mean}} - E_{0,\mathrm{el,l/r}}}{E_{0,\mathrm{el,mean}}} \quad , \tag{5.4}$$

where $E_{0,\mathrm{mean}}$ is the mean elastic modulus of a board, and $E_{0,\mathrm{l/r}}$ is the elastic modulus of the left or right side of a board, was calculated for each board. For the 528 boards, the mean value and the standard deviation of $\Delta E_{0,\mathrm{el}}$ were 0.0 and 0.037. The mean value of 0.0 is inevitable due to the symmetry of $E_{0,\mathrm{l}}$ and $E_{0,\mathrm{r}}$.

With the *KaReMo*$^{+y}$, only the difference of the elastic modulus between the left and right halves of a board is varied. To be on the safe side, the standard deviation of $\Delta E_{0,\mathrm{el}}$ was increased from 0.037 to 0.05 and ΔE was picked from a normal distribution with $N(0.0, 0.05^2)$. The initial value or mean value of the elastic modulus may be determined with the *KaReMo*, or any other value may be chosen.

The *KaReMo*$^{+y}$ can be utilised to determine $E_{0,el}$ and replace the corresponding values in Tables 5.1 to 5.3. The model can be applied to numerically determine the effect of structural imperfections in the y-direction, i.e. the distance between the beam axis and the shear centre. Scattering strengths in the y-direction are not taken into account. If performing numerical Monte Carlo simulations with scattering $E_{0,el}$ with this model, these "numerical experiments" can be utilised to obtain equivalent geometrical imperfections for LTB. An extensive validation of the model based on test results is still pending.
As the influence of the essential macroscopic properties and growth irregularities is not explicitly taken into account, the *KaReMo*$^{+y}$ cannot map the influence of changes in the essential macroscopic properties and growth irregularities. The model is therefore only applicable for softwood GL, where the macroscopic properties and the growth irregularities of the boards are comparable to the experimental investigations of Ormarsson and Cown [126] and the LTB tests in Section 3.4.

5.3.3.5 *KaReMo*$^{++}$

The *KaReMo*$^{++}$ combines the three models described previously. The elastic modulus $E_{0,el}$, the tensile strength $f_{t,0}$, and the compressive strength $f_{c,0}$ of each cell can be determined with the *KaReMo*. In addition, the elastic modulus can be varied over the board width according to the *KaReMo*$^{+y}$. Furthermore, the shear modulus $G_{0,el}$ and the shear strength $f_{v,0}$ of each cell or board can be determined with the *KaReMo*$^{+v}$. For the following FEA, the corresponding values in Tables 5.1 to 5.3 were replaced depending on the application of *KaReMo*$^{++}$.

Figure 5.7: Face of T01, see Section 3.4.

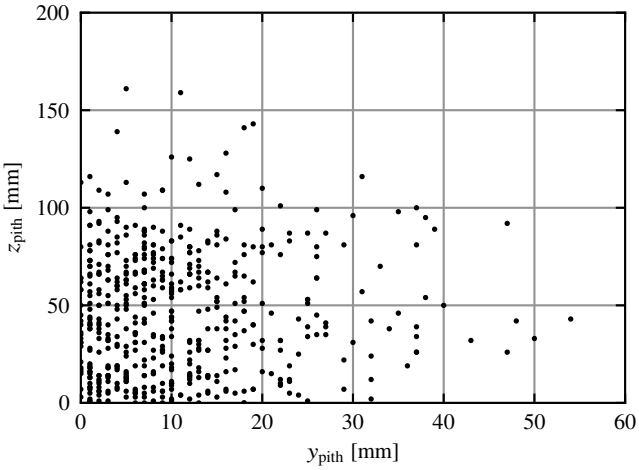

Figure 5.8: Distance of the pith to the centre of the 528 visible board cross-sections of the LTB tests specimen, see Section 3.4; in y- and z-direction.

5.3.3.6 Summary

The models offer the possibility to consider the influence of scattering strengths over the member length and height and the influence of scattering stiffnesses over the member length, height, and width on the load-bearing capacity of imperfection-sensitive timber members in numerical calculations. At the highest level, *numerical simulations* can be carried out with these models in accordance with the *FE-Guidelines*, see Section 5.2.

5.3.4 Geometrical imperfections

In the imperfection measurements described in Section 3.2, it was observed that the geometrical imperfections of timber beams were composed of three parts: (i) the bow imperfections at midspan; (ii) the twist imperfections at midspan; and (iii) the twist imperfections at the fork supports, see Figure 3.6. The total geometrical imperfection of a beam was a superposition of these three parts. The real irregular shape of bow and twist imperfections over the member length, see Figures 3.3 and 3.4, can be represented in analyses by a sinusoidal half-wave, as demonstrated in Section 3.2.4.
For the FEA in this thesis, therefore, the bow and twist imperfections at midspan were assumed in the shape of sinusoidal half-waves. Additionally, twist imperfections at both supports were assumed, which caused a linear twist over the beam length, see Figure 3.6.

Either single values or scattering values were applied for the geometrical imperfections. In analyses with single values of geometrical imperfections, the following values were assumed in line with the 95% quantile values of the measurement results in Section 3.2, see also results of softwood GL beams (without outliers) in Tables 3.3 and 3.4, and fork supports with large tolerances in Table 3.5:

- bow imperfections $e_{y,95} = \dfrac{L}{1000}$ [mm]
- twist imperfections at midspan $e_{\theta,mid,95} = \dfrac{L}{1500 H_{ap}}$ [-]
- twist imperfections at supports $e_{\theta,supp,95} = \dfrac{1}{100}$ [-]

Where L is the member length and H_{ap} is the height of the beam at the apex. On the safe side, the larger values of the twist imperfections at the fork supports with large tolerances (instead of the fork supports with small tolerances) were chosen. Furthermore, it was assumed that outliers of bow imperfections are prevented due to appropriate alignment of the horizontal roof bracing.

In analyses with scattering geometrical imperfections, random values were chosen based on distribution functions obtained from the imperfection measurement results in Section 3.2. The results of all softwood GL and beech LVL beams without outliers and fork supports with large tolerances were utilised, see Tables 3.3, 3.4, and 3.5. On the safe side, fork supports with large tolerances were chosen for the values of the twist imperfections at the supports. Limit values were defined based on the measurement results to avoid unrealistic imperfections. As reasonable approximations of the frequency distributions of the measured imperfections, normal distributions with a mean of zero and the following properties were assumed $N(\mu, \sigma^2, \text{limit})$:

- bow imperfections $\dfrac{e_y}{L}$: $N(0, 0.00043^2, \pm 0.0015)$ [mm/mm]
- twist imperfections at midspan $\dfrac{e_{\theta,mid} H_{ap}}{L}$: $N(0, 0.00027^2, \pm 0.0012)$ [mm/mm]

- twist imperfections at supports $e_{\theta,\text{supp}}$: $N(0, 0.0049^2, \pm 0.02)$ [-]

To represent the correlation between the twist imperfections at both supports, see Section 3.2.4.3, first the twist at one support $e_{\theta,\text{supp},0}$ was determined from the above distribution, then the twist at the other support $e_{\theta,\text{supp},1}$ was determined by the linear regression model with a normally distributed error term e in Equation (3.4).

5.4 Verification

5.4.1 General

The presented FE models were verified according to the *FE guidelines* by Töpler and Kuhlmann [162], see Section 5.2. The most important results, as well as some exemplary results, are discussed below. A comprehensive description is given by Töpler and Kuhlmann [166]. Two cases were assessed:

a. Single-span beams made of GL 24h according to Table 5.1, with ideal fork supports in the beam axis, with dimensions of $480 \cdot 120 \cdot 4000$ mm^3 ($\lambda_{\mathrm{m,rel}} \approx 0.75$), $600 \cdot 120 \cdot 7000$ mm^3 ($\lambda_{\mathrm{m,rel}} \approx 1.10$), and $880 \cdot 120 \cdot 8000$ mm^3 ($\lambda_{\mathrm{m,rel}} \approx 1.40$), with a constant bending moment $M_{\mathrm{y},1}$ applied by variable distributed loads at the end faces, and with bow and twist imperfections $e_{\mathrm{y}} = L/1000$ and $e_{\theta,\mathrm{mid}} = L/1500H_{\mathrm{ap}}$.

b. Pinned columns made of GL75 according to Table 5.3, with supports in the column axis, with dimensions of $200 \cdot 200 \cdot 2000$ mm^3 ($\lambda_{\mathrm{c,rel}} \approx 0.75$), $200 \cdot 200 \cdot 3000$ mm^3 ($\lambda_{\mathrm{c,rel}} \approx 1.10$), and $200 \cdot 200 \cdot 3800$ mm^3 ($\lambda_{\mathrm{c,rel}} \approx 1.40$), with an axial compressive force $N_{\mathrm{x,c}}$ applied by constant distributed loads at the end faces, and a bow imperfection $e_{\mathrm{y}} = L/1000$.

The three slendernesses mentioned were analysed in order to cover the different magnitudes of geometrically and materially nonlinear effects, see Figure 2.4. The size effect for biaxial bending according to Equation (5.2) was only taken into account in the engineering judgement to ensure comparability with calculations using T2O. No scattering material properties according to Section 5.3.3 and no scattering geometrical imperfections according to Section 5.3.4 were taken into account.

5.4.2 Engineering judgement

In the engineering judgement, the essential SRQs, here stresses, internal forces, deformations, load-deformation curves, load-bearing capacities, eigenvalues, and eigenmodes were compared with experience and calculations using T2O with Equations (2.1) to (2.7) and (2.15) to (2.20). The single-span beam with dimensions of $600 \cdot 120 \cdot 7000$ mm^3 ($\lambda_{\mathrm{m,rel}} \approx 1.10$) and the pinned column with dimensions of $200 \cdot 200 \cdot 3000$ mm^3 ($\lambda_{\mathrm{c,rel}} \approx 1.10$) were analysed. For the column, analyses with and without consideration of shear were conducted. A shear modulus $G_{0,\mathrm{el}}$ according to Table 5.3 or an almost infinite value was assumed. Analytical calculations were carried out using Equations (2.3) and (2.8). A comprehensive description of the results is given by Töpler and Kuhlmann [166].

As an example, Figure 5.9 displays the computed horizontal deformations in y-direction v_2 of the single-span beam. These are plausible for a beam at risk of LTB. The other SRQs also corresponded well with experience, see Töpler and Kuhlmann [166].

Table 5.4 lists the internal forces and the horizontal deformations of the member axis at midspan for a defined loading by $N_{\mathrm{x,c}}$ or $M_{\mathrm{y},1}$ from FEA and calculations using T2O. Additionally, the eigenvalues and load-bearing capacities from FEA and analytical

Table 5.4: Comparison of numerical and analytical calculation results for engineering judgement according to the *FE-Guidelines* [162].

	Single-span beam		Pinned column	
	Analytical	FEA	Analytical	FEA
$N_{x,c}$ [kN]	0	0	−1600	−1600
$M_{y,1}$ [kNm]	180	180	0	0
$M_{z,2}$ [kNm]	14.6	9.86	13.8[1] / 16.2[2]	13.5[1] / 14.9[2]
v_2 [mm]	72.8	44.9	5.60[1] / 7.16[2]	5.43[1] / 6.33[2]
Eigenvalue [kNm] or [kN]	198	205	−2460[1] / −2270[2]	−2470[1] / −2280[2]
Load-bearing capacity [kNm] or [kN]	182	199	−2190[1] / −2060[2]	−1790[1] / −1720[2]

[1] Without consideration of shear.
[2] With consideration of shear.

calculations using T2O and Equations (2.3), (2.8), and (2.17) are given.
For the beam, the additional moments $M_{z,2}$ and the horizontal deformations v_2 according to FEA and T2O deviated due to the different degrees of nonlinear behaviour. For the column neglecting shear, the additional moments $M_{z,2}$ and the horizontal deformations v_2 according to FEA and T2O were similar. If considering shear, there were deviations of about 10%, which indicated an overestimation of the geometrically nonlinear behaviour in calculations using T2O with consideration of shear.
The eigenvalues from FEA and analytical calculation were similar. The load-bearing capacity of the beam according to FEA was 4% larger than with calculations using T2O. This minor difference was accepted and was even expected due to the simplifications made in the derivation of the T2O equations, see Section 2.2.1.7. For the column with and

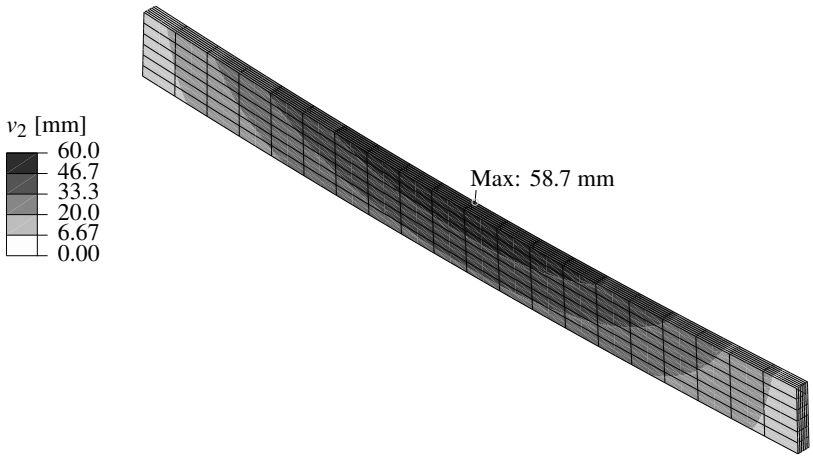

Figure 5.9: Horizontal deformations v_2 of a single-span beam made of GL 24h in mm; dimensions of $600 \cdot 120 \cdot 7000$ mm^3 ($\lambda_{m,rel} \approx 1.10$); ideal fork supports in the beam axis; constant bending moment of $M_{y,1} = 180$ kNm; geometrical imperfections of $e_y = L/1000$ and $e_{\theta,mid} = L/1500 H_{ap}$.

without shear, the load-bearing capacity according to FEA was about 20% smaller than with calculations using T2O. This significant difference indicated inaccuracies of calculations using T2O for GL75 columns, which are assessed in Section 5.5.2.

5.4.3 Discretisation check

In the discretisation check, the influence of the mesh density, the element type, and the size of the load increments on the load-bearing capacity were checked. The aim was to obtain results of high accuracy within minimum computation times. Single-span beams and pinned columns with slendernesses according to Section 5.4.1 were investigated.

The mesh density was varied in width and height between 2 and 10 elements and in length between 10 and 50 elements. A comprehensive description of the results is given in Töpler and Kuhlmann [166]. As an example, Figure 5.10 displays the computed load-bearing capacities $M_{y,1,R}$ of the single-span beam with $\lambda_{m,rel} \approx 1.40$ plotted against the inverse of the number of degrees of freedom DOF^{-1}. The influence of the investigated mesh densities on the load-bearing capacity was negligible, and all results complied with the 1% test of the *FE guidelines* [162], see Section 5.2 and [166]. $10 \cdot 2 \cdot 2$ elements over the length, height, and width were sufficient for the models investigated. For all further FEA, a minimum mesh density of $20 \cdot 6 \cdot 6$ elements over the length, height, and width was chosen.

With the quadratic shape functions and the reduced integration, the 20-node quadratic

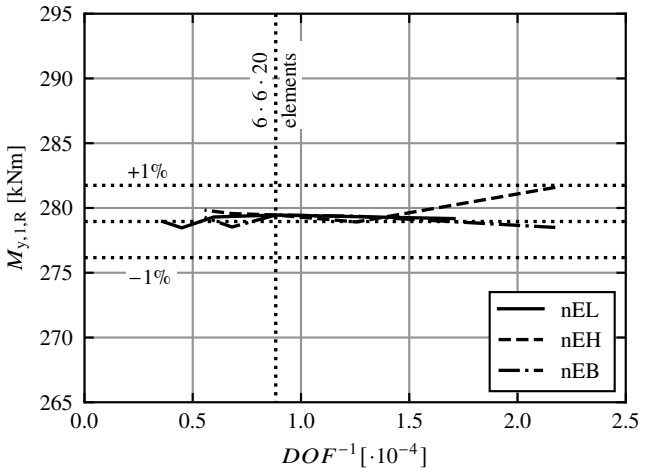

Figure 5.10: Numerically determined load-bearing capacities $M_{y,1,R}$ plotted over the inverse of the number of degrees of freedom DOF^{-1}; variation of the number of elements over length (nEL), height (nEH), and width (nEB); with limits for checking the 1% criterion; single-span beam with $880 \cdot 120 \cdot 8000$ mm^3 ($\lambda_{m,rel} \approx 1.40$).

solid elements C3D20R in Abaqus [1] are well suited to simulate the complex, direction-dependent, nonlinear behaviour of timber.

The maximum size of the load steps was varied between 0.01 and 0.05 of 1.0. The 1% criterion was always met for the load step sizes analysed, see Töpler and Kuhlmann [166]. The maximum size of the load steps was therefore set at 0.05 for all further FEA.

5.4.4 Solver convergence check

The convergence of the solution is checked internally in Abaqus and is therefore guaranteed.

5.4.5 Sensitivity check

In the sensitivity check, the relevant input parameters of the model were varied within realistic ranges, their influence on the relevant SRQs was checked, and it was investigated whether these parameters should be defined with higher precision or not. Single-span beams and pinned columns with slendernesses according to Section 5.4.1 were investigated.

The geometry, the imperfections e_y, $e_{\theta,mid}$, and $e_{\theta,supp}$, the elastic moduli $E_{0,el}$, $G_{0,el}$, and $G_{90,el}$, the proportionality limits $f_{c,0,lin}$, $f_{v,0,lin}$, and $f_{v,90,lin}$, the plastic strain at which the compressive strength is reached $\epsilon_{c,0,pl}$, the strengths $f_{c,0}$, $f_{t,0}$, $f_{v,0}$, and $f_{v,90}$, the plastic moduli $E_{c,0,pl}$, $G_{0,pl}$, and $G_{90,pl}$, and the stiffness of a rotational spring at the supports of the columns about the y-axis K_φ were varied between realistic 5% quantile, mean, and 95% quantile values. A comprehensive description is given by Töpler and Kuhlmann [166].
As an example, Figure 5.11 displays the computed load-horizontal deformation curves of the single-span beam with $L = 7000$ mm and with three different shear moduli $G_{0,el}$. The load-deformation curves were pronouncedly nonlinear due to LTB and were significantly influenced by the shear modulus $G_{0,el}$. The points of the tensile failure and the shear failure were also significantly influenced by the shear modulus $G_{0,el}$.
The results of the sensitivity check are summarised in Table 5.5. A distinction is made between significant influence (> 10%), minor influence (2% to 10%), or negligible influence (< 2%) of the input parameters on the load-bearing capacity. The geometry, the sum of imperfections, the elastic modulus $E_{0,el}$, the compressive strength $f_{c,0}$, the tensile strength $f_{t,0}$, the shear modulus $G_{0,el}$, and a possible rotational spring at the supports had a significant influence on the load-bearing capacity. The linearity limits $f_{c,0,lin}$ and $f_{v,0,lin}$, the plastic strain $\epsilon_{c,0,pl}$, and the shear strength $f_{v,0}$ had a minor influence on the load-bearing capacity. The influence of the plastic stiffnesses $E_{c,0,pl}$ and $G_{0,pl}$, all rolling shear properties, the elastic modulus E_{90}, and the Poisson's ratios was negligible.
On the one hand, these results highlighted that it is generally sufficient to assume reasonable values for transverse stiffnesses, Poisson's ratios, rolling shear properties, and plastic stiffnesses for FEA of imperfection-sensitive timber members and that there is no need for increased accuracy requirements. On the other hand, the results emphasise the importance of accurate values for geometry, imperfections, stiffnesses in grain direction, and compressive strengths (in some cases, also tensile and shear strengths) in grain direction for FEA of imperfection-sensitive timber members.

Table 5.5: Input parameters of the FEA and their influence on the load-bearing capacity of imperfection-sensitive timber members; with significant influence = "++" (> 10%), minor influence = "+" (2% to 10%), negligible influence = "0" (< 2%), not investigated = "-".

	Single-span beams			Pinned columns		
$\lambda_{c/m,rel}$	≈ 0.75	≈ 1.10	≈ 1.40	≈ 0.75	≈ 1.10	≈ 1.40
e_y	0	+	+	+	++	++
$e_{\theta,mid}$	+	+	+	-	-	-
$e_{\theta,supp}$	+	+	+	-	-	-
$E_{0,el}$	0	++	++	+	+	++
$f_{c,0,lin}$	0	0	0	+	+	+
$\epsilon_{c,0,pl}$	0	0	0	+	0	0
$f_{c,0}$	+	+	+	++	++	++
$E_{c,0,pl}$	0	0	0	0	0	0
$f_{t,0}$	++	++	0	0	0	0
$G_{0,el}$	0	+	++	0	0	0
$f_{v,0,lin}$	0	0	+	-	-	-
$G_{0,pl}$	0	0	0	-	-	-
$f_{v,0}$	0	0	+	-	-	-
K_φ	-	-	-	++	++	++

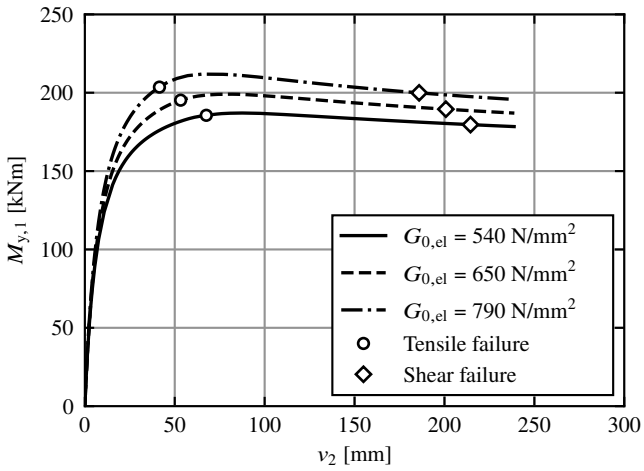

Figure 5.11: Load-displacement behaviour of single-span beams with $\lambda_{m,rel} \approx 1.10$; applied bending moment $M_{y,1}$ plotted over the horizontal deformation of the beam axis at midspan v_2 supplemented by the points of the tensile and the shear failure; variation of the shear modulus $G_{0,el}$.

5.4.6 Imperfection sensitivity check

The imperfection sensitivity was given by default.

5.4.7 Summary

The numerically determined internal forces and deformations were plausible and generally agreed with the internal forces and the deformations calculated using T2O, but also illustrated the inaccuracies of T2O due to the simplifying assumptions in its derivation, see Section 5.4.2. The investigation of the mesh density and the size of the load steps demonstrated that their influence on the load-bearing capacity was negligible for the variations investigated, see Section 5.4.3. Based on this, a mesh density of at least 20 elements in length and 6 elements in height and width was selected for all subsequent FEA. The maximum size of the load steps was set to 0.05 of 1.0. The sensitivity check revealed that the influence of the plastic stiffnesses $E_{c,0,pl}$ and $G_{0,pl}$, all rolling shear properties, the elastic modulus E_{90}, and the Poisson's ratios was negligible, see Section 5.4.5. The other input parameters of the FEA should be selected with medium to high accuracy according to their influence, see Table 5.5.

5.5 Validation

5.5.1 General

The presented FE model was validated according to the *FE guidelines* by Töpler and Kuhlmann [162], see Section 5.2. The FE model was validated with

a. flexural buckling tests on beech LVL columns, see Section 3.3,

b. LTB tests on GL beams, see Section 3.4, and

c. investigations of the *KaReMo* by Frese [74].

5.5.2 Flexural buckling tests on beech LVL columns

The flexural buckling tests S02 to S27 from Section 3.3 were recalculated with the FE model described in Section 5.3. The experimentally and the numerically determined load-deformation curves and load-bearing capacities were compared with each other.

The input values were selected as similar as possible to the tests. The column geometries were selected according to Table A.1, the elastic modulus $E_{0,\mathrm{el}}$ according to Table A.1, the tensile strength according to Dill-Langer and Aicher [37] as $f_{\mathrm{t},0}$ = 100 N/mm^2, which considers the size effect, and the other material properties according to Table 5.3. No imperfections were modelled, as the influence of the load-eccentricities was decisive. A pinned column with rotational springs at the supports with a coefficient of friction of 0.02 according to SKF [147] was modelled to consider friction in the tilting bearings, see Section 3.3.2.2. The compressive force was applied displacement-controlled. The horizontal and the vertical eccentricity of the tilting bearing were considered according to Section 3.3.2. A mesh density of 20 elements in length and 6 elements in height and width was utilised.

The experimentally and the numerically determined load-deformation curves of all flexural buckling tests are given in Annex A.1. As an example, Figure 5.12 displays the experimentally and numerically determined compressive forces $N_{\mathrm{x,c}}$ plotted over the horizontal deformations v_2 of S08. Additionally, results of calculations using T2O according to Equations (2.1) to (2.8) with considering shear and design verification according to Equation (2.54) are displayed. For T2O, the influence of the rotational spring on the effective flexural buckling length was considered according to Petersen [128].
Experimentally and numerically determined load-deformation curves agreed very well. By the comparison of FEA with compressive plasticising (E_{elpl}) and with purely elastic behaviour (E_{el}) in Figure 5.12, it was confirmed that compressive plasticising in grain direction leads to a high point and subsequent drop of the load-deformation curve and a reduction in load-bearing capacity, which has to be considered. In the FEA, as in the tests, the high point of the load-deformation curve was always decisive for the load-bearing capacity and not the tensile strength. In the FEA, tensile failure occurred in 12 cases at smaller horizontal deformations, in 12 cases at similarly large horizontal deformations, and

in 2 cases at larger horizontal deformations than in the experiments. This indicated a slight underestimation of the tensile strength in the FEA.
Before the peak of the experimental curves, calculations using T2O slightly overestimated the deformations. See curves "FEA; E_{el}" and "T2O" in Figure 5.12 in comparison. Results of T2O neglecting shear ($G_{0,el}$ = inf) even approved better with FEA and experiments than with a realistic shear modulus. The compressive plasticising cannot be modelled with T2O, as linear elastic material behaviour is assumed. Therefore, T2O calculations systematically overestimated the load-bearing capacities and underestimated the maximum deformations of the flexural buckling tests, see Figure 5.12 and Annex A.1. This demonstrates the importance of the assumptions with which the T2O equations were derived.

The experimentally and numerically determined load-bearing capacities of all flexural buckling tests are displayed in Table 5.6. Results of FEAs with compressive plasticising in grain direction are given. k_c was determined according to Equation (3.5) with measured cross-sectional dimensions, see Table A.1, and the mean compressive strength $f_{c,0} = -76.9\,\mathrm{N/mm^2}$ from the compression tests, see Table 3.9. $\lambda_{c,rel}$ was calculated with Equation (2.11), measured elastic moduli and geometries of each test specimen according to Table A.1, and the $f_{c,0}$ mentioned above, see also the discussion of Figure 2.7.
The mean and the maximum deviations between the experimentally and the numerically determined load-bearing capacities $N_{x,c,R,exp}/N_{x,c,R,FEA}$ were 1.5% and 5.3%. Equation (5.1) yields $\gamma_{FE} = 1.02$.

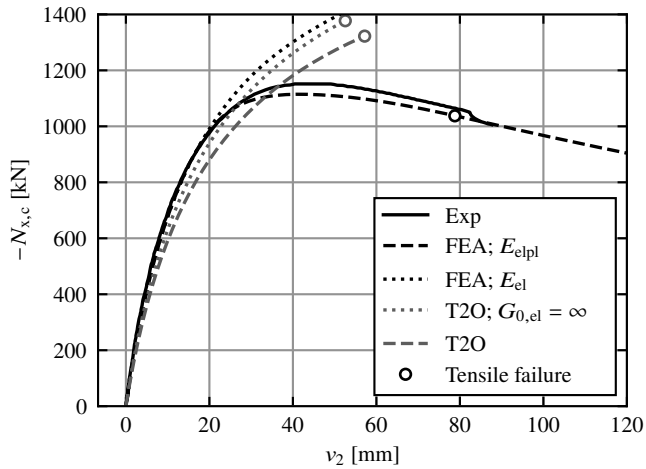

Figure 5.12: Experimentally (Exp) determined load-deformation behaviour of flexural buckling test S08 (beech LVL column with dimensions of $200 \cdot 200 \cdot 3000\,\mathrm{mm^3}$ and a load-eccentricity of $B/10$) with compressive forces $N_{x,c}$ plotted over the horizontal deformations at midspan v_2; comparison with results of FEAs with compressive plasticising (E_{elpl}) and with purely elastic behaviour (E_{el}) and calculations using T2O.

Table 5.6: Comparison of experimentally (Exp) and numerically (FEA) determined load-bearing capacities of the flexural buckling tests on beech LVL GL75 columns.

Series number	$\lambda_{c,rel}$ [1]	$N_{x,c,R,exp}$ [kN]	$k_{c,exp}$	$N_{x,c,R,FEA}$ [kN]	$k_{c,FEA}$	$\frac{N_{x,c,R,exp}}{N_{x,c,R,FEA}}$
S02	2.117	-200	0.186	-200	0.186	0.999
S03	2.149	-193	0.179	-196	0.182	0.981
S04	1.537	-569	0.298	-561	0.294	1.013
S05	1.505	-585	0.307	-577	0.303	1.014
S06	1.499	-601	0.315	-579	0.303	1.038
S07	1.259	-1130	0.375	-1095	0.363	1.032
S08	1.237	-1152	0.382	-1115	0.370	1.033
S09	1.226	-1183	0.392	-1124	0.372	1.053
S10	1.048	-1226	0.409	-1192	0.397	1.029
S11	1.055	-1191	0.398	-1184	0.396	1.006
S12	1.060	-1185	0.396	-1179	0.394	1.005
S13	1.083	-1359	0.460	-1304	0.441	1.043
S14	1.091	-1321	0.446	-1298	0.438	1.018
S15	1.069	-1348	0.455	-1318	0.445	1.022
S16	1.018	-1418	0.471	-1371	0.456	1.034
S17	1.059	-1378	0.458	-1331	0.442	1.036
S18	1.081	-1342	0.446	-1309	0.435	1.025
S19	1.044	-1634	0.545	-1591	0.531	1.027
S20	1.053	-1609	0.536	-1579	0.526	1.019
S21	1.071	-1590	0.528	-1561	0.518	1.019
S22	0.859	-1576	0.526	-1590	0.531	0.991
S23	0.876	-1569	0.522	-1577	0.525	0.995
S24	0.898	-1528	0.509	-1554	0.517	0.984
S25	0.923	-1439	0.481	-1508	0.504	0.954
S26	0.901	-1535	0.513	-1532	0.512	1.002
S27	0.897	-1548	0.518	-1535	0.514	1.008

[1] Calculated with Equation (2.60), measured elastic moduli and geometries of each test specimen according to Table A.1 and $f_{c,0} = -76.9$ N/mm^2 from the compression tests, see Table 3.9.

5.5.3 Lateral torsional buckling tests on GL beams

Each LTB test from Section 3.4 was recalculated with the FE model described in Section 5.3. The experimentally and the numerically determined load-deformation curves and load-bearing capacities were compared with each other. A comprehensive description is given by Töpler and Kuhlmann [166].

The input values were selected as similar as possible to the tests. The beam geometries were selected according to Table B.1, the elastic stiffnesses $E_{0,el}$ and $G_{0,el}$ according to Table B.2, the proportionality limits $f_{c,0,lin}$ according to Table 3.16, the other material properties according to Table 5.1, and the equivalent bow imperfections $e_{y,eq}$ according to

Table B.1. Twist imperfections were neglected. The size effect due to biaxial bending was taken into account by Equation (5.2). For tests with axial compressive forces, a rotational spring with a coefficient of friction of 0.2 according to Schaeffler Technologies GmbH & Co. KG [135] was modelled at the load application points of the axial compressive forces to consider friction in the horizontal support and the yoke joint, see Section 3.4.2.2. The axial compressive force was applied force-controlled, and the vertical load at midspan was applied displacement-controlled. The horizontal and the vertical eccentricities of the vertical load and the sway of the vertical cylinder, see Section 3.4, were included in the model. Realistic support conditions at the lower edge of the beam were considered, i.e. modelling of the support area at the lower edge of the LTB tests. The reinforcements perpendicular to the grain by fully threaded screws were taken into account by coupling of nodes in z-direction. For the 8 m and the 6 m long beams, 67 and 51 elements were chosen in the length and 6 elements each in the height and the width.
As tests T12, T14, and T15 did not display LTB behaviour, the imperfections and the load-eccentricities were set to zero in the FEA.

The experimentally and the numerically determined load-deformation curves of all LTB tests are given in Annex B.1. As an example, Figure 5.13 displays the experimentally and numerically determined vertical load F_z plotted over the horizontal deformation v_2 of T05. Additionally, results of calculations using T2O according to Equations (2.14) to (2.20) with bending design verification according to Equations (2.54) and (2.55) and shear design verification according to Equation (2.69) with $k_{cr} = 1.0$ are shown. The stiffnesses given

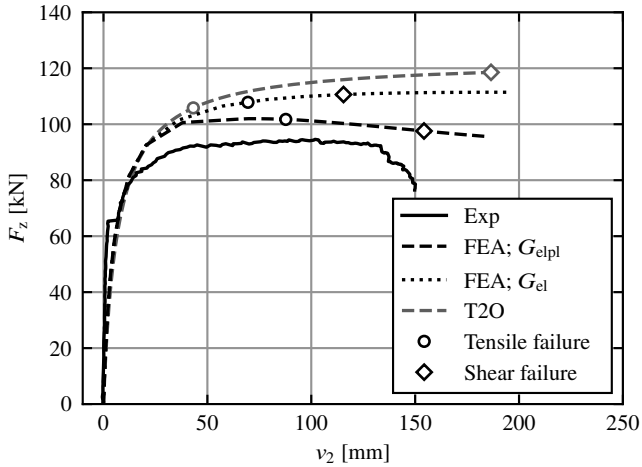

Figure 5.13: Experimentally (Exp) determined load-deformation behaviour of LTB test T05 (GL beam with dimensions of $600 \cdot 120 \cdot 8000$ mm^3) with vertical forces F_z plotted over the horizontal deformations at midspan v_2; comparison with results of FEAs with shear plasticising (G_{elpl}) and with purely elastic shear behaviour (G_{el}) and results of calculations using T2O.

in Table B.2 for analytical calculations were adopted. The horizontal eccentricity of the vertical load plus the measured equivalent bow imperfection in Table B.1 were assumed as bow imperfection. In addition, a twist imperfection at midspan corresponding to the inclination of the vertical cylinder in the test setup was used.
Experimentally and numerically determined load-deformation curves agreed well. By the comparison of FEA with shear plasticising (G_{elpl}) and with purely elastic shear behaviour (G_{el}) in Figure 5.13, it was confirmed that shear plasticising leads to a flattening of the load-deformation curve and a reduction in load-bearing capacity. This was in line with the observations from the LTB tests in Section 3.4, in which probably likewise a local shear failure led to a stiffness and load-bearing capacity reduction. Neglecting the plastic shear behaviour in FEA led to a systematic overestimation of the experimentally determined load-bearing capacities, see Annex B.1. Due to a lack of literature values, the proportionality limit $f_{\mathrm{v,0,lin}}$ was calibrated at the point of "loud cracking" in the LTB tests, see Table 3.16. In the FEA, as in the tests, see Table 3.16, shear failure was decisive for slender beams, and tensile failure was decisive for stocky beams. For the slender beams, the failure occurred in the FEA at similarly large horizontal deformations as in the tests. For the stocky beams, failure occurred in the FEA in 12 out of 16 cases at smaller horizontal deformations than in the tests. This indicates an underestimation of the tensile strength in the FE model. The assumption of the shear strength in the FEA seems to have been appropriate.
Calculations using T2O were well in line with FEA without shear plasticising except for a slight overestimation of resistances, which might be due to the assumption of small deformations in the derivation of the T2O equations. The shear plasticising cannot be modelled with T2O, as linear elastic material behaviour is assumed. Therefore, T2O calculations systematically overestimated the load-bearing capacities and underestimated the deformations of the LTB tests, see Annex B.1.

The experimentally and numerically determined load-bearing capacities of all LTB tests are displayed in Table 5.7. Results of FEAs with shear plasticising are given. k_{m} was determined according to Equation (3.8) with measured cross-sectional dimensions, see Table B.1, and the mean bending strength $f_{\mathrm{m,mean}} = 33.0$ N/mm^2 according to Schilling et al. [141]. $\lambda_{\mathrm{m,rel}}$ was calculated with Equation (2.23), with measured elastic moduli and geometries of each test specimen according to Table B.2, and the $f_{\mathrm{m,mean}}$ mentioned above. The mean and the maximum deviations between the experimentally and the numerically determined load-bearing capacities $F_{\mathrm{z,R,exp}}/F_{\mathrm{z,R,FEA}}$ were 1.2% and 27%. If beams T12, T14, and T15 without pronounced LTB behaviour were neglected, the values improved to 1.0% and 14%. With the results of beams T12, T14, and T15, Equation (5.1) yields $\gamma_{\mathrm{FE}} = 1.17$ and without these test results $\gamma_{\mathrm{FE}} = 1.14$.

Table 5.7: Comparison of experimentally (Exp) and numerically (FEA) determined load-bearing capacities of the LTB tests on softwood GL 24h beam-columns.

Series number	$\lambda_{m,rel}$ [1]	μ_c [2]	$F_{z,R,exp}$ [kN]	$k_{m,exp}$	$F_{z,R,FEA}$ [kN]	$k_{m,FEA}$	$\frac{F_{z,R,exp}}{F_{z,R,FEA}}$
T01	1.086	0.00	106.0	0.608	113.3	0.650	0.936
T02	1.044	0.00	120.5	0.691	122.9	0.705	0.980
T03	1.079	0.00	108.3	0.621	113.7	0.652	0.952
T04	0.990	0.00	88.0	0.727	96.8	0.800	0.909
T05	0.979	0.00	95.1	0.783	102.0	0.839	0.933
T06	0.998	0.20	87.8	0.725	85.7	0.707	1.025
T07	1.005	0.20	85.0	0.701	89.4	0.737	0.951
T08	0.978	0.40	88.3	0.728	88.9	0.733	0.993
T09	1.024	0.40	72.7	0.599	78.0	0.643	0.932
T10	0.995	0.60	76.3	0.630	78.7	0.649	0.970
T11	0.998	0.60	76.9	0.634	79.5	0.655	0.968
T12	0.853	0.00	115.2	1.104	102.8	0.986	1.120
T13	0.812	0.00	117.3	1.127	103.2	0.992	1.136
T14	0.816	0.20	113.9	1.091	103.2	0.988	1.104
T15	0.825	0.20	129.8	1.247	101.9	0.979	1.274
T16	0.814	0.40	97.9	0.940	102.0	0.979	0.960
T17	0.796	0.40	108.9	1.044	102.8	0.986	1.059
T18	0.833	0.60	104.6	1.004	98.2	0.943	1.065
T19	0.812	0.60	107.5	1.034	100.6	0.967	1.069

[1] Calculated with Equation (2.23), with measured elastic moduli and geometries of each test specimen according to Table B.2, and $f_{m,mean} = 33.0$ N/mm^2.

[2] Utilisation ratio of the axial compressive force μ_c, see Table 3.12.

5.5.4 *KaReMo*

The implementations of the *KaReMo* and the *KaReMo*$^{+v}$ were checked by comparative numerical analyses with the following purposes:

a. validation of the bending strengths and stiffnesses of GL beams,

b. validation of the shear strengths of GL beams, and

c. validation of the product of the stiffnesses $E_{0,el} \cdot G_{0,el}$.

The validation was not carried out strictly according to the *FE guidelines* by Töpler and Kuhlmann [162] but rather as a plausibility check. No suitable benchmarks for validating the *KaReMo*$^{+y}$ were known.

The numerical results of Frese [74], Table 7-1, were employed as a benchmark for the validation of the bending strengths and stiffnesses. [74] analysed the bending strengths and stiffnesses of GL beams with dimensions of $600 \cdot 200 \cdot 10{,}800$ mm^3 and a 4-point bending load. Comparative numerical analyses were carried out for grading VIS-2 with a

characteristic tensile strength of the finger joints of 23.5 N/mm^2. The material parameters were selected according to the *KaReMo*, see Section 5.3.3, and Table 5.1. The lamella height was 30 mm. 200 FEAs with scattering material parameters were carried out.
Bending strengths of $f_{m,k}$ = 23.1 N/mm^2 and $f_{m,mean}$ = 30.2 N/mm^2 and local bending stiffnesses of $E_{0,k}$ = 11,600 N/mm^2 and $E_{0,mean}$ = 12,800 N/mm^2 were obtained from own analyses. These bending strengths are 5% to 10% lower than $f_{m,k}$ = 24.2 N/mm^2 and $f_{m,mean}$ = 33.3 N/mm^2 determined by [74]. Approximately 3% of the difference can be explained by the deviating position of the integration points. The bending stiffnesses are similar to the local bending stiffnesses of $E_{0,k}$ = 11,800 N/mm^2 and $E_{0,mean}$ = 12,800 N/mm^2 determined by [74].
With a slight underestimation of the bending strengths, the implementation of the *KaReMo*, which is discussed in this thesis, is well suited for determining the bending strengths and stiffnesses of beams made of GL 24h.

The computation results of Brüninghoff and Klapp [21], Fig. 2.6, and the experimental results of Schickhofer [140] for GL 24h were employed as benchmarks for the validation of the shear strengths. They analysed the bending strengths and stiffnesses of GL beams with dimensions of 3040 · 608 · 100 mm^3 and a 3-point bending load. Deviating to the tests of Schickhofer [140], a rectangular cross-section was utilised in the comparative numerical analyses instead of an I-cross-section. Visual grading VIS-2 was assumed. The material parameters were selected according to the *KaReMo* and the *KaReMo*$^{+v}$, see Section 5.3.3, and Table 5.1. The tensile strength was set at 1000 N/mm^2 in order to prevent tensile failure. The lamella height was 32 mm. 200 FEAs with scattering material parameters were carried out.
Shear strengths of $f_{v,0,k}$ = 3.18 N/mm^2 and $f_{v,0,mean}$ = 3.83 N/mm^2 were obtained from own analyses. These values of the shear strength are similar to $f_{v,0,k}$ = 3.0 N/mm^2 and $f_{v,0,mean}$ = 3.9 N/mm^2, the values determined by [21], and approximately 10% to 15% lower than $f_{v,0,k}$ = 3.6 N/mm^2 to 3.9 N/mm^2 and $f_{v,0,mean}$ = 4.2 N/mm^2 to 4.5 N/mm^2, the values determined by Schickhofer [140].
With a slight underestimation of the shear strengths, the implementation of the *KaReMo*$^{+v}$, which is discussed in this thesis, appears to be well suited for determining the shear strengths of beams made of GL 24h.

The product of the stiffness $E_{0,el} \cdot G_{0,el}$ was investigated, as it significantly influences the eigenvalues of beams at risk of LTB in order to check the implementation of scattering shear stiffnesses.
The investigations by Blaß [11], Table 2, were employed as a benchmark for the validation of $E_{0,el} \cdot G_{0,el}$. [11] analysed the product of the stiffness $E_{0,el} \cdot G_{0,el}$ of GL beams using a simple mechanical model and the measurement results of Görlacher and Kürth [81]. For a rectangular cross-section with dimensions of 600 · 100 · 3000 mm^3, scattering elastic and shear moduli were generated with grading VIS-2 applying the *KaReMo* and the *KaReMo*$^{+v}$, see Section 5.3.3. Analogous to the procedure of [11], the global stiffness $E_{0,el} \cdot G_{0,el}$ of 200 beams with scattering material parameters was determined.
The computed 5% quantile values and mean values of the product $E_{0,el} \cdot G_{0,el}$ were $7.39 \cdot 10^6$ N^2/mm^4 and $8.24 \cdot 10^6$ N^2/mm^4. The values were approximately 10% lower

than the 5% quantile values and mean values of $8.40 \cdot 10^6$ N^2/mm^4 and $9.16 \cdot 10^6$ N^2/mm^4 determined by [11]. This difference was due to the fact that the mean values of the distribution functions of $E_{0,\mathrm{el}}$ and $G_{0,\mathrm{el}}$ utilised in [11], 13700 N/mm^2 and 666 N/mm^2, were larger than the mean values from own FEA with VIS-2, 13100 N/mm^2 and 648 N/mm^2. The COV of the product $E_{0,\mathrm{el}} \cdot G_{0,\mathrm{el}}$ in [11] and own FEA was similar.
With a slightly higher scattering, the implementations of the *KaReMo* and the *KaReMo*$^{+\nu}$ discussed in this thesis are well suited to simulate the product of the stiffnesses $E_{0,\mathrm{el}} \cdot G_{0,\mathrm{el}}$ of members made of GL 24h.

5.5.5 Summary

The validation demonstrated that the stiffness, load-bearing capacity, and failure behaviour of imperfection-sensitive timber members can be modelled with high accuracy by the presented FE model. For doing so, the accurate modelling of the stiffness is of paramount importance.

Significant compressive plasticising in grain direction occurred at the beech LVL columns and needed to be taken into account in the FEA, see Section 5.5.2. For FEA with an experimentally determined stress-strain curve for compression in grain direction and experimentally determined bending stiffnesses, the mean and the maximum deviations between the experimentally and the numerically determined load-bearing capacities were 1.5% and 5.6%.
Significant local shear failure, i.e. shear plasticising, in grain direction occurred at the GL beams and needed to be taken into account in the FEA, see Section 5.5.3. As (i) the shear strength scatters highly, see Section 2.4.4; (ii) the complete load-deformation relationship for torsion cannot be determined in non-destructive preliminary tests; and (iii) no values of the proportionality limit $f_{\mathrm{v},0,\mathrm{lin}}$ of GL beams in torsion were known from literature, see Section 2.3.4, assumptions needed to be made in FEA that were subject to notable uncertainties. This reduced the accuracy of FEA for beams with high shear stresses from torsion. The mean and the maximum deviations between the experimentally and the numerically determined load-bearing capacities at LTB were 1.0% and 14%.
Comparative calculations using T2O demonstrated inaccuracies of T2O due to the simplifying assumptions in its derivation, especially by neglecting the plasticising, see Sections 5.5.2 and 5.5.3.
The validation of the models for the consideration of scattering material properties, the *KaReMo* and the *KaReMo*$^{+\nu}$, demonstrated that they accurately represent the stiffnesses $E_{0,\mathrm{el}}$ and $G_{0,\mathrm{el}}$ and are well suited to determine the bending strengths f_{m} and the shear strengths $f_{\mathrm{v},0}$ of GL 24h with a slight underestimation of the load-bearing capacities, see Section 5.5.4.

The developed FE model reliably reproduces all known relevant physical effects of the load-bearing behaviour of imperfection-sensitive timber beam-columns and can be used for further numerical parameter studies.

5.6 Numerical analysis and parameter studies

5.6.1 General

Two numerical parameter studies with two objectives were conducted:

a. parameter study with scattering geometrical and structural imperfections for deriving the equivalent geometrical imperfection assumptions for design, see Section 5.6.2, and

b. parameter study with varying input parameters for determining the $N_{x,c}$-$M_{y,1}$-interaction for flexural buckling and LTB, see Section 5.6.3.

In parameter study a., scattering geometrical imperfections and scattering material stiffnesses and strengths were taken into account by (i) previously discussed models for scattering basic variables; (ii) sampling with Monte Carlo simulations; (iii) repeated FEA with the sampled input values; and (iv) evaluation of the frequency distributions of the resulting load-bearing capacities. Parameter study b. was conducted with nominal values of the basic variables.

The procedure (i) in case of nominal values for geometry and material parameters corresponded to the methodology of *numerical design calculations with direct resistance check*; (ii) in case of scattering input values for geometry and material parameters corresponded to the methodology of *numerical simulations*; see Section 5.2 and the *FE guidelines* [162]. FEA were performed as *geometrically and materially nonlinear analysis with imperfections* (GMNIA), as the corresponding phenomena are relevant. This type of analysis manifests itself in the chosen material model, imperfection assumptions, and solver settings of the FEA, which are described in Section 5.3.

The computation routine of the FEA is presented in Figure 5.14. The core was the automated

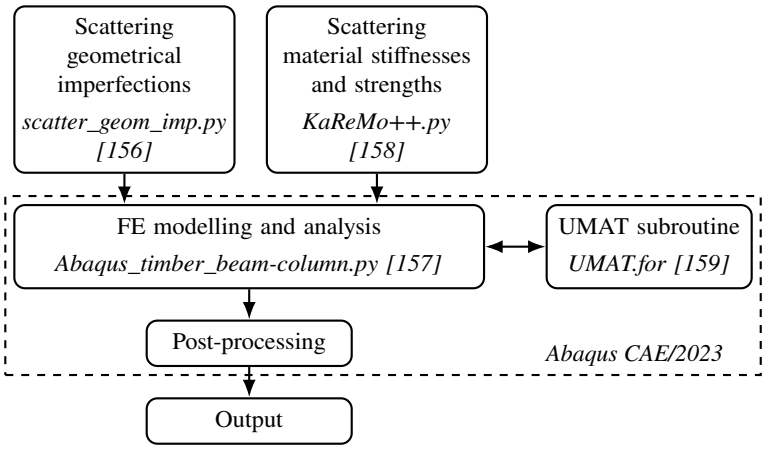

Figure 5.14: Computation routine for FEA of imperfection-sensitive timber members.

FE modelling and analysis using a *Python* input file [157]. Either input values of scattering geometrical imperfections and scattering material properties were generated in advance with two *Python* scripts, [156] and [158], or nominal values of the geometrical imperfections and the material properties were utilised. A user-defined material model was employed for the FEA, which was developed in the Abaqus subroutine *UMAT* [159], see Annex D. The relevant output, e.g. deformations and load-bearing capacities for different failure criteria, was generated in post-processing of the FEA. The *Python* scripts for post-processing are given in [157].

5.6.2 Equivalent geometrical imperfections

FEA with scattering geometrical and structural imperfections were conducted for deriving the equivalent geometrical imperfections for flexural buckling and LTB design of timber beam-columns, covering the effects of both imperfections. Timber members subjected to bending (beams) and to axial compression (columns) with different cross-sectional dimensions were investigated. The variations resulted in over 35,000 FEAs, the results of which are discussed in Section 6.3.

For the beams, scattering values of structural imperfections were simulated with the *KaReMo*$^{+y}$, see Section 5.3.3. Scattering stiffnesses and strengths over the beam length and height were neglected, as these do not significantly influence the structural imperfections at LTB, see Section 2.7.1. GL 24h and a lamella height of 40 mm were chosen. Therefore, characteristic material parameters according to Table 5.8 were selected as initial values and modified with the *KaReMo*$^{+y}$. The failure criterion was the exceeding of the tensile strength $f_{t,0}$ (no size effect according to Equation (5.2)). Shear failure was neglected. Cross-sectional height-to-width ratios of 4, 8, and 12 at a width of 120 mm were modelled. The small width of 120 mm and the small height-to-width ratio of 4 for long-span imperfection-sensitive timber beams, should, due to the low number of lamellae, lead to a minimal lamination effect and consequently high structural imperfections. The influence of imperfections is only significant for medium slendernesses, see Figure 2.4 and Table 5.5. Thus, the member length was varied in seven steps so that relative slendernesses $\lambda_{m,rel}$ of approximately 0.60, 0.70, 0.80, 0.90, 1.00, 1.10, and 1.20 were achieved. The relative slendernesses were calculated according to EN 1995-1-1 [57] with Equation (2.63) and nominal material properties, see also discussions regarding Figure 2.6. For beams with $H/B = 8$ and 12, the low slendernesses were not investigated, as these lead to beam dimensions of $L_{m,ef}/H \leq 2.5$, which are of little relevance for building practice. Additionally, the applicability of the beam theory would be highly questionable for such members, as they would rather act like shell structures. Scattering values of geometrical imperfections were simulated according to Section 5.3.4.

For the columns, scattering values of structural imperfections were simulated with the *KaReMo*, see Section 5.3.3. The FEA thus included scattering strengths, the influence of which had to be eliminated if determining the equivalent geometrical imperfections. GL 24h, visual grading VIS-2, see Frese [74], and a lamella height of 40 mm were chosen. Therefore, mean material parameters according to Table 5.1 were selected as initial values and modified with the *KaReMo*. The failure criterion was the exceeding of the tensile strength $f_{t,0}$. A cross-sectional height-to-width ratio of 1 at widths of 120 mm, 160 mm, 200 mm, and 240 mm was modelled. The small width of 120 mm for imperfection-sensitive timber columns, should, due to the low number of lamellae, lead to a minimal lamination effect and consequently high structural imperfections. The influence of imperfections is only significant for medium slendernesses, see Figure 2.4 and Table 5.5. Thus, the member length was varied in seven steps so that relative slendernesses $\lambda_{c,rel}$ of approximately 0.60, 0.70, 0.80, 0.90, 1.00, 1.10, and 1.20 were achieved. The relative slendernesses were calculated according to EN 1995-1-1 [57] with Equation (2.60) and nominal material properties, see also discussions regarding Figure 2.6. Scattering values of geometrical

Table 5.8: Nominal values for material modelling of GL 24h beams according to EN 14080 [54] supplemented by values from Table 5.1.

	Elastic modulus [N/mm^2]	Proportionality limit [Ratio f_{lin}/f]	Strength [N/mm^2]	Plastic strain at strength [Ratio $\epsilon_{\text{pl}}/\epsilon_{\text{el}}$]	Plastic modulus [N/mm^2]
Tension in L	11,500 [1,2]	-	24.0 [3]	-	-
Compression in L	11,500 [1,2]	0.75	−24.0	0.40	50
Tens. & comp. in R & T	250	-	-	-	-
Shear in LR & LT	650 [1]	0.30	3.5	-	$1.5 \cdot 650$
Shear in RT	54	0.55	1.2	-	$0.5 \cdot 54$

[1] For LTB of softwood GL beams mean values of E_0 and G_0 may be assumed or the product of $E_{0,05}G_{0,05}$ may increased by a factor of 1.4 if calculating $M_{\text{y,cr}}$, see Blaß [11] and DIN EN 1995-1-1/NA [40].
[2] Modified by the *KaReMo*$^{+y}$.
[3] Modified to $f_{\text{t,0,mod}}$.

imperfections were simulated according to Section 5.3.4. A flexural buckling, which produced a flatwise bending moment in the lamellas, was investigated. This orientation is decisive for the influence of the scattering elastic moduli of individual lamellas on the structural imperfections, as the elastic modulus $E_{0,\text{el}}$ varies more between different lamellas than across the width of a lamella, see Figure 5.6 and Equation (5.4).
Single-span beams with ideal fork supports in the member axis and constant bending moments $M_{\text{y},1}$ and pinned columns with axial compressive forces $N_{\text{x,c}}$ were analysed. The constant bending moments was applied force-controlled and the axial compressive forces were applied displacement-controlled.
For each variation of the member geometry, 200 FEAs were carried out with scattering material parameters and scattering geometrical imperfections. Bootstrapping was used to check whether the FEA results converged within the 200 analyses.

The equivalent geometrical imperfections for LTB design of softwood GL beams were determined in four steps:

1. Analyses of the *bending* load-bearing capacities $M_{\text{y,1,R,1}}$ with nominal material parameters according to EN 14080 [54], see Table 5.8, while *neglecting* the geometrically nonlinear behaviour, i.e. LTB. One FEA was conducted for each variation of the member geometry.

2. Analyses of the *bending* load-bearing capacities $M_{\text{y,1,R,2}}$ with nominal material parameters according to EN 14080 [54], see Table 5.8, and scattering $E_{0,\text{el}}$ according to the *KaReMo*$^{+y}$ while *neglecting* the geometrically nonlinear behaviour, i.e. LTB. In this case, to prevent LTB, the DOFs of all nodes in the y-direction had to be fixed. 200 FEAs were conducted for each variation of the member geometry. As stiffnesses attract stresses, the scattering $E_{0,\text{el}}$ across the board width influences the bending load-bearing capacities. Therefore, the modified tensile strength $f_{\text{t,0,mod}}$ of

each beam was determined by linear interpolation, where $M_{y,1,R,2} = M_{y,1,R,1}$ applied: $f_{t,0,mod} = f_{t,0}\, M_{y,1,R,1}/M_{y,1,R,2}$.

3. Analyses of the *LTB* load-bearing capacities $M_{y,1,R,3}$ of the same beams with the same material parameters as in the previous step (200 beams for each variation of the member geometry) with consideration of $f_{t,0,mod}$ and scattering geometrical imperfections.

4. Analyses of the *LTB* load-bearing capacities $M_{y,1,R,4}(e_{\theta,eq})$ with nominal material parameters according to EN 14080 [54], see Table 5.8, bow imperfections of $e_{y,eq} = e_{y,95}$, and stepwise increasing twist imperfections at midspan of $e_{\theta,eq} = 0.0$ to $1.0 \cdot (e_{\theta,mid,95} + e_{\theta,supp,95})$. With $e_{y,95}$, $e_{\theta,mid,95}$, and $e_{\theta,supp,95}$ according to Section 5.3.4. 11 FEAs with stepwise increasing $e_{\theta,eq}$ were conducted for each variation of the member geometry. $e_{y,eq} = L/1000$ was assumed, as this can be applied for both the LTB design of softwood GL beams and the flexural buckling design of softwood GL columns, see Table 3.3. If deviating bow imperfections are chosen for LTB and flexural buckling design, mechanical inconsistencies for combined bending and axial compression cannot be avoided.

The reduction factor for LTB with scattering imperfections was determined by $k_{m,scatter} = M_{y,1,R,3}/M_{y,1,R,1}$. For each variation of the member geometry, 200 values of $k_{m,scatter}$ and the 5% quantile value $k_{m,scatter,05}$ were determined from the 200 FEAs. The reduction factor for LTB with equivalent geometrical imperfections was determined for each variation of the member geometry by $k_{m,eq}(e_{\theta,eq}) = M_{y,1,R,4}(e_{\theta,eq})/M_{y,1,R,1}$. By comparing $k_{m,scatter,05}$ and $k_{m,eq}(e_{\theta,eq})$, the equivalent twist imperfection $e_{\theta,eq}$ was determined for each variation of the member geometry for which $k_{m,eq} = k_{m,scatter,05}$ applied. This equivalent twist imperfection $e_{\theta,eq}$ and the equivalent bow imperfection $e_{y,eq}$ were the equivalent geometrical imperfections that led to the same LTB load-bearing capacity as the 5% quantile value of the LTB load-bearing capacity from FEA with scattering structural and geometrical imperfections.
A determination of the equivalent geometrical imperfections with calculations using T2O, i.e. a calculation of $M_{y,1,R,4}(e_{\theta,eq})$ using T2O, was discarded due to the inaccuracies of the beam theory described in Section 6.2, see also Töpler and Kuhlmann [166].

The equivalent geometrical imperfections for flexural buckling design of softwood GL columns were determined in three steps:

1. Analyses of the *compressive* load-bearing capacities $N_{x,c,R,1}$ with scattering material parameters $E_{0,el}$, $f_{t,0}$, and $f_{c,0}$ according to the *KaReMo* and other material parameters as mean values, see Table 5.1, while *neglecting* the geometrically nonlinear behaviour, i.e. flexural buckling. To prevent the flexural buckling, the DOFs of all nodes in the z-direction had to be fixed. 200 FEAs were conducted for each variation of the member geometry. The 5% quantile values of the compressive load-bearing capacities $N_{x,c,R,1,05}$ were determined for each variation of the member geometry from the distribution functions of $N_{x,c,R,1}$.

2. Analyses of the *flexural buckling* load-bearing capacities $N_{x,c,R,2}$ of the same columns with the same material parameters as in the previous step (200 columns for each

Table 5.9: Nominal values for material modelling of GL 24h columns according to EN 14080 [54] supplemented by values from Table 5.1.

	Elastic modulus [N/mm^2]	Proportionality limit [Ratio f_{lin}/f]	Strength [N/mm^2]	Plastic strain at strength [Ratio $\epsilon_{\text{pl}}/\epsilon_{\text{el}}$]	Plastic modulus [N/mm^2]
Tension in L	9600	-	24.0	-	-
Compression in L	9600	0.75	−24.0	0.40	50
Tens. & comp. in R & T	250	-	-	-	-
Shear in LR & LT	540	0.30	3.5	-	$1.5 \cdot 540$
Shear in RT	54	0.55	1.2	-	$0.5 \cdot 54$

variation of the member geometry) and scattering geometrical imperfections. The 5% quantile values of the flexural buckling load-bearing capacities $N_{\text{x,c,R,2,05}}$ were determined for each variation of the member geometry from the distribution functions of $N_{\text{x,c,R,2}}$.

3. Calculation of the *flexural buckling* load-bearing capacities $N_{\text{x,c,R,3}}(e_{\text{z,eq}})$ using *T2O* according to FprEN 1995-1-1 [69], see Section 2.6.4.1.2, with nominal material parameters according to EN 14080 [54], see Table 5.9, and stepwise increasing bow imperfections $e_{\text{z,eq}}$.

For each variation of the member geometry, the 5% quantile value of the reduction factor for flexural buckling with scattering imperfections was determined by $k_{\text{c,scatter,05}} = N_{\text{x,c,R,2,05}}/N_{\text{x,c,R,1,05}}$. The reduction factor for flexural buckling with equivalent geometrical imperfections was determined for each variation of the member geometry by $k_{\text{c,eq}}(e_{\text{z,eq}}) = N_{\text{x,c,R,3}}(e_{\text{z,eq}})/Af_{\text{c,0,k}}$. By comparing $k_{\text{c,scatter,05}}$ and $k_{\text{c,eq}}(e_{\text{z,eq}})$, the equivalent bow imperfection $e_{\text{z,eq}}$ was determined for each variation of the member geometry for which $k_{\text{c,eq}} = k_{\text{c,scatter,05}}$ applied. These equivalent bow imperfections $e_{\text{z,eq}}$ were the equivalent geometrical imperfections that led to the same flexural buckling load-bearing capacity as the 5% quantile value of the flexural buckling load-bearing capacity from FEA with scattering structural and geometrical imperfections.

5.6.3 $N_{\text{x,c}}$-$M_{\text{y,1}}$-interaction

FEA with varying slenderness, material, and loading were conducted to investigate the interaction relationship of the load-bearing capacity of imperfection-sensitive timber members at combined axial compression and bending. The variations resulted in over 17,000 FEAs, the results of which are discussed in Section 6.3.

Single-span beam-columns with fork supports were investigated, loaded by a constant bending moment, by a uniform line load at the upper edge of the beam-column, or by a concentrated load at midspan at the upper edge of the beam-column. For GL75, only a constant bending moment was investigated. In addition, the axial compressive force was varied between 0% and 100% of the load-bearing capacity in compression. The compressive

force was always applied first and kept constant, and subsequently the bending moment was applied. The loads were applied force-controlled. For the structural system with the constant bending moment, an idealised support in the member axis was modelled, and for the structural systems with the uniform line load or the concentrated load, a realistic support at the lower edge of the beams was modelled. GL 24h, GL 30c, and GL75 with nominal material properties according to EN 14080 [54] and ETA-14/0354 [63] were analysed, see Tables 5.10, 5.11, and 5.12. The mean values of $E_{0,\mathrm{el}}$ and $G_{0,\mathrm{el}}$ were applied consistently for all members, in line with the results of Blaß [11] and the provisions for LTB of softwood GL beams in DIN EN 1995-1-1/NA [40]. The increase of the shear strength with k_{shape} according to EN 1995-1-1 [57] was not taken into account, because k_{shape} takes into account the effect of the shape of the cross-section, see Section 2.6.2.2.1, which may already be partially by considered in the FEA with solid elements. The size effect on the tensile strength due to biaxial bending was included according to Equation (5.2). Further size effects were neglected, as these do not influence the characteristics of the $N_{\mathrm{x,c}}$-$M_{\mathrm{y,1}}$-interaction, only the absolute values of the load-bearing capacities. Based on the results of the parameter study on equivalent geometrical imperfections, see Sections 5.6.2 and 6.3, equivalent bow imperfections and twist imperfections at midspan of $e_{\mathrm{y,eq}} = L/1000$ and $e_{\theta,\mathrm{eq}} = 0.5 \cdot (e_{\theta,\mathrm{mid},95} + e_{\theta,\mathrm{supp},95})$ with $e_{\theta,\mathrm{mid},95} = L/1500 H_{\mathrm{ap}}$ and $e_{\theta,\mathrm{supp},95} = 1/100$ were assumed. Cross-sectional height-to-width ratios of 1, 2, 4, 8, 12, and 16 were modelled with a width of 120 mm. The member length was varied in 31 steps between $2.5H$ and $25H$ or $50H$.

Table 5.10: Nominal values for material modelling of GL 24h beam-columns according to EN 14080 [54] supplemented by values from Table 5.1.

	Elastic modulus [N/mm^2]	Proportionality limit [Ratio f_{lin}/f]	Strength [N/mm^2]	Plastic strain at strength [Ratio $\epsilon_{\mathrm{pl}}/\epsilon_{\mathrm{el}}$]	Plastic modulus [N/mm^2]
Tension in L	11,500	-	24.0 [1]	-	-
Compression in L	11,500	0.75	−24.0	0.40	50
Tens. & comp. in R & T	250	-	-	-	-
Shear in LR & LT	650	0.30	3.50	-	$1.5 \cdot 650$
Shear in RT	54	0.55	1.20	-	$0.5 \cdot 54$

[1] Plus size effect due to biaxial bending according to Equation (5.2).

Table 5.11: Nominal values for material modelling of GL 30c beam-columns according to EN 14080 [54] supplemented by values from Table 5.2.

	Elastic modulus [N/mm^2]	Proportionality limit [Ratio f_{lin}/f]	Strength [N/mm^2]	Plastic strain at strength [Ratio $\epsilon_{\text{pl}}/\epsilon_{\text{el}}$]	Plastic modulus [N/mm^2]
Tension in L	13,000	-	30.0 [1]	-	-
Compression in L	13,000	0.75	−24.5	0.40	50
Tens. & comp. in R & T	250	-	-	-	-
Shear in LR & LT	650	0.30	3.50	-	$1.5 \cdot 650$
Shear in RT	54	0.55	1.20	-	$0.5 \cdot 54$

[1] Plus size effect due to biaxial bending according to Equation (5.2).

Table 5.12: Nominal values for material modelling of GL75 beam-columns according to ETA-14/0354 [63] supplemented by values from Table 5.1, Table 5.3, and Hütter [91].

	Elastic modulus [N/mm^2]	Proportionality limit [Ratio f_{lin}/f]	Strength [N/mm^2]	Plastic strain at strength [Ratio $\epsilon_{\text{pl}}/\epsilon_{\text{el}}$]	Plastic modulus [N/mm^2]
Tension in L	16,800	-	75.0 [1]	-	-
Compression in L	16,800	0.65	−59.4	1.25	50
Tens. & comp. in R & T	900	-	-	-	-
Shear in LR	850	0.30 [2]	4.50	-	$1.5 \cdot 850$ [3]
Shear in LT	850	0.30 [2]	8.00	-	$1.5 \cdot 850$ [3]
Shear in RT	150	0.55 [2]	2.40 [3]	-	$0.5 \cdot 100$ [2]

[1] Plus size effect due to biaxial bending according to Equation (5.2).
[2] Analogous to softwood GL, see Table 5.1.
[3] See Hütter [91].

5.7 Summary

Numerical models and analyses for investigating the load-bearing behaviour of imperfection-sensitive timber members under combined axial compression and bending are discussed in Section 5.

Guidelines for Finite Element Based Design of Timber Structures (*FE guidelines*) were developed by Töpler and Kuhlmann [162], and excerpts relevant to this thesis are presented in Section 5.2. The *FE guidelines* provide (i) guidance on the use of numerical methods for timber design; (ii) minimum requirements on model and software capabilities for specific applications; (iii) boundaries for the safe and correct application of numerical methods; (iv) methods and benchmarks for model verification and validation; (v) possibilities for an expert application of numerical analyses within the safety concept of the Eurocodes.
A parametrised FE model for *Abaqus/CAE 2023* [1] with automated input, output, and post-processing was developed with *Python*, see Sections 5.3 and 5.6. To model the anisotropic elastoplastic material behaviour of wood, a user-defined material model was

implemented in the UMAT subroutine of Abaqus, see Section 5.3.2. To account for the scattering stiffnesses and strengths of wood, the *Karlsruher Rechenmodell* (*KaReMo*), see, e.g. Blaß et al. [14], was extended to include scattering shear strengths and stiffnesses over the member length and height and scattering elastic moduli over the member width, see Section 5.3.3. Furthermore, scattering geometrical imperfections were considered on the basis of the measurement results presented in Section 3.2, see Section 5.3.4.
The FE model was verified in line with the *FE guidelines* [162], i.e. the discretisation and sensitivity to input parameters were checked, see Section 5.4.
The FE model was validated utilising the results of the flexural buckling and LTB tests described in Sections 3.3 and 3.4 and literature values for the *KaReMo*, see Section 5.5. The validation demonstrated that the stiffness, load-bearing capacity, and failure behaviour of imperfection-sensitive timber members can be modelled with high accuracy by the presented FE model. Additionally, the validation highlighted that the compressive plasticising and shear plasticising in grain direction have to be considered if modelling flexural buckling and LTB of timber beam-columns. Comparative calculations using T2O demonstrated inaccuracies of T2O due to the simplifying assumptions in its derivation, see Section 5.5.
Finally, Section 5.6 describes the numerical parameter studies (i) for deriving the equivalent geometrical imperfection assumptions for design; and (ii) for determining the $N_{x,c}$-$M_{y,1}$-interaction for flexural buckling and LTB.

The results of the FEA are discussed in Section 6 together with the experimental results from Section 3 and the analytical derivations from Section 4. This culminated in the formulation of the design concept in Section 7.

6 Results and discussion

6.1 General

In this section, the results of the numerical parameter studies on imperfection-sensitive timber members under combined axial compression and bending described in Section 5.6 are presented. The results are compared with the experimental and analytical investigations in Sections 3 and 4, discussed in the context of the literature, see Section 2, and the design methods in EN 1995-1-1 [57] and FprEN 1995-1-1 [69] are evaluated. In particular

- the equivalent geometrical imperfection assumptions for design, see Section 6.3, and
- the $N_{x,c}$-$M_{y,1}$-interaction for flexural buckling and LTB, see Section 6.4,

are discussed. During the evaluation of the numerical parameter studies, some partially unexpected fundamental aspects emerged that are essential for the interpretation of the results. Therefore, the following aspects are discussed beforehand:

- the influence of cross-sectional warping on the bending load-bearing capacity, see Section 6.2.1;
- the relative slenderness ratio $\lambda_{c/m,rel}$, see Section 6.2.2; and
- the influence of plate bending on the eigenvalues and the load-bearing capacities, see Section 6.2.3.

Based on the results, the proposals for a modification of the design methods in EN 1995-1-1 [57] and FprEN 1995-1-1 [69] were developed, see Section 7.

6.2 Basic aspects

6.2.1 Influence of cross-sectional warping on bending load-bearing capacity

According to Hofmann [88], the total stresses in grain direction σ_0 are composed of the primary stresses due to bending and the secondary stresses due to the obstruction of shear force induced cross-sectional warping, see Figure 6.1. Superimposing primary and secondary stresses increases the edge bending stresses and thus reduces the bending load-bearing capacity. The magnitude of the secondary stresses depends on the ratio of the member length to the height, the type of loading, i.e. the ratio of the bending stresses to the shear stresses, and the ratio of the elastic modulus to the shear modulus, see [88]. The secondary stress components are usually neglected in the bending design verification of timber beams. No investigations from literature were known regarding the influence of the secondary stresses on the total stresses and the bending load-bearing capacity of timber beams.

In own trial tests and FEA, beech LVL beams with a length-to-height ratio below 6 exhibited significant cross-sectional warping due to shear forces, which reduced the bending load-bearing capacity by 10% and more, see Figure 6.2 and Töpler and Kuhlmann [161]. For GL and LVL beams with shear forces and $4 \leq L/H < 6$, [161] recommended a factor k_{warp} to increase the edge bending stresses. For $L/H < 4$, the application of the beam

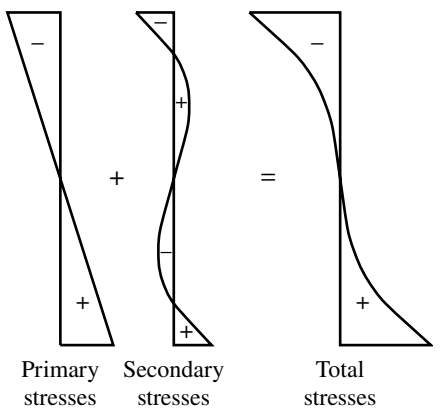

Figure 6.1: Distribution of stresses in grain direction over the beam height of a beam with bending and shear forces; with primary stresses, secondary stresses, and total stresses; from Hofmann [88].

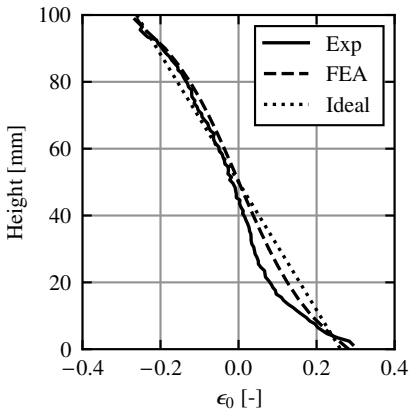

Figure 6.2: Experimentally (Exp) determined strains in grain direction ϵ_0 over the beam height of a beech LVL beam with dimensions of $100 \cdot 100 \cdot 600$ mm^3 at 3-point bending; comparison with results of FEA and an ideal linear strain distribution; from Töpler and Kuhlmann [161].

theory was not endorsed; instead, methods including membrane theory were recommended.

The results of Töpler and Kuhlmann [161] were confirmed by the numerical investigations in this thesis. Figures 6.3 and 6.4 display the reduction factor k_m calculated from the FE results over the relative LTB slenderness ratio $\lambda_{m,rel}$ for loading by a constant bending moment, a uniform line load, or a concentrated force at midspan and $H/B = 4$ and $H/B = 12$. The FE results are those of the parameter study on $N_{x,c}$-$M_{y,1}$-interaction with nominal values for material and geometry, see Sections 5.6.3 and 6.4. k_m was calculated by

$$k_m = \frac{M_{y,1,R,FEA}}{W_y f_{m,k}} \quad , \tag{6.1}$$

where $M_{y,1,R,FEA}$ is the bending load-bearing capacity with LTB from FEA, W_y is the section modulus about the y axis, and $f_{m,k}$ is the characteristic bending strength. $\lambda_{m,rel}$ was calculated according to FprEN 1995-1-1 [69], see Section 2.6.4.1.4.
For beams subjected to shear forces, there was a significant drop in load-bearing capacities for $L/H < 6$ due to significant secondary stresses and cross-sectional warping. For beams with a constant bending moment, this behaviour did not occur due to the lack of shear stresses from shear force, and k_m corresponded to the expected buckling curve, see Figure 2.4.

The influence of the cross-sectional warping on the bending load-bearing capacity needs to be considered in the evaluation of the parameter studies on $N_{x,c}$-$M_{y,1}$-interaction, Section 6.4.

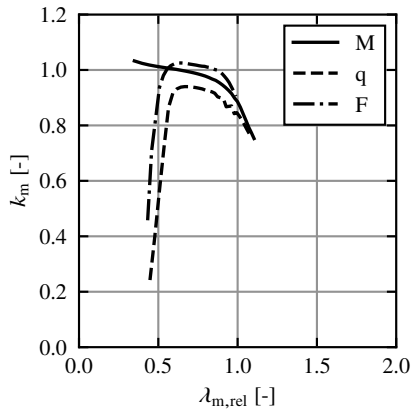

Figure 6.3: Reduction of the load-bearing capacity k_m from FEA plotted over the relative LTB slenderness ratio $\lambda_{m,rel}$ for a constant bending moment (M), a uniform line load (q), and a concentrated load (F); GL 24h and $H/B = 4$.

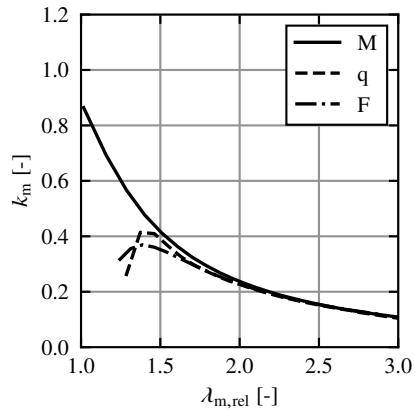

Figure 6.4: Reduction of the load-bearing capacity k_m from FEA plotted over the relative LTB slenderness ratio $\lambda_{m,rel}$ for a constant bending moment (M), a uniform line load (q), and a concentrated load (F); GL 24h and $H/B = 12$.

6.2.2 Relative LTB slenderness ratio

The relative slenderness $\lambda_{c/m,rel}$ for flexural buckling or LTB defined in EN 1995-1-1 [57] allows for a simple formulation of the equations for calculating k_c and k_m, see Equations (2.58), (2.61), and (2.78). $\lambda_{c/m,rel}$ indicates the ratio of the cross-sectional compressive or bending load-bearing capacity to the critical axial compressive force or bending moment, see Equations (2.60) and (2.63). Whereby the cross-sectional load-bearing capacity was well understood, comparatively few experimental investigations of the critical loads were known that only covered some of the materials and geometries relevant in construction, see Section 2.2. Furthermore, no systematic numerical analysis of the critical loads with shell or solid elements, only with beam elements, see Schulze [144], were known. Finally, the equations for calculating the critical loads are based on significant simplifying assumptions, e.g. the beam theory, see Sections 2.2.1.7 and 2.2.2.7.

Figures 6.5 and 6.6 display the ratio of the critical bending moment from FEA to FprEN 1995-1-1 [69] $M_{cr,FEA}/M_{cr,EC5}$ plotted over the relative LTB slenderness ratio $\lambda_{m,rel}$ for loading by a constant bending moment, a uniform line load, or a concentrated force at midspan and $H/B = 4$ and $H/B = 12$. The FE results are those of the parameter study on $N_{x,c}$-$M_{y,1}$-interaction with nominal values for material and geometry, see Sections 5.6.3 and 6.4. $\lambda_{m,rel}$ and $M_{cr,EC5}$ were calculated according to Equations (2.63) and (2.64).
For a constant bending moment, the critical bending moment from FEA was always slightly higher than according to FprEN 1995-1-1 [69]. For $H/B = 12$ the differences increased with decreasing $\lambda_{m,rel}$. This was probably due to the influence of the plate bending on

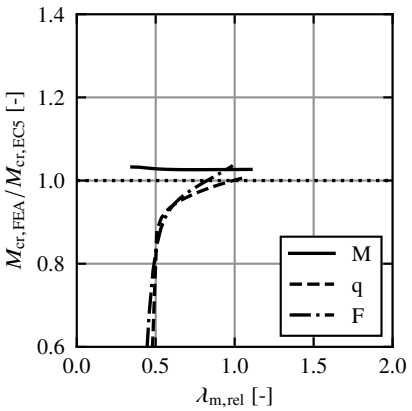

Figure 6.5: Ratio of the critical bending moment from FEA to FprEN 1995-1-1 [69] $M_{cr,FEA}/M_{cr,EC5}$ plotted over the relative LTB slenderness ratio $\lambda_{m,rel}$ for a constant bending moment (M), a uniform line load (q), and a concentrated load (F); GL 24h and $H/B = 4$.

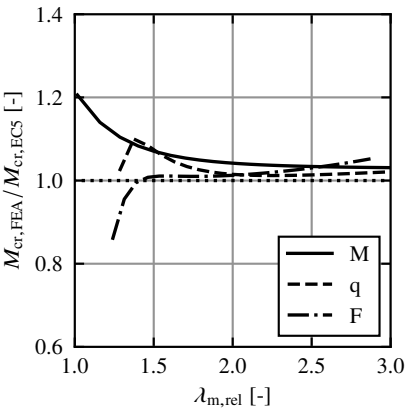

Figure 6.6: Ratio of the critical bending moment from FEA to FprEN 1995-1-1 [69] $M_{cr,FEA}/M_{cr,EC5}$ plotted over the relative LTB slenderness ratio $\lambda_{m,rel}$ for a constant bending moment (M), a uniform line load (q), and a concentrated load (F); GL 24h and $H/B = 12$.

the eigenvalues, see Section 6.2.3. For a uniform line load or a concentrated force at midspan and small $\lambda_{m,rel}$, the critical bending moment from FEA was partly significantly smaller than according to FprEN 1995-1-1 [69]. This corresponded with the influence of the cross-sectional warping due to shear forces and was therefore attributed to this effect. The numerically determined eigenvalues were generally larger than eigenvalues according to FprEN 1995-1-1 [69] or the difference was less than 10% and can thus be neglected in design. Only for a uniform line load or a concentrated force and small $\lambda_{m,rel}$, the eigenvalues according to Equation (2.64) were on the unsafe side.

Figure 6.7 displays the reduction factor k_m from FEA plotted over the relative LTB slenderness ratio according to FEA and FprEN 1995-1-1 [69]. k_m was calculated according to Equation (6.1). Due to the slight underestimation of the critical bending moment by FprEN 1995-1-1 [69] at constant bending moments and large H/B ratios, see also Figure 6.6, the LTB load-bearing capacity was slightly overestimated by FprEN 1995-1-1 [69] by up to 10%.

Figure 6.8 illustrates the reduction factor k_m from FEA plotted over the relative LTB slenderness ratio according to FEA, DIN EN 1995-1-1/NA [40] and FprEN 1995-1-1 [69]. The difference between DIN EN 1995-1-1/NA [40] and FprEN 1995-1-1 [69] is the equation for calculating the effective LTB length $L_{m,ef}$. k_m was calculated according to Equation (6.1).
The equation for determining $L_{m,ef}$ in DIN EN 1995-1-1/NA [40] gave inaccurate results for small relative LTB slenderness ratios at uniform line loads or concentrated forces.

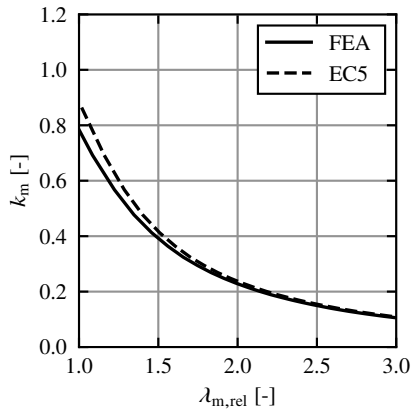

Figure 6.7: Reduction of the load-bearing capacity k_m from FEA plotted over the relative LTB slenderness ratio $\lambda_{m,rel}$ according to FprEN 1995-1-1 [69] (EC5) for a *constant bending moment*; GL 24h and $H/B = 12$.

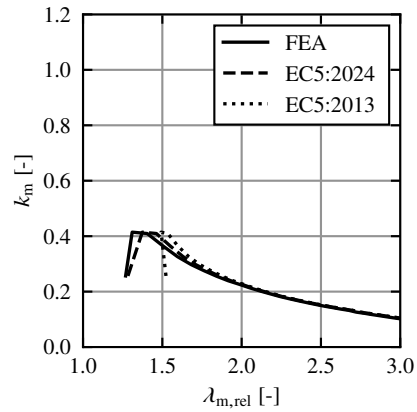

Figure 6.8: Reduction of the load-bearing capacity k_m from FEA plotted over the relative LTB slenderness ratio $\lambda_{m,rel}$ according to FprEN 1995-1-1 [69] (EC5:2024) and DIN EN 1995-1-1/NA [40] (EC5:2013) for a *uniform line load*; GL 24h and $H/B = 12$.

In the following evaluations, the relative LTB slenderness ratio $\lambda_{m,rel}$ according to FprEN 1995-1-1 [69] was therefore always employed. Nevertheless, differences in the critical bending moments between FEA and calculations with FprEN 1995-1-1 [69] can result in differences in load-bearing capacities of up to 10% in addition to the influence of shear warping, see Section 6.2.1.

6.2.3 Influence of plate bending on eigenvalues and load-bearing capacities

The results of the FEAs demonstrated that the LTB deformation behaviour of beams depends on the cross-sectional height-to-width ratio. Figures 6.9 and 6.10 illustrate the LTB behaviour of beams with $H/B = 4$ and $H/B = 12$. At $H/B = 4$, a pure rotation of the cross-section at midspan was observed. At $H/B = 12$, a plate bending around the x-axis combined with a rotation of the cross-section at midspan occurred. The plate bending increased the eigenvalues of the beams by up to 20% compared to analytical calculations with Equation (2.17) with $L_{m,ef}$ according to FprEN 1995-1-1 [69], see Figure 6.6, where the plate bending increased with decreasing length and increasing H/B ratio and was most pronounced for a constant bending moment. The LTB load-bearing capacity depends strongly on the eigenvalue, see Figure 2.4 and Equation (2.21). For a 20% increase of the eigenvalue at $\lambda_{m,rel} = 1.0$, see Figure 6.6, Equations (2.21) and (2.24) yield an approximately 10% increase of k_m from 0.71 to 0.77. The effect of the eigenvalue on the load-bearing capacity becomes visible in comparing Figures 6.4 and 6.6. No reports on this effect at LTB of timber beams were known from literature. No significant stresses perpendicular to the grain occurred due to plate bending.
The reason for this observed influence of the plate bending is probably that the ratio of the buckling stiffness of the compression chord to the plate bending stiffness of the cross-section around the x-axis depends on the ratio of H to B to L, see Figures 6.9 and 6.10. As the

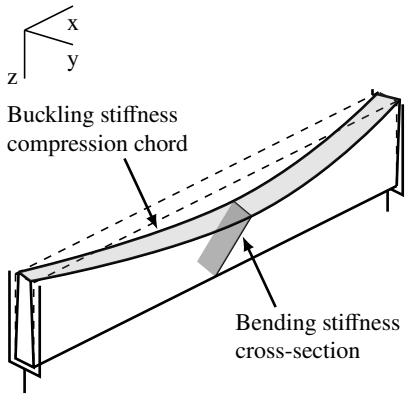

Figure 6.9: Schematic illustration of the LTB deformation behaviour of a timber beam with $H/B = 4$.

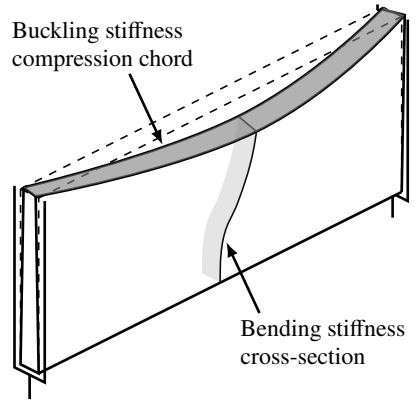

Figure 6.10: Schematic illustration of the LTB deformation behaviour of a timber beam with $H/B = 12$.

H/B ratio increases, the bending stiffness of the cross-section around the x-axis decreases, and also the ratio of the bending stiffness of the cross-section to the buckling stiffness of the compression chord decreases. Therefore, the plate bending is more pronounced, and the flow of forces within the beam changes. Similarly, if the L/B ratio decreases.

The plate bending cannot be modelled with beam theory. Therefore, the calculations of eigenvalues/critical loads, relative LTB slenderness ratios, and load-bearing capacities based on beam theory, e.g. the design equations in EN 1995-1-1 [57] and FprEN 1995-1-1 [69], provide conservative results for beams with large H/B ratios regarding this effect.

The influence of the plate bending on the LTB load-bearing capacity needs to be considered in the evaluation of the parameter studies on $N_{x,c}$-$M_{y,1}$-interaction of beam-columns with constant bending moment, see Section 6.4.

6.3 Equivalent geometrical imperfections

6.3.1 General

Numerical parameter studies on LTB of beams and flexural buckling of columns with scattering geometrical and structural imperfections were conducted, and equivalent geometrical imperfections for design were determined. GL 24h beams with a constant bending moment and GL 24h columns with an axial compressive force were investigated. The focus was on the beams, as no investigations on the influence of scattering geometrical and structural imperfections on the LTB load-bearing capacity of GL beams were known. The investigations on columns were conducted to create a deeper understanding of the influence of structural and geometrical imperfections, to separate the effects of structural and geometrical imperfections, and to evaluate the results of Blaß [9] and Theiler [154]. The FE model and the FEA are described in Sections 5.3 and 5.6.2. The results are discussed subsequently. All results are given in Annex E.

6.3.2 Results

6.3.2.1 Softwood GL beams

The results of the parameter study were, as outlined in Section 5.6.2, the scattering reduction factors k_{m} for seven slenderness ratios and three height-to-width ratios. Examples of the frequency distributions of k_{m} for scattering geometrical and/or structural imperfections with $H/B = 4$ and $\lambda_{\mathrm{m,rel}} = 1.0$ are displayed in Figures 6.11 to 6.13.

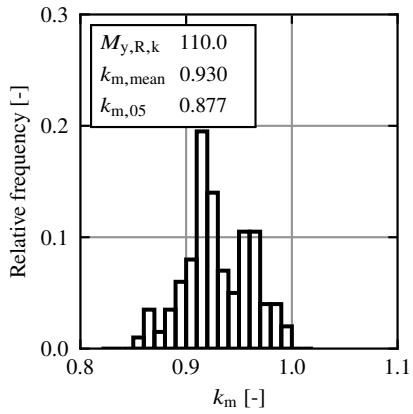

Figure 6.11: Relative frequency distribution of the reduction factor k_{m} from 200 FEAs on GL 24h beams with $H/B = 4$, $\lambda_{\mathrm{m,rel}} = 1.0$, and constant bending moment; with scattering *geometrical imperfections*.

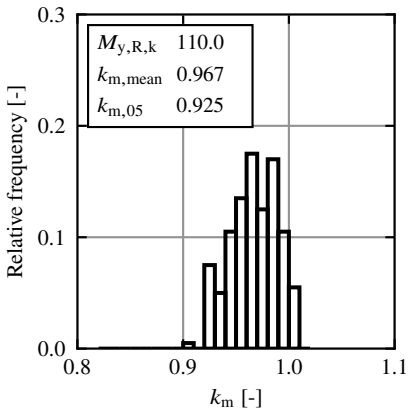

Figure 6.12: Relative frequency distribution of the reduction factor k_{m} from 200 FEAs on GL 24h beams with $H/B = 4$, $\lambda_{\mathrm{m,rel}} = 1.0$, and constant bending moment; with scattering *structural imperfections*.

The characteristic bending load-bearing capacity without LTB according to FEA was $M_{y,R,k}$ = 110.0 kNm. Scattering geometrical imperfections reduced the load-bearing capacity due to LTB by up to 14%, with the 5% quantile value at $k_{m,5}$ = 0.877, see Figure 6.11. The reduction in load-bearing capacity due to scattering structural imperfections was significantly lower, with a 5% quantile value of $k_{m,5}$ = 0.925, see Figure 6.12. For combined scattering geometrical and structural imperfections, see Figure 6.13, $k_{m,5}$ = 0.881 was slightly larger than for purely geometrical imperfections, which is counterintuitive. In other words, structural imperfections that occurred in addition to geometrical imperfections increased the 5% quantile value of the load-bearing capacity in some cases.
A possible cause is illustrated subsequently by an example. In a cross-section where the right half has a lower elastic modulus $E_{0,el}$ than the left half, the shear centre shifts to the left and the beam buckles to the right due to LTB, see Figure 6.14. This LTB leads to a reduction in load-bearing capacity. However, as the right half has a lower stiffness $E_{0,el}$, the lower right cross-sectional corner, which is relevant for the tensile, respectively bending, load-bearing capacity, attracts lower tensile stresses σ_0. This leads to an increase in load-bearing capacity. For beams that had no geometrical imperfections but only structural imperfections, the influence of LTB on the load-bearing capacity dominated in the FEA, and the load-bearing capacity decreased due to LTB, see Figure 6.12. However, if LTB was already triggered by geometrical imperfections, additional structural imperfections apparently did not significantly increase LTB. In contrast, the lower stiffness at the relevant cross-sectional corner reduced the stresses σ_0, which slightly increased the load-bearing capacity, see Figure 6.13 in comparison to Figure 6.11.

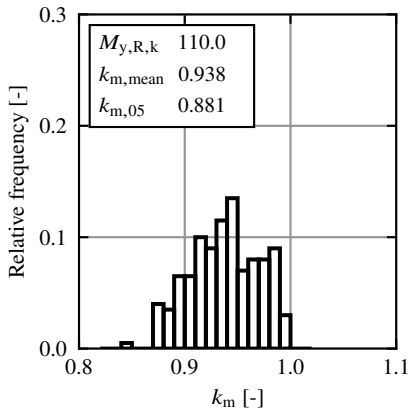

Figure 6.13: Relative frequency distribution of the reduction factor k_m from 200 FEAs on GL 24h beams with $H/B = 4$, $\lambda_{m,rel} = 1.0$, and constant bending moment; with scattering *geometrical and structural imperfections*.

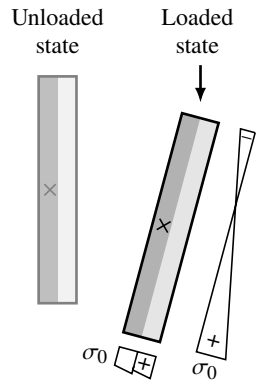

Figure 6.14: Schematic illustration of a cross-section with the influence of a variation of $E_{0,el}$ on the position of the shear centre (×), the LTB behaviour, and the stresses in grain direction σ_0.

Figure 6.15 displays the frequency distributions of the reduction factor k_{m} for scattering geometrical imperfections at $H/B = 4$ as violin plots for the seven investigated relative LTB slenderness ratio $\lambda_{\mathrm{m,rel}}$. The results of all investigated member geometries and scattering geometrical and structural imperfections are given in Annex E.1 and summarised in Table 6.1. k_{m} was determined according to Section 5.6.2. The distribution functions of k_{m}, see Figure 6.11, are plotted as violin plots with 5% quantile values (circles), mean values (middle bars), and 95% quantile values (upper bars). Each violin plot contains the results of 200 FEA. In addition, the results of FEA with bow imperfections of $e_{\mathrm{y,eq}} = L/1000$ and twist imperfections of $e_{\theta,\mathrm{eq}} = 0.5 \cdot (L/1500H_{\mathrm{ap}} + 1/100)$ as equivalent geometrical imperfections are provided. Furthermore, the relative critical bending moment $M_{\mathrm{y,cr}}$ from FEA is given. The relative LTB slenderness ratio $\lambda_{\mathrm{m,rel}}$ was determined according to FprEN 1995-1-1 [69], see Equation (2.80).
The scattering k_{m} values spanned the range between cross-sectional resistance $k_{\mathrm{m}} = 1.0$, the critical bending moment $M_{\mathrm{y,cr}}$, and the typical LTB curve, see Figure 2.4. The influence of imperfections on the load-bearing capacity was largest at $\lambda_{\mathrm{m,rel}} = 1.0$, which was in line with the results of the sensitivity study in Section 5.4.5. The 5% quantile values followed the expected shape of a LTB curve, see Figure 2.4. For $\lambda_{\mathrm{m,rel}} = 1.1$ and 1.2, for a few beams, no significant LTB behaviour occurred before the tensile strength in grain direction was reached because the imperfections were too small.

Table 6.1 summarises the results of all FEAs with scattering imperfections. The relative LTB slenderness ratio $\lambda_{\mathrm{m,rel}}$ was calculated according to EN 1995-1-1 [57] with Equation (2.63)

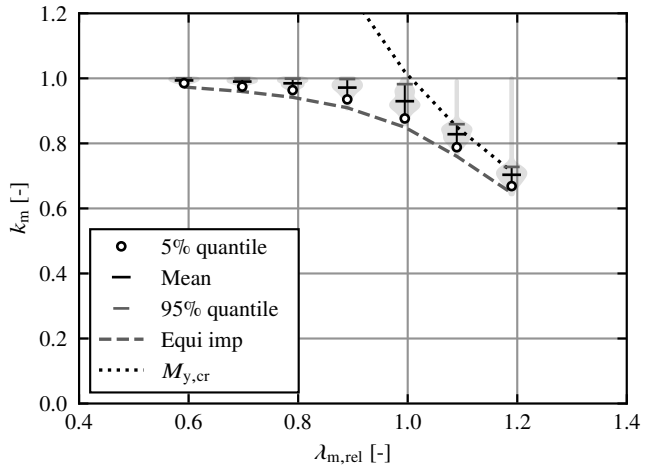

Figure 6.15: Violin plots of the reduction factor k_{m} from FEA on GL 24h beams at seven relative LTB slenderness ratios $\lambda_{\mathrm{m,rel}}$ with $H/B = 4$ and constant bending moment; with scattering *geometrical imperfections*; results of 200 FEAs per violin plot; comparison with critical bending moments $M_{\mathrm{y,cr}}$ from FEA and FEA with equivalent geometrical imperfections (Equi imp).

(EC5) and with numerically determined eigenvalues (FEA). The 5% quantile values of the reduction factor for LTB $k_{m,5}$ were determined from FEA with scattering geometrical imperfections (g), scattering structural imperfections (s), and scattering geometrical and structural imperfections (g+s). The absolute value of the equivalent twist imperfection $e_{\theta,eq}$ and the relative value $e_{\theta,eq}/(e_{\theta,mid,95} + e_{\theta,supp,95})$ calculated according to Section 5.6.2 with $e_{\theta,mid,95}$ and $e_{\theta,supp,95}$ from Section 5.3.4 are given.
For structural imperfections, the reduction in the LTB load-bearing capacity was always lower, and $k_{m,5}$ was higher than for geometrical and combined geometrical and structural imperfections. $k_{m,5}$ for geometrical and combined geometrical and structural imperfections was similar. Thus, structural imperfections acting additionally to geometrical imperfections had no significant effect on the LTB load-bearing capacity. The effect of structural imperfections on the LTB load-bearing capacity can therefore be neglected.
Equivalent twist imperfections $e_{\theta,eq}$ of -9.1% to 51.8% of the sum of the twist imperfections $(e_{\theta,mid,95} + e_{\theta,supp,95})$ were determined in conjunction with an equivalent bow imperfection of $e_{y,eq} = L/1000$. The equivalent twist imperfection $e_{\theta,eq}$ tended to decrease with increasing $\lambda_{m,rel}$ and increasing H/B ratio. For large $\lambda_{m,rel}$ and large H/B ratios, the relative value $e_{\theta,eq}/(e_{\theta,mid,95} + e_{\theta,supp,95})$ was about 0, as the twist imperfections $e_{\theta,mid}$ and $e_{\theta,supp}$ had no significant influence on the load-bearing capacity anymore. Negative equivalent twist imperfections $e_{\theta,eq}$ occurred for large $\lambda_{m,rel}$ and large H/B ratios if the 95% quantile

Table 6.1: Results of the FEAs on softwood GL beams with scattering geometrical and structural imperfections and computed equivalent geometrical imperfections.

H/B	L	$\lambda_{m,rel}$		$k_{m,5}$			$e_{\theta,eq}$	$\frac{e_{\theta,eq}}{e_{\theta,mid,95} + e_{\theta,supp,95}}$
	[mm]	EC5	FEA	g	s	g+s		
4	3450	0.592	0.587	0.985	0.985	0.983	0.00480	0.324
	4800	0.698	0.694	0.974	0.986	0.976	0.00458	0.275
	6150	0.790	0.786	0.964	0.982	0.968	0.00433	0.234
	7800	0.890	0.886	0.935	0.971	0.936	0.00519	0.249
	9750	0.995	0.990	0.877	0.925	0.881	0.00608	0.258
	11700	1.090	1.084	0.788	0.827	0.783	0.00700	0.267
	13950	1.190	1.184	0.669	0.709	0.662	0.00914	0.311
8	2550	0.703	0.655	0.979	0.991	0.977	0.00610	0.518
	3300	0.800	0.761	0.984	0.988	0.984	0.00292	0.238
	4200	0.903	0.871	0.972	0.980	0.972	0.00040	0.031
	5100	0.995	0.969	0.915	0.947	0.908	0.00055	0.041
	6150	1.093	1.071	0.789	0.831	0.789	−0.00058	−0.041
	7350	1.194	1.176	0.666	0.703	0.669	0.00003	0.002
12	3450	0.995	0.906	0.959	0.984	0.944	0.00017	0.015
	4200	1.098	1.022	0.827	0.878	0.816	−0.00020	−0.017
	4950	1.192	1.127	0.708	0.750	0.709	−0.00111	−0.091

EC5 according to FprEN 1995-1-1 [69]
g geometrical imperfections
s structural imperfections
g+s geometrical and structural imperfections

value of the scattering bow imperfections for a specific H/B ratio and $\lambda_{m,rel}$ was by chance lower than $e_{y,eq} = L/1000$.
As the geometrical bow and twist imperfections are independent of each other, see Section 3.2.4.3, the probability that these imperfections are simultaneously larger than $e_{y,95}$, $e_{\theta,mid,95}$, and $e_{\theta,supp,95}$ at a beam is significantly less than 5%. Therefore, when assuming $e_{y,eq} = e_{y,95}$, the equivalent twist imperfections $e_{\theta,eq}$ have to be smaller than the sum $(e_{\theta,mid,95} + e_{\theta,supp,95})$. This is demonstrated by the results of the equivalent twist imperfections $e_{\theta,eq}$ in Table 6.1. The low probability that $e_{y,95}$, $e_{\theta,mid,95}$, and $e_{\theta,supp,95}$ occur simultaneously can be taken into account in the LTB design by reducing the equivalent geometrical imperfections, in this case the equivalent twist imperfections $e_{\theta,eq}$.

For the LTB design of softwood GL beams according to EN 1995-1-1 [57] or FprEN 1995-1-1 [69], the amplitudes of the sinusoidal or parabolic equivalent geometrical imperfections may thus be assumed to be

$$e_{y,eq} = e_{y,eq,95} = \frac{L}{1000} \quad , \tag{6.2}$$

and

$$e_{\theta,eq} = 0.5 \cdot (e_{\theta,mid,95} + e_{\theta,supp,95}) \quad , \tag{6.3}$$

where L is the effective LTB length or the real length of the member, whichever is decisive for the design. $e_{y,eq} = L/1000$ was assumed, as this can be applied for both the LTB design of softwood GL beams and the flexural buckling design of softwood GL columns, see Table 3.3. If deviating bow imperfections are chosen for LTB and flexural buckling design, mechanical inconsistencies for the interaction of axial forces and bending moments cannot be avoided. $e_{\theta,mid,95} = L/1500H_{ap}$ and $e_{\theta,supp,95} = 1/180$ or $1/100$ for low or high tolerances of the fork supports, see also Tables 3.4 and 3.5 and Section 5.3.4. No additional twist imperfections at the supports need to be taken into account in design. The factor 0.5 was chosen on the safe side based on the results in Table 6.1.
For simplification, a pure sinusoidal or parabolic equivalent bow imperfection of

$$e_{y,eq} = \frac{L}{400} \tag{6.4}$$

may be assumed instead of Equations (6.2) and (6.3) for the LTB design of softwood GL beams analogous to EN 1995-1-1 [57], see Figure 6.22.
For pure bending, equivalent geometrical imperfections according to Equations (6.2) and (6.3) or Equation (6.4) lead to similar results, see Figure 6.22. The larger the proportion of the axial compressive force, the more advantageous is the separation of the equivalent geometrical imperfections into bow imperfections and twist imperfections according to Equations (6.2) and (6.3), as twist imperfections do not cause any additional internal forces in the case of axial compressive forces, see Equations (2.1), (2.14), and (2.15).

The 5% quantile values of the reduction factor $k_{m,5}$ from FEA with scattering geometrical imperfections are compared with the results of FEA and calculations using T2O with

equivalent imperfections in Figure 6.16. Calculations using T2O were conducted according to FprEN 1995-1-1 [69], see also Section 2.6.4.1.2. Equivalent bow imperfections and twist imperfections in Equations (6.2) and (6.3) were assumed. For FEA $\lambda_{m,rel,FEA}$ from numerical eigenvalue analyses and for calculations using T2O $\lambda_{m,rel,EC5}$ according to FprEN 1995-1-1 [69], see Equation (2.80), were used. The discrepancy between the relative LTB slenderness ratios $\lambda_{m,rel,EC5}$ and $\lambda_{m,rel,FEA}$ is discussed in Section 6.2.2.
As expected, the relative load-bearing capacity $k_{m,5}$ decreased with increasing slenderness and followed the typical LTB curve, see also Figure 2.4. With increasing H/B ratio, the load-bearing capacity at high slendernesses from FEA slightly decreased, which can also be observed with calculations using T2O. Apart from that, the results of the FEAs with different H/B ratios were similar. The results of FEA with the equivalent imperfection according to Equations (6.2) and (6.3) were similar or slightly on the safe side compared to the 5% quantile values of the reduction factor $k_{m,5}$ from FEA with scattering geometrical imperfections. The same applied to results of calculations using T2O.

6.3.2.2 Softwood GL columns

The results of the parameter study were, as outlined in Section 5.6.2, the scattering load-bearing capacities $N_{x,c,R}$ with and without flexural buckling for seven slenderness ratios and four height-to-width ratios. Examples of the frequency distributions of $N_{x,c,R}$ for $H = 160$ mm and $\lambda_{c,rel} = 1.1$ are displayed in Figures 6.17 to 6.19.
The mean and 5% quantile values of the compressive load-bearing capacity $N_{x,c,R}$ were −943 kN and −836 kN, see Figure 6.17, which were equal to compressive strengths $f_{c,0}$ of

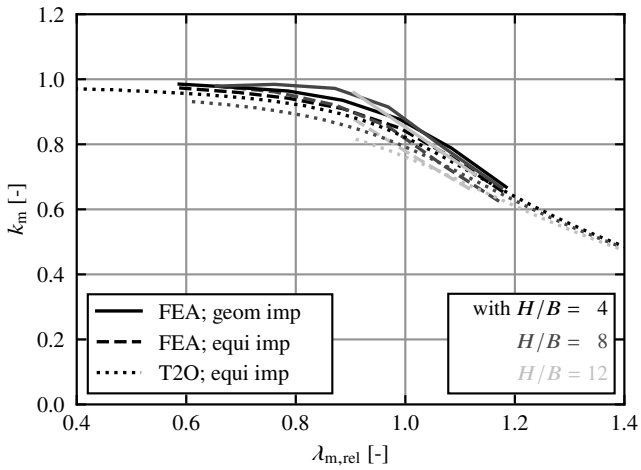

Figure 6.16: 5% quantile values of the reduction factor $k_{m,5}$ from FEA for scattering geometrical imperfections plotted over the relative LTB slenderness ratio $\lambda_{m,rel}$; comparison with FEA and calculations using T2O with equivalent geometrical imperfections; FEA referring to $\lambda_{m,rel,FEA}$ from numerical eigenvalue analyses.

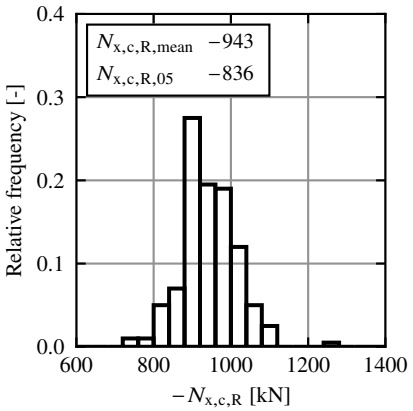

Figure 6.17: Relative frequency distribution of the compressive load-bearing capacity $N_{x,c,R}$ from 200 FEAs on GL 24h columns with H = 160 mm and $\lambda_{c,rel}$ = 1.1; with scattering *structural imperfections*; *without flexural buckling*.

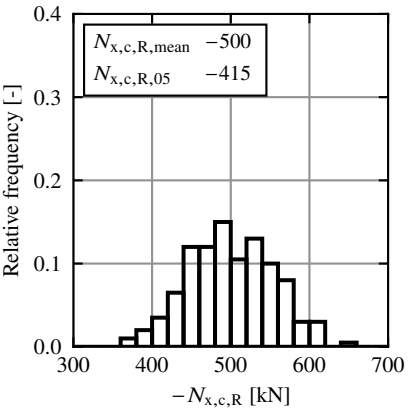

Figure 6.18: Relative frequency distribution of the compressive load-bearing capacity $N_{x,c,R}$ from 200 FEAs on GL 24h columns with H = 160 mm and $\lambda_{c,rel}$ = 1.1; with scattering *structural imperfections*; *with flexural buckling*.

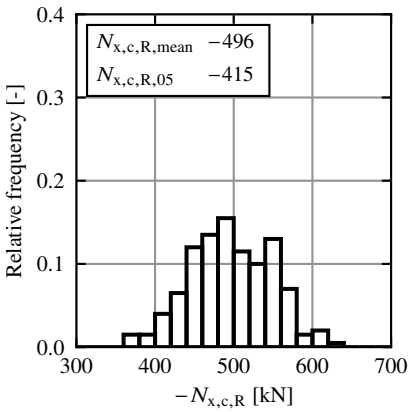

Figure 6.19: Relative frequency distribution of the compressive load-bearing capacity $N_{x,c,R}$ from 200 FEAs on GL 24h columns with H = 160 mm and $\lambda_{c,rel}$ = 1.1; with scattering *geometrical and structural imperfections*; *with flexural buckling*.

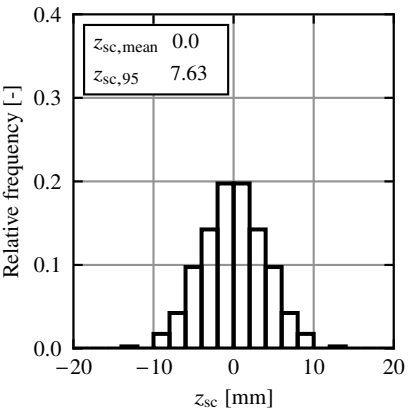

Figure 6.20: Relative frequency distribution of the eccentricity of the shear centre z_{sc} from the input data of the GL 24h columns with H = 160 mm and $\lambda_{c,rel}$ = 1.1; with VIS-2 according to Frese [74].

$-36.8\,\mathrm{N/mm^2}$ and $-32.7\,\mathrm{N/mm^2}$. This is in line with values from literature if considering the negative influence of the size effect due to the higher dimensions compared to compression tests according to EN 408 [60], see Section 2.4.3 and, e.g. Frese et al. [75]. Flexural buckling with scattering geometrical and structural imperfections reduced the load-bearing capacity to $N_{x,c,R,mean} = -496$ kN and $N_{x,c,R,5} = -415$ kN, see Figure 6.19. For purely structural imperfections, the flexural buckling load-bearing capacities were nearly the same, with $N_{x,c,R,mean} = -500$ kN and $N_{x,c,R,5} = -415$ kN, see Figure 6.18. In contrast to the LTB load-bearing capacity in Section 6.3.2.1, the structural imperfections were decisive for the flexural buckling load-bearing capacity.

The frequency distribution of the eccentricity of the shear centre z_{sc} for columns with $H = 160$ mm and $\lambda_{c,rel} = 1.1$ is displayed in Figure 6.20. z_{sc} was calculated with Equation (2.29). As the sign of z_{sc} can be chosen arbitrarily, Figure 6.20 presents the positive and negative values for each z_{sc} determined. This resulted in $2 \cdot 200 = 400$ values and a distribution which is symmetrical around zero.

Figure 6.21 displays the frequency distributions of the compressive load-bearing capacity $N_{x,c,R}$ from FEA with scattering geometrical and structural imperfections and $H = 160$ mm as violin plots for the seven investigated relative flexural buckling slenderness ratios $\lambda_{c,rel}$. Further results are given in Annex E.2. The distribution functions of $N_{x,c,R}$, see Figure 6.21, are plotted as violin plots with 5% quantile values (circles), mean values (middle bars), and 95% quantile values (upper bars). Each violin plot contains the results of 200 FEA.

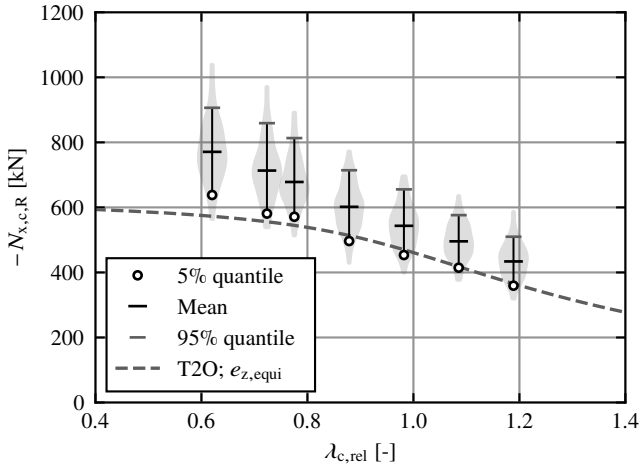

Figure 6.21: Violin plots of the compressive load-bearing resistance $N_{x,c,R}$ from FEA on GL 24h columns at seven relative flexural buckling slenderness ratios $\lambda_{c,rel}$ with $H = 160$ mm; with scattering geometrical and structural imperfections; results of 200 FEAs per violin plot; comparison with design with calculations using T2O with $e_z = L/750$.

In addition, the results of calculations using T2O with characteristic material values and the bow imperfection of $e_z = L/750$ from Figures 2.8 and 2.9 are provided. The relative flexural buckling slenderness ratio $\lambda_{c,rel}$ was calculated according to EN 1995-1-1 [57] with characteristic material values, see Equation (2.60) and Table 5.9. The scattering of $N_{x,c,R}$ was significantly larger than that of k_m in Figure 6.15, as it additionally includes the influence of scattering strengths and stiffnesses. The 5% quantile values followed the expected shape of a flexural buckling curve, see also Figure 2.4, and agreed well with the results of calculations using T2O with a bow imperfection of $e_z = L/750$.

Table 6.2 summarises the results of all FEAs. The relative flexural buckling slenderness ratio $\lambda_{c,rel}$ was calculated according to EN 1995-1-1 [57] with characteristic material values, see Equation (2.60) and Table 5.9. The 5% quantile values of the axial compressive load-bearing capacity without flexural buckling $N_{R,5}$, with flexural buckling and scattering structural imperfections $N_{R,s,5}$, and with flexural buckling and scattering geometrical and structural imperfections $N_{R,g+s,5}$ are given. Furthermore, the 5% quantile values of the reduction factor for flexural buckling $k_{c,5} = N_{R,g+s,5}/N_{R,5}$ and the 95% quantile values of the eccentricity of the shear centre $z_{sc,95}$, see Equation (2.29), are provided. The equivalent bow imperfections $e_{z,eq}$ were determined with two approaches. Firstly, according to Section 5.6.2, $e_{z,eq,kc}$ by comparing the *reduction factor* for flexural buckling from calculations using T2O $k_{c,5,T2O} = N_{R,T2O}/Af_{c,0,k}$ to $k_{c,5}$ from FEA. Secondly, $e_{z,eq,N}$ by comparing the flexural buckling *load-bearing capacity* from calculations using T2O $N_{R,T2O}$ to $N_{R,g+s,5}$ from FEA. Calculations using T2O were conducted according to FprEN 1995-1-1 [69], see Section 2.6.4.1.2. As $N_{R,5}$ from FEA is significantly larger than the characteristic load-bearing capacity $Af_{c,0,k}$ according to EN 1995-1-1 [57] and FprEN 1995-1-1 [69], both methods lead to significantly different equivalent bow imperfections $e_{z,eq}$. The difference in the realistic load-bearing capacity from FEA and the characteristic load-bearing capacity according to EN 1995-1-1 [57] and FprEN 1995-1-1 [69] stems from the systematic underestimation of the characteristic compressive strength in grain direction $f_{c,0,k}$ of softwood GL in SC 1 in EN 14080 [54], see Frese [74] and Schilling et al. [141]. Thus, the second approach considers the positive effect of the underestimation of the characteristic compressive strength of GL 24h in SC 1 in EN 14080 [54].
As expected, the absolute and the relative load-bearing capacities $N_{R,s,5}$, $N_{R,g+s,5}$, and $k_{c,5}$ decreased with increasing slenderness and followed the typical flexural buckling curve, see also Figure 2.4. The differences of the load-bearing capacity due to geometrical and structural imperfections $N_{R,g+s,5}$ to the load-bearing capacity due to structural imperfections $N_{R,s,5}$ were negligibly small. Thus, geometrical imperfections acting additionally to structural imperfections had no significant effect on the flexural buckling load-bearing capacity. The effect of geometrical imperfections on the flexural buckling load-bearing capacity of pinned columns can therefore be neglected.
The eccentricity of the shear centre $z_{sc,95}$ tended to decrease with increasing column length L and increased subproportionally with increasing cross-sectional height H. The former can be attributed to the lamination effect. Similar effects could not be observed for $k_{c,5}$ and $e_{z,eq,kc}$. $e_{z,eq,N}$ even tended to increase with increasing column length L.
While $k_{c,5}$ led to large equivalent bow imperfections $e_{z,eq,kc}$ with a median value of $L/181$, $N_{R,g+s,5}$ led to significantly smaller equivalent bow imperfections $e_{z,eq,N}$ with a median

Table 6.2: Results of the FEAs on softwood GL columns with scattering geometrical and structural imperfections and computed equivalent geometrical imperfections.

H [mm]	L [mm]	$\lambda_{c,rel}$	$N_{R,5}$	$N_{R,s,5}$	$N_{R,g+s,5}$	$k_{c,5}$	$z_{sc,95}$ [mm]	$e_{z,eq,kc}$ [mm]	$e_{z,eq,N}$ [mm]
120	1350	0.620	−487	−357	−357	0.732	8.07	$L/149$	N/A
	1500	0.689	−488	−344	−344	0.704	7.29	$L/158$	$L/12{,}500$
	1800	0.827	−495	−304	−304	0.614	6.75	$L/153$	$L/870$
	1950	0.896	−477	−290	−288	0.605	7.41	$L/181$	$L/810$
	2250	1.034	−460	−243	−243	0.527	6.44	$L/188$	$L/624$
	2400	1.103	−471	−227	−223	0.473	7.02	$L/172$	$L/609$
	2550	1.172	−444	−204	−206	0.463	6.43	$L/206$	$L/639$
160	1800	0.620	−875	−638	−638	0.729	8.27	$L/146$	N/A
	2100	0.724	−874	−581	−581	0.665	9.29	$L/144$	$L/1390$
	2250	0.775	−817	−572	−571	0.699	7.60	$L/199$	$L/1310$
	2550	0.879	−835	−499	−497	0.594	8.30	$L/162$	$L/593$
	2850	0.982	−832	−454	−454	0.545	9.25	$L/175$	$L/602$
	3150	1.085	−836	−415	−415	0.496	7.63	$L/187$	$L/714$
	3450	1.189	−817	−359	−359	0.440	8.45	$L/186$	$L/662$
200	2100	0.579	−1370	−1080	−1080	0.787	8.88	$L/177$	N/A
	2550	0.703	−1350	−1000	−1000	0.744	8.77	$L/201$	N/A
	2850	0.786	−1310	−919	−919	0.700	8.89	$L/206$	$L/2360$
	3300	0.910	−1380	−837	−836	0.605	8.63	$L/189$	$L/1280$
	3600	0.992	−1380	−754	−750	0.545	8.34	$L/181$	$L/939$
	4050	1.116	−1290	−647	−646	0.502	8.44	$L/218$	$L/926$
	4350	1.199	−1270	−587	−583	0.459	8.41	$L/224$	$L/995$
240	2550	0.586	−1930	−1460	−1450	0.748	10.76	$L/146$	N/A
	3000	0.689	−2030	−1410	−1410	0.697	10.38	$L/152$	N/A
	3450	0.793	−1910	−1240	−1240	0.648	9.19	$L/163$	$L/899$
	3900	0.896	−1980	−1180	−1180	0.596	9.47	$L/173$	$L/985$
	4350	0.999	−1860	−1020	−1020	0.547	9.17	$L/187$	$L/653$
	4800	1.103	−1940	−948	−943	0.486	8.73	$L/186$	$L/899$
	5250	1.206	−1860	−805	−800	0.431	9.48	$L/186$	$L/724$
							Median	$L/181$	$L/885$

s Structural imperfections.
g+s Geometrical and structural imperfections.
N/A Not available as some $N_{R,g+s,5}$ fell below $f_{c,0,k} = -24.0$ N/mm^2.

value of $L/885$. The first approach with $k_{c,5}$ yields the same reduction factor $k_{c,5}$ in FEA and calculations using T2O, but the flexural buckling load-bearing capacity in SC 1 is significantly underestimated in calculations using T2O when assuming $f_{c,0,k}$ from EN 14080 [54] and $e_{z,eq,kc}$. The second approach with $N_{R,g+s,5}$ yields the same flexural buckling load-bearing capacity in FEA and calculations using T2O with $f_{c,0,k}$ from EN 14080 [54] and $e_{z,eq,N}$, but the reduction factor $k_{c,5}$ is significantly underestimated in calculations using T2O. This difference in the equivalent bow imperfections between the two evaluation methods is caused by the mentioned underestimation of $f_{c,0,k}$ of GL 24h in SC 1 in EN 14080 [54].

When considering the positive effect of the underestimation of the characteristic compressive strength of softwood GL in SC 1 in EN 14080 [54], the flexural buckling design of softwood GL columns according to EN 1995-1-1 [57] or FprEN 1995-1-1 [69] may be conducted with sinusoidal or parabolic equivalent bow imperfection with an amplitude of

$$e_{z,eq} \approx \frac{L}{600} \quad \text{to} \quad \frac{L}{1000} \quad , \tag{6.5}$$

where L is the column length.

6.3.3 Discussion

6.3.3.1 General

Section 6.3.3 combines the results of own measurements and FEA from Sections 6.3 and 3.2 with the literature review from Section 2.2.3.

6.3.3.2 Softwood GL beams

Investigations regarding imperfections of GL beams were rare and limited to a few measurements of geometrical imperfections, see Brüninghoff [20], Dietsch and Henke [34], Wilden et al. [175], and Section 2.2.3.2. No investigations on structural imperfections of GL beams were known. It is generally assumed that, due to the lamination effect, the influence of geometrical imperfections far outweighs the influence of structural imperfections on the LTB load-bearing capacity. But this assumption still needed to be confirmed.
The equivalent bow imperfection of $e_{y,eq} = L/400$ in EN 1995-1-1 [57] is probably based on engineering judgement supported by imperfection measurements on one building by Brüninghoff [20], see Section 2.2.3.

For the first time, this thesis presents results of analyses on the influence of scattering geometrical and structural imperfections on the LTB load-bearing capacity of GL beams, see Section 6.3.2.1. The assumption that structural imperfections can be neglected in the presence of geometrical imperfections was confirmed, see Figures 6.11 and 6.13. Equivalent geometrical imperfections were determined that allow for a reliable and economic design within the design methods of EN 1995-1-1 [57] and FprEN 1995-1-1 [69], see Equations (6.2) to (6.4). For consistency with the flexural buckling design of softwood GL columns, the same equivalent bow imperfection was chosen for the LTB design of softwood GL beams, namely $e_{y,eq} = L/1000$. Otherwise, mechanical inconsistencies for combined bending and axial compression could not have been avoided. The equivalent bow imperfection of $e_{y,eq} = L/400$ in EN 1995-1-1 [57] leads for pure bending to similar results as the combined equivalent bow and twist imperfections in Equations (6.2) and (6.3) and can therefore be utilised as a simplification in design. For combined bending and axial compression, the separation of the equivalent geometrical imperfections into bow imperfections and twist imperfections is beneficial in design.

Similar to steel structures, see Taras [153] and Section 2.2.2.8, the equivalent twist imperfections in Table 6.1 were not proportional to the length, and, therefore, the assumption of an equivalent geometrical imperfection depending linearly on the length leads to a non-constant reliability over the length. However, the effect of this on the load-bearing capacity was small.

Figure 6.22 presents the comparison of design with these novel equivalent geometrical imperfections and the results of the FEAs for $H/B = 4$. The design was carried out with calculations using T2O according to FprEN 1995-1-1 [69], see Equations (2.15), (2.54), and (2.55), and the equivalent geometrical imperfections in Equations (6.2) and (6.3) or Equation (6.4). Furthermore, calculations were carried out with the k_m-methods in EN 1995-1-1 [57] and FprEN 1995-1-1 [69], see Sections 2.6.2.1.4 and 2.6.4.1.4, and the same equivalent geometrical imperfections. $M_{\mathrm{y,cr}}$ was determined with Equation (2.17).
The results of the k_m-methods and calculations using T2O were similar to the results of the FEAs but slightly on the safe side. The k_m-method from FprEN 1995-1-1 [69] better agreed with the calculations using T2O than the k_m-method from EN 1995-1-1 [57]. The remaining differences highlight the still present inaccuracies of the regression model of the k_m-method in FprEN 1995-1-1 [69]. The differences between calculations using T2O and FEA were partly due to the inaccuracies of the relative LTB slenderness ratio $\lambda_{\mathrm{m,rel}}$ according to FprEN 1995-1-1 [69], see Section 6.2.2.

With the novel equivalent geometrical imperfections, a reliable and economic design of softwood GL beams with the design methods of EN 1995-1-1 [57] and FprEN 1995-1-1

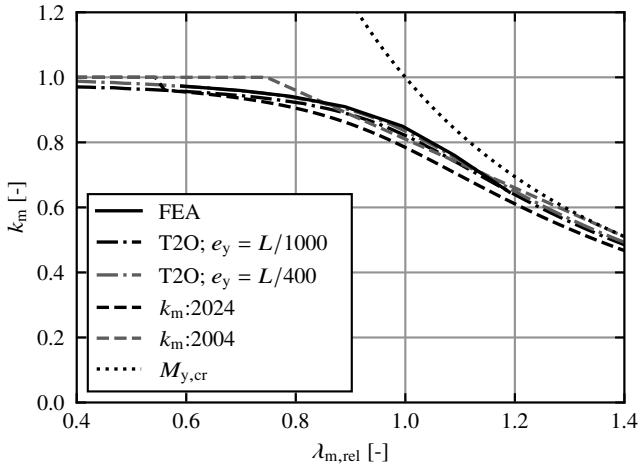

Figure 6.22: Reduction factor k_m from FEA with equivalent geometrical imperfections plotted over the relative LTB slenderness ratio $\lambda_{\mathrm{m,rel}}$; comparison results of the k_m-methods from EN 1995-1-1 [57] and FprEN 1995-1-1 [69] and design with calculations using T2O according to FprEN 1995-1-1 [69]; with $H/B = 4$.

[69] can be conducted. For the first time, equivalent geometrical imperfections of softwood GL beams are available that are based on a sound database of measured geometrical imperfections, see Section 3.2, and comprehensive FEA with scattering structural and geometrical imperfections, see Sections 5.3.4, 5.3.3, 5.6.2, and 6.3.2.1.

6.3.3.3 Softwood GL columns

From the literature, calculations with structural and geometrical imperfections on softwood GL columns by Blaß [9] and Theiler [154], measurements of structural imperfections of softwood GL columns by Theiler [154], and measurements of geometrical imperfections of softwood GL columns by Blaß [9] were known, see also Section 2.2.3.
The equivalent bow imperfection of $e_{y,eq} = L/400$ in EN 1995-1-1 [57] is probably based on engineering judgement supported by imperfection measurements on the GL beams of one building by Brüninghoff [20], see Section 2.2.3, and is inconsistent with the equivalent bow imperfection of $e_{y,eq} \approx L/1000$ implicitly considered in the β_c factor of the k_c-method, see Section 2.2.1.8.

For the first time, this thesis presents results of explicit investigations of the influence of structural imperfections on the flexural buckling load-bearing capacity of softwood GL columns, Section 6.3.2.2.
The frequency distribution of the shear centre z_{sc} in Figure 6.20 was similar to the values determined by Theiler [154], see Figure 2.39 and Section 2.2.3.3. The maximum value determined by [154], $z_{sc,max} = 8.3$ mm, was also similar to the 95% quantile values $z_{sc,95}$ in own analyses, see Table 6.2. The implemented *KaReMo* thus yielded meaningful results for the scattering of the eccentricity of the shear centre and thus of the structural imperfections.
A significant part of the calculated equivalent bow imperfections in Table 6.2 can be attributed to the negative influence of stiffness reduction due to compressive plasticising in grain direction, as discussed at Figures 6.47 and 6.48. The equivalent bow imperfections in Table 6.2 thus include the influence of geometrical imperfections, structural imperfections, and compressive plasticising.
Similar to steel structures, see Taras [153] and Section 2.2.1.8, the equivalent bow imperfections in Table 6.2 were not proportional to the length, and, therefore, the assumption of an equivalent bow imperfection depending linearly on the length leads to a non-constant reliability over the length. However, the effect of this on the load-bearing capacity was small.

Figure 6.23 presents the comparison of own FEA results to calculation results of Blaß [9] and Theiler [154]. [9] conducted investigations on softwood GL columns with the old glued laminated timber grade II, 7 lamellas of 30 mm height each, and scattering geometrical and structural imperfections. [154] conducted investigations on softwood GL 24h columns, 4 lamellas of 40 mm height each, and scattering structural imperfections. [154] neglected geometrical imperfections. In addition, the results of calculations using T2O with characteristic material values and a bow imperfection of $e_z = L/1000$ are provided.
As [154] neglected the geometrical imperfections, the 5% quantile values [154] determined were similar to own FEA but slightly higher, and the mean values [154] determined were significantly higher. The 5% quantile values of [9] were 10% to 15% higher than the results

of own FEA, which was already observed by [154]. The reason was unclear.

Figure 6.24 presents the comparison of design according to EN 1995-1-1 [57] and FprEN 1995-1-1 [69] and the results of own FEA. The design was carried out with calculations using T2O according to FprEN 1995-1-1 [69], see Equations (2.1) and (2.54), and a bow imperfection of $e_z = L/1000$. Furthermore, calculations were carried out with the k_c-method in EN 1995-1-1 [57], see Section 2.6.2.1.3. N_{cr} was determined with Equation (2.17).
For $\lambda_{c,rel} > 0.8$, the results of the k_c-method and calculations using T2O were slightly larger than the results of the own FEA, because the bow imperfection of $L/1000$ was slightly more favourable than the equivalent geometrical imperfections determined in this thesis, see Table 6.2. The bow imperfection for GL contained in $\beta_c = 0.1$ of the k_c-method corresponds approximately to $L/1000$ in comparative calculations with T2O, see Figures 2.8 and 2.9. For $\lambda_{c,rel} < 0.8$, the load-bearing capacities of the k_c-method and calculations using T2O were lower than the results of own FEA because the characteristic compressive $f_{c,0,k}$ strength for GL 24h according to EN 14080 [54], 24.0 N/mm^2, was significantly lower than $f_{c,0,5} = 32.7$ N/mm^2 from the FEA, see Section 6.3.2.2.

The equivalent geometrical imperfection of $e_z = L/1000$ in FprEN 1995-1-1 [69], which is also included in $\beta_c = 0.1$ of the k_c-method in EN 1995-1-1 [57], might thus be slightly too small for flexural buckling design of softwood GL columns. A somewhat more conservative value of $L/750$ might be preferred, see Section 6.3.2.2. However, smaller structural

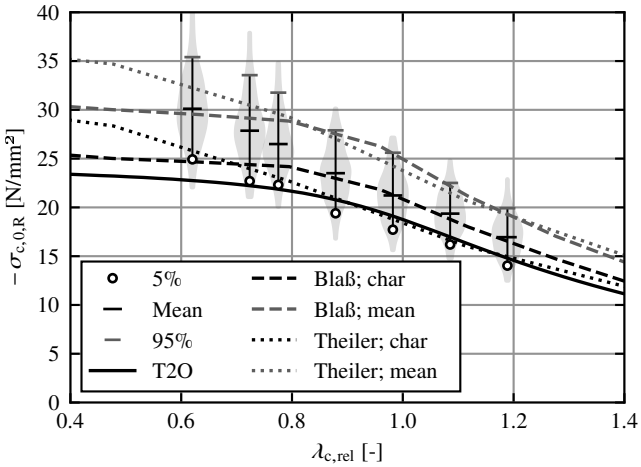

Figure 6.23: Violin plots of the compressive resistance $\sigma_{c,0,R}$ from FEA on GL 24h columns with scattering geometrical and structural imperfections at seven relative flexural buckling slenderness ratios $\lambda_{c,rel}$ with $H = 160$ mm; results of 200 FEAs per violin plot; comparison with results of Blaß [9] and Theiler [154] and design with calculations using T2O with $e_z = L/1000$.

imperfections are to be expected for the larger columns that are common in building practice. Furthermore, $\beta_c = 0.1$ is established in building practice and no comprehensive measurements of actual structural imperfections were known. In this sense, and given the small difference in load-bearing capacity between $e_z = L/1000$ and $L/750$ of < 5% and the consistency with the equivalent bow imperfection for LTB design of beams, it seems reasonable to retain $e_z = L/1000$ and $\beta_c = 0.1$ for the design of softwood GL columns.

The variation of $k_{c,5}$, $z_{sc,95}$, $e_{z,eq,kc}$, and $e_{z,eq,N}$ in Table 6.2 between different relative flexural buckling slenderness ratios $\lambda_{c,rel}$ demonstrates that a higher consistency might have been reached with more than 200 FEAs. However, given the limitations of the computation times and that the investigations of the flexural buckling load-bearing capacity were not the main objective but rather a by-product of this thesis, it was not possible to significantly expand the number of FEAs.

6.3.4 Summary

Numerical parameter studies on LTB of beams and flexural buckling of columns with scattering geometrical according to own measurement results, see Section 3.2, and structural imperfections with a model partly developed in this thesis, see Section 5.3.3, were conducted, and equivalent geometrical imperfections for design were determined.

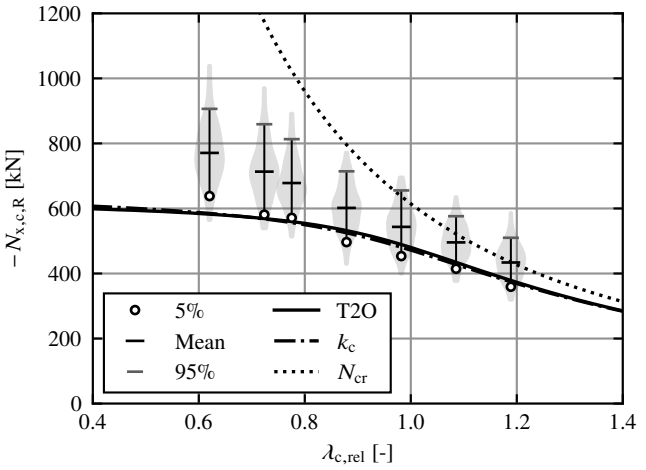

Figure 6.24: Violin plots of the compressive load-bearing capacity $N_{x,c,R}$ from FEA on GL 24h columns with scattering geometrical and structural imperfections at seven relative flexural buckling slenderness ratios $\lambda_{c,rel}$ with $H = 160$ mm; results of 200 FEAs per violin plot; comparison results of the k_c-method from EN 1995-1-1 [57] and design with calculations using T2O with $e_z = L/1000$.

Scattering geometric and structural imperfections cause significant scattering of the LTB and flexural buckling load-bearing capacity of timber beam-columns, see Figures 6.15 and 6.21. For LTB of softwood GL beams, the geometrical imperfections were decisive, and the structural imperfections could be neglected, see Table 6.1. For flexural buckling of pinned softwood GL columns, the structural imperfections were decisive, and the geometrical imperfections did not cause any significant additional reduction in load-bearing capacity, see Table 6.2. The different influence of geometrical and structural imperfections is due to the larger number of lamellas in GL beams compared to columns. Furthermore, the flatwise bending of the lamellas that occurs in flexural buckling of columns is significantly more negative in terms of structural imperfections than the edgewise bending of the lamellas that occurs in LTB of beams, as the elastic modulus $E_{0,\mathrm{el}}$ varies more between different lamellas than across the width of a lamella, see Figure 5.6 and Equation (5.4).
The results of the FEAs on softwood GL columns agreed well with the results of measurements and calculations by Theiler [154], see Figure 6.23. The agreement with the calculation results by Blaß [9] was less good. The reason was unclear.

From the FEA results, equivalent geometrical imperfections were derived, which allow for a reliable and economical design of softwood GL beams, see Equations (6.2) to (6.4). The design approaches for columns in EN 1995-1-1 [57] and FprEN 1995-1-1 [69] were confirmed, see Section 6.3.2.2. These design recommendations have been incorporated into FprEN 1995-1-1 [69].
The findings are summarised in the design proposals for standardisation in Section 7.

6.4 $N_{x,c}$-$M_{y,1}$-interaction

6.4.1 General

Numerical parameter studies on timber beam-columns with varying input parameters were conducted to investigate the $N_{x,c}$-$M_{y,1}$-interaction for flexural buckling and LTB. Varying cross-sectional height-to-width ratios, member lengths, materials, and loadings were analysed.
The FE model and the FEA are described in Sections 5.3 and 5.6.3. The results are discussed subsequently. All results are given in Annex F.

6.4.2 Results

6.4.2.1 General

In general, tensile failure was the decisive failure mode. Shear failure due to shear forces and torsion was only decisive for certain cross-sectional dimensions and loadings. As the focus of this thesis was on tensile failure, beam-columns with such a failure behaviour are discussed in detail in Sections 6.4.2.2 to 6.4.2.4. The implications of shear failure are discussed in Section 6.4.2.5.

6.4.2.2 Influence of the slenderness and the axial compressive force

Figures 6.25 to 6.28 display the reduction factor of the load-bearing capacity k_m from FEA on GL 24h beam-columns with a constant bending moment and four H/B ratios plotted over the relative slenderness ratio $\lambda_{c,rel}$ or $\lambda_{m,rel}$. Additionally, Figures 6.29 to 6.32 display the reduction factors of the load-bearing capacity k_c and k_m from FEA on GL 24h beam-columns with a constant bending moment and four H/B ratios plotted over the length L. The evaluation of the FEA was carried out without considering shear failure. k_c, k_m, $\lambda_{c,rel}$, and $\lambda_{m,rel}$ were calculated with Equations (6.6), (6.1), (2.60), and (2.80). $\mu_c = N_{x,c}/N_{x,c,R}$ is the utilisation ratio the compressive load-bearing capacity with flexural buckling $N_{x,c,R}$, where $N_{x,c}$ is the applied axial compressive force. For $H/B = 1$, k_m is plotted over $\lambda_{c,rel}$ as flexural buckling occurred. For $H/B \geq 2$, k_m is plotted over $\lambda_{m,rel}$ as the $N_{x,c}$-$M_{y,1}$-interaction characteristic of LTB occurred. Due to the realistically chosen member dimensions, only a part of the investigated relative slenderness ratio is covered for each H/B ratio.
For $H/B = 1$, a pronounced compressive plasticising in the grain direction occurred at $\lambda_{c,rel} = 0.3$, which increased the bending load-bearing capacity k_m if an axial compressive force acted simultaneously, see Figure 6.25. For increasing L and $\lambda_{c,rel}$, the influence of plasticising decreased because the compressive forces decreased due to the decreasing critical flexural buckling loads N_{cr}, see Figures 6.25 and 6.29. For $\lambda_{c,rel} \geq 1.0$ to 1.5, k_m was no longer significantly influenced by $\lambda_{c,rel}$, see Figure 6.25. The compressive load-bearing capacity k_c was always influenced by L and $\lambda_{c,rel}$, see Figure 6.29.
For $H/B \geq 2$, a pronounced compressive plasticising in the grain direction occurred at $\lambda_{m,rel} = 0.3$, which increased the bending load-bearing capacity k_m if an axial compressive

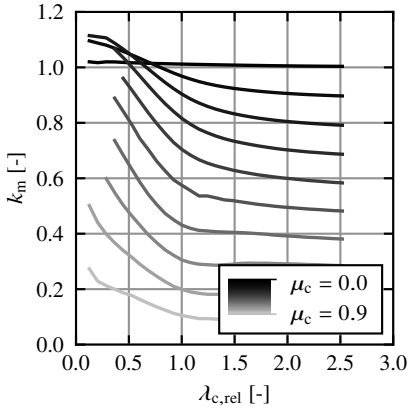

Figure 6.25: Reduction of the load-bearing capacity k_m from FEA plotted over the relative flexural buckling slenderness ratio $\lambda_{c,rel}$ for different utilisation ratios μ_c; with a constant bending moment, GL 24h, $H/B = 1$.

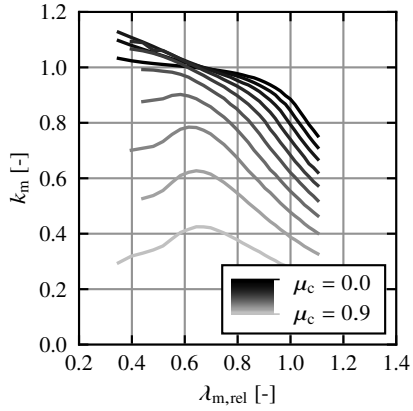

Figure 6.26: Reduction of the load-bearing capacity k_m from FEA plotted over the relative LTB slenderness ratio $\lambda_{m,rel}$ for different utilisation ratios μ_c; with a constant bending moment, GL 24h, $H/B = 4$.

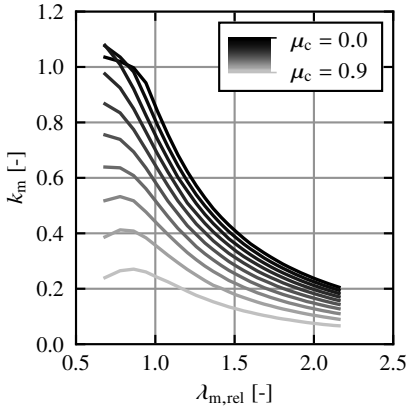

Figure 6.27: Reduction of the load-bearing capacity k_m from FEA plotted over the relative LTB slenderness ratio $\lambda_{m,rel}$ for different utilisation ratios μ_c; with a constant bending moment, GL 24h, $H/B = 8$.

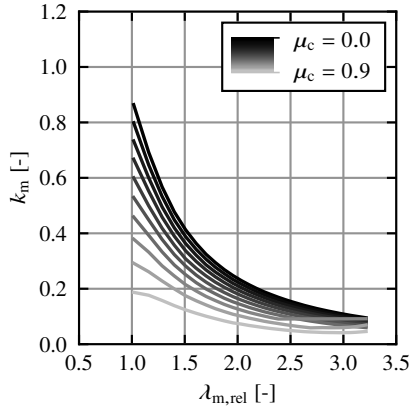

Figure 6.28: Reduction of the load-bearing capacity k_m from FEA plotted over the relative LTB slenderness ratio $\lambda_{m,rel}$ for different utilisation ratios μ_c; with a constant bending moment, GL 24h, $H/B = 12$.

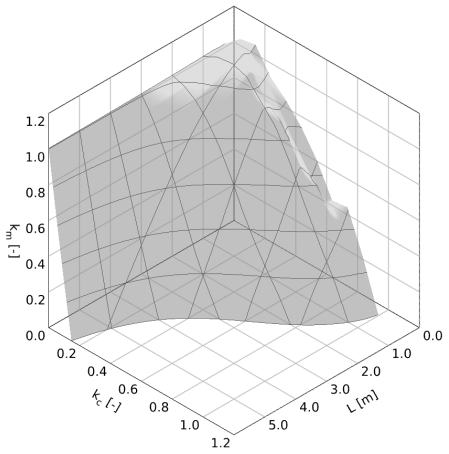

Figure 6.29: Reductions of the load-bearing capacity k_c and k_m from FEA plotted over the member length L; with a constant bending moment, GL 24h, $H/B = 1$.

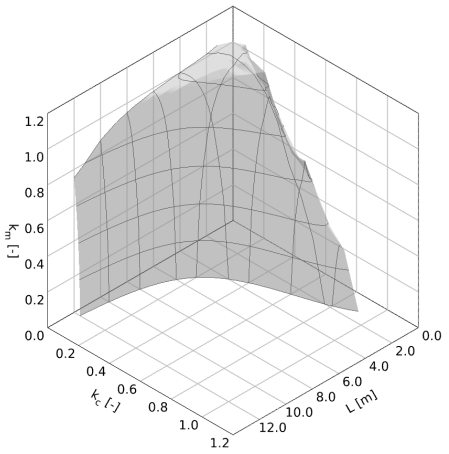

Figure 6.30: Reductions of the load-bearing capacity k_c and k_m from FEA plotted over the member length L; with a constant bending moment, GL 24h, $H/B = 4$.

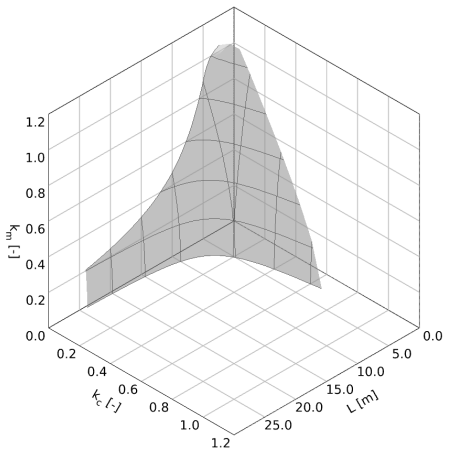

Figure 6.31: Reductions of the load-bearing capacity k_c and k_m from FEA plotted over the member length L; with a constant bending moment, GL 24h, $H/B = 8$.

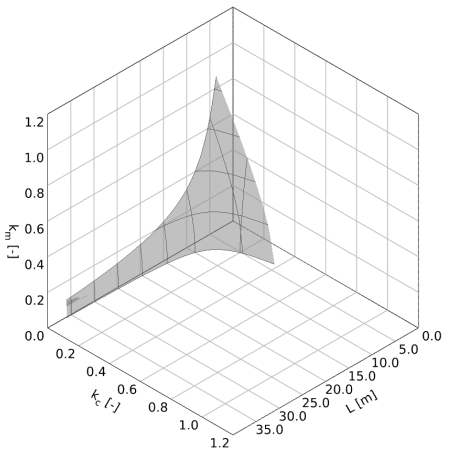

Figure 6.32: Reduction of the load-bearing capacity k_c and k_m from FEA plotted over the member length L; with a constant bending moment, GL 24h, $H/B = 12$.

force acted simultaneously, see Figure 6.26. For increasing $\lambda_{m,rel}$, the influence of plasticising decreased, which partly reduced k_m, see Figures 6.26 and 6.30. With increasing slenderness, this effect was superimposed by the increasing influence of the nonlinear interaction relationship of the critical load, see Section 4.3. Thus, despite decreasing plasticising, there was sometimes an increase in k_m at high μ_c with a peak between $\lambda_{m,rel} = 0.5$ and 0.8, see Figure 6.26. For $\lambda_{m,rel} \geq 0.7$, the k_m-curves followed the known shape of LTB curves, compare Figures 6.26 to 6.28 and Figures 6.30 to 6.32 with Figure 2.4. The k_c-curves always followed the known shape of flexural buckling curves, compare Figures 6.29 to 6.32 with Figure 2.4.

Figures 6.33 and 6.34 display two typical $N_{x,c}$-$M_{y,1}$-interaction diagrams for $H/B = 1$ and 4, GL 24h, a constant bending moment, and varying slendernesses $\lambda_{c,rel}$ and $\lambda_{m,rel}$. The evaluation of the FEA was carried out without considering shear failure. The compressive utilisation ratio $\mu_c = N_{x,c}/N_{x,c,R}$ is plotted over the bending utilisation ratio $\mu_m = M_{y,1}/M_{y,1,R}$. Where $N_{x,c}$ is the applied axial compressive force, $N_{x,c,R}$ is the compressive load-bearing capacity with flexural buckling if only axial compressive forces (no bending moments) are applied, $M_{y,1}$ is the applied bending moment, and $M_{y,1,R}$ is the bending load-bearing capacity with lateral torsional buckling if only bending moments (no axial compressive forces) are applied. This representation makes allows to analyse the change in the $N_{x,c}$-$M_{y,1}$-interaction relationship. At $H/B = 1$, the linear interaction is plotted additionally, i.e. $\mu_c + \mu_m = 1$. Furthermore, the slenderness, for which the bending load-bearing capacities are at most 10% larger than the linear interaction, is highlighted.

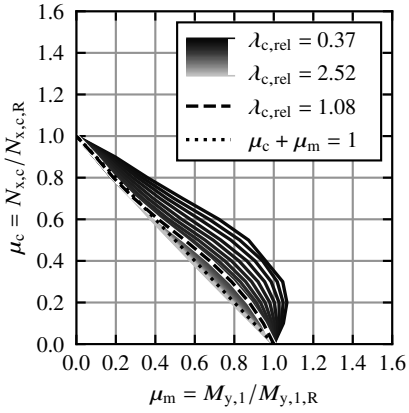

Figure 6.33: Compressive utilisation ratio $\mu_c = N_{x,c}/N_{x,c,R}$ plotted over the bending utilisation ratio $\mu_m = M_{y,1}/M_{y,1,R}$ for different relative flexural buckling slenderness ratios $\lambda_{c,rel}$; GL 24h, constant bending moment, $H/B = 1$.

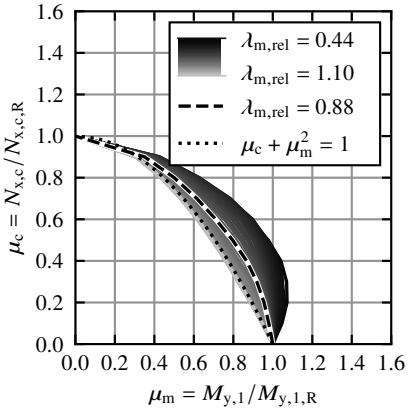

Figure 6.34: Compressive utilisation ratio $\mu_c = N_{x,c}/N_{x,c,R}$ plotted over the bending utilisation ratio $\mu_m = M_{y,1}/M_{y,1,R}$ for different relative LTB slenderness ratios $\lambda_{m,rel}$; GL 24h, constant bending moment, $H/B = 4$.

Above this slenderness, the influence of compressive plasticising on the load-bearing capacity is less than 10% and thus no longer significant. For $H/B \geq 2$, the quadratic interaction is plotted additionally, i.e. $\mu_c + \mu_m^2 = 1$. Furthermore, the slenderness, for which the bending load-bearing capacities are at most 10% larger than the quadratic interaction, is highlighted. Above this slenderness, the influence of compressive plasticising on the load-bearing capacity is less than 10% and thus no longer significant.
For $H/B = 1$, a distinctly nonlinear $N_{x,c}$-$M_{y,1}$-interaction occurred at $\lambda_{c,rel} \approx 0.3$, see Figure 6.33. This nonlinearity of the interaction was particularly pronounced at moderate axial compressive forces and was caused by compressive plasticising in grain direction. With increasing slenderness, the nonlinearity of the interaction decreased until the interaction was almost linear at minimum slendernesses of $\lambda_{c,rel} = 0.79$ (GL75) to 1.08 (GL 24h), see Figures 6.33, F.61, and F.79. For large slendernesses, the compressive load capacities were so low due to the low critical axial compressive forces that no (significant) plasticising occurred, see Figure 6.25, which forced the linearity of the interaction.
For $H/B \geq 2$, the interaction was always distinctly nonlinear, see Figure 6.34. For small slendernesses, the same nonlinear behaviour occurred as for $H/B = 1$ due to compressive plasticising in grain direction. With increasing slenderness, the superposition of the influence of compressive plasticising (materially nonlinear behaviour) and the geometrically nonlinear LTB behaviour, see Section 4.3, resulted in a slight increase in nonlinearity. Subsequently, the nonlinearity decreased and approached the limit of the critical load from Equation (4.10), which was reached at a minimum slendernesses of $\lambda_{m,rel} = 0.60$ (GL75) to 0.88 (GL 24h), see Figure 6.34 and Annex F.3. The load-bearing capacity of the slender beam-columns was equal to the critical load. The nonlinearity of the interaction relationship due to compressive plasticising in the case of stocky members was larger than the nonlinearity due to the geometrically nonlinear LTB behaviour in the case of slender members.
While compressive plasticising in grain direction has a more pronounced effect at low μ_c, the influence of the nonlinear interaction of the critical load is more pronounced at high μ_c. Thus, in the first case, the curvature of the interaction curves is orientated in the direction of the horizontal axis, and, in the second case, in the direction of the vertical axis of Figures 6.33 and 6.34.

6.4.2.3 Influence of the type of loading

Figures 6.35 to 6.36 display the reduction factor of the LTB load-bearing capacity k_m from FEA on GL 24h beam-columns with a constant bending moment (M), a uniform line load (q), and a concentrated load (F) and $H/B = 4$ and 8 plotted over the relative LTB slenderness ratio $\lambda_{m,rel}$. The evaluation of the FEA was carried out without considering shear failure. μ_c is the utilisation ratio the compressive load-bearing capacity with flexural buckling. k_m and $\lambda_{m,rel}$ were calculated with Equations (6.1) and (2.80).
For beam-columns subjected to shear forces with $L/H < 6$, there was a significant drop of the load-bearing capacity due to significant cross-sectional warping, which is discussed in Section 6.2.1, see Figures 6.35 to 6.36. For beam-columns with a constant bending moment, this behaviour did not occur due to the lack of shear stresses from shear forces. For beam-columns subjected to shear forces with $\lambda_{m,rel}$ between about 1.0 and 1.5 and

low μ_c, a reduction in shear stiffness due to shear plasticising occurred, which reduced the load-bearing capacity by up to 20%, see Figure 6.36.

Generally, the $N_{x,c}$-$M_{y,1}$-interaction was a bit more unfavourable for a constant bending moment than for the other loadings, see Annex F. This might have been due to the different stress distributions and the resulting different stiffness reductions caused by compressive plasticising.

6.4.2.4 Influence of the material

Figures 6.37 and 6.38 display two typical $N_{x,c}$-$M_{y,1}$-interaction diagrams for $H/B = 4$, GL 30c and GL75, a constant bending moment, and varying slendernesses $\lambda_{m,rel}$. The evaluation of the FEA was carried out without considering shear failure. The compressive utilisation ratio $\mu_c = N_{x,c}/N_{x,c,R}$ is plotted over the bending utilisation ratio $\mu_m = M_{y,1}/M_{y,1,R}$. Where $N_{x,c}$ is the applied axial compressive force, $N_{x,c,R}$ is the compressive load-bearing capacity with flexural buckling if only axial compressive forces (no bending moments) are applied, $M_{y,1}$ is the applied bending moment, and $M_{y,1,R}$ is the bending load-bearing capacity with lateral torsional buckling if only bending moments (no axial compressive forces) are applied. Additionally, the quadratic interaction is plotted, i.e. $\mu_c + \mu_m^2 = 1$. Furthermore, the slenderness, for which the bending load-bearing capacities are at most 10% larger than the quadratic interaction, is highlighted. Above this slenderness, the influence of compressive plasticising on the load-bearing capacity is less than 10% and thus no longer significant.

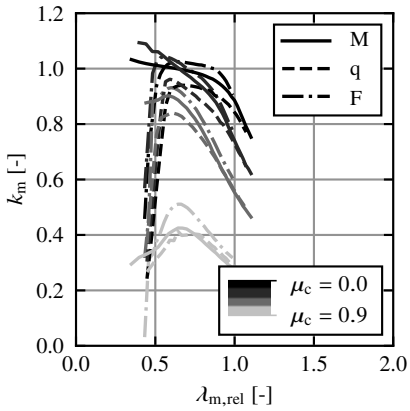

Figure 6.35: Reduction of the load-bearing capacity k_m from FEA plotted over the relative LTB slenderness ratio $\lambda_{m,rel}$ for different utilisation ratios μ_c and constant bending moment (M), a uniform line load (q), and a concentrated load (F); GL 24h and $H/B = 4$.

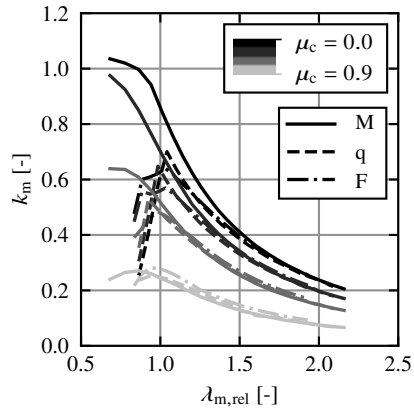

Figure 6.36: Reduction of the load-bearing capacity k_m from FEA plotted over the relative LTB slenderness ratio $\lambda_{m,rel}$ for different utilisation ratios μ_c and constant bending moment (M), a uniform line load (q), and a concentrated load (F); GL 24h and $H/B = 8$.

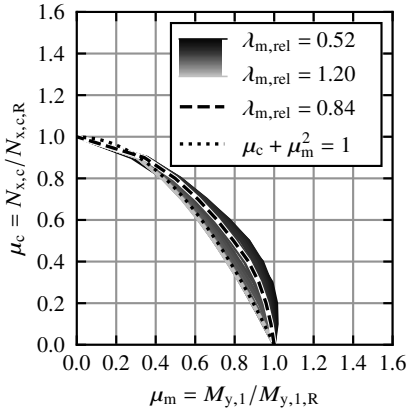

Figure 6.37: Compressive utilisation ratio $\mu_c = N_{x,c}/N_{x,c,R}$ plotted over the bending utilisation ratio $\mu_m = M_{y,1}/M_{y,1,R}$ for different relative flexural buckling slenderness ratios $\lambda_{c,rel}$; GL 30c, constant bending moment, $H/B = 4$.

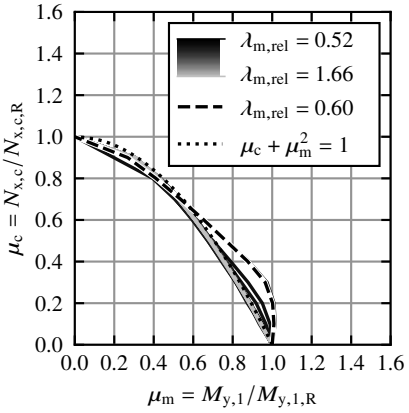

Figure 6.38: Compressive utilisation ratio $\mu_c = N_{x,c}/N_{x,c,R}$ plotted over the bending utilisation ratio $\mu_m = M_{y,1}/M_{y,1,R}$ for different relative LTB slenderness ratios $\lambda_{m,rel}$; GL75, constant bending moment, $H/B = 4$.

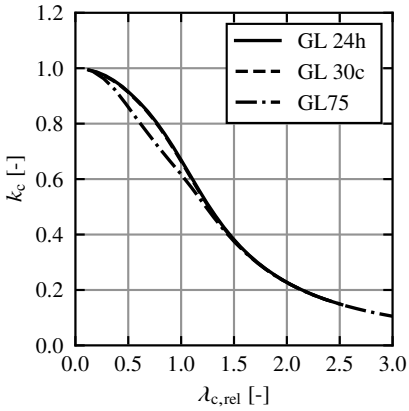

Figure 6.39: Reduction of the load-bearing capacity k_c from FEA plotted over the relative flexural buckling slenderness ratio $\lambda_{c,rel}$ for GL 24h, GL 30c, and GL75; with $H/B = 1$.

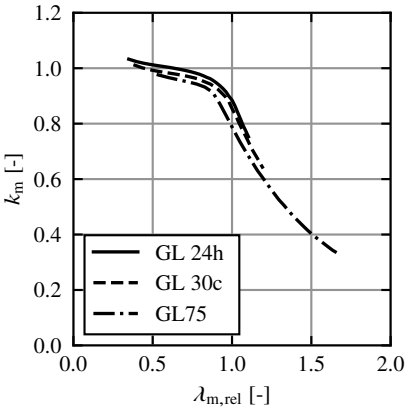

Figure 6.40: Reduction of the load-bearing capacity k_m from FEA plotted over the relative LTB slenderness ratio $\lambda_{m,rel}$ for GL 24h, GL 30c, and GL75; with $H/B = 4$.

For GL75 with medium slendernesses, the positive effect of compressive plasticising was smaller than for GL 24h, compare Figures 6.34 and 6.38. This was due to the earlier and larger compressive plasticising, see Tables 5.10 and 5.12, which reduced the stiffness, increased the geometrically nonlinear deformations, and thus reduced the load-bearing capacities.
The same effect occurred for GL 30c for low slendernesses, compare Figures 6.34 and 6.37, as $f_{c,0,k} < f_{m,k}$. However, for medium slendernesses, there was no increased stiffness reduction, as the proportionality limit $f_{c,0,lin}$ and the plastic strain on reaching the compressive strength $\epsilon_{c,0,pl}$ were chosen to be identical to GL 24h, see Tables 5.10 and 5.11.

Figure 6.39 displays the reduction factor of the load-bearing capacity k_c from FEA on GL 24h, GL 30c, and GL75 columns with an axial compressive force and $H/B = 1$ plotted over the relative flexural buckling slenderness ratio $\lambda_{c,rel}$. Figure 6.40 displays the reduction factor of the load-bearing capacity k_m from FEA on GL 24h, GL 30c, and GL75 beams with a constant bending moment and $H/B = 4$ plotted over the relative LTB slenderness ratio $\lambda_{m,rel}$. The evaluation of the FEA was carried out without considering shear failure. $\lambda_{c,rel}$ and $\lambda_{m,rel}$ were calculated with Equations (2.60) and (2.80), k_m with Equation (6.1), and k_c with

$$k_c = \frac{N_{x,c,R,FEA}}{A f_{c,0,k}} \quad , \tag{6.6}$$

where $N_{x,c,R,FEA}$ is the compressive load-bearing capacity from FEA, A is the cross-sectional area, and $f_{c,0,k}$ is the characteristic compressive strength.
While k_c for GL 24h and GL 30c was identical, a significant reduction of up to 15% occurred for GL75 between $\lambda_{c,rel} = 0.3$ and 1.2. This was due to the earlier and larger compressive plasticising of GL75, see Tables 5.3 and 5.10, which reduced the stiffness, increased the geometrically nonlinear deformations, and thus reduced the load-bearing capacities.
The shape of k_m for GL 24h, GL 30c, and GL75 was similar. The differences in magnitude were due to the fact that in calculations with shell or solid elements and $f_{c,0,k} < f_{m,k}$, the bending load-bearing capacities aimed for in FprEN 1995-1-1 [69] cannot be achieved with the bending strengths according to FprEN 1995-1-1 [69] due to compressive plasticising. The bending strengths in FprEN 1995-1-1 [69] are suitable for calculations with beam elements. This is a fundamental aspect that has to be taken into account if transferring strengths from beams to shell or solid elements, particularly in FEA, and is discussed in CEN/TC 250/SC 5/WG 11.

6.4.2.5 Influence of the shear failure

Figure 6.41 displays the reduction factor of the load-bearing capacity k_m from FEA on GL 24h beam-columns with a concentrated force and $H/B = 8$ plotted over the relative LTB slenderness ratio $\lambda_{m,rel}$. Figure 6.42 displays k_m from FEA on GL75 beam-columns with a constant bending moment and $H/B = 16$ plotted over the relative LTB slenderness ratio $\lambda_{m,rel}$. The evaluation of the FEA was carried out without considering shear failure. k_m and $\lambda_{m,rel}$ were calculated with Equations (6.1) and (2.80). μ_c is the utilisation ratio the compressive load-bearing capacity with flexural buckling.

For beam-columns with low L/H ratios and subjected to shear forces, shear failure was always decisive and reduced the load-bearing capacity, see Figure 6.41. The cause was that the shear forces increased in relation to the bending moments as the length decreased. Shear failure often occurred at stress concentrations near the supports. The limit criterion $L/H = 6$ provided a way to roughly estimate whether shear failure was decisive. This is similar to the limit criterion for cross-sectional warping, see Section 6.2.1.
Shear failure due to torsion was never decisive for GL 24h. With decreasing shear strength $f_{v,k}$ in relation to bending strength $f_{m,k}$, see Tables 5.10 to 5.12, shear failure due to torsion became decisive rarely at GL 30c but more often at GL75 with $H/B > 12$. For GL75 with a constant moment and $H/B > 12$, shear failure due to torsion was governing, see Figure 6.42. The smaller μ_c was, the larger the slenderness range was, in which shear failure due to torsion was decisive. However, the shear load-bearing capacity was only slightly lower than the bending load-bearing capacity.

6.4.3 Discussion

6.4.3.1 General

Section 6.4.3 combines the results of own experiments, analytical investigations, and FEA from Sections 3.3, 3.4, 4, and 6.4 with the literature review from Sections 2.2 to 2.4. The slenderness-dependent $N_{x,c}$-$M_{y,1}$-interaction was investigated. The $N_{x,c}$-$M_{y,2}$(-$M_{z,2}$)-interaction was not investigated, as it is independent of slenderness and was already comprehensively investigated in the literature, see Sections 2.2 to 2.4.

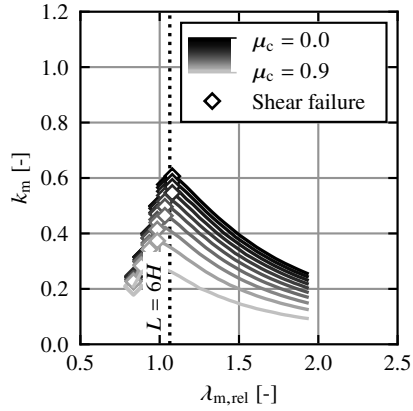

Figure 6.41: Reduction of the load-bearing capacity k_m from FEA plotted over the relative LTB slenderness ratio $\lambda_{m,rel}$ for different utilisation ratios μ_c; with a uniform line load, GL 24h, $H/B = 8$.

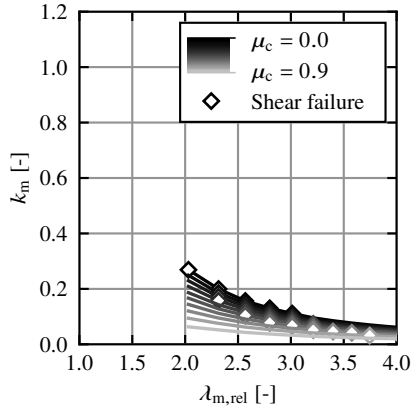

Figure 6.42: Reduction of the load-bearing capacity k_m from FEA plotted over the relative LTB slenderness ratio $\lambda_{m,rel}$ for different utilisation ratios μ_c; with a concentrated force, GL75, $H/B = 16$.

The curves of the reduction of the load-bearing capacity k_m, e.g. Figures 6.25 and 6.26, and the $N_{x,c}$-$M_{y,1}$-interaction diagrams, e.g. Figures 6.33 and 6.34, revealed distinct differences between beam-columns with $H/B = 1$ and $H/B \geq 2$. For beam-columns with $H/B = 1$, flexural buckling, and for beam-columns with $H/B \geq 2$, LTB occurred. This clear distinction was not known to the author from literature. A more detailed investigation of the transition between flexural buckling and LTB was not carried out.

6.4.3.2 Lateral torsional buckling

General

Many parameters that are relevant for the LTB design of softwood GL beam-columns, e.g. the influence of slenderness and axial compressive loads on the LTB load-bearing capacity and on the failure behaviour, were only investigated analytically in literature, see Sections 2.2 to 2.4. For the first time, this thesis combines the results of analytical analyses with extensive numerical analyses validated by experiments. This establishes the basis for the check of the reliability of design models in EN 1995-1-1 [57] and FprEN 1995-1-1 [69].

Comparison with literature

The nonlinear LTB load-deformation behaviour with large horizontal deformations above 80% of the load-bearing capacity and a pronounced plateau (no peak) observed by Wilden et al. [174] and [176], see Section 2.2.2.1, was confirmed by own experiments and FEA, see Sections 3.4.3.2 and 5.5.3.

Moreover, the dependence of the failure behaviour on the slenderness, which was described in the literature, (i) tensile/bending failure for short beams, (ii) stability failure for slender beams, (iii) localised compressive failure in grain direction, and (iv) shear failure due to torsion in more slender beams, see Section 2.2.2.2, could be confirmed by own experiments and FEA, see Sections 3.4.3.2 and 5.5.3. Hörsting [90] reported for calculations using T2O that the shear load-bearing capacity of slender beams is only slightly lower than the bending load-bearing capacity, see Section 2.4.4, which was confirmed in own FEA, see Figure 6.42. Furthermore, it was confirmed that the relevance of the shear strength increases with increasing material grade, as the shear strength does not increase to the same extent as the bending strength. However, in some of the LTB tests, member shear failure was observed at slenderness values, which did not occur in the FEA with GL 24h, see Table 3.16. Since characteristic strengths were assumed in the FEAs, it is possible that the member shear failure in the LTB tests occurred due to an unfavourable combination of low shear strengths with high (bending) tensile strengths. This assumption was supported by the low frequency of member shear failure in the tests (33% for dimensions of $720 \cdot 120 \cdot 8000$ mm^3 and 13% for dimensions of $600 \cdot 120 \cdot 8000$ mm^3).

A novel finding from the experimental and numerical investigations was that for beam-columns subjected to shear forces with $\lambda_{m,rel}$ between about 1.0 and 1.5, a reduction in shear stiffness due to shear plasticising occurred, which reduced the load-bearing capacity by up to 20%, see Sections 3.4.3.2, 5.5.3, and 6.4.2.3. This should be considered in the design. No investigations on the influence of the material and the magnitude of the axial compressive load on this behaviour were conducted, as the stress-strain curve for shear from

torsion must first be investigated in more detail experimentally.

No systematic investigations of the LTB load-bearing behaviour at combined bending and axial compression were known from the literature, see Sections 2.2.2.4. Therefore, the nonlinear $N_{x,c}$-$M_{y,1}$-interaction of the k_m-method, see Equation (2.61), was still under discussion during the revision of FprEN 1995-1-1 [69] in favour of a more conservative linear interaction, see prEN 1995-1-1 [132] and Section 2.6.5. A major result of this thesis is that the nonlinear $N_{x,c}$-$M_{y,1}$-interaction for LTB of slender beam-columns, which was discussed by Eggen [43] and Leicester [117] and is assumed in the k_m-method in EN 1995-1-1 [57], see Sections 2.2.2.4 and 4.3, could be validated experimentally, analytically, and numerically, see Sections 3.4.4, 4.3, and 6.4.2. The results of the FEAs demonstrated that the LTB load-bearing capacity approaches the $N_{x,c}$-$M_{y,1}$-nonlinear interaction curve of the critical LTB load from above and that Equations (2.61) and (4.13) therefore on the safe side for medium and high slendernesses, see Section 6.4.2.
The results of Buchanan et al. [25], see Section 2.3.3.2, and the analytical investigations in Section 4.4 confirmed the FEA results in Section 6.4.2.4, that the positive effect of compressive plasticising is less pronounced for GL75 than for GL 24h as it depends on the ratio of $f_{c,0}$ to f_m.

Further novel findings from the numerical investigations were the pronounced shear force induced shear warping at common ratios of $L/H < 6$ and the plate bending at large H/B ratios, which affected the critical bending moment and the load-bearing capacity, see Sections 6.2.1 to 6.2.3. Both effects are characteristic of the anisotropic material timber, with its large difference between the elastic and shear moduli in grain direction, i.e. the large $E_{0,el}/G_{0,el}$ ratio, and its large difference between the elastic moduli in grain direction and perpendicular to the grain, i.e. the large $E_{0,el}/E_{90,el}$ ratio. For isotropic materials such as steel and concrete, the plate bending can only be observed at significantly higher H/B ratios, and the shear warping can only be observed at significantly smaller ratios of $L/H \leq 2.5$, see Hofmann [88]. No reports on these effects for timber beams were known from literature.

For some timber structures a significant post-critical LTB behaviour can occur, e.g. for timber frames, see Lecomte [114]. However, this did not occur for the investigated timber beam-columns in this thesis.

Comparison with compression and bending design according to FprEN 1995-1-1 [69]

Figures 6.43 to 6.46 display the ratio of the bending load-bearing capacity of design with calculations using T2O and the k_c-k_m-method according to FprEN 1995-1-1 [69] to the load-bearing capacity from FEA $k_{m,EC5}/k_{m,FEA}$ for GL 24h beam-columns with a constant bending moment, a uniform line load, and a concentrated load and $H/B = 4$ and 8 plotted over the relative LTB slenderness ratio $\lambda_{m,rel}$. The evaluation of the FEA was carried out without considering shear failure. A $k_{m,EC5}/k_{m,FEA}$ ratio of less than 1.0 implies that the design methods in FprEN 1995-1-1 [69] were on the safe side. $\lambda_{m,rel}$ was calculated with Equation (2.80). The design was carried out with calculations using T2O according

to FprEN 1995-1-1 [69], see Equations (2.15), (2.54), and (2.55), and the equivalent geometrical imperfections in Equations (6.2) and (6.3). Furthermore, calculations were carried out with the k_c-k_m-method in FprEN 1995-1-1 [69], see Sections 2.6.4.1.3 and 2.6.4.1.4, and the same equivalent geometrical imperfections.
The results of the calculation using T2O were generally closer to those from FEA than the results from the k_c-k_m-method. This was to be expected, as the k_c-k_m-method is a simplification of the design with calculation using T2O. For smaller slenderness ratios, there were larger deviations between the results of the design methods and FEA. With increasing slenderness, the results converged.
For beams subjected to shear forces with $L/H < 6$, see Figures 6.45 and 6.46, the design methods according to FprEN 1995-1-1 [69] significantly overestimated the load-bearing capacity due to neglecting the influence of the cross-sectional warping caused by shear forces. This is discussed in Section 6.2.1.
For $H/B = 4$ and smaller slendernesses, the increasing μ_c ratio caused a compressive plasticising, which is not considered at all in the k_c-k_m-method and is not fully considered in design with calculations using T2O. Therefore, the load-bearing capacities were underestimated by up to 60% by the k_c-k_m-method and by up to 30% by design with calculations using T2O, see Figure 6.43. This effect decreased with increasing slenderness, i.e. increasing H/B ratio and length, and therefore decreasing axial compressive forces and compressive plasticising, see Figures 6.43 and 6.44.
For beam-columns subjected to shear forces with $\lambda_{m,rel}$ between about 1.0 and 1.5 and low μ_c, see Figures 6.45 and 6.46, shear plasticising reduced in shear stiffness, which

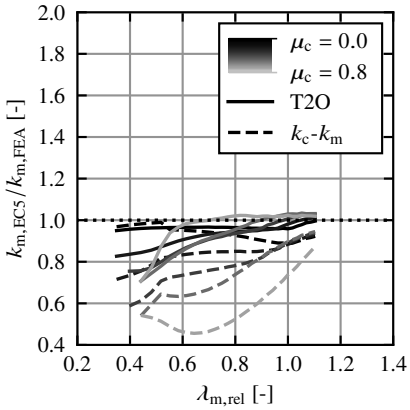

Figure 6.43: Ratio of the bending load-bearing capacity of T2O and the k_c-k_m-method according to FprEN 1995-1-1 [69] to the FEA load-bearing capacity $k_{m,EC5}/k_{m,FEA}$ plotted over the relative LTB slenderness ratio $\lambda_{m,rel}$ for different utilisation ratios μ_c; with a *constant bending moment*, GL 24h, $H/B = 4$.

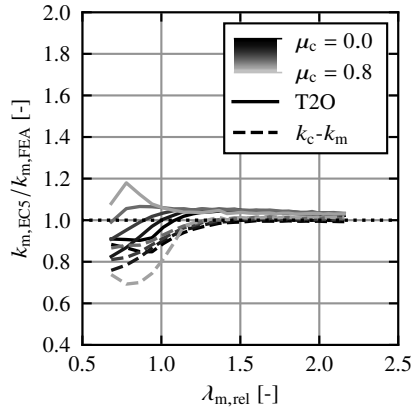

Figure 6.44: Ratio of the bending load-bearing capacity of T2O and the k_c-k_m-method according to FprEN 1995-1-1 [69] to the FEA load-bearing capacity $k_{m,EC5}/k_{m,FEA}$ plotted over the relative LTB slenderness ratio $\lambda_{m,rel}$ for different utilisation ratios μ_c; with a *constant bending moment*, GL 24h, $H/B = 8$.

lowered the load-bearing capacity in FEA by up to 20%. This effect is not covered in the k_c-k_m-method and calculations using T2O according to FprEN 1995-1-1 [69], which therefore overestimated the load-bearing capacities by up to 20%.

Comparison with shear design according to FprEN 1995-1-1 [69]

For beam-columns subjected to shear forces, a comparison of the numerically determined shear load-bearing capacity with the design methods from FprEN 1995-1-1 [69] was not carried out because the shear failure in FEA often occurred in the vicinity of the supports. In the design methods according to FprEN 1995-1-1 [69], on the other hand, the shear stresses are verified at mid-height of beams. This difference led to a strong deviation of the results of FEA and FprEN 1995-1-1 [69] and raised the question of how the shear strengths from the standards can be transferred to stress calculations with shell or solid elements. This transferring of strengths from beams to shell or solid elements, particularly in FEA, is discussed in CEN/TC 250/SC 5/WG 11.

For beam-columns subjected to a constant bending moment, the shear load-bearing capacity was only decisive for large slendernesses and was only slightly smaller than the bending load-bearing capacity, see Figure 6.42. This is due to the fact that for large slendernesses, the decisive torsional moments $M_{x,2}$ as well as the bending moments $M_{z,2}$ occur if the loading $M_{y,1}$ approaches the critical load $M_{y,cr}$, see Equations (2.14) and (2.15). For the investigated beam-columns, the verification of the torsional shear stresses could thus be neglected.

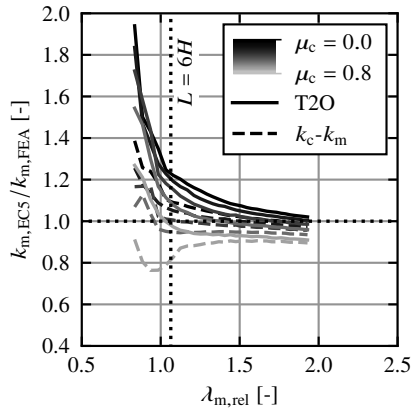

Figure 6.45: Ratio of the bending load-bearing capacity of T2O and the k_c-k_m-method according to FprEN 1995-1-1 [69] to the FEA load-bearing capacity $k_{m,EC5}/k_{m,FEA}$ plotted over the relative LTB slenderness ratio $\lambda_{m,rel}$ for different utilisation ratios μ_c; with a *concentrated force*, GL 24h, $H/B = 8$.

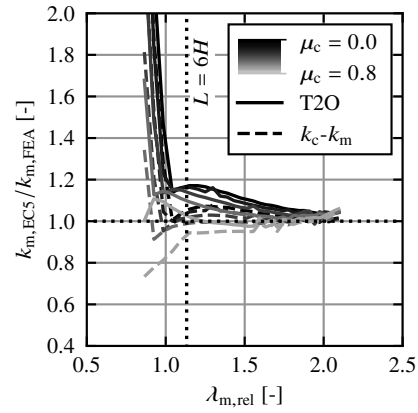

Figure 6.46: Ratio of the bending load-bearing capacity of T2O and the k_c-k_m-method according to FprEN 1995-1-1 [69] to the FEA load-bearing capacity $k_{m,EC5}/k_{m,FEA}$ plotted over the relative LTB slenderness ratio $\lambda_{m,rel}$ for different utilisation ratios μ_c; with a *uniform line load*, GL 24h, $H/B = 8$.

6.4.3.3 Flexural buckling

General

The flexural buckling behaviour of softwood GL columns is sufficiently well investigated and known, see Section 2.2.1. However, there were few studies on other European wood species and wood products, such as by Ehrhart et al. [51] on beech GL. For the first time, this thesis investigated the flexural buckling of columns made of the novel material beech LVL GL75, see ETA-14/0354 [63], which is of particular interest for highly loaded columns in multi-story buildings. This established the basis for the check of the reliability of the extension of the design models in EN 1995-1-1 [57] and FprEN 1995-1-1 [69] to other wood products and species.

Comparison with Literature

The nonlinear flexural buckling load-deformation behaviour with a peak and a subsequent load drop observed by Frangi and Theiler [71], see Section 2.2.1.1, was confirmed by own experiments and FEA, see Sections 3.3.3 and 5.5.2.
Moreover, the dependence of the failure behaviour on slenderness, which was described in the literature, (i) compressive failure in grain direction for short columns, and (ii) stability failure for slender columns, see Section 2.2.1.2, could be confirmed by own experiments and FEA, see Sections 3.3.3 and 5.5.2. In the FEA the peak of the load-deformation curve, see failure criterion C2 in Figure 2.2, was always decisive and not any strength or strain criteria. For flexural buckling design, the limit criterion of the compressive strain discussed by Frese et al. [75], see Section 2.4.3, can therefore be neglected.
The verification in Section 5.4.2 demonstrated that the consideration of the shear modulus can influence the eigenvalue of softwood GL columns by 10%. For precise analyses, it can therefore be beneficial to consider the shear modulus $G_{0,el}$ not only for timber products with low shear stiffness and strength, e.g. CLT, but also for softwood GL.

The linear $N_{x,c}$-$M_{y,1}$-interaction of slender columns and the nonlinear $N_{x,c}$-$M_{y,1}$-interaction of stocky columns reported in the literature by, e.g. Blaß [9], Buchanan et al. [25], Hörsting [90], Steiger and Fontana [150], and Zahn [183], see Section 2.3.3.2, were also found in the FEA, see Section 6.4.2.
[25] reported a pronounced nonlinear $N_{x,c}$-$M_{y,1}$-interaction due to compressive plasticising in grain direction at $L/B = 10 \equiv \lambda_{c,rel} = 0.55$ (for GL 24h), see Figure 2.23. For the k_c-method, Blaß [8] proposed a similar limit value of $\lambda_{c,rel} = 0.50$, above which no plasticising and a linear $N_{x,c}$-$M_{y,1}$-interaction are to be considered. This corresponds to the results of the FEAs, see Figure 6.33 and Annex F. In EN 1995-1-1 [57], the limit value of $\lambda_{c,rel} = 0.50$ was lowered to 0.30, as this is approximately the slenderness of the test specimen at which the characteristic compressive strength $f_{c,0,k}$ was determined, see Brüninghoff and Klapp [22] and Section 2.6.2.1.3. Therefore, $\lambda_{c,rel} = 0.30$ in the k_c-method in EN 1995-1-1 [57] does not represent the limit of plasticising, but it practically implies that the plasticising is no longer considered in the $N_{x,c}$-$M_{y,1}$-interaction, see Section 2.6.2.1.1 and 2.6.2.1.3.
Furthermore, [25] reported an approximately linear interaction at $L/B = 20 \equiv \lambda_{c,rel} = 1.10$ (for GL 24h), see Figure 2.23. This is similar to the limit of $\lambda_{c,rel} = 1.08$ from own FEA on

GL 24h, see Figure 6.33.
[22] suggested an interaction equation with a continuous reduction of the influence of plasticising between $\lambda_{m,rel} = 0$ and 0.9, see Equations (2.27) and (2.28). However, the author doubts whether it is reasonable to assume a dependence of compression plasticising on the relative LTB slenderness ratio $\lambda_{m,rel}$. Furthermore, Equations (2.27) and (2.28) are regression equations lacking the mechanical background.
The results of Buchanan et al. [25], see Section 2.3.3.2, and analytical investigations in Section 4.4 confirmed the FEA results in Section 6.4.2.4, that the positive effect of compressive plasticising is less pronounced for GL75 than for GL 24h as it depends on the ratio of $f_{c,0}$ to f_m.

The experimentally determined flexural buckling load-bearing capacities of the GL75 columns were up to 10% smaller than the characteristic load-bearing capacities according to FprEN 1995-1-1 [69], see Section 3.3.4. Additionally, a 15% drop in load-bearing capacity was observed in FEA between GL 24h and GL75 for slenderness between $\lambda_{c,rel} = 0.3$ and 1.2, see Section 6.4.2.4. This was due to the about five times higher plastic strains of GL75 than softwood if reaching the compressive strength and the resulting decrease of the bending stiffness, see Section 3.3.3.2. Similar reductions in load-bearing capacity were observed by Ehrhart et al. [51] in tests on beech GL columns. The material-specific compressive plasticising can therefore have a significant effect on the flexural buckling load-bearing capacity of columns and should be considered in design.

Comparison with design according to FprEN 1995-1-1 [69]

Figures 6.47 to 6.48 display the ratio of the compressive load-bearing capacity of design with calculations using T2O and the k_c-k_m-method according to FprEN 1995-1-1 [69] to the load-bearing capacity from FEA $k_{c,EC5}/k_{c,FEA}$ for GL 24h and GL75 beam-columns with $H/B = 1$ plotted over the relative flexural buckling slenderness ratio $\lambda_{c,rel}$. The evaluation of the FEA was carried out without considering shear failure. A $k_{c,EC5}/k_{c,FEA}$ ratio of less than 1.0 implies that the design methods in FprEN 1995-1-1 [69] were on the safe side. $\lambda_{c,rel}$ was calculated with Equation (2.60). The design was carried out with calculations using T2O according to FprEN 1995-1-1 [69], see Equations (2.1), (2.54), and (2.55), and the equivalent bow imperfection in Equation (6.2). Furthermore, calculations were carried out with the k_c-k_m-method in FprEN 1995-1-1 [69], see Sections 2.6.4.1.3 and 2.6.4.1.4, and the same equivalent bow imperfection.
For GL 24h and GL 30c, the load-bearing capacities of medium-slender columns with pure axial compressive forces were overestimated by up to 15% according to FprEN 1995-1-1 [69], and for GL75 by up to 35%. For small and large slendernesses, the load-bearing capacities according to FprEN 1995-1-1 [69] and FEA were similar. This and the differences between GL75 and GL 24h or GL 30c, respectively, suggest that the deviations were caused by the neglect of the stiffness reduction due to compression plasticising in grain direction in FprEN 1995-1-1 [69]. This finding provided further insight into the results of FEA on equivalent geometrical imperfections in Section 6.3.2.2. A significant part of the equivalent geometrical imperfections described in Table 6.2 can therefore be attributed to compressive plasticising.

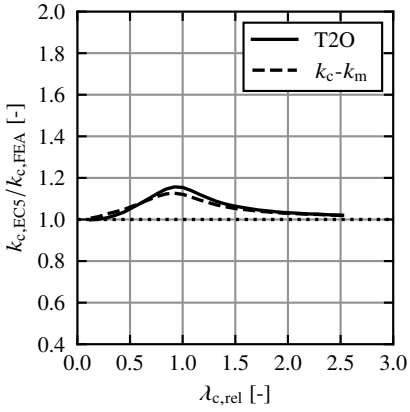

Figure 6.47: Ratio of the compressive load-bearing capacity of T2O and the k_c-k_m-method according to FprEN 1995-1-1 [69] to the FEA load-bearing capacity $k_{c,EC5}/k_{c,FEA}$ plotted over the relative flexural buckling slenderness ratio $\lambda_{c,rel}$ for *GL 24h* and $H/B = 1$.

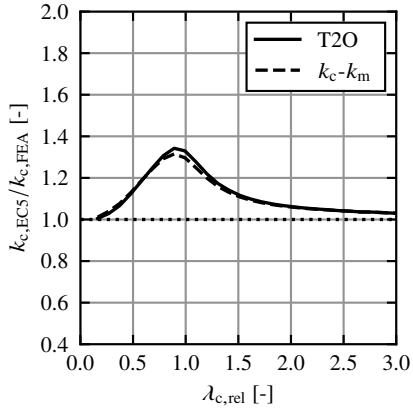

Figure 6.48: Ratio of the compressive load-bearing capacity of T2O and the k_c-k_m-method according to FprEN 1995-1-1 [69] to the FEA load-bearing capacity $k_{c,EC5}/k_{c,FEA}$ plotted over the relative flexural buckling slenderness ratio $\lambda_{c,rel}$ for *GL75* and $H/B = 1$.

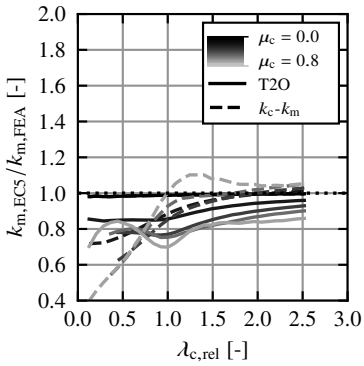

Figure 6.49: Ratio of the bending load-bearing capacity of T2O and the k_c-k_m-method according to FprEN 1995-1-1 [69] to the FEA load-bearing capacity $k_{m,EC5}/k_{m,FEA}$ plotted over the relative flexural buckling slenderness ratio $\lambda_{c,rel}$ for different utilisation ratios μ_c; with a constant bending moment, *GL 24h*, $H/B = 1$.

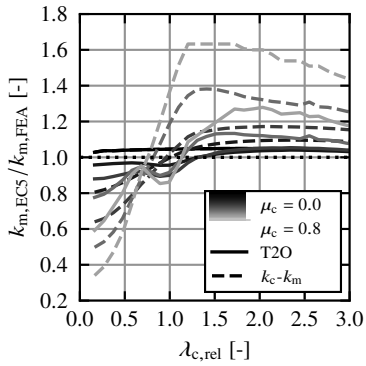

Figure 6.50: Ratio of the bending load-bearing capacity of T2O and the k_c-k_m-method according to FprEN 1995-1-1 [69] to the FEA load-bearing capacity $k_{m,EC5}/k_{m,FEA}$ plotted over the relative flexural buckling slenderness ratio $\lambda_{c,rel}$ for different utilisation ratios μ_c; with a constant bending moment, *GL75*, $H/B = 1$.

Figures 6.49 to 6.50 display the ratio of the bending load-bearing capacity of design with calculations using T2O and the k_c-k_m-method according to FprEN 1995-1-1 [69] to the load-bearing capacity from FEA $k_{m,EC5}/k_{m,FEA}$ for GL 24h and GL75 beam-columns with a constant bending moment, and $H/B = 1$ plotted over the relative flexural buckling slenderness ratio $\lambda_{c,rel}$. The evaluation of the FEA was carried out without considering shear failure. A $k_{m,EC5}/k_{m,FEA}$ ratio of less than 1.0 implies that the design methods in FprEN 1995-1-1 [69] were on the safe side. $\lambda_{c,rel}$ was calculated with Equation (2.60). The design was carried out with calculations using T2O according to FprEN 1995-1-1 [69], see Equations (2.1), (2.54), and (2.55), and the equivalent bow imperfection in Equation (6.2). Furthermore, calculations were carried out with the k_c-k_m-method in FprEN 1995-1-1 [69], see Sections 2.6.4.1.3 and 2.6.4.1.4, and the same equivalent bow imperfection.
The results of the calculation using T2O were generally closer to those from FEA than the results from the k_c-k_m-method. This could be expected, as the k_c-k_m-method is a simplification of the design with calculation using T2O. For GL 24h and GL 30c and small slenderness ratios, there were some larger deviations between the results of the design methods and FEA. With increasing slenderness, the results converged. For GL75 there were large deviations between the results of the design methods and FEA for both small and larger slendernesses.
For small slenderness, an increasing μ_c ratio caused compressive plasticising, which is not considered at all in the k_c-k_m-method and is not fully considered in design with calculations using T2O. Therefore, the load-bearing capacities were underestimated by up to 60% with the k_c-k_m-method and by up to 40% with design with calculations using T2O. This effect decreased with increasing slenderness and therefore decreasing axial compressive forces.
For GL 24h, $\lambda_{c,rel} > 1.0$ and high μ_c ratios, the bending load-bearing capacity was overestimated by up to 10% with the k_c-method, see Figure 6.49, as the geometrically nonlinear component of the bending moment $M_{y,1}$ is neglected in the k_c-method, see Section 2.6.2.1.3. For GL 30c and GL75, $\lambda_{c,rel} > 1.0$ and high μ_c ratios, the bending load-bearing capacity was overestimated by additionally up to 55% with the k_c-method and by additionally up to 25% with calculations using T2O, see Figure 6.50, because the smaller $f_{c,0,k}/f_{m,k}$ ratio and the larger plastic strains $\epsilon_{c,0,pl}$ caused a larger compressive plasticising, see Tables 5.1 to 5.3, which reduced the bending stiffness.

6.4.4 Summary

Numerical parameter studies on LTB and flexural buckling of timber beam-columns with varying cross-sectional height-to-width ratios, member lengths, materials, and loadings were conducted, and the $N_{x,c}$-$M_{y,1}$-interaction was investigated.

The key findings are:

- For timber beam-columns with $H/B = 1$, flexural buckling, and for $H/B \geq 2$, LTB occurs.
- The nonlinear $N_{x,c}$-$M_{y,1}$-interaction for LTB of slender beam-columns, which is assumed in the k_m-method in EN 1995-1-1 [57], see Equation (2.61), can be validated

numerically. This is in line with the experimental results in Section 3.4 and analytical investigations in Section 4.3.

- For beam-columns subjected to shear forces with $L/H < 6$, significant cross-sectional warping occurs, which increases the edge bending stresses and reduces the bending load-bearing capacity. An application limit for the beam theory should be considered in the bending design according to FprEN 1995-1-1 [69].

- For beam-columns subjected to shear forces with $\lambda_{m,rel}$ between about 1.0 and 1.5 and low compressive utilisation ratios μ_c, shear plasticising causes a reduction in shear stiffness, which reduces the LTB load-bearing capacity in FEA by up to 20%. This is in line with the experimental results in Section 3.4 and should be considered additionally in LTB design according to FprEN 1995-1-1 [69].

- For flexural buckling of softwood GL columns with $\lambda_{c,rel}$ between about 0.5 and 1.5, the flexural buckling load-bearing capacity is reduced by up to 15% due to the stiffness reduction caused by compression plasticising in grain direction. For flexural buckling of beech LVL GL75 columns, the reduction in load-bearing capacity increases to up to 25%. At least for beech LVL GL75, this should be considered additionally in flexural buckling design according to FprEN 1995-1-1 [69].

- For flexural buckling of GL 24h columns with $\lambda_{c,rel} > 1.0$ and high compressive utilisation ratios μ_c, the geometrically nonlinear behaviour due to $M_{y,1}$ reduces the bending load-bearing capacity by up to 10%. For flexural buckling of GL 30c and GL75 columns, the more unfavourable compressive plasticising increases the reduction in bending load-bearing capacity to up to 25% and 40%. At least for beech LVL GL75, this should be considered in flexural buckling design according to FprEN 1995-1-1 [69].

The results of the $N_{x,c}$-$M_{y,1}$-interaction agree well with findings from literature. Ehrhart et al. [51] reported similar reductions in load-bearing capacity for beech LVL as are described in this thesis for beech LVL GL75. The observations of the negative influence of shear force induced cross-sectional warping and shear plasticising on the bending and LTB load-bearing capacities are novel.
The nonlinear $N_{x,c}$-$M_{y,1}$-interaction for LTB has been incorporated into the k_m-method in FprEN 1995-1-1 [69] due to the results of this thesis. All findings are summarised in the design proposals for standardisation in Section 7.

6.5 Summary

Section 6 presents the FEA results and combines them with experiments and analytical investigations from Sections 3 and 4 and the literature review from Section 2.
The following key research questions and aims of this thesis, which were developed in Section 2, are addressed: (i) the investigation of the influence of the wood species and the wood product and the influences of the different compressive plasticising on the flexural buckling load-bearing capacity by FEA on softwood GL and beech LVL GL75 columns; (ii) the investigation of the LTB load-bearing capacity at combined axial compression and bending by FEA of softwood GL and beech LVL GL75 beam-columns; and (iii) the derivation of equivalent geometrical imperfections for a reliable LTB and flexural buckling design of timber beam-columns. The results were utilised to derive the design proposals in Section 7.

During the evaluation of the FEA, some partially unexpected fundamental aspects emerged. A significant shear force induced shear warping was observed for $L/H < 6$ which increases the edge bending stresses and thus reduces the bending load-bearing capacity, see Section 6.2.1. Additionally, FEA with solid elements and calculations with FprEN 1995-1-1 [69] result in differences of the critical bending moments of up to 20% which can cause differences in load-bearing capacities of up to 10%, see Section 6.2.2. Finally, a plate bending occurred at FEA with large H/B ratios, which affects the critical bending moment and the load-bearing capacity, see Section 6.2.3.

Numerical parameter studies on LTB of beams and flexural buckling of columns with scattering geometrical and structural imperfections made of GL 24h were conducted, and equivalent geometrical imperfections for design were determined, see Section 6.3. For LTB of softwood GL beams, the geometrical imperfections were decisive, and the structural imperfections could be neglected, see Table 6.1. For flexural buckling of softwood GL columns, the structural imperfections were decisive, and the geometrical imperfections did not cause any significant additional reduction in load-bearing capacity, see Table 6.2. The results agreed well with the results of measurements and calculations by Theiler [154] and measurements of Blaß [9], but less well with calculation results by [9], see Figure 6.23. The reasons were unclear.
From the results of the FEAs, equivalent geometrical imperfections were derived, which allow for a reliable and economical design of softwood GL beams, see Equations (6.2) to (6.4). The design approaches for columns in EN 1995-1-1 [57] and FprEN 1995-1-1 [69] were confirmed, see Section 6.3.2.2. The findings are summarised in the design proposals in Section 7, which were included in FprEN 1995-1-1 [69].

Numerical parameter studies on timber beam-columns with varying input parameters were conducted to investigate the $N_{x,c}$-$M_{y,1}$-interaction at flexural buckling and LTB, see Section 6.4.
The results of the FEAs confirmed the nonlinearity of the $N_{x,c}$-$M_{y,1}$-interaction for LTB, see Figure 6.34, which was also experimentally and analytically observed and is assumed in the k_c-k_m-method in EN 1995-1-1 [57]. This nonlinear $N_{x,c}$-$M_{y,1}$-interaction, typical for LTB, is governing for $H/B \geq 2$. For $H/B = 1$, the linear $N_{x,c}$-$M_{y,1}$-interaction, typical for

flexural buckling, occurs, see Figure 6.33.
For beams with $L/H < 6$ and subjected to shear forces, shear stresses cause a pronounced cross-sectional warping, which significantly reduces the bending load-bearing capacity, see Section 6.2.1. For LTB of beam-columns with significant shear forces and relative LTB slenderness ratios $\lambda_{m,rel}$ between about 1.0 and 1.5, shear plasticising reduced the shear stiffness, which reduced the LTB load-bearing capacity in tests and FEAs by up to 20%. For flexural buckling of GL75 columns with $\lambda_{c,rel}$ between 0.3 and 1.2, the material-specific compressive plasticising in grain direction reduces the load-bearing capacity by about 15% compared to softwood GL, see Figure 6.25. The geometrically nonlinear behaviour due to $M_{y,1}$ reduces the bending load-bearing capacity of medium-slender and slender GL75 columns by up to 40%.

The findings are summarised in the design proposals in Section 7. The nonlinear $N_{x,c}$-$M_{y,1}$-interaction for LTB was included in the k_m-method in FprEN 1995-1-1 [69].

7 Design proposals

7.1 General

This section combines the experimental, analytical, and numerical results as well as the literature review in design proposals for LTB and flexural buckling of timber beam-columns. The design proposals are based on the design models in FprEN 1995-1-1 [69]. These were carefully modified and extended to create (i) mechanically sound, consistent, and experimentally validated design concepts for flexural buckling and LTB of timber beam–columns made of softwood GL and beech LVL and (ii) a consistent set of equivalent geometrical imperfections for flexural buckling and LTB design of timber beam-columns. Emphasis was on improving the reliability of the design methods in FprEN 1995-1-1 [69], as discussed in Section 6.4.3, while covering all relevant physical effects, proposing mechanically meaningful design methods, and ensuring ease-of-use for building practice. The style and the wording are in line with the Eurocodes.
In Section 7.2, the design proposals are presented, in Section 7.3, the background and derivation of the design proposals are discussed, and in Section 7.4, the results of calculations with the design proposals are discussed in comparison with the own experimental and numerical results, the literature, and the results of the design models from FprEN 1995-1-1 [69].

7.2 Design proposals

7.2.1 Structural analysis

7.2.1.1 Member level

(1) The increase in edge bending stresses due to shear-induced cross-sectional warping should be taken into account for members with significant bending and shear stresses in the same plane and a ratio of span-to-height $L/H < 6$. This may be done by analyses with membrane theory.

7.2.1.2 Equivalent geometrical imperfections of beam-columns

(1) The effects of structural and geometrical imperfections of beam-columns should be considered by the equivalent geometrical imperfections in Clauses (2) to (7).

Note 1: The effects of planned or unplanned load-eccentricities are not covered by the equivalent geometrical imperfections.

Note 2: The geometrical imperfections of beams are composed of three parts: the bow imperfections, the twist imperfections at midspan, and the twist imperfections at the fork supports.

Note 3: For flexural buckling, the sway and bow imperfections in Clauses (2) and (3) can be relevant. For lateral torsional buckling, the sway, bow, and twist imperfections in Clauses (3) to (7) can be relevant.

(2) The equivalent sway imperfection $e_{\phi,\mathrm{eq}}$ in radians should be taken as follows:

$$e_{\phi,\mathrm{eq}} = \begin{cases} \frac{1}{200} & \text{for} \quad h \leq 5\ \mathrm{m} \\ \frac{1}{200} \cdot \sqrt{\frac{5}{H}} & \text{for} \quad h > 5\ \mathrm{m} \end{cases} \tag{7.1}$$

where H is the height of the structure or member length in m.

(3) The equivalent bow imperfection $e_{\mathrm{y/z,eq}}$ should be taken as follows:

$$e_{\mathrm{y/z,eq}} = \begin{cases} \frac{L}{400} & \text{for ST} \\ \frac{L}{1000} & \text{for GL and LVL} \end{cases} \tag{7.2}$$

where L is the effective lateral torsional buckling length or the real length of the member, whichever is decisive for the design.

(4) The twist imperfection at midspan $e_{\theta,\mathrm{mid}}$ in radians should be taken as follows:

$$e_{\theta,\mathrm{mid}} = \frac{L}{1500 H_{\mathrm{ap}}} \tag{7.3}$$

where H_{ap} is the height of the beam at the apex.

(5) The twist imperfection at the fork supports $e_{\theta,supp}$ in radians should be taken as follows:

$$e_{\theta,supp} = \begin{cases} \frac{1}{180} & \text{for fork supports with small tolerances} \\ \frac{1}{100} & \text{for fork supports with large tolerances} \end{cases} \tag{7.4}$$

Note: Large tolerances refer to fork supports by means of concrete pockets or similar, and small tolerances refer to fork supports by means of lateral timber members or similar.

(6) In design, the twist imperfection at midspan $e_{\theta,mid}$ and the twist imperfection at the fork supports $e_{\theta,supp}$ may be replaced by an equivalent twist imperfection at midspan $e_{\theta,eq}$:

$$e_{\theta,eq} = 0.5 \cdot (e_{\theta,mid} + e_{\theta,supp}) \tag{7.5}$$

where $e_{\theta,mid}$ and $e_{\theta,supp}$ are the twist imperfections according to Clauses (4) and (5).

Note: This simplification considers the lower probability that the 95% quantile values, i.e. the characteristic values, of the twist imperfection at midspan $e_{\theta,mid}$ and the twist imperfections at the supports $e_{\theta,supp}$ occur simultaneously. It does not represent a mean value.

(7) In design, the equivalent bow imperfection $e_{y,eq}$, the twist imperfection at midspan $e_{\theta,mid}$, and the twist imperfection at the fork supports $e_{\theta,supp}$ may be replaced by an equivalent bow imperfection at midspan $e_{y,eq,simp}$:

$$e_{y,eq,simp} = \frac{L}{400} \quad \text{for GL and LVL} \tag{7.6}$$

Note: For pure bending, equivalent geometrical imperfections according to Clauses (3) and (6) or Clause (7) lead to similar results. The larger the proportion of the axial compressive force, the more advantageous is the separation of the equivalent geometrical imperfections into bow and twist imperfections according to Clauses (3) and (6).

(8) The shapes of equivalent geometrical imperfections may be chosen according to linear bifurcation analysis (LBA) or along experience. For equivalent bow and twist imperfections, sinusoidal or parabolic shapes may be assumed. The decisive shape of the equivalent geometrical imperfection should be chosen so that the maximum effects of actions occur in the respective part of the structure to be designed.

Note: The shapes of the equivalent geometrical imperfections do not need to fulfil the boundary conditions of the structural system, e.g. sway imperfections of clamped columns.

(9) Equivalent bow or sway imperfections of beam-columns may be applied only in one direction, i.e. equivalent geometrical imperfections in the y- and z-directions do not need to be superimposed. All other relevant equivalent geometrical imperfections should be superimposed linearly.

7.2.1.3 Buckling analyses

(1) Geometrical nonlinear analyses may be conducted with numerical or analytical methods (such as the equations in Clauses (5) and (6)).

Note: Analytical methods allow for a straightforward calculation of standard cases, whereas numerical models can be applied universally for buckling problems. Analytical methods can be applied for verification of numerical results, i.e. results of FEAs.

(2) The critical loads, i.e. eigenvalues, may be determined with numerical or analytical methods (such as the equations in Clauses (9) and (10)).

Note: Analytical methods allow for a straightforward calculation of standard cases, whereas numerical models can be applied universally for buckling problems. Analytical methods can be applied for verification of numerical results, i.e. results of FEAs.

(3) Flexural buckling about the z-axis and lateral torsional buckling may be neglected and $M_{x,2,d} = M_{x,1,d}$, $M_{z,2,d} = M_{z,1,d}$, $\theta_{2,d} = \theta_{1,d}$, and $w_{2,d} = w_{1,d}$ may be assumed, if the following limit is met:

$$\alpha_{c,z} \cdot (1 + k_{def,ef,c}) + 0.375 \cdot \alpha_m^2 \cdot (1 + k_{def,ef,m})^2 \leq 0.09 \tag{7.7}$$

with

$$\alpha_{c,y/z} = \frac{N_{x,c,d}}{N_{y/z,cr}} \tag{7.8}$$

$$\alpha_m = \frac{M_{y,1,d}}{M_{y,cr}} \tag{7.9}$$

where $\alpha_{c,y/z}$ is the amplification factor of the axial compressive force due to flexural buckling about the y- or z-axis, $k_{def,ef,c/m}$ are the effective creep coefficients for flexural buckling and lateral torsional buckling according to Equations (7.22) and (7.23), α_m is the amplification factor of the bending moment due to geometrically nonlinear behaviour, $N_{x,c,d}$ is the design axial compressive force with a negative sign for compression, $N_{y/z,cr}$ is the critical axial compressive load for flexural buckling about the y- or z-axis according to Clause (2), $M_{y,1,d}$ is the design bending moment about the y-axis from geometrically linear calculations, and $M_{y,cr}$ is the critical bending moment for lateral torsional buckling according to Clause (2).

(4) Flexural buckling about the y-axis may be neglected and $M_{y,2,d} = M_{y,1,d}$ and $v_{2,d} = v_{1,d}$ may be assumed, if the following limit is met:

$$\alpha_{c,y} \cdot (1 + k_{def,ef,c}) \leq 0.09 \tag{7.10}$$

where $\alpha_{c,y}$ is the amplification factor of the axial compressive force due to flexural buckling about the y-axis according to Equation (7.8), and $k_{def,ef,c}$ is the effective creep coefficient for flexural buckling according to Equation (7.22).

(5) The geometrical nonlinear torsional and bending moments may be determined as follows:

$$M_{x,2,d} = \frac{\pi}{L_{m,ef}} \cdot \frac{M_{y,1,d} k_{pl,m} e_y + \alpha_m^2 G_{0,k} I_x k_{pl,m} e_\theta \cdot (1 + k_{def,ef,m})}{1 - \alpha_{c,z} \cdot (1 + k_{def,ef,c}) - \alpha_m^2 \cdot (1 + k_{def,ef,m})^2} \tag{7.11}$$

$$M_{y,2,d} = \frac{-N_{x,c,d} k_{pl,c} e_z + M_{y,1,d} \cdot (1 + \alpha_{c,y} \delta_y)}{1 - \alpha_{c,y} \cdot (1 + k_{def,ef,c})} \tag{7.12}$$

$$M_{z,2,d} = \frac{\left(-N_{x,c,d} k_{pl,c} + \frac{M_{y,1,d}^2}{G_{0,k} I_x} \cdot k_{pl,m} \cdot (1 + k_{def,ef,m})\right) \cdot e_y + M_{y,1,d} k_{pl,m} e_\theta}{1 - \alpha_{c,z} \cdot (1 + k_{def,ef,c}) - \alpha_m^2 \cdot (1 + k_{def,ef,m})^2} \tag{7.13}$$

where $L_{m,ef}$ is the effective lateral torsional buckling length according to the literature, e.g. FprEN 1995-1-1 [69], $M_{y/z,2,d}$ is the design bending moment about the y- or z-axis according to geometrically linear calculations, $k_{pl,m}$ is a factor considering the material-specific stiffness reduction due to shear plasticising according to Clause (8), $e_{y/z}$ is the bow imperfection in the y- or z-direction, α_m is the amplification factor of the bending moment due to geometrically nonlinear behaviour according to Equation (7.9), $G_{0,k}$ is the characteristic shear modulus in grain direction, I_x is the elastic torsional moment of inertia, e_θ is the twist imperfection, $k_{def,ef,c/m}$ are the effective creep coefficients for flexural buckling and lateral torsional buckling according to Equations (7.22) and (7.23), $\alpha_{c,y/z}$ is the amplification factor of the axial compressive force due to flexural buckling about the y- or z-axis according to Equation (7.8), $N_{x,c,d}$ is the design axial compressive force with a negative sign for compression, $k_{pl,c}$ is a factor considering the material-specific stiffness reduction due to compressive plasticising according to Clause (7), δ_y is the Dischinger-coefficient that accounts for the distribution of $M_{y,1,d}$ if it deviates from a sinusoidal half-wave, according to the literature, e.g. prEN 1995-1-1 [132], $N_{y/z,cr}$ is the critical axial compressive load for flexural buckling about the y- or z-axis according to Clause (2), $E_{0,k}$ is the characteristic elastic modulus in grain direction, $I_{y/z}$ is the elastic moment of inertia about the y- or z-axis, $L_{c,y/z,ef}$ is the effective flexural buckling length about the y- or z-axis according to literature, e.g. DIN EN 1995-1-1/NA [40], and $M_{y,cr}$ is the critical bending moment for lateral torsional buckling according to Clause (2).

Note: $M_{x,2,d}$ in Equation (7.11) is the geometrically nonlinear torsional moment at the fork supports due to lateral torsional buckling, $M_{y,2,d}$ in Equation (7.12) is the geometrically nonlinear bending moment at midspan due to flexural buckling about the y-axis, and $M_{z,2,d}$ in Equation (7.13) is the geometrically nonlinear bending moment at midspan due to lateral torsional buckling.

(6) The geometrical nonlinear rotations and deformations may be determined as follows:

$$\theta_{2,d} = \frac{\frac{M_{y,1,d}}{G_{0,k} I_x} \cdot k_{pl,m} e_y + \alpha_m^2 k_{pl,m} e_\theta \cdot (1 + k_{def,ef,m})}{1 - \alpha_{c,z} \cdot (1 + k_{def,ef,c}) - \alpha_m^2 \cdot (1 + k_{def,ef,m})^2} \tag{7.14}$$

$$v_{2,d} = \frac{(\alpha_{c,z} k_{pl,c} + \alpha_m^2 k_{pl,m} \cdot (1 + k_{def,ef,m})) \cdot e_y + \alpha_m \cdot \frac{G_{0,k} I_x}{M_{y,cr}} \cdot k_{pl,m} e_\theta}{1 - \alpha_{c,z} \cdot (1 + k_{def,ef,c}) - \alpha_m^2 \cdot (1 + k_{def,ef,m})^2} \tag{7.15}$$

$$w_{2,d} = \frac{\alpha_{c,y} k_{pl,c} e_z + \frac{M_{z,1,d}}{-N_{z,cr}} \cdot (1 + \alpha_{c,y} \delta_y)}{1 - \alpha_{c,y} \cdot (1 + k_{def,ef,c})} \tag{7.16}$$

Note: $\theta_{2,d}$ in Equation (7.14) is the geometrically nonlinear torsion at midspan due to lateral torsional buckling, $v_{2,d}$ in Equation (7.15) is the deformation at midspan due to flexural buckling about the y-axis, and $w_{2,d}$ in Equation (7.16) is the geometrically nonlinear deformation at midspan due to lateral torsional buckling.

(7) The influence of the material-specific stiffness reduction due to compressive plasticising should be considered by increasing the equivalent bow imperfections at flexural buckling by $k_{pl,c}$ as follows:

$$k_{pl,c} = \begin{cases} 1.0 & \text{for softwood SL, GL, LVL} \\ 3.0 & \text{for beech SL, GL, LVL} \end{cases} \tag{7.17}$$

(8) The influence of the material-specific stiffness reduction due to shear plasticising should be considered by increasing the equivalent bow and twist imperfections at lateral torsional buckling by $k_{pl,m}$ as follows:

$$k_{pl,m} = \begin{cases} 1.0 & \text{for softwood SL, GL, LVL without significant shear forces} \\ 3.0 & \text{for softwood SL, GL, LVL with significant shear forces} \end{cases} \tag{7.18}$$

(9) The critical axial compressive force and the critical bending moment, i.e. the eigenvalues, may be determined as follows:

$$N_{y/z,cr} = -\frac{\pi^2 E_{0,k} I_{y/z}}{L_{c,y/z,ef}^2} \tag{7.19}$$

$$M_{y,cr} = \frac{\pi}{L_{m,ef}} \cdot \sqrt{E_{0,k} I_z G_{0,k} I_x} \tag{7.20}$$

where $E_{0,k}$ is the characteristic elastic modulus in grain direction, $I_{y/z}$ is the elastic moment of inertia about the y- or z-axis, $L_{c,y/z,ef}$ is the effective flexural buckling length about the y- or z-axis according to literature, e.g. DIN EN 1995-1-1/NA [40] NCI NA.13, $L_{m,ef}$ is the effective lateral torsional buckling length according to the literature, e.g. FprEN 1995-1-1 [69] B.3.2.3, $G_{0,k}$ is the characteristic shear modulus in grain direction, and I_x is the elastic torsional moment of inertia.

(10) For flexural buckling, the influence of the shear stiffness may be considered by replacing $N_{y/z,cr}$ with $N_{y/z,cr,v}$. $N_{y/z,cr,v}$ may be determined as follows:

$$N_{y/z,cr,v} = N_{y/z,cr} \cdot \frac{1}{1 + \frac{N_{y/z,cr}}{G_{0,k} A_s}} \tag{7.21}$$

where $N_{y/z,cr}$ is the critical axial compressive load for flexural buckling according to Clause (2), and A_v is the shear area with $A_v = A/1.2$ for rectangular cross-sections.

(11) For determining the critical bending moment for lateral torsional buckling $M_{y,cr}$ of softwood GL, the elastic modulus $E_{0,k}$ and the shear modulus $G_{0,k}$ may each be increased by a factor of 1.15.

Note: The factor takes into account the low probability that both $E_{0,k}$ and $G_{0,k}$ occur in a member. As $G_{0,k}$ is of minor importance in flexural buckling, the increase cannot be applied to flexural buckling.

7.2.1.4 Long-term behaviour

(1) The influence of creep may be neglected in the flexural buckling verification of columns in SC 1 or if the design value of the permanent and quasi-permanent action is less than 70% of the total action in SC 2 and 3. In this case, $k_{def,ef,c} = 0$ may be assumed.

(2) The influence of creep may be neglected in the lateral torsional buckling verification of beams in SC 1 if the design value of the permanent and quasi-permanent action is less than 50% of the total action. In this case, $k_{def,ef,m} = 0$ may be assumed.

(3) The influence of creep may be considered by reducing $E_{0,k}$ and $G_{0,k}$ by $(1 + k_{def,ef,c/m})$, by creep-amplified imperfections according to FprEN 1995-1-1 [69] B.4.6, or by Equations (7.11) to (7.16).

Note: Creep causes additional deformations over time and does not necessarily reduce stiffnesses. The reduction of $E_{0,k}$ and $G_{0,k}$ by $(1 + k_{def,ef,c/m})$ is only a vehicle to calculate the total deformations including creep.

(4) The effective creep coefficient for flexural buckling should be determined as follows:

$$k_{def,ef,c} = \frac{N_{x,c,d,qper}}{N_{x,c,d,char}} \cdot k_{def} \tag{7.22}$$

where $N_{x,c,d,qper}$ is the design axial compressive force for the quasi-permanent combination of actions and $N_{x,c,d,char}$ is the design axial compressive force for the characteristic combination of actions.

(5) The effective creep coefficient for lateral torsional buckling should be determined as follows:

$$k_{def,ef,m} = \frac{M_{y,1,d,qper}}{M_{y,1,d,char}} \cdot k_{def} \tag{7.23}$$

where $M_{y,1,d,qper}$ is the design bending moment about the y- or z-axis according to geometrically linear calculations for the quasi-permanent combination of actions and $M_{y,1,d,char}$ is the design bending moment about the y- or z-axis according to geometrically linear calculations for the characteristic combination of actions.

7.2.2 Buckling verification of beam-columns

7.2.2.1 General

(1) The buckling verification of beam-columns should be carried out under the consideration of the imperfections in Section 7.2.1.2 either by:

- explicit geometrically nonlinear analyses of internal forces and deformations and verification of cross-sections according to Section 7.2.2.2; or
- geometrical linear analyses of internal forces and deformations and implicit consideration of the geometrical nonlinear behaviour by the factors k_c (considering flexural buckling) and/or k_m (considering lateral torsional buckling) according to Sections 7.2.2.3 and 7.2.2.4.

(2) For buckling verification of beam-columns with geometrical linear analyses of internal forces (k_c- and/or k_m-method) and

- $H/B \approx 1$, the verification should be carried out according to Section 7.2.2.3; and
- $H/B > 2$, the verification should be carried out according to Section 7.2.2.4.

Note: For $H/B \approx 1$, the $N_{x,c}$-$M_{y,1}$-interaction characteristic of flexural buckling occurs, and for $H/B > 2$, the $N_{x,c}$-$M_{y,1}$-interaction characteristic of lateral torsional buckling occurs.

(3) For beam-columns with constant cross-section and $M_{x,1} = 0$ (no planned torsional moment), the shear stresses in grain direction from torsion induced by lateral torsional buckling may be neglected for the verification of the shear stresses.

7.2.2.2 Lateral torsional buckling and flexural buckling with geometrically nonlinear calculation of internal forces

(1) For stresses in grain direction from axial compression and bending, the following should be satisfied:

$$\left(\frac{N_{x,c,d}}{A f_{c,0,d}}\right)^2 + \frac{M_{y,2,d}}{W_y f_{m,y,d}} + k_{red} \cdot \frac{M_{z,2,d}}{W_z f_{m,z,d}} \leq 1.0 \tag{7.24}$$

$$\left(\frac{N_{x,c,d}}{A f_{c,0,d}}\right)^2 + k_{red} \cdot \frac{M_{y,2,d}}{W_y f_{m,y,d}} + \frac{M_{z,2,d}}{W_z f_{m,z,d}} \leq 1.0 \tag{7.25}$$

where $N_{x,c,d}$ is the design axial compressive force, A is the cross-sectional area, $f_{c,0,d}$ is the design compressive strength, $M_{y/z,2,d}$ is the design bending moment about the y- or z-axis from geometrically nonlinear calculations according to Section 7.2.1.3, $W_{y/z}$ is the section modulus about the y- or z-axis, $f_{m,y/z,d}$ is the design bending strength about the y- or z-axis, and k_{red} is a factor for considering the positive size effect on the bending strength at biaxial bending according to FprEN 1995-1-1 [69] 8.1.8.1(2).

(2) For the ratios of the axial compressive force to the critical axial compressive force and of the bending moment to the critical bending moment, the following should be satisfied:

$$\frac{N_{x,c,d}}{N_{z,cr,d}} + \left(\frac{M_{y,1,d}}{M_{y,cr,d}}\right)^2 \leq 1.0 \tag{7.26}$$

$$\frac{N_{x,c,d}}{N_{y,cr,d}} \leq 1.0 \tag{7.27}$$

where $N_{y/z,cr,d}$ is the design critical axial compressive force for flexural buckling and $M_{y,cr,d}$ is the design critical bending moment for lateral torsional buckling according to Section 7.2.1.3 Clause (2) with $E_{0,d} = E_{0,k}/\gamma_M$ and $G_{0,d} = G_{0,k}/\gamma_M$, and γ_M is the partial factor for materials according to FprEN 1995-1-1 [69].

(3) For shear stresses in grain direction from torsion and shear forces, the following should be satisfied:

$$\frac{\tau_{tor,d}}{k_{shape} f_{v,d}} + \left(\frac{\tau_{xy,d}}{k_{v,xy} f_{v,xy,d}}\right)^2 + \left(\frac{\tau_{xz,d}}{k_{v,xz} f_{v,xz,d}}\right)^2 \leq 1.0 \tag{7.28}$$

where $\tau_{tor,d}$ is the design shear stress from torsion, k_{shape} is the factor for considering the effect of the shape of the cross-section according to FprEN 1995-1-1 [69] 8.1.12 (1), $f_{v,(xy/xz,)d}$ is the respective design shear strength, $\tau_{xy/xz,d}$ is the design shear stress from shear forces in the y- or z-direction, and $k_{v,xy/xz}$ is an adjustment factor of the shear strength according to FprEN 1995-1-1 [69] 8.1.11.1(3).

7.2.2.3 Flexural buckling with geometrically linear calculation of internal forces and $H/B \approx 1$ (k_c-method)

(1) Beam-columns should be verified against flexural buckling about the respective axis if the relative slenderness ratio for flexural buckling $\lambda_{c,y/z,rel}$ exceeds the following limit:

$$\lambda_{c,y/z,rel} > 0.3 \tag{7.29}$$

with

$$\lambda_{c,y/z,rel} = \sqrt{\frac{A f_{c,0,k} \cdot (1 + k_{def,ef,c})}{N_{y/z,cr}}} \tag{7.30}$$

where A is the cross-sectional area, $f_{c,0,k}$ is the characteristic compressive strength, $k_{def,ef,c}$ is the effective creep coefficient for flexural buckling according to Equation (7.22), and $N_{y/z,cr}$ is the critical axial compressive load for flexural buckling according to Section 7.2.1.3 Clause (2).

(2) For flexural buckling, the following should be satisfied for stresses in grain direction from axial compression and bending:

$$\frac{N_{x,c,d}}{k_{c,y} A f_{c,0,d}} + \frac{M_{y,1,d}}{W_y f_{m,y,d}} \cdot \left(1 + \frac{N_{x,c,d}}{k_{c,y} A f_{c,0,d}} \cdot \delta_y\right) + k_{red} \cdot \frac{M_{z,1,d}}{W_z f_{m,z,d}} \leq 1.0 \tag{7.31}$$

$$\frac{N_{x,c,d}}{k_{c,z} A f_{c,0,d}} + k_{red} \cdot \frac{M_{y,1,d}}{W_y f_{m,y,d}} + \frac{M_{z,1,d}}{W_z f_{m,z,d}} \cdot \left(1 + \frac{N_{x,c,d}}{k_{c,z} A f_{c,0,d}} \cdot \delta_z\right) \leq 1.0 \tag{7.32}$$

where $N_{x,c,d}$ is the design axial compressive force, $k_{c,y/z}$ is the relative flexural buckling load-bearing capacity according to Clause (3), A is the cross-sectional area, $f_{c,0,d}$ is the design compressive strength, $M_{y/z,1,d}$ is the design bending moment about the y- or z-axis from geometrically linear calculations, $W_{y/z}$ is the section modulus about the y- or z-axis, $f_{m,y/z,d}$ is the design bending strength about the y- or z-axis, $\delta_{y/z}$ is the Dischinger-coefficient that accounts for the distribution of $M_{y/z,1,d}$ if it deviates from a sinusoidal half-wave, according to the literature, e.g. FprEN 1995-1-1 [69] B.4.3 (3), and k_{red} is a factor for considering the positive size effect on the bending strength at biaxial bending according to FprEN 1995-1-1 [69] 8.1.8.1(2).

(3) The relative flexural buckling load-bearing capacity $k_{c,y/z}$ should be determined as follows:

$$k_{c,y/z} = \frac{1}{\phi_{c,y/z} + \sqrt{\phi^2_{c,y/z} - \lambda^2_{c,y/z,rel}}} \tag{7.33}$$

$$\phi_{c,y/z} = 0.5 \cdot (1 + \beta_{c,y/z} \cdot (\lambda_{c,y/z,rel} - 0.3) + \lambda^2_{c,y/z,rel}) \tag{7.34}$$

$$\beta_{c,y/z} = k_{pl,c} \cdot \frac{e_{y/z,eq}}{L} \cdot \pi \cdot \sqrt{\frac{3E_{0,k}}{f_{c,0,k}}} \cdot \frac{f_{c,0,k}}{f_{m,y/z,k}} \tag{7.35}$$

where $\phi_{c,y/z}$ is the intermediate parameter for calculating $k_{c,y/z}$ about the y- or z-axis, $\lambda_{c,y/z,rel}$ is the relative slenderness ratio for flexural buckling according to Equation (7.30), β_c is a fitting factor covering the effects of geometrical and structural imperfections, plasticising, and the $E_{0,k}$ to $f_{c,0,k}$ to $f_{m,y/z,k}$ ratio, $k_{pl,c}$ is a factor considering the material-specific stiffness reduction due to compressive plasticising according to Equation (7.17), $e_{y/z,eq}$ is the equivalent bow imperfection according to Section 7.2.1.2 Clause (3) with the respective length L, $E_{0,k}$ is the characteristic elastic modulus in grain direction, $f_{c,0,k}$ is the characteristic compressive strength, and $f_{m,y/z,k}$ is the characteristic bending strength about the y- or z-axis.

(4) For simplification, the fitting factor $\beta_{c,y/z}$ may be determined as follows:

$$\beta_{c,y/z} = \begin{cases} 0.1 \cdot k_{pl,c} & \text{for GL and LVL} \\ 0.2 \cdot k_{pl,c} & \text{for ST} \end{cases} \tag{7.36}$$

where $k_{pl,c}$ is a factor considering the material-specific stiffness reduction due to compressive plasticising according to Equation (7.17).

7.2.2.4 Lateral torsional buckling and flexural buckling with geometrically linear calculation of internal forces and $H/B \geq 2$ (k_c-k_m-method)

(1) Beam-columns should be verified against lateral torsional buckling (and flexural buckling) if the relative slenderness ratios for lateral torsional buckling $\lambda_{m,rel}$ (and flexural buckling $\lambda_{c,z,rel}$) exceed the following limits:

$$\lambda_{m,rel} > 0.7 \quad (\text{and} \quad \lambda_{c,z,rel} > 0.3) \tag{7.37}$$

with

$$\lambda_{m,rel} = \sqrt{\frac{W_y f_{m,y,k} \cdot (1 + k_{def,ef,m})}{M_{y,cr}}} \tag{7.38}$$

where $\lambda_{c,z,rel}$ is the relative slenderness ratio for flexural buckling according to Equation (7.30), W_y is the section modulus about the y-axis, $f_{m,y,k}$ is the bending strength about the y-axis, $k_{def,ef,m}$ is the effective creep coefficient for lateral torsional buckling according to Equation (7.23), and $M_{y,cr}$ is the critical bending moment for lateral torsional buckling according to Section 7.2.1.3 Clause (2).

(2) For $\lambda_{m,rel} \leq 0.7$, beam-columns should be verified against flexural buckling if the

relative slenderness ratios for flexural buckling $\lambda_{c,z,rel}$ exceeds the following limit:

$$\lambda_{c,z,rel} > 0.3 \tag{7.39}$$

where $\lambda_{c,z,rel}$ is the relative slenderness ratio for flexural buckling according to Equation (7.30). In this case, $k_m = 1.0$ should be assumed.

(3) For flexural buckling and/or lateral torsional buckling, the following should be satisfied for stresses in grain direction from axial compression and bending:

$$\frac{N_{x,c,d}}{k_{c,z} A f_{c,0,d}} + \left(\frac{M_{y,1,d}}{k_m W_y f_{m,y,d}}\right)^2 + \frac{M_{z,1,d}}{W_z f_{m,z,d}} \leq 1.0 \tag{7.40}$$

where $N_{x,c,d}$ is the design axial compressive force, $k_{c,z}$ is the relative flexural buckling load-bearing capacity according to Section 7.2.2.3 Clause (3), A is the cross-sectional area, $f_{c,0,d}$ is the design compressive strength, $M_{y/z,1,d}$ is the design bending moment about the y- or z-axis from geometrically linear calculations, k_m is the relative lateral-torsional buckling load-bearing capacity according to Clause (4), $W_{y/z}$ is the section modulus about the y- or z-axis, and $f_{m,y/z,d}$ is the design bending strength about the y- or z-axis.

(4) The relative lateral torsional buckling load-bearing capacity k_m should be determined as follows:

$$k_m = \frac{1}{\phi_m + \sqrt{\phi_m^2 - \lambda_{m,rel}^2}} \tag{7.41}$$

$$\phi_m = 0.5 \cdot (1 + \beta_m \cdot (\lambda_{m,rel} - 0.7) + \lambda_{m,rel}^2) \tag{7.42}$$

$$\beta_m = k_{pl,m} \cdot \frac{e_y}{L} \cdot \frac{H}{B} \cdot \frac{\pi}{2} \cdot \sqrt{\frac{E_{0,k}}{G_{0,k}}} \tag{7.43}$$

where ϕ_m is the intermediate parameter for calculating k_m, $\lambda_{m,rel}$ is the relative slenderness ratio for lateral torsional buckling according to Equation (7.38), β_m is a fitting factor covering the effects of geometrical and structural imperfections, plasticising, the H to B ratio, and the $E_{0,k}$ to $G_{0,k}$ ratio, $k_{pl,m}$ is a factor considering the material-specific stiffness reduction due to shear plasticising, $e_{y,eq}$ is the equivalent bow imperfection according to Section 7.2.1.2 Clause (3) with the respective length L, H and B are the cross-sectional height and width, $E_{0,k}$ is the characteristic elastic modulus in grain direction, and $G_{0,k}$ is the characteristic shear modulus in grain direction.

Note: The twist imperfections are implicitly included in β_m, as bow and twist imperfections affine to the first eigenmode were assumed in the derivation of Equations (7.41) to (7.43).

(5) For simplification, the fitting factor β_{m} may be determined as follows:

$$\beta_{\mathrm{m}} = \begin{cases} 0.01 \cdot k_{\mathrm{pl,m}} \cdot \frac{H}{B} & \text{for GL and LVL} \\ 0.02 \cdot k_{\mathrm{pl,m}} \cdot \frac{H}{B} & \text{for ST} \end{cases} \tag{7.44}$$

where $k_{\mathrm{pl,m}}$ is a factor considering the material-specific stiffness reduction due to shear plasticising according to Equation (7.18), and H and B are the cross-sectional height and width.

7.3 Background regarding the design proposals

The following aspects are not covered by the design proposals; (i) structural systems composed of several members; (ii) combined bending and axial tension; (iii) loading by a torsional moment $M_{x,1}$; (iv) verification of fork bearings and other adjacent components or members; (v) verifications other than the one of stresses in grain direction; (vi) members with non-constant cross-section over the length; (vii) composite members; (viii) materials other than softwood and beech; and (ix) the determination of eigenvalues or effective flexural buckling and LTB lengths.

Section 7.2.1.1 Clause (1): This clause proposes a limit for the application of the beam theory. The design proposal is based on the results of the FEAs described in Sections 6.2.1 and 6.4 and the experimental and FEAs results by Töpler and Kuhlmann [161] on single-span timber beams with a concentrated force or a uniform line load. The formulation of a more general and precise limit criterion and simplified formulas for considering the increase in bending stress might be possible, based on further experimental and numerical investigations.

Section 7.2.1.2 Clause (1) Note 2: See Figure 2.16.

Section 7.2.1.2 Clause (2): This clause was adopted from EN 1995-1-1 [57] and FprEN 1995-1-1 [69], see Equation (2.53).

Section 7.2.1.2 Clause (3): The design proposal for GL and LVL is based on the results of measurements and FEAs on softwood GL and beech LVL described in Sections 3.2, 5.3.4, 5.3.3, and 6.3 and the results by Ehlbeck and Blaß [44]. The results for softwood GL and beech LVL can be transferred to other wood species, if neither significant differences in the production nor in the assembly nor significantly larger scattering of material properties are expected. The value for SL was adopted from FprEN 1995-1-1 [69], which is based on Ehlbeck and Blaß [44]. The design proposal for GL and LVL was incorporated into FprEN 1995-1-1 [69].

Section 7.2.1.2 Clauses (4) and (5): The design proposals are based on the results of measurements and FEAs on softwood GL and beech LVL described in Section 3.2. The results can be transferred to other wood species, as neither significant differences in the production nor in the assembly are to be expected. The design proposals have been incorporated into FprEN 1995-1-1 [69] with a minor modification of $e_{\theta,\mathrm{supp}}$ for fork supports with small tolerances from $1/180$ to $1/150$, see Equation (2.73).

Section 7.2.1.2 Clause (6): The design proposal is based on the results of the FEAs described in Section 6.3 and has been incorporated into FprEN 1995-1-1 [69].

Section 7.2.1.2 Clause (7): The design proposal is based on the results of measurements and FEAs on softwood GL and beech LVL described in Sections 3.2, 5.3.4, 5.3.3, and 6.3 and in line with EN 1995-1-1 [57]. The results can be transferred to other wood species, if neither significant differences in the production nor in the assembly are expected.

The deviating values of $L/500$ and $L/550$ in FprEN 1995-1-1 [69], see Section 2.6.4.1.2, are based on the calculation of the bow imperfections of a beam with $H < L/15$ at the upper edge, with bow and twist imperfections according to Section 7.2.1.2 (3) to (6). This bow imperfection at the upper edge of a beam seems to deviate from an equivalent bow imperfection determined by fitting to FEA results, see Figure 6.22. As the equivalent bow imperfection determined by fitting represents the actual effect of scattering geometrical and structural imperfections, it should be preferred in design.

Section 7.2.1.2 Clause (8): This clause was adopted from CEN/TC 250/SC 5/WG 3/SG 1 [27].

Section 7.2.1.2 Clause (9): The probability that the 95% quantile value, i.e. the characteristic value, of the bow or sway imperfections in the y- and z-directions occur simultaneously is negligibly small. In addition, the decisive structural imperfections of columns only occur at flatwise bending and not at edgewise bending of the lamellas, see Section 2.7.

Section 7.2.1.3 Clause (3): The limit criterion combines the $N_{x,c}$-$M_{y,1}$-interaction of the critical load, see Equation (4.9), with the slenderness limit criteria of the k_c-k_m-method, see Equations (7.29), (7.37), and (7.39). Thus, the limit criteria of the k_c-k_m-method were extended to geometrical nonlinear analyses. For pure axial compressive forces $N_{x,c}$ or pure bending moments $M_{y,1}$, Equation (7.7) corresponds to Equations (7.29) or (7.37). Therefore, a consistent limit for consideration of flexural buckling and LTB with nonlinear and linear analyses is proposed.

Section 7.2.1.3 Clause (4): The limit criterion corresponds to the slenderness limit criterion of the k_c-method, see Equations (7.29). Thus, the limit criterion of the k_c-method was extended to geometrical nonlinear analyses. Therefore, a consistent limit for consideration of flexural buckling with nonlinear and linear analyses is proposed.

Section 7.2.1.3 Clauses (5) and (6): Equations (7.11) to (7.16) for determining the T2O internal forces and deformations $M_{x,2,d}$, $M_{y,2,d}$, $M_{z,2,d}$, $\theta_{2,d}$, $v_{2,d}$, and $w_{2,d}$ were adopted from prEN 1995-1-1 [132] and Hörsting [90] and extended by the influence of creep deformations according to Schänzlin [137] and [139], see Sections 2.2.1.7, 2.2.2.7, and 2.5. The factors $k_{pl,c}$ and $k_{pl,m}$ were introduced for considering the negative influence of shear and compressive plasticising, see Sections 3.3, 3.4, 5.5, and 6.4. As plasticising affects the load-bearing capacity at similar slenderness ratios as the imperfections, see Figures 6.47 and 6.48, and Section 6.4, $k_{pl,c}$ and $k_{pl,m}$ were introduced in Equations (7.11) to (7.16) as an increase of the imperfections. At first glance, reducing the elastic modulus $E_{0,k}$ and the shear modulus $G_{0,k}$ seems to be the more logical option. However, this reduction in stiffness would have to be formulated depending on the axial compressive force, the flexural buckling slenderness, or the critical axial compressive load. This was rejected because it would result in equations that are far too complex for building practice.

Section 7.2.1.3 Clause (7): $k_{pl,c}$ for considering the stiffness reduction due to compressive plasticising was determined by curve fitting of results from design with calculations using

T2O according to Section 7.2.2.2 to the FE results.

Section 7.2.1.3 Clause (8): $k_{\mathrm{pl,m}}$ was determined by curve fitting of results from design with calculations using T2O according to Section 7.2.2.2 to the FE results. It would be desirable if $k_{\mathrm{pl,m}}$ could be specified depending on the magnitude of the axial compressive load, but further experimental and numerical investigations are required for this.

Section 7.2.1.3 Clause (9): This clause was adopted from FprEN 1995-1-1 [69] B.3.2.2 (1) and B.3.2.3 (1).

Section 7.2.1.3 Clause (10): This clause was introduced as the verification in Section 5.4.2 demonstrated that the consideration of the shear modulus $G_{0,\mathrm{k}}$ can influence the eigenvalue of softwood GL columns by 10%. For precise analyses, it can therefore be beneficial to consider $G_{0,\mathrm{k}}$ not only for timber products with low shear stiffness and strength, e.g. CLT, but also for other timber products like softwood GL. Alternatively, an effective elastic modulus $E_{0,\mathrm{k,eff}}$ may be determined and applied.

Section 7.2.1.3 Clause (11): For considering the low probability that both $E_{0,\mathrm{k}}$ and $G_{0,\mathrm{k}}$ occur in a member, an increase in stiffness is proposed for LTB, based on DIN EN 1995-1-1/NA [40], see Section 2.6.3.2. Deviating from DIN EN 1995-1-1/NA [40], the increase is extended to geometric nonlinear calculations. Blaß [11] and Brandner et al. [19] determined 5% quantile values of the product $E_0 G_0$ for softwood GL beams with $H = 600$ mm, which were 5% to 10% below the product of the mean values $E_{0,\mathrm{mean}} G_{0,\mathrm{mean}}$ ($E_{0,\mathrm{mean}} G_{0,\mathrm{mean}} = 1.2\, E_{0,\mathrm{k}} \cdot 1.2\, G_{0,\mathrm{k}} = 1.44\, E_{0,\mathrm{k}} G_{0,\mathrm{k}}$ for softwood GL according to EN 14080 [54]). Therefore, an increase of $1.15^2 = 1.32$ is proposed, which is approximately 10% below the product of the mean values $E_{0,\mathrm{mean}} G_{0,\mathrm{mean}}$. Given that the argument by [11] regarding (i) the positive influence of the warping torsion for typical length-to-height ratios of beams greater than 10 is negligible according to Hörsting [90] and (ii) the neglect of size effect on the tensile strength due to biaxial bending is irrelevant for high slendernesses, as the stiffnesses govern the load-bearing capacity, it is reasonable from the author's perspective to assume an increase of only $1.15^2 = 1.32$ instead of 1.40 as proposed in DIN EN 1995-1-1/NA [40].

Section 7.2.1.4 Clause (1): This clause was adopted from DIN EN 1995-1-1/NA [40] NCI NA.5.9 (NA.1), see Section 2.6.3.1. As Hartnack and Rautenstrauch [85] did not report any need to consider creep deformations at flexural buckling in SC 1, see Section 2.5.2, and FprEN 1995-1-1 [69] only mistakenly includes SC 1, see Section 2.6.4.1.1, the extension to SC 1 suggested in FprEN 1995-1-1 [69] was rejected. Analogous to [85], it would be possible to differentiate additionally between SC 2 and 3, see Section 2.5.2.

Section 7.2.1.4 Clause (2): The limit criterion is based on the investigations in SC 1 by Hofmann [87], see Section 2.5.3. For LTB of beams in other SCs, no investigations were known. The distinction between flexural buckling and LTB seems reasonable, as torsional creep deformations (typical for LTB) exceed the bending creep deformations (typical for flexural buckling) by many times, see Figure 2.34.

Section 7.2.1.4 Clause (3): This clause is based on FprEN 1995-1-1 [69] B.4.6 and investigations by Abeysekera et al. [2], Hartnack and Rautenstrauch [85], and Schänzlin [137], [139].

Section 7.2.1.4 Clauses (4) and (5): Equations (7.22) and (7.23) were adopted from Schänzlin [137], [139], see Sections 2.5.2 and 2.5.3.

Section 7.2.2.1 Clause (1): This clause was adopted from FprEN 1995-1-1 [69] 8.2.1 (2).

Section 7.2.2.1 Clause (2): The differentiation between $H/B \approx 1$ and $H/B \geq 2$ is based on the results of the FEAs described in Section 6.4. This enables a clear distinction between which $N_{x,c}$-$M_{y,1}$-interaction relationship should be chosen for the verification, which is not possible with EN 1995-1-1 [57] and FprEN 1995-1-1 [69]. Further investigations are necessary for specifying the transition point between flexural buckling and lateral torsional buckling more precisely.

Section 7.2.2.1 Clause (3): The design proposal is based on the results of the FEAs in Section 6.4.2.5 and replaces the limit criterion $L_{m,ef}H/B^2 \leq 225$ in DIN EN 1995-1-1/NA [40] and FprEN 1995-1-1 [69], see Sections 2.6.3.3 and 2.6.4.2. The shear load-bearing capacity from FEAs was only slightly lower than the bending load-bearing capacity from FEA, which was confirmed by the results of Hörsting [90]. Therefore, for LTB with $M_{x,1} = 0$, it seems to be possible to neglect shear from torsion in the verification of the shear stresses.

Section 7.2.2.2 Clause (1): This clause was adopted from EN 1995-1-1 [57] 6.2.4 (1) and FprEN 1995-1-1 [69] 8.1.10 (1), see Section 2.6.2.1.1 and 2.6.4.1.1.

Section 7.2.2.2 Clause (2): This clause was introduced based on discussions in the DIN standardisation committee NA 005-04-01-13 AK. As the flexural buckling and LTB load-bearing capacities for large slenderness are only influenced by the stiffness and not by the strength, see Figure 2.4, the characteristic and design load-bearing capacities according to Section 7.2.2.2 Clause (1) are identical for large slenderness, see Figures 7.9 and 7.10. With respect to the safety concept of the Eurocodes, the partial factor γ_M can be considered for large slendernesses by a reduction of the stiffnesses or the critical loads. It is debatable whether the same partial factor γ_M should be applied to the stiffnesses as to the strengths, as the scatter of the stiffnesses is significantly lower according to Schilling et al. [141]. However, it is generally advisable to maintain a sufficient safety distance from the critical load.

Section 7.2.2.2 Clause (3): This clause was adopted from FprEN 1995-1-1 [69] 8.1.12 (1), see Section 2.6.4.2.1.

Section 7.2.2.3 Clause (1): This clause was adopted from EN 1995-1-1 [57] 6.3.2 (1) and (2) and FprEN 1995-1-1 [69] 8.2.2.2 (1), see Sections 2.6.2.1.3 and 2.6.4.1.3. Equation (7.30) for $\lambda_{c,y/z,rel}$ was adopted from Schänzlin [137] and allows for a mechanically correct

consideration of the influence of creep deformations at flexural buckling, see Section 2.5.2. A different limit criterion than $\lambda_{c,rel} \leq 0.3$ might be adopted for timber products with significantly different $E_{0,k}$ or $f_{c,0,k}$ than softwood as $\lambda_{c,rel}$ of the compression tests for determining $f_{c,0,k}$ might deviate, e.g. $\lambda_{c,rel} \leq 0.4$ for beech LVL GL75, see also [137]. However, this was not proposed in favour of the ease-of-use for the building practice.

Section 7.2.2.3 Clause (2): This clause was adopted from EN 1995-1-1 [57] 6.3.2 (3) and FprEN 1995-1-1 [69] 8.2.2.2 (2), see Sections 2.6.2.1.3 and 2.6.4.1.3, and extended by components to consider the geometrically nonlinear behaviour due to the bending moments $M_{y,1,d}$ and $M_{z,1,d}$ according to Equation (4.8). The necessity of the extension is illustrated by the nonlinearity of the $N_{x,c}$-$M_{y,1}$-interaction in Figures 4.1 and 4.2 and the overestimation of the load-bearing capacities with FprEN 1995-1-1 [69] in Figures 6.49 and 6.50. The slenderness-dependent $N_{x,c}$-$M_{y,1}$-interaction obtained from the FEAs and by Blaß [9] and Buchanan et al. [25], see Figure 6.33 and Section 2.3.3.2, was not implemented in Equations (7.31) and (7.32) in favour of the ease-of-use in the building practice. A proposal for a slenderness-dependent $N_{x,c}$-$M_{y,1}$-interaction was discussed by Töpler and Kuhlmann [166].

Section 7.2.2.3 Clauses (3) and (4): These clauses were adopted from EN 1995-1-1 [57] 6.3.2 (3) and FprEN 1995-1-1 [69] 8.2.2.2 (3), see Sections 2.6.2.1.3 and 2.6.4.1.3. Equations (7.35) and (7.36) for calculating β_c were extended by the factor $k_{pl,c}$ for considering the negative influence of compressive plasticising, see Sections 3.3, 5.5.2, and 6.4. On the safe side, the factor $(1 + k_{def,ef,c})$ derived by Schänzlin [137], see Equation (2.43), was neglected, as it introduces a loading dependency of β_c.

Section 7.2.2.4 Clauses (1) and (2): These clauses were adopted from EN 1995-1-1 [57] 6.3.3 (2) and FprEN 1995-1-1 [69] 8.2.2.3 (1), see Sections 2.6.2.1.4 and 2.6.4.1.4. The separation into two clauses was necessary to allow for $H/B \geq 2$ and flexural buckling the application of the favourable nonlinear $N_{x,c}$-$M_{y,1}$-interaction in Equation (7.40) instead of Equation (7.32). As the bending strength of GL made of softwood was established mainly on the basis of numerical investigations, see e.g. Frese [74], there is no slenderness of test specimens for which the effects of LTB are already included in the bending strength $f_{m,k}$, as this is the case for flexural buckling. Therefore, the limit criterion of $\lambda_{m,rel} \leq 0.7$ was determined based on the point where $k_m = 0.9$ in calculations using T2O according to Section 7.2.2.2. Equation (7.38) was derived analytically in Section 4.5 and allows for a mechanically correct consideration of the influence of creep deformations at LTB. As FprEN 1995-1-1 [69] does not distinguish between bending and torsional creep, the corresponding distinction according to Schänzlin [139], see Section 2.5.3, was neglected. The limit criterion $\lambda_{c,z,rel} \leq 0.3$ is discussed at Section 7.2.2.3 Clause (1).

Section 7.2.2.4 Clause (3): The design proposal was adopted from DIN EN 1995-1-1/NA [40] NCI to 6.3.3 (NA.7), see Section 2.6.3.2. It was validated with the extensive experimental, analytical, and numerical investigations described in Sections 3.4, 4.4, and 6.4. It was incorporated into FprEN 1995-1-1 [69], but with an extension by k_{red}, see Equation (2.77). As there were no investigations known to the author that justified the introduction of k_{red} in

FprEN 1995-1-1 [69], k_{red} was not included in the design proposal. In particular, as the geometrically nonlinear effects due to $M_{z,1}$ are neglected in Equations (2.77) and (7.40). The slenderness-dependent $N_{x,c}$-$M_{y,1}$-interaction obtained from the FEA, see Figure 6.34, was not implemented in Equation (7.40) in favour of the ease-of-use in the building practice. A proposal for a slenderness-dependent $N_{x,c}$-$M_{y,1}$-interaction was discussed by Töpler and Kuhlmann [166].

Section 7.2.2.4 Clauses (4) and (5): The design proposals are based on the analytical investigations described in Section 4.5 and Leicester [118], Taras [153], and Wilden et al. [175]. The limit criterion $\lambda_{m,rel} \leq 0.7$ was determined based on the point where $k_m = 0.9$ in calculations using T2O according to Section 7.2.2.2. Equations (7.43) and (7.44) for calculating β_m were extended by the factor $k_{pl,m}$ for considering the negative influence of shear plasticising, see Sections 3.4, 5.5.3, and 6.4. The factor k_{red} from Equations (4.47) to (4.49) was neglected in Equations (7.41) and (7.42) on the safe side and in favour of the ease-of-use in the building practice.

7.4 Discussion

Figures 7.1 to 7.4 display the ratio of the bending load-bearing capacity of design with calculations using T2O and the k_c-k_m-method according to the design proposal in Section 7.2 to the load-bearing capacity from FEA $k_{m,pro}/k_{m,FEA}$ for GL 24h beam-columns with a constant bending moment, a uniform line load, and a concentrated load and $H/B = 4$ and 8 plotted over the relative LTB slenderness ratio $\lambda_{m,rel}$. A $k_{m,pro}/k_{m,FEA}$ ratio of less than 1.0 implies that the design proposal in Section 7.2 is on the safe side. $\lambda_{m,rel}$ was calculated with Equation (7.38). The design was carried out with calculations using T2O according to Section 7.2.2.2 and with the k_c-k_m-method according to Section 7.2.2.4. Equivalent geometrical imperfections according to Section 7.2.1.2 Clauses (3) and (6) with twist imperfections of fork supports with large tolerances were chosen.
In comparing Figures 7.1 to 7.4 to Figures 6.43 to 6.46, the design proposal yields more reliable results than FprEN 1995-1-1 [69] (i) by differentiating for the $N_{x,c}$-$M_{y,1}$-interaction of the k_c-k_m-method between $H/B \approx 1$ and $H/B \geq 2$, see Section 7.2.2.1, compare, e.g. Figures 6.43 and 7.1; (ii) by considering the shear plasticising for LTB with shear forces with $k_{pl,m}$, compare e.g. Figures 6.46 and 7.4; and (iii) by introducing the application limit of the beam-theory $L/H \geq 6$ for members with shear forces, see Section 7.2.1.1.

Figures 7.5 to 7.6 display the ratio of the bending load-bearing capacity of design with calculations using T2O and the k_c-k_m-method according to the design proposal in Section 7.2 to the load-bearing capacity from FEA $k_{c,pro}/k_{c,FEA}$ for GL 24h and GL75 beam-columns

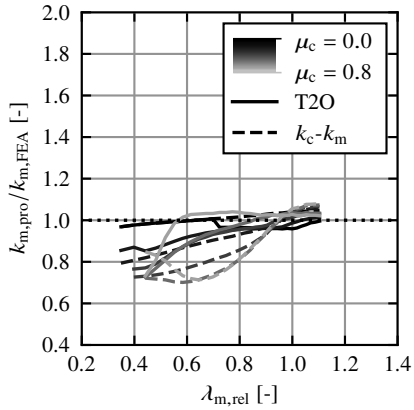

Figure 7.1: Ratio of the bending load-bearing capacity of T2O and the k_c-k_m-method according to the design proposal to the FEA load-bearing capacity $k_{m,pro}/k_{m,FEA}$ plotted over the relative LTB slenderness ratio $\lambda_{m,rel}$ for different utilisation ratios μ_c; with a *constant bending moment*, GL 24h, $H/B = 4$.

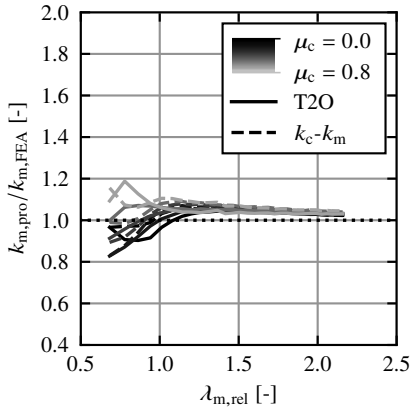

Figure 7.2: Ratio of the bending load-bearing capacity of T2O and the k_c-k_m-method according to the design proposal to the FEA load-bearing capacity $k_{m,pro}/k_{m,FEA}$ plotted over the relative LTB slenderness ratio $\lambda_{m,rel}$ for different utilisation ratios μ_c; with a *constant bending moment*, GL 24h, $H/B = 8$.

with $H/B = 1$ plotted over the relative flexural buckling slenderness ratio $\lambda_{c,rel}$. A $k_{c,pro}/k_{c,FEA}$ ratio of less than 1.0 implies that the design proposal in Section 7.2 are on the safe side. $\lambda_{c,rel}$ was calculated with Equation (7.30). The design was carried out with calculations using T2O according to Section 7.2.2.2 and with the k_c-k_m-method according to Section 7.2.2.4.
For GL 24h and GL 30c the results according to the design proposal and FprEN 1995-1-1 [69] are identical, as no changes were proposed, see Figures 6.47 and 7.5. By considering the compressive plasticising with $k_{pl,c}$ at flexural buckling of GL75, the deviations between the results of the design methods and FEA could be significantly reduced and are in the same range as for GL 24h, compare Figures 7.5 and 7.6.

Figures 7.7 to 7.8 display the ratio of the bending load-bearing capacity of design with calculations using T2O and the k_c-k_m-method according to the design proposal in Section 7.2 to the load-bearing capacity from FEA $k_{m,pro}/k_{m,FEA}$ for GL 24h and GL75 beam-columns with a constant bending moment, and $H/B = 1$ plotted over the relative flexural buckling slenderness ratio $\lambda_{c,rel}$. A $k_{c,pro}/k_{c,FEA}$ ratio of less than 1.0 implies that the design proposal in Section 7.2 are on the safe side. $\lambda_{c,rel}$ was calculated with Equation (7.30). The design was carried out with calculations using T2O according to Section 7.2.2.2 and with the k_c-k_m-method according to Section 7.2.2.4.
In comparing Figures 7.7 and 7.8 to Figures 6.49 to 6.50, the design proposal yields more reliable results than FprEN 1995-1-1 [69] by accounting for the geometrically nonlinear

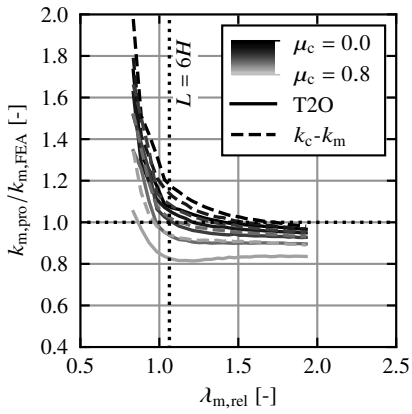

Figure 7.3: Ratio of the bending load-bearing capacity of T2O and the k_c-k_m-method according to the design proposal to the FEA load-bearing capacity $k_{m,pro}/k_{m,FEA}$ plotted over the relative LTB slenderness ratio $\lambda_{m,rel}$ for different utilisation ratios μ_c; with a *concentrated force*, GL 24h, $H/B = 8$.

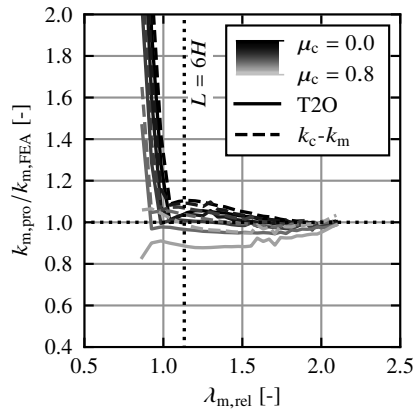

Figure 7.4: Ratio of the bending load-bearing capacity of T2O and the k_c-k_m-method according to the design proposal to the FEA load-bearing capacity $k_{m,pro}/k_{m,FEA}$ plotted over the relative LTB slenderness ratio $\lambda_{m,rel}$ for different utilisation ratios μ_c; with a *uniform line load*, GL 24h, $H/B = 8$.

component of the bending moment $M_{y,1}$ in the k_c-method, see Section 7.2.2.3.

Figure 7.9 displays the characteristic and design load-bearing capacity k_c of design with calculations using T2O and the k_c-method according to FprEN 1995-1-1 [69] and the design proposal in Section 7.2 for GL 24h columns with $H/B = 1$ plotted over the relative flexural buckling slenderness ratio $\lambda_{c,rel}$. Figure 7.10 displays the characteristic and design load-bearing capacities k_m of design with calculations using T2O and the k_m-method according to FprEN 1995-1-1 [69] and the design proposal in Section 7.2 for GL 24h beams with a constant bending moment, and $H/B = 8$ plotted over the relative LTB slenderness ratio $\lambda_{m,rel}$. k_c was calculated by

$$k_c = \frac{N_{x,c,k/d}}{A f_{c,0,k}} \quad , \tag{7.45}$$

where $N_{x,c,k/d}$ is the characteristic or design compressive load-bearing capacity, A is the cross-sectional area, and $f_{c,0,k}$ is the characteristic compressive strength in grain direction. k_m was calculated by

$$k_m = \frac{M_{y,1,k/d}}{W_y f_{m,k}} \quad , \tag{7.46}$$

where $M_{y,1,k/d}$ is the characteristic or design bending load-bearing capacity, W_y is the

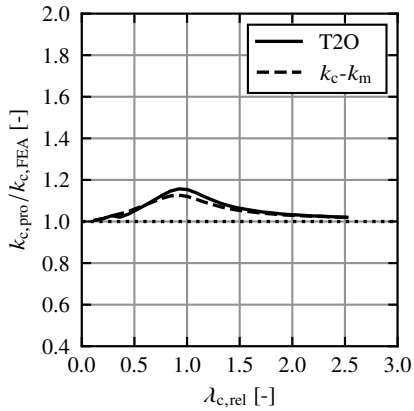

Figure 7.5: Ratio of the compressive load-bearing capacity of T2O and the k_c-k_m-method according to the design proposal to the FEA load-bearing capacity $k_{c,pro}/k_{c,FEA}$ plotted over the relative flexural buckling slenderness ratio $\lambda_{c,rel}$ for *GL 24h* and $H/B = 1$.

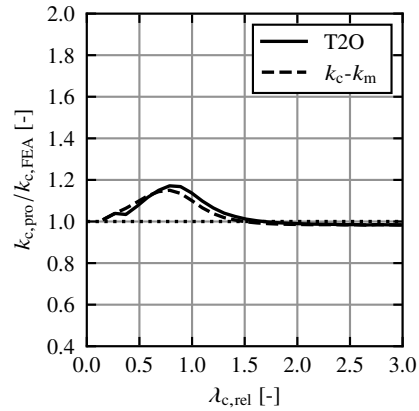

Figure 7.6: Ratio of the compressive load-bearing capacity of T2O and the k_c-k_m-method according to the design proposal to the FEA load-bearing capacity $k_{c,pro}/k_{c,FEA}$ plotted over the relative flexural buckling slenderness ratio $\lambda_{c,rel}$ for *GL75* and $H/B = 1$.

section modulus about the y-axis, and $f_{m,k}$ is the characteristic bending strength. $\lambda_{c,rel}$ and $\lambda_{m,rel}$ were calculated with Equations (7.30) and (7.38). Design with calculations using T2O was carried out according to FprEN 1995-1-1 [69], see Section 2.6.4.1.2, and the design proposal in Section 7.2.2.2. Design with the k_c-k_m-method was carried out according to the design proposal in Section 7.2.2.3. $\gamma_M = 1.0$ and 1.3, $k_{mod} = 1.0$, and $k_{def} = 0.0$ were assumed. N_{cr} and $M_{y,cr}$ were calculated according to Equations (7.19) and (7.20).
The comparison of the characteristic and design load-bearing capacities from design with calculations using T2O demonstrates the importance of the additional stiffness-dependent limit criterion in the design proposal, the limitation of the loading in relation to the critical loads in Equations (7.26) and (7.27). Without this criterion, the characteristic and design load-bearing capacities according to FprEN 1995-1-1 [69] are identical for $\lambda_{c/m,rel} > 1.5$. The k_c-k_m-method implicitly considers this effect, as the resistances are compared to geometrically linear internal forces and not to the geometrically nonlinear internal forces.

Figure 7.11 displays the design load-bearing capacity k_c with and without creep deformations from design with calculations using T2O and the k_c-method according to the design proposal in Section 7.2 for GL 24h columns with $H/B = 1$ plotted over the relative flexural buckling slenderness ratio $\lambda_{c,rel}$. Figure 7.12 displays the design load-bearing capacities k_m with and without creep deformations from design with calculations using T2O and the k_m-method according to the design proposal in Section 7.2 for GL 24h beams with a constant bending moment, and $H/B = 8$ plotted over the relative LTB slenderness ratio $\lambda_{m,rel}$. k_c, k_m, $\lambda_{c,rel}$,

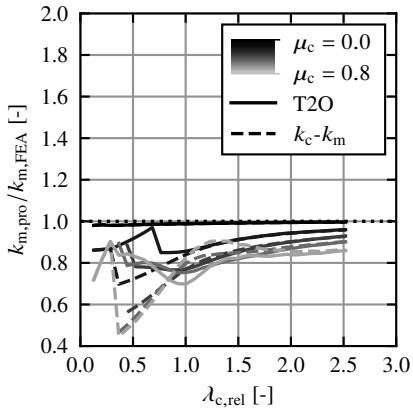

Figure 7.7: Ratio of the bending load-bearing capacity of T2O and the k_c-k_m-method according to the design proposal to the FEA load-bearing capacity $k_{m,pro}/k_{m,FEA}$ plotted over the relative flexural buckling slenderness ratio $\lambda_{c,rel}$ for different utilisation ratios μ_c; with a constant bending moment, *GL 24h*, $H/B = 1$.

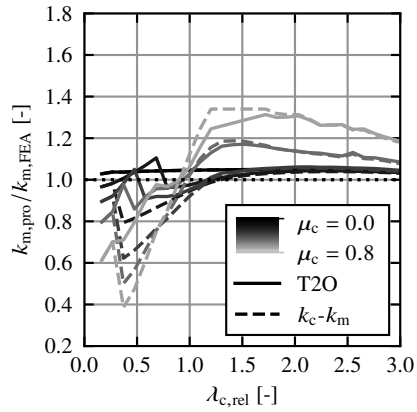

Figure 7.8: Ratio of the bending load-bearing capacity of T2O and the k_c-k_m-method according to the design proposal to the FEA load-bearing capacity $k_{m,pro}/k_{m,FEA}$ plotted over the relative flexural buckling slenderness ratio $\lambda_{c,rel}$ for different utilisation ratios μ_c; with a constant bending moment, *GL75*, $H/B = 1$.

and $\lambda_{m,rel}$ were calculated with Equations (6.6), (6.1), (7.30), and (7.38). $\lambda_{c,rel}$ and $\lambda_{m,rel}$ were calculated with $k_{def} = 0.0$ to allow for a direct comparison of k_c and k_m values. Design with calculations using T2O was carried out according to the design proposal in Section 7.2.2.2. $\gamma_M = 1.3$, $k_{mod} = 1.0$, and $k_{def} = 0.0$ and 0.8 were assumed. N_{cr} and $M_{y,cr}$ were calculated according to Equations (7.19) and (7.20).
k_{def} had a significant effect on the load-bearing capacity at medium and high slenderness. No effect was observed at low slendernesses, as the load-bearing capacity is not influenced by the stiffness but by the strength. The results of the k_c-k_m-method were slightly more conservative. The reason for this is that γ_M and k_{mod} are not included in Equations (7.33) to (7.35) and Equations (7.41) to (7.43). While this would be mechanically correct, it would also reduce the ease-of-use for building practice.

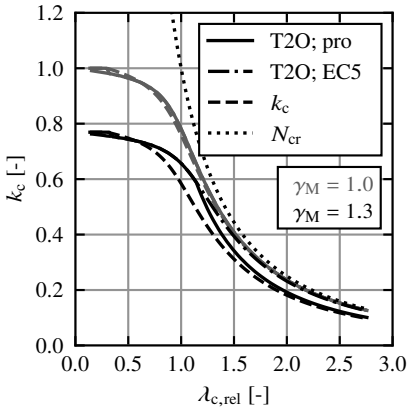

Figure 7.9: Characteristic and design load-bearing capacities k_c from design with calculations using T2O and the k_c-method according to FprEN 1995-1-1 [69] and the design proposal plotted over the relative flexural buckling slenderness ratio $\lambda_{c,rel}$; with the critical flexural buckling load $N_{z,cr}$; with *GL 24h*, and $H/B = 1$.

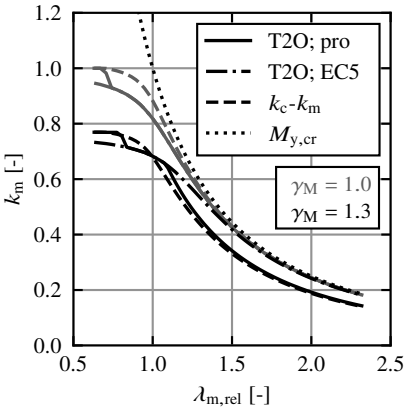

Figure 7.10: Characteristic and design load-bearing capacities k_m from design with calculations using T2O and the k_c-k_m-method according to FprEN 1995-1-1 [69] and the design proposal plotted over the relative LTB slenderness ratio $\lambda_{m,rel}$; with the critical LTB load $M_{y,cr}$; with a constant bending moment, *GL 24h*, and $H/B = 8$.

7.5 Summary

Section 7 presents the design proposals for LTB and flexural buckling of timber beam-columns. The design proposals are based on the design models in FprEN 1995-1-1 [69]. Emphasis was on improving the reliability of the design methods in FprEN 1995-1-1 [69], as discussed in Section 6.4.3, while covering all relevant physical effects, proposing mechanically meaningful design methods, and ensuring ease-of-use for the building practice.

With the limit criterion $L/H \geq 6$, an application limit of the beam theory was introduced in Section 7.2.1.1. This is crucial given that for smaller L/H ratios, the edge bending stresses are significantly increased by shear-induced cross-sectional warping.

Consistent equivalent geometrical imperfections for the design of GL and LVL beam-columns were proposed, see Section 7.2.1.2. These can be utilised for verifications with geometrically nonlinear analyses as well as with geometrically linear analyses (k_c-k_m-method) and distinguish between SL and GL or LVL. This is a significant improvement compared to EN 1995-1-1 [57] and has already been incorporated into FprEN 1995-1-1 [69].

Consistent criteria were proposed for identifying if flexural buckling and LTB can be neglected in geometrically nonlinear and linear analyses, see Equations (7.7), (7.10), (7.29), (7.37), and (7.39).
Introducing the distinction between $H/B \approx 1$ and $H/B > 2$ allows for the first time a clear

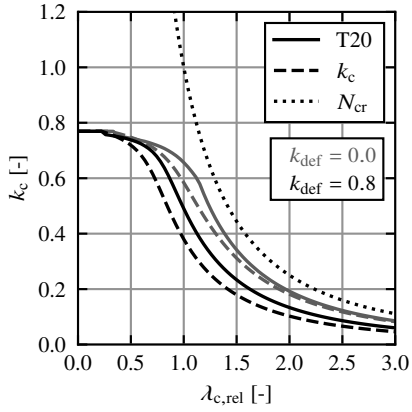

Figure 7.11: Design load-bearing capacities k_c with and without creep deformations from design with calculations using T2O according to the design proposal plotted over the relative flexural buckling slenderness ratio $\lambda_{c,rel}$; with the critical flexural buckling load $N_{z,cr}$; with *GL 24h*, and $H/B = 1$.

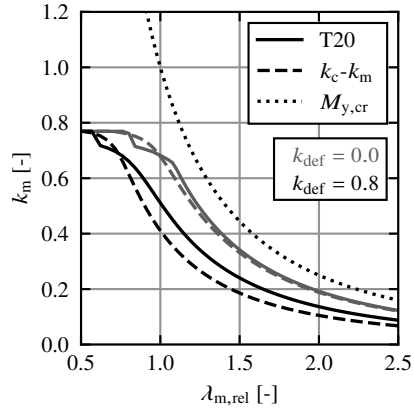

Figure 7.12: Design load-bearing capacities k_m with and without creep deformations from design with calculations using T2O according to the design proposal plotted over the relative LTB slenderness ratio $\lambda_{m,rel}$; with the critical LTB load $M_{y,cr}$; with a constant bending moment, *GL 24h*, and $H/B = 8$.

distinction with the k_c-k_m-method between if the linear $N_{x,c}$-$M_{y,1}$-interaction, which is characteristic of flexural buckling, applies and if the nonlinear $N_{x,c}$-$M_{y,1}$-interaction, which is characteristic of LTB, applies, see Section 7.2.2.1. In contrast to EN 1995-1-1 [57] and FprEN 1995-1-1 [69], it is no longer necessary to check both interactions.
The k_c-method was extended to consider the geometrically nonlinear behaviour due to the bending moments $M_{y,1,d}$ and $M_{z,1,d}$, see Section 7.2.2.3.
For the k_m-method, mechanically sound equations were proposed, see Section 7.2.2.4, which render the regression equations from FprEN 1995-1-1 [69] obsolete.
On the basis of the experimental and numerical investigations, the geometrically nonlinear analyses and geometrically linear analyses were extended by factors for considering the compressive plasticising in grain direction, which is relevant for GL75 columns, and for considering the shear plasticising in grain direction, which is relevant for LTB of beams loaded by shear forces, see Sections 7.2.1.3, 7.2.2.3, and 7.2.2.3.
Furthermore, for verifications with geometrically nonlinear analyses, limit criteria for actions in relation to the critical loads were introduced, see Section 7.2.2.2, which are of major importance, as otherwise the characteristic load-bearing capacities would be equal to the design load-bearing capacities for large slenderness ratios.
Finally, the creep deformations were implemented mechanically correct in the design methods, allowing for a consistent consideration of creep, see Sections 7.2.1.3, 7.2.1.4, 7.2.2.3, and 7.2.2.4.

The comparison with FprEN 1995-1-1 [69] demonstrated that the proposed modifications of the design methods enable a more economical and reliable design of timber beam-columns prone to LTB and flexural buckling, see Section 7.4.

8 Summary and outlook

8.1 Summary

This thesis discusses the load-bearing behaviour and capacity of imperfection-sensitive timber members under combined bending and compression. The main objective of this thesis was to formulate mechanically sound, consistent verification methods for imperfection-sensitive timber members with combined bending and axial compression, i.e. timber beam-columns. These methods should be capable of considering all relevant effects for both softwood *Glued Laminated timber* (GL) and novel timber products, including geometrically and materially nonlinear behaviour, geometrical and structural imperfections, size effects, and long-term behaviour. The overarching objective was to link the flexural buckling and lateral-torsional buckling of timber members on the basis of extensive experimental, analytical, and numerical calculations and thereby establish the basis for a comprehensive understanding of the buckling phenomena of bar-shaped timber members.

The results of three research projects, conducted at the Institute of Structural Design of the University of Stuttgart from 2019 to 2024, are combined within this thesis: DIBt - ZP 52-5-13.194 [107], RP 7-1 of the Cluster of Excellence IntCDC [109], and IGF No. 21285 N [108].

Main parts of this thesis are: (i) the state of the art report in Section 2, (ii) the measurements of geometrical imperfections of timber beams and columns in Section 3.2; (iii) the experimental investigations of the *flexural buckling* behaviour of beech *Laminated Veneer Lumber* (LVL) GL75 in Section 3.3; (iv) the experimental investigations of the *Lateral Torsional Buckling* (LTB) behaviour of full-scale softwood GL beams with combined bending and axial compression in Section 3.4; (v) the analytical investigations on the mechanical background of the stability phenomena in Section 4; (vi) the numerical models and their verification and validation in Section 5; (vii) the combination of the results of the experimental, analytical, and numerical investigations in Section 6; and (viii) the design proposals in Section 7.

In the imperfection measurements, 23 buildings were surveyed with a laser scanner directly after assembly, and the geometrical imperfections of 202 softwood GL beams, 38 beech LVL beams, and 57 beech LVL columns were analysed, see Section 3.2. The geometrical imperfections of the beams could be split into three parts: the bow imperfections, the twist imperfections at midspan, and the twist imperfections at the fork supports, see Figure 3.6. For the softwood GL beams, the 95% quantile values of the equivalent bow imperfections, the equivalent twist imperfections at midspan, and the twist imperfections at the supports were $L/1180$, $L/1600$, and $1/100$. The measured twist imperfections were about 70% of the size of the bow imperfections and can therefore have a significant influence on the LTB load-bearing capacity. The measured bow imperfections of beams agreed well with measured values of columns from literature.

27 flexural buckling tests on beech LVL GL75 columns were conducted, see Section 3.3.

In preceding test, the stress-strain curves of GL75 for compression in grain direction were determined. With a proportionality limit of $f_{c,0,lin} \approx 0.65 f_{c,0}$ and plastic strains of $\epsilon_{c,0,pl} \approx 1.25 \epsilon_{c,0,el}$, beech LVL GL75 exhibited three to five times higher plasticising than softwood. The load-bearing capacity of the columns was always defined by the peak of the load-deformation curve and not a brittle member failure in tension, see Figure 3.21. The experimentally determined load-bearing capacities were up to 10% lower than the characteristic load-bearing capacities according to EN 1995-1-1 [57], see Figure 3.29, which is in line with experimental results of beech GL columns by Ehrhart et al. [52]. This was due to the high plastic strains on reaching the compressive strength and the resulting decrease of the bending stiffness. This has to be considered in the verification of beech LVL GL75 columns.

19 LTB tests on full-scale softwood GL beams with combined bending and axial compression were conducted, see Section 3.4. The load-horizontal displacement behaviour was usually nonlinear with a pronounced plateau, see Figure 3.35. Shear failure occurred in the slender beams and bending failure in the stockier beams, see Figures 3.39 and 3.40. For the slender test specimens, the high twist of the cross-sections led to high torsional shear stresses, which presumably caused early local shear failures. These led to a reduction in stiffnesses, which resulted in higher deformations, and finally up to 20% lower load-bearing capacities. This should be considered in the LTB verification of timber beams. The nonlinear curve of the $N_{x,c}$-$M_{y,1}$-interaction, which is assumed in the k_c-k_m-method in EN 1995-1-1 [57], was confirmed by the test results, see Figure 3.41.

The analytical investigations in Section 4 confirmed that the $N_{x,c}$-$M_{y,1}$-interaction for LTB of slender beam-columns is nonlinear as it approaches the nonlinear limit criterion of the critical load. Furthermore, it was demonstrated that the nonlinear $N_{x,c}$-$M_{y,2}$-interaction with an exponent of two at the compressive term in EN 1995-1-1 [57] represents a mechanically sound limit criterion. Finally, mechanically sound equations for the k_m-method for LTB were derived, see Section 4.5. The consideration of the size effect due to biaxial bending, the consideration of the creep deformations, and, at least in timber construction, the formulation with bow imperfections were novel.

The development, implementation, verification, and validation of a parametrised *Finite Element* (FE) model in *Abaqus/CAE 2023* for numerical analyses of imperfection-sensitive timber members is described in Section 5. A user-defined material model was implemented in the UMAT subroutine of Abaqus to model the anisotropic elastoplastic material behaviour of wood. To account for the scattering stiffnesses and strengths of wood, the *Karlsruher Rechenmodell*, see, e.g. Blaß et al. [14], was extended to include scattering shear strengths and stiffnesses over the member length and height and scattering elastic moduli over the member width. For the first time, this enabled a numerical investigation of the structural imperfections of softwood GL beams. Furthermore, scattering geometrical imperfections were considered on the basis of the imperfection measurements. The models were verified and validated in line with the FE-guidelines [162] and published on *DaRUS*, see [157], [156], [158], and [159].

The numerical parameter studies revealed some partially unexpected fundamental aspects, see Section 6.2. A significant shear force-induced shear warping was observed for $L/H < 6$, which increases the edge bending stresses and thus reduces the bending load-bearing capacity, see Figures 6.1 to 6.3. Additionally, FEA with solid elements and equations from FprEN 1995-1-1 [69] based on beam theory result in differences in the critical bending moments of up to 20%, which can cause differences in load-bearing capacities of up to 10%, see Figure 6.6. Finally, a plate bending occurs at FEA with large H/B ratios, which affects the critical bending moment and the load-bearing capacity.
The numerical parameter study on equivalent geometrical imperfections in Section 6.3 demonstrated that geometrical imperfections are decisive for LTB of softwood GL beams and that structural imperfections can be neglected. In contrast to the flexural buckling of softwood GL columns, where structural imperfections are decisive and geometrical imperfections can be neglected. Consistent equivalent geometrical imperfections were derived, which allow for a reliable and economical design of GL and LVL beam-columns, see Equations (6.2) to (6.4).
The results of the FEA confirmed the nonlinearity of the $N_{x,c}$-$M_{y,1}$-interaction for LTB, see Figure 6.34, which was also experimentally and analytically observed and is assumed in the k_c-k_m-method in EN 1995-1-1 [57]. This nonlinear $N_{x,c}$-$M_{y,1}$-interaction typical for LTB is governing for $H/B \geq 2$. For $H/B = 1$, the linear $N_{x,c}$-$M_{y,1}$-interaction typical for flexural buckling occurs, see Figure 6.33. For LTB of beam-columns with significant shear forces and $1.0 \leq \lambda_{m,rel} \leq 1.5$, shear plasticising reduced the load-bearing capacity by up to 20%. This was in line with the results of the LTB tests. For flexural buckling of medium-slender GL75 columns, i.e. $\lambda_{c,rel} \approx 1.0$, the material-specific compressive plasticising in grain direction reduced the load-bearing capacity by about 15%, see Figure 6.39. This was in line with the results of the flexural buckling tests.

The experimental, analytical, and numerical results were combined and utilised to carefully modify and extend the design models in FprEN 1995-1-1 [69] to create mechanically sound, consistent, and experimentally validated design concepts for imperfection-sensitive timber beam-columns. The design proposals include, among others, (i) the application limit $L/H \geq 6$ for the beam theory in calculations with significant shear forces, (ii) consistent approaches for equivalent geometrical imperfections, (iii) a distinction between the $N_{x,c}$-$M_{y,1}$-interaction at $H/B \approx 1$ and $H/B \geq 2$, (iv) mechanically sound equations for the k_m-method, (v) the factors $k_{pl,m}$ and $k_{pl,c}$ accounting for shear and compressive plasticising, (vi) a limit criterion for geometrically nonlinear internal forces based on the critical load, and (vii) the consistent implementation of creep deformations in the verifications.
The proposed modifications and extensions of the design methods in FprEN 1995-1-1 [69] enable a more economical, reliable, and consistent verification of imperfection-sensitive timber beam-columns.

Through extensive experimental, analytical, and numerical investigations, the load-bearing and failure behaviour in the case of flexural buckling and lateral-torsional buckling could be comprehensively characterised, and both stability phenomena could be combined in consistent analysis and design models. This provides a sound basis for a comprehensive understanding of the buckling phenomena of bar-shaped timber members.

8.2 Outlook

The discussed in-depth investigations of the buckling phenomena of bar-shaped timber members and the formulation of consistent verification methods form a robust foundation upon which subsequent research can build on and expand.

In the LTB tests in Section 3.4, a premature local shear failure due to torsion was presumably observed. Thus, the load-deformation behaviour of softwood GL beams under torsion with the early shear plasticising seems to differ fundamentally from the approximately linear-elastic behaviour under shear from shear force. Hence, experimental investigations of the load-deformation behaviour of softwood GL beams under torsion would be of great benefit, also for refining the presented numerical model.
In this thesis, member shear failure was only touched on briefly, as it did not appear to have a significant influence on the LTB load-bearing capacity, see Figure 6.42. However, parameter studies with scattering shear and bending strengths using the developed numerical model, see Section 5.3.3, could provide more insight into this.
The influence of creep deformations on stability behaviour has been studied little and is only dealt with in a very simplified way in FprEN 1995-1-1 [69]. In particular, due to the high torsional creep, detailed investigations of LTB under long-term behaviour, as initiated by Hofmann [87], are urgently required. To verify the long-term behaviour of real timber structures, deformation measurements similar to the imperfection measurements described in Section 3.2 would be possible with relatively little effort.
The column tests on beech LVL GL75 in Section 3.3 demonstrated that the material-specific elastoplastic behaviour can have a significant influence on the load-bearing capacity. Investigations into the elastoplastic behaviour are therefore required before novel wood species or wood products can be widely applied in the construction sector.
The FEA and own trial tests revealed a significant increase in edge bending stresses due to shear force-induced shear warping, see Section 6.2.1. Relatively simple experimental and numerical investigations could provide important insights into this safety-relevant aspect.
Moreover, the numerical investigations in Section 6 indicated significant differences between eigenvalues from three- and one-dimensional analyses and a flexural buckling at large H/B ratios, which are of interest for further investigations.

Not discussed at all in this thesis were, among others, LTB with combined bending and tension and LTB with planned bending around the weak axis $M_{y,1}$ or torsion $M_{x,1}$. Furthermore, the size effect on the tensile strength at biaxial bending, other member shapes like double-tapered beams, and hybrid members combined of wood products with significantly different stiffnesses and/or strengths were not investigated. Finally, the torsional moments at fork supports and the effect of bracings were not addressed. Some of these aspects have been investigated in the literature only analytically, some only partially, and some not yet at all.

Researchers interested in the stability phenomena of timber members are therefore likely to encounter no shortage of topics to explore in the coming decades.

References

[1] Abaqus (2023). *Simulia User Assistance 2023*. Dassault Systèmes SE.

[2] Abeysekera, I., I. Feltham, and A. Lawrence (2021). “Buckling of slender timber beam-columns under combined loading, including creep”. In: *Proceedings of the 8th meeting of International Network on Timber Engineering Research (INTER)*. 54-2-1, online.

[3] Aicher, S. (1990). “Investigation on the torsional properties of vertical glulam including "warping torsion" of orthotropoic materials”. In: *Otto-Graf-Journal* 1, pp. 9–35.

[4] Aicher, S. and G. Dill-Langer (2000). “Basic considerations to rolling shear modulus in wooden boards”. In: *Otto-Graf-Journal* 11, pp. 157–165.

[5] Aicher, S. and D. Ohnesorge (2011). “Shear strength of glued laminated timber made from European beech timber”. In: *European Journal of Wood and Wood Products* 69, pp. 143–154. DOI: 10.1007/s00107-009-0399-9.

[6] Ballio, G. and F. M. Mazzolani (1983). *Theory and design of steel structures*. New York, US: Chapman and Hall. ISBN: 0-412-23660-5.

[7] Blank, L., G. Fink, R. Jockwer, and A. Frangi (2017). “Quasi-brittle fracture and size effect of glued laminated timber beams”. In: *European Journal of Wood and Wood Products* 75, pp. 667–681. DOI: 10.1007/s00107-017-1156-0.

[8] Blaß, H. J. (1987a). “Design of timber columns”. In: *CIB-W18*. 20-2-2, Dublin, Ireland.

[9] Blaß, H. J. (1987b). “Tragfähigkeit von Druckstäben aus Brettschichtholz unter Berücksichtigung streuender Einflussgrößen”. Phd thesis. University of Karlsruhe, Karlsruhe, Germany.

[10] Blaß, H. J. (1988). “Einfluss des Kriechens auf die Tragfähigkeit von Holzdruckstäben”. In: *Holz als Roh- und Werkstoff* 46, pp. 405–411.

[11] Blaß, H. J. (2005). *Ermittlung des 5%-Quantils des Produkts aus Elastizitätsmodul und Torsionsschubmodul für Brettschichtholz*. Research report for Studiengemeinschaft Holzleimbau e.V. (unpublished), see also CEN/TC 124 WG3 N0021. University of Karlsruhe, Karlsruhe, Germany.

[12] Blaß, H. J., J. Ehlbeck, and L. Kurzweil (1998). *Untersuchungen zur Zugfestigkeit von Brettschichtholz im Hinblick auf Normungsvorschläge*. Research report. Universität Fredericiana zu Karlsruhe, Karlsruhe, Germany. DOI: 10.5445/IR/354598.

[13] Blaß, H. J. and M. Frese (2002). *Entwicklung eines Sortierverfahrens für die kombinierte maschinelle und visuelle Festigkeitssortierung*. Research report. Universität Fredericiana zu Karlsruhe, Karlsruhe, Germany.

[14] Blaß, H. J., M. Frese, P. Glos, J. K. Denzler, P. Linsenmann, and A. Ranta-Maunus (2008). *Zuverlässigkeit von Fichten-Brettschichtholz mit modifiziertem Aufbau*. Research report. University of Karlsruhe, Karlsruhe, Germany. DOI: 10.5445/KSP/1000008462.

[15] Blaß, H. J. and O. Krüger (2010). *Schubverstärkung von Holz mit Holzschrauben und Gewindestangen*. Research report. Karlsruhe Institute of Technology, Karlsruhe, Germany. DOI: 10.5445/KSP/1000020518.

[16] Bodig, J. and B. A. Jayne (1982). *Mechanics of wood and wood composites*. Malabar, Florida, US: Krieger publishing company. ISBN: 0-89464-777-6.

[17] Brandner, R. (2024). "Fatigue behaviour of in tension axially-loaded self-tapping screws". In: *Proceedings of the 11th meeting of International Network on Timber Engineering Research (INTER)*. 57-7-1, Padova, Italy.

[18] Brandner, R., W. Gatternig, and G. Schickhofer (2012). "Determination of shear strength of structural and glued laminated timber". In: *CIB-W18*. 45-12-2, Växjö, Sweden.

[19] Brandner, R., E. Gehri, T. Bogensperger, and G. Schickhofer (2007). "Determination of modulus of shear and elasticity of glued laminated timber and related examinations". In: *CIB-W18*. 40-12-2, Bled, Slovenia.

[20] Brüninghoff, H. (1973). "Spannungen und Stabilität bei quergestützten Brettschichtholzträgern". Phd thesis. University of Karlsruhe, Karlsruhe, Germany.

[21] Brüninghoff, H. and H. Klapp (2005a). "Shear strength of glued laminated timber". In: *CIB-W18*. 38-6-3, Karlsruhe, Germany.

[22] Brüninghoff, H. and H. Klapp (2005b). "Stabilitätsnachweis im Holzbau – Biegedrillknicken mit Normalkraft". In: *Bauen mit Holz* 10, pp. 27–33.

[23] BS-Holz-Merkblatt (2022). Studiengemeinschaft Holzleimbau e.V., Wuppertal, Germany.

[24] Buchanan, A. H. (1984). "Strength model and design methods for bending and axial load interaction in timber members". Phd thesis. University of British Columbia, Vancouver, Canada.

[25] Buchanan, A. H., K. C. Johns, and B. Madsen (1985). "Column design methods for timber engineering". In: *CIB-W18*. 18-2-1, Beit Oren, Israel.

[26] Burger, N. (1998). "Einfluss der Holzabmessungen auf die Zugfestigkeit von Schnittholz unter Zugbeanspruchung in Faserrichtung". Phd thesis. Ludwig Maximilian University of Munich, Munich, Germany.

[27] CEN/TC 250/SC 5/WG 3/SG 1 (2021). *Revised design rules for Section 7 – Based on Project team 3 Sub-task 3 (1) Milestone 4*. CEN/TC 250/SC 5/WG 3 N 288.

[28] Chen, W.-F. and T. Atsuta (1976). *Theory of beam-columns – In-plane behavior and design*. New York, US: McGraw-Hill. ISBN: 0-07-010754-8.

[29] Chen, W.-F. and T. Atsuta (1977). *Theory of beam-columns – Space behavior and design*. New York, US: McGraw-Hill. ISBN: 0-07-010759-9.

[30] Colling, F. (1990). "Tragfähigkeit von Biegeträgern aus Brettschichtholz in Abhängigkeit von den festigkeitsrelevanten Einflußgrößen". Phd thesis. University of Karlsruhe, Karlsruhe, Germany. DOI: 10.5445/IR/20490.

[31] Dahl, K. B. and K. A. Malo (2009). "Nonlinear shear properties of spruce softwood: experimental results". In: *Wood Science and Technology* 43, pp. 539–558. DOI: 10.1007/s00226-009-0247-4.

[32] Dahlblom, O., S. Ormarsson, and H. Petersson (1996). "Simulation of wood deformation processes in drying and other types of environmental loading". In: *Annals of Forest Science* 53, pp. 857–866.

[33] Dietsch, P., A. Gamper, M. Merk, and H. Schopbach (2012). *Film project for educational purposes: failure mechanisms in timber structures [DVD]*. Technical University of Munich, Munich, Germany. URL: https://www.youtube.com/watch?v=Z_IB3K4kLxQ.

[34] Dietsch, P. and K. Henke (2010). *Verformungsmessungen an weitgespannten Brettschichtholzträgern zur Ermittlung horizontaler Verformungen*. Research report. Technical University of Munich, Munich, Germany.

[35] Dill-Langer, G. and S. Aicher (2013). *Glulam composed of glued laminated veneer lumber made of beech wood – superior performance in compression loading*. Ed. by S. Aicher, H. W. Reinhardt, and H. Garrecht. Materials and Joints in Timber Structures. RILEM Bookseries, vol 9. Dordrecht, Netherlands: Springer. DOI: 10.1007/978-94-007-7811-5_55.

[36] Dill-Langer, G. and S. Aicher (2014). "Tragfähigkeit und Baupotenziale von Buchen-Furnierschichtholz". In: *20. Internationales Holzbau Forum (IHF)*. Garmisch-Partenkirchen, Germany.

[37] Dill-Langer, G. and S. Aicher (2015). "BauBuche im XXL-Format – Versuche und Europäische technische Zulassung". In: *3. Stuttgarter Holzbau-Symposium*. Stuttgart, Germany, pp. 79–87.

[38] DIN 1052 (2004). *Entwurf, Berechnung und Bemessung von Holzbauwerken – Allgemeine Bemessungsregeln und Bemessungsregeln für den Hochbau*. German Institute of Standardization (DIN), Berlin, Germany.

[39] DIN 68364 (2003). *Kennwerte von Holzarten – Rohdichte, Elastizitätsmodul und Festigkeiten*. German Institute of Standardization (DIN), Berlin, Germany.

[40] DIN EN 1995-1-1/NA (2013). *Nationaler Anhang – National festgelegte Parameter – Eurocode 5: Bemessung und Konstruktion von Holzbauten – Teil 1-1: Allgemeines – Allgemeine Regeln und Regeln für den Hochbau*. German Institute of Standardization (DIN), Berlin, Germany.

[41] Dlubal Software GmbH (2023). *RFEM 6.05*. Tiefenbach, Germany.

[42] Eberhardsteiner, J. (2002). *Mechanisches Verhalten von Fichtenholz*. Wien, Austria: Springer-Verlag. ISBN: 3-211-83763-9.

[43] Eggen, T. E. (2021). "Buckling and geometrical nonlinear beam-type analyses of timber structures". Phd thesis. Norwegian University of Science and Technology, Trondheim, Norway.

[44] Ehlbeck, J. and H. J. Blaß (1987). *Zuverlässigkeit von Holzdruckstäben*. Research report. University of Karlsruhe, Karlsruhe, Germany. DOI: 10.5445/IR/1000173252.

[45] Ehlbeck, J. and F. Colling (1987). *Biegefestigkeit von Brettschichtholz in Abhängigkeit von Rohdichte, Elastizitätsmodul, Ästigkeit und Keilzinkung der Lamellen, der Lage der Keilzinkung sowie von der Trägerhöhe*. Research report. University of Karlsruhe, Karlsruhe, Germany. DOI: 10.5445/IR/1000173250.

[46] Ehlbeck, J. and F. Colling (1992). *Biegefestigkeit von Brettschichtholz in Abhängigkeit von den Eigenschaften der Brettlamellen im Hinblick auf Normungsvorschläge*. Research report. University of Karlsruhe, Karlsruhe, Germany. DOI: 10.5445/IR/1000173293.

[47] Ehlbeck, J., F. Colling, and R. Görlacher (1984). *Einfluss keilgezinkter Lamellen auf die Biegefestigkeit von Brettschichtholzträgern*. Research report. University of Karlsruhe, Karlsruhe, Germany.

[48] Ehlbeck, J., F. Colling, and R. Görlacher (1985). "Einfluss keilgezinkter Lamellen auf die Biegefestigkeit von Brettschichtholzträgern – Eingangsdaten für das Rechenmodell". In: *Holz als Roh- und Werkstoff* 43, pp. 369–373.

[49] Ehrhart, T. (2019). "European beech glued laminated timber". Phd thesis. ETH Zurich, Zurich, Switzerland. DOI: 10.3929/ethz-b-000402805.

[50] Ehrhart, T. and R. Brandner (2018). "Rolling shear: test configurations and properties of some European soft- and hardwood species". In: *Engineering Structures* 172, pp. 554–572. DOI: 10.1016/j.engstruct.2018.05.118.

[51] Ehrhart, T., R. Steiger, and A. Frangi (2021a). "Influence of the moisture content on the compressive strength and modulus of elasticity parallel to the grain of engineered hardwood products (EHP)". In: *Proceedings of the 8th meeting of International Network on Timber Engineering Research (INTER)*. 54-12-2, online.

[52] Ehrhart, T., R. Steiger, A. Frangi, T. Strahm, and A. Bernasconi (2019). "Compressive strength and buckling resistance of GLT columns made of European beech (fagus sylvatica l.)" In: *Proceedings of the 6th meeting of International Network on Timber Engineering Research (INTER)*. 52-12-1, Tacoma, USA.

[53] Ehrhart, T., R. Steiger, A. Frangi, T. Strahm, and A. Bernasconi (2021b). *Laubholzstützen – Druckfestigkeit und E-Modul parallel zur Faserrichtung und Einfluss der Holzfeuchte*. Research report, WHFF-CH 2020.11. ETH Zurich, Zurich, Switzerland.

[54] EN 14080 (2013). *Timber structures – Glued laminated timber and glued solid timber – Requirements*. European Committee for Standardization (CEN), Brussels, Belgium.

[55] EN 1990 (2010). *Eurocode 0 – Basis of structural design*. European Committee for Standardization (CEN), Brussels, Belgium, with corrections and amendments + A1:2005 and AC:2010.

[56] EN 1993-1-1 (2005). *Eurocode 3 – Design of steel structures – Part 1-1: General rules and rules for buildings*. European Committee for Standardization (CEN), Brussels, Belgium, with corrections and amendments + AC:2009.

[57] EN 1995-1-1 (2004). *Eurocode 5 – Design of timber structures – Part 1-1: General – Common rules and rules for buildings*. European Committee for Standardization (CEN), Brussels, Belgium, with corrections and amendments + AC:2006, A1:2008, and A2:2014.

[58] EN 26891 (1991). *Timber structures – Joints made with mechanical fasteners; General principles for the determlnation of strength and deformation characteristics (ISO 6891 : 1983)*. European Committee for Standardization (CEN), Brussels, Belgium.

[59] EN 384 (2016). *Structural timber – Determination of characteristic values of mechanical properties and density*. European Committee for Standardization (CEN), Brussels, Belgium, with corrections and amendments + A2:2022.

[60] EN 408 (2010). *Structural timber and glued laminated timber – Determination of some physical and mechanical properties*. European Committee for Standardization (CEN), Brussels, Belgium, with corrections and amendments + A1:2012.

[61] Engesser, F. (1891). "Die Knickfestigkeit gerader Stäbe". In: *Centralblatt der Bauverwaltung* 11.49, pp. 483–486.

[62] Ersvik, O. and G. Alpsten (1970). *Experimental investigation of the column strength of wide-flange shapes ME 200 A, roller straightened in different ways,* Report 19.3. Swedish Institute of Steel Construction, Stockholm, Sweden.

[63] ETA-14/0354 (2018). *Beam BauBuche GL75*. Austria Institute of Construction Engineering (OIB), Vienna, Austria.

[64] Fink, G. (2014). "Influence of varying material properties on the load-bearing capacity of glued laminated timber". Phd thesis. ETH Zurich, Zurich, Switzerland. DOI: 10.3929/ethz-a-010294974.

[65] Fink, G., J. Köhler, and A. Frangi (2013). *Bending tests on glued laminated timber beams with well-known material properties*. Research report. ETH Zurich, Zurich, Switzerland.

[66] Fischer, L. (2003). "Charakteristische Werte – ihre Bedeutung und Berechnung". In: *Bauingenieur* 78, pp. 179–187.

[67] Flaig, M. (2013). "Biegeträger aus Brettsperrholz bei Beanspruchung in Plattenebene". Phd thesis. Karlsruhe Institute of Technology, Karlsruhe, Germany. DOI: 10.5445/KSP/1000035587.

[68] FprEN 1993-1-14 (2024). *Eurocode 3 – Design of steel structures – Part 1-14: Design assisted by finite element analysis*. CEN/TC 250/SC 3 N 4020. European Committee for Standardization (CEN): Brussels, Belgium.

[69] FprEN 1995-1-1 (2024). *Eurocode 5 – Design of timber structures – Part 1-1: General rules and rules for buildings (Version 3f)*. CEN/TC 250/SC 5 N 2196. European Committee for Standardization (CEN): Brussels, Belgium.

[70] FprEN 1995-3 (2024). *Eurocode 5 – Design of timber structures – Part 3: Execution*. CEN/TC 250/SC 5 N 2163. European Committee for Standardization (CEN): Brussels, Belgium.

[71] Frangi, A. and M. Theiler (2015). *Knickversuche mit Brettschichtholzstützen unter exzentrischer Normalkraftbeanspruchung*. Research report. ETH Zurich, Zurich, Switzerland.

[72] Franke, S., B. Franke, and M. Magnière (2016). "Load carrying capacity of cracked beams". In: *Proceedings of the 14th World Conference of Timber Engineering (WCTE)*. Vienna, Austria.

[73] Frese, M. (2006). "Die Biegefestigkeit von Brettschichtholz aus Buche: Experimentelle und numerische Untersuchungen zum Laminierungseffekt". Phd thesis. Universität Fredericiana zu Karlsruhe, Karlsruhe, Germany. DOI: 10.5445/KSP/1000004599.

[74] Frese, M. (2016). "Computergestützte Verfahren zur pragmatischen Beurteilung der Tragwiderstände von Brettschichtholz: Zusammenfassung exemplarischer Simulationsstudien". Habilitation. Karlsruhe Institute of Technology, Karlsruhe, Germany. DOI: 10.5445/KSP/1000052710.

[75] Frese, M., M. Enders-Comberg, H. J. Blaß, and P. Glos (2012). "Compressive strength of spruce glulam". In: *European Journal of Wood and Wood Products* 70, pp. 801–809. DOI: 10.1007/s00107-012-0623-x.

[76] Gatternig, W. (2012). "Prüftechnische Ermittlung der Schubfestigkeit von Vollholz und Analyse des Größeneinflusses". Master thesis. Graz University of Technology, Graz, Austria.

[77] Glos, P. (1978). "Berichte zur Zuverlässigkeitstheorie der Bauwerke: Zur Bestimmung des Festigkeitsverhaltens von Brettschichtholz bei Druckbeanspruchung aus Werkstoff- und Einwirkungskenngrößen". Heft 35/1978. Phd thesis. Technical University of Munich, Munich, Germany.

[78] Glos, P. (1981). *Berichte zur Zuverlässigkeitstheorie der Bauwerke: Zur Modellierung des Festigkeitsverhaltens von Bauholz bei Druck-, Zug- und Biegebeanspruchung*. Heft 61/1981. Technical University of Munich, Munich, Germany.

[79] Glos, P. and J. K. Denzler (2004). *Kalibrierung der charakteristischen Schubfestigkeitskennwerte für Vollholz in EN 338 entsprechend den Rahmenbedingungen der nationalen Sortiernorm*. Research report. Technical University of Munich, Munich, Germany.

[80] Görlacher, R. (1990). "Klassifizierung von Brettschichtholzlamellen durch Messung von Longitudinalschwingungen". Phd thesis. University of Karlsruhe, Karlsruhe, Germany. DOI: 10.5445/IR/1490.

[81] Görlacher, R. and J. Kürth (1994). "Determination of shear modulus". In: *CIB-W18*. 27-10-1, Sidney, Australia.

[82] Gressel, P. (1982). "Kriechverhalten von Holz und Holzwerkstoffen – Auswirkungen auf den Formänderungsnachweis". In: *Ingenieurholzbau in Forschung und Praxis – Karl Möhler gewidmet*. Ed. by J. Ehlbeck, G. Steck, and H. Blumer. Karlsruhe, Germany: Bruderverlag, pp. 55–66.

[83] Grosse, M. (2005). "Zur numerischen Simulation des physikalisch nichtlinearen Kurzzeittragverhaltens von Nadelholz am Beispiel von Holz-Beton-Verbundkonstruktionen". Phd thesis. Bauhaus-Universität Weimar, Weimar, Germany.

[84] Gupta, R. and T. Siller (2005). "Shear strength of structural composite lumber using torsion tests". In: *Journal of Testing and Evaluation* 33.2, pp. 110–117.

[85] Hartnack, R. and K. Rautenstrauch (2005). "Long-term load bearing of wooden columns influenced by climate: view on code". In: *CIB-W18*. 38-2-1, Karlsruhe, Germany.

[86] Heimeshoff, B. (1986). "Berechnung und Ausführung von Holzbauwerken". In: *Ingenieur-Holzbau 86*. Leinfelden-Echterdingen, Germany.

[87] Hofmann, R. (2022). "Stabilität und Langzeitverhalten schlanker Brettschichtholzträger". Phd thesis. University of Stuttgart, Stuttgart, Germany. DOI: 10.18419/opus-12674.

[88] Hofmann, T. J. (1992). "Beitrag zur verfeinerten Balkentheorie". Phd thesis. University of Stuttgart, Stuttgart, Germany.

[89] Hooley, R. F. and B. Madsen (1964). "Lateral stability of glued laminated beams". In: *Journal of Structural Division* ST3, pp. 201–218.

[90] Hörsting, O.-P. (2008). "Zum Tragverhalten druck- und biegebeanspruchter Holzbauteile". Phd thesis. Technische Universität Carolo-Wilhelmina zu Braunschweig, Braunschweig, Germany. DOI: 10.24355/dbbs.084-200807140200-0.

[91] Hütter, V. (2017). "Bestimmung der Rollschubfestigkeiten und -steifigkeiten von Furnierschichthölzern aus Laubholz". Bachelor thesis. Karlsruhe Institute of Technology, Karlsruhe, Germany.

[92] JCSS (2006). "3.5 Properties of timber". In: *JCSS probabilistic model code – Part 3: resistance models*. Joint Committee of Structural Safety (JCSS).

[93] Johansson, C.-J. (2003). “Grading of timber with respect to mechanical properties”. In: *Timber Engineering*. Ed. by S. Thelandersson and H. J. Larsen. Chichester, United Kingdom: Wiley. Chap. 10, pp. 23–43.

[94] Kenel, A. and U. Meierhofer (1998). *Holz / Beton-Verbund unter langfristiger Beanspruchung*. Research report 115/39. Swiss Federal Laboratories for Materials Science and Technology (EMPA), Dübendorf, Switzerland.

[95] Kersken-Bradley, M. (1981). “Beanspruchbarkeit von Bauteilquerschnitten bei streuenden Kenngrößen des Kraftverformungsverhaltens innerhalb des Querschnitts”. Phd thesis. Technical University of Munich, Munich, Germany.

[96] Kessel, M. H. (2012). *Imperfektionen von satteldachförmigen Fachwerkträgern aus Holz*. Research report. Technical University of Braunschweig, Braunschweig, Germany.

[97] Kessel, M. H. (2022). *Considerations on the relationship between stability and imperfections*. CEN/TC 250/SC 5/WG 3 N 417.

[98] Kessel, M. H., A. Kühl, and C. Hall (2015). *Überprüfung und Ergänzung der Imperfektionsannahmen und Montageregeln der DIN EN 1995-1-1 für Nagelplattenkonstruktionen zur Steigerung ihrer Sicherheit und Wirtschaftlichkeit*. Research report. Ingenieurbüro kgs, Hildesheim, Germany.

[99] Kessel, M. H. and A. Mertinaschk (2001). *Imperfektionsmessungen an Nagelplattenbindern*. Research report, AiF No. 11631 N. Technical University of Braunschweig, Braunschweig, Germany.

[100] Kessel, M. H., F. Schönhoff, and O.-P. Hörsting (2005). “Zum Nachweis von druckbeanspruchten Bauteilen nach DIN 1052:2004-08 – Teil 1”. In: *Bauen mit Holz* 12, pp. 88–96.

[101] Kessel, M. H., M. Sieder, and H. Kreuzinger (2020). *Bracing of the main girder of a pedestrian bridge*. CEN/TC 250/SC 5/WG 3 N 153.

[102] Khokhar, A., H. Zhang, and D. Ridley-Ellis (2010). “The shear strength, and failure modes, of timber joists obtained from torsion test method”. In: *Proceedings of the 11th World Conference of Timber Engineering (WCTE)*. Trentino, Italy.

[103] Kollmann, F. and W. A. Côté (1968). *Principles of Wood Science and Technology: I – Solid Wood*. Berlin – Heidelberg, Germany: Springer-Verlag.

[104] Köppel, N., J. Töpler, and U. Kuhlmann (2019). “Investigation of lateral torsional buckling of timber beams subjected to combined bending and axial compression”. In: *25. Internationales Holzbau Forum (IHF)*. Garmisch-Partenkirchen, Germany.

[105] Kuck, E. (2015). “Untersuchungen von Querschnittsschwächungen durch Verbindungsmittel in druckbeanspruchten Bauteilen aus Buchenfurnierschichtholz”. Bachelor thesis. Karlsruhe Institute of Technology, Karlsruhe, Germany.

[106] Kuhlmann, U. and F. Jörg (2019). *Interaktionsbeziehungen für Normalkraft, Biegemomente und Torsion: Harmonisierung und Ergänzung der Stabilitätsnachweise*

für Stäbe mit Standard-Walzprofilen. Research report, IGF No. 19044 N. Institute of Structural Design, University of Stuttgart, Stuttgart, Germany.

[107] Kuhlmann, U. and J. Töpler (2020–2022). *Imperfektionsmessungen an stabilitätsgefährdeten Holzbauteilen*. Research Project, DIBt P 52-5- 13.194-2048/19, Institute of Structural Design, University of Stuttgart, Stuttgart, Germany.

[108] Kuhlmann, U. and J. Töpler (2021–2023). *Optimierung des Ersatzstabverfahrens für biegedrillknickgefährdete Bauteile aus Holz unter Momenten-Normalkraft-Belastung*. Research Project, IGF No. 21285 N, Institute of Structural Design, University of Stuttgart, Stuttgart, Germany.

[109] Kuhlmann, U., J. Töpler, J. Gauß, and L. Buchholz (2019–2022). *Development of an integrated approach of testing and numerical verifications which respects and further develops the basic rules of the eurocodes*. Research Project, DFG Cluster of Excellence: Integrative Computational Design and Construction for Architecture, EXC 2120/1–390831618, RP 7-1, Institute of Structural Design, University of Stuttgart, Stuttgart, Germany.

[110] Lam, F. and J.-K. Oh (2018). "Performance of Canadian glulam columns with new laminae E requirements". In: *Engineering Structures* 172, pp. 85–93.

[111] Larsen, H. J. (1977). "Laterally loaded timber columns: tests and theory". In: *CIB-W18*. 8-15-1, Brussels, Belgium.

[112] Larsen, H. J. (1980). *Strength of glued laminated beams*. Report No. 8004. Aalborg University, Aalborg, Denmark.

[113] Larsen, H. J. and E. Theilgaard (1979). "Laterally loaded timber columns". In: *Journal of Structural Division* ST7, pp. 1347–1363.

[114] Lecomte, C. (2017). *Lateral torsional buckling of bended Kerto elements: A code oriented reseach on the stability design of Kerto members subjected to bending and/or compression*. Metsä Wood, Paris, France.

[115] Leica Geosystems AG (2013). *Leica ScanStation P20 – User Manual*. Heerbrugg, Switzerland.

[116] Leicester, R. H. (1986). "Creep buckling strength of timber beams and columns". In: *CIB-W18*. 19-2-1, Florence, Italy.

[117] Leicester, R. H. (1988a). "Beam-column formulae for design codes". In: *CIB-W18*. 21-2-2, Parksville, Vancouver Island, Canada.

[118] Leicester, R. H. (1988b). "Format for buckling strength". In: *CIB-W18*. 21-2-1, Parksville, Vancouver Island, Canada.

[119] Lindner, J. and R. Giezelt (1984). "Imperfektionsannahmen für Stützenschiefstellungen". In: *Stahlbau* 53.4, pp. 910–921.

[120] Lukas, J., J. Töpler, and U. Kuhlmann (2023). "Investigations of lateral torsional buckling of timber beams under combined bending and compression". In: *27. Internationales Holzbau Forum (IHF)*. Innsbruck, Austria.

[121] Möhler, K. and K. Hemmer (1976). *Untersuchungen über die Festigkeit und das Dauerstandsverhalten von Nadelholz und Brettschichtholz bei Torsionsbeanspruchung*. Research report. University of Karlsruhe, Karlsruhe, Germany.

[122] Möhler, K. and K. Hemmer (1977). "Verformungs- und Festigkeitsverhalten von Nadelvoll- und Brettschichtholz bei Torsionsbeanspruchung". In: *Holz als Roh- und Werkstoff* 35, pp. 473–478.

[123] Narcy, A., D. T. Pham, G. Forêt, and L. A. (2023). "Comparison of CLT buckling strength criteria with experimental results". In: *Proceedings of the 10th meeting of International Network on Timber Engineering Research (INTER)*. 56-2-1, Biel/Bienne, Switzerland.

[124] Neuhaus, F.-H. (1981). "Elastizitätszahlen von Fichtenholz in Abhängigkeit von der Holzfeuchtigkeit". Phd thesis. Ruhr University Bochum, Bochum, Germany.

[125] Niemz, P. and W. Sonderegger (2017). *Holzphysik*. Munich, Germany: Carl Hanser Verlag. ISBN: 978-3-446-44526-0.

[126] Ormarsson, S. and D. Cown (2005). "Moisture related distortion of timber boards of radiata pine: comparison with Norway spruce". In: *Wood and Fibre Science* 37.3, pp. 424–436.

[127] Pawlowski, R., K. Henke, P. Schregle, and S. Winter (2013). "Überwachung von Bauwerksverformungen mittels digitaler Bildverarbeitung". In: *Bauingenieur* 88.5, pp. 214–221.

[128] Petersen, C. (1980). *Elasto- und plasto-statische Berechnungsverfahren druckbeanspruchter Tragwerke – Nachweisformen gegen Knicken, Kippen, Beulen*. Braunschweig / Wiesbaden, Germany: Friedr. Vieweg & Sohn. ISBN: 3-528-08663-7.

[129] Poulsen, J. S. (1997). "Compression in clear wood". Phd thesis. Danmarks Tekniske Universitet, Lyngby, Denmark.

[130] Pourostad, V. (2024). "Stabilitätsverhalten von nicht-rechteckigen Beulfeldern und von ausgesteiften Beulfeldern unter mehrachsigen Beanspruchungen". Phd thesis. Institute of Structural Design, University of Stuttgart, Stuttgart, Germany. DOI: 10.18419/opus-15380.

[131] prEN 1995-1-1 (2023). *Background documents to prEN 1995-1-1:2023*. CEN/TC 250/SC 5/N 1809.

[132] prEN 1995-1-1 (2024). *Eurocode 5 – Design of timber structures – Part 1-1: General rules and rules for buildings (Version 2a)*. CEN/TC 250/SC 5 N 2077. European Committee for Standardization (CEN): Brussels, Belgium.

[133] Rautenstrauch, K. and P. Becker (1998). "Zur Berücksichtigung des Kriechens bei Druckstäben aus Holz". In: *Bautechnik* 75.11, pp. 23–29.

[134] Rondal, J. and R. Maquoi (1978). "Analytical formulation of the new European buckling curves". In: *Acier – Stahl – Steel* 43.1, pp. 23–29.

[135] Schaeffler Technologies GmbH & Co. KG (2011). *Gelenklager, Gleitbuchsen, Gelenkköpfe – Katalog 238*. Herzogenaurach, Germany.

[136] Schänzlin, J. (2010). "Modeling the long-term behavior of structural timber for typical serviceclass-II-conditions in South-West Germany". Habilitation. Institute of Structural Design, Stuttgart, Germany. DOI: 10.18419/opus-348.

[137] Schänzlin, J. (2020). *k_c-method – consideration of creep deformations*. Institute for timber design, Biberach University of Applied Sciences, Biberach, Germany.

[138] Schänzlin, J. (2023). *Umdruck zu den Vorlesungen: Holzbau (12550) und Ingenieurholzbau (12560)*. University of Stuttgart, Stuttgart, Germany.

[139] Schänzlin, J. (2024). *Creep & torsional buckling – determination of the value k_{crit}*. Institute for timber design, Biberach University of Applied Sciences, Biberach, Germany.

[140] Schickhofer, G. (2001). "Determination of shear strength values for GLT using visual and machine graded spruce laminations". In: *CIB-W18*. 34-12-6, Venice, Italy.

[141] Schilling, S., P. Palma, and A. Frangi (2021). "Probabilistic description of the mechanical properties of glued laminated timber made from softwood". In: *Proceedings of the 8th meeting of International Network on Timber Engineering Research (INTER)*. 54-12-4, online. DOI: 10.3929/ethz-b-000505371.

[142] Schulte, C. (2022). "Entwicklung eines Rechenmodells zur Bestimmung der Tragfähigkeit von stabilitätsgefährdeten Brettschichtholzträgern unter Berücksichtigung streuender Einflußgrößen". Phd thesis. Ruhr University Bochum, Bochum, Germany. DOI: 10.5445/IR/13742002.

[143] Schulz, G. (1968). "Traglastermittlung von planmäßig mittig belasteten Druckstäben aus Baustahl unter Berücksichtigung von geometrischen und strukturellen Imperfektionen". Phd thesis. Graz University of Technology, Graz, Germany.

[144] Schulze, S. (2017). "Numerische Auswertung der Ersatzstablängen von kippgefährdeten Holzbauteilen und Vergleich mit der Lösung aus der DIN EN 1995-1-1". Project report. Technical University of Braunschweig, Braunschweig, Germany.

[145] Sedlacek, G., H. Stangenberg, J. Lindner, T. Glitsch, R. Kindmann, and C. Wolf (2004). *Forschung für die Praxis P 554 – Untersuchungen zum Einfluss der Torsionseffekte auf die plastische Querschnittstragfähigkeit und die Bauteiltragfähigkeit von Stahlprofilen*. Research report. RWTH Aachen, Technical University of Berlin, Ruhr University Bochum, Aachen, Berlin, Bochum, Germany.

[146] Sieder, R. and R. Brandner (2022). "Probabilistic models for the tensile properties of split boards and their application for the prediction of bending properties of engineered timber products made of Norway spruce". In: *Buildings* 12. DOI: 10.3390/buildings12081143.

[147] SKF (2021). *GE 90 TXE-2LS Radial spherical plain bearings – Technical specification*. Gothenburg, Sweden.

[148] Spengler, R. (1986). "Festigkeitsverhalten von Brettelementen aus Fichte unter zweiachsiger Beanspruchung". In: *Baukonstruktion und Holzbau: Beiträge aus Lehre und Forschung. o. Prof. Dr.-Ing. Bodo Heimeshoff zum 60. Geburtstag*. Ed. by R. Spengler. Munich, Germany: Lehrstuhl für Baukonstruktion und Holzbau, Technical University of Munich, pp. 125–157.

[149] Steffen, A., C.-J. Johanssen, and E.-W. Wormuth (1997). "Study of the relationship between flatwise and edgewise moduli of elasticity of sawn timber as a means to improve mechanical strength grading technology". In: *Holz als Roh- und Werkstoff* 55, pp. 245–253.

[150] Steiger, R. and M. Fontana (2005). "Bending moment and axial force interacting on solid timber beams". In: *Materials and Structures* 38, pp. 507–513. DOI: 10.1007/BF02479541.

[151] Suomen rakentamismääräyskokoelma B 10 (78). *Puurakenteet Ohjeet*. Sisäasiainministeriö, Helsinki, Finland.

[152] Tapia, C. and S. Aicher (2022). "Size effect of glulam made of oak wood under consideration of the finite weakest link theory". In: *Proceedings of the 9th meeting of International Network on Timber Engineering Research (INTER)*. 55-12-2, Bad Aibling, Germany.

[153] Taras, A. (2010). "Contribution to the development of consistent stability design rules for steel members". Phd thesis. Graz University of Technology, Graz, Austria. DOI: 10.3217/1smsn-1bq83.

[154] Theiler, M. (2014). "Stabilität von axial auf Druck beanspruchten Bauteilen aus Vollholz und Brettschichtholz". Phd thesis. ETH Zurich, Zurich, Switzerland. DOI: 10.3929/ethz-a-010273734.

[155] Töpler, J. (2022). *Flexural buckling of beech LVL columns*. Experimental report, research project RP 7, DFG cluster of excellence EXC 2120/1 – 390831618. Institute of Structural Design, University of Stuttgart, Stuttgart, Germany. DOI: 10.18419/opus-16327.

[156] Töpler, J. (2025a). *Source code for: generating scattering geometrical imperfections*. Version V1. DOI: 10.18419/DARUS-5060.

[157] Töpler, J. (2025b). *Source code for: geometrically and materially nonlinear numerical analysis of timber beam-columns with Abaqus/CAE (Abaqus_timber_beam-column)*. Version V1. DOI: 10.18419/DARUS-5059.

[158] Töpler, J. (2025c). *Source code for: KaReMo++*. Version V1. DOI: https://doi.org/10.18419/DARUS-5061.

[159] Töpler, J. (2025d). *Source code for: UMAT subroutine for material modelling of timber with Abaqus*. Version V1. DOI: https://doi.org/10.18419/DARUS-5062.

[160] Töpler, J., L. Buchholz, J. Lukas, and U. Kuhlmann (2023a). "Guidelines for a finite element based design of timber structures and their exemplary application on modelling of beech LVL". In: *Buildings* 13.1143. DOI: 10.3390/buildings13020393.

[161] Töpler, J. and U. Kuhlmann (2022a). "Experimentelle und numerische Untersuchungen von Brettschichtholz aus Buchen-Furnierschichtholz (BauBuche)". In: *Doktorandenkolloquium Holzbau Forschung und Praxis*. Stuttgart, Germany, pp. 131–139. DOI: 10.18419/opus-12607.

[162] Töpler, J. and U. Kuhlmann (2022b). *Guidelines for a finite element based design of timber structures*. Mitteilung No. 2022-36X, Institute of Structural Design, University of Stuttgart, Germany. DOI: 10.18419/opus-12769.

[163] Töpler, J. and U. Kuhlmann (2022c). *Imperfektionsmessungen an stabilitätsgefährdeten Holzbauteilen*. Research report, DIBt P 52-5- 13.194-2048/19. Institute of Structural Design, University of Stuttgart, Stuttgart, Germany. DOI: 10.18419/opus-12578.

[164] Töpler, J. and U. Kuhlmann (2022d). "In-plane buckling of beech LVL columns". In: *Proceedings of the 9th meeting of International Network on Timber Engineering Research (INTER)*. 55-2-1, Bad Aibling, Germany. DOI: 10.18419/opus-12610.

[165] Töpler, J. and U. Kuhlmann (2023). *Measurement data: Laser scanning of timber buildings*. Version V1. DOI: 10.18419/darus-3304.

[166] Töpler, J. and U. Kuhlmann (2024). *Optimierung des Ersatzstabverfahrens für biegedrillknickgefährdete Bauteile aus Holz unter Momenten-Normalkraft-Belastung*. Research report, IGF No. 21285 N. Institute of Structural Design, University of Stuttgart, Stuttgart, Germany.

[167] Töpler, J. and U. Kuhlmann (2025a). *Experimental data: Flexural buckling of beech LVL columns*. Version V1. DOI: 10.18419/DARUS-5058.

[168] Töpler, J. and U. Kuhlmann (2025b). *Experimental data: Lateral torsional buckling of softwood glulam beams with combined bending and axial compressions*. Version V1. DOI: 10.18419/DARUS-5057.

[169] Töpler, J., M. Schweigler, R. Lemaître, P. Palma, M. Schenk, P. Grönquist, C. Tapia, G. Hochreiner, and U. Kuhlmann (2023b). "Finite element based design of timber structures". In: *Proceedings of the 10th meeting of International Network on Timber Engineering Research (INTER)*. 56-102-1, Biel/Bienne, Switzerland. DOI: 10.18419/opus-13594.

[170] TROTEC GmbH & Co. KG (Version 2.0). *T2000 Praxishandbuch*. Heinsberg, Germany.

[171] van der Put, T. A. C. M. (1991). "Discussion of failure criterion for combined bending and compression". In: *CIB-W18*. 24-6-1, Oxford, England.

[172] van der Put, T. A. C. M. (2010). "Failure criterion for timber beams loaded in bending, compression and shear". In: *Wood Material Science and Engineering* 1, pp. 41–49. DOI: 10.1080/17480270903582163.

[173] Weibull, W. (1939). *A statistical theory of the strength of materials*. Stockholm, Sweden: Generalstabens litografiska anstalts förlag.

[174] Wilden, V., B. Hoffmeister, and M. Feldmann (2022). “Ein mechanisch konsistenter Ansatz für den Stabilitätsnachweis für Holzträger unter Druck und Biegung um die starke Achse”. In: *Doktorandenkolloquium Holzbau Forschung und Praxis*. Stuttgart, Germany, pp. 165–173.

[175] Wilden, V., B. Hoffmeister, and M. Feldmann (2023). “Ein mechanisch konsistenter Ansatz für den Stabilitätsnachweis für Holzträger unter Druck und Biegung um die starke Achse, Teil 1 – Herleitungen”. In: *Bautechnik* 100.Sonderheft Holzbau, pp. 19–30. DOI: 10.1002/bate.202200073.

[176] Wilden, V., B. Hoffmeister, and M. Feldmann (2024). “Ein mechanisch konsistenter Ansatz für den Stabilitätsnachweis für Holzträger unter Druck und Biegung um die starke Achse – Teil 2: Versuche und Numerik”. In: *Bautechnik* 101. DOI: 10.1002/bate.202400020.

[177] Windeck, L. and H. J. Blaß (2017). *Prüfbericht Nr. 176121 – Versuche an Brettschichtholz aus Buchen- und Nadel-Furnierschichtholz zur Ermittlung des Querdruckbeiwertes $k_{c,90}$ (unpublished)*. Experimental report. Karlsruhe Institute of Technology, Karlsruhe, Germany.

[178] Xiao, Q. (2014). “Lateral torsional buckling of wood beams”. Master thesis. University of Ottawa, Ottawa, Canada.

[179] Ylinen, A. (1956). “A method for determining the buckling stress and the required cross-sectional area for centrally loaded straight columns in elastic and inelastic range”. In: *Publications of the International Association for Bridge and Structural Engineering* 16, pp. 529–550. DOI: 10.5169/seals-15082.

[180] Yoshihara, H. and A. Suzuki (2005). “Shear stress/shear strain relation of wood obtained by asymmetrie four-point bending test of side-tapered specimen”. In: *Journal of Testing and Evaluation* 33.1, pp. 55–60.

[181] Zahn, J. J. (1982). *Strength of lumber under combined bending and compression*. Research report. University of Minnesota, Minnesota, US.

[182] Zahn, J. J. (1984). *Design of wood members und combined load*. Research report. Forest Products Laboratory, Madison, US.

[183] Zahn, J. J. (1986). “Design of wood members und combined load”. In: *Journal of Structural Engineering* 112.9, pp. 2109–2126. DOI: 10.1061/(ASCE)0733-9445(1986)112:9(2109).

[184] Zahn, J. J. (1992). “Re-examination of Ylinen and other column equations”. In: *Journal of Structural Engineering* 118.10, pp. 2716–2728. DOI: 10.1061/(ASCE) 0733-9445(1992)118:10(2716).

[185] Zahn, J. J. and D. R. Rammer (1995). “Design of glued laminated timber columns”. In: *Journal of Structural Engineering* 121.12, pp. 1789–1794. DOI: 10.1061/ (ASCE)0733-9445(1995)121:12(1789).

Appendix A

Data of flexural buckling tests on beech LVL columns

A.1 Flexural buckling tests

The experimentally determined load-deformation curves of the 26 flexural buckling tests on beech LVL GL75 columns from the research project RP 7-1 of the Cluster of Excellence IntCDC [109] are presented in the following. The results of column S01 are not displayed as, in this case, the lower support acted as an unplanned restraint due to high friction. The x-axis displays the horizontal deformation at midspan v, and the y-axis exhibits the compressive force $N_{x,c}$. The experimental results are compared with results of FEA with compressive plasticising and calculations using T2O from the validation in Section 5.5.2.

In Table A.1, the dimensions of the test specimens, the density, the elastic modulus in grain direction from preceding elastic bending tests, and the maximum load are given. The height represents the cross-sectional dimension in the direction of the buckling. It is the mean value of measurements at both sides and at the bottom, middle, and top of each column.

The tests are discussed in Section 3.3. The experimental data are also available at Töpler and Kuhlmann [167].

Table A.1: Data of the flexural buckling tests on beech LVL GL75 columns.

Specimen number	L [mm]	H [mm]	B [mm]	ρ [kg/m^3]	$E_{0,el}$ [N/mm^2]	$N_{x,c,R}$ [kN]
S02	2998	119.2	119.1	797.0	16,030	−200
S03	2998	119.4	119.3	788.6	15,510	−193
S04	3003	159.1	158.0	807.8	17,139	−569
S05	2999	159.1	158.1	803.6	17,836	−585
S06	3003	159.1	158.0	807.6	18,014	−601
S07	3002	200.0	198.1	791.1	16,160	−1130
S08	2999	200.0	198.1	802.5	16,702	−1152
S09	3002	199.9	198.0	806.4	17,059	−1183
S10	2499	199.3	198.0	806.4	16,863	−1226
S11	2504	199.2	197.8	794.0	16,747	−1191
S12	2499	199.2	197.7	798.7	16,520	−1185
S13	2498	198.0	199.8	791.5	16,006	−1359
S14	2499	198.1	199.9	792.3	15,786	−1321
S15	2504	198.1	199.7	790.4	16,497	−1348
S16	2498	199.7	198.1	808.4	17,182	−1418
S17	2504	199.7	198.1	787.3	16,524	−1378
S18	2503	199.8	198.0	805.0	15,837	−1342
S19	2498	199.5	198.1	809.4	16,987	−1634
S20	2503	199.5	198.0	809.9	16,740	−1609
S21	2503	199.8	198.0	802.5	16,134	−1590
S22	2003	199.4	199.1	818.7	17,006	−1576
S23	2000	199.6	199.1	805.1	16,286	−1569
S24	2003	199.5	199.2	786.6	15,540	−1528
S25	2000	199.2	199.8	797.6	14,718	−1439
S26	2003	199.2	199.8	811.9	15,498	−1535
S27	2000	199.1	199.8	816.2	15,603	−1548
			Mean	801.4	16,420	
			COV	0.0113	0.0463	

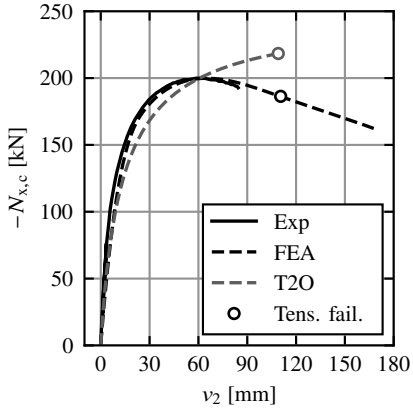

Figure A.1: Experimentally (Exp) determined load-deformation behaviour of flexural buckling test S02 with compressive forces $N_{x,c}$ plotted over the horizontal deformations at midspan v_2; comparison with FEA and calculations using T2O.

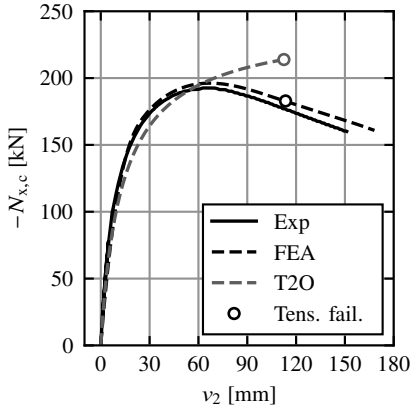

Figure A.2: Experimentally (Exp) determined load-deformation behaviour of flexural buckling test S03 with compressive forces $N_{x,c}$ plotted over the horizontal deformations at midspan v_2; comparison with FEA and calculations using T2O.

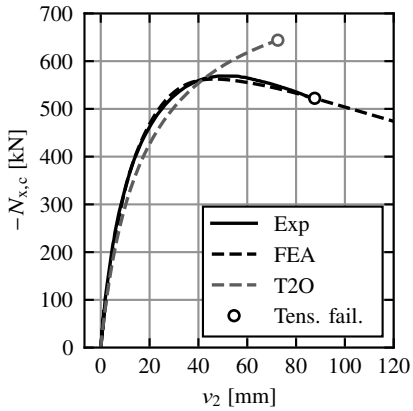

Figure A.3: Experimentally (Exp) determined load-deformation behaviour of flexural buckling test S04 with compressive forces $N_{x,c}$ plotted over the horizontal deformations at midspan v_2; comparison with FEA and calculations using T2O.

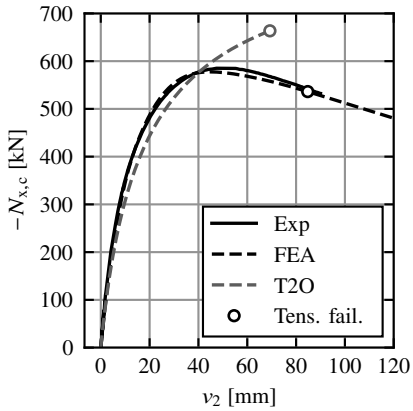

Figure A.4: Experimentally (Exp) determined load-deformation behaviour of flexural buckling test S05 with compressive forces $N_{x,c}$ plotted over the horizontal deformations at midspan v_2; comparison with FEA and calculations using T2O.

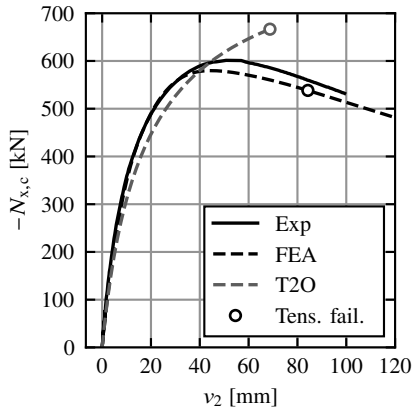

Figure A.5: Experimentally (Exp) determined load-deformation behaviour of flexural buckling test S06 with compressive forces $N_{x,c}$ plotted over the horizontal deformations at midspan v_2; comparison with FEA and calculations using T2O.

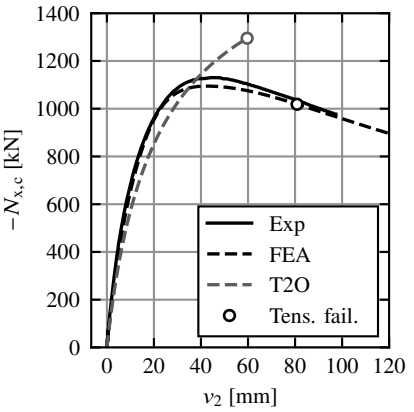

Figure A.6: Experimentally (Exp) determined load-deformation behaviour of flexural buckling test S07 with compressive forces $N_{x,c}$ plotted over the horizontal deformations at midspan v_2; comparison with FEA and calculations using T2O.

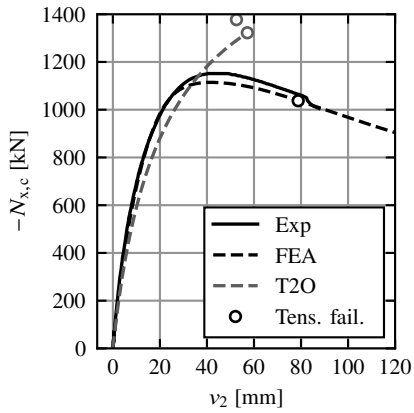

Figure A.7: Experimentally (Exp) determined load-deformation behaviour of flexural buckling test S08 with compressive forces $N_{x,c}$ plotted over the horizontal deformations at midspan v_2; comparison with FEA and calculations using T2O.

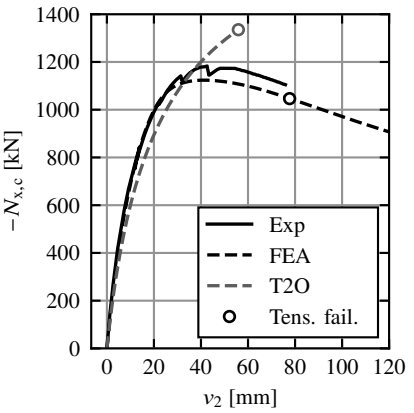

Figure A.8: Experimentally (Exp) determined load-deformation behaviour of flexural buckling test S09 with compressive forces $N_{x,c}$ plotted over the horizontal deformations at midspan v_2; comparison with FEA and calculations using T2O.

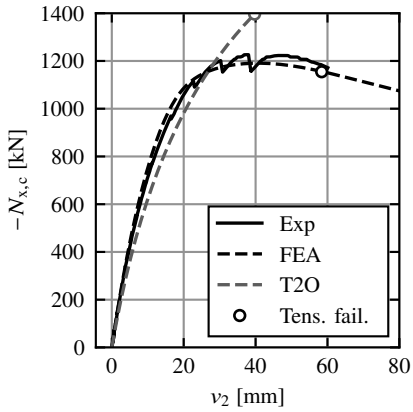

Figure A.9: Experimentally (Exp) determined load-deformation behaviour of flexural buckling test S10 with compressive forces $N_{x,c}$ plotted over the horizontal deformations at midspan v_2; comparison with FEA and calculations using T2O.

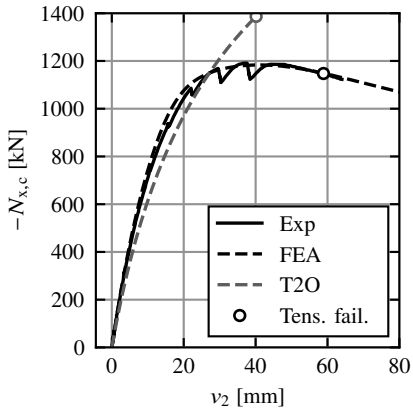

Figure A.10: Experimentally (Exp) determined load-deformation behaviour of flexural buckling test S11 with compressive forces $N_{x,c}$ plotted over the horizontal deformations at midspan v_2; comparison with FEA and calculations using T2O.

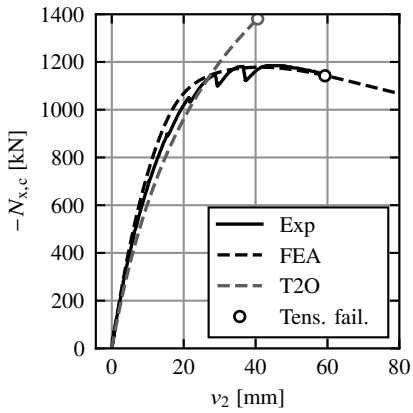

Figure A.11: Experimentally (Exp) determined load-deformation behaviour of flexural buckling test S12 with compressive forces $N_{x,c}$ plotted over the horizontal deformations at midspan v_2; comparison with FEA and calculations using T2O.

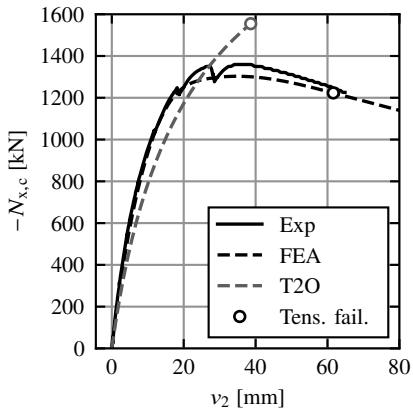

Figure A.12: Experimentally (Exp) determined load-deformation behaviour of flexural buckling test S13 with compressive forces $N_{x,c}$ plotted over the horizontal deformations at midspan v_2; comparison with FEA and calculations using T2O.

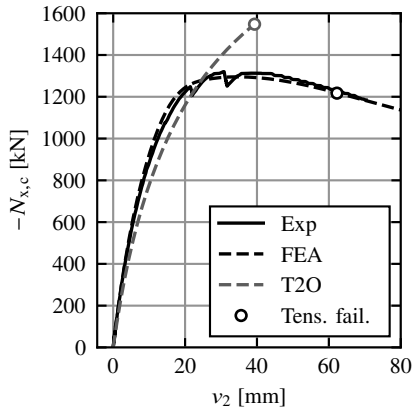

Figure A.13: Experimentally (Exp) determined load-deformation behaviour of flexural buckling test S14 with compressive forces $N_{x,c}$ plotted over the horizontal deformations at midspan v_2; comparison with FEA and calculations using T2O.

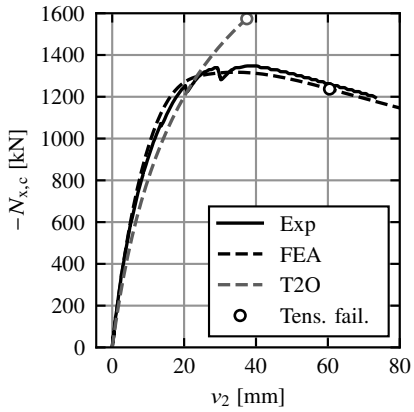

Figure A.14: Experimentally (Exp) determined load-deformation behaviour of flexural buckling test S15 with compressive forces $N_{x,c}$ plotted over the horizontal deformations at midspan v_2; comparison with FEA and calculations using T2O.

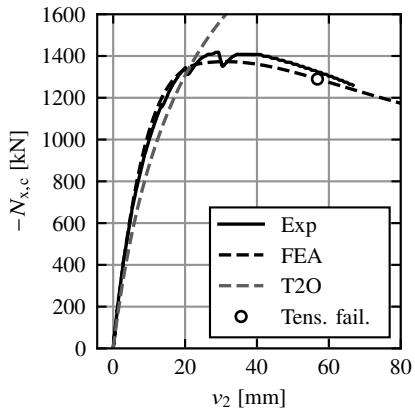

Figure A.15: Experimentally (Exp) determined load-deformation behaviour of flexural buckling test S16 with compressive forces $N_{x,c}$ plotted over the horizontal deformations at midspan v_2; comparison with FEA and calculations using T2O.

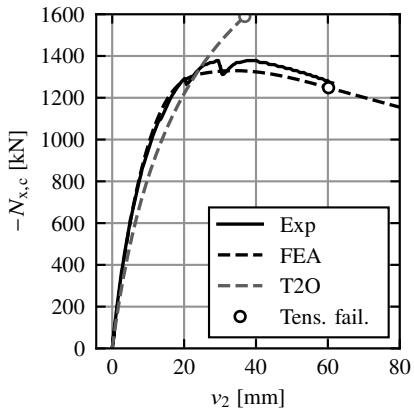

Figure A.16: Experimentally (Exp) determined load-deformation behaviour of flexural buckling test S17 with compressive forces $N_{x,c}$ plotted over the horizontal deformations at midspan v_2; comparison with FEA and calculations using T2O.

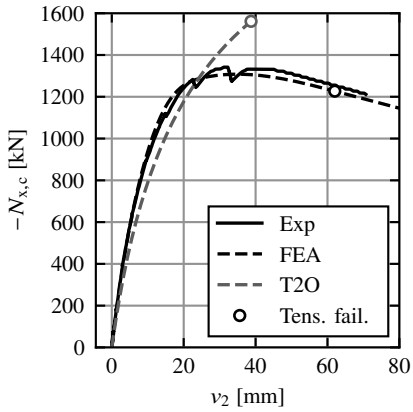

Figure A.17: Experimentally (Exp) determined load-deformation behaviour of flexural buckling test S18 with compressive forces $N_{x,c}$ plotted over the horizontal deformations at midspan v_2; comparison with FEA and calculations using T2O.

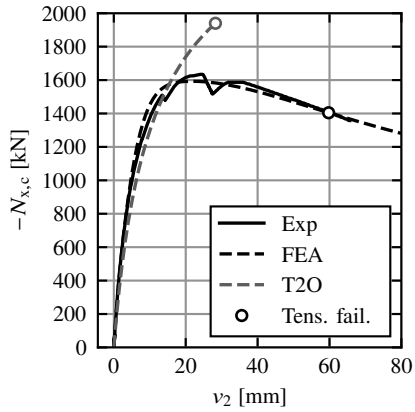

Figure A.18: Experimentally (Exp) determined load-deformation behaviour of flexural buckling test S19 with compressive forces $N_{x,c}$ plotted over the horizontal deformations at midspan v_2; comparison with FEA and calculations using T2O.

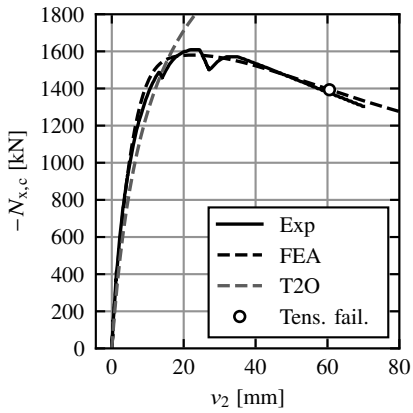

Figure A.19: Experimentally (Exp) determined load-deformation behaviour of flexural buckling test S20 with compressive forces $N_{x,c}$ plotted over the horizontal deformations at midspan v_2; comparison with FEA and calculations using T2O.

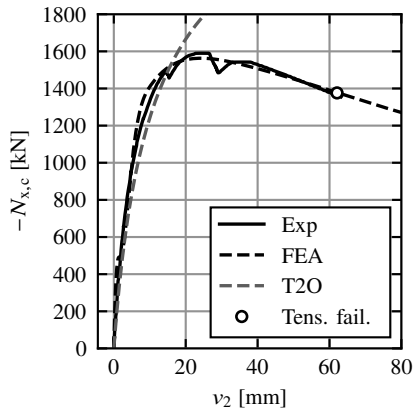

Figure A.20: Experimentally (Exp) determined load-deformation behaviour of flexural buckling test S21 with compressive forces $N_{x,c}$ plotted over the horizontal deformations at midspan v_2; comparison with FEA and calculations using T2O.

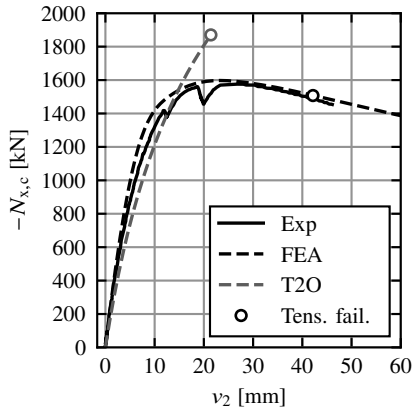

Figure A.21: Experimentally (Exp) determined load-deformation behaviour of flexural buckling test S22 with compressive forces $N_{x,c}$ plotted over the horizontal deformations at midspan v_2; comparison with FEA and calculations using T2O.

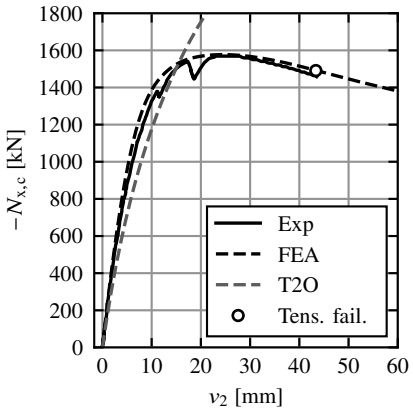

Figure A.22: Experimentally (Exp) determined load-deformation behaviour of flexural buckling test S23 with compressive forces $N_{x,c}$ plotted over the horizontal deformations at midspan v_2; comparison with FEA and calculations using T2O.

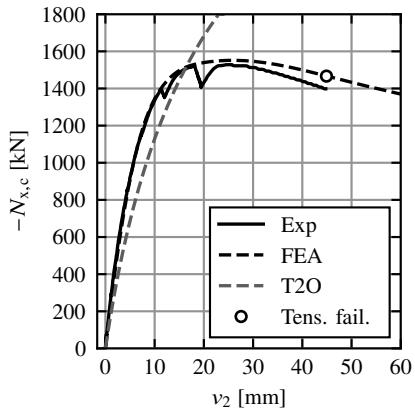

Figure A.23: Experimentally (Exp) determined load-deformation behaviour of flexural buckling test S24 with compressive forces $N_{x,c}$ plotted over the horizontal deformations at midspan v_2; comparison with FEA and calculations using T2O.

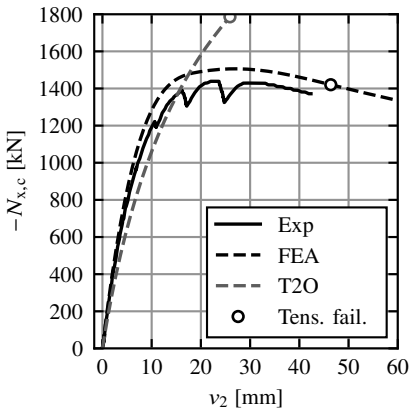

Figure A.24: Experimentally (Exp) determined load-deformation behaviour of flexural buckling test S25 with compressive forces $N_{x,c}$ plotted over the horizontal deformations at midspan v_2; comparison with FEA and calculations using T2O.

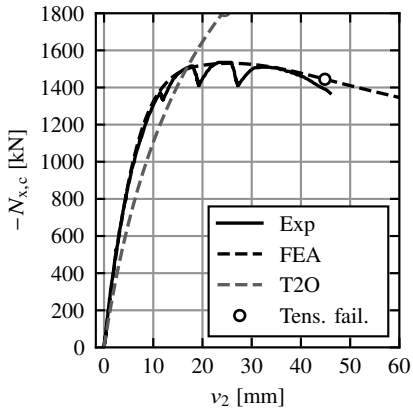

Figure A.25: Experimentally (Exp) determined load-deformation behaviour of flexural buckling test S26 with compressive forces $N_{x,c}$ plotted over the horizontal deformations at midspan v_2; comparison with FEA and calculations using T2O.

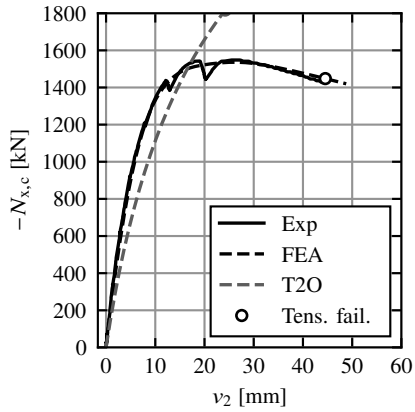

Figure A.26: Experimentally (Exp) determined load-deformation behaviour of flexural buckling test S27 with compressive forces $N_{x,c}$ plotted over the horizontal deformations at midspan v_2; comparison with FEA and calculations using T2O.

A.2 Preceding compression tests

The experimentally determined stress-strain curves of the five preceding compression tests in grain direction on beech LVL GL75 from the research project RP 7-1 of the Cluster of Excellence IntCDC [109] are presented in the following. The initial length of the displacement transducers, between which the deformations and $\epsilon_{c,0}$ were determined, was 230 mm. The x-axis displays the strains in grain direction ϵ_0, and the y-axis exhibits the stresses in grain direction σ_0.

In Table A.2, the test specimen dimensions, the density, the elastic modulus in grain direction $E_{0,el}$, the proportionality limit in grain direction $f_{c,0,lin}$, the compressive strength in grain direction $f_{c,0}$, and the plastic strain in grain direction on reaching the compressive strength $\epsilon_{c,0,pl}$ are given, see also Figure 3.24. The first number of the test specimen number indicates the lamella and the second a consecutive number within a lamella. One to two test specimens each from three lamellas were tested.

The tests are discussed in Section 3.3. The experimental data are also available at Töpler and Kuhlmann [167].

Table A.2: Data of the compression tests in grain direction on beech LVL GL75.

Specimen number	L [mm]	H [mm]	B [mm]	ρ [kg/m^3]	$E_{0,el}$ [N/mm^2]	$f_{c,0,lin}$ [$\cdot f_{c,0}$]	$f_{c,0}$ [N/mm^2]	$\epsilon_{c,0,pl}$ [$\cdot\epsilon_{c,0,el}$]
2.1	300.0	119.5	50.2	800.1	15,947	0.664	−75.8	1.12
3.2	300.0	119.0	50.2	793.7	15,613	0.673	−74.3	1.12
3.2	300.0	119.0	50.2	802.3	16,379	0.642	−74.5	1.08
4.1	300.0	119.3	49.8	797.0	16,221	0.644	−80.4	1.33
4.2	300.0	119.3	50.3	799.2	16,919	0.689	−79.8	1.65
			Mean	798.5	16,216	0.662	−76.9	1.26
			COV	0.00411	0.0302	0.0301	0.0384	0.188

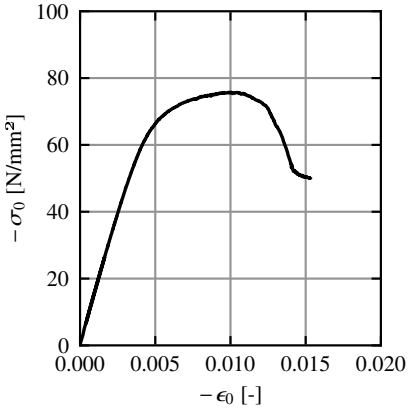

Figure A.27: Compression test 2.1 with stresses σ_0 plotted over strains ϵ_0.

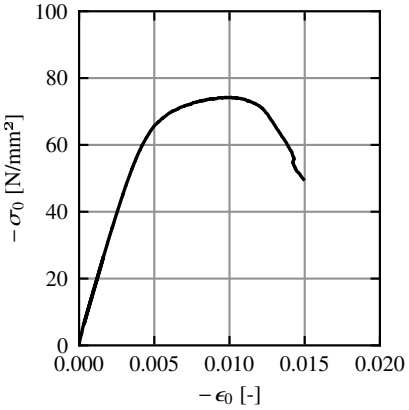

Figure A.28: Compression test 3.1 with stresses σ_0 plotted over strains ϵ_0.

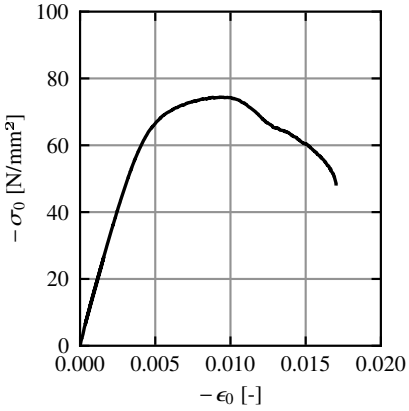

Figure A.29: Compression test 3.2 with stresses σ_0 plotted over strains ϵ_0.

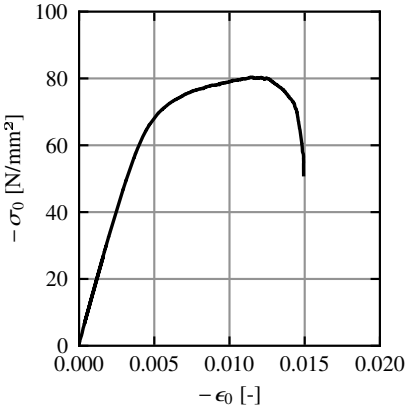

Figure A.30: Compression test 4.1 with stresses σ_0 plotted over strains ϵ_0.

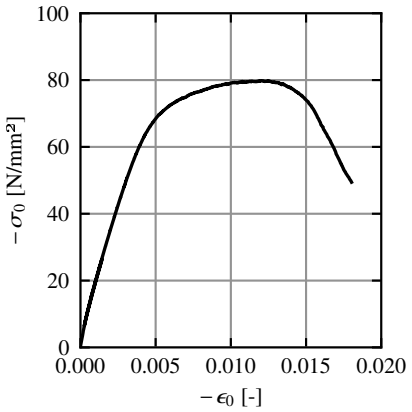

Figure A.31: Compression test 4.2 with stresses σ_0 plotted over strains ϵ_0.

Appendix B

Data of lateral torsional buckling tests on glulam beams

B.1 Lateral torsional buckling tests

The experimentally determined load-deformation curves of the 19 LTB tests on softwood GL 24h beams from the research project IGF No. 21285 N [108] are presented in the following. The x axis displays the horizontal deformation of the beam axis at midspan v, and the y axis exhibits the vertical force at midspan F_z. The results are compared with FEA with shear plasticising and calculations using T2O according to FprEN 1995-1-1 [69] (EC5) and the design proposal in Section 7 (prop), see also Section 5.5.3.
Calculations using T2O according to FprEN 1995-1-1 [69] better represented the initial stiffness of the LTB tests as no shear plasticising is considered. Calculations using T2O according to the design proposal in Section 7 better represented the load-bearing capacity and maximum deformations of the LTB tests, as the shear plasticising is considered with the factor $k_{pl,m}$ from Section 7.2.1.3 (6). For T12 to T19, calculations using T2O according to the design proposal in Section 7 systematically underestimated the load-bearing capacity. This indicated an underestimation of the bending strength, which was assumed to be $f_{m,mean}$ = 33.0 N/mm^2 according to Schilling et al. [141].

In Table B.1, the dimensions of the test specimens, the density, the wood moisture content, the equivalent geometrical imperfection, see Equation (3.7), and the maximum load are given. The height and width were measured at midspan. The equivalent geometrical imperfection $e_{y,eq}$ was not determined for T01. Likewise for T15 to T19, as these were aligned horizontally at midspan using a jack.

The tests are discussed in Section 3.4. The experimental data are also available at Töpler and Kuhlmann [168].

Table B.1: Data of the LTB tests on softwood GL 24h beams.

Specimen number	L [mm]	H [mm]	B [mm]	ρ [kg/m^3]	u [%]	$e_{y,eq}$ [mm]	$F_{z,R}$ [kN]
T01	8000	721.2	120.1	440.6	11.5	-	106.0
T02	8000	721.7	120.0	458.1	11.7	-3.0	120.5
T03	8000	721.6	119.9	450.1	10.6	-3.9	108.3
T04	8000	601.6	119.8	447.0	10.4	-2.9	88.0
T05	8000	601.9	120.2	451.9	10.3	-2.1	95.1
T06	8000	601.1	120.1	443.1	10.1	0.0	87.8
T07	8000	601.4	120.1	439.1	9.7	-1.3	85.0
T08	8000	601.7	119.9	458.4	11.2	-1.3	88.3
T09	8000	601.8	120.1	428.8	11.7	-0.4	72.7
T10	8000	601.8	119.9	441.2	10.8	-0.8	76.3
T11	8000	601.6	120.1	442.7	10.2	-1.6	76.9
T12	6000	481.8	120.1	418.8	9.4	-6.7	115.2
T13	6000	481.6	120.0	448.2	9.6	-3.8	117.3
T14	6000	481.9	120.1	441.7	9.8	-1.4	113.9
T15	6000	481.5	120.0	439.5	10.4	-	129.8
T16	6000	481.4	120.1	439.0	9.8	-	97.9
T17	6000	481.5	120.2	462.0	9.9	-	108.9
T18	6000	481.5	120.1	436.1	10.2	-	104.6
T19	6000	481.2	120.0	456.9	11.0	-	107.5
			Mean	444.4	10.4	-2.2	
			COV	0.0240	0.068	-0.81	

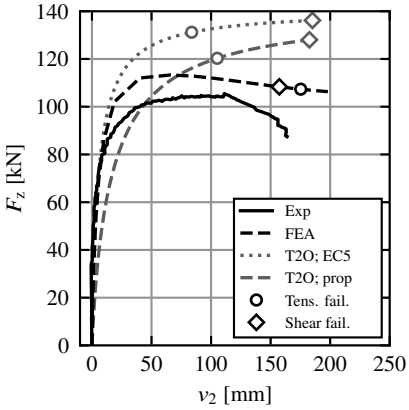

Figure B.1: Experimentally (Exp) determined load-deformation behaviour of LTB test T01 with vertical forces F_z plotted over the horizontal deformations at midspan v_2; comparison with FEA and calculations using T2O.

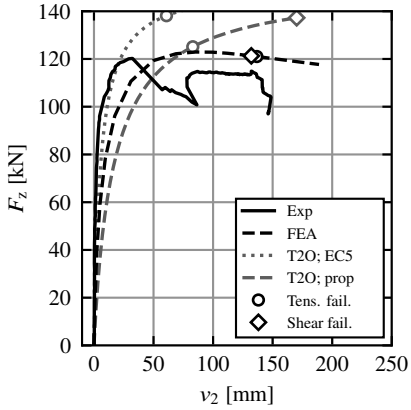

Figure B.2: Experimentally (Exp) determined load-deformation behaviour of LTB test T02 with vertical forces F_z plotted over the horizontal deformations at midspan v_2; comparison with FEA and calculations using T2O.

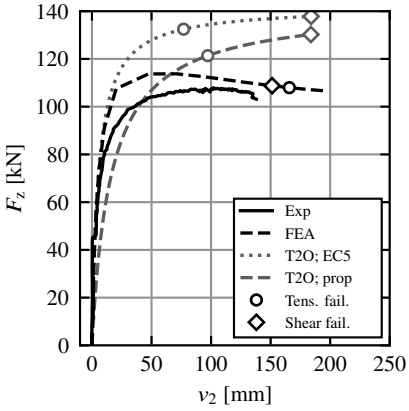

Figure B.3: Experimentally (Exp) determined load-deformation behaviour of LTB test T03 with vertical forces F_z plotted over the horizontal deformations at midspan v_2; comparison with FEA and calculations using T2O.

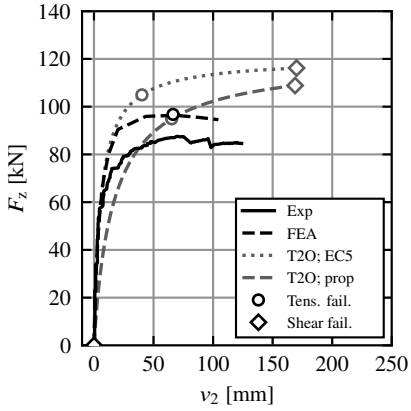

Figure B.4: Experimentally (Exp) determined load-deformation behaviour of LTB test T04 with vertical forces F_z plotted over the horizontal deformations at midspan v_2; comparison with FEA and calculations using T2O.

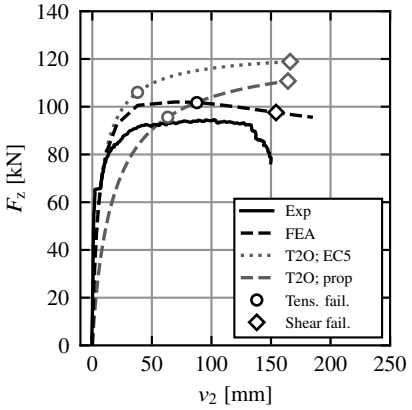

Figure B.5: Experimentally (Exp) determined load-deformation behaviour of LTB test T05 with vertical forces F_z plotted over the horizontal deformations at midspan v_2; comparison with FEA and calculations using T2O.

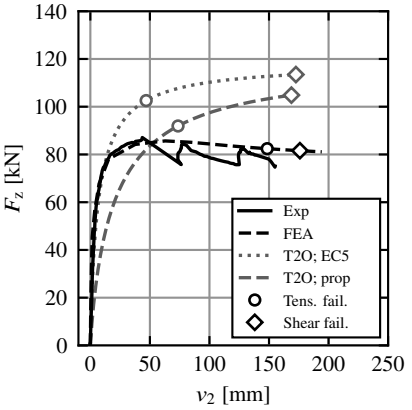

Figure B.6: Experimentally (Exp) determined load-deformation behaviour of LTB test T06 with vertical forces F_z plotted over the horizontal deformations at midspan v_2; comparison with FEA and calculations using T2O.

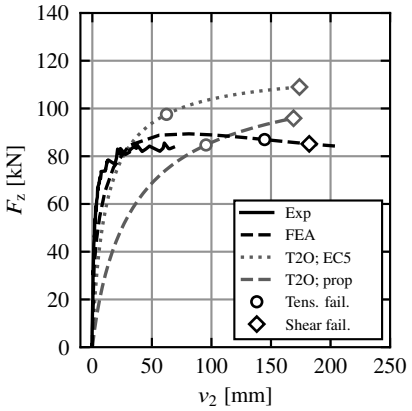

Figure B.7: Experimentally (Exp) determined load-deformation behaviour of LTB test T07 with vertical forces F_z plotted over the horizontal deformations at midspan v_2; comparison with FEA and calculations using T2O.

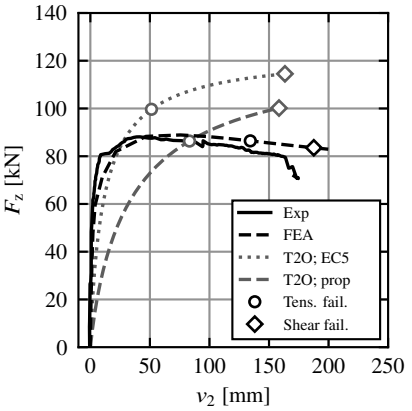

Figure B.8: Experimentally (Exp) determined load-deformation behaviour of LTB test T08 with vertical forces F_z plotted over the horizontal deformations at midspan v_2; comparison with FEA and calculations using T2O.

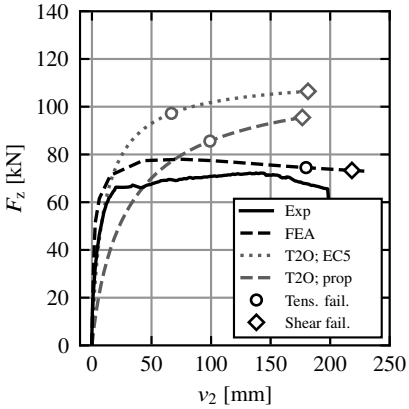

Figure B.9: Experimentally (Exp) determined load-deformation behaviour of LTB test T09 with vertical forces F_z plotted over the horizontal deformations at midspan v_2; comparison with FEA and calculations using T2O.

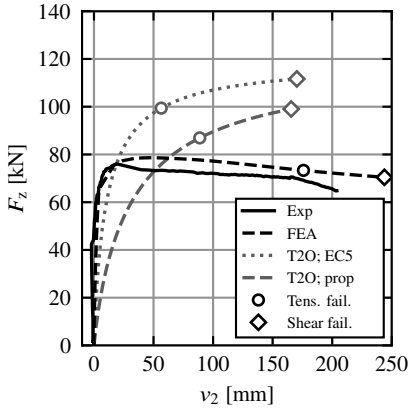

Figure B.10: Experimentally (Exp) determined load-deformation behaviour of LTB test T10 with vertical forces F_z plotted over the horizontal deformations at midspan v_2; comparison with FEA and calculations using T2O.

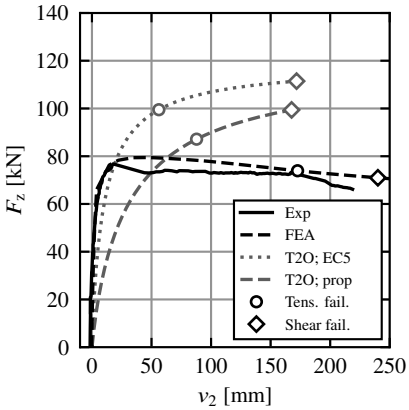

Figure B.11: Experimentally (Exp) determined load-deformation behaviour of LTB test T11 with vertical forces F_z plotted over the horizontal deformations at midspan v_2; comparison with FEA and calculations using T2O.

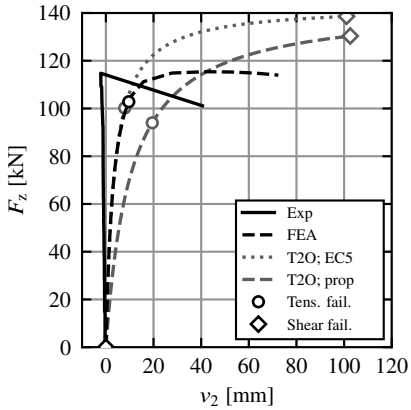

Figure B.12: Experimentally (Exp) determined load-deformation behaviour of LTB test T12 with vertical forces F_z plotted over the horizontal deformations at midspan v_2; comparison with FEA and calculations using T2O.

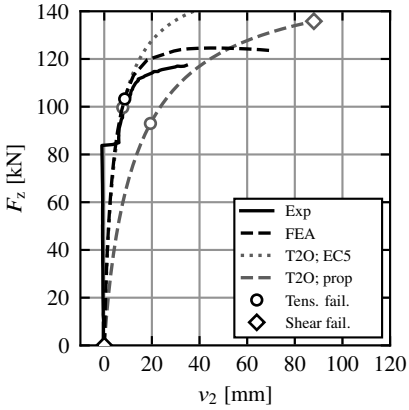

Figure B.13: Experimentally (Exp) determined load-deformation behaviour of LTB test T13 with vertical forces F_z plotted over the horizontal deformations at midspan v_2; comparison with FEA and calculations using T2O.

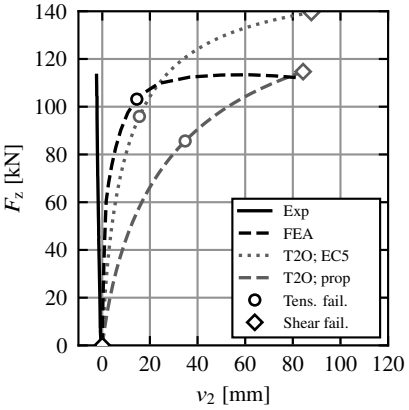

Figure B.14: Experimentally (Exp) determined load-deformation behaviour of LTB test T14 with vertical forces F_z plotted over the horizontal deformations at midspan v_2; comparison with FEA and calculations using T2O.

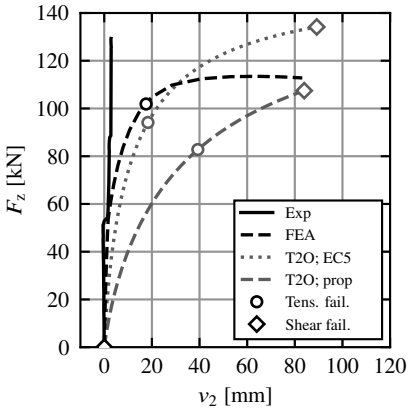

Figure B.15: Experimentally (Exp) determined load-deformation behaviour of LTB test T15 with vertical forces F_z plotted over the horizontal deformations at midspan v_2; comparison with FEA and calculations using T2O.

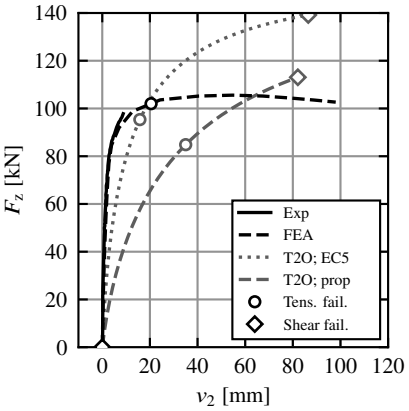

Figure B.16: Experimentally (Exp) determined load-deformation behaviour of LTB test T16 with vertical forces F_z plotted over the horizontal deformations at midspan v_2; comparison with FEA and calculations using T2O.

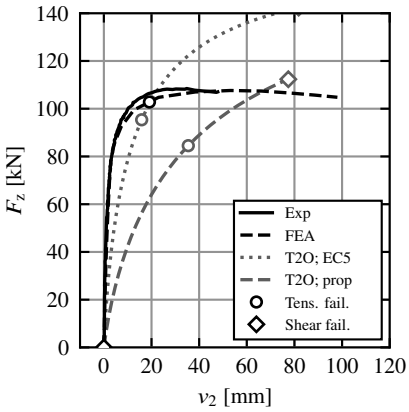

Figure B.17: Experimentally (Exp) determined load-deformation behaviour of LTB test T17 with vertical forces F_z plotted over the horizontal deformations at midspan v_2; comparison with FEA and calculations using T2O.

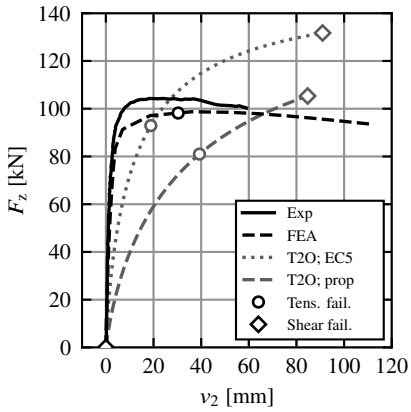

Figure B.18: Experimentally (Exp) determined load-deformation behaviour of LTB test T18 with vertical forces F_z plotted over the horizontal deformations at midspan v_2; comparison with FEA and calculations using T2O.

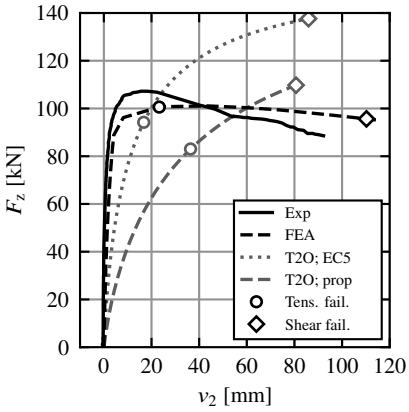

Figure B.19: Experimentally (Exp) determined load-deformation behaviour of LTB test T19 with vertical forces F_z plotted over the horizontal deformations at midspan v_2; comparison with FEA and calculations using T2O.

B.2 Preceding bending and torsion tests

In Table B.2, the analytically (Ana) and numerically (FEA) determined elastic and shear moduli in grain direction of the preceding elastic bending and torsion tests on the LTB test specimens made of softwood GL 24h from the research project IGF No. 21285 N [108] are given.

The tests are discussed in Section 3.4. The experimental data are also available at Töpler and Kuhlmann [168].

Table B.2: Data of the preceding elastic bending and torsion tests on the LTB test specimens made of softwood GL 24h.

Specimen	$E_{0,el,y}$ [N/mm^2]		$E_{0,el,z}$ [N/mm^2]		$E_{0,el,mean}$ [N/mm^2]		$G_{0,el}$ [N/mm^2]	
number	Ana	FEA	Ana	FEA	Ana	FEA	Ana	FEA
T01	11,224	11,768	11,569	11,516	11,397	11,642	851	779
T02	13,878	14,734	13,207	13,152	13,543	13,943	859	778
T03	12,032	12,662	12,412	12,357	12,222	12,510	830	755
T04	12,404	12,705	12,312	12,263	12,358	12,484	831	773
T05	12,743	13,065	12,498	12,449	12,621	12,757	841	781
T06	11,918	12,191	12,662	12,614	12,290	12,403	802	744
T07	11,883	12,155	11,547	11,500	11,715	11,828	813	757
T08	12,900	13,229	13,100	13,051	13,000	13,140	832	771
T09	10,774	10,993	11,271	11,223	11,023	11,108	799	745
T10	11,488	11,743	12,064	12,017	11,776	11,880	843	786
T11	11,744	12,011	12,112	12,064	11,928	12,038	822	765
T12	10,863	11,071	11,311	11,269	11,087	11,170	688	646
T13	11,520	11,765	12,556	12,511	12,038	12,138	769	726
T14	10,696	10,906	11,299	11,256	10,998	11,081	803	763
T15	11,101	11,323	11,435	11,392	11,268	11,358	764	723
T16	11,114	11,338	11,662	11,618	11,388	11,478	792	750
T17	10,871	11,091	11,820	11,776	11,346	11,434	852	812
T18	13,251	13,572	12,624	12,579	12,938	13,076	672	625
T19	12,055	12,322	12,394	12,349	12,225	12,336	759	714
Mean	11,814	12,139	12,098	12,050	11,956	12,095	801	747
COV	0.0760	0.0830	0.0503	0.0503	0.0609	0.0644	0.0650	0.0616

B.3 Preceding compression tests

The experimentally determined stress-strain curves of the eight preceding compression tests in grain direction on softwood GL 24h from the research project IGF No. 21285 N [108] are presented in the following. The initial length of the displacement transducers, between which the deformations and $\epsilon_{c,0}$ were determined, was 180 mm. The x-axis displays the strains in grain direction ϵ_0, and the y-axis exhibits the stresses in grain direction σ_0.

In Table B.3, the measured of the test specimen dimensions, the density, the elastic modulus in grain direction $E_{0,el}$, the proportionality limit in grain direction $f_{c,0,lin}$, the compressive strength in grain direction $f_{c,0}$, and the plastic strain in grain direction on reaching the compressive strength $\epsilon_{c,0,pl}$ are given, see also Figure 3.34. The first number of the test specimen number indicates the lamella and the second a consecutive number within a lamella. Two test specimens each were tested from four lamellas. $\epsilon_{c,0,pl}$ of test 3.1 could not be determined as one displacement transducer fell off to the end of the test. As $f_{c,0,lin}$ of test 2.2 was an outlier, the mean value of $f_{c,0,lin}$ was also determined without test 2.2.

The tests are discussed in Section 3.3. The experimental data are also available at Töpler and Kuhlmann [168].

Table B.3: Data of the compression tests in grain direction on softwood GL 24h.

Specimen number	L [mm]	H [mm]	B [mm]	ρ [kg/m^3]	$E_{0,el}$ [N/mm^2]	$f_{c,0,lin}$ [$\cdot f_{c,0}$]	$f_{c,0}$ [N/mm^2]	$\epsilon_{c,0,pl}$ [$\cdot\epsilon_{c,0,el}$]
1.1	300.0	120.0	40.7	497.4	8970	0.716	−35.1	0.823
1.2	300.0	119.9	40.7	495.4	11,587	0.804	−46.4	0.438
2.1	300.0	120.0	40.6	530.0	14,541	0.676	−45.4	0.289
2.2	300.0	120.0	40.6	525.0	15,029	0.469	−50.2	0.470
3.1	300.0	120.1	40.8	473.9	12,488	0.853	−43.8	-
3.2	300.0	120.0	40.7	491.1	10,529	0.643	−38.8	0.512
4.1	300.0	120.1	40.8	420.3	11,613	0.703	−43.0	0.378
4.2	300.0	119.9	40.8	407.1	11,803	0.782	−43.4	0.257
			Mean	480.0	12,070	0.706	−43.2	0.452
		Mean without 2.2		-	-	0.739	-	-
			COV	0.0935	0.164	0.168	0.107	0.415

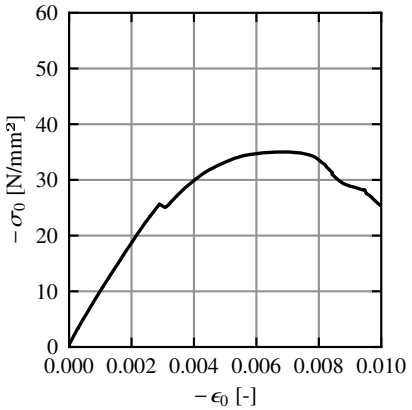

Figure B.20: Compression test 1.1 with stresses σ_0 plotted over strains ϵ_0.

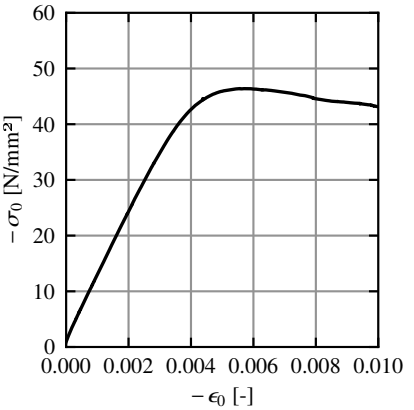

Figure B.21: Compression test 1.2; stresses σ_0 plotted over strains ϵ_0.

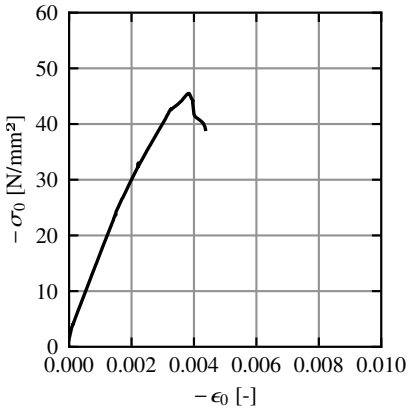

Figure B.22: Compression test 2.1 with stresses σ_0 plotted over strains ϵ_0.

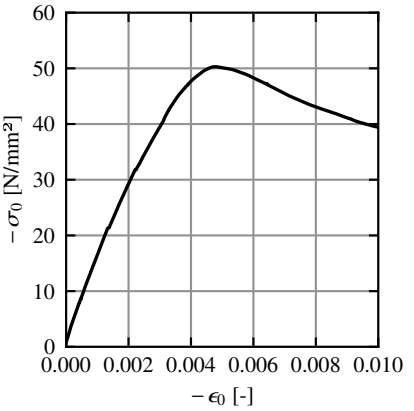

Figure B.23: Compression test 2.2 with stresses σ_0 plotted over strains ϵ_0.

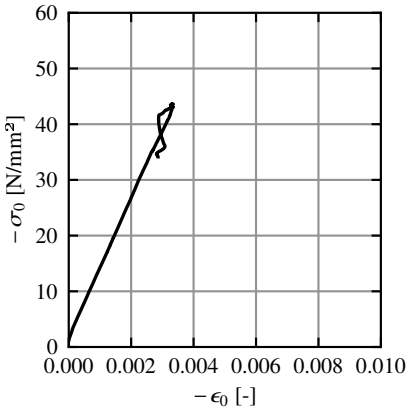

Figure B.24: Compression test 3.1 with stresses σ_0 plotted over strains ϵ_0.

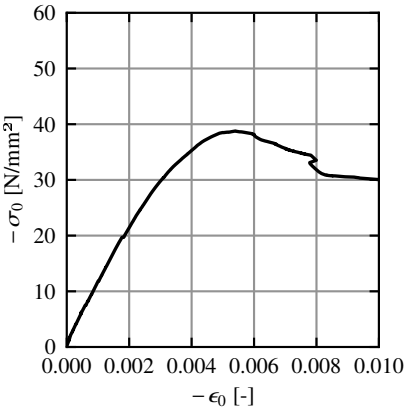

Figure B.25: Compression test 3.2 with stresses σ_0 plotted over strains ϵ_0.

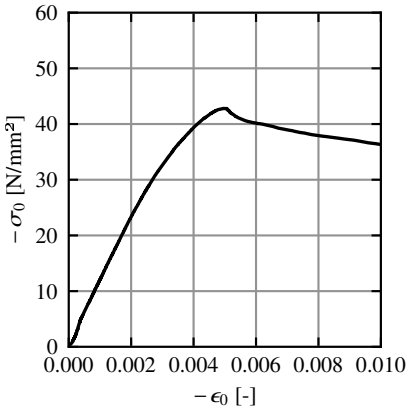

Figure B.26: Compression test 4.1 with stresses σ_0 plotted over strains ϵ_0.

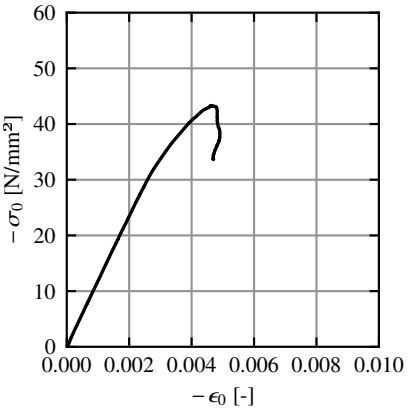

Figure B.27: Compression test 4.2 with stresses σ_0 plotted over strains ϵ_0.

Appendix C

Reduction factor k_c accounting for flexural buckling

In practice, simplified design models are often adopted for flexural buckling design, which assume geometrically linear internal forces (T1O) and a reduction factor k_c to account for flexural buckling. The common model for calculating k_c is discussed in Sections 2.2.1.8, 2.6.2.1.3, and 2.6.4.1.3.
Schänzlin [137] discussed a mechanically sound analytical derivation of the reduction factor for considering flexural buckling k_c that includes the creep deformations, see also Equations (2.43) and (2.44). As this analytical derivation of k_c was not widely used or known in timber construction when this thesis was prepared, the complete derivation from Schänzlin [137] is given here.

For pure axial compressive forces, the bending moment $M_{y,2}$ from Equation (2.42) is

$$M_{y,2} = \frac{-N_{x,c} e_z}{1 - \alpha_{c,y} \cdot (1 + k_{def,eff})} \quad , \tag{C.1}$$

where $N_{x,c}$ is the axial compressive force with a negative sign for compression, e_z is the bow imperfection in the z-direction, $\alpha_{c,y}$ is the amplification factor of the axial compressive force due to flexural buckling about the y-axis according to Equation (2.2), and where $k_{def,eff}$ is the effective creep deformation coefficient according to Equation (2.41).
A linear $N_{x,c}$-$M_{y,2}$-interaction is assumed, as

$$\frac{N_{x,c}}{A f_{c,0}} + \frac{M_{y,2}}{W_y f_m} \leq 1.0 \quad , \tag{C.2}$$

where A is the cross-sectional area, $f_{c,0}$ and f_m are the compressive and bending strengths in grain direction, and W_y is the section modulus about the y-axis.
Inserting Equation (C.1) into Equation (C.2) yields

$$\begin{aligned} &\frac{\sigma_{c,0}^2}{f_{c,0}^2} \cdot (1 + k_{def,eff}) \\ &- \frac{\sigma_{c,0}}{f_{c,0}} \cdot \left(\frac{\sigma_{c,y,cr}}{f_{c,0}} + \frac{A f_{c,0}}{W_z f_m} \cdot e_z \cdot \frac{\sigma_{c,y,cr}}{f_{c,0}} + (1 + k_{def,eff}) \right) + \frac{\sigma_{c,y,cr}}{f_{c,0}} = 0 \quad , \end{aligned} \tag{C.3}$$

where $\sigma_{c,0} = N_{x,c}/A$ is the axial compressive stress, and $\sigma_{c,y,cr} = N_{y,cr}/A$ is the critical axial compressive stress. This equation is the quadratic form of the flexural buckling load-bearing capacity and is equal to the *Ayrton-Perry approach* discussed in Section 2.2.1.8.

With the definition of the reduction factor for flexural buckling

$$k_{c,y} = \frac{\sigma_{c,0}}{f_{c,0}} \quad , \tag{C.4}$$

the definition of the relative slenderness ratio for flexural buckling, see also Equation (2.44),

$$\lambda^2_{c,y,rel} = \frac{f_{c,0} \cdot (1 + k_{def,eff})}{\sigma_{c,y,cr}} \quad , \tag{C.5}$$

and the definition of the fitting factor, see also Equation (2.43),

$$\beta_{c,y} = \frac{e_y}{L} \cdot \pi \cdot \sqrt{\frac{3E_{0,el}}{f_{c,0} \cdot (1 + k_{def,eff})}} \cdot \frac{f_{c,0}}{f_m} \quad , \tag{C.6}$$

where $E_{0,el}$ is the elastic modulus in grain direction, Equation (C.3) can be simplified to

$$k^2_{c,y}\, \lambda^2_{c,y,rel} - k_{c,y} \cdot \left(1 + \beta_{c,y}\, \lambda_{c,y,rel} + \lambda^2_{c,y,rel}\right) + 1 = 0 \quad . \tag{C.7}$$

This quadratic equation can be solved for $k_{c,y}$, where the smaller of the two results is

$$\begin{aligned} k_{c,y} = & \frac{1}{\lambda^2_{c,y,rel}} \cdot 0.5 \cdot \left(1 + \beta_{c,y}\, \lambda_{c,y,rel} + \lambda^2_{c,y,rel}\right) \\ & - \sqrt{\left(\frac{1}{\lambda^2_{c,y,rel}} \cdot 0.5 \cdot \left((1 + \beta_{c,y}\, \lambda_{c,y,rel} + \lambda^2_{c,y,rel}\right)\right)^2 - \frac{1}{\lambda^2_{c,y,rel}}} \quad . \end{aligned} \tag{C.8}$$

By the introduction of

$$\phi_{c,y} = 0.5 \cdot \left(1 + \beta_{c,y}\, \lambda_{c,y,rel} + \lambda^2_{c,y,rel}\right) \quad , \tag{C.9}$$

Equation (C.8) can be simplified to

$$k_{c,y} = \frac{\phi_{c,y} - \sqrt{\phi^2_{c,y} - \lambda^2_{c,y,rel}}}{\lambda^2_{c,y,rel}} \quad . \tag{C.10}$$

Expanding the numerator and denominator by $\phi_{c,y} + \sqrt{\phi^2_{c,y} - \lambda^2_{c,y,rel}}$ yields

$$k_{c,y} = \frac{1}{\phi_{c,y} + \sqrt{\phi^2_{c,y} - \lambda^2_{c,y,rel}}} \quad . \tag{C.11}$$

The reduction factor for flexural buckling in compressive design with geometrically linear calculations $k_{c,y}$ can thus be calculated by means of Equations (C.11) and (C.9).

Appendix D

UMAT subroutine for modelling of elastoplastic behaviour of timber

D.1 General

This Annex provides background information on the developed UMAT subroutine [159], which is applied in the FEA in Sections 5 and 6. The UMAT subroutine is capable of modelling orthotropic behaviour with brittle failure for tension in the x-direction, ellipsoid elastoplastic behaviour for compression in grain direction (x-direction), and bilinear elastoplastic behaviour for shear in the xy-, xz-, and yz-planes. A stress interaction is only considered for the three shear components.
By modification of the input parameters, it is possible to achieve bilinear or purely elastic behaviour for compression in grain direction. In the same manner, it is possible to achieve purely elastic behaviour in one or multiple shear planes and for tension in grain direction. According to the common sign convention, compressive stresses and strains are negative.

The UMAT subroutine was written in *Fortran 77* and is available on *DaRUS* [159]. For using the modifiable Fortran code, a corresponding compiler is necessary for Abaqus. The *standardU.dll* contains the already compiled UMAT and can be used directly without a compiler in Abaqus CAE/2023.

D.2 Tension in grain direction

Linear elastic behaviour until brittle failure is assumed for tension in the x-direction, i.e. in grain direction, see Figure 5.2. Brittle failure is implemented by means of element deletion. The element deletion criterion was modified so that the elements are deleted if the tensile strength is exceeded at one of the 8 integration points of a C3D20R element. This is necessary due to the variable tensile stresses caused by bending over the element height and width. After failure and deletion of the first element convergence problems can occur if using implicit solution methods.

D.3 Compression in grain direction

The stress-strain curve for compression in the x-direction, i.e. in grain direction, is divided into three segments, see Figure 5.4. Segment 1: linear elastic behaviour, segment 2: ellipsoid plasticising, and segment 3: linear plasticising.

In segment 1, linear elastic behaviour until reaching the proportionality limit $f_{c,0,lin}$ is assumed:

$$\sigma_0(\epsilon_0) = \epsilon_0 \cdot E_{0,el} \quad \text{for} \quad \sigma_0 \geq f_{c,0,lin} \quad , \tag{D.1}$$

where σ_0 is the stress in grain direction, ϵ_0 is the strain in grain direction, and $E_{0,el}$ is the elastic modulus in grain direction.

In segment 2, plastic strains are computed based on an ellipse, see Figure 5.5, with the proportionality limit $f_{c,0,lin}$ on the horizontal axis of the ellipse to the compressive strength $f_{c,0}$ on the vertical axis. The general equation for this ellipse is

$$\frac{(\epsilon_{0,pl} - \epsilon_{c,0,pl})^2}{\epsilon_{c,0,pl}^2} + \frac{(\sigma_0 - f_{c,0,lin})^2}{(f_{c,0} - f_{c,0,lin})^2} = 1 \quad \text{for} \quad f_{c,0,lin} \geq \sigma_0 \geq f_{c,0} \quad , \tag{D.2}$$

where $\epsilon_{0,pl}$ is the plastic strain in grain direction, $\epsilon_{c,0,pl}$ is the plastic strain in the x-direction on reaching the compressive strength, and $f_{c,0}$ is the compressive strength in grain direction. Substituting

$$\epsilon_{0,pl} = \epsilon_0 - \epsilon_{0,el} \quad , \tag{D.3}$$

$$\sigma_0 = \epsilon_{0,el} \cdot E_{0,el} \quad , \tag{D.4}$$

where ϵ_0 is the total strain in grain direction and $\epsilon_{0,el}$ is the elastic strain in grain direction, and transforming Equation (D.2) yields $\epsilon_{0,el}$ as a function of ϵ_0. The *Python* library *SymPy* can be recommended for solving this equation. In this way, the proportion of plastic and elastic strains can be determined for any given total strain.

In segment 3, a linear plasticising with gradient $E_{0,pl}$ is assumed, see Figure 5.5. The total gradient, i.e. the tangent elastic modulus $E_{0,pl}$, is given by

$$\frac{1}{E_{0,T}} = \frac{1}{E_{0,el}} + \frac{1}{E_{0,pl}} \quad , \tag{D.5}$$

where $E_{0,pl}$ is the plastic modulus in grain direction. Substituting $E_{0,T} = \delta\sigma_0/\delta\epsilon_0$ and $\delta\sigma_0 = \delta\epsilon_{0,el} \cdot E_{0,el}$ and transforming Equation (D.5) yields the additional elastic strains

$$\delta\epsilon_{0,el} = \frac{\delta\epsilon_0 \cdot E_{0,pl}}{E_{0,el} + E_{0,pl}} \quad \text{for} \quad \sigma_0 \leq f_{c,0} \quad , \tag{D.6}$$

where $\delta\epsilon_0$ is the additional total strain in grain direction given for each increment of the FEA at each integration point. The additional plastic strains $\delta\epsilon_{0,pl}$ can be computed using Equation (D.3).

For a continuous stress-strain curve, the tangent intersection point of $E_{0,\mathrm{T}}$ with the ellipse has to be selected as the transition point between segments 2 and 3. The tangent intersection point can be determined by equating the derivative of the ellipse equation, see Equation (D.2), with E_{T}. This yields

$$\epsilon_{\mathrm{c},0,\mathrm{pl},\mathrm{int}} = \epsilon_{\mathrm{c},0,\mathrm{pl}} + E_{0,\mathrm{pl}} \cdot \epsilon_{\mathrm{c},0,\mathrm{pl}}^2 \cdot \sqrt{\frac{1}{(E_{0,\mathrm{pl}} \cdot \epsilon_{\mathrm{c},0,\mathrm{pl}})^2 + (f_{\mathrm{c},0} - f_{\mathrm{c},0,\mathrm{lin}})^2}} \quad , \tag{D.7}$$

$$f_{\mathrm{c},0,\mathrm{int}} = f_{\mathrm{c},0,\mathrm{lin}} - (f_{\mathrm{c},0} - f_{\mathrm{c},0,\mathrm{lin}})^2 \cdot \sqrt{\frac{1}{(E_{0,\mathrm{pl}} \cdot \epsilon_{\mathrm{c},0,\mathrm{pl}})^2 + (f_{\mathrm{c},0} - f_{\mathrm{c},0,\mathrm{lin}})^2}} \quad , \tag{D.8}$$

where $\epsilon_{\mathrm{c},0,\mathrm{pl},\mathrm{int}}$ is the plastic strain in grain direction at the intersection point and $f_{\mathrm{c},0,\mathrm{int}}$ is the stress in grain direction at the intersection point. Using $f_{\mathrm{c},0,\mathrm{int}}$ instead of $f_{\mathrm{c},0}$ as the limit criterion for σ_0 in Equations (D.2) and (D.6) results in a continuous stress-strain curve.

For unloading and reloading, a linear elastic behaviour with $E_{0,\mathrm{el}}$ is assumed. No failure criterion was implemented.

D.4 Shear

The described shear behaviour was implemented for positive and negative shear stresses in all three planes xy, xz, and yz. The stress-strain curve is divided into two segments, see Figure 5.3. Segment 1: linear elastic behaviour and segment 2: linear plasticising.

In segment 1, linear elastic behaviour until reaching the proportionality limit $f_{\mathrm{v,lin}}$ is assumed:

$$\tau(\gamma) = \gamma \cdot G_{\mathrm{el}} \quad \text{for} \quad |\tau| \leq |f_{\mathrm{v,lin}}| \quad , \tag{D.9}$$

where τ is the shear stress in the xy-, xz-, or yz-plane, γ is the total shear strain in the xy-, xz-, or yz-plane, and G_{el} is the elastic shear modulus in the xy-, xz-, or yz-plane.

In segment 2, a linear plasticising with gradient G_{pl} is assumed. The total gradient, i.e. the tangent shear modulus G_{T}, is given by

$$\frac{1}{G_{\mathrm{T}}} = \frac{1}{G_{\mathrm{el}}} + \frac{1}{G_{\mathrm{pl}}} \quad , \tag{D.10}$$

where G_{pl} is the plastic shear modulus. Substituting $G_{\mathrm{T}} = \delta\tau/\delta\gamma$ and $\delta\tau = \delta\gamma_{\mathrm{el}} \cdot G_{\mathrm{el}}$ and transforming Equation (D.10) yields the additional elastic shear strains

$$\delta\gamma_{\mathrm{el}} = \frac{\delta\gamma \cdot G_{\mathrm{pl}}}{G_{\mathrm{el}} + G_{\mathrm{pl}}} \quad \text{for} \quad |\tau| \geq |f_{\mathrm{v}}| \quad , \tag{D.11}$$

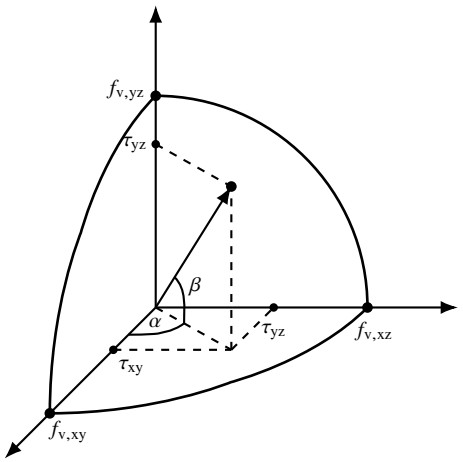

Figure D.1: Visualisation of the proportional limit for shear interaction.

where $\delta\gamma$ is the additional total shear strain in the xy-, xz-, or yz-plane given for each increment of the FEA at each integration point. The additional plastic shear strains $\delta\gamma_{pl}$ can be computed by

$$\delta\gamma_{pl} = \delta\gamma - \delta\gamma_{el} \quad . \tag{D.12}$$

Based on FprEN 1995-1-1 [69], a quadratic interaction of the shear stresses is assumed for determining the proportional limit, see Figure D.1 and

$$\left(\frac{\tau_{xy}}{f_{v,xy,lin}}\right)^2 + \left(\frac{\tau_{xz}}{f_{v,xz,lin}}\right)^2 + \left(\frac{\tau_{yz}}{f_{v,yz,lin}}\right)^2 = 1 \quad , \tag{D.13}$$

where $\tau_{xy/xz/yz}$ are the respective shear stresses in the xy-, xz-, and yz-planes and $f_{v,xy/xz/yz,lin}$ are the respective proportional limits in the xy-, xz-, and yz-planes.
The value of $f_{v,lin}$ can be calculated by

$$f_{v,lin} = \frac{abc}{\sqrt{a^2b^2\sin^2\beta + c^2(b^2\cos^2\alpha + a^2\sin^2\alpha)\cos^2\beta}} \quad , \tag{D.14}$$

where $a = f_{v,xy,lin}$ is the shear proportionality limit in the xy-plane, $b = f_{v,xz,lin}$ is the shear proportionality limit in the xz-plane, $c = f_{v,yz,lin}$ is the shear proportionality limit in the yz-plane, and for α and β see Figure D.1. This is the general equation for the radius of an ellipsoid at given angles α and β.

For unloading and reloading, a linear elastic behaviour is assumed. No failure criterion was implemented.

Appendix E

Results of FEA on equivalent geometrical imperfections

E.1 Softwood GL beams

This Annex provides the results of the numerical parameter studies on LTB of timber beams with scattering geometrical and structural imperfections, see Sections 5.6.2 and 6.3.2.1.

In Figures E.1 to E.9, the frequency distributions of the reduction factor k_{m} for scattering geometrical and structural imperfections are plotted as violin plots for the seven investigated relative LTB slenderness ratios $\lambda_{\mathrm{m,rel}}$. k_{m} is the quotient of the load-bearing capacity with LTB to the load-bearing capacity without LTB. The violin plots are supplemented by their 5% quantile values (circles), mean values (middle bars), and 95% quantile values (upper bars). Each violin plot contains the results of 200 FEA. In addition, the results of FEA with bow imperfections of $e_{\mathrm{y,eq}} = L/1000$ and twist imperfections of $e_{\theta,\mathrm{eq}} = 0.5 \cdot (L/1500H_{\mathrm{ap}} + 1/100)$ as equivalent geometrical imperfections are provided. Furthermore, the relative critical bending moment $M_{\mathrm{y,cr}}$ from FEA is given. The relative LTB slenderness ratio $\lambda_{\mathrm{m,rel}}$ was determined according to FprEN 1995-1-1 [69], see Equation (2.80).

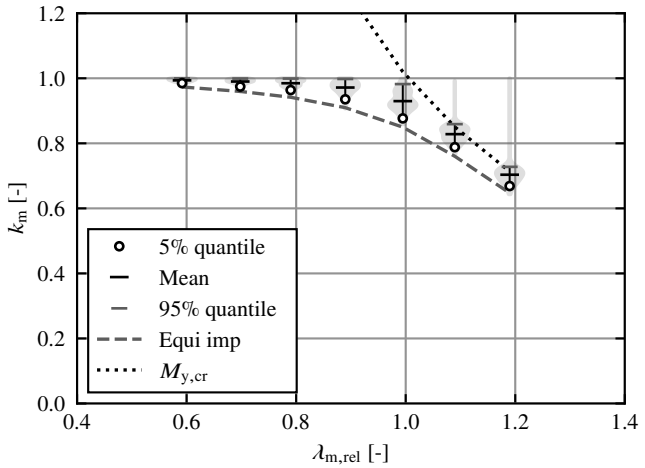

Figure E.1: Violin plots of the reduction factor k_m from FEA on GL 24h beams at seven relative LTB slenderness ratios $\lambda_{m,rel}$ with constant bending moment; with scattering *geometrical imperfections*; results of 200 FEA per violin plot; $H/B = 4$.

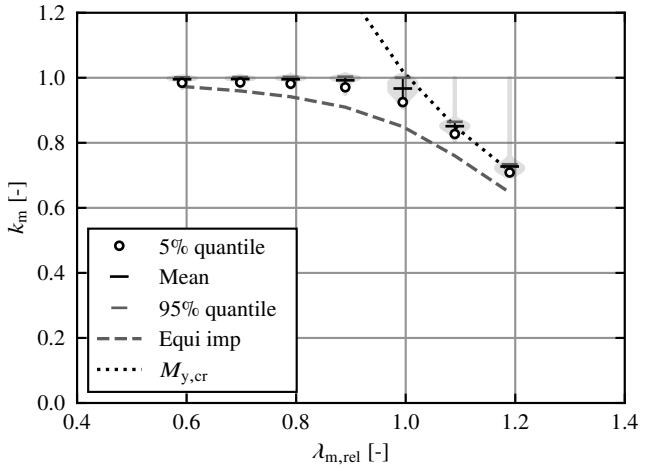

Figure E.2: Violin plots of the reduction factor k_m from FEA on GL 24h beams at seven relative LTB slenderness ratios $\lambda_{m,rel}$ with constant bending moment; with scattering *structural imperfections*; results of 200 FEA per violin plot; $H/B = 4$.

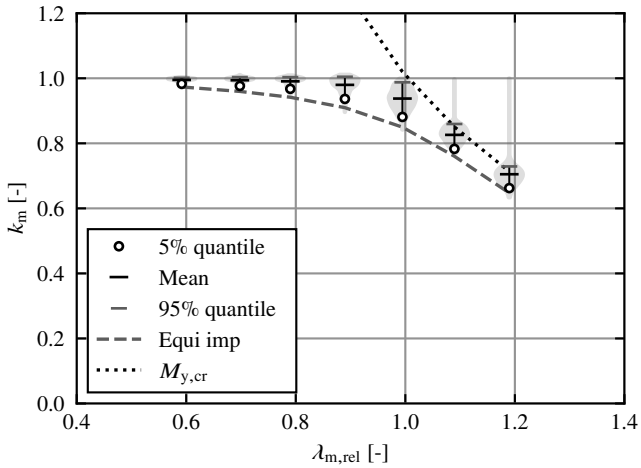

Figure E.3: Violin plots of the reduction factor k_m from FEA on GL 24h beams at seven relative LTB slenderness ratios $\lambda_{m,rel}$ with constant bending moment; with scattering *geometrical and structural imperfections*; results of 200 FEA per violin plot; $H/B = 4$.

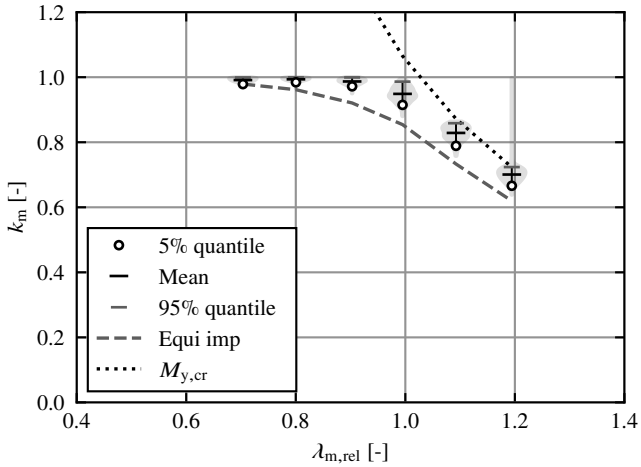

Figure E.4: Violin plots of the reduction factor k_m from FEA on GL 24h beams at seven relative LTB slenderness ratios $\lambda_{m,rel}$ with constant bending moment; with scattering *geometrical imperfections*; results of 200 FEA per violin plot; $H/B = 8$.

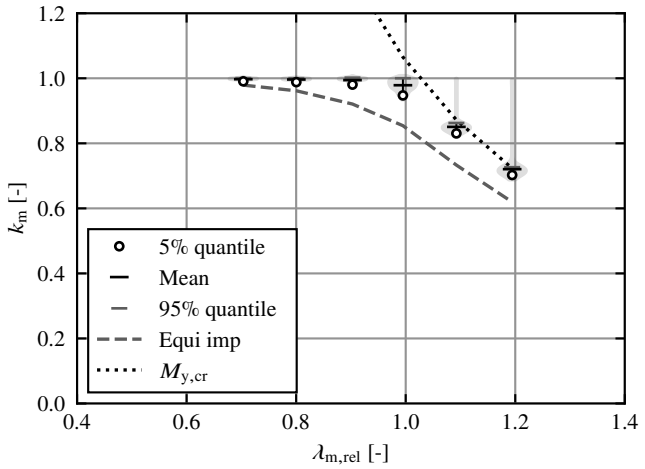

Figure E.5: Violin plots of the reduction factor k_m from FEA on GL 24h beams at seven relative LTB slenderness ratios $\lambda_{m,rel}$ with constant bending moment; with scattering *structural imperfections*; results of 200 FEA per violin plot; $H/B = 8$.

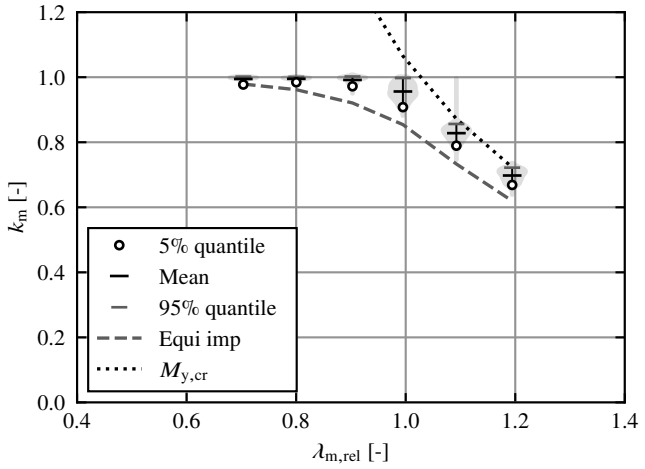

Figure E.6: Violin plots of the reduction factor k_m from FEA on GL 24h beams at seven relative LTB slenderness ratios $\lambda_{m,rel}$ with constant bending moment; with scattering *geometrical and structural imperfections*; results of 200 FEA per violin plot; $H/B = 8$.

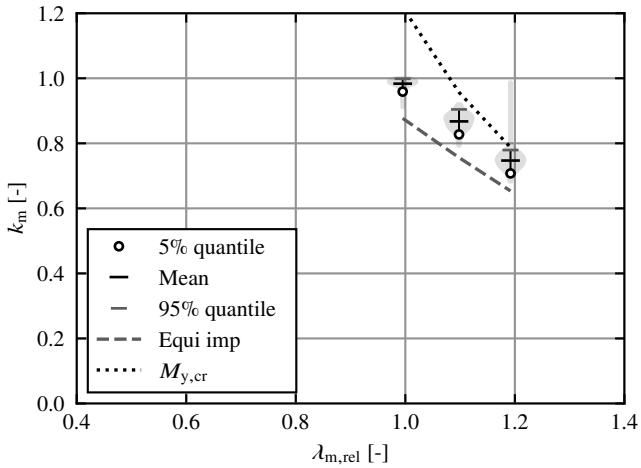

Figure E.7: Violin plots of the reduction factor k_m from FEA on GL 24h beams at seven relative LTB slenderness ratios $\lambda_{m,rel}$ with constant bending moment; with scattering *geometrical imperfections*; results of 200 FEA per violin plot; $H/B = 12$.

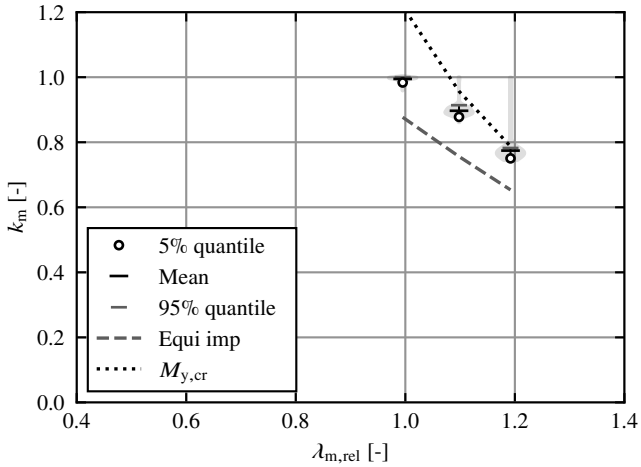

Figure E.8: Violin plots of the reduction factor k_m from FEA on GL 24h beams at seven relative LTB slenderness ratios $\lambda_{m,rel}$ with constant bending moment; with scattering *structural imperfections*; results of 200 FEA per violin plot; $H/B = 12$.

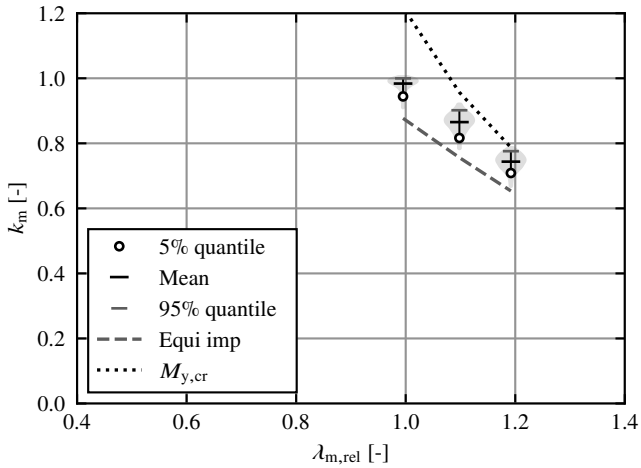

Figure E.9: Violin plots of the reduction factor k_m from FEA on GL 24h beams at seven relative LTB slenderness ratios $\lambda_{m,rel}$ with constant bending moment; with scattering *geometrical and structural imperfections*; results of 200 FEA per violin plot; $H/B = 12$.

E.2 Softwood GL columns

This Annex provides the results of the numerical parameter studies on flexural buckling of timber columns with scattering geometrical and structural imperfections, see Sections 5.6.2 and 6.3.2.2.

In Figures E.10 to E.17, the frequency distributions of the axial compressive load-bearing capacities $N_{x,c,R}$ for scattering geometrical and structural imperfections are plotted as violin plots for the seven investigated relative flexural buckling slenderness ratios $\lambda_{c,rel}$. The violin plots are supplemented by their 5% quantile values (circles), mean values (middle bars), and 95% quantile values (upper bars). Each violin plot contains the results of 200 FEA. In addition, the results of calculations using T2O with characteristic material values and a bow imperfection of $e_{z,eq} = L/750$ are provided. The relative flexural buckling slenderness ratio $\lambda_{c,rel}$ was determined according to EN 1995-1-1 [57], see Equation (2.60).

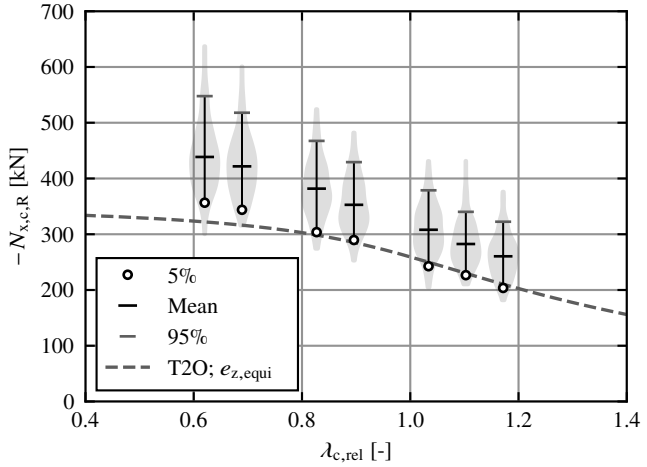

Figure E.10: Violin plots of the axial compressive load-bearing capacities $N_{x,c,R}$ from FEA on GL 24h columns at seven relative LTB slenderness ratios $\lambda_{c,rel}$; with scattering *structural imperfections*; results of 200 FEA per violin plot; H = 120 mm.

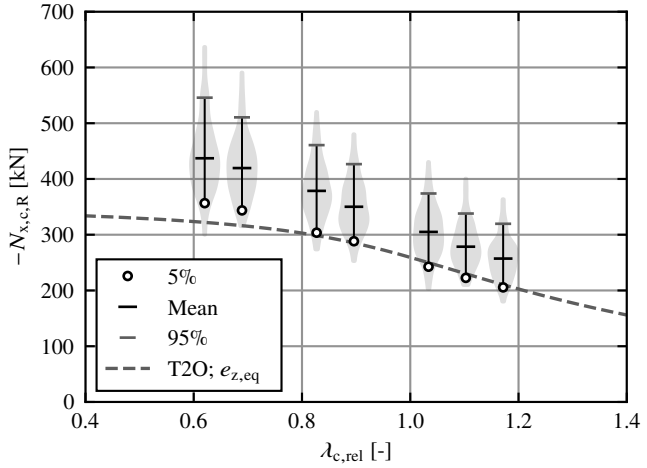

Figure E.11: Violin plots of the reduction factor k_m from FEA on GL 24h beams at seven relative LTB slenderness ratios $\lambda_{m,rel}$ with constant bending moment; with scattering *geometrical and structural imperfections*; results of 200 FEA per violin plot; H = 120 mm.

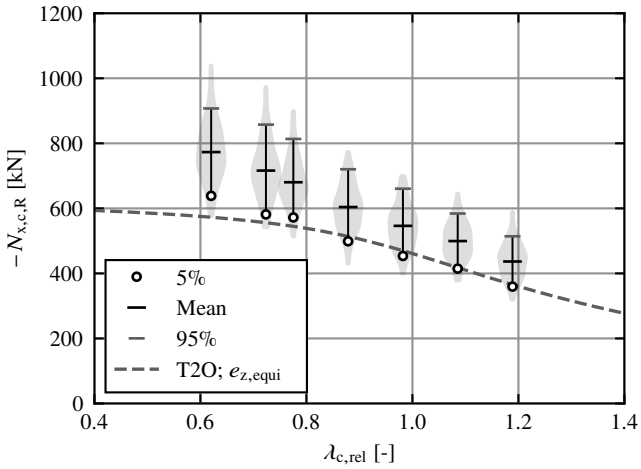

Figure E.12: Violin plots of the axial compressive load-bearing capacities $N_{x,c,R}$ from FEA on GL 24h columns at seven relative LTB slenderness ratios $\lambda_{c,rel}$; with scattering *structural imperfections*; results of 200 FEA per violin plot; H = 160 mm.

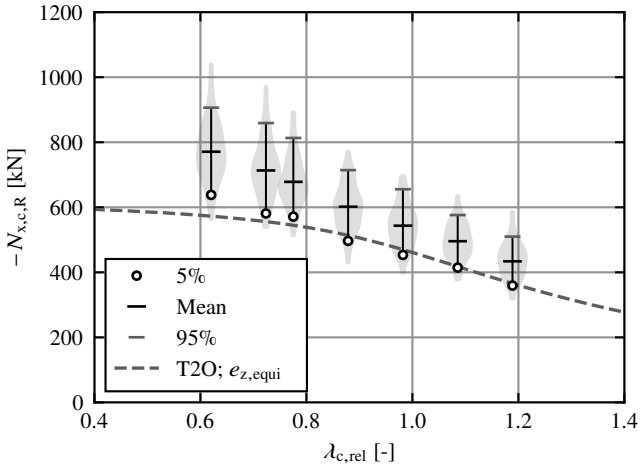

Figure E.13: Violin plots of the reduction factor k_m from FEA on GL 24h beams at seven relative LTB slenderness ratios $\lambda_{m,rel}$ with constant bending moment; with scattering *geometrical and structural imperfections*; results of 200 FEA per violin plot; H = 160 mm.

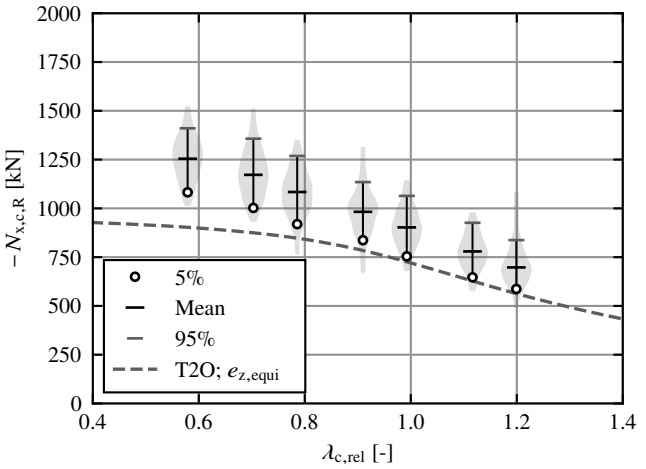

Figure E.14: Violin plots of the axial compressive load-bearing capacities $N_{x,c,R}$ from FEA on GL 24h columns at seven relative LTB slenderness ratios $\lambda_{c,rel}$; with scattering *structural imperfections*; results of 200 FEA per violin plot; H = 200 mm.

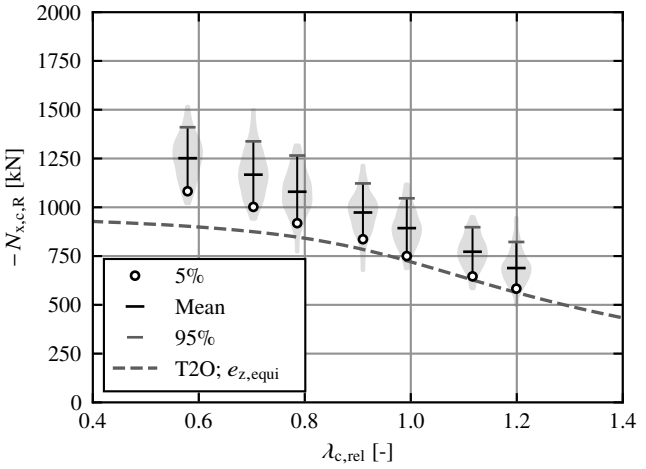

Figure E.15: Violin plots of the reduction factor k_m from FEA on GL 24h beams at seven relative LTB slenderness ratios $\lambda_{m,rel}$ with constant bending moment; with scattering *geometrical and structural imperfections*; results of 200 FEA per violin plot; H = 200 mm.

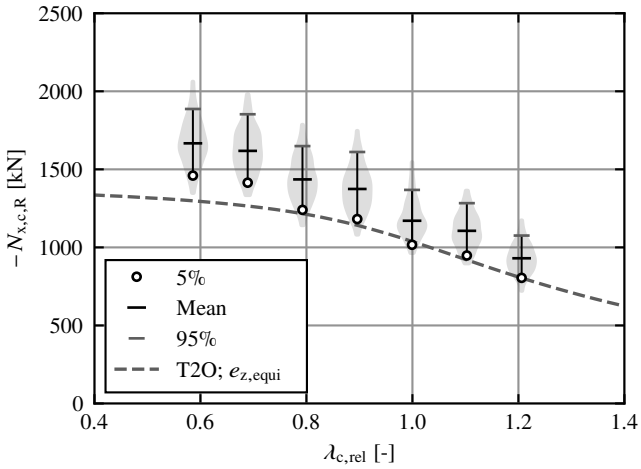

Figure E.16: Violin plots of the axial compressive load-bearing capacities $N_{x,c,R}$ from FEA on GL 24h columns at seven relative LTB slenderness ratios $\lambda_{c,rel}$; with scattering *structural imperfections*; results of 200 FEA per violin plot; H = 240 mm.

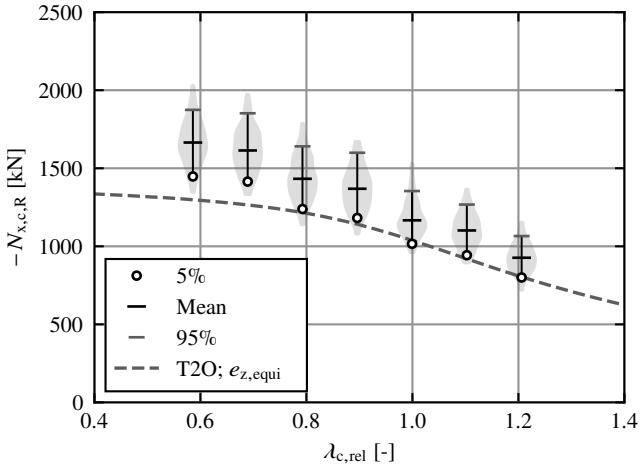

Figure E.17: Violin plots of the reduction factor k_m from FEA on GL 24h beams at seven relative LTB slenderness ratios $\lambda_{m,rel}$ with constant bending moment; with scattering *geometrical and structural imperfections*; results of 200 FEA per violin plot; H = 240 mm.

Appendix F

Results of FEA on $N_{x,c}$-$M_{y,1}$-interaction

F.1 General

This Annex provides the results of the numerical parameter studies on the $N_{x,c}$-$M_{y,1}$-interaction of imperfection-sensitive timber beam-columns, see Sections 5.6.3 and 6.4.

F.2 $k_{c/m}$ in dependence of $\lambda_{c/m,rel}$

In Figures F.1 to F.42, the reduction factor of the load-bearing capacity $k_{c/m}$ from FEA is plotted over the relative slenderness ratio $\lambda_{c/m,rel}$ for loading by a constant bending moment (M), a uniform line load (q), or a concentrated force at midspan (F). The evaluation of the FEA was carried out without considering shear failure. k_m, $\lambda_{c,rel}$, and $\lambda_{m,rel}$ were calculated with Equations (6.1), (2.60), and (2.80). μ_c is the utilisation ratio of the axial compressive resistance considering flexural buckling.

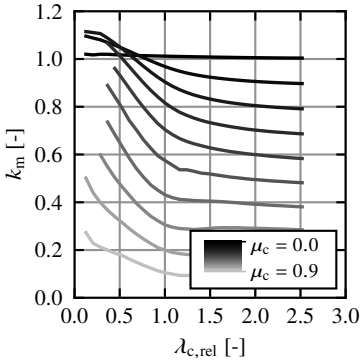

Figure F.1: GL 24h, H = 120 mm, M.

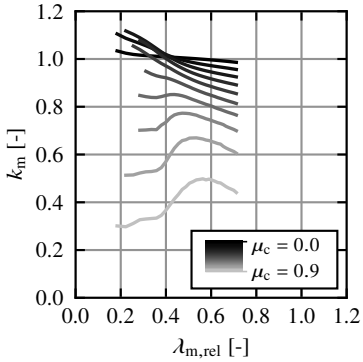

Figure F.2: GL 24h, H = 240 mm, M.

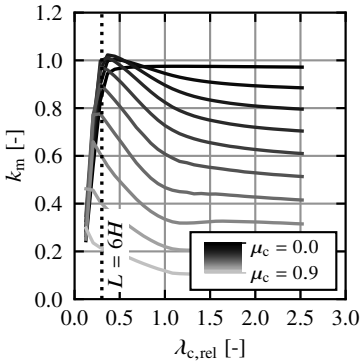

Figure F.3: GL 24h, H = 120 mm, q.

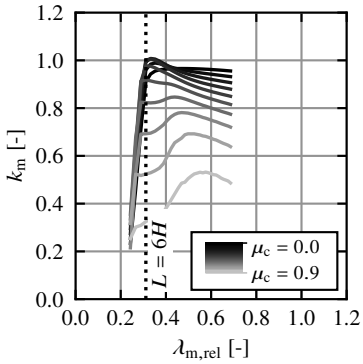

Figure F.4: GL 24h, H = 240 mm, q.

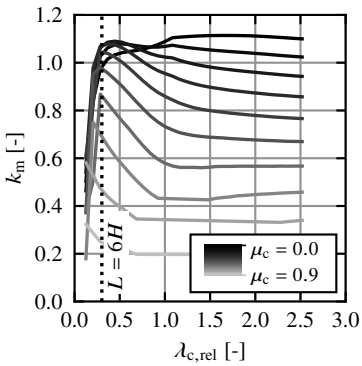

Figure F.5: GL 24h, H = 120 mm, F.

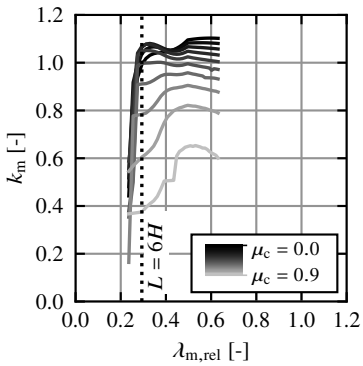

Figure F.6: GL 24h, H = 240 mm, F.

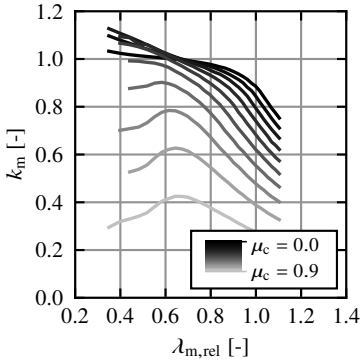

Figure F.7: GL 24h, H = 480 mm, M.

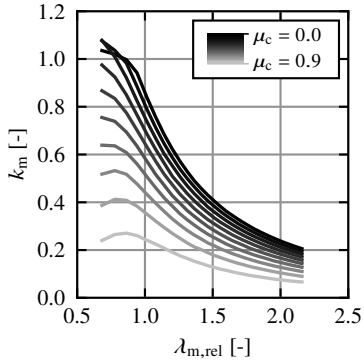

Figure F.8: GL 24h, H = 960 mm, M.

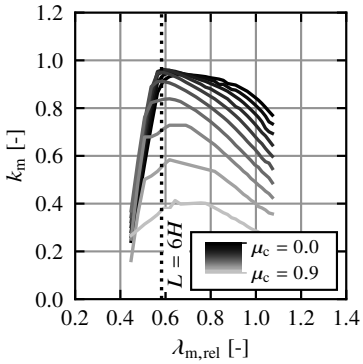

Figure F.9: GL 24h, H = 480 mm, q.

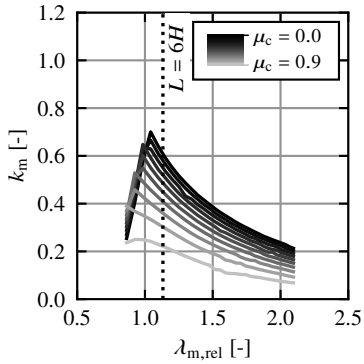

Figure F.10: GL 24h, H = 960 mm, q.

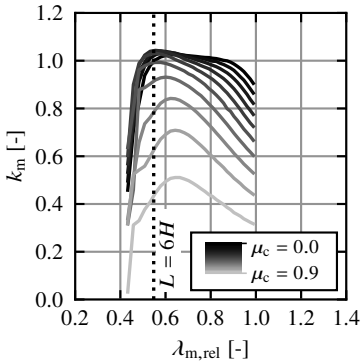

Figure F.11: GL 24h, H = 480 mm, F.

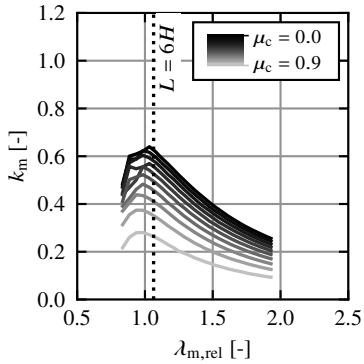

Figure F.12: GL 24h, H = 960 mm, F.

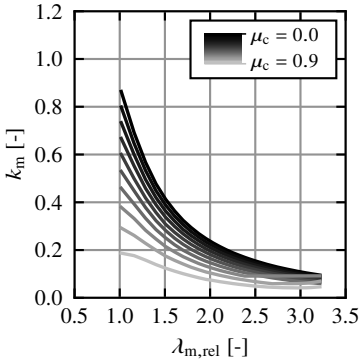

Figure F.13: GL 24h, H = 1440 mm, M.

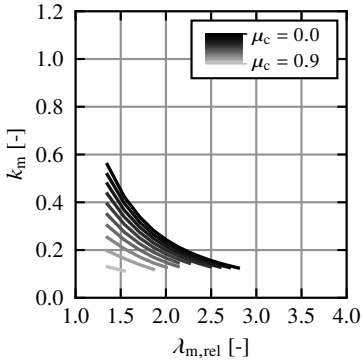

Figure F.14: GL 24h, H = 1920 mm, M.

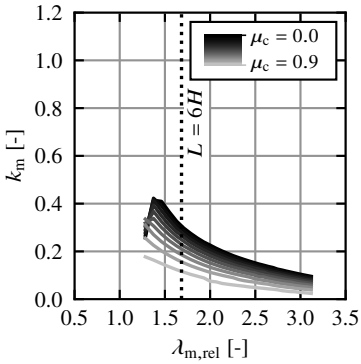

Figure F.15: GL 24h, H = 1440 mm, q.

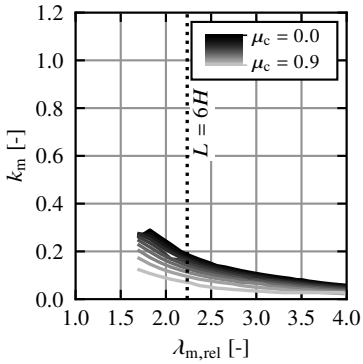

Figure F.16: GL 24h, H = 1920 mm, q.

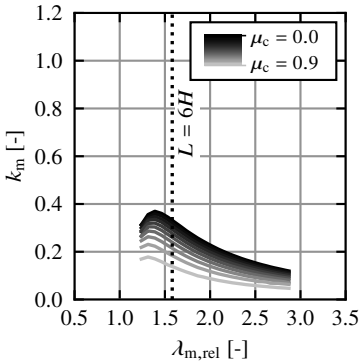

Figure F.17: GL 24h, H = 1440 mm, F.

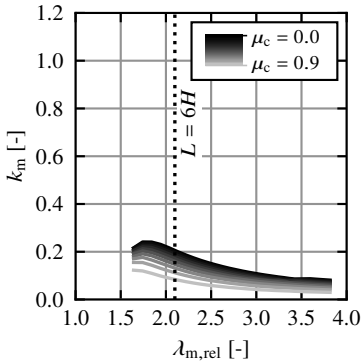

Figure F.18: GL 24h, H = 1920 mm, F.

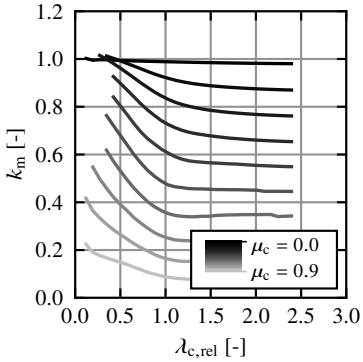

Figure F.19: GL 30c, H = 120 mm, M.

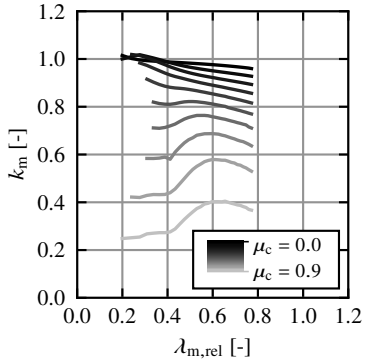

Figure F.20: GL 30c, H = 240 mm, M.

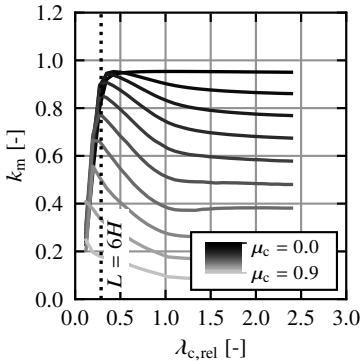

Figure F.21: GL 30c, H = 120 mm, q.

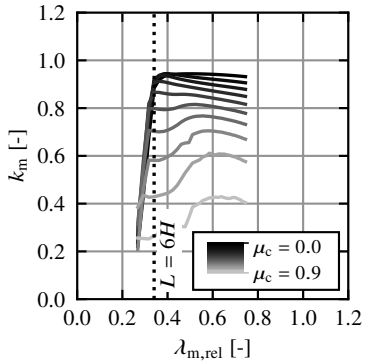

Figure F.22: GL 30c, H = 240 mm, q.

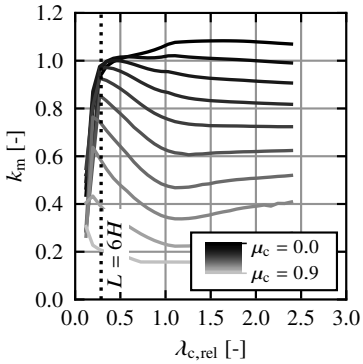

Figure F.23: GL 30c, H = 120 mm, F.

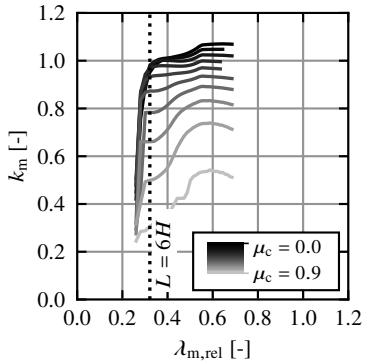

Figure F.24: GL 30c, H = 240 mm, F.

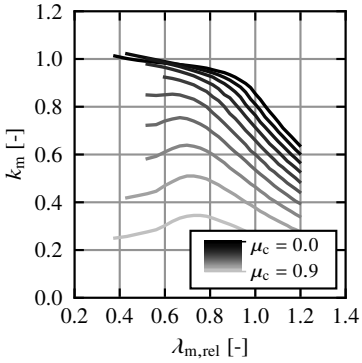

Figure F.25: GL 30c, H = 480 mm, M.

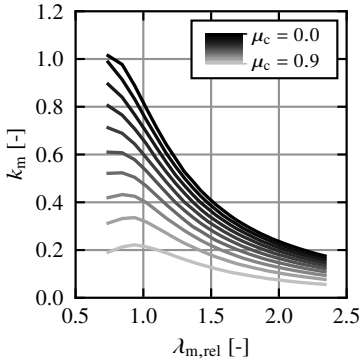

Figure F.26: GL 30c, H = 960 mm, M.

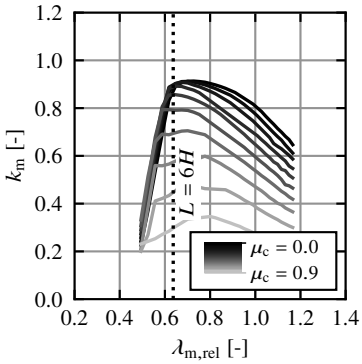

Figure F.27: GL 30c, H = 480 mm, q.

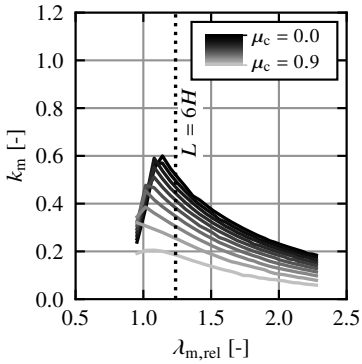

Figure F.28: GL 30c, H = 960 mm, q.

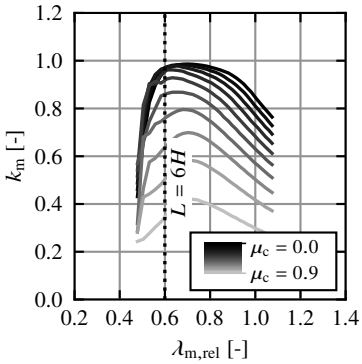

Figure F.29: GL 30c, H = 480 mm, F.

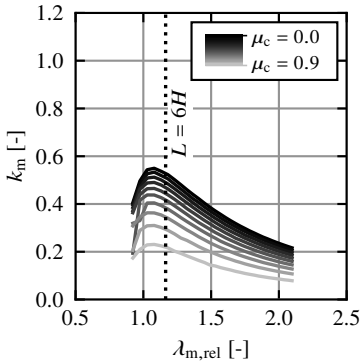

Figure F.30: GL 30c, H = 960 mm, F.

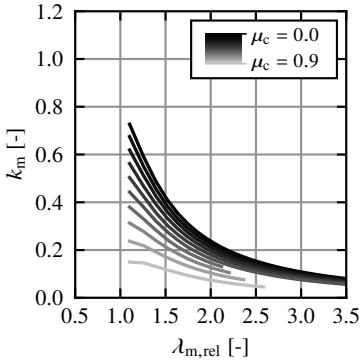

Figure F.31: GL 30c, H = 1440 mm, M.

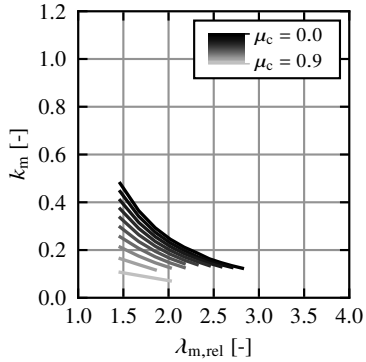

Figure F.32: GL 30c, H = 1920 mm, M.

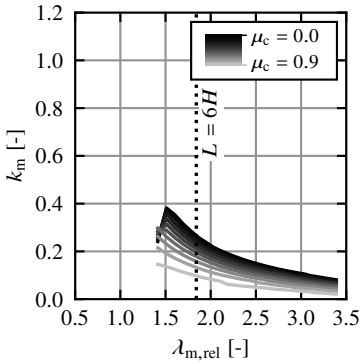

Figure F.33: GL 30c, H = 1440 mm, q.

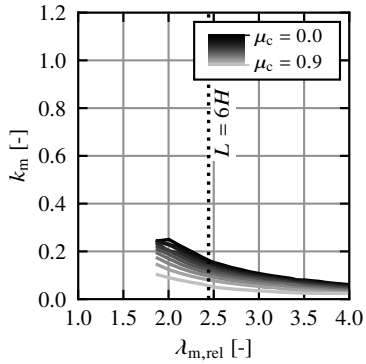

Figure F.34: GL 30c, H = 1920 mm, q.

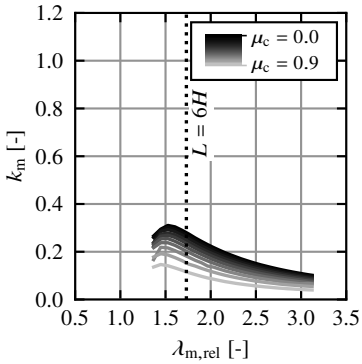

Figure F.35: GL 30c, H = 1440 mm, F.

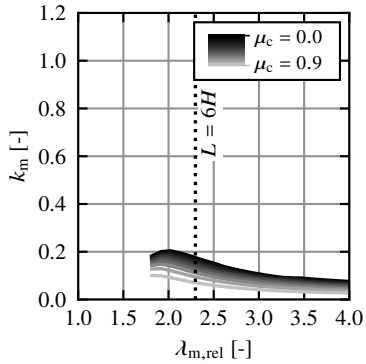

Figure F.36: GL 30c, H = 1920 mm, F.

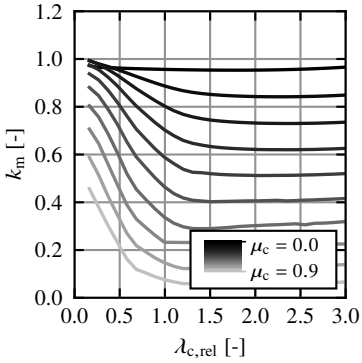

Figure F.37: GL75, H = 120 mm, M.

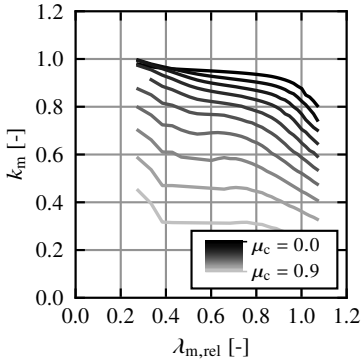

Figure F.38: GL75, H = 240 mm, M.

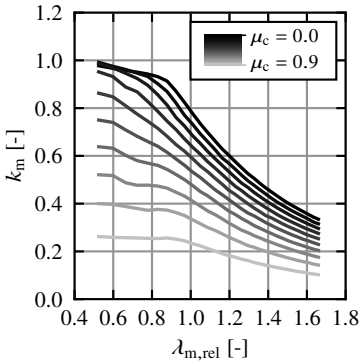

Figure F.39: GL75, H = 480 mm, M.

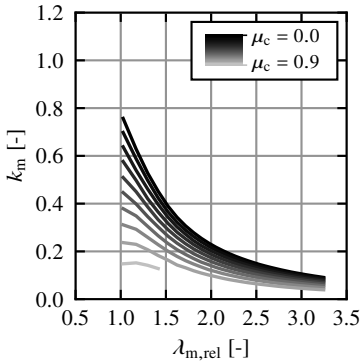

Figure F.40: GL75, H = 960 mm, M.

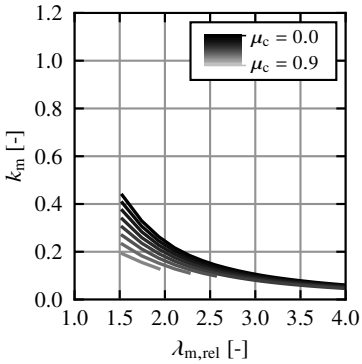

Figure F.41: GL75, H = 1440 mm, M.

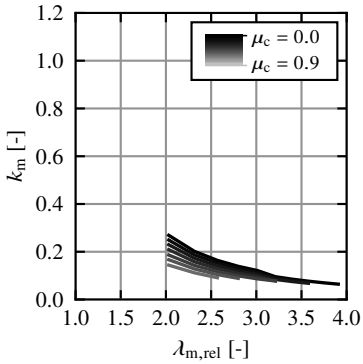

Figure F.42: GL75, H = 1920 mm, M.

F.3 $N_{x,c}$-$M_{y,1}$-interaction

In Figures F.43 to F.84, the $N_{x,c}$-$M_{y,1}$-interaction is plotted for varying slendernesses $\lambda_{c,rel}$ and $\lambda_{m,rel}$. The evaluation of the FEA was carried out without considering shear failure. The relative load-bearing capacities are displayed as ratios of the bending or compressive load-bearing capacity to the load-bearing capacity for pure bending or pure compression (including stability behaviour). At $H/B = 1$, the linear interaction is plotted additionally, i.e. $\mu_c + \mu_m = 1$. Furthermore, the slenderness, where the bending load-bearing capacities are at most 10% greater than the linear interaction, is highlighted. For $H/B \geq 2$, the quadratic interaction is plotted additionally, i.e. $\mu_c + \mu_m^2 = 1$. Furthermore, the slenderness for which the bending load-bearing capacities are at most 10% greater than the quadratic interaction is highlighted.

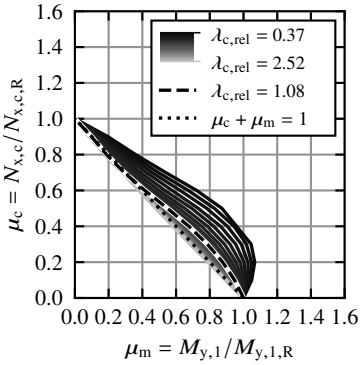

Figure F.43: GL 24h, $H = 120$ mm, M.

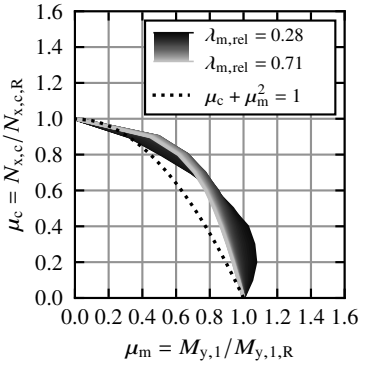

Figure F.44: GL 24h, $H = 240$ mm, M.

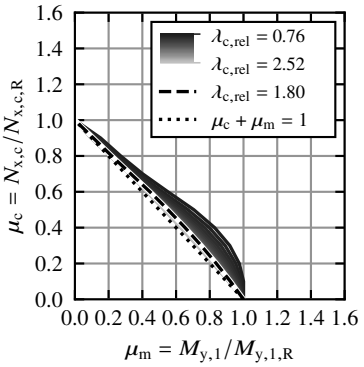

Figure F.45: GL 24h, $H = 120$ mm, q.

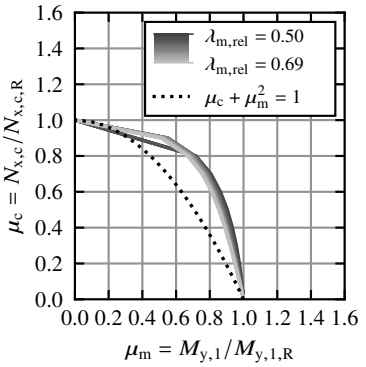

Figure F.46: GL 24h, $H = 240$ mm, q.

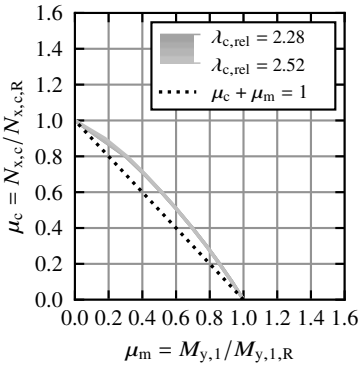

Figure F.47: GL 24h, $H = 120$ mm, F.

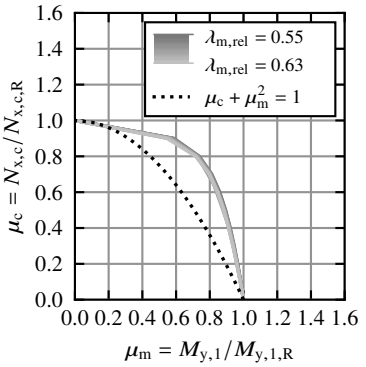

Figure F.48: GL 24h, $H = 240$ mm, F.

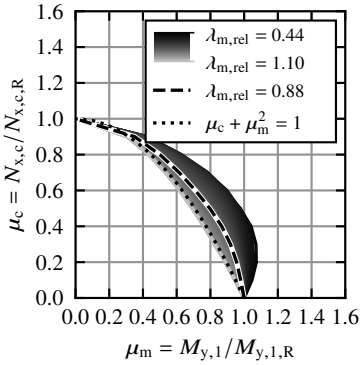

Figure F.49: GL 24h, H = 480 mm, M.

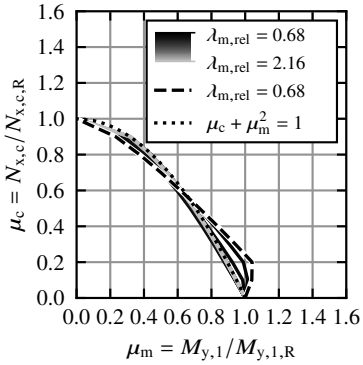

Figure F.50: GL 24h, H = 960 mm, M.

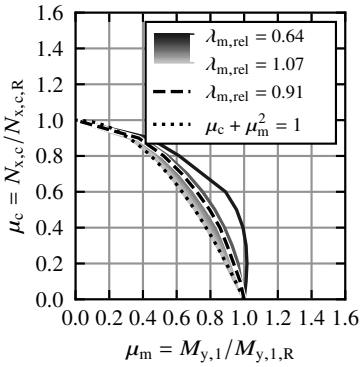

Figure F.51: GL 24h, H = 480 mm, q.

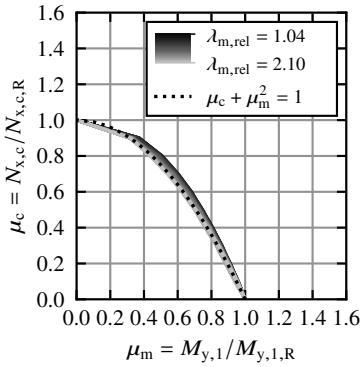

Figure F.52: GL 24h, H = 960 mm, q.

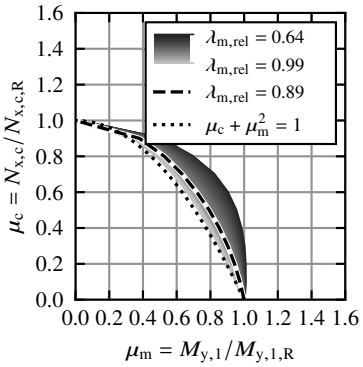

Figure F.53: GL 24h, H = 480 mm, F.

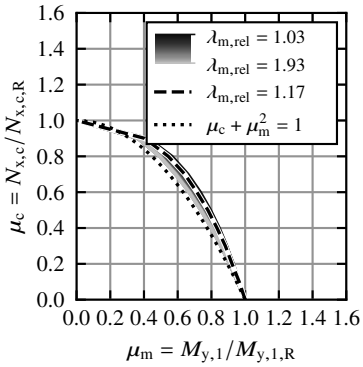

Figure F.54: GL 24h, H = 960 mm, F.

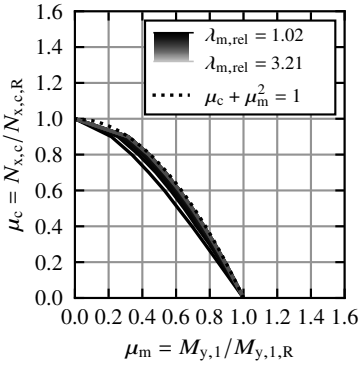

Figure F.55: GL 24h, H = 1440 mm, M.

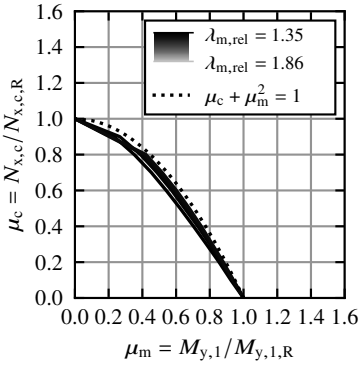

Figure F.56: GL 24h, H = 1920 mm, M.

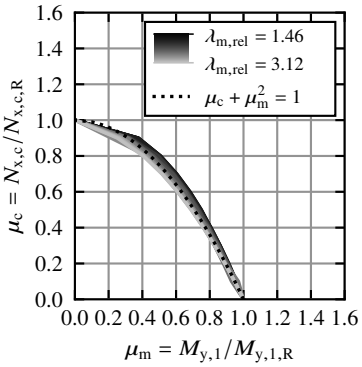

Figure F.57: GL 24h, H = 1440 mm, q.

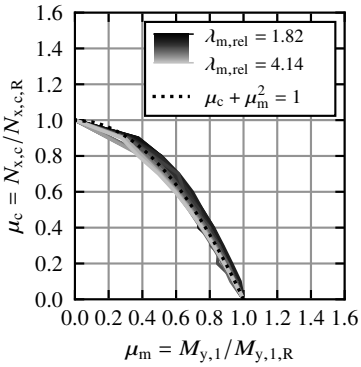

Figure F.58: GL 24h, H = 1920 mm, q.

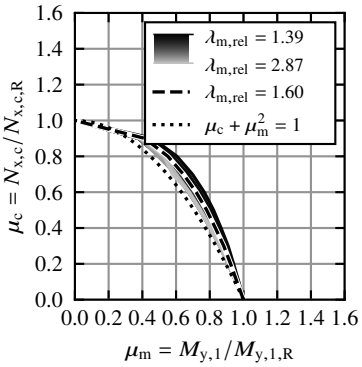

Figure F.59: GL 24h, H = 1440 mm, F.

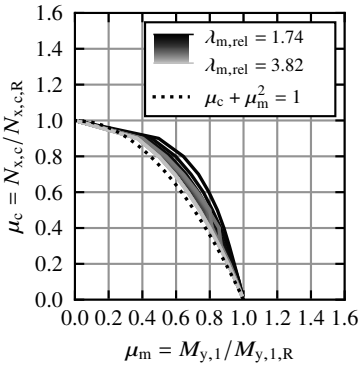

Figure F.60: GL 24h, H = 1920 mm, F.

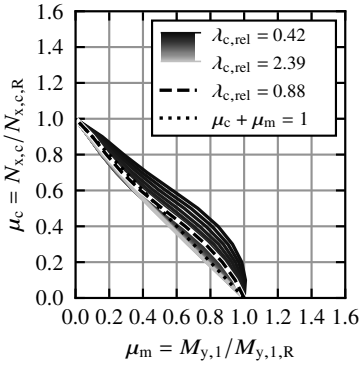

Figure F.61: GL 30c, H = 120 mm, M.

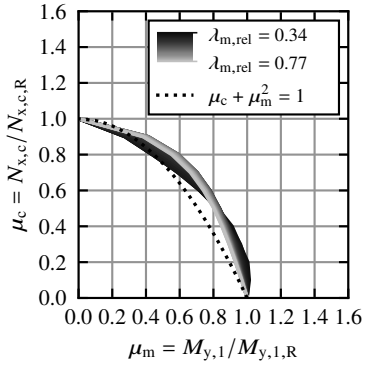

Figure F.62: GL 30c, H = 240 mm, M.

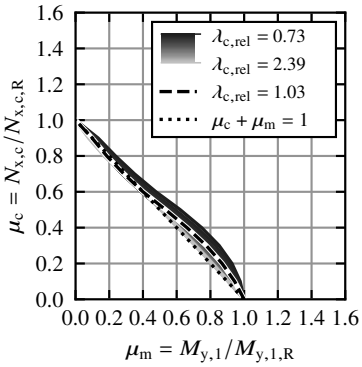

Figure F.63: GL 30c, H = 120 mm, q.

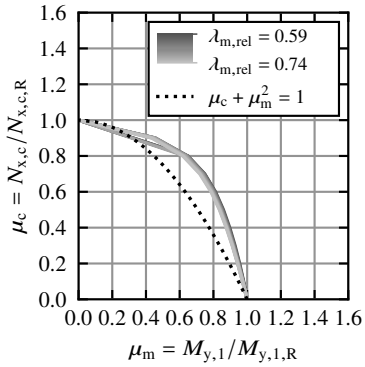

Figure F.64: GL 30c, H = 240 mm, q.

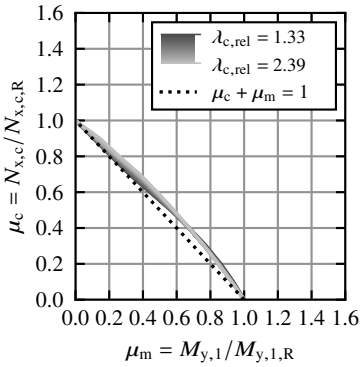

Figure F.65: GL 30c, H = 120 mm, F.

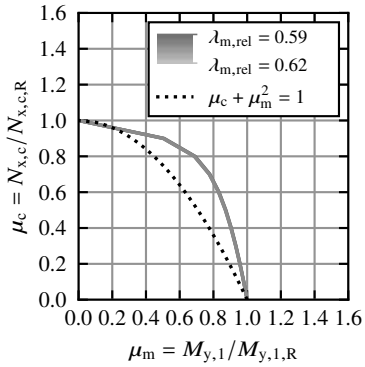

Figure F.66: GL 30c, H = 240 mm, F.

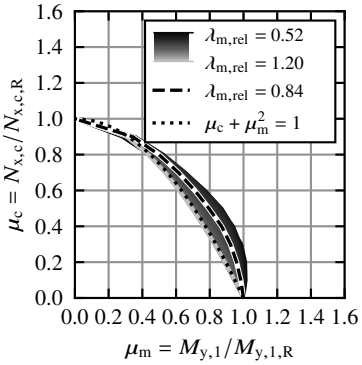

Figure F.67: GL 30c, H = 480 mm, M.

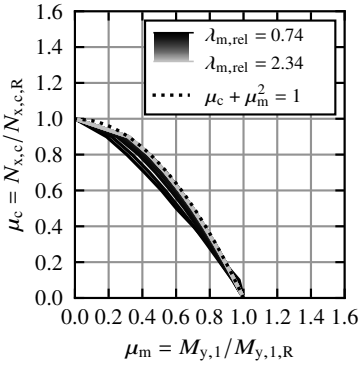

Figure F.68: GL 30c, H = 960 mm, M.

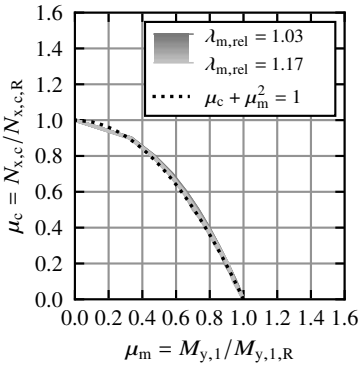

Figure F.69: GL 30c, H = 480 mm, q.

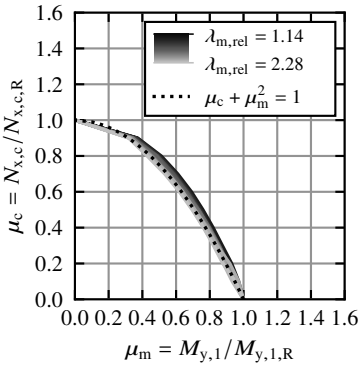

Figure F.70: GL 30c, H = 960 mm, q.

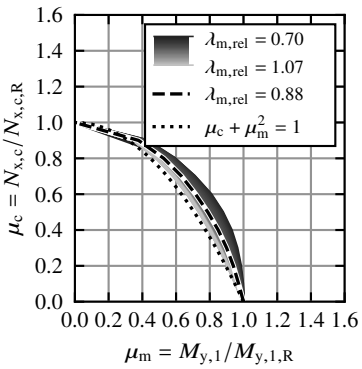

Figure F.71: GL 30c, H = 480 mm, F.

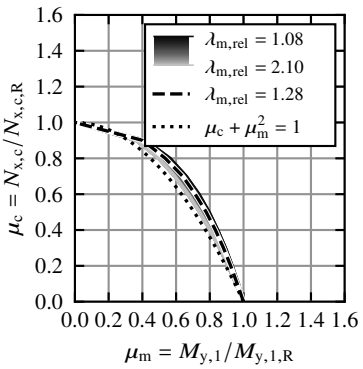

Figure F.72: GL 30c, H = 960 mm, F.

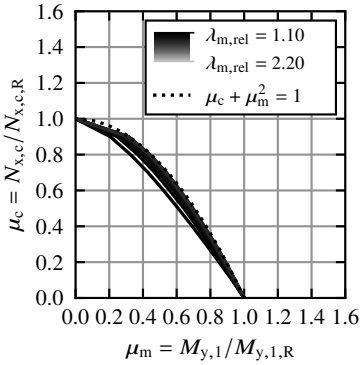

Figure F.73: GL 30c, H = 1440 mm, M.

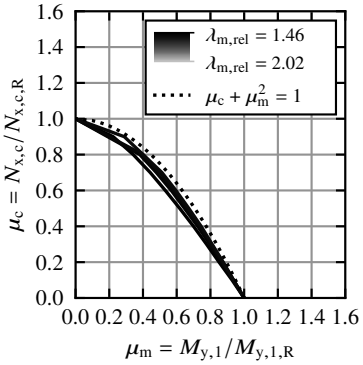

Figure F.74: GL 30c, H = 1920 mm, M.

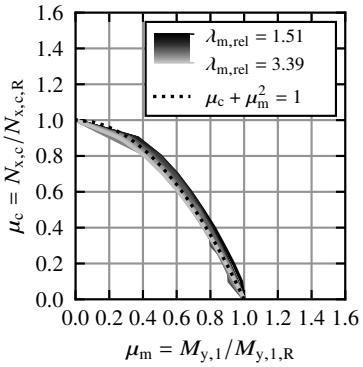

Figure F.75: GL 30c, H = 1440 mm, q.

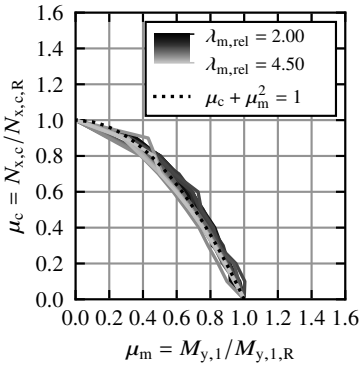

Figure F.76: GL 30c, H = 1920 mm, q.

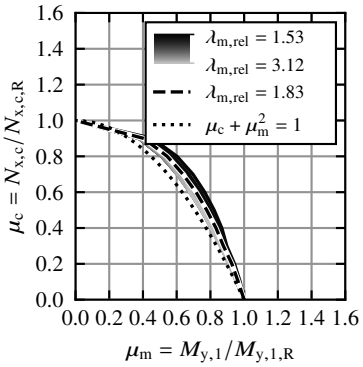

Figure F.77: GL 30c, H = 1440 mm, F.

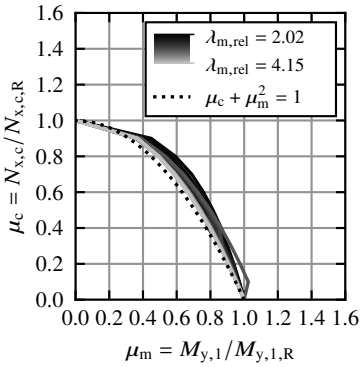

Figure F.78: GL 30c, H = 1920 mm, F.

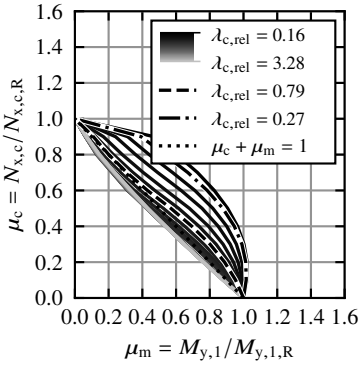

Figure F.79: GL75, H = 120 mm, M.

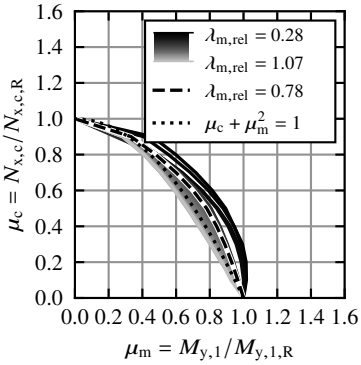

Figure F.80: GL75, H = 240 mm, M.

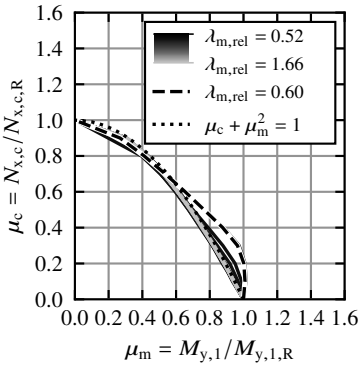

Figure F.81: GL75, H = 480 mm, M.

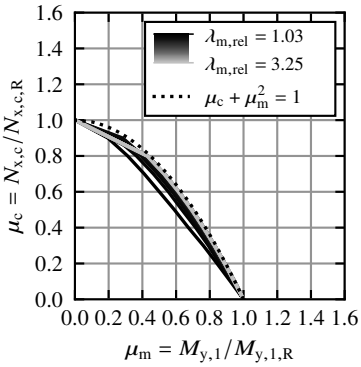

Figure F.82: GL75, H = 960 mm, M.

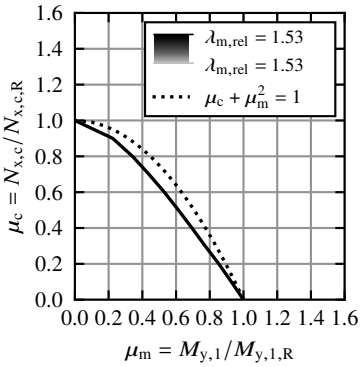

Figure F.83: GL75, H = 1440 mm, M.

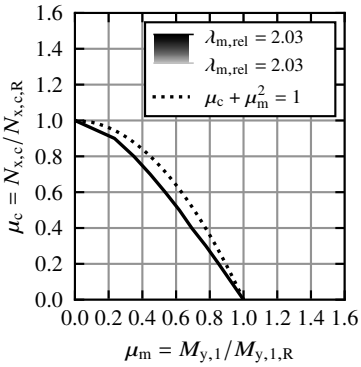

Figure F.84: GL75, H = 1920 mm, M.

F.4 Comparison of design proposals with FEA

In Figures F.85 to F.126, the ratio of the bending load-bearing capacity of design with calculations using T2O and the k_c-k_m-method according to the design proposal in Section 7 to the load-bearing capacity from FEA $k_{m,pro}/k_{m,FEA}$ is plotted over the relative slenderness ratio $\lambda_{c/m,rel}$. The evaluation of the FEA was carried out without considering shear failure. $\lambda_{c,rel}$ and $\lambda_{m,rel}$ were calculated with Equations (2.60) and (2.80).

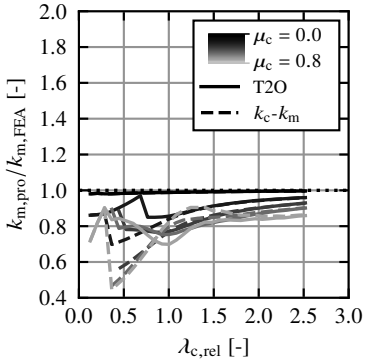

Figure F.85: GL 24h, H = 120 mm, M.

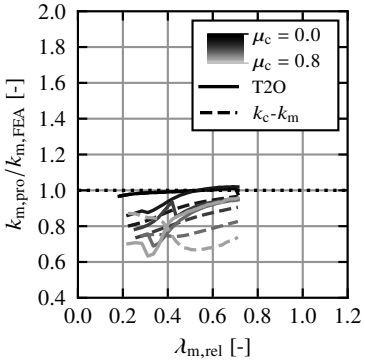

Figure F.86: GL 24h, H = 240 mm, M.

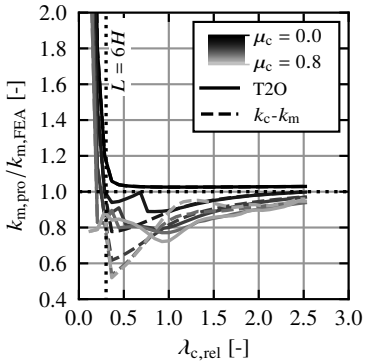

Figure F.87: GL 24h, H = 120 mm, q.

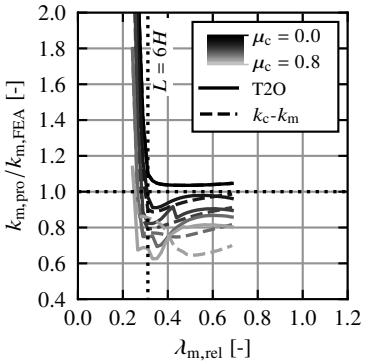

Figure F.88: GL 24h, H = 240 mm, q.

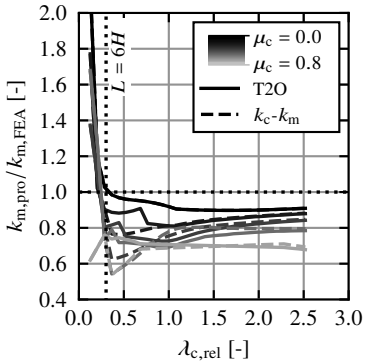

Figure F.89: GL 24h, H = 120 mm, F.

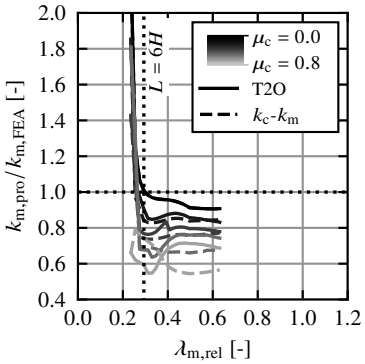

Figure F.90: GL 24h, H = 240 mm, F.

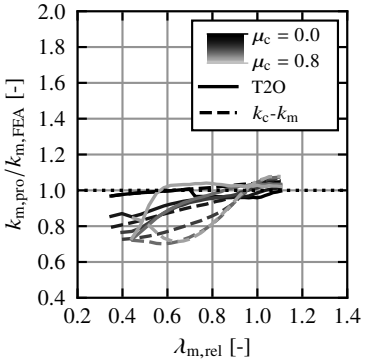

Figure F.91: GL 24h, H = 480 mm, M.

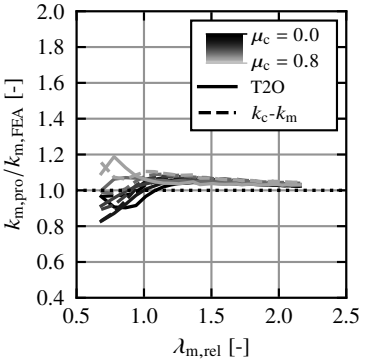

Figure F.92: GL 24h, H = 960 mm, M.

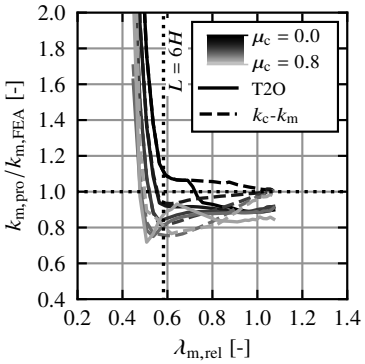

Figure F.93: GL 24h, H = 480 mm, q.

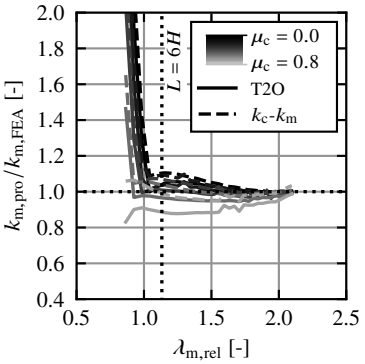

Figure F.94: GL 24h, H = 960 mm, q.

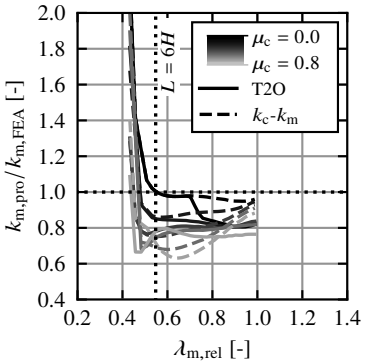

Figure F.95: GL 24h, H = 480 mm, F.

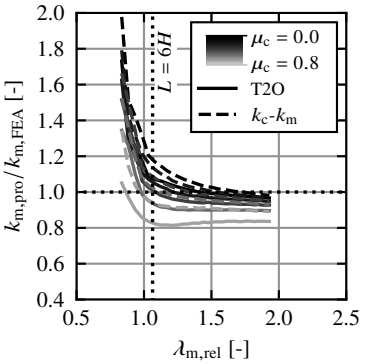

Figure F.96: GL 24h, H = 960 mm, F.

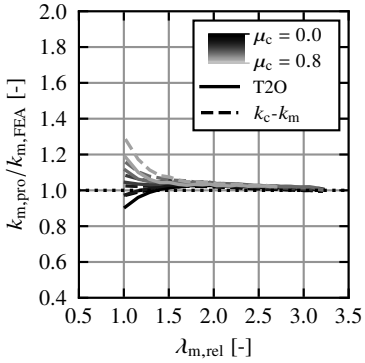

Figure F.97: GL 24h, H = 1440 mm, M.

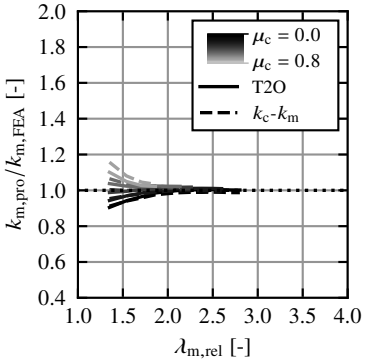

Figure F.98: GL 24h, H = 1920 mm, M.

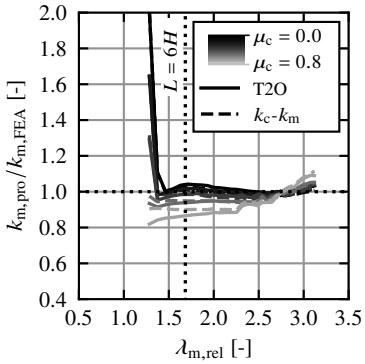

Figure F.99: GL 24h, H = 1440 mm, q.

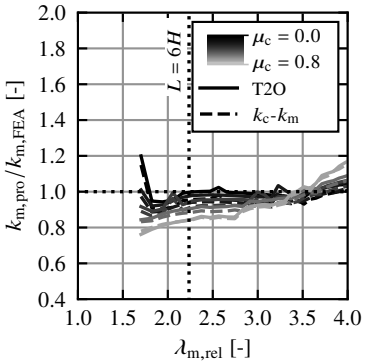

Figure F.100: GL 24h, H = 1920 mm, q.

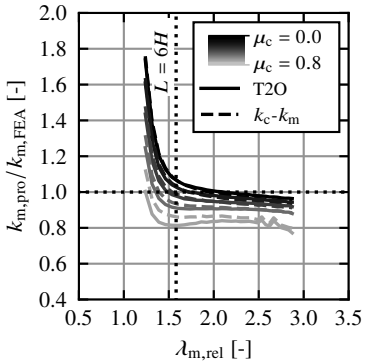

Figure F.101: GL 24h, H = 1440 mm, F.

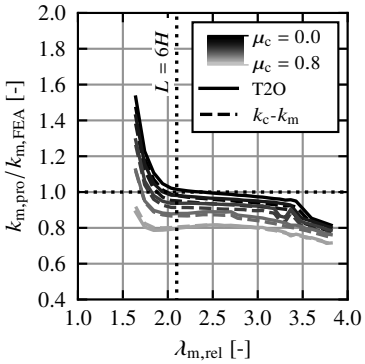

Figure F.102: GL 24h, H = 1920 mm, F.

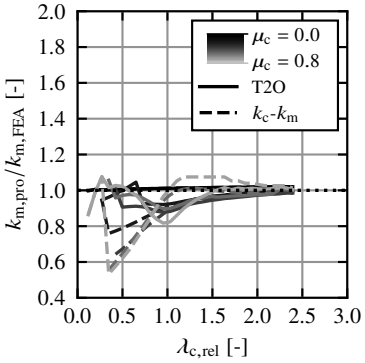

Figure F.103: GL 30c, H = 120 mm, M.

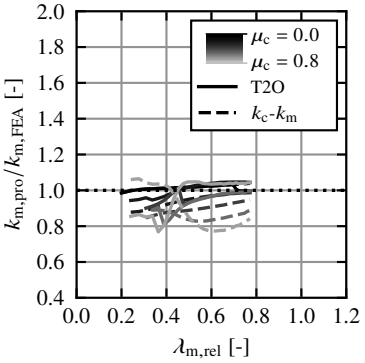

Figure F.104: GL 30c, H = 240 mm, M.

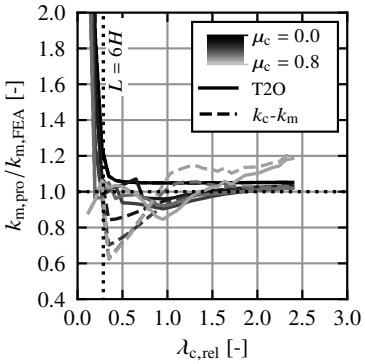

Figure F.105: GL 30c, H = 120 mm, q.

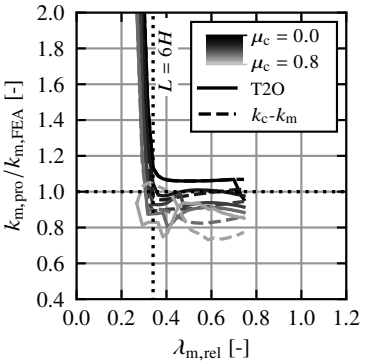

Figure F.106: GL 30c, H = 240 mm, q.

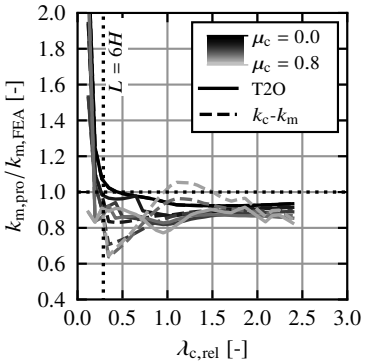

Figure F.107: GL 30c, H = 120 mm, F.

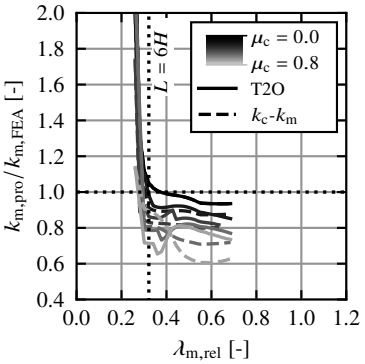

Figure F.108: GL 30c, H = 240 mm, F.

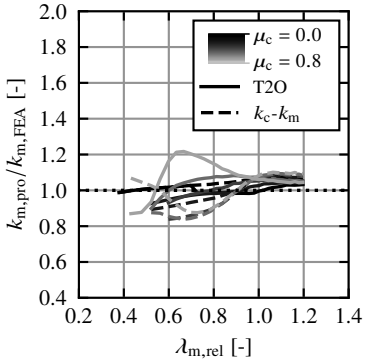

Figure F.109: GL 30c, H = 480 mm, M.

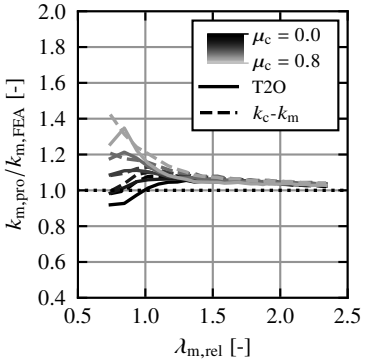

Figure F.110: GL 30c, H = 960 mm, M.

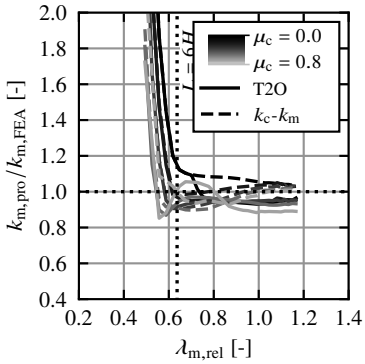

Figure F.111: GL 30c, H = 480 mm, q.

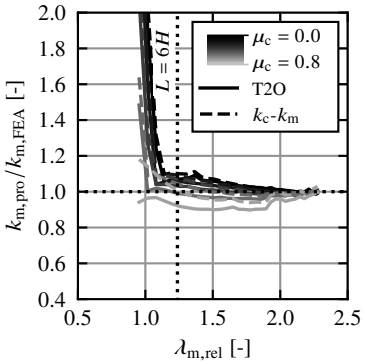

Figure F.112: GL 30c, H = 960 mm, q.

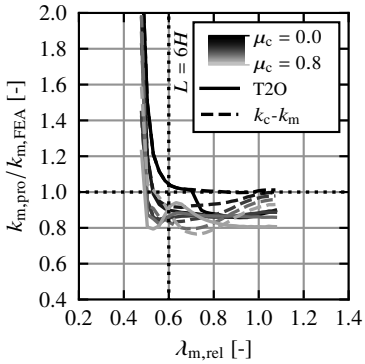

Figure F.113: GL 30c, H = 480 mm, F.

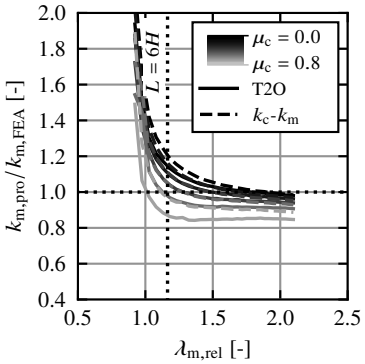

Figure F.114: GL 30c, H = 960 mm, F.

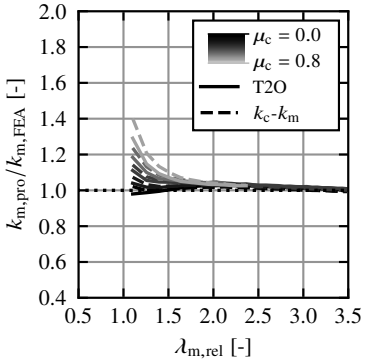

Figure F.115: GL 30c, H = 1440 mm, M.

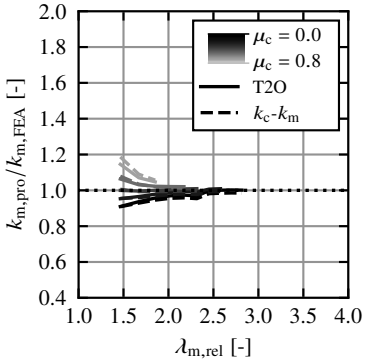

Figure F.116: GL 30c, H = 1920 mm, M.

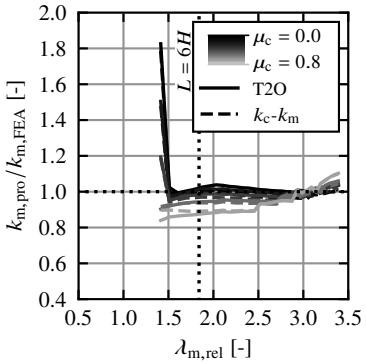

Figure F.117: GL 30c, H = 1440 mm, q.

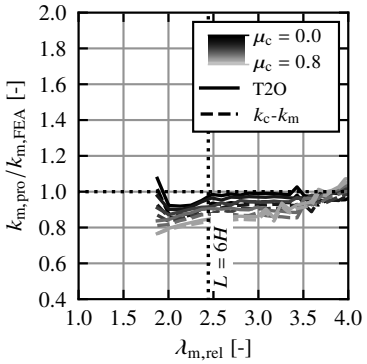

Figure F.118: GL 30c, H = 1920 mm, q.

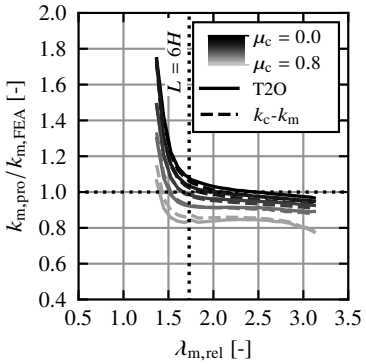

Figure F.119: GL 30c, H = 1440 mm, F.

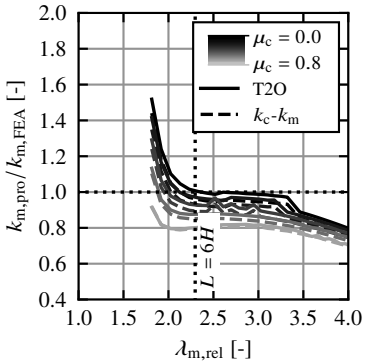

Figure F.120: GL 30c, H = 1920 mm, F.

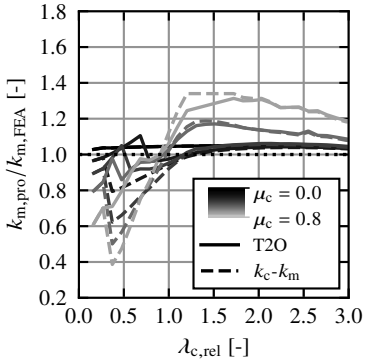

Figure F.121: GL75, H = 120 mm, M.

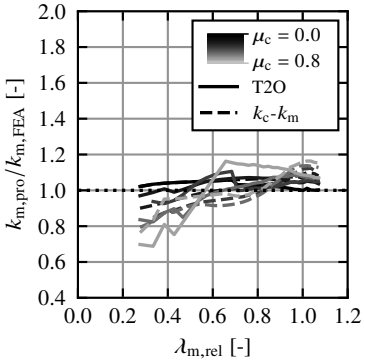

Figure F.122: GL75, H = 240 mm, M.

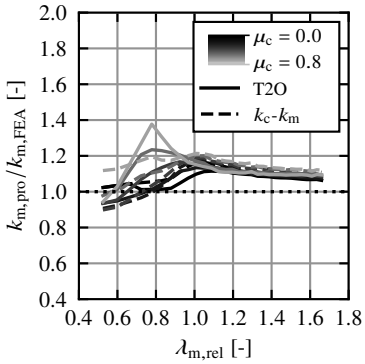

Figure F.123: GL75, H = 480 mm, M.

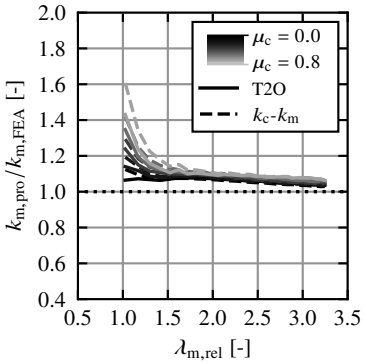

Figure F.124: GL75, H = 960 mm, M.

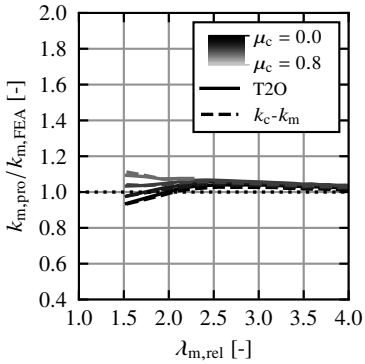

Figure F.125: GL75, H = 1440 mm, M.

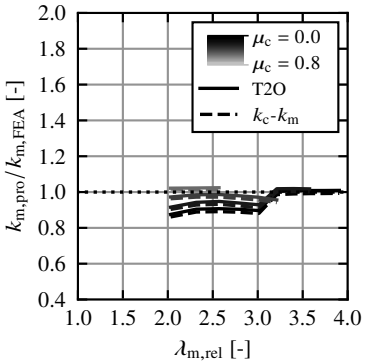

Figure F.126: GL75, H = 1920 mm, M.